UNIVERSITÀ DEGLI STUDI DI MESSINA

DOTTORATO DI RICERCA IN FISICA

XXX CICLO

Coherent Resonant Coupling of States with Different Excitations Numbers in Hybrid Quantum Systems

Vincenzo Macrì

Coordinatore Dottorato:

Chiar.mo Prof. L. Torrisi

Relatore:

Chiar.mo Prof. S. Savasta

Triennio 2014/2017

Coherent Resonant Coupling of States with Different Excitations Numbers in Hybrid Quantum Systems

Vincenzo Macrì

2017

List of Publications

I. **Single-step arbitrary control of mechanical quantum states in ultrastrong optomechanics**
Luigi Garziano, Roberto Stassi, Vincenzo Macrí, Salvatore Savasta, and Omar Di Stefano
Physical Review A ***91***, 023809 (2015)

II. **Multiphoton quantum Rabi oscillations in ultrastrong cavity QED**
Luigi Garziano, Roberto Stassi, Vincenzo Macrí, Anton Frisk Kockum, Salvatore Savasta and Franco Nori
Physical Review A ***92***, 063830 (2015)

III. **Deterministic synthesis of mechanical *NOON* states in ultrastrong optomechanics**
Vincenzo Macrí, Luigi Garziano, Alessandro Ridolfo, Omar Di Stefano, and Salvatore Savasta
Physical Review A ***94***, 013817 (2016)

IV. **A single photon can simultaneously excite two or more atoms**
Luigi Garziano, Vincenzo Macrí, Roberto Stassi, Omar Di Stefano, Franco Nori and Salvatore Savasta
Physical Review Letters ***117***, 043601 (2016)
APS Physics Focus ***9***, 83 (2016)

V. **Frequency conversion in ultrastrong cavity QED**
Anton Frisk Kockum, Vincenzo Macrí, Luigi Garziano, Salvatore Savasta, Franco Nori
Scientific Reports ***7***, 5313 (2017)

VI. **Deterministic quantum nonlinear optics with single atoms and virtual photons**
Anton Frisk Kockum, Adam Miranowicz, Vincenzo Macrí, Salvatore Savasta, Franco Nori
Physical Review A ***95***, 063849 (2017)

VII. **Quantum Nonlinear Optics without Photons**
Roberto Stassi, Vincenzo Macrí, Anton Frisk Kockum, Omar Di Stefano, Adam Miranowicz, Salvatore Savasta, Franco Nori
Physical Review A ***96***, 023818 (2017)

VIII. **Nonperturbative Dynamical Casimir Effect in Optomechanical Systems: Vacuum Casimir-Rabi Splittings**
Vincenzo Macrí, Alessandro Ridolfo, Omar Di Stefano, Anton Frisk Kockum, Franco Nori and Salvatore Savasta
arXiv:1706.04134: submitted to Physical Review X (2017)

Acknowledgements

I would like to thank my supervisor Salvatore Savasta. He has been much more than a supervisor, I would dare to say a mentor. He has always encouraged me in every single proposal that I have ever made with him, involving me with his infinite enthusiasm. Thanks for giving me the key that opens the door for a better understanding of the wonderful world of quantum mechanics, also for giving me the opportunity to work in the fascinating field of quantum optics. The physics I learned from you is the best intellectual experience I have ever had. You are a good friend of mine.

I want to thank with all the affection I am capable of, my colleagues and friends Luigi Garziano, Omar Di Stefano, Roberto Stassi and Alessandro Ridolfo for stimulating discussions, all the time we worked together and for all the fun we've had in these three years. Time in your company was for me a source of happiness. I want you to know that you are a second family to me.

Contents

Introduction

Since the early days of its birth, Quantum Mechanics has been applied to explain the properties and the behavior of a wide range of natural systems, and it has had tremendous success also as a fundamental physical theory. Atomic, molecular, and solid state-systems are just a few examples of physical systems whose behavior has been understood by applying Quantum Mechanics [1, 2]. Mainly, quantum physics developed through the first half of the twentieth century largely by understanding how light and matter interacts.

Since its invention in 1960, the laser has revolutionized both the study of optics and our understanding of the nature of light, prompting the emergence of Quantum Optics, a new field where the interaction between light and matter is dealt at fundamental level. Quantum description of light and matter is necessary to understand at fundamental level, the dynamics of atoms, and their interaction with the electromagnetic field. Quantum Optics experiments were originally performed with natural atoms, sometimes placed in cavities formed by mirrors, where a standing-wave electromagnetic field can exist for a long time and interacts with them. Serge Haroche and David Wineland demonstrated that single atoms could be used to probe photon states in a microwave cavity and, conversely, that single ions could be trapped, cooled, and probed with laser light [3–5]. In both cases, the measurements are gentle enough to allow for continuous manipulation of these fragile quantum systems. One of the first big achievements for both research groups was to create and measure a superposition state known as a *Schrödinger cat state* . They won the Nobel Prize in Physics 2012 for their contribution to this field over the years [6, 7]. This approach is known as cavity quantum electrodynamics (cavity QED) [8–11].

In atom-cavity systems one can distinguish four different coupling regimes: When the atom-cavity coupling strength is slower than all the loss rates

($g \ll \kappa, \gamma$), the system is in the *weak* coupling regime; when $g > \kappa, \gamma$, the *strong* coupling regime is achieved; When the coupling strength starts approaching the transition frequency of the atom or the resonance frequency of the cavity mode ($g \sim \omega_q, \omega_c$), the system enters the *ultrastrong* (USC) regime (see Chapter 1). Finally, when the coupling strength goes beyond the transition frequency of the atom or the resonance frequency of the cavity mode $g > \omega_q, \omega_c$, the atom-cavity systems fall in the (still little explored) *deep* coupling regime.

Microscopic systems, such as atoms (or spins), are given by nature and can easily be made as identical unit of information (qubits) with long coherence times ($\simeq 1ms$), but they operate slowly because of their weak coupling to external fields, and have limited scalability, namely, it is difficult to individually control many atoms working as qubits. The most versatile and promising framework for quantum optics experimental is that of superconducting circuits [12–16], often referred to as circuit quantum electrodynamics (circuit QED). In the case of circuit QED, the 1D transmission line resonator consists of a section of superconducting coplanar waveguide (CPW SC resonator). It is used to guide microwave photons to and from superconducting artificial atoms. They possess anharmonically-spaced discrete energy levels. Hence, by selecting the frequeny of the driving field, it is possible to excite only one transition, so that they can behave like to two-level atoms (qubits). SC qubits come in different varieties but they are all based on Josephson junctions [17], which provide the required nonlinearity, in combination with traditional circuit elements like capacitances C and inductances L (see Chapter 1.4). Although not microscopic in size, they can still behave quantum mechanically, allowing the observation of quantum coherence on a macroscopic scale, when they operate at temperatures of tens of mK. SC qubits are sensitive to environmental noise from extrinsic and intrinsic decoherence sources which limits the coherence times but, unlike atom-cavity interaction, they can couple strongly to the electromagnetic fields, confined in a SC waveguide-resonator or in a LC resonator [18], playing the role of cavities, which makes fast gate operations possible with current technology. Phenomena which occur in cavity QED (with artificial atoms) are expected

to manifest in circuit QED setups, using SC qubits and microwave photons. Cavity QED and circuit QED systems, can be described by similar Hamiltonians. Hence, by using circuit QED it is possible to explore regimes that are very hard to reach with natural atoms in optical cavities. The general picture, not only sees the circuit QED as an area where one can experience new effects beyond regimes allowed with natural atoms but also, represents the most promising framework for the realization of quantum computers.

Another quantum system with a great potential for development of new quantum technologies is Cavity Optomechanics, where the interaction between light and mechanical vibrations is studied [19–23]. The typical experimental setup is an optical cavity where one of the mirrors can move as mechanical harmonic oscillator. If the vibrational energy of the movable mirror becomes larger than the thermal energy $k_B T$, the mechanical oscillation can behave quantum mechanically. The quantized vibrations of the mirror then couples to the photons in the cavity due to radiation pressure. This kind of setup has been realized in a large variety of systems in recent years [24–28]. However, the observation of quantum behavior is challenging since it requires cooling the mechanical motion to extremely low temperatures and the ability to generate nonclassical states.

It is possible to realize an analogue of cavity optomechanics in SC circuit without any moving parts [29]. The circuit consists of a coplanar transmission line with an electrical length that can be changed at a few percent of the speed of light. The length is changed by modulating the inductance of a superconducting quantum interference device (SQUID) which is, two Josephson junctions which form a loop [30], acting as an effective movable mirror. The movement is simulated by tuning the magnetic field passing through the loop. Using this type of SC systems, it has been possible to observe the creation of real photons out of vacuum fluctuations as in dynamical Casimir effect (DCE) occurs, where a mobile mirror undergoing relativistic motion convert virtual photons into directly observable real photons [31]. In particular, it was observed in a SC resonator terminated by a SQUID whose inductance was modulated at high frequency [32]. In that case, the boundary conditions of the system are modulated by an effective motion, producing a paramet-

ric amplification of vacuum fluctuations (*parametric*-DCE [33–38]). These optical experiment do not demonstrate the conversion of mechanical energy into photons as predicted by the dynamical Casimir effect. In Paper 5.8 I investigate the DCE in real cavity optomechanical systems, also showing how vacuum emission can originate from the free evolution di an initial pure mechanical excited state, proving in this way the conversion of mechanical energy into elettromagnetic energy.

Much of the interesting physics sees the use of cross-systems: artificial and natural atoms together with optomechanical systems are the blocks of construction of the newborn quantum engineering. There are many ongoing efforts to create *hybrid quantum system* (HQS), that combine the best characteristics of different systems while avoiding their shortcomings [39]. The fundamental requirement for the realization of a functional HQS is the ability to communicate, with high fidelity, quantum states and properties between its different components. To make this possible it is necessary that the subsystems interact each other. The interaction between subsystems is described by the perturbative part of the total Hamiltonian. The perturbation gives rise to coherent resonant coupling between states nearly degenerate including those which not conserve the number of excitations. In quantum systems whose Hamiltonian depends on a variable parameter, two energy levels can cross for some value of this parameter. If the Hamiltonian is perturbed by an interaction which couples the levels, the degeneracy at the crossing is broken and the levels repel. The perturbation, not only modifies the energy eigenvalues but also mix the old eigenstates (bare states) into the new ones (dressed states). The effective coupling rate between the subsystems must be large enough to allow quantum-state transfer between them within the shortest coherence time, giving rise to observable *avoided-level crossings*. In Appendix A is given an analytical method to estimate, by means of the time-dependent perturbation theory, the coherent resonant coupling between two degenerate quantum states induced by a constant perturbation. Avoided-level crossings play an important role in quantum mechanics. Many of the effects studied in this thesis work can be explained and understood in terms of avoided level crossings arising from some interaction between subsystems,

able to remove degeneracy between quantum states.

One of the most interesting and widely studied HQS consists of individual natural atoms (SC qubit) coupled to an optical cavity (SC resonator). The weak and strong coupling regime of this system has been widely studied to explore fundamental physics effects and, also for applications in the field of quantum information [40, 41]. In weak coupling regime, where the coupling strength is lower than the losses, there are many signicant physical phenomena that have been experimentally demonstrated such as Purcell effect [42], which describes the enhancement of spontaneous emission rates of atoms when they are matched in a resonant cavity. In strong coupling regime, where the coupling strength is much greater than the losses, Rabi oscillations have been experimentally demonstrated [43], where an atom and a cavity electromagnetic mode can exchange a photon frequently, before coherence is lost, and the bare states of the atom and the cavity mode mix to form new dressed-energy eigenstates which are coherent superpositions of atom and photon excitations, also known as polaritons. Moreover, the atom and cavity resonances exhibit a ladder of avoided crossings as predicted by the well-known Jaynes-Cummings (JC) model (see Sec. 1.2). The lowest energy avoided crossing is referred to as vacuum-Rabi splitting. The regime of particular interest, for this thesis work, is that of ultrastrong copling (USC) regime that arises when the coupling strength becomes comparable to (or even larger than) the transition frequency of the atom (SC qubit) or the resonance frequency of the cavity mode (SC resonator). Recently, due to experimental progress in the development of circuit QED systems, it has been possible to experimentally achieve the USC regime [18]. It presents a great variety of new exciting effects [18, 44–47] that are not observed in the conventional weak and strong-coupling regimes. These new exciting effects cannot be described by the standard JC Hamiltonian. The fully interaction between atom and cavity (SC qubit-resonator), can be described by Rabi Hamiltonian (see Sec. 1.3). Unlike the JC Hamiltonian, the counter-rotating terms contained in the Rabi Hamiltonian become relevant, and the total number of excitations is not preserved. The transmission spectra of the combined system has revealed avoided-level crossings that cannot be explained by the JC

model. Instead, they are caused by the simultaneous creation (annihilation) of two excitations, one in the qubit and one in a resonator mode, while annihilating (creating) only one excitation in a different resonator mode. These describe an interesting example of an avoided-level crossing involving states with a different excitation number. Since then a number of novel processes based on avoided-level crossing in the absence of excitation number conservation has been theoretically predicted, many of these are the subject of this thesis. Indeed, part of this thesis aims to show that analogues of many nonlinear optics effects can also be realized within the cavity QED (also looking at the circuit QED where a generalized Rabi Haimiltonian can be defined, Sec. 1.4), by coupling one or more resonator modes to one or more two-level atoms (Dicke model [48]). The dynamic of system is studied excitating the atoms or the cavities by applying external electromagnetic drive, gaussian π-pulses or continuous way.

In general, when the intensity of light increase nonliner effets of the medium emerge. This nonlinear response can give rise to a host of effects, including frequency conversion and amplification, many of which have important technological applications [49–52]. After the high-intensity light of a laser made possible the first experimental demonstration of second-harmonic generation (frequency up-conversion) in 1961 [53], many more nonlinear optics effects have been demonstrated using a variety of nonlinear media, inspired investigations of analogous effects in other types of waves [54–60]. Just as nonlinear optics effects usually require very high light intensity to manifest clearly, the higher-order processes that I consider in this thesis work require a very strong light-matter coupling to become noticeable.

Following this line of research, I contributed to realizing multiphoton reversible absorption and emission, as Paper 5.2 reported. In this case, a single qubit coupled ultrastrongly to a resonator can exhibit anomalous vacuum Rabi oscillations where *two* or *more* photons are jointly emitted by the qubit into the resonator and reabsorbed by the qubit in a reversible and coherent process. Moreover, we have shown in Paper 5.4 that a single photon is able to excite *two* or *more* atoms at the same time. Also, we propose in Paper 5.7 an analogous physical process where one excited atom directly transfers its

excitation to a pair of spatially separated atoms with probability approaching one, the interaction being mediated by the exchange of *virtual* rather than *real* photons. More generally, it has been shown that the USC regime opens the door to higher-order processes, where virtual photons are created and annihilated, and an effective deterministic coupling between two levels (whose degeneracy at the crossing is broken) of such a system can be created. In Paper 5.5 analogues of various three-wave and four-wave mixing (frequency conversion) processes have been realized. The proposed frequency-conversion scheme is deterministic and allows for a variety of different frequency conversion processes in the same setup. The setup should be possible to implement in state-of-the-art circuit QED, but the idea also applies to other cavity QED systems. To complete the circle, in Paper 5.6 we show how analogues of a large number of well-known nonlinear optics phenomena can be realized with one or more two-level atoms coupled to one or more resonator modes. Through higher-order processes, where virtual photons are created and annihilated, an effective deterministic coupling between two states of such a system can be created. In this way, analogues higher-harmonic and subharmonic-generation (up and down-conversion), multiphoton absorption, parametric amplification, Raman and hyper-Raman scattering, the Kerr effect, and other nonlinear processes can be realized, without the need for intense input light fields.

The remainder of this thesis work focuses to another HQS constituted by a mechanical oscillator coupled, via radiation pressure, to an optical cavity: Cavity Optomechanics (see Chapter 2). This type of HQSs are promising for the study of fundamental quantum effects on a mesoscopic or macroscopic scale. In particulary, I refer to dynamical Casimir effect (DCE) where the generation of photons from the quantum vacuum is due to rapid changes of the geometry (the positions of some boundaries). In Paper 5.8, we show that this fundamental physical process originates from avoided-level crossings involving states with a different number of excitations. Actually, within this approach, we show that DCE effect can be described without considering any time dependent Hamiltonian (see Sec. 2.1). The only time dependent Hamiltonian term considered in our study is the one describing the external drive

of the mobile mirror. We show that the resonant generation of photons from the vacuum is determined by a ladder of mirror-field vacuum Rabi splittings. When the loss rates are lower than the corresponding frequency splittings, a reversible exchange of energy between the vibrating mirror and the cavity field, which we call vacuum Casimir-Rabi oscillations, can be observed. We also find that the dynamical Casimir effect can create steady state entanglement between the oscillating mirror and the radiation produced by its motion in the vacuum field. We show that vacuum radiation can originate from the free evolution of an initial pure mechanical excited state, in analogy with the spontaneous emission from excited atoms. Moreover, we find that resonant production of photons out from the vacuum can be observed for mechanical frequencies lower than the cavity mode frequency. Hence, this coupling regime, which experimentsare rapidly approaching, removes one of the major obstacles for the observation of this long sought effect. I believe that this theoretical framework provides a more fundamental explanation of the DCE. Notice that fundamental processes in quantum field theory are described by interaction Hamiltonians which do not depend parametrically on time. On the technological point, cavity optomechanics is a rapidly developing field [23], and constitutes a promising light-mechanics interface to realize HQSs for the manipulation and detection of mechanical motion, for applications in quantum information processing and storage in long-lived phonon states. Paper 5.1 is devoted to highlight the importance of the ultrastrong coupling regime in optomechanical systems for the synthesis of arbitrary superposition of mechanical quantum states. Here, we propose a new cavity-optomechanics protocol working in the ultrastrong regime which, in a single step, forces the ground state of a mechanical oscillator to evolve into an arbitrary quantum state in a completely controlled and deterministic manner. In this case we adopt the *standard* optomechanical Hamiltonian (see Sec. 2.2), which differ from DCE optomecanical Hamiltonian (Law Hamiltonian [61]), because the terms that oscillate very quickly are neglected, when the oscillation frequencies of the mirror are much smaller than the frequency spacing of neighboring cavity modes. The protocol results efficient and robust against decoherence, thermal noise and imperfect cooling. Moreover, the single-step

protocol is compared with the most recently proposed multi-step algorithms. We show that in the ultrastrong coupling regime the single-step protocol leads to a significantly reduction of the preparation time. This type of analysis ends with Paper 5.3, which is thought in order to realize an extension of the Paper 5.1, by designing a protocol for the deterministic preparation of entangled *NOON* mechanical states on demand, where the system is constituted by two identical, optically-coupled optomechanical systems.

Overview of the thesis

The thesis is structured as follows: after an introductory text where I have given an overview of the field (placing the work of the appended published Papers in their proper context), follow few chapters in which are reported mainly review the theoretical tools used.

In Chapter 1, the quantum theory of light-matter interaction in cavity QED is presented. I review how to formulate a quantum mechanical description of weak and strong coupling light-matter interaction in cavity QED, where the rotating wave approximation can be safely made. I refer to the Jaynes-Cummings Hamiltonian. Following, I focus on the peculiarities of the ultrastrong coupling regime. In particular, it is pointed out that in this regime the rotating wave approximation cannot be safely made and counter-rotating terms in the interaction Hamiltonian have to be taken into account. In this case I refer to Rabi Hamiltonian. Finally, in the context of the circuit QED where the quantum Rabi model can be generalized, I introduce the amount of longitudinal and transversal couplings as, for example, in experiments with USC of flux qubits to resonators [18, 45, 62]. This generalized quantum Rabi model does not impose any restrictions on the number of excitations.

Chapter 2 is devoted to describe the correct formulation of the interaction between a moving mirror and radiation pressure. I discuss the canonical quantization of both the field and the motion of the mirror, in order to derive a nonrelativistic Hamiltonian of a one-dimensional mirror-field coupled system in a cavity configuration. This approach leads to a more detailed description of a typical cavity optomechanics setup, in terms of a Hamiltonian known as Law Hamiltonian [61]. This theoretical framework provides a more fundamental explanation of the Casimir dynamic effect, and opens the doors to a possible experimental observation of light emission from mechanical

motion. Moreover, a description of the cavity optomechanical system in the standard case is derived as a particular case of the Law approach, when the frequencies of the mirror are much smaller than the frequency spacing of neighboring cavity modes. In this case one can neglect the terms that oscillate very quickly, adopting a rotating-wave-approximation (RWA). The standard optomechanical Hamiltonian has been used to successfully describe most of the experiments to date [23].

Chapter 3 is devoted to the description of the right procedure to calculate the input-output relations, the output photon emission rate, and the n-th order correlation fuctions in the ultrastrong coupling regime [63]. Indeed, an inconvenient issue arising in the ultrastrong coupling regime when considering the usual normal order correlation functions. It fails in to describe the output photon emission rate and photon statistics in the ultrastrong coupling regime. A clear evidence of this fact is that the standard input-output relations would for example predict, for a vacuum input, a finite output photon flux. Moreover, an incautious application of these standard relations for a system in its dressed ground state, which now contains a finite number of photons due to the counter-rotating terms in the Rabi Hamiltonian, would therefore predict an unphysical stream of output photons. The last part of this chapter it is also shown how this theory is actually valid for every degree of light-matter interaction, since the standard relations are recovered in the limit of low values of the atom-cavity coupling strength.

In Chapter 4 we look at open quantum systems, where a small quantum system is coupled to an environment with a large number of degrees of freedom, in order to describe the correct formulation of dissipation in the ultrastrong coupling regime. Indeed, it has been recently demonstrated that, while the standard quantum optical master equation can be safely used to describe the dynamics of the system in the weak and strong coupling regimes, in the ultrastrong coupling regime this standard approach fails to correctly describe the dissipation processes and leads to unphysical results as well [64]. The proper procedure that solves such issues and leads to the dressed master equation is described in detail.

Chapter 5 is an overview of the published paperss. Briefly in chronolog-

ical order of publication, Paper 5.1 analyzes a protocol working in the USC regime which in a single step forces the ground state of a mechanical oscillator to evolve into an arbitrary quantum state in a completely controlled and deterministic manner. Paper 5.2 shows that a system consisting of a single qubit coupled ultrastrongly to a resonator can exhibit anomalous vacuum Rabi oscillations. An avoided level crossing resulting from the coupling between the states with diffrent excitation numbers(due to the presence of counterrotating terms in the system Hamiltonian), explain the physical process where two or more photons are jointly emitted by the qubit into the resonator and reabsorbed by the qubit in a reversible and coherent process. Paper 5.3 proposes a protocol for the deterministic preparation of entangled *NOON* states or even more general mechanical states between two identical, optically coupled optomechanical systems. This approach extends the proposed scheme in Paper 5.1. Paper 5.4 is a proof-of-principle theoretical demonstration of an exciting new effect in cavity QED. Considering two separate atoms interacting with a single optical mode, when the frequency of the resonator field is twice the atomic transition frequency, it is possible to show that there exists a resonant coupling between one photon and two atoms, via intermediate virtual states connected by counter-rotating processes. If the resonator is prepared in its one-photon state, the photon can be jointly absorbed by the two atoms in their ground state which will both reach their excited state with a probability close to one. This work was selected as Editors Suggestion for *Physical Review Letters* ***117***, 043601 (2016). It was also featured in the *APS Physics Focus* ***9***, 83 (2016), and widely covered by the popular media all over the world. Paper 5.5 is thought in order to implement a new method for frequency conversion of photons, which is both versatile and deterministic. We have shown that a system with two resonators ultrastrongly coupled to a single qubit can be used to realize both single and multiphoton frequency conversion processes. The conversion can be exquisitely controlled by tuning the qubit frequency to bring the desired frequency-conversion transitions on or off resonance. Paper 5.6 shows how analogues of a large number of well-known nonlinear-optics phenomena can be realized with one or more qubit coupled to one or more resonator modes.

Through higher-order processes, where virtual photons are created and annihilated, an effective deterministic resonant coupling between two states of such a system can be created. In this way, analogues of three-wave mixing, four-wave mixing, higher-harmonic and -subharmonic generation (up- and down-conversion), multiphoton absorption, parametric amplification, Raman and hyper-Raman scattering, the Kerr effect, and other nonlinear processes can be realized. The recent experimental progress in ultrastrong light-matter coupling let us think that, many of these nonlinear-optics analogues can be realized with currently available technology. In Paper 5.7 one describes nonlinear optical processes with qubits, where only virtual photons are involved. The results presented here open the way to nonlinear optical processes without real photons. Instead, virtual photons, which are not subject to losses and decoherence, drive the interaction between N spatially separated and nondegenerate qubits. Finally, in Paper 5.8 we explain the dynamical Casimir effect, describing quantum mechanically both the cavity field and the oscillating mirror (optomechanical systems), neither adopting parametric or perturbative approximations, nor dynamics linearization. We show that the resonant generation of photons from the vacuum is determined by a ladder of mirror-field vacuum Rabi splittings. We find that vacuum emission can even originate from the free evolution of an initial pure mechanical excited state, in analogy with the spontaneous emission from excited atoms. By considering a coherent drive of the mirror and a master equation approach to take into account the losses, I were able to study the DCE from the weak to the ultrastrong limit. My coauthors and myself found that, when the coupling between the mobile mirror and the cavity field is not a negligible amount of the mechanical and optical resonance frequencies, a resonant production of photons out from the vacuum can be observed for mechanical frequencies lower than the cavity mode frequency. Hence, this coupling regime, which experiments are rapidly approaching, removes one of the major obstacles to the observation of this long sought effect.

We conclude in Chapter 6 by summarizing my work and looking to the future. There are indeed many interesting directions to pursue in the field of quantum optics.

Chapter 1

Cavity QED

The general problem of a physical system interacting with light involve the complex internal structure of the system (atom, molecule, solid, etc.) and the infinite number of modes of the electromagnetic field, which are described as independent harmonic oscillators. In cavity QED one can considers one or more atoms placed inside a resonant cavity which supports one or more discrete modes of the electromagnetic field, and whose resonance frequency can be properly adjusted with respect to the transition frequencies of each atoms. The problem can be simplified if one considers one cavity mode of frequency ω_c and only one atomic resonant transition between two atomic states $|g\rangle$ and $|e\rangle$, with energy separation is $E_{\rm e} - E_{\rm g} = \hbar(\omega_e - \omega_g) \equiv \hbar\omega_q$. All of the other cavity modes do not couple to the atom due to the large frequency mismatch and can therefore be neglected. In this case one may adopt a very simple model consisting in a single cavity mode interacting with a two-level atom (qubit) Fig. 1.1.

1.1 Light-Matter Interaction in Cavity QED

In cavity QED, the qubit-cavity interaction is essentially described by three parameters: the qubit-cavity coupling strength g, the cavity photon decay rate $\kappa = t_\kappa^{-1}$ (where t_κ is the cavity photon lifetime) and the qubit decay rate into non-cavity modes $\gamma = t_\gamma^{-1}$ (where t_γ is the qubit excited state lifetime). The expression for the qubit-cavity coupling strength g is obtained considering the interaction between the qubit and the the zero-point fluctuations of

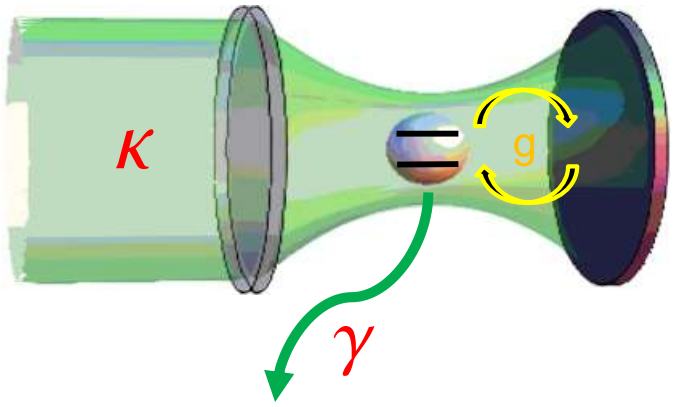

Figure 1.1: qubit inside a single-mode resonant cavity. The light-matter interaction is described by three parameters: the qubit-field interaction strength g, the cavity photon decay rate κ and the qubit decay rate into non-cavity modes γ.

the electromagnetic field in the cavity, and it is given by [40]:

$$g = \sqrt{\frac{d_{eg}^2 \omega_c}{2\hbar\epsilon_0 V_0}}, \tag{1.1}$$

where ω_c is the angular cavity frequency, ϵ_0 is the electric permittivity, V_0 is the cavity volume and d_{eg} is the dipole moment associated to the qubit transition. When the qubit-cavity coupling strength is slower than all loss rates ($g \ll \kappa, \gamma$), the system is in the weak coupling regime and photons emitted by the qubit escape the cavity before being reabsorbed, a process analogous to the free-space spontaneous emission. On the contrary, when $g \gg \kappa, \gamma$, the system enters the so-called strong coupling regime, in which the periodic exchange of the excitation between the qubit and the cavity is faster than the *irreversible* processes due to photon losses into non-cavity modes. In this case, the photon emission is a *reversible* process in which the photon is absorbed by the qubit before it can leave the cavity. In the strong coupling regime, the bare states of the qubit and the cavity mode mix to form new dressed energy eigenstates which are coherent superpositions of qubit and photon excitations, also known as polaritons. Moreover, the qubit and cavity resonances exhibit an avoided crossing and the resulting splitting is referred to as the "vacuum-Rabi" splitting [65]. When the qubit-cavity coupling

strength becomes comparable to the transition frequency of the qubit or the resonance frequency of the cavity mode $g/\omega_{c,q} \simeq 1$, the system enters the ultrastrong coupling regime (USC) which presents a great variety of new exciting effects that are not observed in the conventional weak and strong-coupling regimes [44, 46, 47]. Recently, due to the experimental progress in the development of circuit quantum electrodynamics (circuit QED) systems, where superconducting artificial qubits are coupled to on-chip cavities, it has been possible to experimentally achieve the USC regime [18, 45, 66, 67]. This regime has also been achieved with photochromic molecules [68], by using intersubband transitions in semiconductor structures [69, 70] or, by coupling the cyclotron transition of a high-mobility two-dimensional electron gas to the photonic modes of an array of electronic split-ring resonators [71]. In order to describe the interaction of a qubit with the quantized field of a cavity, we need to introduce the Pauli spin operators $\sigma_z, \sigma_y, \sigma_x$,

$$\sigma_z = \sigma_+\sigma_- - \sigma_-\sigma_+ = \begin{pmatrix} 1 & 0 \\ 0 & -1 \end{pmatrix} = |e\rangle\langle e| - |g\rangle\langle g| \tag{1.2}$$

$$\sigma_x = \sigma_- + \sigma_+ = \begin{pmatrix} 0 & 1 \\ 1 & 0 \end{pmatrix} = |g\rangle\langle e| + |e\rangle\langle g| \tag{1.3}$$

$$\sigma_y = i(\sigma_- - \sigma_+) = \begin{pmatrix} 0 & -i \\ i & 0 \end{pmatrix} = i(|g\rangle\langle e| - |e\rangle\langle g|) \tag{1.4}$$

and, the raising and lowering operators σ_+ and σ_-,

$$\sigma_+ = \begin{pmatrix} 0 & 1 \\ 0 & 0 \end{pmatrix} = |e\rangle\langle g| \tag{1.5}$$

$$\sigma_- = \begin{pmatrix} 0 & 0 \\ 1 & 0 \end{pmatrix} = |g\rangle\langle e| \tag{1.6}$$

$$\tag{1.7}$$

all of them expressed in the bare basis $\{|g\rangle, |e\rangle\}$. The raising operators σ_+ produces a transition from the lower to the upper state and the lowering operator σ_- has the opposite effect. The σ_z operator coincides with the

corresponding Pauli spin matrix, while the pseudo-spin raising and lowering operators can be related to the Pauli matrices through the relation $\sigma_\pm = \frac{1}{2}[\sigma_x \pm i\sigma_y]$. The total Hamiltonian for the system,

$$H = H_\mathrm{A} + H_\mathrm{F} + V \tag{1.8}$$

contains three terms describing the qubit H_A, the cavity field H_F and the the qubit-cavity interaction V. In terms of the qubit operators, the qubit Hamiltonian is given by

$$H_\mathrm{A} = \frac{1}{2}\hbar\omega_\mathrm{q}\sigma_z = \frac{1}{2}\hbar\omega_\mathrm{q}\,|e\rangle\langle e| - \frac{1}{2}\hbar\omega_\mathrm{q}\,|g\rangle\langle g| \tag{1.9}$$

In Eq. (1.9) the zero point of energy has been chosen half-way between levels $|e\rangle$ and $|g\rangle$, so that the energy of the state $|e\rangle$ is $E_\mathrm{e} = \frac{1}{2}\hbar\omega_\mathrm{q}$ and that of $|g\rangle$ is $E_\mathrm{g} = -\frac{1}{2}\hbar\omega_\mathrm{q}$. The Hamiltonian for the cavity field is

$$H_\mathrm{F} = \hbar\omega_\mathrm{c} a^\dagger a, \tag{1.10}$$

where $a^\dagger$ and a are, respectively, the bosonic creation and annihilation operators for the cavity mode. Finally, in the dipole approximation, the qubit-cavity interaction has the standard form

$$V = -d \cdot E = -d \cdot \epsilon E(\mathbf{r_0})(a + a^\dagger), \tag{1.11}$$

where $E(\mathbf{r_0})$ is the the electric field at the qubit position $\mathbf{r_0}$ and $\epsilon = (\hbar\omega_\mathrm{c}/\epsilon_0 V_0)^{\frac{1}{2}}$ is the field per photon within the cavity volume V_0. The dipole-moment operator can be expressed as

$$d = |g\rangle\langle g|\, d\, |e\rangle\langle e| + |e\rangle\langle e|\, d\, |g\rangle\langle g| = d_\mathrm{ge}\sigma_- + d_\mathrm{eg}\sigma_+ \tag{1.12}$$

If we assume, without loss of generality, that the matrix elements of the dipole-moment operator are real ($\langle g\,|d|\,e\rangle = \langle e\,|d|\,g\rangle$) and define the qubit-cavity coupling strength as

$$\hbar g \equiv -\langle e\,|d \cdot \epsilon|\,g\rangle\, E(r_0), \tag{1.13}$$

we can write the the qubit-cavity interaction Hamiltonian as,

$$V = \hbar g(\sigma_+ + \sigma_-)(a + a^\dagger) = \hbar g\sigma_x(a + a^\dagger). \tag{1.14}$$

With the Eq. (1.9), Eq. (1.10) and Eq. (1.14), the total Hamiltonian for the system becomes:

$$H = \frac{1}{2}\hbar\omega_{\rm q}\sigma_z + \hbar\omega_{\rm c}a^\dagger a + \hbar g\sigma_x(a + a^\dagger) \tag{1.15}$$

it is known as *Rabi Hamiltonian*. Eq. (1.15) describes the full qubit-cavity interaction without any approximation.

1.2 Jaynes-Cummings Hamiltonian

In the interaction picture, the qubit and field operators become,

$$U_{\rm A}^\dagger(t)\sigma_\pm U_{\rm A}(t) = \sigma_\pm e^{\pm i\omega_{\rm q}t}, \tag{1.16}$$

$$U_{\rm F}^\dagger(t)aU_{\rm F}(t) = ae^{-i\omega_{\rm c}t}, \tag{1.17}$$

$$U_{\rm F}^\dagger(t)a^\dagger U_{\rm F}(t) = a^\dagger e^{i\omega_{\rm c}t}, \tag{1.18}$$

where $U_{\rm A} = e^{-\frac{i}{\hbar}H_{\rm A}t}$ and $U_{\rm F} = e^{-\frac{i}{\hbar}H_{\rm F}t}$ are the free evolution operators for the qubit and the free field, respectively. The qubit-cavity interaction (1.14) in the interaction picture becomes:

$$\begin{aligned}\tilde{V} = e^{\frac{i}{\hbar}H_0t}Ve^{-\frac{i}{\hbar}H_0t} &= \hbar g(a\sigma_+e^{-i(\omega_{\rm c}-\omega_{\rm q})} + a^\dagger\sigma_-e^{i(\omega_{\rm c}-\omega_{\rm q})}) \\ &+ \hbar g(a\sigma_-e^{-i(\omega_{\rm c}+\omega_{\rm q})} + a^\dagger\sigma_+e^{i(\omega_{\rm c}+\omega_{\rm q})}).\end{aligned} \tag{1.19}$$

In this interaction Hamiltonian, the term of the form $a^\dagger\sigma_-$ corresponds to the process of qubit transition from the upper to the lower state and creation of one photon, while the term $a\sigma_+$ describes the inverse process, both of which are near-resonant and oscillate at frequencies $\pm(\omega_{\rm c}-\omega_{\rm q})$. On the other hand, the terms $a\sigma_-$ and $a^\dagger\sigma_+$, which in the interaction picture oscillate with the sum frequencies $\pm(\omega_{\rm c}+\omega_{\rm q})$, describe the nonresonant processes in which the qubit and the field are excited or de-excited simultaneously. Actually, exami-

nation of Eq. (1.19) reveals that these terms do not conserve the total energy of the system. Thus, for $E_e > E_g$, the operator combination $a\sigma_-$ annihilates a photon and induces a transition from the higher energy state $|e\rangle$ to the lower energy state $|g\rangle$, in clear violation of energy conservation. A similar violation occurs for the combination $a^\dagger\sigma_+$, in which a photon is created during the transition $|g\rangle \to |e\rangle$. When $\kappa, \gamma \ll g \ll \omega_{q,c}$ (the system is in the weak or strong coupling regime), these nonresonant terms are dropped in the rotating wave approximation (RWA) and the total Hamiltonian becomes

$$H = \frac{1}{2}\hbar\omega_q\sigma_z + \hbar\omega_c a^\dagger a + \hbar g(a\sigma_+ + a^\dagger\sigma_-) \tag{1.20}$$

A two-level system coupled to a single-mode electromagnetic field in the RWA approximation is known as the Jaynes-Cummings (JC) model [65]. In order to obtain a solution for the problem of qubit-cavity interaction, we need to specify the complete state of the system in terms of the states of both qubit and field. In the energy eigenstate representation, the basis states of the field are the number Fock states $|n\rangle$, with $n = 0, 1, 2, \ldots$ Considering the total excitation number operator $\mathcal{N}_{\text{exc}} \equiv a^\dagger a + \sigma_+\sigma_-$, it is easy to verify that it commutes with the total system Hamiltonian, *i.e.*, $[H, \mathcal{N}_{\text{exc}}] = 0$. This implies that the JC Hamiltonian in Eq. (1.20) conserves the total number of excitations and the interaction can only couple the states $|e\rangle|n\rangle \equiv |e, n\rangle$ and $|g\rangle|n+1\rangle \equiv |g, n+1\rangle$, whose energies are

$$E_{e,n} = \langle e, n|H|e, n\rangle = n\hbar\omega_c + \frac{\hbar}{2}\omega_q, \tag{1.21}$$

$$\begin{aligned} E_{g,n+1} = \langle g, n+1|H|g, n+1\rangle =& \hbar\omega_c(n+1) - \frac{\hbar}{2}\omega_q \\ =& E_{e,n} + \hbar\Delta, \end{aligned} \tag{1.22}$$

where $\Delta \equiv \omega_c - \omega_q$ is the detuning; when $\Delta = 0$, the bare states $|e, n\rangle$ and $|g, n+1\rangle$ are degenerate (see Fig. 1.2). Thus, the Hamiltonian in Eq. (1.20)

is block diagonal with two by two blocks and the off-diagonal elements are

$$\langle e,n|\,\hbar g(a\sigma_+ + a^\dagger\sigma_-)\,|g,n+1\rangle = \langle g,n+1|\,\hbar g(a\sigma_+ + a^\dagger\sigma_-)\,|e,n\rangle = \hbar g\sqrt{n+1}. \tag{1.23}$$

The Jaynes-Cummings Hamiltonian can also be split into the sum $H = \sum_n H_n$ with each term

$$H_n = E_{e,n}\begin{bmatrix}1 & 0\\ 0 & 1\end{bmatrix} + \hbar\begin{bmatrix}0 & g\sqrt{n+1}\\ g\sqrt{n+1} & \Delta\end{bmatrix}, \tag{1.24}$$

acting on its own subspace $\mathbb{H}_n = \{|e,n\rangle, |g,n+1\rangle\}$, with $n = 0,1,2,\ldots$ Diagonalizing the matrix in (1.24), we find the eigenvalues

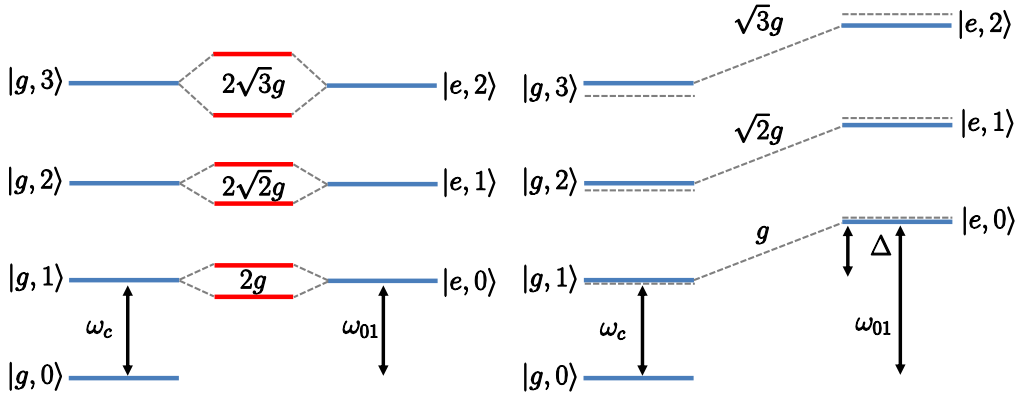

Figure 1.2: Jaynes-Cummings ladder or 'dressed-qubit' level structure. (left panel) Degenerate case $\omega_c = \omega_q$. The degenerate levels mix and split by an amount proportional to the vacuum Rabi splitting g. (right panel) Dispersive case $\omega_q = \omega_c + \Delta$. For $\Delta > 0$ the level repulsion causes the cavity frequency to decrease when the qubit is in the ground state and increase when the qubit is in the excited state.

$$\lambda_\pm^n = \frac{1}{\hbar}E_{e,n} + \frac{1}{2}\Delta \pm \bar{\Omega} \tag{1.25}$$

with $\bar{\Omega} \equiv \sqrt{g^2(n+1) + (\Delta/2)^2}$, and the corresponding eigenstates

$$|\pm_n\rangle = \frac{1}{\sqrt{N_\pm}}\left[\left(\bar{\Omega} \mp \frac{1}{2}\Delta\right)|e,n\rangle \pm g\sqrt{n+1}\,|g,n+1\rangle\right], \tag{1.26}$$

where $N_\pm = (\bar{\Omega} \mp \frac{1}{2}\Delta) + g^2(n+1)$ are the normalization constants. These are known as the dressed states of the JC Hamiltonian (Eq. (1.20)). At resonance, when $\Delta = 0$, we have

$$\lambda_\pm = \frac{1}{\hbar} E_{e,n} \pm g\sqrt{n+1}, \tag{1.27}$$

and

$$|\pm_n\rangle = \frac{1}{\sqrt{2}}[|e,n\rangle \pm |g,n+1\rangle]. \tag{1.28}$$

These dressed states, also called polaritons, are given by the symmetric $|+_n\rangle$ and antisymmetric $|-_n\rangle$ superposition of the bare states $|e,n\rangle$ and $|g,n+1\rangle$ and are split by the amount $\lambda_+^{(n)} - \lambda_-^{(n)} = 2g\sqrt{n+1}$, which is twice the matrix element of (1.23). One of the most important feature of the strong coupling regime is the possibility to observe the so-called vacuum Rabi oscillations [6], a coherent and reversible process in which the qubit and the cavity exchange a single quantum excitation. Vacuum Rabi oscillations is a "classical" example of coherent resonant coupling of states that in, this case, conserve the number of excitations (see Fig. 1.3). Specifically, if the system is prepared in the state $|e,0\rangle$, *i.e.*, the qubit is excited with no photons in the cavity, it will undergo Rabi oscillations between the states $|e,0\rangle$ and $|g,1\rangle$ at a frequency $\Omega_{\text{Rabi}} = g$. This means that the cavity field stimulates the qubit decay into the cavity, so that the qubit is deexcited and the photon number increases by one. Subsequently, the qubit is reexcited after the reabsorption of the emitted photon, and so forth. Controlling these oscillatory dynamics quickly relative to the vacuum Rabi frequency, enables remarkable capabilities such as Fock state generation and deterministic synthesis of quantum states of light. In Paper 5.2, We show that in the so-called ultrastrong coupling regime the concept of vacuum Rabi oscillations can strongly modified, enabling multiphoton exchanges between the qubit and the cavity. These anomalous Rabi oscillations can be exploited for the realization of efficient Fock-state sources of light and complex entangled states of artificial qubits.

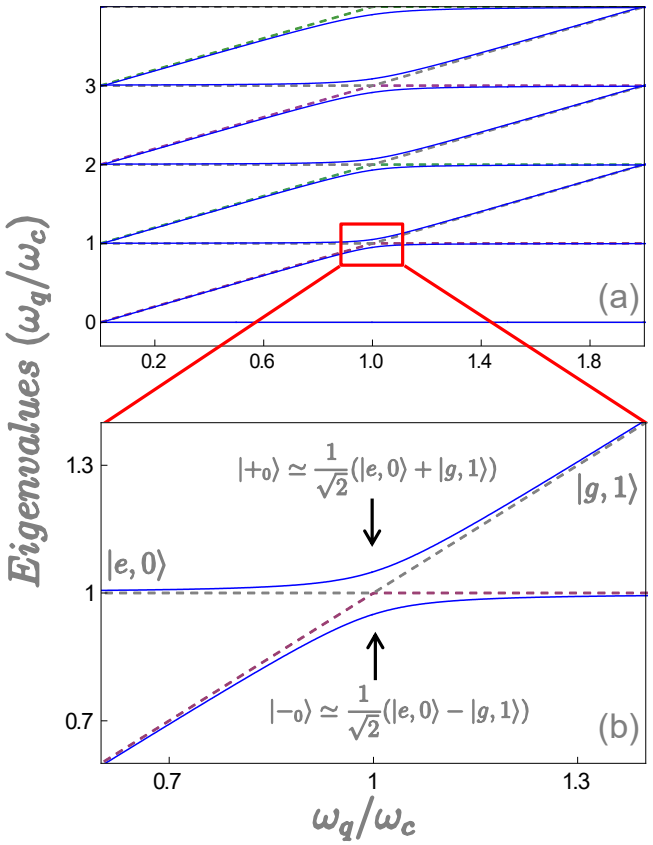

Figure 1.3: (a) Lowest energy levels of the system JC Hamiltonian as a function of the ratio between the qubit and the cavity frequency for qubit-cavity coupling strength g/ω_c = 0.05 (blue continous line). At the resonances $\omega_c = \omega_q$ a ladder of avoided crossings are clearly visible. The grey-dashed lines describe the eigenenergies of the JC Hamiltonian for $g/\omega_c = 0.02$. It is clearly visible a decrease of the splitting $\lambda_+^{(n)} - \lambda_-^{(n)} = 2g\sqrt{n+1}$, when the qubit-cavity coupling strength decrease. (b) display enlarged views of two boxed regions in (a), showing avoided level crossing due to hybridizations of $|e,0\rangle$ and $|g,1\rangle$ (vacuum-Rabi splittings).

1.3 Rabi Hamiltonian

As discussed above, when the qubit-cavity coupling strength $g/\omega_{q,c} \simeq 1$ the system enters in USC regime. This light-matter regime presents a great variety of new exciting effects [18, 44–47] that are not observed in the conventional weak- and strong-coupling regimes. In order to describe these and other new effects, we need to use the Rabi Hamiltonian which takes account

the full qubit-cavity interaction,

$$H_{\mathrm{R}} = \frac{\hbar}{2}\omega_{\mathrm{q}}\sigma_z + \hbar\omega_{\mathrm{c}}a^\dagger a + \hbar g\sigma_x(a + a^\dagger). \tag{1.29}$$

Eq. (1.29) contains the counter-rotating terms $a\sigma_-$, $a^\dagger\sigma_+$, which lead to experimentally observable consequences. Actually, these terms can be neglected only in the case in which the ratio $g/\omega_{\mathrm{c}} \ll 1$, and this can be understood considering that $a\sigma_-$, $a^\dagger\sigma_+$ couples the states $|g, n\rangle$ and $|e, n+1\rangle$ that differ by two excitations

$$\langle e, n+1|\, \hbar g(a\sigma_- + a^\dagger\sigma_+)\, |g, n\rangle = \langle g, n|\, \hbar g(a\sigma_- + a^\dagger\sigma_+)\, |e, n+1\rangle \approx \hbar g, \tag{1.30}$$

while the energy difference between the bare states (at resonance) is

$$\langle e, n+1|\, H_0\, |e, n+1\rangle - \langle g, n|\, H_0\, |g, n\rangle \approx 2\hbar\omega_{\mathrm{c}}, \tag{1.31}$$

where $H_0 = \frac{1}{2}\hbar\omega_{\mathrm{q}}\sigma_z + \hbar\omega_{\mathrm{c}}a^\dagger a$. Eq. (1.30) and Eq. (1.31) show that the counter-rotating terms become relevant only when the coupling strength g becomes comparable to or much larger than the transition frequency of the atom or the resonance frequency of the cavity mode. It is immediate to verify that the total number of excitations is not preserved, $[H_{\mathrm{R}}, \mathcal{N}_{\mathrm{exc}}] \neq 0$, while the parity is [72]. Namely, $[\mathcal{P}, H_R] = 0$ with the unity parity operator $\mathcal{P} = e^{i\pi\mathcal{N}_{\mathrm{exc}}}$. As important consequence of the non conservation of the total number of excitations, the ground state of the system is no longer the vacuum state $|g, 0\rangle$ of the JC model. A new vacuum state $|G\rangle$ now appears, which contains both atom and resonator excitations

$$|G\rangle = \sum_{k=0}^{\infty}(c^G_{\mathrm{g},2k}|\mathrm{g}, 2k\rangle + c^G_{\mathrm{e},2k+1}|\mathrm{e}, 2k+1\rangle). \tag{1.32}$$

Unless a time-dependent perturbation of the light-matter coupling is applied to the system, these excitations have to be considered "virtual" as they cannot be experimentally detected [44]. Another important feature of the dressed ground state $|G\rangle$ is that, in contrast to what happens to the

JC ground state $|g,0\rangle$, its energy depends on the coupling rate g/ω_c (see Fig. 1.4). This implies that the number of virtual photons bound in the dressed ground state dependents from the coupling strength. Actually, it increases as the coupling strength increases. The dressed states of the Rabi

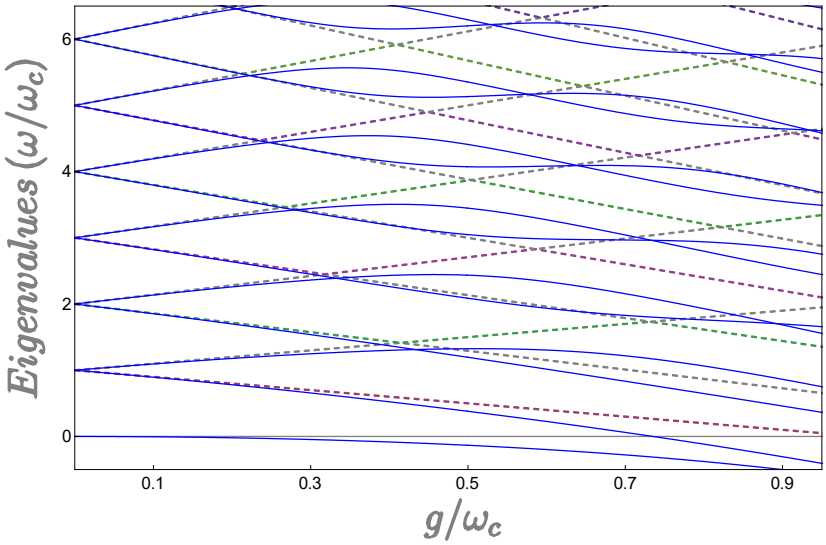

Figure 1.4: Energy spectrum of H_R as function of the coupling strength in the non-dispersive regime ($\Delta = \omega_c - \omega_q = 0$) for the Jaynes-Cummings model (dashed line) and the Rabi Hamiltonian (solid blue line) containing the counter-rotating terms.

Hamiltonian can be expanded in terms of the bare states

$$|j,+\rangle = \sum_{k=0}^{\infty}(c^{j^+}_{g,2k}|g,2k\rangle + c^{j^+}_{e,2k+1}|e,2k+1\rangle), \tag{1.33}$$

$$|j,-\rangle = \sum_{k=0}^{\infty}(c^{j^-}_{g,2k+1}|g,2k+1\rangle + c^{j^-}_{e,2k}|e,2k\rangle), \tag{1.34}$$

where $|j,+\rangle$ and $|j,-\rangle$ indicate, respectively, the even- and odd-parity eigenstates. Although the analytical spectrum of H_R has recently been found [73], it is defined in terms of the power series of a transcendental function. An approximate, but more simple form, can be found in the intermediate regime, referred to as the Bloch-Siegert (BS) regime, where the coupling strength g is small with respect to $\omega_c + \omega_q$, with the system still being in the ultrastrong

coupling regime. This is done using the unitary transformation

$$U = e^{[\Lambda\left(a\sigma_- - a^\dagger\sigma_+\right)+\xi\left(a^2-a^{\dagger 2}\right)\sigma_z]}, \tag{1.35}$$

where $\Lambda = g/(\omega_\mathrm{c}+\omega_\mathrm{q})$, and $\xi = g\Lambda/2\omega_\mathrm{c}$. This yields the BS Hamiltonian

$$U^\dagger H_\mathrm{R} U \simeq H_\mathrm{BS} = (\omega_\mathrm{c}+\mu\sigma_z)\, a^\dagger a + \frac{\tilde{\omega}_\mathrm{q}}{2}\sigma_z + gI_+, \tag{1.36}$$

where $I_+ = a\sigma_+ + a^\dagger\sigma_-$, $\tilde{\omega}_\mathrm{q} = \omega_\mathrm{q}+\mu$, and $\mu = g^2/(\omega_\mathrm{c}+\omega_\mathrm{q})$. This Hamiltonian is similar to the JC Hamiltonian, but contains BS shifts μ on qubit and resonator frequencies. Since the BS Hamiltonian in Eq. (1.36) is block diagonal, its eigenstates can be found exactly to be

$$|n,+\rangle = -\sin\theta_n\,|e,n-1\rangle + \cos\theta_n\,|g,n\rangle\,, \tag{1.37}$$

$$|n,-\rangle = \cos\theta_n\,|e,n-1\rangle + \sin\theta_n\,|g,n\rangle\,, \tag{1.38}$$

where θ_n is BS mixing angle

$$\theta_n = \arctan\left[\frac{\Delta_n^\mathrm{BS} - \sqrt{(\Delta_n^\mathrm{BS})^2+4g^2n}}{2g\sqrt{n}}\right], \tag{1.39}$$

and $\Delta_n^\mathrm{BS} = \omega_\mathrm{q}-\omega_\mathrm{c}+2\mu n$. To second order in Λ, the excited eigenstates $\widetilde{|n,\pm\rangle}$ of the Rabi Hamiltonian in the bare basis are then given by

$$\widetilde{|n,\pm\rangle} = U\,|n,\pm\rangle\,, \tag{1.40}$$

while the ground state takes the form

$$|G\rangle = U|g,0\rangle \simeq \left(1-\frac{\Lambda^2}{2}\right)|g,0\rangle - \Lambda|e,1\rangle + \xi\sqrt{2}|g,2\rangle. \tag{1.41}$$

Eq. (1.41) cleary shows an important feature of the dressed ground state $|G\rangle$. In contrast to the JC ground state $|g,0\rangle$, its energy depends on the coupling rate g/ω_c (see Fig. 1.4). This implies that the number of virtual photons bound in the dressed ground state dependents from the coupling strength. Actually, it increases as the coupling strength increases. $|G\rangle$ is a squeezed

vacuum containing a finite number of virtual photons. This is one of the most important feature of the ultrastrong coupling regime as, for example, in the presence of nonadiabatic modulations [44], induced Raman transitions [74], spontaneous decay mechanisms [46], or sudden on-off switches of the light-matter interaction [75], these virtual photons can be converted to real ones, giving rise to a stream of quantum vacuum radiation. Moreover, in the ultrastrong coupling regime the resonator field $X = a + a^{\dagger}$ can display a non-zero vacuum first-order coherence $|\langle G|a|G\rangle|^2 / \langle G|a^{\dagger}a|G\rangle \neq 0$, a situation that does not occur in the JC model, where the vacuum first-order coherence is strictly zero (see Chapter 3). This property is very important in circuit QED systems constitued by a flux qubit coupled to an on-chip coplanar resonator, as a non-zero expectation value of the resonator field in the system ground state $|G\rangle$ can lead to a vacuum-induced parity-symmetry breaking on an additional artificial atom [76].

1.4 Look at circuit QED: Generalized Rabi Hamiltonian

The last two decades have seen a greatly increased interest in using superconducting quantum circuits (SQCs), based on Josephson junctions [17], for implementing quantum bits (the basic units of quantum information or qubit). Starting from experiments on macroscopic quantum coherence in devices where Cooper pairs tunnel between small superconducting islands [77], It has also been demonstrated that SQCs possess discrete energy levels and behave like atoms, often referred to as superconducting (SC) qubit. Usually, SC qubits interact with a quantized microwave electromagnetic field. They referred to as circuit QED, the study of the interaction between a quantized microwave electromagnetic field and SC qubit. In microwave photonics with SQC the basic building blocks of cavity QED (natural atoms and optical cavities), are replaced with SC qubit and SC resonators, respectively, as shown in Fig. 1.5. There are three basic types of SQC based on Josephson junctions, called *charge*, *flux*, and *phase* SQC [14, 78]. Just like natural atoms, SQC is

multi-level system but when we limit our study to only the two lowest-energy levels (two-level system), a SC qubit can be defined. SC resonators, which usually are constructed from electrical circuits, are used to store or guide microwave photons, transferring quantum information between SC qubits. The simplest resonator is the LC circuit, consisting of a capacitor C connected in series with an inductor L [79]. Other SQC devices can be described in terms of lumped-element LC circuits, e.g., SC cavities, transmission-line resonators, and waveguides. Transmission lines most commonly appear in SQC devices in the form of coplanar waveguides (CPWs) [80,81]. A CPW consists of a central conductor, inserted in a slot of the ground plane. By terminating a length of CPW with capacitors, functioning like Fabry-Perot cavity mirrors, a CPW resonator is formed. Phenomena which occur quantum op-

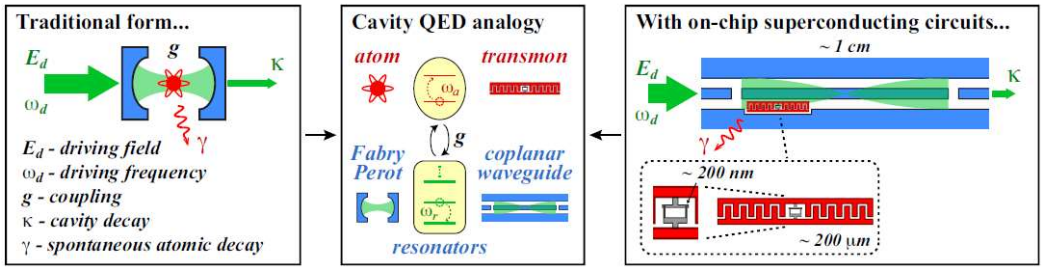

Figure 1.5: Analogy between traditional cavity QED and its SC circuit based form. The cavity mirrors in the circuit form are capacitors in the waveguide (gaps in the central conductor). The artificial atom shown, a transmon (a type of SC charge qubit), is an anharmonic electronic oscillator, a parallel capacitor and nonlinear SC quantum interference device (SQUID) inductor. Its two lowest energy levels form a qubit, coupling to the waveguide via its electric dipole. The figure shows a nonlinear resonator, created by inserting a SQUID in the waveguides central conductor, illustrating the platforms flexibility.

tics, using natural atoms and optical photons, are expected to also manifest in setups using SC qubits and microwave photons [12, 13, 82]. Experiments show that, unlike cavity QED, SC qubits can be strongly and ultra-strongly coupled to a SC resonator [18], opening many new possibilities for studying the interaction beyond the nature permissive regimes [66]. For example, one can reach the USC regime, where the strength of the coupling between the SC qubit and the SC resonator is on the same order as the bare transition frequencies in the system. Moreover, the coupling between a SC qubit and a SC resonator can be tunable in situ [83–86].

The general Hamiltonian describing the interaction between a SC qubit and a SC resonator can be written as [12, 13, 87, 88],

$$H = \frac{1}{2}\hbar\omega_{\mathrm{q}}\sigma_z + \hbar\omega_{\mathrm{c}}a^{\dagger}a + \hbar g(a + a^{\dagger})(\sigma_x \cos\theta + \sigma_z \sin\theta) \tag{1.42}$$

where θ parameterizes the amount of longitudinal and transversal couplings as, for example, in experiments with USC of flux qubits to resonators [18, 45, 62]. It corresponds to breaking the inversion symmetry of the potential energy of the SC qubit. This generalized quantum Rabi model does not impose any restrictions on the number of excitations.

Chapter 2

Cavity Optomechanics

Cavity Optomechanics explores the interaction, via radiation pressure, between the electromagnetic field in an optical resonator and a mobile mirror (mechanical oscillator)(see Fig. 2.1). Mechanical oscillators are at the

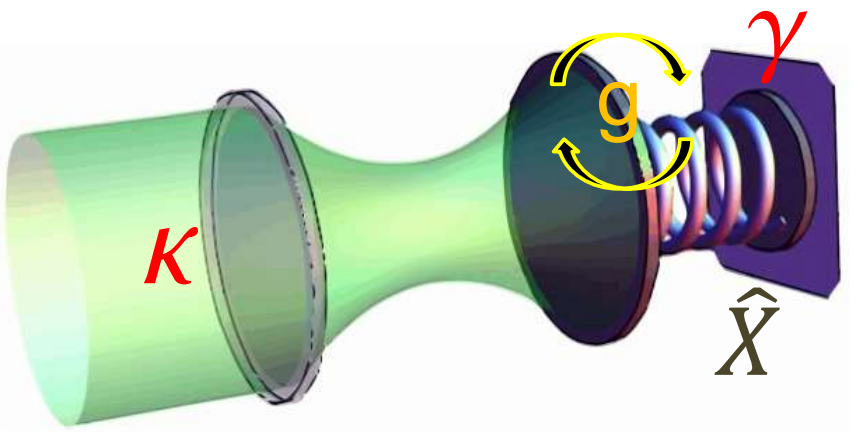

Figure 2.1: Optomechanics setup: a mechanical oscillator with frequency ω_M is coupled via radiation pressure, with a single-mode cavity with frequency ω_c. The moving mirror-cavity field interaction strength is g, while κ is the cavity photon decay rate and γ is the mirror decay rate into non-cavity modes.

heart of many precision experiments, such as highly sensitive detection of small forces, displacements, and accelerations [23, 89, 90] and can exhibit exceptionally low dissipation. Recently, many groups have devoted considerable effort to this type of *hybrid quantum systems* (HQSs) and various designs for the observations of quantum behavior in these systems have been studied. For example, The generation of quantum entanglement [91–94],

quantum measurement [95], high precision displacement detection [96], and cooling [97–99] have been demonstrated. Moreover, since quantum superpositions are the main resources for quantum information processing, many theoretical proposals and experimental demonstrations have been presented in order to generate arbitrary superpositions of different mechanical Fock states [94, 100–102]. Paper 5.1 and Paper 5.3 are devoted to the study of the ultrastrong (or single-photon) coupling regime in optomechanical systems [21,103,104] (using *standard* optomechanical Hamiltonian, see Sec. 2.2), which is achieved when the radiation pressure of a single photon displaces the mechanical resonator by more than its zero-point uncertainty [105]. In particular, in Paper 5.1 I contributed to the development of a new single-step protocol for the preparation of arbitrary quantum superpositions of mechanical Fock states whose efficiency and robustness have been tested in the presence of decoherence, thermal noise, and imperfect cooling. The results obtained in Paper 5.1 were inspirational for the developments reported in Paper 5.3, where a protocol for the deterministic preparation of entangled *NOON* mechanical states on demand is proposed. In this case, the system is constituted by two identical optically-coupled optomechanical systems. This type of HQS is also promising for the study of fundamental quantum effects on a mesoscopic or macroscopic scale as the dynamical Casimir effect (DCE) [31, 106–108]. It predicts the generation of photons from the quantum vacuum due to rapid changes of the geometry (the positions of some boundaries). In Paper 5.8, we show that this fundamental physical process originates from *avoided-level crossings* involving also states with different excitations number. In this paper we show that the DCE can be described without considering any time dependent Hamiltonian. The main purpose of this chapter is just to derive the Hamiltonian describing this process, due to C.K. Law [61]. It is a non-relativistic Hamiltonian describing the interaction, due to the radiation pressure, between a moving mirror and the cavity field, constructed directly from the canonical quantization of both the field and the motion of the mirror, and using the equation of motion of the moving mirror (regarded as a mechanical harmonic oscillator) and the wave equation (with appropriate boundary conditions) of the field (see Sec. 2.1). When

the mechanical frequency is much smaller than the cavity frequency (which is the most common experimental situation), the rapidly oscillating terms in the Law optomechanical Hamiltonian can be neglected (rotating wave apprixmation (RWA)). With this approximation, the resulting *standard* optomechamical Hamiltonian conserves the number of photons and it can be analytically diagonalized (see Sec. 2.2).

2.1 Law optomechanical Hamiltonian

Let's start by considering a one-dimensional cavity formed by two perfectly reflecting mirrors. One of the mirrors is fixed at the position $X = 0$ and the other one move in a potential well $V(q)$. The potential well $V(q)$ at $q = 0$ acts like an infinite potential wall which forbids the moving mirror from penetrating through the fixed mirror. The vector potential $A(x,t)$ of the cavity field is defined in the region $0 \leqslant x \leqslant q(t)$ ($q(t)$ is the position of the movable mirror), and obeys the wave equation ($c = 1$),

$$\frac{\partial^2 A(x,t)}{\partial x^2} = \frac{\partial^2 A(x,t)}{\partial t^2}. \tag{2.1}$$

We need to use the time-dependent boundary conditions $A(0,t) = A(q(t),t) = 0$. So that, the electric field is always zero in the rest frame of the mirror surface. The non-relativistic equation of motion of the mirror is given by (m is the mirror mass),

$$m\ddot{q} = -\frac{\partial V(q)}{\partial q} + \frac{1}{2}\left(\frac{\partial A(x,t)}{\partial x}\right)^2_{x=q(t)}. \tag{2.2}$$

The second term of the right side of Eq. (2.2) is the radiation pressure force. It can be derived from the radiation pressure force appearing in the rest frame of the movable mirror. We now define a set of generalized coordinates Q_k which is the mode decomposition of the field,

$$Q_k = \sqrt{\frac{2}{q(t)}}\int_0^{q(t)} dx A(x,t)\sin\left(\frac{k\pi x}{q(t)}\right) \qquad k \,\epsilon\, \mathbb{N}. \tag{2.3}$$

Unlike the usual situation, the mode basis functions used here are determined by the instantaneous position of the mirror. From Eq. (2.3) and the completeness of the mode functions, the vector potential is written:

$$A(x,t) = \sum_{k=1}^{\infty} Q_k(t)\sqrt{\frac{2}{q(t)}}\sin\left(\frac{k\pi x}{q(t)}\right). \tag{2.4}$$

With the Eq. (2.4) and the orthogonality of the mode functions $Q_k(t)$, Eq. (2.1) and Eq. (2.2) become:

$$\begin{aligned}\ddot{Q}_k =& -\omega_k^2 Q_k + 2\frac{\dot{q}}{q}\sum_j g_{kj}\dot{Q}_j + \frac{\ddot{q}q-\dot{q}^2}{q^2}\sum_j g_{kj}Q_j + \frac{\dot{q}^2}{q^2}\sum_{jl} g_{jk}g_{jl}Q_l,\\ m\ddot{q} =& -\frac{\partial V(q)}{\partial q} + \frac{1}{q}\sum_{kj}(-1)^{k+j}\omega_k\omega_j Q_k Q_j,\end{aligned} \tag{2.5}$$

where the position-dependent frequencies ω_k and the dimensionless coefficients g_{kj} are given by

$$\begin{aligned}\omega_k(q) =& \frac{k\pi}{q},\\ g_{kj} =& \begin{cases}(-1)^{k+j}\frac{2kj}{j^2-k^2} & ,k\neq j\\ 0 & ,k=j\end{cases}\end{aligned} \tag{2.6}$$

By examining Eq. (2.5), we find that one can construct a Lagrangian $\mathcal{L}$,

$$\begin{aligned}\mathcal{L}(q,\dot{q},Q_k,\dot{Q}_k) =& \frac{1}{2}\sum_k\left[\dot{Q}_k^2 - \omega_k^2(q)Q_k^2\right] + \frac{1}{2}m\dot{q}^2 - v(q)\\ &-\frac{\dot{q}}{q}\sum_{jk} g_{kj}\dot{Q}_k Q_j + \frac{\dot{q}^2}{2q^2}\sum_{jkl} g_{kj}g_{kl}Q_l Q_j.\end{aligned} \tag{2.7}$$

So that, the corresponding Hamiltonian associated with this $\mathcal{L}$ is defined by

$$\mathcal{H}(P_k,Q_j,p,q) = \frac{1}{2m}\left(p + \frac{1}{q}\sum_{jk} g_{kj}P_k Q_j\right)^2 + V(q) + \frac{1}{2}\sum_k\left[P_k^2 + \omega_k^2 Q_k^2\right], \tag{2.8}$$

where P_k and p are canonical momenta conjugate to Q_k and q, defined as

$$\begin{aligned} P_k &= \dot{Q}_k - \frac{\dot{q}}{q}\sum_{jk} g_{kj} P_k Q_j \\ p &= m\dot{q} - \frac{1}{q}\sum_{jk} g_{kj} P_k Q_j. \end{aligned} \tag{2.9}$$

The Hamiltonian in Eq. (2.8) is a more general expression because the mirror is included as a dynamical degree of freedom, and so allows us to consider the effects of radiation pressure.

At this point, we can follow the canonical quantization procedure. We let the canonical momenta (P_k, p) and their conjugate variables Q_k, q be operators, with the commutation relations

$$\begin{aligned} &\left[\hat{q}, \hat{Q}_j\right] = \left[\hat{q}, \hat{P}_k\right] = \left[\hat{p}, \hat{Q}_j\right] = \left[\hat{p}, \hat{P}_k\right] = 0 \\ &[\hat{q}, \hat{p}] = i\hbar \qquad \left[\hat{Q}_j, \hat{P}_k\right] = i\hbar. \end{aligned} \tag{2.10}$$

We define the cavity-length-dependent creation and annihilation operators for each cavity mode by

$$\begin{aligned} \hat{a}_k(\hat{q}) &= \sqrt{\frac{1}{2\hbar\omega_k(\hat{q})}}\left[\omega_k(\hat{q})\hat{Q}_k + i\hat{P}_k\right] \\ \hat{a}_k^\dagger(\hat{q}) &= \sqrt{\frac{1}{2\hbar\omega_k(\hat{q})}}\left[\omega_k(\hat{q})\hat{Q}_k - i\hat{P}_k\right]. \end{aligned} \tag{2.11}$$

where the dependence on the operator $\hat{q}$ indicates that for each position of the mirror one has a set of *Fock* states associated with that position. The creation and annihilation operators are not defined when the cavity has zero length ($q = 0$). To fix this problem one imposes a boundary condition on the wave function such that, the wave function is identically zero at $q = 0$.

The Hamiltonian operator now reads

$$\hat{H}' = \frac{(\hat{p} + \hat{\Gamma})^2}{2m} + V(\hat{q}) + \hbar\sum_k \omega_k(\hat{q})\left[\hat{a}_k^\dagger\hat{a}_k + \frac{1}{2}\right], \tag{2.12}$$

where

$$\hat{\Gamma} = \frac{i\hbar}{2\hat{q}} \sum_{kj} g_{kj} \left[\frac{k}{j}\right]^{\frac{1}{2}} \left[\hat{a}_k^\dagger \hat{a}_j^\dagger - \hat{a}_k a_j + \hat{a}_k^\dagger a_j - \hat{a}_j^\dagger a_k\right]. \tag{2.13}$$

The vacuum field energy appearing in Eq. (2.12) is divergent and is the origin of the Casimir force. Following the usual procedure [109] one obtain the Casimir energy $\hbar\pi/24q$ for one-dimensional space, which is finite because the cancellation of the divergent parts of the vacuum pressure came from both sides of the mirror [110]. This is an approximation, since it only counts the static part (the Casimir effect) of the interaction between the mirror and the outside field. The dynamic part, which describes the changing of the field outside the cavity, is ignored. Nevertheless, in most physical situations where the cavity field is dominant this is a good approximation. At this point we can consider the cavity optmechanical case, where the motion of the mobile mirror is that of a mechanical resonator. In this case, the mirror is bounded by a potential $V(\hat{q})$ which keeps the mirror moving around a certain equilibrium position l_0, and the radiation pressure force acts as a small perturbation. When the mobile mirror displacement $\hat{X} = \hat{q} - l_0$ is small compared with l_0, one can write $\hat{\Gamma} \approx \hat{\Gamma}|_{\hat{q}=l_0} = \hat{\Gamma}_0$ which is the operator $\hat{\Gamma}$ evaluated at the equilibrium position. Furthermore, for the small parameter $\hat{X}/l_0$ one make the following expansions:

$$\begin{aligned} \hat{a}_k(\hat{q}) &\approx \hat{a}_{k0} - \frac{\hat{X}}{2l_0}\hat{a}_k^\dagger \\ \omega_k(\hat{q}) &\approx \omega_{k0}\left(1 - \frac{\hat{X}}{l_0}\right) \end{aligned} \tag{2.14}$$

where $\hat{a}_{k0}$ and ω_{k0} denote the annihilation operator and the frequency associated with the equilibrium position, respectively. Using the relations Eq. (2.14) and unitary transformation $U = \exp(i\hat{X}\Gamma_0/\hbar)$, the Hamiltonian operator (Eq. (2.12)), $\hat{H}'$ becomes:

$$\hat{H} = \frac{\hat{p}^2}{2m} + V(\hat{X}) + \hbar\sum_k \omega_{k0}\hat{a}_{k0}^\dagger \hat{a}_{k0} - \hat{X}\hat{F}_0, \tag{2.15}$$

where $\hat{F}_0$ is the normally ordered radiation pressure force,

$$\hat{F}_0 = \frac{\hbar}{2l_0}\sum_{kj}(-1)^{k+j}\sqrt{\omega_{k0}\omega_{j0}}\left[\hat{a}^\dagger_{k0}\hat{a}^\dagger_{j0} + \hat{a}_{k0}a_{j0} + \hat{a}^\dagger_{k0}a_{j0} + \hat{a}^\dagger_{j0}a_{k0}\right]. \quad (2.16)$$

At this point, one can consider only one mode of the cavity field. So that, in Eq. (2.15) with Eq. (2.16) we have $k = j = 1$. Also, one can expressed the the mobile mirror energy and the mobile mirror displacement in term of the creation and annihilation phonon operator

$$\begin{aligned}\hat{b} &= \sqrt{\frac{1}{2\hbar\omega_M}}\left[\omega_M\hat{X} + i\hat{p}\right]\\ \hat{b}^\dagger &= \sqrt{\frac{1}{2\hbar\omega_M}}\left[\omega_M\hat{X} - i\hat{p}\right],\end{aligned} \quad (2.17)$$

so that, Eq. (2.15) with Eq. (2.16) becomes

$$H = \hbar\omega_{\mathrm{R}}a^\dagger a + \hbar\omega_{\mathrm{M}}b^\dagger b + \hbar g(b^\dagger + b)(a^\dagger + a)^2, \quad (2.18)$$

where ω_{R} is the resonator frequency, ω_{M} is the mechanical frequency, and $g = Gx_{zpf}$ is the optomechanical coupling strength. x_{zpf} is the zero-point fluctuation amplitude of the vibrating mirror and G is a coupling parameter. Eq. (2.18) is the time-independent Hamiltonian due to C.K. Law [61] which describes, in a non-relativistic way, the interaction due to the radiation pressure between a moving mirror and one mode of the cavity field. Eq. (2.18) is used in Paper 5.8 in oredr to described DCE in cavity optomechanical system. When the mechanical frequency is much smaller than the cavity frequency the quadratic term in Eq. (2.18) can be neglected, because it connects bare states with an energy difference $2\hbar\omega_R \pm \hbar\omega_M$. With this approximation, the resulting Hamiltonian Eq. (2.19),

$$H = \hbar\omega_{\mathrm{R}}a^\dagger a + \hbar\omega_{\mathrm{M}}b^\dagger b + \hbar g a^\dagger a(b^\dagger + b), \quad (2.19)$$

conserves the number of photons and can be analytically diagonalized, how shown in Chapter 2.2

2.2 Standard optomechanical Hamiltonian

I will describe the diagonalization procedure for the standard optomechanical Hamiltonian:

$$H = \hbar\omega_{\mathrm{R}} a^{\dagger}a + \hbar\omega_{\mathrm{M}} b^{\dagger}b + \hbar g\, a^{\dagger}a(b + b^{\dagger}) \,, \tag{2.20}$$

It can be easily verified that the Hamiltonian in Eq. (2.20) commutes with the photon number operator $\mathcal{N} \equiv a^{\dagger}a$

$$[H, \mathcal{N}] = 0. \tag{2.21}$$

Since the photon number n is a good quantum number, the total system Hilbert space can be decomposed into many subspaces, in each of which the number of photons n is fixed.

Our purpose is to eliminate the photon-phonon coupling term in the Hamiltonian in Eq. (2.20). This can be accomplished by performing a canonical transformation of the form:

$$\bar{H} = e^{S} H e^{-S} \tag{2.22}$$

Clearly, the transformation must be unitary to preserve the hermiticity of the Hamilton operator. This implies that the transformations generator S in Eq. (2.22) must be anti-Hermitian, *e.g.*, $S^{\dagger} = -S$. The appropriate choice for S to eliminate the photon-phonon coupling is

$$S = \frac{g}{\omega_{\mathrm{M}}} a^{\dagger}a(b^{\dagger} - b). \tag{2.23}$$

The essential building block of the calculation consists of exploiting the Baker-Campbell-Hausdorff formula, which reads

$$\begin{aligned} e^{A}Be^{-A} =& \sum_{m=0}^{\infty} \frac{1}{m!}[A, B]_m \\ =& B + [A, B] + \frac{1}{2}[A, [A, B]] + \frac{1}{6}[A, [A, [A, B]]] + \dots \end{aligned} \tag{2.24}$$

For the transformation of the relevant operators, one thus obtains

$$\bar{a} = a, \tag{2.25}$$

$$\bar{a}^\dagger = a^\dagger, \tag{2.26}$$

$$\bar{b} = e^S b\, e^{-S} = \sum_{n=0}^{\infty} \frac{(g/\omega_{\mathrm{M}})^n (a^\dagger a)^n}{n!} [(b^\dagger - b), b]_n = b - \frac{g}{\omega_{\mathrm{M}}}(a^\dagger a), \tag{2.27}$$

$$\bar{b}^\dagger = b^\dagger - \frac{g}{\omega_{\mathrm{M}}}(a^\dagger a), \tag{2.28}$$

After substituting Eqs. (2.25-2.28) in Eq. (2.22), we obtain the transformed diagonal Hamiltonian

$$\bar{H} = \hbar\omega_{\mathrm{R}} a^\dagger a + \hbar\omega_{\mathrm{M}} b^\dagger b - \frac{\hbar g^2}{\omega_{\mathrm{M}}} (a^\dagger a)^2. \tag{2.29}$$

The Hamiltonian of the n-th subspace is then given by:

$$\bar{H}^{(n)} = \langle n|\bar{H}|n\rangle = \hbar\omega_{\mathrm{M}} b^\dagger b + n\,\hbar\omega_{\mathrm{R}} - n^2 \frac{\hbar g^2}{\omega_{\mathrm{M}}}. \tag{2.30}$$

Moreover, labeling the eigenstates of $\bar{H}^{(n)}$ with $|n, m_n\rangle$, where n and m_n are, respectively, the number of photons and mechanical excitations (phonons), one obtains:

$$\begin{aligned} \bar{H}^{(n)}|n, m_n\rangle =& \left(\hbar\omega_{\mathrm{M}} b^\dagger b + n\hbar\omega_{\mathrm{R}} - \frac{n^2\hbar g^2}{\omega_{\mathrm{M}}}\right)|n, m_n\rangle \\ =& \left(m\hbar\omega_{\mathrm{M}} + n\hbar\omega_{\mathrm{R}} - \frac{n^2\hbar g^2}{\omega_{\mathrm{M}}}\right)|n, m_n\rangle \\ =& E_{nm}|n, m_n\rangle, \end{aligned} \tag{2.31}$$

where we have used the simple relation

$$b^\dagger b|n, m_n\rangle = m|n, m_n\rangle \tag{2.32}$$

and then defined the eigenvalues as

$$E_{nm} = m\hbar\omega_{\mathrm{M}} + n\hbar\omega_{\mathrm{R}} - \frac{n^2\hbar g^2}{\omega_{\mathrm{M}}}. \tag{2.33}$$

Chapter 3

Photodetection in USC Regime

In the ultrastrong coupling regime the standard normal order correlation functions fail to describe the output photon emission rate and photon statistics. A clear evidence of this fact is that the standard input-output relations would predict, for example, a finite output photon flux proportional to the average number of cavity photons for a vacuum input [44, 63, 64], *i.e.*, $\langle A^-_{\rm out}(t)A^+_{\rm out}(t)\rangle \propto \langle a^\dagger(t)a(t)\rangle$, where $A^+_{\rm out}(t)$ and $A^-_{\rm out}(t)$ are the positive and negative components of the output field operator, respectively. Moreover, an incautious application of these standard relations for a system in its dressed ground state, would predict an unphysical stream of output photons. Indeed, the new dressed ground state now contains a finite number of photons (Eq. (1.32)), due to the counter-rotating terms in the Rabi Hamiltonian (Eq. (1.29)),

$$\left\langle G \left| a^\dagger a \right| G \right\rangle \neq 0\,. \tag{3.1}$$

In order to find the right procedure to calculate the output photon emission rate, namely, the rate of photons that are actually absorbed by a photodetector, we must come back to the Glauber work [111].

3.1 Standard Photodetection Theory

Usually, all devices that measure the intensity of a light beam depend on the absorption of photons that induce an observable response in the absorbing system. In particular, an ideal broadband detector consists of a single atom that becomes ionized in the act of absorbing a photon, so that the electron

detached from the atom makes its presence known as an electrical pulse. With initial $|I\rangle$ and final $|F\rangle$ state, the matrix element of the atom-field interaction Hamiltonian in Eq. (1.11) between these states is

$$\langle F\,|V|\,I\rangle = \langle F\,|-\mathbf{d}\cdot\mathbf{E}(\mathbf{r})|\,I\rangle = \left\langle F\,\middle|-\mathbf{d}\cdot\mathbf{E}^{+}(\mathbf{r})\middle|\,I\right\rangle, \tag{3.2}$$

where $\mathbf{d}$ is the dipole moment operator and $\mathbf{E}(\mathbf{r})$ is the the general quantized electric field in the Schrödinger representation with $\mathbf{k}\cdot\mathbf{r} \ll 1$

$$\mathbf{E}(\mathbf{r},t) = i\sum_{\mathbf{k}\lambda}\sqrt{\frac{\hbar\omega_k}{2\epsilon_0 V}}\left[a_{\mathbf{k}\lambda}e^{i(\mathbf{k}\cdot\mathbf{r}-\omega_k t)} - a^{\dagger}_{\mathbf{k}\lambda}e^{-i(\mathbf{k}\cdot\mathbf{r}-\omega_k t)}\right]. \tag{3.3}$$

The general quantized electric field in Eq. (3.3) can be decomposed in its positive- and negative-frequency components

$$\begin{aligned}\mathbf{E}^{+}(\mathbf{r},t) &= i\sum_{\mathbf{k}\lambda}\sqrt{\frac{\hbar\omega_k}{2\epsilon_0 V}}a_{\mathbf{k}\lambda}e^{i(\mathbf{k}\cdot\mathbf{r}-\omega_k t)}\\ \mathbf{E}^{-}(\mathbf{r},t) &= i\sum_{\mathbf{k}\lambda}\sqrt{\frac{\hbar\omega_k}{2\epsilon_0 V}}a^{\dagger}_{\mathbf{k}\lambda}e^{-i(\mathbf{k}\cdot\mathbf{r}-\omega_k t)},\end{aligned} \tag{3.4}$$

In Eq. (3.2) only the positive-frequency component $\mathbf{E}^{+}(\mathbf{r},t)$ appears, which contains the annihilation operator and is therefore the operator responsible for the absorption process. The initial state $|I\rangle$ consists of an atom in the ground state $|g\rangle$ and a radiation field in a general state $|i\rangle$ (that is not necessarily a photon number state or a product of such states), while the final state $|F\rangle$ consists of an atomic state $|e\rangle$ in the continuum and a radiation field in a general state $|f\rangle$. Since the dipole moment operator $\mathbf{d}$ acts only on the atomic states while $\mathbf{E}^{+}(\mathbf{r},t)$ acts only on the states of the field, Eq. (3.2) can be factorized:

$$\langle F\,|V|\,I\rangle = -\langle e\,|\mathbf{d}|\,g\rangle\cdot\left\langle f\,\middle|\mathbf{E}^{+}(\mathbf{r})\middle|\,i\right\rangle. \tag{3.5}$$

As the transition probability is proportional to $|\langle F|V|I\rangle|^2$, the probability that the field will undergo a transition $|i\rangle \to |f\rangle$ is proportional to

$$|\langle f|\mathbf{E}^+(\mathbf{r})|i\rangle|^2. \tag{3.6}$$

In practice, the final state $|f\rangle$ of the radiation field is rarely, if ever, observed; for this reason, it is necessary to sum the transition probability over all possible final states to which transitions from $|i\rangle$ are allowed:

$$\sum_f |\langle f|\mathbf{E}^+(\mathbf{r})|i\rangle|^2 = \sum_f \langle i|\mathbf{E}^-(\mathbf{r})|f\rangle \cdot \langle f|\mathbf{E}^+(\mathbf{r})|i\rangle . \tag{3.7}$$

Using the completeness relation $\sum_f |f\rangle\langle f| = 1$ in Eq. (3.7) and considering that the initial state is often a mixed state and cannot be prepared with infinite precision so that it is more realistic to resort to average values, one finds that the transition probability or the output of the one-atom detector is proportional to

$$\{\langle i|\mathbf{E}^-(\mathbf{r})\mathbf{E}^+(\mathbf{r})|i\rangle\}_{av} = \langle \mathbf{E}^-(\mathbf{r})\mathbf{E}^+(\mathbf{r})\rangle \tag{3.8}$$

It is important to note that, since $\mathbf{E}^-(\mathbf{r})$ and $\mathbf{E}^+(\mathbf{r})$ do not commute, the order in which they appear in Eq. (3.8) is significant. In fact, whereas in the classical case the order in which the fields are written in a product such as $\langle \mathbf{E}^*(\mathbf{x_1})\mathbf{E}(\mathbf{x_2})\rangle$ is not relevant, in a quantum formulation the operators must be always be written in *normal order* [112], that is, all operators of the field oscillating at negative frequencies lie to the left of those oscillating at positive frequencies.

3.2 Standard Input-Output Theory

In the standard input-output theory it is considered a system interacting weakly with an external multi-mode field. The feature of the system are not taken into account in the first moment, that is, the system can in turn be composed of two or more subsystems in strong-, weak- or ultrastrong-interaction

between their. The external multi-mode field (*e.g.*, a transmission line), can be modeled as an assembly of harmonic oscillators, that is, a thermal bath. The system-bath coupling Hamiltonian can be written as

$$H_{\mathrm{SB}} = \sum_n \alpha_n (b_n + b_n^\dagger) X, \tag{3.9}$$

where b_n and $b_n^\dagger$ are the bosonic operators for the n-th bath mode, X is a particular one of the system operators (*e.g.*, the intracavity field operator $X = a + a^\dagger$) that couples with the external bath, and α_n is the coupling strength to the mode n. According to the input-output theory for resonators, where the bath is explicitly treated as an external cavity field in order to determine the effect of the intracavity dynamics on the quantum statistics of the output field, the output field operator can be related through a boundary condition to the intracavity field and the input field operators [113].

The input and output field operators (see Fig. 3.1) are defined as ($\hbar = 1$)

$$A_{\mathrm{in}}(t) = \frac{1}{2}\int_0^\infty \mathrm{d}\omega \sqrt{\frac{\hbar}{\pi\omega v}} \left\{ b\left(\omega, t_0\right) e^{-i\omega(t-t_0)} + b^\dagger\left(\omega, t_0\right) e^{i\omega(t-t_0)} \right\}, \tag{3.10}$$

$$A_{\mathrm{out}}(t) = \frac{1}{2}\int_0^\infty \mathrm{d}\omega \sqrt{\frac{\hbar}{\pi\omega v}} \left\{ b\left(\omega, t_1\right) e^{-i\omega(t-t_1)} + b^\dagger\left(\omega, t_1\right) e^{i\omega(t-t_1)} \right\}, \tag{3.11}$$

in which $t_0 < t$ (the input) is an initial time in the remote past, $t_1 > t$ (the output) is assumed to be in the remote future and v is the speed of light in the transmission line.

The positive- and negative-frequency components of the input and output fields are given by

$$A_{\mathrm{out}}^+(t) = \frac{1}{2}\int_0^\infty \mathrm{d}\omega \sqrt{\frac{\hbar}{\pi\omega v}} b\left(\omega, t_1\right) e^{-i\omega(t-t_1)}, \tag{3.12}$$

$$A_{\mathrm{out}}^-(t) = \left[A_{\mathrm{out}}^+(t)\right]^\dagger \tag{3.13}$$

and

$$A_{\mathrm{in}}^+(t) = \frac{1}{2}\int_0^\infty \mathrm{d}\omega \sqrt{\frac{\hbar}{\pi\omega v}} b\left(\omega, t_0\right) e^{-i\omega(t-t_0)}, \tag{3.14}$$

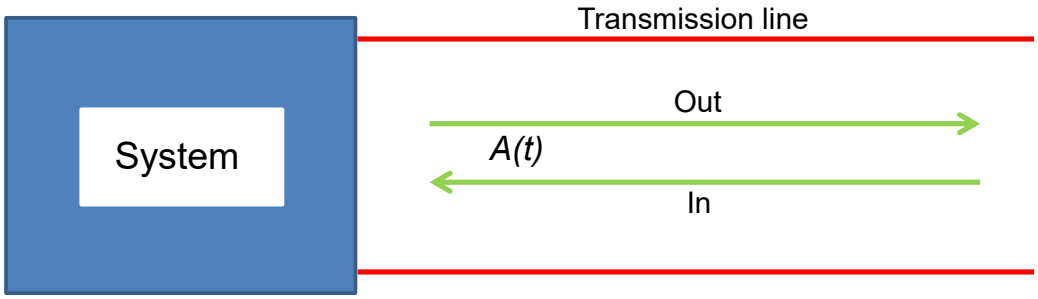

Figure 3.1: sketch of a system interacting with a input and output fields (*reservoir* in this specific case. It is represented by a transmission line). The system is a rather small localized object which interacts with a one-sided field which streams in from the left, interacts with the system, and streams out to the left. Damping appears as *radiation* damping.

$$A_{\text{in}}^{-}(t) = [A_{\text{in}}^{+}(t)]^{\dagger}, \tag{3.15}$$

respectively, so that

$$A_{\text{in}}(t) = A_{\text{in}}^{+}(t) + A_{\text{in}}^{-}(t), \tag{3.16}$$

$$A_{\text{out}}(t) = A_{\text{out}}^{+}(t) + A_{\text{out}}^{-}(t). \tag{3.17}$$

In the Markovian approximation, valid when the system-bath interaction is weak, the input-output relation can be written as [114]

$$A_{\text{out}}(t) = A_{\text{in}}(t) - \sqrt{\frac{\hbar\kappa}{2\omega_{\text{c}}v}}X, \tag{3.18}$$

where the rate κ represents the cavity loss due to the interaction of the single cavity mode ω_{c} with the continuum of the external modes. By taking the Fourier transform of Eq. (3.18) and summing up only the components at positive frequency, we obtain

$$A_{\text{out}}^{+} = A_{\text{in}}^{+} - \sqrt{\frac{\hbar\kappa}{2\omega_{\text{c}}v}}X^{+}. \tag{3.19}$$

According to Eq. (3.8), the extracavity emission rate is given by $\langle A_{\text{out}}^{-}A_{\text{out}}^{+}\rangle$ and, for the case of an input in the vacuum state, it can be readily obtained

by applying the input-output relation (3.19):

$$2\omega_c v\langle A_{\text{out}}^- A_{\text{out}}^+\rangle = \kappa\langle X^- X^+\rangle \tag{3.20}$$

In standard quantum optics, the photon emission rate is just proportional to the cavity photon number, *i.e.*, $\langle X^- X^+\rangle \propto \langle a^\dagger a\rangle$ since, according to their actual dynamics, the negative- and positive-frequency components of X are simply proportional, respectively, to the creation and annihilation operators $a^\dagger$ and a.

$$2\omega_c v\langle A_{\text{out}}^- A_{\text{out}}^+\rangle \propto \kappa\langle a^\dagger a\rangle \tag{3.21}$$

3.3 Look at USC regime

So far, we have not taken into account the feature of the system. In cavity QED, when the coupling strength fall into USC regime, due to the presence of the counter-rotating terms in the Rabi Hamiltonian (Eq. (1.29)), Eq. (3.21) is no longer valid. This can be observed by considering the Heisenberg equation of motion for the annihilation operator a:

$$\dot{a} = -\frac{i}{\hbar}[a, H_{\text{R}}] = -\frac{i}{\hbar}[\omega_c a + g(\sigma_- + \sigma_+)]. \tag{3.22}$$

In addition to the first two terms, proportional to the operators a and σ_- and oscillating at positive frequencies, the right-hand side of Eq. (3.22) also contains a term proportional to σ_-, which oscillates at negative frequency. This implies that the solution of Eq. (3.22) will be of the form:

$$a(t) \sim e^{-i\omega_c t} + \ldots e^{-i\omega_q t} + \ldots e^{i\omega_q t}. \tag{3.23}$$

A similar result can be obtained for the dynamics of the creation operator $a^\dagger$. Eq. (3.23) clearly shows that, in the presence of the counter-rotating terms, the annihilation operator a is not the positive-frequency component of the cavity field operator as it now contains a mixing of positive and negative frequencies. Similarly, the negative-frequency component of the cavity field operator will not coincide with the creation operator $a^\dagger$. In general, that

result remain valid for any Hybrid quantum system (HQS) in USC regime and a new approach to measuring the extracavity emission rate is required.

In the cavity QED case, in order to find the actual positive- and negative-frequency components of the electric-field operator X (or any other boson-field) in the Schrödinger picture, we first expand it in the dressed basis $\{|j\rangle, |k\rangle\}$ of the energy eigenstates of the Rabi Hamiltonian (Eq. (1.29)) [63]:

$$X^{(S)} = \sum_{j,k} |j\rangle\langle j| X^{(S)} |k\rangle\langle k| = \sum_{j,k} X_{jk} |j\rangle\langle k| . \tag{3.24}$$

In the case of a generic HQS, we first expand it in the dressed basis of the energy eigenstates of the total Hamiltonian. Given the relation between the Heisenberg and Schrödinger pictures for the operator X

$$X^{(H)}(t) = U^{\dagger}(t) X^{(S)} U(t), \tag{3.25}$$

where $U(t) = exp(-iH_{\mathrm{R}}t/\hbar)$, and substituting Eq. (3.24) in Eq. (3.25), we obtain

$$X^{(H)}(t) = \sum_{j,k} X_{jk}\, e^{\frac{i}{\hbar}\omega_j t} |j\rangle\langle k| e^{-\frac{i}{\hbar}\omega_k t} = \sum_{j,k} X_{jk}\, e^{-\frac{i}{\hbar}(\omega_k - \omega_j)t} |j\rangle\langle k|, \tag{3.26}$$

where $X_{jk} \equiv \langle j | X | k \rangle$. Looking at Eq. (3.26), we can observe that the positive- and negative-frequency components of the electric-field operator X are obtained, respectively, for $k > j$ (so that $\omega_k > \omega_j$) and $k < j$ (so that $\omega_k < \omega_j$):

$$\begin{aligned} X^{+} &= \sum_{j,k>j} X_{jk} |j\rangle\langle k|, \\ X^{-} &= \sum_{j,k<j} X_{jk} |j\rangle\langle k| . \end{aligned} \tag{3.27}$$

The most noteworthy aspect of these results is that, in the ultrastrong coupling regime, one correctly obtains $X^{+}|G\rangle = 0$ for the system in its ground state $|G\rangle$ in contrast to $a|G\rangle \neq 0$.

Moreover, as the dressed ground state $|G\rangle$ contains only virtual photons,

while the operator $N \equiv X^- X^+$ represents the physical photons that can be experimentally detected, we correctly obtain that

$$\left\langle G \left| X^- X^+ \right| G \right\rangle = 0. \tag{3.28}$$

In the same way, Eqs.(3.27) can be used to calculate the quantum mechanical zero-delay n-th order coherence function for an input field in the dressed ground state [63]

$$g^{(n)}(t,t) \equiv \frac{\langle (X^-(t))^n (X^+(t))^n \rangle}{\langle X^-(t) X^+(t) \rangle^n}, \tag{3.29}$$

considering that, in the limit $g \to 0$, the field operators X^- and X^+ reduce to the standard photon operators $a^\dagger, a$ and the standard relation

$$g^{(n)}(t,t) \equiv \frac{\langle (a^\dagger(t))^n (a(t))^n \rangle}{\langle (a^\dagger(t))(a(t)) \rangle^n}, \tag{3.30}$$

for the time-dependent zero-delay normalized n-th order correlation function is recovered.

Chapter 4

Dissipation

In all physical processes there is an associated loss mechanism so, quantum mechanical systems must always be regarded as open systems. Any realistic system is subjected to a coupling to an environment which influences it in a non-negligible way. Most interesting systems are too complicated to be described, in practice, by the underlying microscopic laws of physics. Since perfect isolation of quantum systems is not possible, a complete microscopic description of the enviromental degrees of freedom is not feasible if not only partially. A microscopic approach would not provide the desidered solution to the problem since, even if a solution of the microscopic evolution equations were possible, it would give a huge amount of information useless for a realistic description. Therefore, we need to seek for a simpler probabilistic description of an open system's dynamics and to use a theory that allows the treatment of complex systems (which involve even an infinite number of degrees of freedom) by restricting the mathematical formulation to a small number of relevant variables. An important property of the quantum dynamics of an open system is that, in contrast to the case of closed systems, it cannot, in general, be represented in terms of a unitary time evolution. For this reason in many cases it turns out to be useful to use, instead, the so-called master-equation approach, in which the dynamics of an open system is formulated by means of an appropriate equation of motion for its density matrix operator. Many cavity QED and circuit QED experiments are accurately described by neglecting the light-matter interaction when the dissipative part of the master equation is obtained. That is a simplification that leads to the so-called *standard quantum optical master equation* [114–116].

It has been recently demonstrated that, in the atom-field system case when the interaction strength increases up to the breakdown of the RWA and the system enters the ultrastrong coupling regime, the standard master equation fails to correctly describe the dissipation processes and leads to unphysical results as well [12]. In general, for hybrid quantum systems in USC regime where the interaction between the subsystems define new *dressed eigenstates*, we need to use a proper procedure that take account the hybridization of the subsystems. The proper procedure leads to the *dressed master equation* and, it will be described in Sec. 4.1. In Sec. 4.1.1 and Sec. 4.1.2, a dressed master equation is obatained in the optical and optomechanical case, respectively.

4.1 Dressed Master Equation

An open system S is a quantum system which is coupled to another system B usually called *reservoir*. It represents a subsystem of the combined total system $S + B$ (see Fig. 4.1). The term *reservoir* refers to an environment with an infinite number of degrees of freedom such that the frequencies of the reservoir modes form a continuum. As will be seen, it is this property which generally leads to an irreversible behaviour of the open quantum system. As a consequence of its internal dynamics and of the interaction with the external environment B, the state of the subsystem S will change over the time. This interaction leads to a certain system-environment correlations such that the resulting state changes of S can no longer be represented in terms of unitary Hamiltonian dynamics. The dynamics of the subystem S induced by the Hamiltonian evolution of the total system is often referred to as *reduced system dynamics*. We denote by $\mathcal{H}_{\mathrm{S}}$ the Hilbert space of the system and by $\mathcal{H}_{\mathrm{B}}$ the Hilbert space of the *reservoir*. The Hilbert space of the total system is then given by the tensor product space $\mathcal{H}_{\mathrm{S}} \otimes \mathcal{H}_{\mathrm{B}}$. The total Hamiltonian of the system is assumed to be of the form

$$H = H_{\mathrm{S}} + H_{\mathrm{B}} + H_{\mathrm{SB}}, \tag{4.1}$$

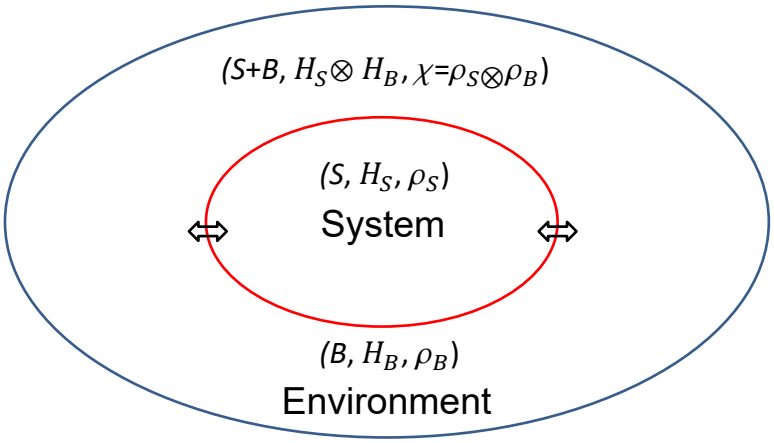

Figure 4.1: Schematic picture of an open quantum system.

where H_{S} and H_{B} denote respectively, the free Hamiltonian of the system S and of the *reservoir* B and H_{SB} describs the Hamiltonian interaction between the system and the *reservoir*. We will denote by $\chi(t)$ the density operator for the total system $S+B$ and the reduced density operator $\rho(t)$ by

$$\rho(t) = tr_B[\chi(t)], \tag{4.2}$$

where the trace is taken on the *reservoir* states. If O is an operator of the Hilbert space of the system S, its average can be calculated in the Schrödinger picture by having knowledge of $\rho(t)$ alone:

$$\langle O \rangle = tr_{(S\otimes B)}[O\,\chi(t)] = tr_S\{O\,tr_B[\chi(t)]\} = tr_S[O\rho(t)]. \tag{4.3}$$

In the master-equation approach, the fundamental task is to isolate and determine the interesting physical properties of the system S by obtaining an equation for $\rho(t)$ with the properties of the *reservoir* entering only as parameters. The Schrödinger equation for $\chi(t)$ reads ($\hbar = 1$):

$$\dot{\chi} = \frac{1}{i\hbar}[H, \chi] \tag{4.4}$$

where H is given by Eq. (4.1). In order to separate the rapid motion generated by $H_{\mathrm{S}} + H_{\mathrm{B}}$ from the slow motion generated by the interaction H_{SB}, it

is convenient to transform Eq. (4.4) in the interaction picture

$$\tilde{\chi}(t) = e^{\frac{i}{\hbar}(H_S+H_B)t}\,\chi\, e^{-\frac{i}{\hbar}(H_S+H_B)t}, \tag{4.5}$$

so that from Eq. (4.1) and Eq. (4.4) we obtain

$$\dot{\tilde{\chi}} = \frac{1}{i\hbar}[\tilde{H}_{SB}(t), \tilde{\chi}], \tag{4.6}$$

where $\tilde{H}_{SB}(t)$ is explicity time-dependent

$$\tilde{H}_{SB}(t) = e^{\frac{i}{\hbar}(H_S+H_B)t}\, H_{SB}\, e^{-\frac{i}{\hbar}(H_S+H_B)t}. \tag{4.7}$$

Eq. (4.6) can be integrated formally to give

$$\tilde{\chi}(t) = \chi(0) + \frac{1}{i\hbar}\int_0^t dt'\,[\tilde{H}_{SB}(t'), \tilde{\chi}(t')], \tag{4.8}$$

and after substituting $\tilde{\chi}(t)$ in the commutator in Eq. (4.6), we obtain:

$$\dot{\tilde{\chi}}(t) = \frac{1}{i\hbar}[\tilde{H}_{SB}(t), \tilde{\chi}(0)] - \frac{1}{\hbar^2}\int_0^t dt'\,[\tilde{H}_{SB}(t), [\tilde{H}_{SB}(t'), \tilde{\chi}(t')]] \tag{4.9}$$

This equation is exact, as we have simply written Eq. (4.4) in a convenient way in order to identify some reasonable approximations. The first assumption is that the interaction is turned on at $t = 0$, so that no correlations exist between the system and the *reservoir* before this initial time. Then, the total system density matrix $\chi(0) = \tilde{\chi}(0)$ can be factorized

$$\chi(0) = \rho(0)B_0, \tag{4.10}$$

where B_0 is the initial *reservoir* density operator. After tracing over the *reservoir*, Eq. (4.9) gives

$$\dot{\tilde{\rho}} = -\frac{1}{\hbar^2}\int_0^t dt'\, tr_B\{[\tilde{H}_{SB}(t), [\tilde{H}_{SB}(t'), \tilde{\chi}(t')]]\}, \tag{4.11}$$

where we assumed that $tr_B[\tilde{H}_{\rm SB}(t)B_0] = 0$, a result that is guaranteed if the *reservoir* operators coupling to S have zero mean in the state B_0. Although the system and the *reservoir* are not supposed to interact at $t = 0$, at later times correlations may arise due to the coupling of the system and the *reservoir* through the interaction Hamiltonian $H_{\rm SB}$. If the coupling is weak, at all times $\chi(t)$ will only show deviations of order of $H_{\rm SB}$ from an uncorrelated state. Moreover, since the *reservoir* B is a large system, its state should be virtually unaffected by the coupling to S so that we can write

$$\tilde{\chi}(t) = \tilde{\rho}(t)B_0 + \mathcal{O}(H_{\rm SB}). \tag{4.12}$$

As the system-reservoir interaction is considered to be weak, terms higher than second order in $H_{\rm SB}$ can be neglected [117], and Eq. (4.11) can be written as

$$\dot{\tilde{\rho}} = -\frac{1}{\hbar^2}\int_0^t dt'\, tr_B\{[\tilde{H}_{\rm SB}(t), [\tilde{H}_{\rm SB}(t'), \tilde{\rho}(t')B_0]]\}. \tag{4.13}$$

This approximation is referred to as the *Born approximation*.

Eq. (4.13) is still a complicated equation and, in particular, it is not Markovian, since the future evolution of $\tilde{\rho}(t)$ depends on its past history through the integration over $\tilde{\rho}(t')$ (conversely, the time evolution of a Markovian system depends only on its present state). However, a Markovian behavior seems reasonable because, if the *reservoir* is a large system mantained at thermal equilibrium (bath), it is not expected to preserve the minor changes induced by its interaction with S for very long; not for long enough to significantly affect the future evolution of S. On the basis of these physical grounds, one can make the so-called *Markov approximation* by substituting $\tilde{\rho}(t')$ for $\tilde{\rho}(t)$ in Eq. (4.13) to obtain the *Born-Markov master equation*

$$\dot{\tilde{\rho}} = -\frac{1}{\hbar^2}\int_0^t dt'\, tr_B\{[\tilde{H}_{\rm SB}(t), [\tilde{H}_{\rm SB}(t'), \tilde{\rho}(t)B_0]]\}. \tag{4.14}$$

The Born-Markov approximation performed above do not guarantee, however, that the resulting Eq. (4.14) gives rise a first-order linear differential

equation for the reduced density matrix, which is known as quantum Markovian master equation in *Lindblad* form. One therefore performs a further *secular* approximation which involves an averaging over the rapidly oscillating terms in the master equation and is known as the rotating wave approximation. To explain the procedure let us write the Schrodinger picture interaction Hamiltonian, $\tilde{H}_{\rm SB}$ in the form

$$\tilde{H}_{\rm SB} = \sum_i \tilde{S}_i \tilde{B}_i, \tag{4.15}$$

where $\tilde{S}_i = \tilde{S}_i^\dagger$ are system operators in the Hilbert space of S and $\tilde{B}_i = \tilde{B}_i^\dagger$ are i independent baths operators (reservoir of quantum harmonic oscillators at thermal equilibrium), each one described by the free Hamiltonian, $H_{\rm B} = \hbar \sum_m \nu_m \hat{b}_m^\dagger \hat{b}_m$ in the Hilbert space of B, where $\tilde{b}_m^\dagger, \tilde{b}_m$ are ladder operators for the bathmode m with frequency ν_m.

In cavity QED and cavity optomechanical, system operators can always be written as sum of ladder operators, weakly coupled to independent baths. In that cases Eq. (4.15) becomes

$$H_{\rm SB} = \hbar \sum_{i,m} \alpha_{i,m} (s_i + s_i^\dagger)(b_{i,m} + b_{i,m}^\dagger). \tag{4.16}$$

For the qubit $s_i, s_i^\dagger \to \sigma_-, \sigma_+$, for the resonator $s_i, s_i^\dagger \to a, a^\dagger$, while for the mobile mirror $s_i, s_i^\dagger \to c, c^\dagger$. Cavity QED and cavity optomechanical systems have a total excitation number with well-defined parity. Since the dressed states (eigenstates of the total Hamiltonian system $H_{\rm S}$), also have a well-defined parity and the operator s_i, $s_i^\dagger$ change the excitaion number by one, it is easy to verify that the system operators flip the parity when applied on a state. So it follows that, the diagonal matrix elements of the system operators respect with the dressed basis $\{|j\rangle\}$ are zero, $\langle j| \tilde{S}_i |j\rangle = S_{jj}^i = 0$. The secular approximation is easily carried out if one decomposes the interaction Hamiltonian $\tilde{H}_{\rm SB}$ into eigenoperators of the system Hamiltonian $H_{\rm S}$. Expressing the system Hamiltonian $H_{\rm S}$ in the dressed basis of its energy

eigenstates

$$H_{\mathrm{S}} = \sum_j E_j \left|j\right\rangle\!\left\langle j\right|, \tag{4.17}$$

we can define the eigenoperators as follow

$$\tilde{S}_i(\omega) = \sum_{k-j=\omega} S^i_{jk} \left|j\right\rangle\!\left\langle k\right|. \tag{4.18}$$

The sum in this expression is extended over all energy eigenvalues j and k of $\tilde{H}_{\mathrm{S}}$ with a fixed energy difference of ω so, summing over all energy differences and employing the completeness relation, we get

$$\tilde{S}_i = \sum_\omega \tilde{S}_i(\omega) = \sum_\omega \tilde{S}_i^\dagger(\omega). \tag{4.19}$$

An immediate consequence of this definition is that the following relations are satisfied,

$$\begin{aligned}
&[\tilde{H}_{\mathrm{S}}, \tilde{S}_i(\omega)] = -\omega \tilde{S}_i(\omega) \\
&[\tilde{H}_{\mathrm{S}}, \tilde{S}_i^\dagger(\omega)] = \omega \tilde{S}_i^\dagger(\omega) \\
&[\tilde{H}_{\mathrm{S}}, \tilde{S}_i^\dagger(\omega)\tilde{S}_l(\omega)] = 0 \\
&\tilde{S}_i^\dagger(\omega) = \tilde{S}_i(-\omega) \\
&\tilde{S}_i(0) = 0.
\end{aligned} \tag{4.20}$$

The corresponding interaction picture operators take the form

$$e^{\frac{i}{\hbar}H_{\mathrm{S}}t}\tilde{S}_i(\omega)e^{-\frac{i}{\hbar}H_{\mathrm{S}}t} = e^{-i\omega t}\tilde{S}_i(\omega), \quad e^{\frac{i}{\hbar}H_{\mathrm{S}}t}\tilde{S}_i^\dagger(\omega)e^{-\frac{i}{\hbar}H_{\mathrm{S}}t} = e^{i\omega t}\tilde{S}_i^\dagger(\omega). \tag{4.21}$$

With the Eq. (4.20) the interaction Hamiltonian $\tilde{H}_{\mathrm{SB}}$ into interaction picture can be separate in negative and positive frequencies and, it can put in very simple form

$$\begin{aligned}
\tilde{H}_{\mathrm{SB}}(t) &= \hbar \sum_l \left\{ \sum_{\omega>0} e^{-i\omega t}\tilde{S}_l(\omega)\tilde{B}_l^\dagger(t) + \sum_{\omega<0} e^{i\omega t}\tilde{S}_l(-\omega)\tilde{B}_l(t) \right\} \\
&= \hbar \sum_l [\tilde{S}_l(t)\tilde{B}_l^\dagger(t) + \tilde{S}_l^\dagger(t)\tilde{B}_l(t)].
\end{aligned} \tag{4.22}$$

where

$$\begin{aligned}\tilde{B}_l(t) &= \sum_m \alpha_{l,m} b_{l,m} e^{-i\nu_{l,m}t} \\ \tilde{S}_l(t) &= \sum_{\omega>0} \tilde{S}_l(\omega) e^{-i\omega t}\end{aligned} \tag{4.23}$$

Inserting Eq. (4.22) into the master equation Eq. (4.14), we obtain

$$\begin{aligned}\dot{\tilde{\rho}}(t) = \sum_l \Bigg\{ &\int_0^t dt' \, [\tilde{S}_l(t')\tilde{\rho}(t)\tilde{S}_l(t) - \tilde{S}_l(t)\tilde{S}_l(t')\tilde{\rho}(t)]\langle \tilde{B}_l^\dagger(t)\tilde{B}_l^\dagger(t')\rangle \\ &+ \int_0^t dt' \, [\tilde{S}_l^\dagger(t')\tilde{\rho}(t)\tilde{S}_l^\dagger(t) - \tilde{S}_l^\dagger(t)\tilde{S}_l^\dagger(t')\tilde{\rho}(t)]\langle \tilde{B}_l(t)\tilde{B}_l(t')\rangle \\ &+ \int_0^t dt' \, [\tilde{S}_l^\dagger(t')\tilde{\rho}(t)\tilde{S}_l(t) - \tilde{S}_l(t)\tilde{S}_l^\dagger(t')\tilde{\rho}(t)]\langle \tilde{B}_l^\dagger(t)\tilde{B}_l(t')\rangle \\ &+ \int_0^t dt' \, [\tilde{S}_l(t')\tilde{\rho}(t)\tilde{S}_l^\dagger(t) - \tilde{S}_l^\dagger(t)\tilde{S}_l(t')\tilde{\rho}(t)]\langle \tilde{B}_l(t)\tilde{B}_l^\dagger(t')\rangle + H.c. \Bigg\}.\end{aligned} \tag{4.24}$$

The reservoir correlation functions in Eq. (4.24) can be evaluated explicitly:

$$\begin{aligned}\langle \tilde{B}_l(t)\tilde{B}_l(t')\rangle &= \langle \tilde{B}_l^\dagger(t)\tilde{B}_l^\dagger(t')\rangle = 0 \\ \langle \tilde{B}_l^\dagger(t)\tilde{B}_l(t')\rangle &= \sum_m |\alpha_{l,m}|^2 e^{i\nu_{l,m}(t-t')} \, \bar{n}(\nu_{l,m}, T) \\ \langle \tilde{B}_l(t)\tilde{B}_l^\dagger(t')\rangle &= \sum_m |\alpha_{l,m}|^2 e^{-i\nu_{l,m}(t-t')} \, \big[\bar{n}(\nu_{l,m}, T) + 1\big],\end{aligned} \tag{4.25}$$

where $\bar{n}(\nu_{l,m}, T) = \left[e^{(\hbar\nu_{l,m}/k_{\mathrm{B}}T)} - 1\right]^{-1}$ is the mean photon number for an oscillator with frequency $\nu_{l,m}$ in thermal equilibrium at temperature T. The nonvanishing reservoir correlation functions Eq. (4.25) involve a summation over the reservoir oscillators. This summation can be changed to an integration by introducing the density of states $g(\nu)$ such that $g(\nu)d\nu$ gives the number of oscillators with frequencies in the interval ν to $\nu + d\nu$. The

reservoir correlation functions then become

$$\begin{aligned}\langle \tilde{B}_l^\dagger(t)\tilde{B}_l(t')\rangle &= \int_0^\infty d\nu_l\, g(\nu_l)|\alpha(\nu_l)|^2\, \bar{n}(\nu_l,T)e^{i\nu_l(t-t')}\\ \langle \tilde{B}_l(t)\tilde{B}_l^\dagger(t')\rangle &= \int_0^\infty d\nu_l\, g(\nu_l)|\alpha(\nu_l)|^2\, \big[\bar{n}(\nu_l,T)+1\big]e^{-i\nu_l(t-t')}.\end{aligned} \tag{4.26}$$

Inserting Eq. (4.23) and Eq. (4.26), into the master equation Eq. (4.24) and, defining $\tau = t - t'$ we obtain

$$\dot{\tilde{\rho}}(t) = \sum_l \sum_{(\omega,\omega')>0} \Big[\mathcal{A}^l_{\omega,\omega'}(t) + \mathcal{B}^l_{\omega,\omega'}(t) + \mathcal{C}^l_{\omega,\omega'}(t) + \mathcal{D}^l_{\omega,\omega'}(t)\Big], \tag{4.27}$$

where

$$\begin{aligned}\mathcal{A}^l_{\omega,\omega'}(t) = &\int_0^t d\tau\, e^{i(\omega-\omega')t}\, e^{i\omega'\tau}\Big(\tilde{S}_l^\dagger(\omega')\tilde{\rho}(t)\tilde{S}_l(\omega) - \tilde{S}_l(\omega)\tilde{S}_l^\dagger(\omega')\tilde{\rho}(t)\Big)\\ &\times \int_0^\infty d\nu_l\, g(\nu_l)|\alpha(\nu_l)|^2\, \bar{n}(\nu_l,T)e^{i\nu_l\tau},\end{aligned} \tag{4.28}$$

$$\begin{aligned}\mathcal{B}^l_{\omega,\omega'}(t) = &\int_0^t d\tau\, e^{i(\omega-\omega')t}\, e^{-i\omega'\tau}\Big(\tilde{S}_l(\omega)\tilde{\rho}(t)\tilde{S}_l^\dagger(\omega') - \tilde{S}_l^\dagger(\omega')\tilde{S}_l(\omega)\tilde{\rho}(t)\Big)\\ &\times \int_0^\infty d\nu_l\, g(\nu_l)|\alpha(\nu_l)|^2\, \big[\bar{n}(\nu_l,T)+1\big]e^{-i\nu_l\tau},\end{aligned} \tag{4.29}$$

$$\begin{aligned}\mathcal{C}^l_{\omega,\omega'}(t) = &\int_0^t d\tau\, e^{i(\omega-\omega')t}\, e^{-i\omega'\tau}\Big(\tilde{S}_l^\dagger(\omega')\tilde{\rho}(t)\tilde{S}_l(\omega) - \tilde{\rho}(t)\tilde{S}_l(\omega)\tilde{S}_l^\dagger(\omega')\Big)\\ &\times \int_0^\infty d\nu_l\, g(\nu_l)|\alpha(\nu_l)|^2\, \bar{n}(\nu_l,T)e^{-i\nu_l\tau},\end{aligned} \tag{4.30}$$

$$\begin{aligned}\mathcal{D}^l_{\omega,\omega'}(t) = &\int_0^t d\tau\, e^{i(\omega-\omega')t}\, e^{i\omega'\tau}\Big(\tilde{S}_l(\omega)\tilde{\rho}(t)\tilde{S}_l^\dagger(\omega') - \tilde{\rho}(t)\tilde{S}_l^\dagger(\omega')\tilde{S}_l(\omega)\Big)\\ &\times \int_0^\infty d\nu_l\, g(\nu_l)|\alpha(\nu_l)|^2\, \big[\bar{n}(\nu_l,T)+1\big]e^{i\nu_l\tau}.\end{aligned} \tag{4.31}$$

The basic condition underlying the Markov approximation is that the reservoir correlation functions Eq. (4.26), decay sufficiently fast over a time t_B which is small compared to the system relaxation time t_S. It is important to note that a decay of the correlations can only be strictly valid for an environment which is infinitely large and involves a continuum of frequencies. In

the typical situation the reservoir is provided by a collection of harmonic oscillator modes. This time scale t_S is defined by a typical value for $\left|\omega - \omega^{'}\right|^{-1}$, that is by a typical value for the inverse of the frequency differences involved. If t_S is large compared to the relaxation time t_B of the bath the terms of the form $\exp[i(\omega - \omega^{'})t)]$ in Eq. (4.27), may be neglected since they oscillate very rapidly during the time t_B over which $\tilde{\rho}(t)$ varies appreciably. In practice, we are often interested only in a subset of the energy levels of the system for which all transitions have different frequencies. In this *secular* approximation, rapidly oscillating terms proportional to $\exp[i(\omega - \omega^{'})t)]$ for $\omega \neq \omega^{'}$ are neglected, ensuring that the quantum master equation is in Lindblad form. The corresponding condition is that the inverse frequency differences involved in the problem are small compared to the relaxation time of the system, that is $t_S \sim \left|\omega - \omega^{'}\right|^{-1} \ll t_B$. After setting $\omega = \omega^{'}$, Eq. (4.27) becomes

$$\dot{\tilde{\rho}}(t) = \sum_l \sum_{\omega>0} \left[\mathcal{A}^l_\omega(t) + \mathcal{B}^l_\omega(t) + \mathcal{C}^l_\omega(t) + \mathcal{D}^l_\omega(t) \right]. \tag{4.32}$$

Since t is a time typical of the time scale for $\tilde{\rho}(t)$ and the τ integration is dominated by much shorter times characterizing the decay of reservoir correlation functions, we can extend the τ integration to infinity and evaluate the integrals

$$\int_0^t d\tau \int_0^\infty d\nu \, e^{\pm i(\nu+\omega)\tau} g(\nu) |\alpha(\nu)|^2, \tag{4.33}$$

$$\int_0^t d\tau \int_0^\infty d\nu \, e^{\pm i(\nu+\omega)\tau} g(\nu) |\alpha(\nu)|^2 \, \bar{n}(\nu, T), \tag{4.34}$$

using the realation

$$\lim_{t\to\infty} \int_0^t d\tau \, e^{\pm i(\nu+\omega)\tau} = \pi\delta(\nu+\omega) \mp i \frac{P}{(\nu+\omega)}, \tag{4.35}$$

where P is Cauchy's principal value. If we consider that the term $\delta(\nu+\omega)$ is non-zero only for $\nu = -\omega$, and define the *Lamb shifts*

$$L_\omega = \frac{P}{2\pi} \int_0^\infty d\nu \, \frac{\Gamma(\nu)}{\nu+\omega}, \tag{4.36}$$

$$L'_\omega = \frac{P}{2\pi}\int_0^\infty d\nu\, \frac{\Gamma(\nu)\,\bar{n}(\nu,T)}{\nu+\omega}, \tag{4.37}$$

caused by coupling to the environment, Eq. (4.32) becomes

$$\dot{\tilde{\rho}}(t) = \sum_l \sum_{\omega>0} \left[\bar{\boldsymbol{\mathcal{A}}}^l_\omega(t) + \bar{\boldsymbol{\mathcal{B}}}^l_\omega(t) + \bar{\boldsymbol{\mathcal{C}}}^l_\omega(t) \right], \tag{4.38}$$

with

$$\begin{aligned}\bar{\boldsymbol{\mathcal{A}}}^l_\omega(t) =& \Big(2\tilde{S}_l^\dagger(\omega)\tilde{\rho}(t)\tilde{S}_l(\omega) - \tilde{S}_l(\omega)\tilde{S}_l^\dagger(\omega)\tilde{\rho}(t) - \tilde{\rho}(t)\tilde{S}_l(\omega)\tilde{S}_l^\dagger(\omega)\Big) \\ & \times \pi g(\omega)|\alpha(\omega)|^2\,\bar{n}(\omega,T),\end{aligned} \tag{4.39}$$

$$\begin{aligned}\bar{\boldsymbol{\mathcal{B}}}^l_\omega(t) =& \Big(2\tilde{S}_l(\omega)\tilde{\rho}(t)\tilde{S}_l^\dagger(\omega) - \tilde{S}_l^\dagger(\omega)\tilde{S}_l(\omega)\tilde{\rho}(t) - \tilde{\rho}(t)\tilde{S}_l^\dagger(\omega)\tilde{S}_l(\omega)\Big) \\ & \times \pi g(\omega)|\alpha(\omega)|^2\big[\bar{n}(\omega,T)+1\big],\end{aligned} \tag{4.40}$$

$$\begin{aligned}\bar{\boldsymbol{\mathcal{C}}}^l_\omega(t) =& -i\Big\{L'_\omega\big[\tilde{S}_l^\dagger(\omega)\tilde{S}_l(\omega)\tilde{\rho}(t) - \tilde{\rho}(t)\tilde{S}_l^\dagger(\omega)\tilde{S}_l(\omega) + \tilde{\rho}(t)\tilde{S}_l(\omega)\tilde{S}_l^\dagger(\omega) \\ & - \tilde{S}_l(\omega)\tilde{S}_l^\dagger(\omega)\tilde{\rho}(t)\big] + L_\omega\big[\tilde{S}_l^\dagger(\omega)\tilde{S}_l(\omega)\tilde{\rho}(t) - \tilde{\rho}(t)\tilde{S}_l^\dagger(\omega)\tilde{S}_l(\omega)\big]\Big\}.\end{aligned} \tag{4.41}$$

Finally, after defining the relaxation rate

$$\Gamma(\omega) = 2\pi g(\omega)|\alpha(\omega)|^2, \tag{4.42}$$

and the *Lindblad* superoperator $\mathcal{D}[O]\rho = \frac{1}{2}(2O\rho\,O^\dagger - \rho\,O^\dagger O - O^\dagger O\rho)$, we obtain the *dressed master equation* in the interaction picture:

$$\begin{aligned}\dot{\tilde{\rho}}(t) =& \sum_{l,\omega>0}\Gamma(\omega)\bar{n}(\omega,T)\mathcal{D}[\tilde{S}_l^\dagger(\omega)]\tilde{\rho}(t) + \sum_{l,\omega>0}\Gamma(\omega)(1+\bar{n}(\omega,T))\mathcal{D}[\tilde{S}_l(\omega)]\tilde{\rho}(t) \\ & - i\sum_{l,\omega>0}\Big\{L'_\omega\big[\big(\tilde{S}_l^\dagger(\omega)\tilde{S}_l(\omega) - \tilde{S}_l(\omega)\tilde{S}_l^\dagger(\omega)\big),\tilde{\rho}(t)\big] + L_\omega\big[\tilde{S}_l^\dagger(\omega)\tilde{S}_l(\omega),\tilde{\rho}(t)\big]\Big\}.\end{aligned} \tag{4.43}$$

Transforming back to the Schrödinger picture, Eq. (4.43) gives

$$\begin{aligned}\dot{\rho}(t) = &-\frac{i}{\hbar}[H'_{\mathrm{S}}, \rho(t)] + \sum_{l,\omega>0} \Gamma(\omega)\bar{n}(\omega, T)\mathcal{D}[\tilde{S}_l^{\dagger}(\omega)]\tilde{\rho}(t) \\ &+ \sum_{l,\omega>0} \Gamma(\omega)(1+\bar{n}(\omega, T))\mathcal{D}[\tilde{S}_l(\omega)]\tilde{\rho}(t),\end{aligned} \tag{4.44}$$

where we have defined the *Lamb-shifted* system Hamiltonian

$$H'_{\mathrm{S}} = H_{\mathrm{S}} - \sum_{l,\omega>0} \Big\{ L'_{\omega}\big(\tilde{S}_l^{\dagger}(\omega)\tilde{S}_l(\omega) - \tilde{S}_l(\omega)\tilde{S}_l^{\dagger}(\omega)\big) + L_{\omega}\tilde{S}_l^{\dagger}(\omega)\tilde{S}_l(\omega)\Big\}. \tag{4.45}$$

In most cases, the *Lamb-shifts* L_{ω} and L'_{ω} in Eq. (4.45) are small and can be neglected.

4.1.1 Optical Dressed Master Equation

When the atom-field interaction increases up to the breakdown of the RWA, the standard master equation approach leads to unphysical predictions. Since in the ultrastrong coupling regime $|g, 0\rangle$ is no longer the ground state, optical standard master equation will bring the ultrastrongly coupled qubit-resonator system outside of its true ground state $|G\rangle$. Indeed, if the system is initially prepared in the ground state $|G\rangle$, relaxation will generate photons in excess to those already present in the ground state even at $T = 0$, in which case no energy should be added to the system [64]. Furthermore, in the presence of a strong qubit-resonator coupling, transitions at widely separated frequencies appear, breaking down the standard white noise approximation. To avoid such annoyances, the qubit-resonator coupling and colored baths must be included in the treatment of dissipation. In this case, it is not possible to assign a unique dissipation channel to each bath mentioned above. Indeed, rather than transitions between eigenstates of the free Hamiltonian, $H_0 = \hbar\omega_{\mathrm{c}}a^{\dagger}a + \hbar\omega_{\mathrm{q}}\sigma_z/2$, coupling to the baths leads to transitions between the qubit-resonator entangled eigenstates $\{|G\rangle, |j, \pm\rangle\}$ of the Rabi Hamiltonian H_{R} (Eq. (1.29)). To simplify the notation, these states will be denoted below as $|j\rangle$, j increasing with energy. These states

can be approximated analytically or found exactly numerically. In order to properly treat the dissipation effects in cavity QED in USC regime, we need to use the *dressed master equation* (Eq. (4.44)) that, takes into account the qubit-resonator coupling neglecting high-frequency terms. In the dissipation process will be involved transitions between eigenstates, $|j\rangle \leftrightarrow |k\rangle$, at a rate that depends on the noise spectral density at frequency $\Delta_{kj} \equiv \hbar\omega_k - \hbar\omega_j = \omega$, where $\hbar\omega_j$ is the energy eigenvalue of $|j\rangle$, *i.e.*, $H_{\mathrm{R}}|j\rangle = \hbar\omega_j|j\rangle$. We need to distinguish between two different channels of losses, one for the cavity and one for the qubit. So that, we have to calculate the eigenoperators (using Eq. (4.18)), for the cavity $X = (a + a^\dagger)$

$$\tilde{S}^{(c)}_{jk}(\omega) = \kappa(\Delta_{kj})\langle j|X|k\rangle|j\rangle\langle k| = \Gamma^{jk}_{\kappa}(\omega)|j\rangle\langle k|, \tag{4.46}$$

and for the qubit $\sigma_x = (\sigma_- + \sigma_+)$

$$\tilde{S}^{(q)}_{jk}(\omega) = \gamma(\Delta_{kj})\langle j|\sigma_x|k\rangle|j\rangle\langle k| = \Gamma^{jk}_{\gamma}(\omega)|j\rangle\langle k|, \tag{4.47}$$

where the relaxation rates are,

$$\Gamma^{jk}_{\kappa}(\omega) = \kappa(\omega)|X^{jk}|^2, \tag{4.48}$$

$$\Gamma^{jk}_{\gamma}(\omega) = \gamma(\omega)|\sigma^{jk}_x|^2. \tag{4.49}$$

In Eq. (4.48) and (4.49), the rates $\kappa(\omega)$ and $\gamma(\omega)$ are proportional to noise spectra, respectively for resonator and qubit environments. With these replacements and neglecting the *Lamb-shifts* L_ω and L'_ω since they are small, dressed master equation for qubit-resonetor system is written as:

$$\dot{\rho}(t) = -\frac{i}{\hbar}[H_{\mathrm{R}}, \rho(t)] + \mathcal{L}\rho(t), \tag{4.50}$$

where

$$\begin{aligned}\mathcal{L}\rho(t) = &\sum_{k-j=\omega>0} \Gamma_{\kappa}^{jk}(\omega)(1+\bar{n}_{\kappa}(\Delta_{kj},T))\mathcal{D}[\tilde{S}_{jk}^{(c)}(\omega)]\rho(t) \\ &+ \sum_{k-j=\omega>0} \Gamma_{\gamma}^{jk}(\omega)(1+\bar{n}_{\gamma}(\Delta_{kj},T))\mathcal{D}[\tilde{S}_{jk}^{(q)}(\omega)]\rho(t) \\ &+ \sum_{k-j=\omega>0} \Gamma_{\kappa}^{jk}(\omega)\bar{n}_{\kappa}(\Delta_{kj},T)\mathcal{D}[\tilde{S}_{jk}^{\dagger(c)}(\omega)]\rho(t) \\ &+ \sum_{k-j=\omega>0} \Gamma_{\gamma}^{jk}(\omega)\bar{n}_{\gamma}(\Delta_{kj},T)\mathcal{D}[\tilde{S}_{jk}^{\dagger(q)}(\omega)]\rho(t).\end{aligned} \tag{4.51}$$

The four terms in Eq. (4.51) are contributions from the resonator and qubit baths that caused energy relaxation in the quantum optical master equation. The *dressed* Lindbladian solves the problem stated before. Indeed, at $T = 0$, rather than exciting the system, dissipators accounting for relaxation in Eq. (4.51) lead to decay to the true ground state $|G\rangle$. In the limit $g/\omega_{\rm c} \ll 1$, the *dressed* Lindbladian converges to the *standard* Lindbladian. Optical dressed master equation has been used in Paper 5.2, Paper 5.4-5.7, since the systems studied in there was in USC regime.

4.1.2 Optomachanical Dressed Master Equation

Paper 5.1 and 5.2, have been realized with the purpose of create arbitrary quantum superposition states and entangled *NOON* states (even more general mechanical states), respectively, of mobile mirrors in a completely controlled and deterministic manner. The first protocol use a standard optomechanical system (see Chapter 2.2) in USC regime while, the second use two identical optically coupled standard optomechanical systems, each one in own USC regime. In order to test the efficiency and robustness in presence of decoherence, thermal noise, and imperfect cooling, the use of the dressed master equation has been necessary. In this subsection, I will show how a dressed optomechanical master equation is obtained stared with the result obtained in Chapter 2.2 and uising Eq. (4.44) [118].

In standard optomechanical systems, where a mechanical oscillator is parametrically coupled to an optical cavity via radiation-pressure interac-

tion, the total Hamiltonian Eq. (2.20) conserves the photon number. It follow that, the total Hamiltonian can be diagonalized separately in each n-photon subspace. In each of these subspaces, the Hamiltonian describes a harmonic oscillator with mechanical frequency ω_M which is displaced by $-nX_0$, where $X_0 = 2X_{zpf}g/\omega_M$ is the displacement caused by one photon (see Chapter 2.2). The eigenvalues are $E_{nm} = n\hbar\omega_R - \frac{n^2\hbar g^2}{\omega_M} + m\hbar\omega_M$ while, the general quantum state of such system is

$$|n, m^{(n)}\rangle = |n\rangle \; e^{n\,\beta_0(\hat{b}^\dagger - \hat{b})}|m^{(n)}\rangle\,, \tag{4.52}$$

where $\beta_0 = g/\omega_M$ and, the integer $m^{(n)}$ represents the vibrational excitations of the mechanical resonator in the corresponding n-photon subspace. Here the mechanical Fock state $|m^{(n)}\rangle$ is shifted with a displacement $n\,\beta_0$ proportional to the cavity photon number n. In other words, the photon Fock state in the eigenstates is dressed by phonon excitations due to the optomechanical coupling. In the ultrastrong coupling regime ($g \sim \omega_M$), the dressed states are strongly affected by the optomechanical coupling. We need to distinguish between two different channels of losses, one for the cavity and one for the mobile mirror. So that, we have to calculate the eigenoperators Eq. (4.18) for the cavity $X_c = (a + a^\dagger)$, using the dressed states of the total system. For every fixed n, we have to define the eigenoperators associated to each possible transition between the n- and $(n\pm1)$- manifold energy levels in order to derive the correct dressed master equation. We define the eigenoperators

$$\tilde{S}_c^{(n)}(\omega_m) = \tilde{A}^{(n)}(\omega_m) + [\tilde{A}^{(n)}(\omega_m)]^\dagger = [\tilde{S}_c^{(n)}(\omega_m)]^\dagger \tag{4.53}$$

$$\tilde{A}^{(n)}(\omega_m) = \sum_{\omega_{m^{(n)}} - \omega_{m^{(n-1)}}} A^{(n)}_{m^{(n)},m^{(n-1)}} \left|n-1, m^{(n-1)}\right\rangle\!\left\langle n, m^{(n)}\right|, \tag{4.54}$$

with $A^{(n)}_{m^{(n)},m^{(n-1)}} = \sqrt{n}\langle m^{(n-1)}|m^{(n)}\rangle$ which contains many phonon sideband. For the mobile mirror $X_m = (b + b^\dagger)$, using the phonon dressed operator $c = b - \beta_0 a^\dagger a$, we get

$$\tilde{S}_M^{(n)}(\omega_m) = \tilde{C}^{(n)}(\omega_m) + [\tilde{C}^{(n)}(\omega_m)]^\dagger = [\tilde{S}_M^{(n)}(\omega_m)]^\dagger = \tilde{S}_M^{(n)}(-\omega_m) \tag{4.55}$$

$$\tilde{C}^{(n)}(\omega_m) = \sum_{\omega_{m^{(n)}} - \omega_{(m-1)^{(n)}}} C^{(n)}_{m^{(n)},(m-1)^{(n)}} \left|n, m^{(n)}\right\rangle\!\left\langle n, (m-1)^{(n)}\right|, \tag{4.56}$$

with $C^{(n)}_{m^{(n)},(m-1)^{(n)}} = \sqrt{m}\langle(m-1)^{(n)}|m^{(n)}\rangle$ which contains phonon transition between mechanical states belonging at the same n-manifold. All these transitions occur at frequency ω_M. From phonon dressed operators definition, we also have to take account of pure dephasing term $\beta_0 a^\dagger a$, due to the low-frequency part of the mechanical noise and inducing dephasing between different photon number states [119],

$$\tilde{N}^{(n)}(\omega_m) = \sum_{\omega_{m^{(n)}} - \omega_{m'^{(n)}}} N^{(n)}_{m^{(n)},m'^{(n)}} \left|n, m^{(n)}\right\rangle\!\left\langle n, m'^{(n)}\right|, \tag{4.57}$$

with $N^{(n)}_{m^{(n)},m'^{(n)}} = n\langle m'^{(n)}|m^{(n)}\rangle$. With $\omega_c \gg \omega_M$ the cavity-bath spectral density $\Gamma_c(\omega)$ can be assumed to be flat over the whole range of relevant phonon sidebands with $\Gamma_c(\omega) = \kappa/2\pi$, κ being the cavity damping rate. We also assume that the mechanical bath spectral density is of Ohmic form with $\Gamma_M(\omega) = \gamma_m\omega/2\pi\omega_m$, γ_m being the mechanical damping rate. At high temperature, this spectral density corresponds to a white noise on the mechanical mode. With these replacements and neglecting the *Lamb-shifts* L_ω and L'_ω since they are small, dressed master equation for standard optomechanical system is written as:

$$\dot{\rho}(t) = -\frac{i}{\hbar}[H,\rho(t)] + \sum_n \mathcal{L}_n\rho(t), \tag{4.58}$$

where

$$\begin{aligned}\mathcal{L}_n\rho(t) =& \kappa\sum_n(1+2\bar{n}(\omega,T))\mathcal{D}[\tilde{S}_c^{(n)}(\omega_m)]\rho(t)\\ &+\gamma_m\sum_n(1+2\bar{n}(\omega,T))\mathcal{D}[\tilde{S}_M^{(n)}(\omega_m)]\rho(t)\\ &+8\gamma_m(K_BT/\omega_m)\beta_0^2\sum_n\mathcal{D}[\tilde{N}^{(n)}(\omega_m)]\rho(t).\end{aligned} \tag{4.59}$$

The last term is the extra dephasing term.

In Paper 5.8, the dynamical Casimir effect has been studied using the

Law optomechanical Hamiltonian Eq. (2.18), that can not be analytically diagonized. In that case, in order to properly deal with the dissipation effects, we have to use a *dressed* master equation which is similar to Eq. (4.50) with *dressed* Lindbladian given by Eq. (4.51), but has substantial differences. Eq. (4.50) is not applicable in the presence of equally spaced (even approximately) energy levels, as in the Law optomechanical Hamiltonian happens. In this case we write the master equation without making the post-trace rotating-wave approximation, which means that, we do not adopt the secular approximation. Following Ref. [120], the correct *dressed* master equation assuming that the baths are at zero temperature $T = 0$, is written as follows:

$$\dot{\rho}(t) = -\frac{i}{\hbar}[H, \rho(t)] + \kappa\mathcal{L}_c\rho(t) + \gamma_m\mathcal{L}_M\rho(t), \tag{4.60}$$

where

$$\begin{aligned}
\mathcal{L}_n\rho(t) =& \kappa\mathcal{D}[\tilde{S}_c]\rho(t) \\
\mathcal{L}_n\rho(t) =& \gamma_m\mathcal{D}[\tilde{S}_M]\rho(t) \\
\tilde{S}_c =& \sum_{\omega_k>\omega_j} \left\langle j \left| (a^\dagger + a) \right| k \right\rangle |j\rangle\langle k| \\
\tilde{S}_M =& \sum_{\omega_k>\omega_j} \left\langle j \left| (b^\dagger + b) \right| k \right\rangle |j\rangle\langle k| .
\end{aligned} \tag{4.61}$$

Chapter 5

Paper overview

5.1 Paper I: Single-step arbitrary control of mechanical quantum states in ultrastrong optomechanics

Single-step arbitrary control of mechanical quantum states in ultrastrong optomechanics

L. Garziano,[1] R. Stassi,[2] V. Macrí,[1] S. Savasta,[1] and O. Di Stefano[1]

[1]*Dipartimento di Fisica e di Scienze Terra Terra, Università di Messina, Viale F. Stagno d'Alcontres 31, I-98166 Messina, Italy*

[2]*Dipartimento di Fisica e Chimica, Group of Interdisciplinary Physics, Università di Palermo and CNISM, Viale delle Scienze, I-90128 Palermo, Italy*

(Received 5 September 2014; revised manuscript received 17 December 2014; published 5 February 2015)

We describe how ultrastrong interactions in optomechanical systems can be used to force the system ground state to evolve into an arbitrary quantum state of mechanical motion in a completely controlled and deterministic manner. If the target quantum state is a superposition of N Fock states, it can be obtained by applying in single-step N classical optical signals of different frequencies for a common time interval. This protocol can be applied to various strongly interacting quantum systems as trapped ions beyond the Lamb-Dicke regime and cavity QED into the ultrastrong coupling regime.

DOI: 10.1103/PhysRevA.91.023809 PACS number(s): 42.50.Wk, 07.10.Cm, 37.30.+i, 42.65.−k

I. INTRODUCTION

Mechanical oscillators are at the heart of many precision experiments, such as highly sensitive detection of small forces, displacements, and accelerations [1,2] and can exhibit exceptionally low dissipation. Optical forces due to radiation pressure offer the possibility to control the motion of such engineered micromechanical or nanomechanical oscillators [3–8]. The manipulation and detection of mechanical motion in the quantum regime using light is promising for applications in quantum information processing [9], where optomechanical devices could serve as coherent light-matter interfaces which may allow for storage of quantum information in long-lived phonon states [10]. Mechanical oscillators in the quantum regime are systems with great potential in quantum metrology and sensing [7]. At the same time, they offer a route towards fundamental tests of quantum mechanics in a hitherto inaccessible parameter regime of size and mass [11]. First demonstrations of cooling mechanical resonators to the quantum ground state [12–15] have attracted great interest and opened the door towards the quantum regime of optomechanics. Achievements towards the control of optomechanical interactions at the quantum level are the demonstrations of optomechanically induced transparency [16,17] and of quantum-coherent coupling of a mechanical oscillator with an optical cavity mode [18–20]. In addition, quantum control at the single-phonon level has been demonstrated, by coupling a piezoelectrical dilatation oscillator to a superconducting qubit [21]. Despite substantial experimental advances, a full access to the quantum regime remains extremely challenging. Optomechanics experiments are rapidly approaching the ultrastrong (or single-photon) coupling regime [6,22–24], where the radiation pressure of a single photon displaces the mechanical resonator by more than its zero-point uncertainty [25]. This regime is attracting great interest also in cavity QED because it can give rise to novel quantum effects [26–30]. Realizing this ultrastrong coupling (USC) regime in optomechanical systems will facilitate the creation of quantum mechanical states of the mechanical resonator, as well as the characterization of such states by measuring the cavity photon field [23,25].

Here, we propose a cavity-optomechanics protocol working in the USC regime which in a single step forces the ground state of a mechanical oscillator to evolve into an arbitrary quantum state in a completely controlled and deterministic manner. An equivalent control of the electromagnetic field of an optical resonator mode has been demonstrated in the context of cavity quantum electrodynamics [31–33] and later in circuit quantum electrodynamics [34]. The general strategy for creating such states was first described by Law and Eberly in the context of cavity QED [35]. A quantum superposition of states with the highest Fock state $|N\rangle$ requires sequentially exciting N times the qubit into the proper superposition state and then performing each of the N times a partial transfer to the resonator. This strategy was later generalized to superpositions of arbitrary motional states of a trapped ion by Gardiner *et al.* [36] and Kneer and Law [37]. Recently, Xu *et al.* demonstrated that the Hamiltonian of the optomechanical systems can be reduced, in the strong single-photon optomechanical coupling regime when the photon blockade occurs, to one describing the interaction between a driven two-level trapped ion and the vibrating modes [38]. Hence, they proposed the application of the strategy of Ref. [35] for the synthesis of arbitrary nonclassical motional states in optomechanical systems. No experiments to realize these proposals in trapped ions and in mechanical resonators have been reported so far. The strategy here proposed, in contrast to the Law and Eberly algorithm, consists of a single step independently on the highest desired Fock state $|N\rangle$, being the only limitation the strength of the optomechanics interaction. In this way, the preparation time can be significantly reduced (see Sec.IV). Since a key requirement for synthesizing arbitrary quantum states is that the preparation time needs to be much shorter than the decoherence time, the here proposed scheme provides a promising strategy to fully control the quantum state of massive mechanical oscillators. The framework here presented is an example of how the USC regime can favor the generation and control of mechanical quantum states. Moreover, the proposed strategy can be applied to other systems such as trapped ions [39] and and cavity QED into the USC regime [26,29,40,41].

II. MODEL

We consider the standard model of optomechanical systems where a mechanical oscillator is parametrically coupled to an optical cavity [see Fig. 1(a)]. The total Hamiltonian of the

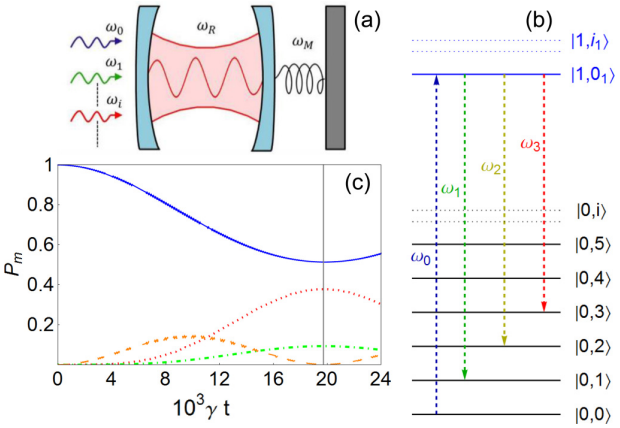

FIG. 1. (Color online) (a) Optomechanics setup: a mechanical oscillator with frequency $\omega_{\rm M}$ is parametrically coupled with a single-mode cavity driven by external driving fields. (b) Scheme of the involved energy levels of the optomechanical system and external driving fields: the frequency ω_0 of the pump field corresponds to the energy gap between the intermediate state $|1,0_1\rangle$ and the ground state $|0,0\rangle$. Other external driving fields with frequencies $\omega_k = \omega_0 - k\omega_{\rm M}$ are sent in order to depopulate the intermediate state towards the $|0,m\rangle$ states. (c) Time evolution of the occupation probabilities $P_m(t) = \langle 0,m|\rho(t)|0,m\rangle$ for the mechanical states with $m = 0$ (solid blue line), $m = 2$ (dotted red line), and $m = 4$ (dotted-dashed green line). Dashed orange line describes the evolution of the occupation probability for the intermediate state $|1,0_1\rangle$. Vertical line indicates the instant of time $t = t^*$ at which the *a priori* determined quantum state $|\bar{\psi}\rangle = \frac{1}{\sqrt{2}}(|0,0\rangle + \frac{2}{\sqrt{5}}|0,2\rangle + \frac{1}{\sqrt{5}}|0,4\rangle)$ is obtained. Parameters are $\omega_{\rm R}/\omega_{\rm M} = 500$, $g/\omega_{\rm M} = 1$, $\kappa/\omega_{\rm M} = 5\times10^{-5}$, $\gamma/\kappa = 0.1$, and $A_0/\omega_{\rm M} = 5\times10^{-3}$.

system is ($\hbar = 1$)

$$\hat{H}_0 = \omega_{\rm R}\hat{a}^\dagger\hat{a} + \omega_{\rm M}\hat{b}^\dagger\hat{b} + g\hat{a}^\dagger\hat{a}(\hat{b} + \hat{b}^\dagger), \tag{1}$$

where $\omega_{\rm R}$ is the resonator frequency, $\omega_{\rm M}$ is the mechanical frequency, and $g = \omega'_{\rm R}x_{\rm ZPF}$ is the optomechanical coupling. $x_{\rm ZPF} = (2M\omega_{\rm M})^{-1/2}$ represents the zero-point uncertainty, where M is the mass of the mechanical oscillator and $\omega'_{\rm R}$ is the derivative of the resonator energy with respect to the mechanical oscillator position x. Finally, $\hat{a}$ and $\hat{b}$ are the standard bosonic annihilation operators for the cavity mode and the mechanical oscillator, respectively. As the total Hamiltonian (1) conserves the photon number ($[\hat{a}^\dagger\hat{a}, \hat{H}_0] = 0$), it can be diagonalized separately in each n-photon subspace. In each of these subspaces, the Hamiltonian describes a harmonic oscillator with frequency $\omega_{\rm M}$ which is displaced by $-nx_0$, where $x_0 = 2x_{\rm ZPF}g/\omega_{\rm M}$ is the displacement caused by one photon. The general quantum state of such system is $|n,m_n\rangle$, where the integer m_n represents the vibrational excitations of the mechanical resonator in the corresponding n-photon subspace. The eigenvalues of (1) are $E_{nm} = n\omega_{\rm R} - \frac{n^2g^2}{\omega_{\rm M}} + m\omega_{\rm M}$. In the manifold with $n = 0$, the states $|0,m_0\rangle$ (simply labeled $|0,m\rangle$) are the eigenstates of the harmonic oscillator decoupled from the cavity.

In this article, we describe a single-step protocol in order to construct an arbitrary superposition of quantum mechanical states $|\bar{\psi}\rangle = \sum_{m=0}^{N}\bar{c}_{0m}|0,m\rangle$. We consider that the system is initially prepared in the state $|0,0\rangle$ (no photons in the cavity and the mechanical oscillator in its ground state). Then, we apply an external pump driving field $\mathcal{A}_0(t) = A_0e^{i(\omega_0t+\phi_0)}$ able to populate the $|1,0_1\rangle$ state, where ω_0 is the energy gap between the $|1,0_1\rangle$ and $|0,0\rangle$ states and A_0,ϕ_0 are the amplitude and the phase of the pump beam, respectively. At the same time, other driving fields $\mathcal{A}_m(t) = A_me^{i(\omega_mt+\phi_m)}$ are sent in the system in order to depopulate the intermediate state $|1,0_1\rangle$ towards the $|0,m\rangle$ states [see Fig. 1(b)]. The $|1,0_1\rangle$ state represents the mechanical ground state of the $n = 1$ manifold displaced harmonic oscillator. It corresponds to a mechanical coherent state that can be expanded in terms of the bare mechanical states $|m\rangle$ with the well-known expression

$$|0_1\rangle = \sum_{m=0}^{\infty} d_m|m\rangle, \tag{2}$$

with

$$d_m = \frac{(-1)^m}{\sqrt{m!}}\left(\frac{g}{\omega_M}\right)^m e^{-\frac{1}{2}(g/\omega_{\rm M})^2}. \tag{3}$$

This excitation scheme shares some analogies with a recently proposed Raman interaction in ultrastrong cavity QED in which the intermediate states are dressed by vacuum field [41]. Generally speaking, the experimental realization of quantum superpositions containing mechanical Fock states with high-m values is very challenging. For example, in circuit QED experiments, superpositions of Fock states up to $m = 9$ have been realized so far. This limitation is mainly due to the fact that when the vibrational number m increases, the decay time of the corresponding quantum states decreases while a longer preparation time is required. Although the protocol here proposed may reduce the preparation time, it seems to have an inherent limitation: the stimulated-emission transition $|1,0_1\rangle \to |0,m\rangle$ (completing the Raman process) cannot occur if $m\omega_{\rm M} \lesssim \omega_{\rm R}$. Actually this protocol can work, at least in principle, even for superpositions including Fock states m such that $m\omega_{\rm M} > \omega_{\rm R}$. Indeed, this limitation can be overcome by (i) exciting a higher energy level $|1,k_1\rangle$ instead of $|1,0_1\rangle$, or (ii) sending the pump drive in order to excite the ancilla state $|1,0_1\rangle$ together with additional drives at frequencies $\omega_m = m\omega_{\rm M} - \omega_0$. In this case, the latter external drives induce absorption processes instead of stimulated emissions.

The total Hamiltonian of our system is thus given by

$$\hat{H} = \hat{H}_0 + \hat{H}_D, \tag{4}$$

where $\hat{H}_D$ describes the external driving of the cavity:

$$\hat{H}_D = \sum_{i=0}^{N} A_i\cos(\omega_it + \phi_i)(\hat{a} + \hat{a}^\dagger). \tag{5}$$

In Eq. (5), N is the highest vibrational mechanical quantum level populated in the driving pump process and $A_i = \sqrt{\kappa}\,\mathcal{E}_i$, where $\mathcal{E}_i$ are the external drive amplitudes, κ is the cavity damping rate, and $\sqrt{\kappa}$ represents the coupling of the cavity mode with the external modes. Throughout this article, we will consider this coupling constant and independent of the cavity frequency.

We now move to the frame that diagonalizes the system Hamiltonian $\hat{H}_0$ expressing the driving Hamiltonian in the

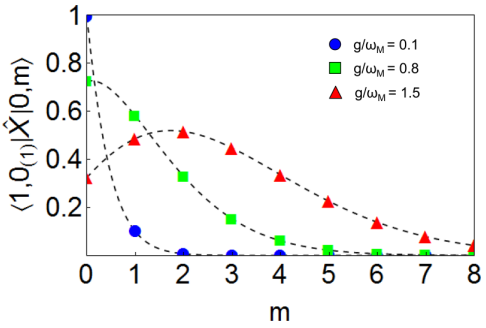

FIG. 2. (Color online) Transition matrix elements $\langle 1,0_1|\hat{X}|0,m\rangle$ between the intermediate state $|1,0_1\rangle$ and the mechanical states $|0,m\rangle$ as a function of the vibrational quantum number m for different values of the optomechanical coupling rate: $g/\omega_{\rm M} = 0.1$ (blue filled circles), $g/\omega_{\rm M} = 0.8$ (green filled squares), $g/\omega_{\rm M} = 1.5$ (red filled triangles). It can be noticed that for low values of the coupling rate $g/\omega_{\rm M}$, i.e., when the system is not in the optomechanical ultrastrong coupling regime, only the first mechanical states can be coupled. On the other hand, when the coupling strength increases, the transition matrix elements $\langle 1,0_1|\hat{X}|0,m\rangle$ become non-negligible even for higher values of m.

dressed basis, and focus our attention on the case in which the driving fields are on resonance with the transitions $|1,0_1\rangle \rightarrow |0,m\rangle$, i.e., $\omega_0 - \omega_k = k\omega_{\rm M}$. In the interaction picture with respect to $\hat{H}_0$, neglecting the counter-rotating terms [rotating wave approximation (RWA)], $\hat{H}_D$ can be approximated with an effective driving Hamiltonian:

$$\hat{H}_{\rm eff} = \sum_{m=0}^{N} A'_m e^{i\phi_m}|0,m\rangle\langle 1,0_1| + \text{H.c.}, \tag{6}$$

where the effective amplitudes A'_m of the driving fields are given by

$$A'_m = (A_m/2)\langle 0,m|\hat{X}|1,0_1\rangle, \tag{7}$$

with $\hat{X} \equiv \hat{a} + \hat{a}^\dagger$. The effective driving amplitudes are then proportional to the transition matrix elements between the intermediate state $|1,0_1\rangle$ and the mechanical states $|0,m\rangle$. Using Eqs. (2) and (3), it is easy to show that $\langle 1,0_1|\hat{X}|0,m\rangle = d_m$. It is important to note that if the coupling rate $g/\omega_{\rm M}$ is not strong enough, i.e., the system is not in the optomechanical USC regime, only the first mechanical states can be coupled (see Fig. 2). On the other hand, as shown in Fig. 2, when the coupling strength increases, the transition matrix elements $\langle 1,0_1|\hat{X}|0,m\rangle$ become non-negligible even for higher values of m. The optomechanical USC regime is then an essential feature in order to obtain an arbitrary superposition of mechanical quantum states $|0,m\rangle$.

In order to calculate the time evolution of the system, we expand the generic system quantum state in the eigenstates of $\hat{H}_0$ that are populated by the driving pumps and are effectively involved in the dynamics, i.e., $|\psi(t)\rangle = \sum_{m=0}^{N} c_{0m}(t)|0,m\rangle + c_{10}(t)|1,0_1\rangle$ and then we solve the Schrödinger equation with the initial condition $|\psi(t=0)\rangle = |0,0\rangle$. In this way, we obtain a set of coupled differential equations for the $c_{0m}(t), c_{10}(t)$ coefficients that can be analytically solved. The exact solution for the time evolution of the coefficients reads as

$$c_{10}(t) = -i\frac{\sin(\theta t)}{\sqrt{1+\eta}}e^{-i\phi_0}, \tag{8}$$

$$c_{00}(t) = \frac{\eta + \cos(\theta t)}{1+\eta}, \tag{9}$$

$$c_{0m}(t) = -\tfrac{1-\cos(\theta t)}{1+\eta}\tfrac{A'_m}{A'_0}e^{i(\phi_m-\phi_0)}, \quad m = 1,\ldots,N \tag{10}$$

where $\eta = \sum A'^2_m/A'^2_0$ and $\theta = A'_0\sqrt{1+\eta}$. In order to obtain an arbitrary superposition of mechanical quantum states $|0,m\rangle$, we need to find the instant of time t^* in which the intermediate state $|1,0_1\rangle$ is totally depopulated, i.e., $c_{10}(t^*) = 0$. From Eq. (8) it is possible to verify that this condition is satisfied for $t^* = (2l+1)\pi/\theta$ with $l \in \mathbb{N}$. The time t^* represents the specific instant of time at which the pump and the driving fields must be switched off in order to have no contribution for the intermediate state $|1,0_1\rangle$. Of course, the most convenient choice is the shortest possible t^* corresponding to $l = 0$. The target state $|\bar{\psi}\rangle = \sum_{m=0}^{N}\bar{c}_{0m}|0,m\rangle$ is determined *a priori* with an appropriate initial choice of the complex coefficients $\bar{c}_{0m} = \bar{C}_{0m}e^{i\bar{\varphi}_{0m}}$. Once the arbitrary target state has been chosen and the pump amplitude and phase A_0, ϕ_0 have been arbitrarily fixed, from Eqs. (9) and (10) it is simple to obtain the relations that must be satisfied by the amplitudes and phases of the external driving field:

$$A_m = A_0\frac{\bar{C}_{0m}}{1-\bar{C}_{00}}\frac{\langle 1,0_1|\hat{X}|0,0\rangle}{\langle 1,0_1|\hat{X}|0,m\rangle}, \quad m = 1,\ldots,N \tag{11}$$

$$\phi_m = \bar{\varphi}_{0m} + \phi_0 - \pi. \tag{12}$$

It is worth noticing that the required external driving amplitudes A_m depend on the ratio $\langle 1,0_1|\hat{X}|0,0\rangle/\langle 1,0_1|\hat{X}|0,m\rangle$. Such a ratio can be very high for high-m values and for small normalized optomechanical couplings $g/\omega_{\rm M}$. In this case, the required external drive could be so high to produce undesired off-resonance excitations as well as heating and eventually damage of the experimental device. On the contrary, the USC regime has the effect of both decreasing the numerator and increasing the denominator in the ratio (see Fig. 2), thus lowering the required driving power. In order to correctly describe the quantum dynamics of the system, dissipation induced by its coupling to the environment needs to be considered. We assume that the cavity and the mechanical oscillator are weakly coupled with two different baths of harmonic oscillators at a temperature T so that the the standard Born-Markov approximation can be employed. The dynamics of the system is then described by the quantum master equation

$$\dot{\rho}(t) = -i[\hat{H}_0,\rho(t)] + \kappa\mathcal{D}[\hat{a}]\rho(t) + \gamma(n_{\rm th}+1)\mathcal{D}[\hat{b}]\rho(t) + \gamma n_{\rm th}\mathcal{D}[\hat{b}^\dagger]\rho(t), \tag{13}$$

where $\mathcal{D}[\hat{O}]\rho = \frac{1}{2}(2\hat{O}\rho\hat{O}^\dagger - \rho\hat{O}^\dagger\hat{O} - \hat{O}^\dagger\hat{O}\rho)$ is the standard dissipator in Lindblad form, $n_{\rm th} = (e^{\hbar\omega_{\rm M}/k_BT} - 1)^{-1}$, and γ and κ are the mechanical and cavity damping rates, respectively.

Equation (11) clearly shows the key role played by the optomechanical coupling g for the protocol operation. Before concluding this section, relying on the Rabi problem,

we briefly discuss the requirements that the other system parameters and external driving amplitudes have to satisfy.

According to the Rabi formula, the population transfer time among two generic states is inversely proportional to the driving amplitude. In order to get the desired state with a high fidelity, the preparation time needs to be significantly lower than the decay times. Hence, assuming that the relevant matrix elements $\langle 1,0_1|\hat{X}|0,m\rangle \approx 1$, it is required that $\kappa,\gamma \ll A_0$. Moreover, in order to prevent undesired off-resonance excitations of nearby mechanical Fock states, it is required that $A_0 \ll \omega_{\rm M}$. Considering $\kappa \approx \gamma$, we have

$$1 \ll \frac{A_0}{\gamma} \ll Q_{\rm M}, \tag{14}$$

where $Q_{\rm M} = \omega_{\rm M}/\gamma$ is the mechanical quality factor.

III. NUMERICAL RESULTS

In this article, unless otherwise stated, we will consider the following system parameters: $\omega_{\rm R}/\omega_{\rm M} = 500$, $g/\omega_{\rm M} = 1$, $\kappa/\omega_{\rm M} = 5\times10^{-4}$, $\gamma/\kappa = 0.1$, and $A_0/\omega_{\rm M} = 5\times10^{-3}$. Figure 1(c) shows the time evolution of the occupation probabilities $P_m(t) = \langle 0,m|\rho(t)|0,m\rangle$ for $m = 0,2,4$ under the influence of three external optical drives of frequencies ω_0, ω_2, ω_4 chosen in order to generate the target quantum state $|\bar{\psi}\rangle = \frac{1}{\sqrt{2}}(|0,0\rangle + \frac{2}{\sqrt{5}}|0,2\rangle + \frac{1}{\sqrt{5}}|0,4\rangle)$. The vertical line indicates the analytically evaluated instant of time $t = t^*$ at which the target state $|\bar{\psi}\rangle$ can be experimentally obtained switching off the pump and all the external driving fields. The occupation probability $\langle 1,0_1|\rho(t)|1,0_1\rangle$ for the intermediate state is shown as well. The key feature of this single-step protocol is that the state $|1,0_1\rangle$ acts as an "ancilla" state whose occupation goes to zero at $t = t^*$.

The study of the dynamical evolution of the probabilities $P_m(t)$ is not sufficient for the complete characterization of the quantum mechanical state $|\psi\rangle$. Indeed, two different quantum superpositions $|\psi_a\rangle$ and $|\psi_b\rangle$ differing only in the relative phases of the mechanical Fock states cannot be distinguished. The quantum state can be univocally characterized by employing Wigner tomography. Following the scheme developed by Leibfried *et al.* [42], the reconstruction of the density matrix and Wigner function of the mechanical quantum state can be obtained. Once the target state $|\bar{\psi}\rangle$ is synthesized, the reconstruction mapping can be realized applying to this state coherent displacements provided by a classical driving field of frequency ω_0 with different amplitudes and phases, and then measuring the number-state populations. In analogy with Wigner tomography for trapped ions, a proposal for optomechanical quantum states reconstruction has been recently presented by Vanner *et al.* [43].

In order to probe the creation of complex superpositions by the above-described algorithm, in Fig. 3 we compare the Wigner functions for two synthesized states $|\psi_1\rangle$ and $|\psi_2\rangle$, corresponding to the target states $|\bar{\psi}_1\rangle = \frac{1}{\sqrt{3}}(|0\rangle + |1\rangle + |3\rangle)$ and $|\bar{\psi}_2\rangle = \frac{1}{\sqrt{3}}(|0\rangle + i|1\rangle + |3\rangle)$ differing only in the relative phase of the mechanical Fock state $|1\rangle$. In Figs. 3(a) and 3(b), numerical calculations are carried out considering the system at $T = 0$ and in the absence of thermal noise. The master equation is solved numerically including the interaction of the mechanical oscillator and the cavity with their reservoirs and under the effect of the Hamiltonian in Eq. (4). Cooling in the single-photon strong coupling regime of cavity optomechanics has been recently analyzed [44]. In real optomechanical systems, however, ground-state cooling is never complete and the interaction with a finite-temperature reservoir has to be taken into account. Figures 3(c) and 3(d) display the Wigner functions of the same two synthesized states with the system initially prepared in a thermal state with a mean occupation number $\langle \hat{b}^\dagger\hat{b}\rangle = 0.2$ and interacting with a reservoir at finite temperature ($n_{\rm th} = 0.8$). The fidelities $F = \sqrt{\langle\bar{\psi}|\rho|\bar{\psi}\rangle}$ between the desired target states $|\bar{\psi}\rangle$ and the density matrices ρ of the synthesized states are, from Figs. 3(a) to 3(d), $F = 0.98,0.98,0.90,0.90$. It can be noticed that the effects of the thermal noise and the interaction of the system with a finite-temperature reservoir modify the Wigner tomography of the two synthesized states. However, they continue to display nonclassical features (i.e., negative values of the Wigner function) and are in good agreement with the corresponding desired target states as shown by the resulting fidelities.

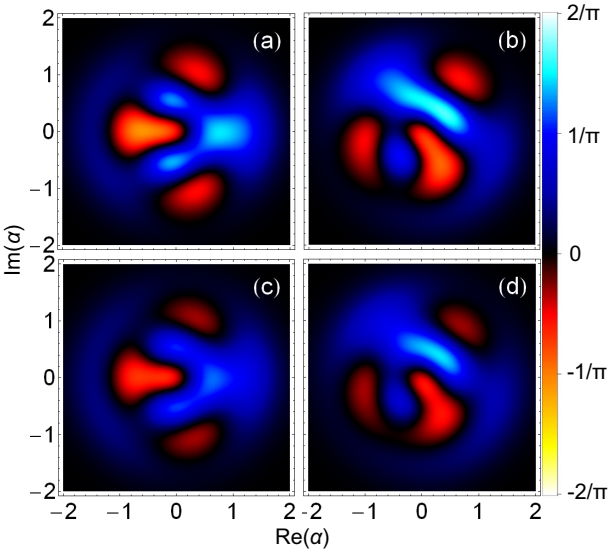

FIG. 3. (Color online) Quantum tomography of two synthesized states (a) $|\psi\rangle = \frac{1}{\sqrt{3}}(|0\rangle + |1\rangle + |3\rangle)$ and (b) $|\psi\rangle = \frac{1}{\sqrt{3}}(|0\rangle + i|1\rangle + |3\rangle)$ for the system initially prepared in a pure ground state at $T = 0$. Wigner functions of the same two states synthesized starting from a thermal distribution with mean occupation number $\langle \hat{b}^\dagger\hat{b}\rangle = 0.2$ and in the presence of a $T \neq 0$ reservoir ($n_{\rm th} = 0.8$) are displayed in (c) and (d). Parameters are the same as in Fig. 1.

Finally, in Fig. 4 we show the effects of thermal noise on the synthesis and decoherence of the state $|\psi_3\rangle = \frac{1}{\sqrt{2}}(|0\rangle + |3\rangle)$. The same state is synthesized both at $T = 0$ and starting from a pure ground state [Fig. 4(a)] and at finite T with the system initially prepared in a thermal distribution with a mean occupation number $\langle \hat{b}^\dagger\hat{b}\rangle = 0.1$ [Fig. 4(b)]. The time t^* at which we synthesize the state in both configurations by switching off all the external drives is shorter than the decoherence time, so that the two Wigner functions display

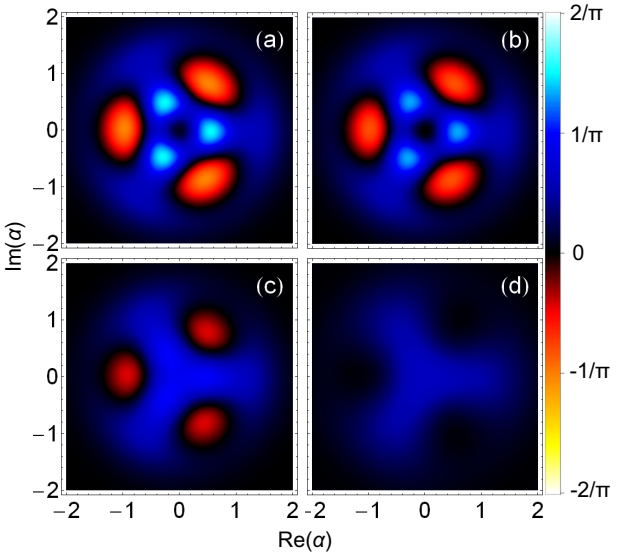

FIG. 4. (Color online) Quantum tomography of the state $|\psi\rangle = \frac{1}{\sqrt{2}}(|0\rangle + |3\rangle)$ for (a) the system at $T = 0$ and initially prepared in a pure ground state and (b) the system at finite $T(n_{\rm th} = 0.8)$ and initially prepared in a thermal distribution with a mean occupation number $\langle\hat{b}^\dagger\hat{b}\rangle = 0.1$. The effects of decoherence after the system has evolved for a coherence time $\gamma(t' - t^*) = 0.3$ are shown for both configurations in (c) and (d), respectively. Other parameters are the same as in Fig. 1.

only few differences. We now study the free evolution of the state $|\psi_3\rangle$ in both cases for the same reservoir interaction time $\gamma(t' - t^*) = 0.3$. Differently for the case in which the system is prepared at $T = 0$ [Fig. 4(c)], the effects of thermal noise at a finite T are quite relevant as the coherence of the state is completely destroyed and nonclassical features in the Wigner function disappear [Fig. 4(d)].The high degree of decoherence is also confirmed by the low value of the fidelity ($F = 0.63$) obtained; in the other cases, fidelities of the synthesized states are, from Figs. 4(a) to 4(c), $F = 0.99,0.93,0.81$.

IV. COMPARISON WITH RECENTLY PROPOSED PROTOCOLS

In recent years, the engineering of quantum states in optomechanical systems has attracted considerable attention. By considering an optomechanical cavity which contains a Kerr medium, Tan proposed a scheme for deterministically preparing a mechanical quantum superposition between vacuum and an arbitrary Fock state [45]. Recently, Xu *et al.* applied the well-known Law-Eberly algorithm to optomechanical systems [38], showing that arbitrary superpositions $|\bar{\psi}\rangle = \sum_{m=0}^{N} \bar{C}_{0m} e^{i\bar{\varphi}_{0m}} |0,m\rangle$ of different phonon number states can be prepared. Specifically, the authors consider separately two different regimes corresponding to (i) $g/\omega_{\rm M} \ll 1$ and (ii) the USC regime $g/\omega_{\rm M} \sim 1$. Protocol (i) applies to optomechanical systems an algorithm developed for trapped ions in the Lamb-Dicke regime [36], while (ii) exploits a protocol for engineering arbitrary motional and entangled states of a single trapped ion beyond the Lamb-Dicke limit [46].

In this section, we make a comparison between our protocol and the method recently proposed by Xu *et al.*, comparing the resulting preparation times for different quantum superpositions. We focus on the regime (ii) mainly because the protocol here proposed operates only in the USC regime. Moreover, protocol (i) requires additional excitation processes with respect to (ii) and hence requires longer preparation times.

Applying algorithm (ii), Xu *et al.* have shown that in the USC regime an arbitrary superposition $|\bar{\psi}\rangle = \sum_{m=0}^{N} \bar{C}_{0m} e^{i\bar{\varphi}_{0m}} |0,m\rangle$ of different phonon number states can be prepared by sequentially applying N red-sideband excitations after a single-carrier process. If the system is initially prepared in the ground state $|0,0\rangle$, the carrier process populates the $|1,0\rangle$ state by the application of an external driving field with the frequency matching condition $\omega_d = \omega_0$ for a time interval $t_0^c = \arccos(\bar{C}_{00})/\Omega_0$, where $\Omega_0 = (A_0/2)\langle 1,0_1|\hat{X}|0,0\rangle$ is the effective Rabi frequency. After the carrier process, N red-sideband excitations are sequentially applied to the cavity with the frequency matching conditions $\omega_d = \omega_0 - \omega_{\rm M}, \omega_0 - 2\omega_{\rm M}, \ldots, \omega_0 - N\omega_{\rm M}$ for the time intervals $t_1^r, \ldots, t_N^r$, respectively. Every red-sideband excitation process links the transitions between $|1,0\rangle$ and $|0,m\rangle$ with an effective Rabi frequency $\Omega_m = (A_0/2)\langle 1,0_1|\hat{X}|0,m\rangle$. The time intervals t_m^r, properly chosen in order to obtain the desired superposition, can be obtained analytically [46] and are given by

$$t_m^r = \arcsin\left[\bar{C}_{0m}\left(1 - \sum_{j=0}^{m-1}\bar{C}_{0j}^2\right)^{-1/2}\right] \Big/ \Omega_m, \quad 1 \leqslant m \leqslant N-1. \tag{15}$$

The time interval $t_N^r = \pi/2\Omega_N$ of the last step satisfies the condition $\sin(\Omega_N t_N^r) = 1$ which ensures that the intermediate state $|1,0\rangle$ is completely depopulated. The total preparation time is then $\tilde{t}^* = t_0^c + \sum_{m=1}^{N} t_m^r$. Unlike the above-described protocol, our method consists of a single step independently on the highest desired Fock state $|N\rangle$. The pump driving field and the other external driving fields are sent simultaneously for the time interval $t^* = \pi/\theta$, where $\theta = [A_0'^2 + \sum_{m=1}^{N} A_m'^2]^{1/2}$ is the effective Rabi frequency.

In order to make a comparison, we consider the system initially prepared in its ground state $|0,0\rangle$ and then synthesize different superpositions $|\bar{\psi}\rangle = \frac{1}{\sqrt{N+1}}\sum_{m=0}^{N}|0,m\rangle$ with $N = 1,2,3,4$ by applying once the single-step protocol and then the

TABLE I. Numerical values of the dimensionless preparation time for the synthesis of different superpositions $|\bar{\psi}\rangle = \frac{1}{\sqrt{N+1}}\sum_{m=0}^{N}|0,m\rangle$. The second and the third columns show, respectively, the preparation times obtained by using the single-step protocol and the multistep scheme (ii). The ratio $t^*/\tilde{t}^*$ is also shown.

$\|\Psi\rangle$	gt^*	$g\tilde{t}^*$	$t^*/\tilde{t}^*$
$\frac{1}{\sqrt{2}}(\|0\rangle + \|1\rangle)$	136	211.7	0.64
$\frac{1}{\sqrt{3}}(\|0\rangle + \|1\rangle + \|2\rangle)$	163.4	284.9	0.57
$\frac{1}{2}(\|0\rangle + \|1\rangle + \|2\rangle + \|3\rangle)$	177.7	357	0.5
$\frac{1}{\sqrt{5}}(\|0\rangle + \|1\rangle + \|2\rangle + \|3\rangle + \|4\rangle)$	187	454.3	0.41

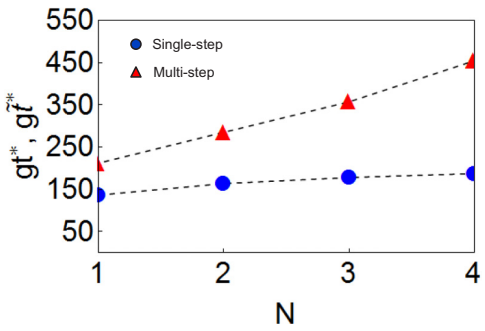

FIG. 5. (Color online) Plot of the dimensionless preparation time for a quantum superposition $|\tilde{\psi}\rangle = \frac{1}{\sqrt{N+1}} \sum_{m=0}^{N} |0,m\rangle$ as a function of the highest Fock-state number N. Red filled triangles represent the preparation time $g\tilde{t}^*$ required for the protocol proposed by Xu *et al.*, while blue filled circles display the preparation time gt^* for the single-step protocol. It can be noticed that the preparation times required by the single-step protocol are lower and tend to saturate at increasing values of N.

multistep algorithm (ii). In both cases, system parameters are $g/\omega_M = 1.5$, $A_0/\omega_M = 8 \times 10^{-2}$. We neglect damping effects for both the protocols. If they would be included, the result would be that the protocol with lower preparation times would provide better fidelities.

It is important to point out that in the procedure proposed by Xu *et al.*, the same pump amplitude A_0 is used both for the carrier and the red-sideband excitation processes, while in our scheme we use different amplitudes A_m [related to the pump amplitude A_0 by Eq. (11)] for every external driving field. We have chosen the highest possible value for A_0 in order to obtain a good preparation of the target state without exciting undesired transitions; notice also that in the regime here considered it results that $A_m \leqslant A_0$. Numerical values of the dimensionless preparation times gt^* and $g\tilde{t}^*$ for different quantum superpositions of N mechanical Fock states are reported in Table I and are also displayed in Fig. 5. The figure not only shows clearly that the single-step protocol here proposed requires lower preparation times, but also indicates that its preparation time tends to saturate at increasing values of N in contrast to the multistep protocol.

V. CONCLUSION

We presented a strategy for the preparation of arbitrary quantum superpositions of mechanical Fock states. The proposed scheme consists of a single step where all the classical optical excitations are sent for a common time interval. We tested the efficiency and robustness of this protocol by calculating fidelities and Wigner functions in presence of decoherence, thermal noise, and imperfect cooling. In addition, we compared this single-step protocol with a recently presented multistep algorithm [38], showing that in the USC regime the preparation time can be significantly reduced with our protocol. Our quantum control scheme can be applied to various strongly interacting quantum systems as trapped ions beyond the Lamb-Dicke regime by applying the same excitation scheme as in Fig. 1(b) where the photon and phonon states $|0(1),m\rangle$ are replaced by the atomic and motional states $|g(e),m\rangle$, and cavity QED into the USC regime with three level atoms. In this latter case, it is sufficient to apply the here described protocol to the cascade three-level systems described in Refs. [40,41,47]. Moreover, we expect that this framework can be generalized for further applications in quantum optomechanics as, for example, the generation of complex entangled states in coupled mechanical resonators.

[1] D. Rugar, R. Budakian, H. Mamin, and B. Chui, Nature (London) **430**, 329 (2004).
[2] A. G. Krause, M. Winger, T. D. Blasius, Q. Lin, and O. Painter, Nat. Photon. **6**, 768 (2012).
[3] S. Bose, K. Jacobs, and P. L. Knight, Phys. Rev. A **59**, 3204 (1999).
[4] W. Marshall, C. Simon, R. Penrose, and D. Bouwmeester, Phys. Rev. Lett. **91**, 130401 (2003).
[5] T. J. Kippenberg and K. J. Vahala, Science **321**, 1172 (2008).
[6] F. Marquardt and S. M. Girvin, Physics **2**, 40 (2009).
[7] M. Aspelmeyer, S. Gröblacher, K. Hammerer, and N. Kiesel, J. Opt. Soc. Am. B **27**, A189 (2010).
[8] M. Aspelmeyer, T. J. Kippenberg, and F. Marquardt, Rev. Mod. Phys. **86**, 1391 (2014).
[9] K. Stannigel, P. Komar, S. J. M. Habraken, S. D. Bennett, M. D. Lukin, P. Zoller, and P. Rabl, Phys. Rev. Lett. **109**, 013603 (2012).
[10] P. Meystre, Ann. Phys. (Berlin) **525**, 215 (2013).
[11] O. Romero-Isart, A. C. Pflanzer, F. Blaser, R. Kaltenbaek, N. Kiesel, M. Aspelmeyer, and J. I. Cirac, Phys. Rev. Lett. **107**, 020405 (2011).
[12] J. Teufel, T. Donner, M. Castellanos-Beltran, J. Harlow, and K. Lehnert, Nat. Nanotechnol. **4**, 820 (2009).
[13] A. Schliesser, O. Arcizet, R. Riviere, G. Anetsberger, and T. Kippenberg, Nat. Phys. **5**, 509 (2009).
[14] S. Gröblacher, J. B. Hertzberg, M. R. Vanner, G. D. Cole, S. Gigan, K. Schwab, and M. Aspelmeyer, Nat. Phys. **5**, 485 (2009).
[15] T. Rocheleau, T. Ndukum, C. Macklin, J. Hertzberg, A. Clerk, and K. Schwab, Nature (London) **463**, 72 (2009).
[16] S. Weis, R. Rivière, S. Deléglise, E. Gavartin, O. Arcizet, A. Schliesser, and T. J. Kippenberg, Science **330**, 1520 (2010).
[17] A. H. Safavi-Naeini, T. M. Alegre, J. Chan, M. Eichenfield, M. Winger, Q. Lin, J. T. Hill, D. E. Chang, and O. Painter, Nature (London) **472**, 69 (2011).
[18] S. Gröblacher, K. Hammerer, M. R. Vanner, and M. Aspelmeyer, Nature (London) **460**, 724 (2009).
[19] J. D. Teufel, D. Li, M. Allman, K. Cicak, A. Sirois, J. Whittaker, and R. Simmonds, Nature (London) **471**, 204 (2011).
[20] E. Verhagen, S. Deléglise, S. Weis, A. Schliesser, and T. J. Kippenberg, Nature (London) **482**, 63 (2012).
[21] A. D. O'Connell, M. Hofheinz, M. Ansmann, R. C. Bialczak, M. Lenander, E. Lucero, M. Neeley, D. Sank, H. Wang, M. Weides *et al.*, Nature (London) **464**, 697 (2010).

[22] J.-M. Pirkkalainen, S. Cho, J. Li, G. Paraoanu, P. Hakonen, and M. Sillanpää, Nature (London) **494**, 211 (2013).
[23] A. Rimberg, M. Blencowe, A. Armour, and P. Nation, New J. Phys. **16**, 055008 (2014).
[24] T. T. Heikkilä, F. Massel, J. Tuorila, R. Khan, and M. A. Sillanpää, Phys. Rev. Lett. **112**, 203603 (2014).
[25] A. Nunnenkamp, K. Børkje, and S. M. Girvin, Phys. Rev. Lett. **107**, 063602 (2011).
[26] T. Niemczyk, F. Deppe, H. Huebl, E. Menzel, F. Hocke, M. Schwarz, J. J. García-Ripoll, D. Zueco, T. Hümmer, E. Solano *et al.*, Nat. Phys. **6**, 772 (2010).
[27] A. Ridolfo, M. Leib, S. Savasta, and M. J. Hartmann, Phys. Rev. Lett. **109**, 193602 (2012).
[28] A. Ridolfo, S. Savasta, and M. J. Hartmann, Phys. Rev. Lett. **110**, 163601 (2013).
[29] L. Garziano, A. Ridolfo, R. Stassi, O. Di Stefano, and S. Savasta, Phys. Rev. A **88**, 063829 (2013).
[30] L. Garziano, R. Stassi, A. Ridolfo, O. Di Stefano, and S. Savasta, Phys. Rev. A **90**, 043817 (2014).
[31] S. Bose, K. Jacobs, and P. Knight, Phys. Rev. A **56**, 4175 (1997).
[32] S. Deleglise, I. Dotsenko, C. Sayrin, J. Bernu, M. Brune, J.-M. Raimond, and S. Haroche, Nature (London) **455**, 510 (2008).
[33] D. Kleckner, I. Pikovski, E. Jeffrey, L. Ament, E. Eliel, J. Van Den Brink, and D. Bouwmeester, New J. Phys. **10**, 095020 (2008).
[34] M. Hofheinz, H. Wang, M. Ansmann, R. C. Bialczak, E. Lucero, M. Neeley, A. O'Connell, D. Sank, J. Wenner, J. M. Martinis *et al.*, Nature (London) **459**, 546 (2009).
[35] C. K. Law and J. H. Eberly, Phys. Rev. Lett. **76**, 1055 (1996).
[36] S. A. Gardiner, J. I. Cirac, and P. Zoller, Phys. Rev. A **55**, 1683 (1997).
[37] B. Kneer and C. K. Law, Phys. Rev. A **57**, 2096 (1998).
[38] X.-W. Xu, H. Wang, J. Zhang, and Y. X. Liu, Phys. Rev. A **88**, 063819 (2013).
[39] D. Leibfried, R. Blatt, C. Monroe, and D. Wineland, Rev. Mod. Phys. **75**, 281 (2003).
[40] R. Stassi, A. Ridolfo, O. Di Stefano, M. J. Hartmann, and S. Savasta, Phys. Rev. Lett. **110**, 243601 (2013).
[41] J.-F. Huang and C. K. Law, Phys. Rev. A **89**, 033827 (2014).
[42] D. Leibfried, D. M. Meekhof, B. E. King, C. Monroe, W. M. Itano, and D. J. Wineland, Phys. Rev. Lett. **77**, 4281 (1996).
[43] M. R. Vanner, I. Pikovski, G. D. Cole, M. Kim, Č. Brukner, K. Hammerer, G. J. Milburn, and M. Aspelmeyer, Proc. Natl. Acad. Sci. USA **108**, 16182 (2011).
[44] A. Nunnenkamp, K. Børkje, and S. M. Girvin, Phys. Rev. A **85**, 051803(R) (2012).
[45] H. Tan, Phys. Rev. A **89**, 053829 (2014).
[46] L. F. Wei, Y.-x. Liu, and F. Nori, Phys. Rev. A **70**, 063801 (2004).
[47] A. Ridolfo, R. Vilardi, O. Di Stefano, S. Portolan, and S. Savasta, Phys. Rev. Lett. **106**, 013601 (2011).

5.2 Paper II: Multiphoton quantum Rabi oscillations in ultrastrong cavity QED

PHYSICAL REVIEW A **92**, 063830 (2015)

Multiphoton quantum Rabi oscillations in ultrastrong cavity QED

Luigi Garziano,[1,2] Roberto Stassi,[1,2] Vincenzo Macrì,[1] Anton Frisk Kockum,[2] Salvatore Savasta,[1,2] and Franco Nori[2,3]
[1]*Dipartimento di Fisica e di Scienze della Terra, Università di Messina, I-98166 Messina, Italy*
[2]*CEMS, RIKEN, Saitama 351-0198, Japan*
[3]*Department of Physics, University of Michigan, Ann Arbor, Michigan 48109-1040, USA*
(Received 20 September 2015; published 18 December 2015)

When an atom is strongly coupled to a cavity, the two systems can exchange a *single* photon through a coherent Rabi oscillation. This process enables precise quantum-state engineering and manipulation of atoms and photons in a cavity, which play a central role in quantum information and measurement. Recently, a new regime of cavity QED was reached experimentally where the strength of the interaction between light and artificial atoms (qubits) becomes comparable to the atomic transition frequency or the resonance frequency of the cavity mode. Here we show that this regime can strongly modify the concept of vacuum Rabi oscillations, enabling multiphoton exchanges between the qubit and the resonator. We find that experimental state-of-the-art circuit-QED systems can undergo *two*- and *three*-photon vacuum Rabi oscillations. These anomalous Rabi oscillations can be exploited for the realization of efficient Fock-state sources of light and complex entangled states of qubits.

DOI: 10.1103/PhysRevA.92.063830 PACS number(s): 42.50.Pq, 42.50.Ct, 85.25.Cp, 84.40.Az

I. INTRODUCTION

Light-matter interaction in the strong-coupling regime is a coherent reversible process in which a photon is absorbed and reemitted by an electronic transition at a rate equal to the coupling energy divided by the Planck constant [1,2]. Reaching the light-matter strong-coupling regime has been a major focus of research in atomic physics and quantum optics for several decades and has driven the field of cavity quantum electrodynamics (QED) [3,4]. The strong-coupling regime has been observed, in both the time and frequency domains, in a variety of systems [5], when an electronic transition is resonantly coupled to a cavity (optical resonator) and the coupling rate exceeds the rates of relaxation and decoherence of both the electronic transition and the field. Cavity QED effects with individual qubits have been intensively studied in solid state systems by replacing natural atoms with artificial atoms, such as quantum dots [6,7] and Josephson circuits [8–11]. The strong-coupling regime, when reached with a single qubit, enables a high degree of manipulation and control of quantum systems [12]. For example, by exploiting the strong-coupling regime of cavity QED, the preparation and measurement of arbitrary quantum states in a completely controlled and deterministic manner have been achieved [13,14] and Schrödinger's cat states of radiation have been prepared and reconstructed [15,16]. Basic steps in quantum information processing, including the deterministic entanglement of atoms and the realization of quantum gates using atoms and photons as quantum bits, have also been demonstrated [2,17,18].

Recently, a new regime of cavity QED, where the coupling rate becomes an appreciable fraction of the unperturbed frequency of the bare systems, has been experimentally reached in a variety of solid state systems [19–27]. In this so-called ultrastrong-coupling (USC) regime, the routinely invoked rotating-wave approximation (RWA) is no longer applicable and the antiresonant terms in the interaction Hamiltonian significantly change the standard cavity QED scenarios (see, e.g., Refs. [28–36]). Although in principle counterrotating terms exist in any real light-matter interaction Hamiltonian, their effects become prominent only in the USC limit [37]. Usually, light-matter USC is reached by coupling the resonator with a large number of molecules or more generally electronic transitions. Ultrastrong coupling with a single qubit has been achieved only by using superconducting circuits based on Josephson junctions, which exhibit macroscopic quantum coherence and giant dipole moments as artificial atoms [20,21,38].

One interesting feature of the USC regime is that the number of excitations in the cavity-emitter system is no longer conserved, even in the absence of drives and dissipation. Measurements on a superconducting circuit QED system in the USC regime have shown clear evidence of this feature [21]. Specifically, by tuning the qubit transition frequency (by adjusting the external flux bias threading the qubit) and measuring the cavity transmission, an anticrossing arising from the coupling between states with a different number of excitations has been observed. In particular, the measurements evidence the resonant coupling of the states $|\phi_1\rangle = |g,0,0,1\rangle$ and $|\phi_2\rangle = |e,1,0,0\rangle$, where the kets indicate the states of the qubit and of the first three resonator modes. This level anticrossing occurs when $\omega_q + \omega_1^r \approx \omega_3^r$, where ω_q is the transition frequency of the artificial atom and the ω_m^r are the resonance frequencies of the cavity modes. The dominant contributions to the resulting eigenstates $|\psi_\pm\rangle$ are approximate symmetric and antisymmetric superpositions of the degenerate states $|\phi_1\rangle$ and $|\phi_2\rangle$. The coupling between these two states, determining the anticrossing, originates from counterrotating terms in the interaction Hamiltonian that do not conserve the number of excitations. Indeed, the resulting effect of the action of these counterrotating terms on, e.g., the $|\phi_2\rangle$ state is the annihilation of two excitations, one in the $m = 1$ mode and one in the qubit, and the simultaneous creation of a single excitation in the $m = 3$ mode. Such a process can result only from counterrotating terms, but it would not be possible within the RWA.

Very recently it was shown [39] that, when the frequency of the cavity field is near one-third of the atomic transition frequency, there exists a resonant three-photon coupling via intermediate states connected by counterrotating processes. The resonant quantum Rabi oscillations, occurring when

the atom and the cavity mode can exchange one excitation quantum in a reversible way, play a key role in the manipulation of atomic and field states for quantum information processing [12]. Here we show that a system consisting of a single qubit coupled ultrastrongly to a resonator can exhibit anomalous vacuum Rabi oscillations where *two* or *three* photons are jointly emitted by the qubit into the resonator and reabsorbed by the qubit in a reversible and coherent process. We focus on the case of a flux qubit coupled to a coplanar-waveguide resonator, a system where the USC regime with a single artificial atom has been demonstrated [21]. We find that this effect can be observed at coupling rates of the same order as those already reached in these systems [21,38].

II. DISSIPATION AND PHOTODETECTION IN THE USC REGIME

In order to demonstrate multiphoton quantum Rabi oscillations in USC cavity QED, we calculate the time evolution of the mean output photon fluxes and higher-order normally ordered photon correlations. It has been shown that, in the USC regime, the usual normally ordered correlation functions fail to describe the output photon emission rate and photon statistics. Clear evidence of this is that the standard input-output relations predict, even for a vacuum input and the system in the ground state, a finite output photon flux proportional to the average number of cavity photons [32,40,41], i.e., $\langle \hat{A}^{-}_{\rm out}(t)\hat{A}^{+}_{\rm out}(t)\rangle \propto \langle \hat{a}^{\dagger}(t)\hat{a}(t)\rangle$, where $\hat{A}^{+}_{\rm out}(t)$ and $\hat{A}^{-}_{\rm out}(t)$ are the positive- and negative-frequency components of the output field operator and $\hat{a}$ and $\hat{a}^{\dagger}$ are the destruction and creation operators for cavity photons. A solution to this problem was proposed in Ref. [32]. Considering, for the sake of simplicity, a single-mode resonator, it is possible to derive the correct output photon emission rate and correlation functions by expressing the cavity electric-field operator $\hat{X} = \hat{a} + \hat{a}^{\dagger}$ in the atom-cavity dressed basis. Once the cavity electric-field operator has been expressed in the dressed basis, it has to be decomposed into its positive- and negative-frequency components $\hat{X}^{+}$ and $\hat{X}^{-}$ [32]. Expanding the $\hat{X}$ operator in terms of the energy eigenstates $|j\rangle$ (with $\hbar\omega_j$ the corresponding eigenvalues) of the system Hamiltonian $\hat{H}$, one finds the relations

$$\hat{X}^{+} = \sum_{j,k>j} X_{jk}|j\rangle\langle k|, \quad \hat{X}^{-} = (\hat{X}^{+})^{\dagger}, \tag{1}$$

where $X_{jk} \equiv \langle j|(\hat{a}^{\dagger} + \hat{a})|k\rangle$ and the states are labeled such that $\omega_k > \omega_j$ for $k > j$. The resulting positive frequency output operator can be expressed as

$$\hat{A}^{+}_{\rm out}(t) = \hat{A}^{+}_{\rm in}(t) - \sqrt{\kappa}C_0\hat{X}^{+}, \tag{2}$$

where κ is the loss rate of the resonator due to the coupling to the external in-out modes and C_0 is a constant proportional to the zero-point fluctuation amplitude of the resonator [42]. Two aspects of these results are noteworthy. First of all, we note that in the USC regime, one correctly obtains $\hat{X}^{+}|0\rangle = 0$ for the system in its ground state $|0\rangle$ in contrast to $\hat{a}|0\rangle \neq 0$. Moreover, we note that the positive-frequency component of $\hat{X}$ is not simply proportional to the photon annihilation operator $\hat{a}$. As a consequence, for arbitrary degrees of light-matter interaction, the output photon flux emitted by a resonator can be expressed as $\Phi_{\rm out} = \kappa\langle \hat{X}^{-}\hat{X}^{+}\rangle$. Similarly, the output delayed coincidence rate is proportional to the two-photon correlation function $\langle \hat{X}^{-}(t)\hat{X}^{-}(t+\tau)\hat{X}^{+}(t+\tau)\hat{X}^{+}(t)\rangle$. In quantum optics, it is well known that the signal directly emitted from the qubit is proportional to $\langle \hat{\sigma}_{+}\hat{\sigma}_{-}\rangle$. In circuit QED systems, this emission can be detected by coupling the qubit to an additional microwave antenna [14]. Indeed, in the USC regime the qubit emission rate becomes proportional to the qubit mean excitation number $\langle \hat{C}^{-}\hat{C}^{+}\rangle$, where $\hat{C}^{\pm}$ are the qubit positive- and negative-frequency operators, defined as $\hat{C}^{+} = \sum_{j,k>j} C_{jk}|j\rangle\langle k|$ and $\hat{C}^{-} = (\hat{C}^{+})^{\dagger}$, with $C_{jk} \equiv \langle j|(\hat{\sigma}_{-} + \hat{\sigma}_{+})|k\rangle$.

In order to properly describe the system dynamics, including dissipation and decoherence effects, the coupling to the environment needs to be considered. We adopt the master-equation approach. However, in the USC regime the description offered by the standard quantum-optical master equation breaks down [43]. Following Refs. [41,44], we express the system-bath interaction Hamiltonian in the basis formed by the energy eigenstates of $\hat{H}$. We consider $T = 0$ temperature reservoirs (the generalization to $T \neq 0$ reservoirs is straightforward). By applying the standard Markov approximation and tracing out the reservoir degrees of freedom, we arrive at the master equation for the density-matrix operator $\hat{\rho}(t)$,

$$\dot{\hat{\rho}} = \frac{i}{\hbar}[\hat{\rho}(t), \hat{H}] + \mathcal{L}_{\rm damp}\hat{\rho}(t) + \mathcal{L}_{\phi}\hat{\rho}(t), \tag{3}$$

where $\mathcal{L}_{\rm damp}\hat{\rho}(t) = \sum_{j,k>j}(\Gamma^{jk}_{\kappa} + \Gamma^{jk}_{\gamma})\mathcal{D}[|j\rangle\langle k|]\hat{\rho}(t)$, with $\mathcal{D}[\hat{O}]\hat{\rho} = \frac{1}{2}(2\hat{O}\hat{\rho}\hat{O}^{\dagger} - \hat{\rho}\hat{O}^{\dagger}\hat{O} - \hat{O}^{\dagger}\hat{O}\hat{\rho})$, describes dissipation effects arising from the resonator and qubit reservoirs. These cause transitions between eigenstates at rates

$$\Gamma^{jk}_{\kappa} = \kappa|\langle j|\hat{X}|k\rangle|^2, \tag{4}$$

$$\Gamma^{jk}_{\gamma} = \gamma|\langle j|\hat{\sigma}_x|k\rangle|^2, \tag{5}$$

where κ and γ are decay rates, here assumed to be spectrally constant, induced by the resonator and qubit reservoirs. Pure dephasing effects affecting the qubit are described in Eq. (3) by the last term $\mathcal{L}_{\phi}\hat{\rho}(t) = \mathcal{D}[\sum_j \Phi_j|j\rangle\langle j|]\hat{\rho}(t)$, where $\Phi_j = \sqrt{\gamma_{\phi}/2}\langle j|\hat{\sigma}_z|j\rangle$, and γ_{ϕ} is the pure dephasing rate. Note that only the most relevant diagonal contributions have been included.

III. RESULTS

Here we study a flux qubit coupled to a coplanar resonator in the USC regime. For suitable junctions, the qubit potential landscape is a double-well potential, where the two minima correspond to states with clockwise and counterclockwise persistent currents $\pm I_{\rm p}$ [10,11]. When the flux offset $\delta\Phi_x \equiv \Phi_{\rm ext} - \Phi_0/2 = 0$, where $\Phi_{\rm ext}$ is the external flux threading the qubit and Φ_0 is the flux quantum, the two lowest-energy states are separated by an energy gap Δ. In the qubit eigenbasis, the qubit Hamiltonian reads $\hat{H}_{\rm q} = \hbar\omega_{\rm q}\hat{\sigma}_z/2$, where $\hbar\omega_{\rm q} = \sqrt{\Delta^2 + (2I_{\rm p}\delta\Phi_x)^2}$ is the qubit transition frequency, which can be adjusted by an external flux bias. We note that the two-level approximation is well justified because of the large anharmonicity of this superconducting artificial atom.

The resonator modes are described as harmonic oscillators $\hat{H}_m = \hbar\omega_m^{\rm r}\hat{a}_m^\dagger\hat{a}_m$, where $\omega_m^{\rm r}$ is the resonance frequency, m is the resonator-mode index, and $\hat{a}_m^\dagger$ ($\hat{a}_m$) is the bosonic creation (annihilation) operator for the mth resonator mode. We will consider $\lambda/2$ and $\lambda/4$ resonators. Then the quantum circuit can be described by the extended Rabi Hamiltonian

$$\hat{H} = \hat{H}_{\rm q} + \sum_m [\hat{H}_m + \hbar g_m \hat{X}_m(\cos\theta\hat{\sigma}_x + \sin\theta\hat{\sigma}_z)]. \quad (6)$$

Here $\hat{X}_m = \hat{a}_m + \hat{a}_m^\dagger$, $\hat{\sigma}_{x,z}$ denote Pauli operators, g_m is the coupling rate of the qubit to the mth cavity mode, and the flux dependence is encoded in $\cos\theta = \Delta/\omega_{\rm q}$. The operator $\hat{\sigma}_x$ is conveniently expressed as the sum of the qubit raising $\hat{\sigma}_+$ and lowering $\hat{\sigma}_-$ operators, which in the Heisenberg picture and for $g_m = 0$ oscillate as $\exp(i\omega_{\rm q}t)$ (negative frequency) and $\exp(-i\omega_{\rm q}t)$ (positive frequency), respectively. Thus, in contrast to the Jaynes-Cummings (JC) model [45], the Hamiltonian in Eq. (6) explicitly contains counterrotating terms of the form $\hat{\sigma}_+\hat{a}_m^\dagger$, $\hat{\sigma}_-\hat{a}_m$, $\hat{\sigma}_z\hat{a}_m^\dagger$, and $\hat{\sigma}_z\hat{a}_m$. Considering only one resonator mode and a flux offset $\delta\Phi_x = 0$, the Hamiltonian in Eq. (6) reduces to the standard Rabi Hamiltonian.

A. Two-photon quantum Rabi oscillations

We first consider the case of a flux qubit coupled to a $\lambda/2$ superconducting transmission-line resonator with resonance frequencies $\omega_m^{\rm r} = m\pi c/L$, where L is the resonator length. We use the qubit parameters $\Delta/h = 2.25$ GHz and $2I_{\rm p} = 630$ nA, as in Ref. [21]. We are interested in the situation where the qubit transition energy is approximately twice that of the fundamental resonator mode: $\omega_{\rm q} \approx 2\omega_1^{\rm r}$. We consider the qubit to be positioned at the center of the resonator so that it does not interact with the resonator mode $m = 2$ [see Fig. 1(a)]. The other resonator modes are much higher in energy, detuned with respect to the qubit transition frequency by an amount significantly larger than the coupling rate $\omega_m^{\rm r} - \omega_{\rm q} \approx (m-2)\omega_1^{\rm r}$, providing only moderate energy shifts for the coupling rates $g_m/\omega_m^{\rm r} \lesssim 0.2$ considered here. We will thus only take into account the interaction of the qubit with the fundamental resonator mode. We diagonalize numerically the Hamiltonian from Eq. (6) and indicate the resulting energy eigenvalues and eigenstates as $\hbar\omega_i$ and $|i\rangle$ with $i = 0,1,\ldots$, choosing the labeling of the states such that $\omega_k > \omega_j$ for $k > j$.

Figure 1(b) shows the frequency differences $\omega_{i,0} = \omega_i - \omega_0$ for the lowest-energy states as a function of the qubit transition frequency, which can be tuned by changing the external flux bias $\delta\Phi_x$. The red dashed curves correspond to calculations obtained neglecting all the counterrotating terms (the JC model). We observe a spectrum with two large-splitting anticrossings around $\omega_{\rm q} \approx \omega_1^r$, which appear for both the dashed and the solid curves. In the JC picture, they correspond to the resonant coupling between states with the same number of excitations. The lowest-energy avoided crossing results from the coherent coupling of the states $|e,0\rangle$ and $|g,1\rangle$, where g (e) indicates the ground (excited) state of the qubit and the second entry in the kets represents the photon number. When the splitting reaches its minimum, the resulting system

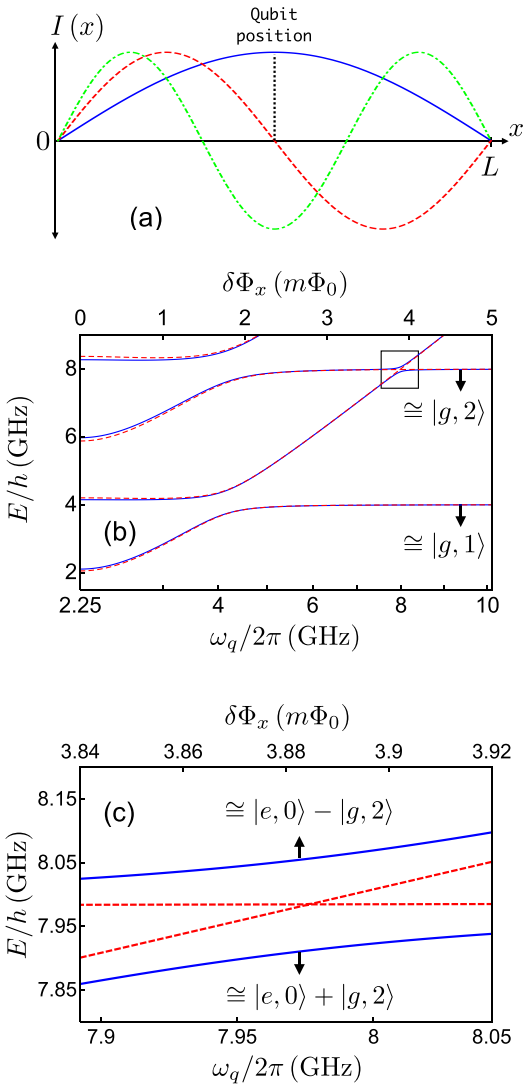

FIG. 1. (Color online) (a) Sketch of the distribution of the first three resonator modes $m = 1,2,3$ of a transmission-line $\lambda/2$ resonator. The resonance frequency of the first mode (blue solid curve) is set to $\omega_1^{\rm r}/2\pi = 4$ GHz. The qubit is positioned at the center of the resonator so that it does not interact with the mode $m = 2$ (red dashed curve) and is off-resonance with the mode $m = 3$ (green dot-dashed curve) mode. The bare resonance frequencies of the second and third modes are $\omega_2^{\rm r} = 2\omega_1^{\rm r}$ and $\omega_3^{\rm r} = 3\omega_1^{\rm r}$, respectively. The qubit parameters are $\Delta/h = 2.25$ GHz and $2I_{\rm p} = 630$ nA. (b) Frequency differences $\omega_{i,0} = \omega_i - \omega_0$ for the lowest-energy dressed states as a function of the qubit transition frequency $\omega_{\rm q}$ (which can be tuned by changing the external flux bias $\delta\Phi_x$) for the JC model (red dashed curves) and the extended Rabi Hamiltonian (blue solid curves). We consider a normalized coupling rate $g_1/\omega_1^{\rm r} = 0.15$ between the qubit and the resonator. In both cases the ground state level is not displayed. (c) Avoided level crossing (blue solid curves) resulting from the coupling between the states $|e,0\rangle$ and $|g,2\rangle$ due to the presence of counterrotating terms in the system Hamiltonian. The energy splitting reaches its minimum at $\omega_{\rm q}/2\pi \approx 7.97$ GHz $\approx 2(\omega_1^{\rm r}/2\pi)$. The anticrossing is not present in the JC model (red dashed lines), since it arises from the coherent coupling between states with a different number of excitations.

eigenstates are

$$\frac{1}{\sqrt{2}}(|e,0\rangle \pm |g,1\rangle). \tag{7}$$

The higher-energy large avoided crossing in the plot corresponds to the second rung of the JC ladder, arising from the coupling of $|e,1\rangle$ and $|g,2\rangle$. Only small quantitative deviations between the eigenenergies in the JC and in the extended Rabi model can be observed.

When the counterrotating terms are taken into account, the states $|i\rangle$ are no longer eigenstates of the total number of the excitation operator $\hat{N}_{\rm exc} = \hat{a}^\dagger a + \hat{\sigma}_+\hat{\sigma}_-$. For example, the system ground state can be expressed as a superposition $|0\rangle = \sum_n c^0_{gn}|g,n\rangle + c^0_{en}|e,n\rangle$ of bare states also involving nonzero excitations. Of course, when the normalized coupling $g_1/\omega_1^{\rm r} \ll 1$, only the coefficient c^0_{g0} is significantly different from zero. Moreover, for $\theta = 0$ parity is conserved [46,47] and only states with an even number of excitations contribute to $|0\rangle$. The nonconservation of the total excitation number also affects the excited dressed states $|j\rangle = \sum_n c^j_{gn}|g,n\rangle + c^j_{en}|e,n\rangle$. As a consequence, the dressed states $|1\rangle$ and $|2\rangle$ at the minimum splitting do not correspond to the simple JC picture of Eq. (7).

The solid line levels in Fig. 1(b) also display a smaller-amplitude avoided crossing when $\omega_{\rm q} \approx 2\omega_1^{\rm r}$. Observing that just outside this avoided-crossing region one level remains flat as a function of the flux offset $\delta\Phi_x$ with energy $\omega \approx 2\omega_1^{\rm r}$ while the other shows a linear behavior with $\omega_{\rm q}$, the splitting originates from the hybridization of the states $|e,0\rangle$ and $|g,2\rangle$. This avoided crossing behavior is better shown in Fig. 1(c) and the resulting states are well approximated by the states $\frac{1}{\sqrt{2}}(|e,0\rangle \pm |g,2\rangle)$. This splitting is not present in the RWA, where the coherent coupling between states with a different number of excitations is not allowed, nor does it occur with the standard Rabi Hamiltonian ($\theta = 0$).

Following the procedure described in Ref. [39], such a two-photon coupling between the bare states $|e,0\rangle$ and $|g,2\rangle$ can be analytically described by an effective Hamiltonian (see the Appendix). As displayed in Fig. 2, the coupling between $|e,0\rangle$ and $|g,2\rangle$ can only occur via the intermediate states $|g,1\rangle$ and $|e,1\rangle$. Indeed, if the system is initially prepared in the state $|e,0\rangle$, two different processes can occur: Either (i) the counterrotating term $\hat{a}_1^\dagger\hat{\sigma}_z$ enables a virtual transition $|e,0\rangle \to |e,1\rangle$ and then the term $\hat{a}_1^\dagger\hat{\sigma}_-$ leads to the final transition to the state $|g,2\rangle$ or (ii) the term $\hat{a}_1^\dagger\hat{\sigma}_-$ enables the transition $|e,0\rangle \to |g,1\rangle$, which is followed by the virtual transition $|g,1\rangle \to |g,2\rangle$ induced by the term $\hat{a}_1^\dagger\hat{\sigma}_z$.

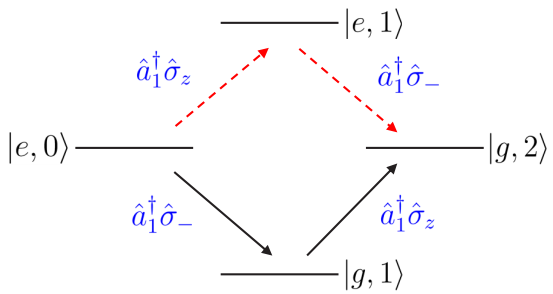

FIG. 2. (Color online) Coupling between the bare states $|e,0\rangle$ and $|g,2\rangle$ via the intermediate states $|g,1\rangle$ and $|e,1\rangle$. The red dashed arrows and the solid black arrows indicate, respectively, the two different processes describing the two-photon resonant coupling between $|e,0\rangle$ and $|g,2\rangle$.

In order to obtain an analytical description of the effective coupling, we first reduce the extended Rabi Hamiltonian to the truncated Hilbert space composed of the bare states $|e,0\rangle$, $|g,1\rangle$, $|e,1\rangle$, and $|g,2\rangle$. The matrix form of the reduced Hamiltonian becomes

$$\frac{\hat{H}_{\rm r}}{\hbar} = \begin{pmatrix} \frac{\omega_{\rm q}}{2} & g_1\cos\theta & g_1\sin\theta & 0 \\ g_1\cos\theta & \omega_1^{\rm r} - \frac{\omega_{\rm q}}{2} & 0 & -\sqrt{2}g_1\sin\theta \\ g_1\sin\theta & 0 & \omega_1^{\rm r} + \frac{\omega_{\rm q}}{2} & \sqrt{2}g_1\cos\theta \\ 0 & -\sqrt{2}g_1\sin\theta & \sqrt{2}g_1\cos\theta & 2\omega_1^{\rm r} - \frac{\omega_{\rm q}}{2} \end{pmatrix}, \tag{8}$$

where the order of columns and rows is $|e,0\rangle$, $|g,1\rangle$, $|e,1\rangle$, and $|g,2\rangle$. Near the two-photon resonance when $\omega_{\rm q} \approx 2\omega_1^{\rm r}$, the intermediate states $|g,1\rangle$ and $|e,1\rangle$ can be adiabatically eliminated (see the Appendix), leading to the effective Hamiltonian

$$\begin{aligned} \hat{H}_{\rm eff} = &\left(\frac{\omega_{\rm q}}{2} + \frac{2g_1^2}{\omega_{\rm q}}\cos(2\theta)\right)|e,0\rangle\langle e,0| \\ &+ \left(2\omega_1^{\rm r} - \frac{\omega_{\rm q}}{2} - \frac{4g_1^2}{\omega_{\rm q}}\cos(2\theta)\right)|g,2\rangle\langle g,2| \\ &- \Omega_{\rm eff}^{\rm (2ph)}(|e,0\rangle\langle g,2| + |g,2\rangle\langle e,0|), \end{aligned} \tag{9}$$

which describes the effective two-photon coupling between $|e,0\rangle$ and $|g,2\rangle$, with an effective two-photon Rabi frequency

$$\Omega_{\rm eff}^{\rm (2ph)} \equiv \frac{2\sqrt{2}g_1^2\sin(2\theta)}{\omega_{\rm q}}. \tag{10}$$

A key theoretical issue of the USC regime is the distinction between bare (unobservable) excitations and physical particles that can be detected. For example, when the counterrotating terms are relevant, the mean photon number in the system ground state is different from zero, $\langle 0|\hat{a}^\dagger\hat{a}|0\rangle \neq 0$. However, these photons are actually virtual since they do not correspond to real particles that can be detected in a photon-counting experiment. According to this analysis, the presence of an n-photon contribution in a specific eigenstate of the system does not imply that the system can emit n photons when prepared in this state. In order to fully understand and characterize this avoided crossing not present in the RWA, a more quantitative analysis is required. In the following, we therefore calculate the output signals and correlations that can be measured in a photodetection experiment.

In order to probe the anomalous avoided crossing shown in Figs. 1(b) and 1(c), we consider the case where the qubit is directly excited via a microwave antenna by an optical Gaussian pulse. The corresponding driving Hamiltonian is

$$\hat{H}_{\rm d} = \mathcal{E}(t)\cos(\omega t)\hat{\sigma}_x, \tag{11}$$

where $\mathcal{E}(t) = A\exp[-(t-t_0)^2/2\tau^2]/\tau\sqrt{2\pi}$. Here A and τ are the amplitude and the standard deviation of the Gaussian pulse, respectively. We consider the zero-detuning case by choosing the flux offset $\delta\Phi_x$ corresponding to the qubit frequency $\omega_{\rm q}/2\pi \simeq 7.97$ GHz, where the splitting in Fig. 1(b)

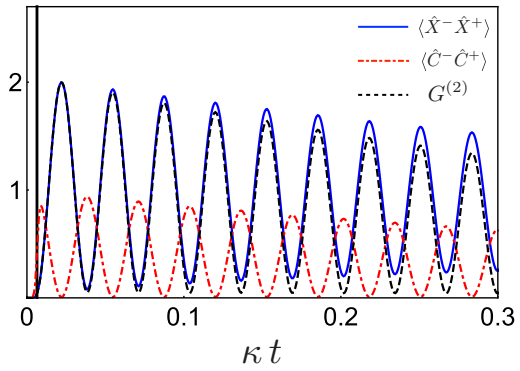

FIG. 3. (Color online) Time evolution of the cavity mean photon number $\langle \hat{X}^- \hat{X}^+ \rangle$ (blue solid curve), the qubit mean excitation number $\langle \hat{C}^- \hat{C}^+ \rangle$ (red dot-dashed curve), and the zero-delay two-photon correlation function $G^{(2)}(t)$ (dashed black curve) after the arrival of a π-like Gaussian pulse initially exciting the qubit (the black vertical line on the far left shows the wave-packet peak arrival time). The amplitude and the central frequency of the pulse are $A/\omega_1^r = 8.7 \times 10^{-2}$ and $\omega = (\omega_{3,0} + \omega_{2,0})/2$, respectively. After the arrival of the pulse, the system undergoes vacuum Rabi oscillations showing the reversible excitation exchange of two photons between the qubit and the resonator. Initially, $\langle \hat{X}^- \hat{X}^+ \rangle$ and $G^{(2)}(t)$ almost coincide. This perfect two-photon correlation is a signature that photons are actually emitted in pairs. The resonator and qubit damping rates are $\kappa/\omega_1^r = 1.8 \times 10^{-4}$ and $\gamma/\omega_1^r = 1.8 \times 10^{-4}$, respectively.

is at its minimum. The central frequency of the pulse has been chosen to be in the middle of the two split transition energies $\omega = (\omega_{3,0} + \omega_{2,0})/2$.

The cavity output photon flux and the photon flux emitted by the qubit directly coupled to a microwave antenna are proportional to $\langle \hat{X}^- \hat{X}^+ \rangle$ and $\langle \hat{C}^- \hat{C}^+ \rangle$, respectively. Figure 3 displays the dynamics of these two quantities and of the zero-delay two-photon correlation function $G^{(2)}(t) = \langle \hat{X}^-(t)\hat{X}^-(t)\hat{X}^+(t)\hat{X}^+(t) \rangle$ (dashed black curve) after the arrival of a π-like pulse initially exciting the qubit described by the Hamiltonian (11). Calculations in Fig. 3 have been carried out in the absence of pure dephasing ($\gamma_\phi = 0$). Results for $\gamma_\phi \neq 0$ are shown in Fig. 4. Vacuum Rabi oscillations showing the reversible excitation exchange between the qubit and the resonator are clearly visible in Fig. 3. The pulse time width is not much narrower than the Rabi period, so the qubit excitation is partially transferred to the cavity during the pulse arrival. Therefore, the first peak of the qubit mean excitation number in Fig. 3 is slightly lower than the second one. We observe that the mean intracavity physical photon number at its first maximum is very close to 2. This is an initial hint that when the qubit is in the ground state the resonator mode acquires two photons. However, the output measured signals are proportional and not equal to $\langle \hat{X}^- \hat{X}^+ \rangle$, so from this kind of measurement it is not possible to certify that the qubit and the resonator are actually exchanging two quanta. We also observe that at early times $\langle \hat{X}^- \hat{X}^+ \rangle$ and $G^{(2)}(t)$ almost coincide. This is a signature of perfect two-photon correlation: The probability of the system to emit one photon is equal to the probability to emit a photon pair. During the system evolution, higher values of the local minima of $\langle \hat{X}^- \hat{X}^+ \rangle$ are observed due to the decay from the

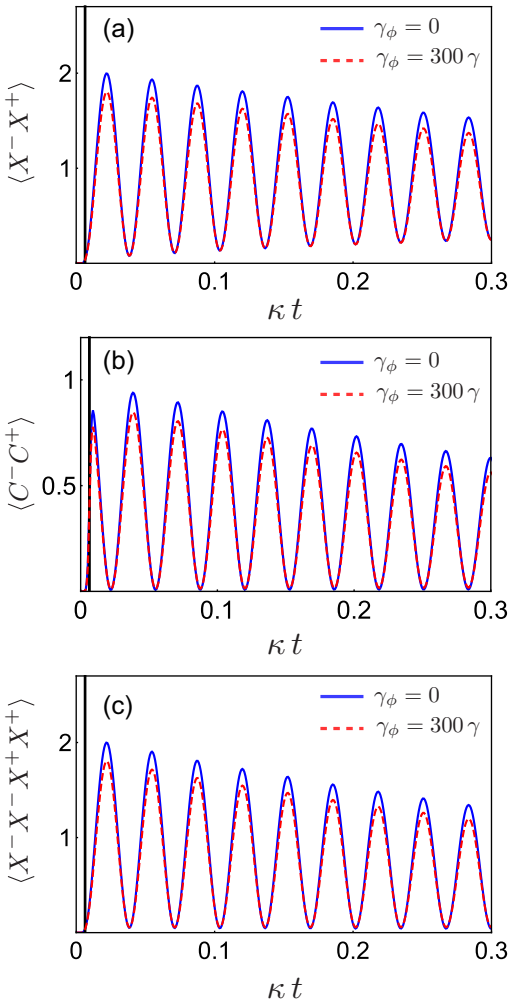

FIG. 4. (Color online) Effects of strong pure dephasing (dashed curves) on the dynamics of (a) the mean photon number $\langle \hat{X}^- \hat{X}^+ \rangle$, (b) the effective qubit population $\langle \hat{C}^- \hat{C}^+ \rangle$, and (c) the two-photon correlation function $\langle \hat{X}^- \hat{X}^- \hat{X}^+ \hat{X}^+ \rangle$. Calculations have been performed with the same parameters as in Fig. 3 with the addition of a pure dephasing rate $\gamma_\phi = 300\gamma$. Solid curves display numerical results obtained in the absence of pure dephasing, $\gamma_\phi = 0$. It can be observed that the physics of multiphoton vacuum Rabi oscillations is not significantly altered by the effects of pure dephasing.

two-photon state to the one-photon state (out of resonance with respect to the qubit) caused by the photon escape from the resonator. However, the two-photon correlation function $\langle \hat{X}^-(t)\hat{X}^-(t)\hat{X}^+(t)\hat{X}^+(t) \rangle$ goes almost to zero every time the qubit is maximally excited. This different behavior indicates that the qubit does not absorb single photons but only photon pairs. The period of a complete population oscillation is $2\pi/\Omega_{\rm eff}^{(2ph)}$, where $2\Omega_{\rm eff}^{(2ph)}$ is the minimum splitting in Fig. 1(c).

Ordinary quantum vacuum oscillations have already been demonstrated in circuit-QED systems (e.g., [10,48]). The dynamics observed in Fig. 3 can also be obtained by first preparing the qubit in its excited state by employing a π pulse.

Then the π pulse can be followed by a shift pulse that brings the qubit into resonance with the resonator for the desired duration in order to observe the coupled dynamics as in Ref. [48]. If the shift pulse has a duration $\delta t = 2\pi/\Omega_{\rm eff}^{(2{\rm ph})}$, the Fock state $n = 2$ is directly generated. After the switch-off of the shift pulse, the qubit is out of resonance with the resonator and the Fock state can escape from the cavity through an input-output port and be detected. Hence two-photon Rabi oscillations can be exploited for fast and efficient generation of two-photon states.

The influence of strong pure dephasing effects is shown in Fig. 4. Calculations have been performed with the same parameters used in Fig. 3 with the addition of a pure dephasing rate $\gamma_\phi = 300\gamma$. Figure 4 compares the dynamics of the mean photon number [Fig. 4(a)], the qubit effective population [Fig. 4(b)], and the two-photon correlation [Fig. 4(c)] in the absence (solid curves) and in the presence (dashed curves) of pure dephasing. The figure shows that strong pure dephasing does not significantly alter the physics of multiphoton vacuum Rabi oscillations and the main effect of dephasing is to make the excitation pulse less effective.

B. Three-photon quantum Rabi oscillations

Very recently, it was shown [39] that the strong coupling of a single qubit with three photons can be achieved in the USC regime when the frequency of the cavity field is near one-third of the atomic transition frequency. In this case, parity-symmetry breaking is not required and this effect can occur also at $\theta = 0$. Hence, it could be observed also in systems such as natural atoms or molecules displaying parity symmetry. One possible problem with this configuration is that the qubit can also interact resonantly with the one-photon state of the mode $m = 3$ of the resonator. In this case the qubit would interact with both one- and three-photon states. We show that the undesired one-photon resonant coupling of the qubit with a resonator mode can be avoided by considering a $\lambda/4$ resonator, whose resonance frequencies are $\omega_m^{\rm r} = (2m-1)\pi c/2L$, with $m = 1,2,3,\ldots$ [see Fig. 5(a)]. As shown in Fig. 5(a), the qubit is positioned so that it does not interact with the mode $m = 2$ with resonance frequency $\omega_2^{\rm r} = 3\omega_1^{\rm r}$. The qubit parameters are $\Delta/h = 4.25$ GHz and $2I_{\rm p} = 630$ nA. In the present case we are interested in the situation where the qubit transition energy is approximately three times that of the fundamental resonator mode $\omega_{\rm q} \approx 3\omega_1^{\rm r}$. The mode $m = 3$ has resonance frequency $\omega_3^{\rm r} = 5\omega_1^{\rm r}$, which is much larger than $\omega_{\rm q}$. Hence, also in this case we can consider the interaction of the qubit with only the fundamental resonator mode.

Figure 5(b) displays the frequency differences $\omega_{i,0}$ for the lowest-energy states as a function of the qubit transition frequency. The red dashed curves corresponds to calculations obtained neglecting all the counterrotating terms (JC model). We observe a spectrum with two large-splitting anticrossings, which appear only in the solid curves plus a smaller avoided crossing magnified in Fig. 5(c). The lowest-energy splitting corresponds to a two-photon vacuum Rabi splitting. When it reaches its minimum (at $\omega_{\rm q} \approx 2\omega_1^{\rm r}$), the corresponding hybridized states are analogous to those whose dynamics has been described in Fig. 3. They can be approximately

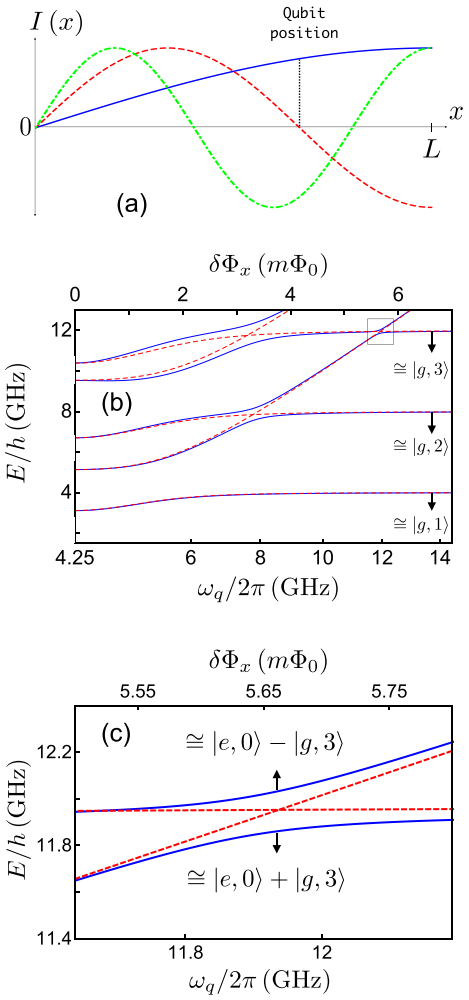

FIG. 5. (Color online) (a) Sketch of the distribution of the first three resonator modes $m = 1,2,3$ of a transmission-line $\lambda/4$ resonator. The resonance frequency of the first mode (blue solid curve) is $\omega_1^{\rm r} = 4$ GHz. The qubit is positioned so that it does not interact with the mode $m = 2$ (red dashed curve) with resonance frequency $\omega_2^{\rm r} = 3\omega_1^{\rm r}$. The mode $m = 3$ (green dot-dashed curve) has resonance frequency $\omega_3^{\rm r} = 5\omega_1^{\rm r}$, which is much larger than $\omega_{\rm q}$, so only the interaction of the qubit with the fundamental resonator mode must be considered. The qubit parameters are $\Delta/h = 4.25$ GHz and $2I_{\rm p} = 630$ nA. (b) Frequency differences $\omega_{i,0} = \omega_i - \omega_0$ for the lowest-energy dressed states as a function of the qubit transition frequency $\omega_{\rm q}$ (which can be tuned by changing the external flux bias $\delta\Phi_x$) for the JC model (red dashed curves) and the extended Rabi Hamiltonian (blue solid curves) explicitly containing counterrotating terms. We consider a normalized coupling rate $g_1/\omega_1^{\rm r} = 0.25$ between the qubit and the resonator. The spectrum shows two large-splitting anticrossings, which appear only in the continuous curves, plus a smaller avoided crossing, which is magnified in (c). (c) Three-photon vacuum Rabi splitting (blue solid curves) resulting from the coupling between the states $|e,0\rangle$ and $|g,3\rangle$ due to the presence of counterrotating terms in the system Hamiltonian. The energy splitting reaches its minimum at $\omega_{\rm q}/2\pi \approx 11.89$ GHz $\approx 3(\omega_1^{\rm r}/2\pi)$. The anticrossing is not present in the JC model (red dashed curves), since it arises from the coherent coupling between states with a different number of excitations.

expressed as

$$\frac{1}{\sqrt{2}}(|e,0\rangle \pm |g,2\rangle). \tag{12}$$

The second avoided crossing at higher energy corresponds to the second rung of the two-photon Rabi ladder and the corresponding approximated hybridized states (at the minimum splitting) are

$$\frac{1}{\sqrt{2}}(|e,1\rangle \pm |g,3\rangle). \tag{13}$$

The third smallest splitting, occurring at $\omega_q \approx 3\omega_1^r$, corresponds to a three-photon vacuum Rabi splitting. Here a single qubit is resonantly coupled with a three-photon state, resulting, at the minimum splitting, in the approximated eigenstates

$$\frac{1}{\sqrt{2}}(|e,0\rangle \pm |g,3\rangle)\,. \tag{14}$$

Figure 6 displays the system dynamics after the arrival of a π-like pulse exciting the qubit described by the Hamiltonian (11). Specifically, Fig. 6(a) shows the time evolution of $\langle \hat{X}^-\hat{X}^+\rangle$ and $\langle \hat{C}^-\hat{C}^+\rangle$. Calculations have been carried out in the absence of pure dephasing ($\gamma_\phi = 0$). Vacuum Rabi oscillations showing the reversible excitation exchange between the qubit and the resonator are clearly visible. We observe that the mean intracavity physical photon number at its first maximum is very close to 3. This is an initial hint that when the qubit is in the ground state the resonator mode is in a three-photon state. The period of a complete population oscillation is $2\pi/\Omega_{\rm eff}^{(3ph)}$, where $2\Omega_{\rm eff}^{(3ph)}$ is the minimum splitting in Fig. 5(c).

Figure 6(b) displays the time evolution of the zero-delay three-photon correlation function $G^{(3)}(t) = \langle \hat{X}^-(t)\hat{X}^-(t)\hat{X}^-(t)\hat{X}^+(t)\hat{X}^+(t)\hat{X}^+(t)\rangle$ together with the intracavity photon number $\langle \hat{X}^-\hat{X}^+\rangle$ for comparison. At early times the peak values of $G^{(3)}(t)$ are approximately two times higher than those of the mean photon number $\langle \hat{X}^-(t)\hat{X}^+(t)\rangle$. This is a specific feature of three-photon Fock states and indicates an almost-perfect three-photon correlation. We observe that $G^{(3)}(t)$ at early times reaches a peak value slightly beyond 6. This indicates that the system has a non-negligible probability to emit more than three photons. This is confirmed by the presence of a nonzero four-photon correlation function. Analyzing the different transitions contributing to $G^{(3)}(t)$, we can attribute this effect to additional low-frequency transition $|4\rangle \rightarrow |3\rangle$. These transitions between Rabi-split states occur when parity symmetry is broken [33] and in this case produce a four-photon cascade $|4\rangle \rightarrow |3\rangle \rightarrow |2\rangle \rightarrow |1\rangle \rightarrow |0\rangle$. This small contribution cannot be observed if its low frequency is outside the frequency-detection window. Analogously to the two-photon case (see Fig. 4), pure dephasing does not significantly affect the dynamics of multiphoton quantum Rabi oscillations (plot not shown).

C. Generation of entangled Greenberger-Horne-Zeilinger states

Standard vacuum Rabi oscillations have been exploited for the realization of atom-atom entanglement (see, e.g., Ref. [2]). Here we show that the multiphoton Rabi oscillations can be directly applied to the deterministic realization of more complex entangled states. As an initial application we discuss

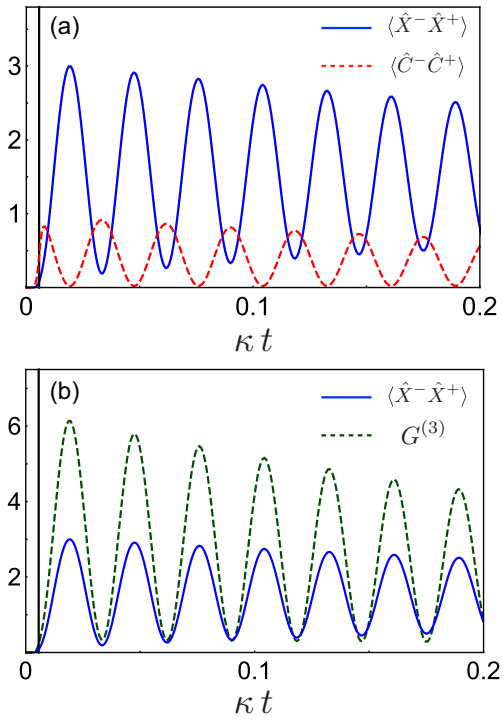

FIG. 6. (Color online) (a) Temporal evolution of the cavity mean photon number $\langle \hat{X}^-\hat{X}^+\rangle$ (blue solid curve) and the qubit mean excitation number $\langle \hat{C}^-\hat{C}^+\rangle$ (red dashed curve) after the arrival of a π-like Gaussian pulse exciting the qubit (the black vertical line on the far left shows the wave-packet center time). The amplitude and the central frequency of the pulse are $A/\omega_1^r = 9.4 \times 10^{-2}$ and $\omega = (\omega_{4,0} + \omega_{3,0})/2$, respectively. After the arrival of the pulse, the system undergoes vacuum Rabi oscillations showing the reversible excitation exchange between the qubit and the resonator. The fact that the mean intracavity physical photon number at its first maximum is very close to 3 is an initial signature that, when the qubit is in its ground state, the resonator mode is in a three-photon state. (b) Time evolution of the zero-delay three-photon function $G^{(3)}(t)$ (dashed green curve) together with the intracavity photon number $\langle \hat{X}^-\hat{X}^+\rangle$ (solid blue curve). The first peak value of the three-photon correlation function is approximately two times higher than that of the mean photon number, a signature of an almost-perfect three-photon correlation. The parameters for the resonator and qubit losses are the same as in Fig. 3.

the deterministic realization of multiatom Greenberger-Horne-Zeilinger (GHZ) states [49] by using only one resonator. The GHZ states lead to striking violations of local realism and are an important resource for quantum information processing [50], quantum cryptography [51], and error correction protocols [52]. Superconducting circuits have been used to study GHZ states (see, e.g., Refs. [53,54]).

Consider a resonator coupled to qubit 1 in the USC regime where two-photon vacuum Rabi oscillations can occur. The resonator also interacts in the strong- (not ultrastrong-) coupling regime with two additional qubits (2 and 3). Although the coupling rates between the resonator and the qubits are fixed, the qubit-resonator interaction can be switched on and

off by adjusting the qubit frequencies [14]. The protocol is simple and consists of three steps, one for each qubit. The different qubits do not interact directly with each other. They interact one at a time with the same resonator. We start by exciting the ultrastrongly coupled qubit 1 with a π pulse. Then, by changing the flux offset (at time $t = 0$), we drive it into resonance with the two-photon state of the resonator [Fig. 1(c)]. The system state at time t is $|\psi\rangle = \cos(\Omega_{\rm eff}^{(2ph)}t)|e,g,g,0\rangle + \sin(\Omega_{\rm eff}^{(2ph)}t)|g,g,g,2\rangle$. We let the qubit interact for a $\pi/2$ Rabi rotation so that the resulting state is

$$\frac{1}{\sqrt{2}}(|e,g,g,0\rangle + |g,g,g,2\rangle). \tag{15}$$

We then drive the qubit back out of resonance, stopping the Rabi rotation. The new state of the system now consists of the Einstein-Podolsky-Rosen pair constituted by qubit 1 and the resonator described in Eq. (15). Detecting qubit 1 in a given quantum state instantaneously collapses the cavity mode in the correlated field state. For example, detecting this qubit in the ground state $|g\rangle$ amounts to preparing a *two-photon* Fock state in the cavity. Qubits 2 and 3 are still in a factorized state.

The second step consists of driving qubit 2 into resonance with the one-photon state of the first resonator mode for a π rotation time so that the resulting state is $(|e,g,g,0\rangle - |g,e,g,1\rangle)/\sqrt{2}$. For the third step, we similarly drive the third qubit into resonance with the first resonator mode for a π rotation. The resulting state is $(|e,g,g,0\rangle + |g,e,e,0\rangle)/\sqrt{2}$. At this point, the photon state can be factored out, leaving us with a three-qubit GHZ-like entangled state. We note that the excitation of qubits 2 and 3 is conditioned on the presence of photons in the resonator. The excitation swapping between the resonator and qubits 2 and 3 carries away the cavity photons and transfers the entanglement of qubit 1 with the resonator to the other two qubits. A more conventional GHZ state can be obtained by performing a final local operation on qubit 1, e.g., by sending a further π pulse to the first qubit, so that the resulting final state is $(|g,g,g,0\rangle + |e,e,e,0\rangle)/\sqrt{2}$. This procedure can be easily generalized to four or more qubits. In general, if n-photon Rabi oscillations are achieved, then $(n+1)$-qubit GHZ states can be produced. We note that this protocol does not need the initial synthesis of photonic or atomic superposition states [55,56].

IV. CONCLUSION

We have investigated vacuum Rabi oscillations in the USC regime. According to the Jaynes-Cummings model, the qubit and the resonator can exchange a single excitation quantum through a coherent Rabi oscillation process. Such Rabi oscillations play a key role in the manipulation of atomic and field states for quantum information processing [12]. Our theoretical predictions show clear evidence for physics beyond the Jaynes-Cummings model and extend the concept of quantum Rabi oscillations. We find that multiphoton reversible exchanges between an individual qubit and a resonator can be observed in the USC regime. Specifically, we have shown that experimental state-of-the-art circuit-QED systems can undergo two- and three-photon vacuum Rabi oscillations. Still increasing the coupling rate, a higher number of photons can be exchanged with the qubit during a single Rabi oscillation. These anomalous Rabi oscillations can be exploited for the realization of efficient Fock-state sources of light and for the implementation of novel protocols for the control and manipulation of atomic and field states.

ACKNOWLEDGMENTS

We thank O. Di Stefano and Chui-Ping Yang for useful discussions. This work was partially supported by the RIKEN iTHES Project, the MURI Center for Dynamic Magneto-Optics via the AFOSR Grant No. FA9550-14-1-0040, the IMPACT program of JST, a Grant-in-Aid for Scientific Research (A), and the MPNS COST Action MP1403 Nanoscale Quantum Optics. A.F.K. acknowledges support from a JSPS Postdoctoral Fellowship for Overseas Researchers.

APPENDIX: ANALYTICAL DERIVATION OF THE TWO-PHOTON-QUBIT EFFECTIVE HAMILTONIAN

In this Appendix we derive the analytical expression for the effective Hamiltonian in Eq. (9), describing the two-photon coupling between the states $|e,0\rangle$ and $|g,2\rangle$. We start from the reduced Hamiltonian in Eq. (8) and then move to the rotating frame with frequency $\omega_{\rm q}/2$, obtaining the transformed reduced Hamiltonian

$$\frac{\hat{H}_{\rm r}'}{\hbar} = \begin{pmatrix} 0 & g_1\sin\theta & g_1\cos\theta & 0 \\ g_1\sin\theta & \omega_1^{\rm r} & 0 & \sqrt{2}g_1\cos\theta \\ g_1\cos\theta & 0 & \omega_1^{\rm r}-\omega_{\rm q} & -\sqrt{2}g_1\sin\theta \\ 0 & \sqrt{2}g_1\cos\theta & -\sqrt{2}g_1\sin\theta & 2\omega_1^{\rm r}-\omega_{\rm q}\,. \end{pmatrix}. \tag{A1}$$

Now the order of columns and rows is $|e,0\rangle$, $|e,1\rangle$, $|g,1\rangle$, and $|g,2\rangle$. After the transformation, an arbitrary state of the system in this truncated Hilbert space can be denoted by $(c1,c2,c3,c4)^T$ and the Schrödinger equation with Hamiltonian $\hat{H}_{\rm r}'$ gives

$$i\dot{c}_1 = (g_1\sin\theta)c_2 + (g_1\cos\theta)c_3, \tag{A2}$$

$$i\dot{c}_2 = \omega_1^{\rm r}c_2 + (g_1\sin\theta)c_1 + (\sqrt{2}g_1\cos\theta)c_4, \tag{A3}$$

$$i\dot{c}_3 = \left(\omega_1^{\rm r}-\omega_{\rm q}\right)c_3 + (g_1\cos\theta)c_1 - (\sqrt{2}g_1\sin\theta)c_4, \tag{A4}$$

$$i\dot{c}_4 = \left(2\omega_1^{\rm r}-\omega_{\rm q}\right)c_4 + (\sqrt{2}g_1\cos\theta)c_2 - (\sqrt{2}g_1\sin\theta)c_3\,. \tag{A5}$$

For $g_1/\omega_1^{\rm r} \ll 1$, the adiabatic elimination in Eqs. (A3) and (A4) can be applied [39] and the coefficients c_2 and c_3 can be approximated as

$$c_2 \approx -\frac{g_1}{\omega_1^{\rm r}}(\sin\theta c_1 + \sqrt{2}\cos\theta c_4), \tag{A6}$$

$$c_3 \approx -\frac{g_1}{\left(\omega_1^{\rm r}-\omega_{\rm q}\right)}(\cos\theta c_1 - \sqrt{2}\sin\theta c_4). \tag{A7}$$

The coupled equations for c_1 and c_4 are obtained by substituting these results in Eqs. (A2) and (A5):

$$i\dot{c}_1 \approx \frac{g_1^2\left(\omega_q \sin^2(2\theta) - \omega_1^r\right)}{\omega_1^r\left(\omega_1^r - \omega_q\right)} c_1 + \frac{\sqrt{2}g_1^2\omega_q \sin(2\theta)}{2\omega_1^r\left(\omega_1^r - \omega_q\right)} c_4, \tag{A8}$$

$$i\dot{c}_4 \approx \frac{-2g_1^2\left(\omega_1^r - \omega_q \cos^2\theta\right) + \omega_1^r\left[2\left(\omega_1^r\right)^2 - 3\omega_1^r\omega_q + \omega_q^2\right]}{\omega_1^r\left(\omega_1^r - \omega_q\right)} c_4 + \frac{\sqrt{2}g_1^2\omega_q \sin(2\theta)}{2\omega_1^r\left(\omega_1^r - \omega_q\right)} c_1. \tag{A9}$$

Considering the near-resonance case $\omega_1^r \approx \omega_q/2$, transforming back to the laboratory frame and keeping only the g_1^2 dependence terms in the diagonal elements, the effective Hamiltonian in Eq. (9) is obtained. According to the effective Hamiltonian (9), the ratio of the minimum splitting at the avoided crossing [see Fig. 1(c)] to the qubit frequency ω_q is given by

$$\frac{2\Omega_{\text{eff}}^{(2\text{ph})}}{\omega_q} = 4\sqrt{2}\sin(2\theta)\left(\frac{g_1}{\omega_q}\right)^2. \tag{A10}$$

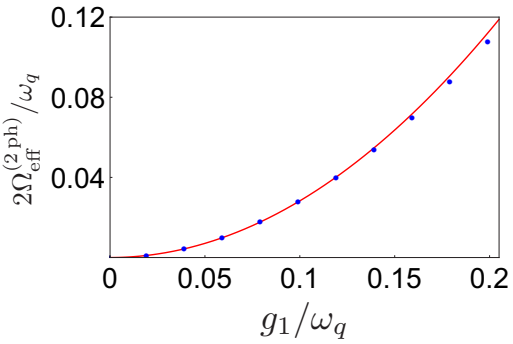

FIG. 7. (Color online) Comparison between the minimum energy splitting $2\Omega_{\text{eff}}^{(2\text{ph})}/\omega_q$ obtained analytically (red solid curve) and numerically (blue points) as a function of g_1/ω_q for $\theta = \pi/4$.

A comparison between analytical and numerical results for the minimum energy splitting $2\Omega_{\text{eff}}^{(2\text{ph})}/\omega_q$ is shown in Fig. 7 as a function of g_1/ω_q.

[1] M. Brune, F. Schmidt-Kaler, A. Maali, J. Dreyer, E. Hagley, J. M. Raimond, and S. Haroche, Quantum Rabi Oscillation: A Direct Test of Field Quantization in a Cavity, Phys. Rev. Lett. **76**, 1800 (1996).

[2] J. M. Raimond, M. Brune, and S. Haroche, Manipulating quantum entanglement with atoms and photons in a cavity, Rev. Mod. Phys. **73**, 565 (2001).

[3] R. J. Thompson, G. Rempe, and H. J. Kimble, Observation of Normal-Mode Splitting for an Atom in an Optical Cavity, Phys. Rev. Lett. **68**, 1132 (1992).

[4] S. Haroche and J. M. Raimond, *Exploring the Quantum: Atoms, Cavities and Photons* (Oxford University Press, Oxford, 2006).

[5] A. Auffeves, D. Gerace, R. Maxime, S. Portolan, M. F. Santos, L. C. Kwek, and C. Miniatura, *Strong Light-Matter Coupling: From Atoms to Solid-State Physics* (World Scientific, Singapore, 2013).

[6] T. Yoshie, A. Scherer, J. Hendrickson, G. Khitrova, H. M. Gibbs, G. Rupper, C. Ell, O. B. Shchekin, and D. G. Deppe, Vacuum Rabi splitting with a single quantum dot in a photonic crystal nanocavity, Nature (London) **432**, 200 (2004).

[7] J. P. Reithmaier, G. Sek, A. Löffler, C. Hofmann, S. Kuhn, S. Reitzenstein, L. V. Keldysh, V. D. Kulakovskii, T. L. Reinecke, and A. Forchel, Strong coupling in a single quantum dot–semiconductor microcavity system, Nature (London) **432**, 197 (2004).

[8] A. Blais, R. S. Huang, A. Wallraff, S. M. Girvin, and R. J. Schoelkopf, Cavity quantum electrodynamics for superconducting electrical circuits: An architecture for quantum computation, Phys. Rev. A **69**, 062320 (2004).

[9] A. Wallraff, D. I. Schuster, A. Blais, L. Frunzio, R. S. Huang, J. Majer, S. Kumar, S. M. Girvin, and R. J. Schoelkopf, Strong coupling of a single photon to a superconducting qubit using circuit quantum electrodynamics, Nature (London) **431**, 162 (2004).

[10] I. Chiorescu, P. Bertet, K. Semba, Y. Nakamura, C. J. P. M. Harmans, and J. E. Mooij, Coherent dynamics of a flux qubit coupled to a harmonic oscillator, Nature (London) **431**, 159 (2004).

[11] J. Q. You and F. Nori, Atomic physics and quantum optics using superconducting circuits, Nature (London) **474**, 589 (2011).

[12] S. Haroche, Nobel lecture: Controlling photons in a box and exploring the quantum to classical boundary, Rev. Mod. Phys. **85**, 1083 (2013).

[13] S. Deleglise, I. Dotsenko, C. Sayrin, J. Bernu, M. Brune, J. M. Raimond, and S. Haroche, Reconstruction of non-classical cavity field states with snapshots of their decoherence, Nature (London) **455**, 510 (2008).

[14] M. Hofheinz, H. Wang, M. Ansmann, R. C. Bialczak, E. Lucero, M. Neeley, A. D. O'Connell, D. Sank, J. Wenner, J. M. Martinis, and A. N. Cleland, Synthesizing arbitrary quantum states in a superconducting resonator, Nature (London) **459**, 546 (2009).

[15] S. Haroche, M. Brune, and J. M. Raimond, Atomic clocks for controlling light fields, Phys. Today **66**(1), 27 (2013).

[16] B. Vlastakis, G. Kirchmair, Z. Leghtas, S. E. Nigg, L. Frunzio, S. M. Girvin, M. Mirrahimi, M. H. Devoret, and R. J. Schoelkopf, Deterministically encoding quantum information using 100-photon Schrödinger cat states, Science **342**, 607 (2013).

[17] J. Q. You and F. Nori, Superconducting circuits and quantum information, Phys. Today **58**(11), 42 (2005).

[18] H. J. Kimble, The quantum internet, Nature (London) **453**, 1023 (2008).

[19] G. Günter, A. A. Anappara, J. Hees, A. Sell, G. Biasiol, L. Sorba, S. De Liberato, C. Ciuti, A. Tredicucci, A. Leitenstorfer, and R. Huber, Sub-cycle switch-on of ultrastrong light–matter interaction, Nature (London) **458**, 178 (2009).

[20] P. Forn-Díaz, J. Lisenfeld, D. Marcos, J. J. García-Ripoll, E. Solano, C. J. P. M. Harmans, and J. E. Mooij, Observation of the Bloch-Siegert Shift in a Qubit-Oscillator System in the

Ultrastrong Coupling Regime, Phys. Rev. Lett. **105**, 237001 (2010).
[21] T. Niemczyk, F. Deppe, H. Huebl, E. P. Menzel, F. Hocke, M. J. Schwarz, J. J. García-Ripoll, D. Zueco, T. Hümmer, E. Solano, A. Marx, and R. Gross, Circuit quantum electrodynamics in the ultrastrong-coupling regime, Nat. Phys. **6**, 772 (2010).
[22] T. Schwartz, J. A. Hutchison, C. Genet, and T. W. Ebbesen, Reversible Switching of Ultrastrong Light-Molecule Coupling, Phys. Rev. Lett. **106**, 196405 (2011).
[23] M. Geiser, F. Castellano, G. Scalari, M. Beck, L. Nevou, and J. Faist, Ultrastrong Coupling Regime and Plasmon Polaritons in Parabolic Semiconductor Quantum Wells, Phys. Rev. Lett. **108**, 106402 (2012).
[24] G. Scalari, C. Maissen, D. Turčinková, D. Hagenmüller, S. De Liberato, C. Ciuti, C. Reichl, D. Schuh, W. Wegscheider, M. Beck, and J. Faist, Ultrastrong coupling of the cyclotron transition of a 2D electron gas to a THz metamaterial, Science **335**, 1323 (2012).
[25] S. Gambino, M. Mazzeo, A. Genco, O. Di Stefano, S. Savasta, S. Patane, D. Ballarini, F. Mangione, G. Lerario, D. Sanvitto, and G. Gigli, Exploring light–matter interaction phenomena under ultrastrong coupling regime, ACS Photon. **1**, 1042 (2014).
[26] M. Goryachev, W. G. Farr, D. L. Creedon, Y. Fan, M. Kostylev, and M. E. Tobar, High-Cooperativity Cavity QED with Magnons at Microwave Frequencies, Phys. Rev. Appl. **2**, 054002 (2014).
[27] C. Maissen, G. Scalari, F. Valmorra, M. Beck, J. Faist, S. Cibella, R. Leoni, C. Reichl, C. Charpentier, and W. Wegscheider, Ultrastrong coupling in the near field of complementary split-ring resonators, Phys. Rev. B **90**, 205309 (2014).
[28] S. De Liberato, C. Ciuti, and I. Carusotto, Quantum Vacuum Radiation Spectra from a Semiconductor Microcavity with a Time-Modulated Vacuum Rabi Frequency, Phys. Rev. Lett. **98**, 103602 (2007).
[29] S. Ashhab and F. Nori, Qubit-oscillator systems in the ultrastrong-coupling regime and their potential for preparing nonclassical states, Phys. Rev. A **81**, 042311 (2010).
[30] X. Cao, J. Q. You, H. Zheng, A. G. Kofman, and F. Nori, Dynamics and quantum Zeno effect for a qubit in either a low-or high-frequency bath beyond the rotating-wave approximation, Phys. Rev. A **82**, 022119 (2010).
[31] X. Cao, J. Q. You, H. Zheng, and F. Nori, A qubit strongly coupled to a resonant cavity: Asymmetry of the spontaneous emission spectrum beyond the rotating wave approximation, New J. Phys. **13**, 073002 (2011).
[32] A. Ridolfo, M. Leib, S. Savasta, and M. J. Hartmann, Photon Blockade in the Ultrastrong Coupling Regime, Phys. Rev. Lett. **109**, 193602 (2012).
[33] A. Ridolfo, S. Savasta, and M. J. Hartmann, Nonclassical Radiation from Thermal Cavities in the Ultrastrong Coupling Regime, Phys. Rev. Lett. **110**, 163601 (2013).
[34] R. Stassi, A. Ridolfo, O. Di Stefano, M. J. Hartmann, and S. Savasta, Spontaneous Conversion from Virtual to Real Photons in the Ultrastrong-Coupling Regime, Phys. Rev. Lett. **110**, 243601 (2013).
[35] J.-F. Huang and C. K. Law, Photon emission via vacuum-dressed intermediate states under ultrastrong coupling, Phys. Rev. A **89**, 033827 (2014).
[36] A. Cacciola, O. Di Stefano, R. Stassi, R. Saija, and S. Savasta, Ultrastrong coupling of plasmons and excitons in a nanoshell, ACS Nano **8**, 11483 (2014).
[37] L. Garziano, R. Stassi, A. Ridolfo, O. Di Stefano, and S. Savasta, Vacuum-induced symmetry breaking in a superconducting quantum circuit, Phys. Rev. A **90**, 043817 (2014).
[38] A. Baust *et al.*, Ultrastrong coupling in two-resonator circuit QED, arXiv:1412.7372.
[39] K. K. W. Ma and C. K. Law, Three-photon resonance and adiabatic passage in the large-detuning Rabi model, Phys. Rev. A **92**, 023842 (2015).
[40] S. De Liberato, D. Gerace, I. Carusotto, and C. Ciuti, Extracavity quantum vacuum radiation from a single qubit, Phys. Rev. A **80**, 053810 (2009).
[41] F. Beaudoin, J. M. Gambetta, and A. Blais, Dissipation and ultrastrong coupling in circuit QED, Phys. Rev. A **84**, 043832 (2011).
[42] L. Garziano, A. Ridolfo, R. Stassi, O. Di Stefano, and S. Savasta, Switching on and off of ultrastrong light-matter interaction: Photon statistics of quantum vacuum radiation, Phys. Rev. A **88**, 063829 (2013).
[43] S. Agarwal, S. M. Hashemi Rafsanjani, and J. H. Eberly, Dissipation of the Rabi model beyond the Jaynes-Cummings approximation: quasi-degenerate qubit and ultra-strong coupling, J. Phys. B **46**, 224017 (2013).
[44] H.-P. Breuer and F. Petruccione, *The Theory of Open Quantum Systems* (Oxford University Press, Oxford, 2002).
[45] E. T. Jaynes and F. W. Cummings, Comparison of quantum and semiclassical radiation theories with application to the beam maser, Proc. IEEE **51**, 89 (1963).
[46] Y. X. Liu, J. Q. You, L. F. Wei, C. P. Sun, and F. Nori, Optical Selection Rules and Phase-Dependent Adiabatic State Control in a Superconducting Quantum Circuit, Phys. Rev. Lett. **95**, 087001 (2005).
[47] D. Braak, Integrability of the Rabi model, Phys. Rev. Lett. **107**, 100401 (2011).
[48] J. Johansson, S. Saito, T. Meno, H. Nakano, M. Ueda, K. Semba, and H. Takayanagi, Vacuum Rabi Oscillations in a Macroscopic Superconducting Qubit LC Oscillator System, Phys. Rev. Lett. **96**, 127006 (2006).
[49] D. M. Greenberger, M. A. Horne, A. Shimony, and A. Zeilinger, Bell's theorem without inequalities, Am. J. Phys. **58**, 1131 (1990).
[50] S. Bose, V. Vedral, and P. L. Knight, Multiparticle generalization of entanglement swapping, Phys. Rev. A **57**, 822 (1998).
[51] R. Cleve, D. Gottesman, and H.-K. Lo, How to Share a Quantum Secret, Phys. Rev. Lett. **83**, 648 (1999).
[52] D. P. Di Vincenzo and P. W. Shor, Fault-Tolerant Error Correction with Efficient Quantum Codes, Phys. Rev. Lett. **77**, 3260 (1996).
[53] L. F. Wei, Y. X. Liu, and F. Nori, Generation and Control of Greenberger-Horne-Zeilinger Entanglement in Superconducting Circuits, Phys. Rev. Lett. **96**, 246803 (2006).
[54] C.-P. Yang, Q.-P. Su, S.-B. Zheng, and F. Nori, Entangling superconducting qubits in a multi-cavity system, arXiv:1506.06108.
[55] J. I. Cirac and P. Zoller, Preparation of macroscopic superpositions in many-atom systems, Phys. Rev. A **50**, R2799 (1994).
[56] S.-B. Zheng, One-Step Synthesis of Multiatom Greenberger-Horne-Zeilinger States, Phys. Rev. Lett. **87**, 230404 (2001).

5.3 Paper III: Deterministic synthesis of mechanical *NOON* states in ultrastrong optomechanics

PHYSICAL REVIEW A **94**, 013817 (2016)

Deterministic synthesis of mechanical NOON states in ultrastrong optomechanics

V. Macrí, L. Garziano, A. Ridolfo, O. Di Stefano, and S. Savasta
Dipartimento di Fisica e di Scienze Terra Terra, Università di Messina, Viale F. Stagno d'Alcontres 31, I-98166 Messina, Italy
(Received 18 May 2016; published 8 July 2016)

We propose a protocol for the deterministic preparation of entangled NOON mechanical states. The system is constituted by two identical, optically coupled optomechanical systems. The protocol consists of two steps. In the first, one of the two optical resonators is excited by a resonant external π-like Gaussian optical pulse. When the optical excitation coherently partly transfers to the second cavity, the second step starts. It consists of sending simultaneously two additional π-like Gaussian optical pulses, one at each optical resonator, with specific frequencies. In the optomechanical ultrastrong coupling regime, when the coupling strength becomes a significant fraction of the mechanical frequency, we show that NOON mechanical states with quite high Fock states can be deterministically obtained. The operating range of this protocol is carefully analyzed. Calculations have been carried out taking into account the presence of decoherence, thermal noise, and imperfect cooling.

DOI: 10.1103/PhysRevA.94.013817

I. INTRODUCTION

Cavity optomechanics studies optical cavities and mechanical resonators interacting via radiation pressure and mechanical back-action. The manipulation and detection of mechanical motion in the quantum regime using radiation pressure is promising for applications in quantum information processing [1,2], where optomechanical devices could serve as coherent light-matter interfaces which may allow for storage of quantum information in long-lived phonon states [3]. Specifically, hybrid systems, consisting of electromagnetic resonators and mechanical oscillators constitute a promising platform for realizing quantum memory or quantum state transfer among different nodes of a quantum network [4–7].

Mechanical oscillators in the quantum regime are also systems with great potential in sensing and quantum metrology [8–15]. Moreover, they could offer a route to new tests of quantum theory at unprecedented size and mass scales. These experiments could help the understanding of decoherence processes in massive objects. These systems are promising as a means to control and observe quantum superpositions of macroscopic objects [16–18]. The optomechanical interaction can also be exploited to create interesting quantum states in both the optical and the mechanical subsystems and to create entangled states between the two subsystems or between different mechanical systems. One of the most straightforward applications of quantum optomechanics, regarding the manipulation of the photon quantum states, consists of squeezing the noise of the light beam [19–21]. A review of the current efforts toward demonstrating shot-noise effects and squeezing in optomechanical experiments can be found in Ref. [22]. The realizations of cavity optomechanical systems with both atomic clouds and photonic crystal cavities have allowed the demonstration of mechanical-induced optical squeezing at the quantum level [23,24].

The generation of nonclassical mechanical states requires cooling of the system to its ground state. Experimentally, ground-state cooling with conventional cryogenics can be reached only for high-frequency mechanical oscillators. The first demonstration of quantum control at the single-phonon level was demonstrated with a ∼6-GHz piezoelectric mechanical oscillator cooled below 50 mK [25]. For lower-frequency mechanical oscillators, ground-state cooling can be obtained by combining cryogenic precooling with dynamical back-action laser cooling. Optical feedback cooling based on the radiation pressure force was demonstrated in the vibrational modes of a macroscopic end-mirror [26]. Radiation-pressure cavity cooling, for suspended micromirrors [27] and for microtoroids [28], has also been demonstrated. It has been shown that, starting from the system ground state, it is possible, in principle, to synthesize arbitrary mechanical quantum states in a completely controlled and deterministic manner [29]. The general strategy for creating such states was described by Law and Eberly in the context of cavity QED [30]. Quantum state engineering of the electromagnetic field of an optical mode has been demonstrated in the context of cavity quantum electrodynamics and in circuit quantum electrodynamics [31–34]. The approach by Xu *et al.* [29] applies to optomechanical systems the protocols developed for the synthesis of arbitrary motional states of a trapped ion [35–37], inspired by the Law and Eberly protocol [30]. Recently, Garziano *et al.* proposed a different cavity-optomechanics protocol working in the ultrastrong-coupling (USC) regime, which in a single step forces the ground state of a mechanical oscillator to evolve into the target quantum state in a completely controlled and deterministic manner, the only limitation being the strength of the optomechanics interaction [38].

The classification of the different interaction regimes based on the interaction strength is not universal. In analogy with cavity QED, the USC regime can be referred to as the regime where the coupling strength g_M becomes comparable to the transition frequency of the mechanical resonator ω_M [38]. This regime is also known as beyond Lamb-Dicke [37,39]. The regime where the radiation pressure of a single photon displaces the mechanical resonator by more than its zero-point uncertainty, corresponding to $g_M \geqslant \omega_M$, has been designated as the single-photon strong-coupling regime [40]. Optomechanics experiments are rapidly approaching the USC regime [11]. Achieving it in optomechanical systems will facilitate the creation of quantum mechanical states of the mechanical resonator, as well as the characterization of such states by measuring the cavity photon field [40–42]. USC is

attracting great interest also in cavity QED because it can give rise to novel quantum effects [43–49].

In the single-photon strong-coupling regime, it has been shown that, starting from a superposition of photon states inside the cavity, it is possible to create a Schrödinger cat-type state, where a microscopic degree of freedom (the optical cavity mode) is entangled with a "macroscopic" degree of freedom (the vibrating mirror) [31,50,51]. Experimental schemes for obtaining entanglement between mechanical motion and the optical cavity have also been analyzed for the continuous-variable case [52,53]. Recently, it has been shown that a suitable time-dependent modulation of the drive can improve the efficiency of photon-phonon entanglement [54].

Several different protocols and techniques have been proposed in order to create entanglement of spatially separated mechanical oscillators, exploiting radiation pressure [55,56]. A heralded probabilistic scheme, working in the optomechanical USC regime, to generate mechanical NOON states [57,58] with arbitrary phonon numbers by measuring the sideband photons has been proposed [59]. Using sideband excitations, it has been shown that arbitrary entangled states of vibrational modes of different membranes embedded inside a cavity can be produced in principle by sequentially applying a series of classical pulses with specific frequencies, phases, and durations [39]. In the case of two mechanical resonators coupled to the same driven cavity mode, a realistic protocol for the heralded preparation and readout of mechanical Bell states has been proposed [60,61]. A scheme to transfer continuous variable entanglement from the squeezed light to the mechanical motion of movable mirrors has been recently proposed [62].

Here we propose a protocol for the deterministic preparation of entangled NOON states or even more general mechanical states between two identical, optically coupled optomechanical systems. Two key features of this scheme are the following: (i) entanglement can be generated with a few steps independently of the highest phonon number present in the entangled state, and (ii) the protocol is deterministic. This approach extends a recently proposed scheme for a single-step arbitrary control of mechanical quantum states in a single optomechanical system in the USC regime [38]. The system here studied has already been proposed to generate quantum entanglement between two mechanical resonators involving zero- and one-phonon states [63], by considering a large photon hopping regime. The protocol here presented is an example of how the USC regime can favor the generation and control of mechanical quantum entangled states.

II. MODEL

We start by considering two identical, optically coupled optomechanical systems (see Fig. 1). We mainly focus on the USC regime, although we also present results obtained for lower coupling rates.

The total Hamiltonian of the system is ($\hbar = 1$)

$$\hat{H}_S = \sum_{i=1}^{2} \hat{H}_0^{(i)} + \hat{H}_I, \tag{1}$$

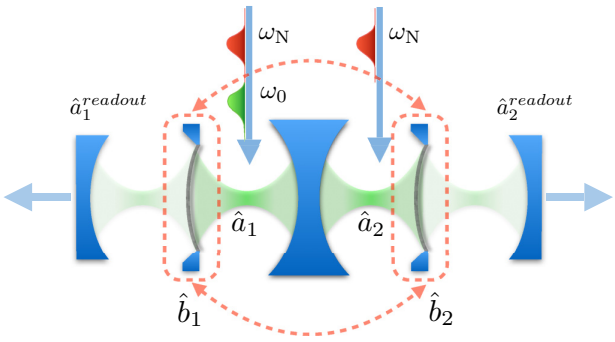

FIG. 1. Schematic setup of two identical optically coupled optomechanical systems. Each mechanical oscillator, with frequency ω_M, is parametrically coupled with a single-mode optical resonator and/or cavity, which can be driven by external π-like Gaussian optical pulses with specific central frequencies. One cavity mirror can be added to the end of both the optomechanical systems for optical readout.

where

$$\hat{H}_0^{(i)} = \omega_R \hat{a}_i^\dagger \hat{a}_i + \omega_M \hat{b}_i^\dagger \hat{b}_i + g_M \hat{a}_i^\dagger \hat{a}_i (\hat{b}_i + \hat{b}_i^\dagger) \tag{2}$$

describes the two uncoupled optomechanical systems and

$$\hat{H}_I = g_R (\hat{a}_1^\dagger \hat{a}_2 + \hat{a}_1 \hat{a}_2^\dagger) \tag{3}$$

describes their optical coupling, where g_R is the coupling rate between the two optical resonators. In Eq. (2), ω_R is the resonance frequency of the optical resonator, ω_M is the mechanical resonance frequency, and $g_M = \omega_R' x_{\rm ZPF}$ is the optomechanical coupling. Here $x_{\rm ZPF} = (2\mathcal{M}\omega_M)^{-1/2}$, representing the zero-point uncertainty, where $\mathcal{M}$ is the mass of the mechanical oscillator and ω_M' is the derivative of the resonator energy with respect to the mechanical oscillator position. The operators $\hat{a}_i$ and $\hat{b}_i$ are, respectively, the standard Bosonic annihilation operators for the ith cavity mode and the mechanical oscillator. In Eq. (3), the counter-rotating terms proportional to $\hat{a}_1^\dagger \hat{a}_2^\dagger$ and $\hat{a}_1 \hat{a}_2$ have been dropped, owing to the smallness of the coupling strength between the two optical resonators, with respect to their resonance frequency, considered in this work.

The two optomechanical systems interact only via optical coupling. When $g_R = 0$, i.e., there is no interaction between the two cavities, each Hamiltonian in Eq. (2) conserves its photon number ($[\hat{a}_i^\dagger \hat{a}_i, \hat{H}_0^{(i)}] = 0$), and it can be diagonalized separately. In each n-photonic Fock subspace, the Hamiltonian describes a harmonic oscillator with frequency ω_M which is displaced by $-n x_0$, where $x_0 = 2 x_{\rm ZPF}\, g_M^2/\omega_M$ is the displacement caused by a single photon. The eigenvalues of the Hamiltonian in Eq. (2) are $E_{nm}^{(i)} = n\omega_R - \frac{n^2 g_M^2}{\omega_M} + m\omega_M$, and the corresponding eigenstates can be expressed as

$$|n,m\rangle_i = |n\rangle_i e^{n\beta_0(\hat{b}_i^\dagger - \hat{b}_i)} |m\rangle_i, \tag{4}$$

where $\beta_0 = g_M/\omega_M$ and $|m\rangle_i = (1/\sqrt{m!})(b_i^\dagger)^m |0\rangle_i$. The $|1,0\rangle_i$ state represents the mechanical ground state of the $n = 1$ manifold displaced harmonic oscillator. It corresponds to a mechanical coherent state that can be expanded in terms of the

bare mechanical states $|m\rangle_i$ with the well-known expression

$$|1,0\rangle_i = |1\rangle_i \sum_{m=0}^{\infty} d_m |m\rangle_i, \tag{5}$$

with

$$d_m = \frac{(-\beta_0)^m}{\sqrt{m!}} e^{-\frac{1}{2}\beta_0^2}. \tag{6}$$

If $g_R = 0$, the eigenstates of the Hamiltonian in Eq. (1) can be written as

$$|n_1,m_1,n_2,m_2\rangle = |n_1,m_1\rangle_1 \otimes |n_2,m_2\rangle_2, \tag{7}$$

where the integers n_i and m_i represent, respectively, the number of photons and vibrational excitation in the ith optomechanical system.

III. THE PROTOCOL

We first describe the two-step protocol for the *deterministic* preparation of mechanical entangled NOON states:

$$|\bar{\psi}\rangle = \alpha|0,N,0,0\rangle + \beta e^{i\varphi}|0,0,0,N\rangle, \quad \alpha,\beta \in \mathbb{R}^+. \tag{8}$$

We consider that the two optical cavities are interacting ($g_R \neq 0$), and the system is initially prepared in its ground state $|0,0,0,0\rangle$ (no photons in the cavities and the mechanical oscillators are in their ground state). We neglect the coupling of the system with its environment, in this initial presentation, in order to focus on the key points of the protocol. The influence of pulse width and transition matrix elements on the achievement of the target quantum state is discussed below under the subsection "Operating limits."

The first step consists of the excitation of one of the two optical resonators (e.g., resonator 1) by an external π-like Gaussian optical pulse resonant with the transition $|0,0,0,0\rangle \leftrightarrow |1,m,0,0\rangle$ (pulse 1). Since the system is totally symmetrical, results do not change if we apply pulse 1 to either cavity 1 or cavity 2. In the following we consider the case where pulse 1 is sent to cavity 1. In the regimes here investigated, where the optomechanical coupling induces the photon blockade, the resulting state is $|1,m,0,0\rangle$. For $g_R \neq 0$ this state is not an eigenstate of the Hamiltonian in Eq. (1). As a consequence, the system will undergo Rabi-like oscillations and the time evolution of the state of the system will be given by

$$|\psi(t)\rangle = \cos(g_R t)|1,m,0,0\rangle - i\sin(g_R t)|0,0,1,m\rangle. \tag{9}$$

This energy exchange between the two resonators can be interrupted by sending simultaneously two additional optical π pulses, (pulses 2 and 3, one exciting each cavity) resonant with the transition $|1,m\rangle_i \rightarrow |0,N\rangle_i$ (step 2). If we want to create a NOON state with specific probability amplitudes $\beta = \sin(g_R t^*)$, $\alpha = \cos(g_R t^*)$, these two additional optical pulses must be sent at $t^* = g_R^{-1}\arctan(\beta/\alpha)$. A key point is that the ket $|0,0\rangle_i$ will remain unchanged after the arrival of such pulses, because the central frequency of the pulse is very far from the transition frequency of $|0,0\rangle_i \rightarrow |1,0\rangle_i$ as schematically shown in Fig. 2. This will produce the desired entangled mechanical state. If the two optical pulses have the same phase, the following state is obtained,

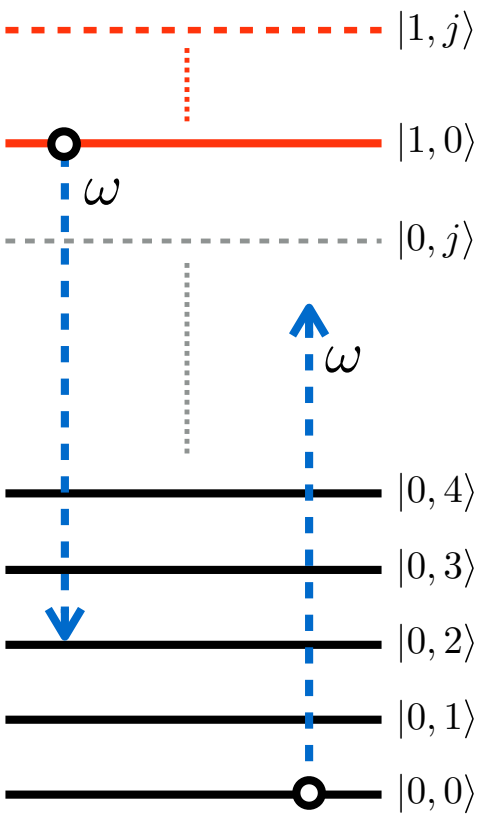

FIG. 2. Scheme of the lowest energy levels for a single optomechanical system. If the system is in the state $|1,0\rangle$, a resonant optical π pulse, described by the blue arrow, induces the transition $|1,0\rangle \rightarrow |0,2\rangle$. If the system is in the state $|0,0\rangle$, no transitions can be induced by the same pulse.

$$|\bar{\psi}\rangle = \alpha\,|0,N,0,0\rangle - i\beta\,|0,0,0,N\rangle, \tag{10}$$

which, dropping the factorized photonic kets, can be also written as

$$|\bar{\psi}\rangle_{\rm mech} = \alpha\,|N,0\rangle_{\rm mech} - i\beta\,|0,N\rangle_{\rm mech}. \tag{11}$$

The highest mechanical number state N that can be obtained in this NOON state strongly depends on the normalized mechanical coupling strength β_0.

We now proceed to a more detailed description of the protocol. The total system Hamiltonian in the presence of the input optical pulses (dissipation and decoherence effects are described later by the master equation approach) reads

$$\hat{H} = \hat{H}_S + \hat{H}_d^{(0)}(t) + \sum_{i=1}^{2} \hat{H}_d^{(i)}(t), \tag{12}$$

where

$$\hat{H}_d^{(0)}(t) = \mathcal{E}_0(t)\cos(\omega_0 t)\hat{X}_1 \tag{13}$$

describes the external driving pulse 1 (first step), with $\mathcal{E}_0(t) = \sqrt{\kappa}\,A_0\,\mathcal{G}_\Delta(t-t_0)$. Here, A_0 is the pulse

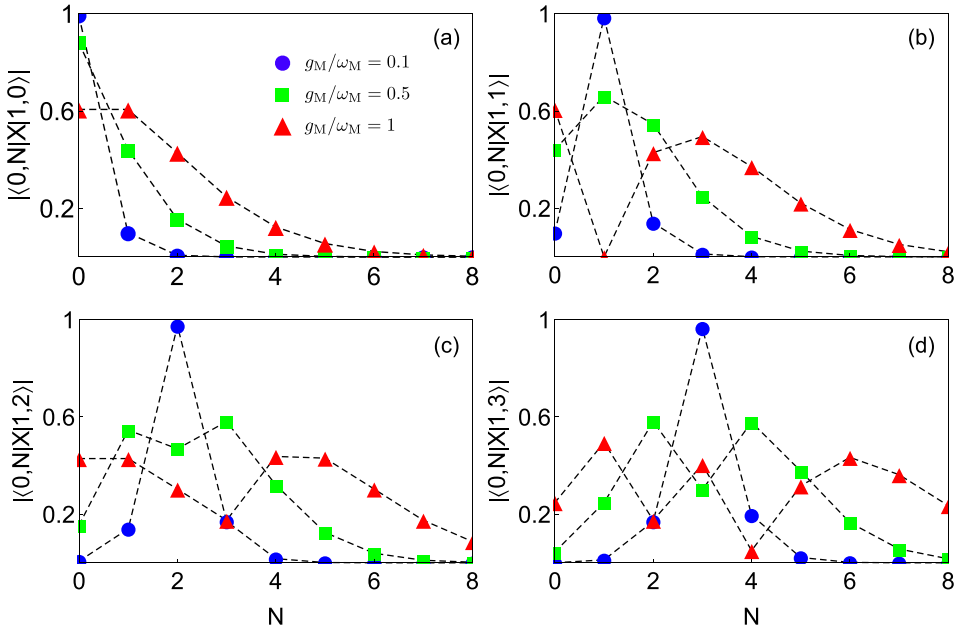

FIG. 3. Transition matrix elements $\langle 0,N|\hat{X}|1,m\rangle$ between the intermediate state $|1,m\rangle$ and the mechanical state $|0,N\rangle$ as a function of the vibrational quantum number N for different values of the optomechanical coupling rates $g_M/\omega_M = 0.1$ (blue solid circles), $g_M/\omega_M = 0.5$ (green solid squares), and $g_M/\omega_M = 1$ (red solid triangles), when the ancilla state has phonon numbers (a) $m = 0$, (b) $m = 1$, (c) $m = 2$, and (d) $m = 3$.

amplitude, κ is the cavity damping rate, and $\mathcal{G}_\Delta(t-t_0) = \exp[-(t-t_0)^2/(2\Delta^2)]/(\Delta\sqrt{2\pi})$ is a normalized Gaussian function describing the pulse shape. Moreover, $\hat{X}_1 = \hat{a}_1^\dagger + \hat{a}_1$ and $\omega_0 = E_{1m} - E_{00}$ is the energy gap between the *ancilla* state $|1,m,0,0\rangle$ and the ground state $|0,0,0,0\rangle$. We now move to the frame that diagonalizes the system Hamiltonian $\hat{H}_S$ by expressing the driving Hamiltonian in the dressed basis of the system energy eigenstates, and we can focus our attention on the case in which the driving fields are resonant with the transitions $|1,m,0,0\rangle \leftrightarrow |0,0,0,0\rangle$. In the interaction picture (with respect to $\hat{H}_S$) and neglecting the nonresonant time-oscillating terms, $\hat{H}_d^{(0)}$ reduces to the following effective driving Hamiltonian:

$$\hat{H}_{\rm eff}^{(0)} = \mathcal{E}_m(t)|0,0,0,0\rangle\langle 1,m,0,0| + \text{H.c.}, \tag{14}$$

where the effective amplitude $\mathcal{E}_m(t)$ of the driving field is given by

$$\mathcal{E}_m(t) = \frac{\mathcal{E}_0(t)}{2}\langle 0,0,0,0|\hat{X}_1|1,m,0,0\rangle. \tag{15}$$

The necessary and sufficient condition to ensure that the *ancilla* state is completely populated by external drive pulse is $\int_{-\infty}^{\infty}|\mathcal{E}_m(t)|dt = \pi$. This condition is fulfilled if $A_0\sqrt{\kappa}|\langle 0,0,0,0|\hat{X}_{(1)}|1,m,0,0\rangle| = \pi$. As described above, since the two cavities are optically coupled, after the arrival of the first pulse at cavity 1, the excitation spontaneously transfers towards the second cavity, and the resulting state is the superposition in Eq. (9).

The last term in Eq. (12) describes the equal (except for a possible phase factor) external driving pulses that are sent to both the cavities in the second step. The driving Hamiltonian $\hat{H}_d^{(i)}$ corresponding to excitation of the ith cavity can be expressed as

$$\hat{H}_d^{(i)} = \sum_{j=1}^{k}\mathcal{E}_j(t)\cos\left(\omega_j t + \eta_j^{(i)}\right)\hat{X}_i. \tag{16}$$

In order to depopulate the intermediate ancilla state $|1,m\rangle_i$ towards the $|0,m'\rangle_i$ states, two optical π-like pulses at both cavities have to be sent, at the same instant of time t^*. Then, the target NOON state $|\bar{\psi}\rangle$, in Eq. (8), can be obtained by sending, at each cavity, one quasimonochromatic optical pulse with central frequency $\omega_N = E_{1m} - E_{0N}$. Following the above-described procedure, $\hat{H}_d^{(1)}$ can be approximated by the effective driving Hamiltonian:

$$\hat{H}_{\rm eff}^{(1)} = \mathcal{E}_{m,N}(t)e^{i\eta_N^{(1)}}|0,N,0,0\rangle\langle 1,m,0,0| + \text{H.c.}, \tag{17}$$

where the effective amplitudes $\mathcal{E}_{m,N}(t)$ of the driving fields are given by

$$\mathcal{E}_{m,N}(t) = \frac{\mathcal{E}_1(t)}{2}\langle 0,N,0,0|\hat{X}_1|1,m,0,0\rangle, \tag{18}$$

with $\mathcal{E}_1(t) = \sqrt{\kappa}A_1\mathcal{G}_\Delta(t-t_1)$. In this case, the complete transfer of the excitation from the ancilla states to the mechanical states $|0,N,0,0\rangle$ or $|0,0,0,N\rangle$ is obtained if the condition $A_1\sqrt{\kappa}|\langle 0,N,0,0|\hat{X}_1|1,m,0,0\rangle| = \pi$ is fulfilled. Once such a transfer is completed, the desired NOON state in Eq. (8) is obtained, provided that the two pulses display the following phase difference:

$$\eta_N^{(2)} - \eta_N^{(1)} = \varphi + \pi/2. \tag{19}$$

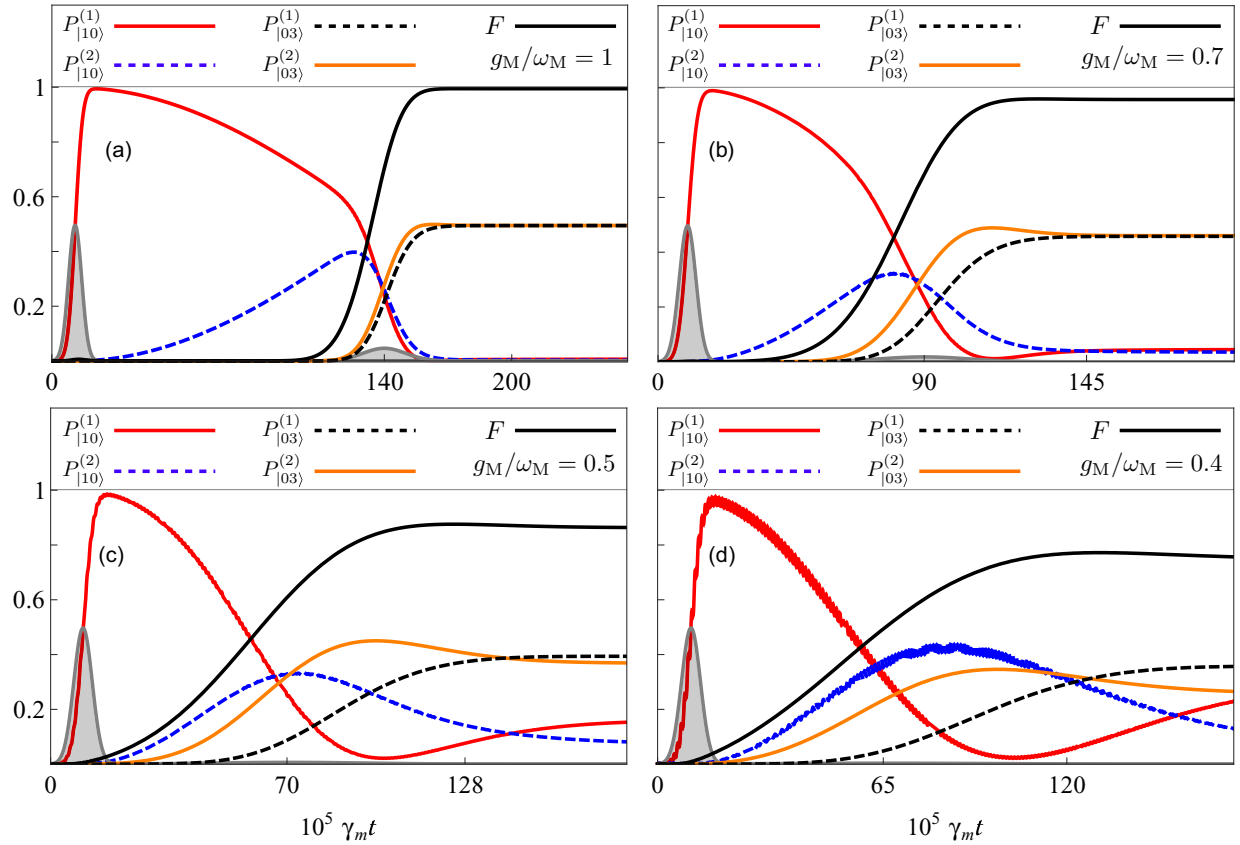

FIG. 4. Time evolution of the occupation probabilities $P^{(1)}_{|1,0\rangle}(t)$, $P^{(2)}_{|1,0\rangle}(t)$, $P^{(1)}_{|0,3\rangle}(t)$, and $P^{(2)}_{|0,3\rangle}(t)$, under the influence of three external π-like Gaussian pulses (gray solid curves). The first pulse, of central frequency ω_0, excites cavity 1. The other two, of central frequency ω_3, have the same arrival time and are sent one to each cavity. The amplitude, phase, and central frequencies of the pulses are chosen in order to generate the target NOON state $|\bar{\psi}\rangle_{\rm mech} = (|3,0\rangle_{\rm mech} - i|0,3\rangle_{\rm mech})/\sqrt{2}$. The time evolution of the fidelity F is also shown. Calculations are displayed for four different coupling mechanical rates: (a) $g_M/\omega_M = 1.0$ ($F_{\rm MAX} = 0.98$), (b) $g_M/\omega_M = 0.7$ ($F_{\rm MAX} = 0.95$), (c) $g_M/\omega_M = 0.5$ ($F_{\rm MAX} = 0.87$), and (d) $g_M/\omega_M = 0.4$ ($F_{\rm MAX} = 0.77$). For both optomechanical systems the other parameters are $\omega_R/\omega_M = 500$, $\kappa/\omega_M = 5 \times 10^{-5}$, $\gamma_m/\kappa = 0.1$, and $g_R/\omega_M = 8 \times 10^{-3}$.

We observe that this protocol can be extended to the implementation of general entangled states. Actually, it is possible to obtain entangled mechanical superpositions of the given

$$|\bar{\Phi}\rangle = \alpha|\Psi\rangle_1 \otimes |0,0\rangle_2 + \beta e^{i\varphi}|0,0\rangle_1 \otimes |\Psi\rangle_2, \qquad (20)$$

which we refer to as the $\Psi OO\Psi$ states, where $|\Psi\rangle_i = \sum_{m=0}^{N} c_m^{(i)}|0,m\rangle_i$ are arbitrary superpositions of one mechanical oscillator. In this case the first step needs no modifications, while the driving Hamltonian in Eq. (16) (second step) includes additional optical pulses ($k > 1$). The effective driving Hamiltonian, describing the jth pulse is

$$\hat{H}^{(1)}_{\rm eff_{(j)}} = \mathcal{E}^{(j)}_{m,m'}(t)e^{i\eta^{(j)}_{m,m'}}|0,m',0,0\rangle\langle 1,m,0,0| + \text{H.c.}, \qquad (21)$$

where the effective amplitudes $\mathcal{E}^{(j)}_{m,m'}(t)$ of the driving fields are given by

$$\mathcal{E}^{(j)}_{m,m'}(t) = \frac{\mathcal{E}_j(t)}{2}\langle 0,m',0,0|\hat{X}_1|1,m,0,0\rangle. \qquad (22)$$

The complete excitation transfer from the ancilla state to the final mechanical superpositions requires the following condition: $A_j\sqrt{\kappa}|\langle 0,m',0,0|\hat{X}_1|1,m,0,0\rangle| = |c^{(1)}_{m'}|\pi$.

In order to correctly describe the quantum dynamics of the system, dissipation induced by its coupling to the environment needs to be considered. We adopt the master equation approach. In the USC regime the description offered by the standard quantum optical master equation breaks down. Following Ref. [64], we exploit a master equation in the dressed state basis, which works for arbitrary optomechanical coupling strengths,

$$\begin{aligned}\dot{\rho}(t) = i[\rho(t),\hat{H}] &+ \sum_{j=1}^{2}\gamma_m^j(n_{\rm th}+1)\mathcal{D}[\hat{C}_j]\rho(t) \\ &+ \sum_{j=1}^{2}\gamma_m^j n_{\rm th}\mathcal{D}[\hat{C}_j^\dagger]\rho(t) + \sum_{j=1}^{2}\kappa_j\mathcal{D}[\hat{a}_j]\rho(t) \\ &+ \sum_{j=1}^{2}\phi_\gamma^j\mathcal{D}[\hat{N}_j]\rho(t), \qquad (23)\end{aligned}$$

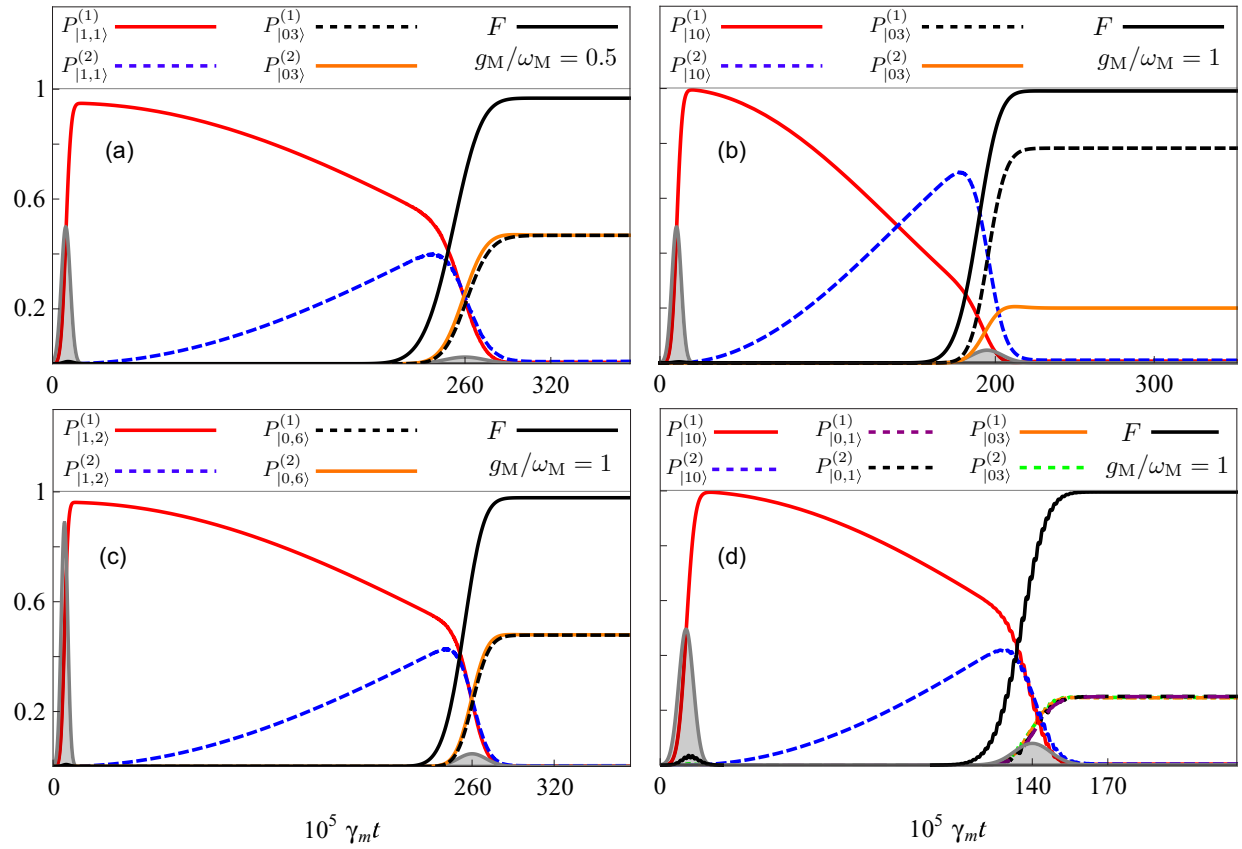

FIG. 5. Examples of time evolution of occupation probabilities and fidelities F for different entangled target states. (a) $|\bar{\psi}\rangle_{\rm mech} = (|3,0\rangle_{\rm mech} - i|0,3\rangle_{\rm mech})/\sqrt{2}$. The dynamics is calculated exploiting the ancilla state $|1,1\rangle$ and for $g_M/\omega_M = 0.5$. The achieved maximal fidelity is $F_{\rm MAX} = 0.963$. (b) Target state: $|\bar{\psi}\rangle_{\rm mech} = (2|3,0\rangle_{\rm mech} - i|0,3\rangle_{\rm mech})/\sqrt{5}$. Here the dynamics is calculated exploiting the ancilla state $|1,0\rangle$ and for $g_M/\omega_M = 1$, with $F_{\rm MAX} = 0.993$. (c) Target state: $|\bar{\psi}\rangle_{\rm mech} = (|6,0\rangle_{\rm mech} - i|0,6\rangle_{\rm mech})/\sqrt{2}$. We calculate the dynamics by starting from the ancilla state $|1,2\rangle$ and for $g_M/\omega_M = 1$, with $F_{\rm MAX} = 0.933$. (d) The target state is the $\bar{\Psi}OO\bar{\Psi}$ state, $|\bar{\Psi}\rangle_{\rm mech} = (|\Psi\rangle_{\rm mech}|0\rangle_{\rm mech} - i|0\rangle_{\rm mech}|\Psi\rangle_{\rm mech})/\sqrt{2}$, where $|\Psi\rangle_{\rm mech} = (|1\rangle_{\rm mech} + |3\rangle_{\rm mech})/\sqrt{2}$. The dynamics is calculated exploiting the ancilla state $|1,0\rangle$ and for $g_M/\omega_M = 1$ and $F_{\rm MAX} = 0.993$ is obtained. For both the optomechanical systems and for all four panels the other parameters are $\omega_R/\omega_M = 500$, $\kappa/\omega_M = 5 \times 10^{-5}$, $\gamma_m/\kappa = 0.1$, and $g_R/\omega_M = 8 \times 10^{-3}$.

where $\mathcal{D}[\hat{O}]\hat{\rho} = \frac{1}{2}(2\hat{O}\hat{\rho}\hat{O}^\dagger - \hat{\rho}\hat{O}^\dagger\hat{O} - \hat{O}^\dagger\hat{O}\hat{\rho})$ describes dissipation effects arising from the resonator and the mechanical reservoirs, and $\hat{C}_j = \hat{b}_j - (g_M/\omega_M)\hat{N}_j$ and $\hat{N}_j = \hat{a}_j^\dagger a_j$ are the displacement operator and the photon number operator, respectively. The optical cavity modes are affected by temperature-dependent pure dephasing effects, induced by the optomechanical coupling [64]. Such pure dephasing is taken into account by the last term of Eq. (23), where the coefficients $\phi_\gamma^j = 4K_B T\gamma_m^j g_M/\omega_M^2$ represent the decoherence rates.

Once the target state has been synthesized, there remains the problem of detecting it experimentally, or at least of quantifying its entanglement. The nonclassical nature of this mechanical state can be demonstrated by applying a readout laser on the lower sideband to map the phononic state to a photonic mode and performing an autocorrelation measurement [60,65]. The mechanical excitation is thus coherently mapped onto the external optical cavity $\hat{a}_i^{\rm readout}$. Alternatively, a full quantum tomography of the mechanical state might be carried out. The quantum state can be univocally characterized by employing Wigner tomography. Following the scheme developed by Leibfried *et al.* [66], the reconstruction of the density matrix and the Wigner function of the mechanical quantum state can be obtained. Once the target state is synthesized, the reconstruction mapping can be realized by applying to this state coherent displacements provided by a classical driving field of frequency ω_0 with different amplitudes and phases and then measuring the number-state populations. In analogy with Wigner tomography for trapped ions, a proposal for reconstruction of optomechanical quantum states has been recently presented by Vanner *et al.* [67].

Operating limits

We briefly discuss the requirements that the system parameters and external driving amplitudes have to fulfill for the correct working of this protocol. We observe that Eqs. (13) and (16), beyond the desired resonant contributions shown in Eqs. (14) and (17) respectively, contain also nonresonant (time-oscillating) terms which may induce undesired transitions. In order to face this problem, we can reduce it to a two-state system in the presence of an external pulse. This problem

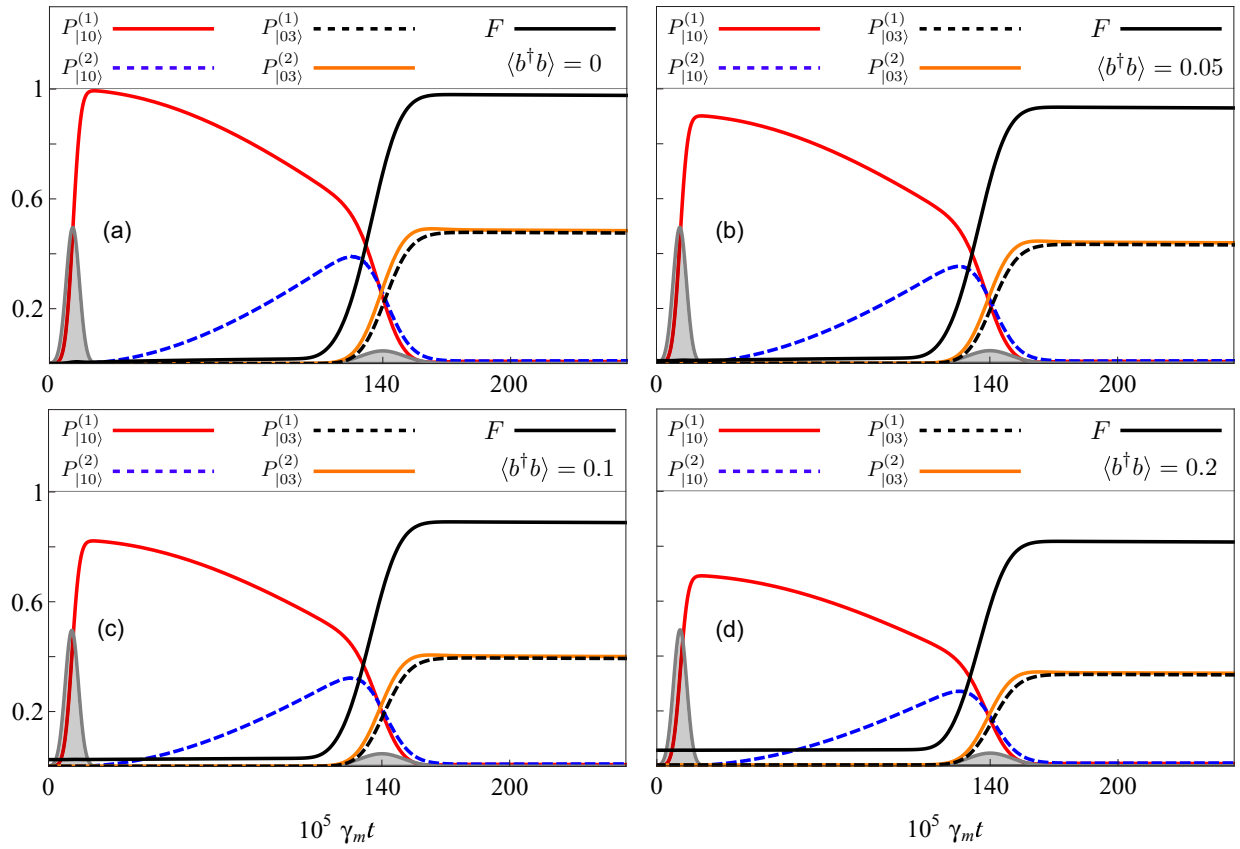

FIG. 6. Time evolution of occupation probabilities $P^{(1)}_{|1,0\rangle}(t)$, $P^{(2)}_{|1,0\rangle}(t)$, $P^{(1)}_{|0,3\rangle}(t)$, and $P^{(2)}_{|0,3\rangle}(t)$, and of the fidelity F during the generation of the target NOON state $|\bar{\psi}\rangle_{\rm mech} = (|3,0\rangle_{\rm mech} - i|0,3\rangle_{\rm mech})/\sqrt{2}$. Here the effects of thermal noise and pure dephasing have been included. In each panel the initial state corresponds to a thermal mechanical state at equilibrium with the mechanical reservoir. Panel (a) has been obtained considering a zero-temperature mechanical reservoir ($\langle \hat{b}^\dagger \hat{b}\rangle = 0$). Panels (b) and (c) have been obtained considering reservoirs with increasing values of thermal noise. The increase of noise determines the lowering of the fidelity. For both the optomechanical systems the other parameters are $\omega_R/\omega_M = 500$, $\kappa/\omega_M = 5 \times 10^{-5}$, $\gamma_m/\kappa = 0.1$, $g_M/\omega_M = 1$, and $g_R/\omega_M = 8 \times 10^{-3}$.

can be easily solved when the central frequency of the pulse is equal to the transition frequency as in Eqs. (14) and (17). However, the general solution for an arbitrary exciting field is much more complicated [68]. It is simpler if the system is subjected to a rectangular exciting pulse. Assuming this pulse shape in Eqs. (13) and (16) [$\mathcal{E}_j(t) = \mathcal{E}$], according to the Rabi problem [68], the probability of undesired adjacent transitions is small if $\mathcal{E}/\omega_M < 1$. Since we are actually considering a Gaussian pulse, we replace the constant amplitude $\mathcal{E}$ with its peak value, thus obtaining: $\sqrt{k}AX_{N\pm1}/(\sqrt{2\pi}\omega_M\Delta) < 1$ where $X_{N\pm1} = \langle 0,N \pm 1,0,0|\hat{X}_1|1,m,0,0\rangle$. Since we are using a π pulse for the desired transition between the ancilla states $|1,m\rangle_i$ and the zero-photon mechanical states $|0,N\rangle_i$, the amplitude A is determined by $\sqrt{\kappa}A = \pi/X_N$. We thus obtain $\omega_M\,\Delta > (X_{N\pm1}/X_N)$. Of course the pulse duration has to be much smaller than the damping rates. Hence the protocol works if the following condition is fulfilled:

$$Q_M \gg \omega_M\,\Delta > \frac{X_{N\pm1}}{X_N}, \tag{24}$$

where $Q_M = \omega_M/\gamma$ is the mechanical quality factor, and we assume $\gamma > \kappa$. Equation (24) shows that the protocol may fail for ratios $X_{N\pm1}/X_N \gg 1$. In general, a normalized coupling β_0 not much smaller than 1 ensure ratios not much larger than 1.

We complete this section analyzing how the coupling β_0 influences the matrix elements. The matrix elements in Eqs. (15) and (18) can be easily derived using Eqs. (4)–(6):

$$\langle 0,N,0,0|\hat{X}_1|1,m,0,0\rangle = \sum_{k=0}^{m} \frac{\sqrt{m!\,N!}}{k!(m-k)!(N-m-k)!}\,\beta_0^k\,d_{N-m-k}. \tag{25}$$

Figure 3 shows the transition matrix elements $\langle 0,N,0,0|\hat{X}_1|1,m,0,0\rangle$ as a function of the vibrational quantum number N for different values of the optomechanical coupling rates g_M/ω_M and considering the cases in which the ancilla state has, respectively, phonon number $m = 0$, 1, 2, and 3 . We note that in order to create NOON states with increasing N, higher values of g_M/ω_M are required, because if the coupling rate is not strong enough, i.e., the system is not in the optomechanical USC regime, only the first mechanical states can be coupled. In order to synthesize the target state, the protocol requires that both the transitions $|0,0,0,0\rangle \leftrightarrow |1,m,0,0\rangle$ and $|1,m,0,0\rangle \leftrightarrow |0,N,0,0\rangle$ are possible; namely, Eqs. (15)

and (18), $\langle 0,0,0,0|\hat{X}_1|1,m,0,0\rangle$ and $\langle 0,N,0,0|\hat{X}_1|1,m,0,0\rangle$, have to be significantly different from zero. Figures 3(a)–3(d) clearly show that, if the coupling rate g_M/ω_M is too low (blue circles), this last condition is not fulfilled. In fact, for every fixed value of the ancilla state phonon number m the only relevant transition matrix elements $\langle 0,N,0,0|\hat{X}_1|1,m,0,0\rangle$ are those with $m = N$. Specifically, when $m = 0$ and for low values of the optomechanical coupling rate only the first mechanical states can be coupled. On the other hand, when $m > 0$ the result is that $\langle 0,0,0,0|\hat{X}_1|1,m,0,0\rangle$ always displays a very small value and this implies that the ancilla state cannot be efficiently populated.

IV. NUMERICAL RESULTS

In this article, unless otherwise stated, we consider the following system parameters for the two identical optomechanical systems:$\omega_R/\omega_M = 500$, $g_M/\omega_M = 1$, $\kappa/\omega_M = 5\times10^{-5}$, $\gamma_m/\kappa = 0.1$, and $g_R/\omega_M = 8\times10^{-3}$. We use $P^{(1)}_{|n,m\rangle}(t) = \langle n,m,0,0|\rho(t)|n,m,0,0\rangle$ and $P^{(2)}_{|n,m\rangle}(t) = \langle 0,0,n,m|\rho(t)|0,0,n,m\rangle$ to indicate, respectively, the time evolution of the occupation probabilities for the states of system 1 and system 2.

In Figs. 4 and 5, we present numerical calculations carried out considering the system at $T = 0$ K, i.e., in the absence of thermal noise. Figure 4 displays the time evolution of occupation probabilities $P^{(1)}_{|1,0\rangle}(t)$, $P^{(1)}_{|0,3\rangle}(t)$, $P^{(2)}_{|1,0\rangle}(t)$, and $P^{(2)}_{|0,3\rangle}(t)$ under the influence of three external π pulses of central frequency ω_0 and ω_3 chosen in order to generate the target NOON state $|\bar{\psi}\rangle_{\rm mech} = \frac{1}{\sqrt{2}}(|3,0\rangle_{\rm mech} - i|0,3\rangle_{\rm mech})$ for optomechanical coupling rates $g_M/\omega_M = 1.0$ (a), $g_M/\omega_M = 0.7$ (b), $g_M/\omega_M = 0.5$ (c), and $g_M/\omega_M = 0.4$ (d). Following the protocol described in Sec. III, in order to synthesize the mechanical NOON state $|\bar{\psi}\rangle_{\rm mech} = \frac{1}{\sqrt{2}}(|3,0\rangle_{\rm mech} - i|0,3\rangle_{\rm mech})$, a π pulse (first gray solid curve) of central frequency ω_0 was sent to system 1 in order to completely populate the ancilla state $|1,0\rangle_1$: $P^{(1)}_{|1,0\rangle}(t) \simeq 1$. Then, at the instant of time $t^* = \pi/4g_R$ we sent two additional π pulses of central frequency ω_3 (second gray solid curve) to both systems in order to depopulate the superposition $|\psi(t)\rangle$ state in Eq. (9), towards pure mechanical states $|0,3\rangle_1$ and $|0,3\rangle_2$, so that $P^{(1)}_{|0,3\rangle}(t) = P^{(2)}_{|0,3\rangle}(t) = 0.5$. In order to quantify the correspondence between the achieved and the target states, we exploit the fidelity. We observe that when g_M/ω_M decreases, the transition matrix elements between the intermediate ancilla state and the mechanical states decrease contributing to a decrease of the occupation probabilities. The fidelities $F = \sqrt{\langle\bar{\psi}|\rho|\bar{\psi}\rangle}$ between the desired target states $|\bar{\psi}\rangle$ and the density matrices ρ of the synthesized states are, from Figs. 4(a) to 4(d), $F = 0.98$, 0.95, 0.87, and 0.77. This shows that, choosing the state $|1,0\rangle_1$ as the ancilla state, the protocol is less efficient for low values of the mechanical coupling rate g_M/ω_M.

In Fig. 5(a) we show the dynamics describing the synthesis of the same mechanical NOON state $|\bar{\psi}\rangle_{\rm mech} = \frac{1}{\sqrt{2}}(|3,0\rangle_{\rm mech} - i|0,3\rangle_{\rm mech})$ as in Fig. 4(c), choosing as the ancilla state the state $|1,1\rangle_1$ rather than $|1,0\rangle_1$. Numerical results show that, for the same value of the optomechanical coupling rate ($g_M/\omega_M = 0.5$), the choice of a higher-energy ancilla state leads to an improvement in the synthesis of the target state, as confirmed by the higher value of the fidelity [$F = 0.963$ compared with $F = 0.87$ in Fig. 4(c)]. Figure 5(b) shows the dynamics leading to the synthesis of the target quantum NOON state $|\bar{\psi}\rangle_{\rm mech} = \frac{2}{\sqrt{5}}|3,0\rangle_{\rm mech} - \frac{i}{\sqrt{5}}|0,3\rangle_{\rm mech}$. In this case the second Gaussian pulse must be sent at the instant of time $t^* = g_R^{-1}\arctan(1/2)$. Figure 5(c) shows how it is possible to apply the here present protocol to realize mechanical NOON states with a higher mechanical Fock-state number N. Specifically, it displays the realization of the NOON state $|\bar{\psi}\rangle_{\rm mech} = \frac{1}{\sqrt{2}}(|6,0\rangle_{\rm mech} - i|0,6\rangle_{\rm mech})$ by choosing the state $|1,2\rangle_1$ as the ancilla state. From Fig. 3(d), it would seem more convenient to use the ancilla state $|1,3\rangle_1$, being $\langle 0,6,0,0|\hat{X}_1|1,3,0,0\rangle > \langle 0,6,0,0|\hat{X}_1|1,2,0,0\rangle$. However, numerical calculations show that a choice of the ancilla state $|1,3\rangle_1$ implies a longer time training which could lower the probabilities of synthesizing the state in the presence of thermal noise. Finally, in Fig. 5(d) we realize the target quantum state $|\bar{\Psi}\rangle_{\rm mech} = \frac{1}{\sqrt{2}}[\frac{1}{\sqrt{2}}(|1,0\rangle_{\rm mech} + |3,0\rangle_{\rm mech}) - i\frac{1}{\sqrt{2}}(|0,1\rangle_{\rm mech} + |0,3\rangle_{\rm mech})]$, showing how the here proposed protocol can be effectively used to synthesize, with high

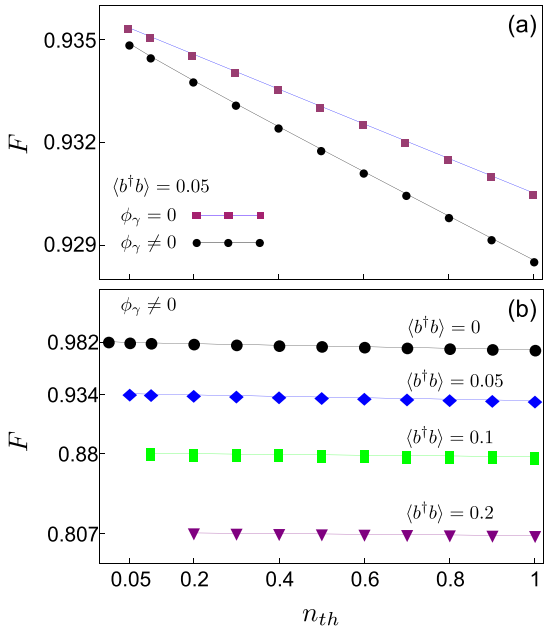

FIG. 7. The effects of thermal noise on the calculation of the fidelities when we apply the protocol for the synthesis of the target quantum NOON state $|\bar{\psi}\rangle_{\rm mech} = (|3,0\rangle_{\rm mech} - i|0,3\rangle_{\rm mech})/\sqrt{2}$. (a) Trend of the fidelity as a function of $n_{\rm th}$ when the system is initially prepared in a thermal state with the mean occupation number $\langle\hat{b}^\dagger\hat{b}\rangle = 0.05$, in the presence and in the absence of pure dephasing ϕ_γ. The fidelity decreases faster when the effects of dephasing are taken into account. (b) Trend of fidelities as a function of $n_{\rm th}$ when the system is initially prepared in different thermal states with increasing mean occupation number $\langle\hat{b}^\dagger\hat{b}\rangle$ and in the presence of pure dephasing ϕ_γ. For both optomechanical systems the other parameters are $\omega_R/\omega_M = 500, \kappa/\omega_M = 5\times10^{-5}, \gamma_m/\kappa = 0.1, g_M/\omega_M = 1$, and $g_R/\omega_M = 8\times10^{-3}$.

fidelity, more general entangled mechanical superposition $\Psi O O \Psi$ states.

In real optomechanical systems, ground-state cooling is never complete and the interaction with a finite-temperature reservoir also has to be taken into account. In order to describe the influence of the dissipation and decoherence processes, we solve numerically the dressed master equation, Eq. (23). Figure 6 shows the effects of thermal noise on the synthesis of the state $|\bar{\psi}\rangle_{\rm mech} = \frac{1}{\sqrt{2}}(|3,0\rangle_{\rm mech} - i|0,3\rangle_{\rm mech})$, when the system is initially prepared in a thermal state with mean occupation numbers $\langle \hat{b}^\dagger \hat{b}\rangle = 0$ (a), 0.05 (b), 0.1 (c), and 0.2 (d). Here we consider the case where the mechanical system is in thermal equilibrium with the reservoir. The effects of the pure dephasing ϕ_γ induced by the optomechanical coupling, described in the last term of Eq. (23), are also considered. It can be observed that the effects of thermal noise can be relevant as confirmed by the lower values of the fidelities obtained as the temperature increases. In Fig. 7 we consider the effects of thermal noise on the calculation of the fidelities when we apply the protocol for the synthesis of the target quantum NOON state $|\bar{\psi}\rangle_{\rm mech} = \frac{1}{\sqrt{2}}(|3,0\rangle_{\rm mech} - i|0,3\rangle_{\rm mech})$. Specifically, Fig. 7(a) shows the trend of the fidelity as a function of the mechanical reservoir noise $n_{\rm th}$ when the system is initially prepared in a thermal state with a small mean occupation number $\langle \hat{b}^\dagger \hat{b}\rangle = 0.05$. Calculations have been performed both in the presence and in the absence of pure dephasing ϕ_γ. It can be observed that, for increasing value of temperature, the fidelity decreases faster when the effects of dephasing are taken into account [see Eq. (23)]. Finally, in Fig. 7(b) we show the trend of fidelities as a function of the mean occupation number $n_{\rm th}$ of the mechanical reservoir when the system is initially prepared in different thermal states with increasing mean occupation number $\langle \hat{b}^\dagger \hat{b}\rangle = 0, 0.05, 0.1$, and 0.2 and in presence of pure dephasing ϕ_γ.

V. CONCLUSION

We presented a strategy for the preparation of the maximally entangled mechanical NOON states in optomechanical systems in a completely controlled and deterministic manner. In the optomechanical USC regime, when the coupling strength becomes a significant fraction of the mechanical frequency, we have shown that NOON mechanical states with quite high Fock states can be deterministically obtained within a few-step protocol. The framework presented here provides an example of how the USC regime can favor the generation of entangled mechanical quantum states. Such states can be viewed as a benchmark for multimode state preparation and coherent control capabilities. Moreover they play an important role in quantum metrology and sensing [69,70]. The generation of mechanical NOON states offers a route towards fundamental tests of quantum mechanics, such as the effects of decoherence on many-particle entanglement [71,72] and the quantum-classical crossover in a parameter regime beyond microscopic sizes and masses [73].

One key feature of the protocol presented here is that it consists of a few operations independently of the specific Fock state in the target NOON states. In the ideal case the system starts in its ground state. The protocol starts sending a π pulse to one optical resonator with central frequency equal to the frequency difference between an ancilla state $|1,j\rangle$ and the ground state. Then, the system is subject to a spontaneous Rabi-like oscillation able to partly transfer the excitation to the second optomechanical system. The final step consists of sending simultaneously two additional π-like Gaussian optical pulses, one at each optical resonator, with a central frequency corresponding to the frequency difference between the ancilla state and the final desired mechanical Fock state.

The operating range of this protocol has been carefully analyzed. We tested the efficiency and robustness of this protocol by applying it to different situations, calculating fidelities in the presence of decoherence and thermal noise, and including the effects of dephasing and imperfect cooling. This approach can also be exploited for obtaining more general entangled states. For example, we have shown that, within a two-step operation, $\Psi O O \Psi$ states can be synthesized. These many-body entangled states realize the situation where one of the two resonators is in an arbitrary superposition of Fock states, with the other in its ground state and vice versa.

[1] K. Stannigel, P. Komar, S. J. M. Habraken, S. D. Bennett, M. D. Lukin, P. Zoller, and P. Rabl, Optomechanical Quantum Information Processing with Photons and Phonons, Phys. Rev. Lett. **109**, 013603 (2012).

[2] M. Aspelmeyer, T. J. Kippenberg, and F. Marquardt, Cavity optomechanics, Rev. Mod. Phys. **86**, 1391 (2014).

[3] P. Meystre, A short walk through quantum optomechanics, Ann. Phys. (Berlin) **525**, 215 (2013).

[4] Y.-D. Wang and A. A. Clerk, Using Interference for High Fidelity Quantum State Transfer in Optomechanics, Phys. Rev. Lett. **108**, 153603 (2012).

[5] S. A. McGee, D. Meiser, C. A. Regal, K. W. Lehnert, and M. J. Holland, Mechanical resonators for storage and transfer of electrical and optical quantum states, Phys. Rev. A **87**, 053818 (2013).

[6] T. A. Palomaki, J. W. Harlow, J. D. Teufel, R. W. Simmonds, and K. W. Lehnert, Coherent state transfer between itinerant microwave fields and a mechanical oscillator, Nature (London) **495**, 210 (2013).

[7] Eyob A. Sete and H. Eleuch, High-efficiency quantum state transfer and quantum memory using a mechanical oscillator, Phys. Rev. A **91**, 032309 (2015).

[8] M. Aspelmeyer, S. Gröblacher, Klemens Hammerer, and N. Kiesel, Quantum optomechanicsthrowing a glance, J. Opt. Soc. Am. B **27**, A189 (2010).

[9] T. J. Kippenberg and K. J. Vahala, Cavity optomechanics: Back-action at the mesoscale, Science **321**, 1172 (2008).

[10] I. Favero and K. Karrai, Optomechanics of deformable optical cavities, Nat. Photonics **3**, 201 (2009).

[11] F. Marquardt and S. M. Girvin, Optomechanics, Physics **2**, 40 (2009).

[12] D. Van Thourhout and J. Roels, Optomechanical device actuation through the optical gradient force, Nat. Photonics **4**, 211 (2010).

[13] M. Poot and H. S. J. van der Zant, Mechanical systems in the quantum regime, Phys. Rep. **511**, 273 (2012).
[14] X. Y. Lü, Y. Wu, J. R. Johansson, H. Jing, J. Zhang, and F. Nori, Squeezed Optomechanics with Phase-Matched Amplification and Dissipation, Phys. Phys. Lett. **114**, 093602 (2015).
[15] G. Vacanti, M. Paternostro, G. M. Palma, M. S. Kim, and V. Vedral, Nonclassicality of optomechanical devices in experimentally realistic operating regimes, Phys. Rev. A **88**, 013851 (2013).
[16] S. Bose, K. Jacobs, and P. L. Knight, Scheme to probe the decoherence of a macroscopic object, Phys. Rev. A **59**, 3204 (1999).
[17] W. Marshall, C. Simon, R. Penrose, and D. Bouwmeester, Towards Quantum Superpositions of a Mirror, Phys. Rev. Lett. **91**, 130401 (2003).
[18] B. Pepper, R. Ghobadi, E. Jeffrey, C. Simon, and D. Bouwmeester, Optomechanical Superpositions via Nested Interferometry, Phys. Rev. Lett. **109**, 023601 (2012).
[19] S. P. Vyatchanin and A. B. Matsko, Quantum limit on force measurements, JETP **77**, 218 (1993).
[20] C. Fabre, M. Pinard, S. Bourzeix, A. Heidmann, E. Giacobino, and S. Reynaud, Quantum-noise reduction using a cavity with a movable mirror, Phys. Rev. A **49**, 1337 (1994).
[21] S. Mancini and P. Tombesi, Quantum noise reduction by radiation pressure, Phys. Rev. A **49**, 4055 (1994).
[22] P. Verlot, A. Tavernarakis, C. Molinelli, A. Kuhn, T. Antoni, S. Gras, T. Briant, P. F. Cohadon, A. Heidmann, and L. Pinard, Towards the experimental demonstration of quantum radiation pressure noise, C. R. Physs **12**, 826 (2011).
[23] D. W. C. Brooks, T. Botter, S. Schreppler, T. P. Purdy, N. Brahms, and D. M. Stamper-Kurn, Non-classical light generated by quantum-noise-driven cavity optomechanics, Nature (London) **488**, 476 (2012).
[24] A. H. Safavi-Naeini, S. Gröblacher, J. T. Hill, J. Chan, M. Aspelmeyer, and O. Painter, Squeezed light from a silicon micromechanical resonator, Nature (London) **500**, 185 (2013).
[25] A. D. O'Connell, M. Hofheinz, M. Ansmann, R. C. Bialczak, M. Lenander, E. Lucero, D. Neeley, M. Sank, H. Wang, and M. Weides, Quantum ground state and single-phonon control of a mechanical resonator, Nature (London) **464**, 697 (2010).
[26] P. F. Cohadon, A. Heidmann, and M. Pinard, Cooling of a Mirror by Radiation Pressure, Phys. Rev. Lett. **83**, 3174 (1999).
[27] O. Arcizet, P. F. Cohadon, T. Briant, M. Pinard, and Antoine Heidmann, Radiation-pressure cooling and optomechanical instability of a micromirror, Nature (London) **444**, 71 (2006).
[28] A. Schliesser, P. Del'Haye, N. Nooshi, K. J. Vahala, and T. J. Kippenberg, Radiation Pressure Cooling of a Micromechanical Oscillator using Dynamical Backaction, Phys. Rev. Lett. **97**, 243905 (2006).
[29] X.-w. Xu, H. Wang, J. Zhang, and Y.-x. Liu, Engineering of nonclassical motional states in optomechanical systems, Phys. Rev. A **88**, 063819 (2013).
[30] C. K. Law and J. H. Eberly, Arbitrary Control of a Quantum Electromagnetic Field, Phys. Rev. Lett. **76**, 1055 (1996).
[31] S. Bose, K. Jacobs, and P. L. Knight, Preparation of nonclassical states in cavities with a moving mirror, Phys. Rev. A **56**, 4175 (1997).
[32] S. Deleglise, I. Dotsenko, C. Sayrin, J. Bernu, M. Brune, J. M. Raimond, and S. Haroche, Reconstruction of non-classical cavity field states with snapshots of their decoherence, Nature (London) **455**, 510 (2008).
[33] D. Kleckner, I. Pikovski, E. Jeffrey, L. Ament, E. Eliel, J. Van Den Brink, and D. Bouwmeester, Creating and verifying a quantum superposition in a micro-optomechanical system, New J. Phys. **10**, 095020 (2008).
[34] M. Hofheinz, H. Wang, M. Ansmann, R. C. Bialczak, E. Lucero, M. Neeley, A. D. O'Connell, D. Sank, J. Wenner, and J. M. Martinis, Synthesizing arbitrary quantum states in a superconducting resonator, Nature (London) **459**, 546 (2009).
[35] S. A. Gardiner, J. I. Cirac, and P. Zoller, Nonclassical states and measurement of general motional observables of a trapped ion, Phys. Rev. A **55**, 1683 (1997).
[36] B. Kneer and C. K. Law, Preparation of arbitrary entangled quantum states of a trapped ion, Phys. Rev. A **57**, 2096 (1998).
[37] L. F. Wei, Y.-x. Liu, and F. Nori, Engineering quantum pure states of a trapped cold ion beyond the Lamb-Dicke limit, Phys. Rev. A **70**, 063801 (2004).
[38] L. Garziano, R. Stassi, V. Macrí, S. Savasta, and O. Di Stefano, Single-step arbitrary control of mechanical quantum states in ultrastrong optomechanics, Phys. Rev. A **91**, 023809 (2015).
[39] X. W. Xu, Y. J. Zhao, and Y. X. Liu, Entangled-state engineering of vibrational modes in a multimembrane optomechanical system, Phys. Rev. A **88**, 022325 (2013).
[40] A. Nunnenkamp, K. Børkje, and S. M. Girvin, Single-Photon Optomechanics, Phys. Rev. Lett. **107**, 063602 (2011).
[41] A. J. Rimberg, M. P. Blencowe, A. D. Armour, and P. D. Nation, A cavity-Cooper pair transistor scheme for investigating quantum optomechanics in the ultra-strong coupling regime, New J. Phys. **16**, 055008 (2014).
[42] T. T. Heikkilä, F. Massel, J. Tuorila, R. Khan, and M. A. Sillanpää, Enhancing Optomechanical Coupling via the Josephson Effect, Phys. Rev. Lett. **112**, 203603 (2014).
[43] T. Niemczyk, F. Deppe, H. Huebl, E. P. Menzel, F. Hocke, M. J. Schwarz, J. J. García-Ripoll, D. Zueco, T. Hümmer, and E. Solano, Circuit quantum electrodynamics in the ultrastrong-coupling regime, Nat. Phys. **6**, 772 (2010).
[44] A. Ridolfo, M. Leib, S. Savasta, and M. J. Hartmann, Photon Blockade in the Ultrastrong Coupling Regime, Phys. Rev. Lett. **109**, 193602 (2012).
[45] S. Ashhab and F. Nori, Qubit-oscillator systems in the ultrastrong-coupling regime and their potential for preparing nonclassical states, Phys. Rev. A **81**, 042311 (2010).
[46] A. Ridolfo, S. Savasta, and M. J. Hartmann, Nonclassical Radiation from Thermal Cavities in the Ultrastrong Coupling Regime, Phys. Rev. Lett. **110**, 163601 (2013).
[47] L. Garziano, A. Ridolfo, R. Stassi, O. Di Stefano, and S. Savasta, Switching on and off of ultrastrong light-matter interaction: Photon statistics of quantum vacuum radiation, Phys. Rev. A **88**, 063829 (2013).
[48] J. F. Huang and C. K. Law, Photon emission via vacuum-dressed intermediate states under ultrastrong coupling, Phys. Rev. A **89**, 033827 (2014).
[49] L. Garziano, R. Stassi, A. Ridolfo, O. Di Stefano, and S. Savasta, Vacuum-induced symmetry breaking in a superconducting quantum circuit, Phys. Rev. A **90**, 043817 (2014).
[50] S. Mancini, V. I. Man'ko, and P. Tombesi, Ponderomotive control of quantum macroscopic coherence, Phys. Rev. A **55**, 3042 (1997).

[51] J. Q. Liao, C. K. Law, L. M. Kuang, and F. Nori, Enhancement of mechanical effects of single photons in modulated two-mode optomechanics, Phys. Rev. A **92**, 013822 (2015).
[52] M. Paternostro, D. Vitali, S. Gigan, M. S. Kim, C. Brukner, J. Eisert, and M. Aspelmeyer, Creating and Probing Multipartite Macroscopic Entanglement with Light, Phys. Rev. Lett. **99**, 250401 (2007).
[53] D. Vitali, S. Gigan, A. Ferreira, H. R. Böhm, P. Tombesi, A. Guerreiro, V. Vedral, A. Zeilinger, and M. Aspelmeyer, Optomechanical Entanglement Between a Movable Mirror and a Cavity Field, Phys. Rev. Lett. **98**, 030405 (2007).
[54] A. Mari and J. Eisert, Opto-and electro-mechanical entanglement improved by modulation, New J. Phys. **14**, 075014 (2012).
[55] J. Zhang, K. Peng, and S. L. Braunstein, Quantum-state transfer from light to macroscopic oscillators, Phys. Rev. A **68**, 013808 (2003).
[56] G. Vacanti, M. Paternostro, G. M. Palma, and V. Vedral, Optomechanical to mechanical entanglement transformation, New. J. Phys. **10**, 095014 (2008).
[57] B. C. Sanders, Quantum dynamics of the nonlinear rotator and the effects of continual spin measurement, Phys. Rev. A **40**, 2417 (1989).
[58] A. N. Boto, P. Kok, D. S. Abrams, S. L. Braunstein, C. P. Williams, and J. P. Dowling, Quantum Interferometric Optical Lithography: Exploiting Entanglement to Beat the Diffraction Limit, Phys. Rev. Lett. **85**, 2733 (2000).
[59] X. X. Ren, H. K. Li, M. Y. Yan, Y. C. Liu, Y. F. Xiao, and Q. Gong, Single-photon transport and mechanical NOON-state generation in microcavity optomechanics, Phys. Rev. A **87**, 033807 (2013).
[60] H. Flayac and V. Savona, Heralded Preparation and Readout of Entangled Phonons in a Photonic Crystal Cavity, Phys. Rev. Lett. **113**, 143603 (2014).
[61] G. De Chiara, M. Paternostro, and G. M. Palma, Entanglement detection in hybrid optomechanical systems, Phys. Rev. A **83**, 052324 (2011).
[62] Eyob A. Sete, Hichem Eleuch, and C. H. Raymond Ooi, Light-to-matter entanglement transfer in optomechanics, J. Opt. Soc. Am. B **31**, 2821 (2014).
[63] J. Q. Liao, Q. Q. Wu, and F. Nori, Entangling two macroscopic mechanical mirrors in a two-cavity optomechanical system, Phys. Rev. A **89**, 014302 (2014).
[64] D. Hu, S. Y. Huang, J. Q. Liao, L. Tian, and H. S. Goan, Quantum coherence in ultrastrong optomechanics, Phys. Rev. A **91**, 013812 (2015).
[65] C. Galland, N. Sangouard, N. Piro, N. Gisin, and T. J. Kippenberg, Heralded Single-Phonon Preparation, Storage, and Readout in Cavity Optomechanics, Phys. Rev. Lett. **112**, 143602 (2014).
[66] D. Leibfried, D. M. Meekhof, B. E. King, C. H. Monroe, W. M. Itano, and D. J. Wineland, Experimental Determination of the Motional Quantum State of a Trapped Atom, Phys. Rev. Lett. **77**, 4281 (1996).
[67] M. R. Vanner, I. Pikovski, G. D. Cole, M. S. Kim, Č. Brukner, K. Hammerer, G. J. Milburn, and M. Aspelmeyer, Pulsed quantum optomechanics, Proc. Nat. Acad. Sci. USA **108**, 16182 (2011).
[68] L. Mandel and E. Wolf, *Optical Coherence and Quantum Optics* (Cambridge University Press, Cambridge, UK, 1995).
[69] H. Lee, P. Kok, and J. P. Dowling, A quantum rosetta stone for interferometry, J. Mod. Opt. **49**, 2325 (2002).
[70] M. W. Mitchell, J. S. Lundeen, and A. M. Steinberg, Super-resolving phase measurements with a multiphoton entangled state, Nature (London) **429**, 161 (2004).
[71] L. Aolita, R. Chaves, D. Cavalcanti, A. Acín, and L. Davidovich, Scaling Laws for the Decay of Multiqubit Entanglement, Phys. Rev. Lett. **100**, 080501 (2008).
[72] H. S. Eisenberg, G. Khoury, G. A. Durkin, C. Simon, and D. Bouwmeester, Quantum Entanglement of a Large Number of Photons, Phys. Rev. Lett. **93**, 193901 (2004).
[73] S. L. Adler and A. Bassi, Is quantum theory exact?, Science **325**, 275 (2009).

5.4 Paper IV: A single photon can simultaneously excite two or more atoms

One Photon Can Simultaneously Excite Two or More Atoms

Luigi Garziano,[1,2] Vincenzo Macrì,[1] Roberto Stassi,[1,2] Omar Di Stefano,[1] Franco Nori,[2,3] and Salvatore Savasta[1,2]
[1]Dipartimento di Scienze Matematiche e Informatiche, Scienze Fisiche e Scienze della Terra (MIFT), Università di Messina, I-98166 Messina, Italy
[2]CEMS, RIKEN, Saitama 351-0198, Japan
[3]Physics Department, The University of Michigan, Ann Arbor, Michigan 48109-1040, USA
(Received 25 January 2016; published 22 July 2016)

We consider two separate atoms interacting with a single-mode optical or microwave resonator. When the frequency of the resonator field is twice the atomic transition frequency, we show that there exists a resonant coupling between *one* photon and *two* atoms, via intermediate virtual states connected by counterrotating processes. If the resonator is prepared in its one-photon state, the photon can be jointly absorbed by the two atoms in their ground state which will both reach their excited state with a probability close to one. Like ordinary quantum Rabi oscillations, this process is coherent and reversible, so that two atoms in their excited state will undergo a downward transition jointly emitting a single cavity photon. This joint absorption and emission process can also occur with three atoms. The parameters used to investigate this process correspond to experimentally demonstrated values in circuit quantum electrodynamics systems.

DOI: 10.1103/PhysRevLett.117.043601

Multiphoton excitation and emission processes were predicted in 1931 by Göppert-Mayer in her doctoral dissertation on the theory of two-photon quantum transitions [1]. Two-photon absorption consists in the simultaneous absorption of two photons of identical or different frequencies by an atom or a molecule. Two-photon excitation is now a powerful spectroscopic and diagnostic tool [2,3]. One may wonder if the reverse phenomenon, i.e., joint multiatom emission of one photon or multiatom excitation with a single photon, is ever possible. We show that these processes not only can be enabled by the strong correlation between the states of the atoms and those of the field occurring in cavity quantum electrodynamics (QED) [4], but they can even take place with probability approaching one.

Cavity QED investigates the interaction of confined electromagnetic field modes with natural or artificial atoms under conditions where the quantum nature of light affects the system dynamics [5,6]. A high degree of manipulation and control of quantum systems can be reached in the strong-coupling regime, where the atom-field coupling rate is dominant with respect to the loss and decoherence rates. This paves the way for many interesting physical applications [6–9]. Cavity QED is also very promising for the realization of quantum gates [10–12] and quantum networks for quantum computational tasks [13–15]. Many of the proposed concepts, pioneered with flying atoms, have been adapted and further developed using superconducting artificial atoms in the electromagnetic field of microwave resonators, giving rise to the rapidly growing field of circuit QED, which is very promising for future quantum technologies [8,9,12,16–19]. In these systems, coupling rates between an individual qubit and a single electromagnetic mode of the order of 10% of the unperturbed frequency of the bare subsystems have been experimentally reached [20–23]. Such a coupling rate is significantly higher than that obtained using natural atoms. Such an ultrastrong coupling (USC) opens the door to the study of the physics of virtual processes which do not conserve the number of excitations governed by the counterrotating terms in the interaction Hamiltonian [24–33]. Recently, it has been shown that these excitation-number-nonconserving processes enable higher-order atom-field resonant transitions, making possible coherent and reversible multiphoton exchanges between the qubit and the resonator [34–36].

Here we examine a quantum system constituted by two two-level atoms coupled to a single-mode resonator in the regime where the field-atom detuning $\Delta = \omega_c - \omega_q$ is large as compared to their coupling rate λ (ω_c and ω_q are the resonance frequency of the cavity mode and the qubit transition frequency). We investigate the situation where the two qubits are initially in their ground state and one photon is present in the resonator, corresponding to the initial state $|g, g, 1\rangle$. We find that, if $\omega_c \approx 2\omega_q$, a single cavity photon is able to excite simultaneously two independent atoms. During this process no parametric down-conversion, splitting the initial photon into observable pairs of photons at frequency $\omega_c/2$, occurs. The cavity photon is directly and jointly absorbed by the two atoms. As shown in Fig. 1, the initial state $|g, g, 1\rangle$ goes to virtual intermediate states that do not conserve the energy, but comes back to the real final state $|e, e, 0\rangle$ that does conserve energy (the additional virtual transitions contributing to the process are shown in Fig. S1 of the Supplemental Material

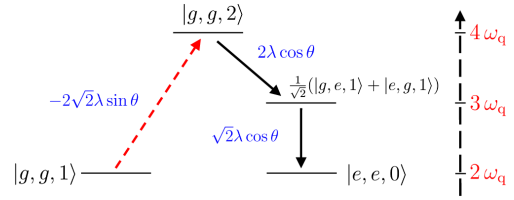

FIG. 1. Sketch of the process giving the main contribution to the effective coupling between the bare states $|g,g,1\rangle$ and $|e,e,0\rangle$, via intermediate virtual transitions. Here, the excitation-number-nonconserving processes are represented by arrowed dashed line. The transition matrix elements are also shown.

[37]). If $\omega_c \approx 3\omega_q$, the simultaneous excitation of three atoms, $|g,g,g,1\rangle \rightarrow |e,e,e,0\rangle$, is also possible (see Fig. S3 of the Supplemental Material [37]). If the coupling is sufficiently strong, even a higher number of atoms can be excited with a single photon. Owing to optical selection rules, the two-atom process requires parity-symmetry breaking of the atomic potentials, which can be easily achieved in superconducting artificial atoms [34,38,39]. On the contrary, the three-atom process does not need broken symmetry.

The Hamiltonian describing the system consisting of a single cavity mode interacting with two or more identical qubits with possible symmetry-broken potentials is given by [20,31]

$$\hat{H}_0 = \hat{H}_q + \hat{H}_c + \lambda\hat{X}\sum_i(\cos\theta\hat{\sigma}_x^{(i)} + \sin\theta\hat{\sigma}_z^{(i)}), \qquad (1)$$

where $\hat{H}_q = (\omega_q/2)\sum_i\hat{\sigma}_z^{(i)}$ and $\hat{H}_c = \omega_c\hat{a}^\dagger\hat{a}$ describe the qubit and cavity Hamiltonians in the absence of interaction, $\hat{X} = \hat{a} + \hat{a}^\dagger$, $\hat{\sigma}_x^{(i)}$ and $\hat{\sigma}_z^{(i)}$ are Pauli operators for the ith qubit, and λ is the coupling rate of each qubit to the cavity mode. For $\theta = 0$, parity is conserved. For flux qubits, this angle, as well as the transition frequency ω_q, can be continuously tuned by changing the external flux bias [20,38]. For the sake of simplicity, Eq. (1) describes identical qubits, but this is not an essential point. In contrast to the Jaynes-Cummings model, the Hamiltonian in Eq. (1) explicitly contains counterrotating terms of the form $\hat{\sigma}_+^{(i)}\hat{a}^\dagger$, $\hat{\sigma}_-^{(i)}\hat{a}$, $\hat{\sigma}_z^{(i)}\hat{a}^\dagger$, and $\hat{\sigma}_z^{(i)}\hat{a}$. The first (second) term creates (destroys) two excitations while the third (fourth) term creates (destroys) one excitation. The presence of counterrotating terms in the interaction Hamiltonian enables four different paths which, starting from the initial state $|g,g,1\rangle$, reach the final state $|e,e,0\rangle$ (see Supplemental Material [37]). Each path includes three virtual transitions involving out-of-resonance intermediate states. Figure 1 displays only the process that gives the main contribution to the effective coupling between the bare states $|g,g,1\rangle$ and $|e,e,0\rangle$. Higher-order processes, depending on the atom-field interaction strength, can also contribute. By applying standard third-order perturbation theory, we obtain the following effective coupling rate: $\Omega_{\rm eff}/\omega_q \equiv (8/3)(\lambda/\omega_q)^3\sin\theta\cos^2\theta$. The analytical derivation of the effective coupling rate as a function of λ/ω_q is presented in Sec. I of Supplemental Material [37]. Already at a coupling rate $\lambda/\omega_q = 0.1$, an effective (two qubits)-(one photon) coupling rate $\Omega_{\rm eff}/\omega_q \sim 10^{-3}$ can be obtained, corresponding, e.g., to an effective Rabi splitting $2\Omega_{\rm eff} \simeq 12$ MHz, for a flux qubit with transition frequency $\omega_q = 6$ GHz. We observe that $\Omega_{\rm eff}$ strongly depends on the mixing angle θ, and it is maximum for $\theta = \arccos\sqrt{2/3}$.

We diagonalize numerically the Hamiltonian in Eq. (1) for the case of two qubits and indicate the resulting energy eigenvalues and eigenstates as $\hbar\omega_i$ and $|i\rangle$, with $i = 0, 1, \ldots$, choosing the labeling of the states such that $\omega_k > \omega_j$ for $k > j$. We use a normalized coupling rate $\lambda/\omega_q = 0.1$ and an angle $\theta = \pi/6$. Figure 2(a) shows the frequency differences $\omega_{i,0} = \omega_i - \omega_0$ for the lowest energy states as a function of the resonator frequency. Starting from the lowest excited states of the spectrum, a large splitting anticrossing around $\omega_c/\omega_q = 1$ can be observed [see arrows in Fig. 2(a)]. It corresponds to the standard

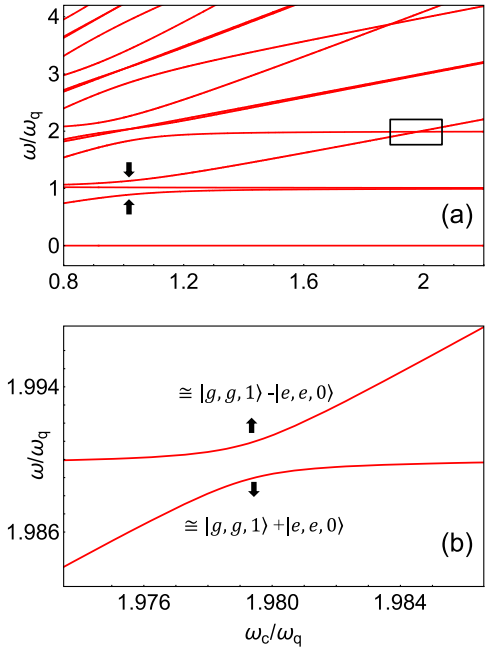

FIG. 2. (a) Frequency differences $\omega_{i,0} = \omega_i - \omega_0$ for the lowest energy eigenstates of Hamiltonian Eq. (1) as a function of ω_c/ω_q. Here, we consider a normalized coupling rate $\lambda/\omega_q = 0.1$ between the resonator and each of the qubits. We used $\theta = \pi/6$. The black arrows indicate the ordinary vacuum splitting arising from the coupling between the states $|g,g,1\rangle$ and $(1/\sqrt{2})(|g,e,0\rangle + |e,g,0\rangle)$. (b) Enlarged view of the spectral region delimited by a square in (a). This shows an avoided-level crossing, demonstrating the coupling between the states $|g,g,1\rangle$ and $|e,e,0\rangle$ due to the presence of counterrotating terms in the system Hamiltonian.

vacuum Rabi splitting, which appears also when neglecting the counterrotating terms. The straight line at $E/\omega_q = 1$ corresponds to the dark antisymmetric state $(|g,e,0\rangle - |e,g,0\rangle)/\sqrt{2}$. Even larger splitting anticrossings around $\omega_c/\omega_q = 1$ can be observed at higher E values. These correspond to the second and third rung of the Jaynes-Cummings ladder. We are interested in the region around $\omega_c/\omega_q = 2$, where the levels three and four display an apparent crossing at $E/\omega_q \approx 2$. Actually, what appears as a crossing on this scale turns out to be a splitting anticrossing on an enlarged view as in Fig. 2(b). Observing that just outside this avoided-crossing region one level remains flat as a function of ω_c with energy $\omega \approx 2\omega_q$, while the other grows as ω_c, this splitting clearly originates from the hybridization of the states $|e,e,0\rangle$ and $|g,g,1\rangle$. The resulting states are well approximated by the states $(|e,e,0\rangle \pm |g,g,1\rangle)/\sqrt{2}$. This splitting is not present in the rotating-wave approximation (RWA), where the coherent coupling between states with a different number of excitations is not allowed, nor does it occur in the absence of symmetry breaking ($\theta = 0$). The normalized splitting has a value $2\Omega_{\rm eff}/\omega_q = 1.97 \times 10^{-3}$, which is in good agreement with 2×10^{-3}, obtained within perturbation theory. This observed hybridization opens the way to the observation of weird effects such as the simultaneous excitations of *two* qubits with only *one* cavity photon. Such a coupling between the states $|e,e,0\rangle$ and $|g,g,1\rangle$ can be analytically described by the effective interaction Hamiltonian $H_{\rm eff} = -\Omega_{\rm eff}(|e,e,0\rangle\langle g,g,1| + \text{H.c.})$.

A key theoretical issue of the USC regime is the distinction between bare (unobservable) excitations and physical particles that can be detected [28,40]. For example, when the counterrotating terms are taken into account, the mean photon number in the system ground state becomes different from zero: $\langle 0|\hat{a}^\dagger\hat{a}|0\rangle \neq 0$. However, these photons are actually virtual [40] because they do not correspond to real particles that can be detected in a photon-counting experiment. The same problem holds for the excited states. According to these analyses, the presence of an n-photon contribution in a specific eigenstate of the system does not imply that the system can emit n photons when prepared in this state.

In order to fully understand and characterize this anomalous avoided crossing not present in the RWA, a more quantitative analysis is required. In the following, we therefore calculate the output signals and correlations which can be measured in a photodetection experiment. We fix the cavity frequency at the value where the splitting between level 3 and 4 is minimum. Instead of starting from the ideal initial state $(|3\rangle - |4\rangle)/\sqrt{2} \approx |g,g,1\rangle$, more realistically, we consider the system initially in its ground state $|0\rangle \approx |g,g,0\rangle$ and study the direct excitation of the cavity by an electromagnetic Gaussian pulse with central frequency $\omega_d = (\omega_{4,0} + \omega_{3,0})/2$. In this strongly dispersive regime, the resonator displays very low anharmonicity, so that for a strong system excitation such as that induced by a π pulse, higher-energy states of the resonator (as the state $|8\rangle \simeq |g,g,2\rangle$) can be resonantly populated. This problem can be avoided by feeding the system with a single-photon input or by probing the system in the weak-excitation regime. However, in order to achieve a deterministic transition $|g,g,1\rangle \to |e,e,0\rangle$, a useful route involves introducing a Kerr nonlinearity into the resonator, able to activate a photon blockade. In circuit QED this can be realized by introducing some additional Josephson junction, or coupling the resonator with weakly detuned artificial atoms [41]. This additional nonlinearity can be described by the Hamiltonian term $\hat{H}_K = \mu\hat{a}^{\dagger 2}\hat{a}^2$. The driving Hamiltonian, describing the system excitation by a coherent electromagnetic pulse, is $\hat{H}_d(t) = \mathcal{E}(t)\cos(\omega t)\hat{X}$, where $\mathcal{E}(t) = A\exp[-(t-t_0)^2/(2\tau^2)]/(\tau\sqrt{2\pi})$. Here, A and τ are the amplitude and the standard deviation of the Gaussian pulse, respectively. A includes the factor $\sqrt{\kappa}$, where κ is the loss rate through the cavity port. The system is thus under the influence of the total Hamiltonian $\hat{H} = \hat{H}_0 + \hat{H}_K + \hat{H}_d(t)$.

The output photon flux emitted by a resonator can be expressed as $\Phi_{\rm out} = \kappa\langle\hat{X}^-\hat{X}^+\rangle$, where $\hat{X}^+ = \sum_{j,k>j} X_{jk}|j\rangle\langle k|$ and $\hat{X}^- = (\hat{X}^+)^\dagger$, with $X_{jk} \equiv \langle j|(\hat{a}^\dagger + \hat{a})|k\rangle$, are the positive and negative frequency cavity-photon operators [30,36]. Neglecting the counterrotating terms, or in the limit of negligible coupling rates, they coincide with $\hat{a}$ and $\hat{a}^\dagger$, respectively. The signal directly emitted from the qubit is proportional to the qubit mean excitation number $\langle\hat{C}^-\hat{C}^+\rangle$, where $\hat{C}^\pm$ are the qubit positive and negative frequency operators, defined as $\hat{C}^+ = \sum_{j,k>j} C_{jk}|j\rangle\langle k|$ and $\hat{C}^- = (\hat{C}^+)^\dagger$, with $C_{jk} \equiv \langle j|(\hat{\sigma}_- + \hat{\sigma}_+)|k\rangle$ [30,36]. Neglecting the counterrotating terms, or in the limit of negligible coupling rates, they coincide with $\hat{\sigma}_-$ and $\hat{\sigma}_+$, respectively. In circuit QED systems, this emission can be detected by coupling the qubit to an additional microwave antenna [8].

Thanks to the photon-blockade effect, induced by the Kerr interaction $\hat{H}_K$, it is possible to resonantly excite the split states $|3\rangle$ and $|4\rangle$ with a π pulse, so that after the pulse arrival the population is completely transferred from the ground state to only these two energy levels. We use a pulse width $\tau = 1/(4\omega_{43})$. Figure 3(a) displays the numerically calculated dynamics of the photon number $\langle\hat{X}^-\hat{X}^+\rangle$, of the mean excitation number $\langle\hat{C}_1^-\hat{C}_1^+\rangle$ for qubit 1 (which, of course, coincides with that of qubit 2), and of the two-qubit correlation $G_q^{(2)} \equiv \langle\hat{C}_1^-\hat{C}_2^-\hat{C}_2^+\hat{C}_1^+\rangle$. Vacuum Rabi oscillations showing the reversible excitation exchange between the qubits and the resonator are clearly visible. We observe that, after a half Rabi period, $\Omega_{\rm eff}t = \pi/2$, the excitation is fully transferred to the two qubits which reach an excitation probability approaching one. Hence, not only the multiatom absorption of a single photon is possible, but it can essentially be deterministic. We observe that the

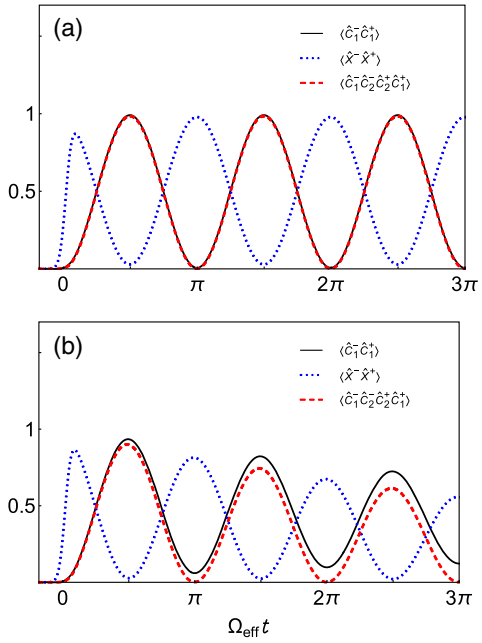

FIG. 3. (a) Time evolution of the cavity mean photon number $\langle\hat{X}^-\hat{X}^+\rangle$ (dotted blue curve), qubit 1 mean excitation number $\langle\hat{C}_1^-\hat{C}_1^+\rangle$ (continuous black curve), and the zero-delay two-qubit correlation function $G_q^{(2)}=\langle\hat{C}_1^-\hat{C}_2^-\hat{C}_2^+\hat{C}_1^+\rangle$ (dashed red curve) after the arrival of a π-like Gaussian pulse initially exciting the resonator. After the arrival of the pulse, the system undergoes vacuum Rabi oscillations showing the reversible joint absorption and reemission of one photon by two qubits. $\langle\hat{C}_1^-\hat{C}_1^+\rangle$ and $G_q^{(2)}(t)$ are almost coincident. This perfect two-qubit correlation is a signature that the two qubits are jointly excited. (b) Time evolution of the cavity mean photon number (dotted blue curve), the qubit mean excitation number, and the two-qubit correlation as in (a), but including the effect of cavity damping and atomic decay. The corresponding rates are $\kappa=\gamma=4\times10^{-5}\omega_q$.

single-qubit excitation $\langle\hat{C}_i^-\hat{C}_i^+\rangle$ and $G_q^{(2)}$ almost coincide at any time. This almost-perfect two-qubit correlation is a clear signature of the joint excitation: if one qubit gets excited, the probability that the other one is also excited is very close to one. In summary, an electromagnetic pulse is able, thanks to the photon-blockade effect, to generate a *single* cavity photon, which then gets jointly absorbed by a *couple* of qubits. The resonant coupling can be stopped at this time, e.g., by changing the resonance frequency of the qubits. If not, the reverse process starts, where two qubits jointly emit a *single* photon: $|e,e,0\rangle\rightarrow|g,g,1\rangle$. We observe that $\langle\hat{X}^-\hat{X}^+\rangle$ is not exactly zero at the photon minima. This occurs because the two-qubit excited state, owing to the same processes inducing its coupling with the one-photon state, acquires a dipole transition matrix element, so that this state is able to emit photons. We find that this effects increases when increasing the atom-field coupling strength λ (see Fig. S6 of Supplemental Material [37]). In order to exclude that this joint qubit excitation does not occur via more conventional paths, involving the creation of photon pairs and/or a one-qubit–one-photon excitation, we have also calculated the photonic second-order correlation function $G_c^{(2)}\equiv\langle(\hat{X}^-)^2(\hat{X}^+)^2\rangle$ and the qubit-cavity correlation $G_{\rm qc}^{(2)}\equiv\langle\hat{C}_i^-\hat{X}^-\hat{X}^+\hat{C}_i^+\rangle$. We find that their value is more than 2 orders of magnitude lower than that of the two-qubit correlation $G_q^{(2)}$. Calculations have been performed considering two-level atoms [see Eq. (1)]. Although flux qubits (generally employed to realize the USC regime with individual atoms) display very high anharmomicity (see, e.g., Ref. [19]), it is interesting to investigate if significant competing effects, lowering the correlation, can arise from the presence of additional atomic transitions. This analysis is carried out in Sec. IV of Supplemental Material [37].

Figure 3(a) has been obtained without including loss effects. The influence of cavity field damping and atomic decay on the process can be studied by the master equation approach. We consider the system interacting with zero-temperature baths. By using the Born-Markov approximation without the post-trace RWA [35], the resulting master equation for the reduced density matrix of the system is

$$\dot{\hat{\rho}}=i[\hat{\rho}(t),\hat{H}]+\kappa\mathcal{D}[\hat{X}^+]\hat{\rho}+\gamma\sum_i\mathcal{D}[\hat{C}_i^+]\hat{\rho},\qquad(2)$$

where the superoperator $\mathcal{D}$ is defined as $\mathcal{D}[\hat{O}]\hat{\rho}=\frac{1}{2}(2\hat{O}\,\hat{\rho}\,\hat{O}^\dagger-\hat{\rho}\hat{O}^\dagger\hat{O}-\hat{O}^\dagger\hat{O}\,\hat{\rho})$. We use $\kappa=\gamma=3\times10^{-5}\omega_q$. Figure 3(b) shows how the cavity losses and the atomic decay affect the system dynamics. As expected, the vacuum Rabi oscillations undergo damping and, as expected, the two-qubit correlation is more fragile to losses. Finally, we have also considered the case of nonidentical qubits. We find that also in this case, for qubit transition frequencies such that $\omega_{q1}+\omega_{q2}\simeq\omega_c$, it results $\langle\hat{C}_1^-\hat{C}_1^+\rangle=\langle\hat{C}_2^-\hat{C}_2^+\rangle\simeq G_q^{(2)}$ (see Fig. S9 in Supplemental Material [37]). This result further confirms the simultaneous and joint nature of this multiatom process.

The processes described here can be observed by placing two superconducting artificial atoms at opposite ends of a superconducting transmission line resonator [42]. These multiatom excitation and emission processes can find useful applications for the development of novel quantum technologies. Conditional quantum-state transfer is a first possible application: the quantum information stored in one of the two qubits can be transferred to the resonator conditioned by the state of the second qubit. We also observe that the quantum Rabi oscillations displayed in Fig. 3 imply that a hybrid entangled Greenberger-Horne-Zeilinger (GHZ) state, $(|g,g,1\rangle+|e,e,0\rangle)/\sqrt{2}$, can be obtained by an elementary quantum Rabi process after a time $t=\pi/(4\Omega_{\rm eff})$. This state can be stored by just changing the transition frequency of one of the two qubits. Besides possible applications, the puzzling results

presented here, showing that *one* photon can divide its energy into *two* spatially separated atoms, and that vacuum fluctuations [43] can induce separate atoms to behave as a single quantum entity (as testified by the one-photon transition matrix element acquired by the transition $|g,g\rangle \rightarrow |e,e\rangle$), provide new insights into the quantum aspects of the interaction between light and matter.

This work is partially supported by the RIKEN iTHES Project, the MURI Center for Dynamic Magneto-Optics via the AFOSR Award No. FA9550-14-1-0040, the IMPACT program of JST, a Grant-in-Aid for Scientific Research (A), and the MPNS COST Action MP1403 Nanoscale Quantum Optics. We also acknowledge the support of a grant from the John Templeton Foundation.

[1] M. Göppert-Mayer, Über elementarakte mit zwei quantensprüngen, Ann. Phys. (Berlin) **401**, 273 (1931).
[2] W. Denk, J. H. Strickler, and W. W Webb, Two-photon laser scanning fluorescence microscopy, Science **248**, 73 (1990).
[3] P. T. C. So, C. Y. Dong, B. R. Masters, and K. M. Berland, Two-photon excitation fluorescence microscopy, Annu. Rev. Biomed. Eng. **2**, 399 (2000).
[4] S. Haroche and J. M. Raimond, *Exploring the Quantum: Atoms, Cavities and Photons* (Oxford University Press, Oxford, 2006).
[5] S. Haroche, Nobel lecture: Controlling photons in a box and exploring the quantum to classical boundary, Rev. Mod. Phys. **85**, 1083 (2013).
[6] S. Haroche, M. Brune, and J. M. Raimond, Atomic clocks for controlling light fields, Phys. Today **66**, No. 1, 27 (2013).
[7] S. Deleglise, I. Dotsenko, C. Sayrin, J. Bernu, M. Brune, J. M. Raimond, and S. Haroche, Reconstruction of non-classical cavity field states with snapshots of their decoherence, Nature (London) **455**, 510 (2008).
[8] M. Hofheinz, H. Wang, M. Ansmann, R. C. Bialczak, E. Lucero, M. Neeley, A. D. O'Connell, D. Sank, J. Wenner, J. M. Martinis, and A. N. Cleland, Synthesizing arbitrary quantum states in a superconducting resonator, Nature (London) **459**, 546 (2009).
[9] B. Vlastakis, G. Kirchmair, Z. Leghtas, S. E. Nigg, L. Frunzio, S. M. Girvin, M. Mirrahimi, M. H. Devoret, and R. J. Schoelkopf, Deterministically encoding quantum information using 100-photon Schrödinger cat states, Science **342**, 607 (2013).
[10] A. Rauschenbeutel, G. Nogues, S. Osnaghi, P. Bertet, M. Brune, J. M. Raimond, and S. Haroche, Coherent Operation of a Tunable Quantum Phase Gate in Cavity QED, Phys. Rev. Lett. **83**, 5166 (1999).
[11] S.-B. Zheng and G.-C. Guo, Efficient Scheme for Two-Atom Entanglement and Quantum Information Processing in Cavity QED, Phys. Rev. Lett. **85**, 2392 (2000).
[12] J. Q. You and F. Nori, Superconducting circuits and quantum information, Phys. Today **58**, 42 (2005).
[13] D. Felinto, C.-W. Chou, J. Laurat, E. W. Schomburg, H. De Riedmatten, and H. J. Kimble, Conditional control of the quantum states of remote atomic memories for quantum networking, Nat. Phys. **2**, 844 (2006).
[14] H. J. Kimble, The quantum internet, Nature (London) **453**, 1023 (2008).
[15] S. Ritter, C. Nölleke, C. Hahn, A. Reiserer, A. Neuzner, M. Uphoff, M. Mücke, E. Figueroa, J. Bochmann, and G. Rempe, An elementary quantum network of single atoms in optical cavities, Nature (London) **484**, 195 (2012).
[16] J. Q. You and F. Nori, Quantum information processing with superconducting qubits in a microwave field, Phys. Rev. B **68**, 064509 (2003).
[17] A. Blais, R. S. Huang, A. Wallraff, S. M. Girvin, and R. J. Schoelkopf, Cavity quantum electrodynamics for superconducting electrical circuits: An architecture for quantum computation, Phys. Rev. A **69**, 062320 (2004).
[18] A. Wallraff, D. I. Schuster, A. Blais, L. Frunzio, R. S. Huang, J. Majer, S. Kumar, S. M. Girvin, and R. J. Schoelkopf, Strong coupling of a single photon to a superconducting qubit using circuit quantum electrodynamics, Nature (London) **431**, 162 (2004).
[19] I. Chiorescu, P. Bertet, K. Semba, Y. Nakamura, C. J. P. M. Harmans, and J. E. Mooij, Coherent dynamics of a flux qubit coupled to a harmonic oscillator, Nature (London) **431**, 159 (2004).
[20] T. Niemczyk, F. Deppe, H. Huebl, E. P. Menzel, F. Hocke, M. J. Schwarz, J. J. García-Ripoll, D. Zueco, T. Hümmer, E. Solano, A. Marx, and R. Gross, Circuit quantum electrodynamics in the ultrastrong-coupling regime, Nat. Phys. **6**, 772 (2010).
[21] P. Forn-Díaz, J. Lisenfeld, D. Marcos, J. J. García-Ripoll, E. Solano, C. J. P. M. Harmans, and J. E. Mooij, Observation of the Bloch-Siegert Shift in a Qubit-Oscillator System in the Ultrastrong Coupling Regime, Phys. Rev. Lett. **105**, 237001 (2010).
[22] A. Fedorov, A. K. Feofanov, P. Macha, P. Forn-Díaz, C. J. P. M. Harmans, and J. E. Mooij, Strong Coupling of a Quantum Oscillator to a Flux Qubit at Its Symmetry Point, Phys. Rev. Lett. **105**, 060503 (2010).
[23] P. Forn-Díaz, G. Romero, C. J. P. M. Harmans, E. Solano, and J. E. Mooij, Broken selection rule in the quantum Rabi model, Sci. Rep. **6**, 26720 (2016).
[24] S. De Liberato, D. Gerace, I. Carusotto, and C. Ciuti, Extracavity quantum vacuum radiation from a single qubit, Phys. Rev. A **80**, 053810 (2009).
[25] Q. Ai, Y. Li, H. Zheng, and C. P. Sun, Quantum anti-Zeno effect without rotating wave approximation, Phys. Rev. A **81**, 042116 (2010).
[26] X. Cao, J. Q. You, H. Zheng, A. G. Kofman, and F. Nori, Dynamics and quantum Zeno effect for a qubit in either a low- or high-frequency bath beyond the rotating-wave approximation, Phys. Rev. A **82**, 022119 (2010).
[27] X. Cao, J. Q. You, H. Zheng, and F. Nori, A qubit strongly coupled to a resonant cavity: Asymmetry of the spontaneous emission spectrum beyond the rotating wave approximation, New J. Phys. **13**, 073002 (2011).
[28] R. Stassi, A. Ridolfo, O. Di Stefano, M. J. Hartmann, and S. Savasta, Spontaneous Conversion from Virtual to Real Photons in the Ultrastrong-Coupling Regime, Phys. Rev. Lett. **110**, 243601 (2013).
[29] A. Ridolfo, S. Savasta, and M. J. Hartmann, Nonclassical Radiation from Thermal Cavities in the Ultrastrong Coupling Regime, Phys. Rev. Lett. **110**, 163601 (2013).

[30] L. Garziano, A. Ridolfo, R. Stassi, O. Di Stefano, and S. Savasta, Switching on and off of ultrastrong light-matter interaction: Photon statistics of quantum vacuum radiation, Phys. Rev. A **88**, 063829 (2013).

[31] L. Garziano, R. Stassi, A. Ridolfo, O. Di Stefano, and S. Savasta, Vacuum-induced symmetry breaking in a superconducting quantum circuit, Phys. Rev. A **90**, 043817 (2014).

[32] J.-F. Huang and C. K. Law, Photon emission via vacuum-dressed intermediate states under ultrastrong coupling, Phys. Rev. A **89**, 033827 (2014).

[33] Y.-J. Zhao, Y.-L. Liu, Y.-X. Liu, and F. Nori, Generating nonclassical photon states via longitudinal couplings between superconducting qubits and microwave fields, Phys. Rev. A **91**, 053820 (2015).

[34] G. Zhu, D. G. Ferguson, V. E. Manucharyan, and J. Koch, Circuit QED with fluxonium qubits: Theory of the dispersive regime, Phys. Rev. B **87**, 024510 (2013).

[35] K. K. W. Ma and C. K. Law, Three-photon resonance and adiabatic passage in the large-detuning Rabi model, Phys. Rev. A **92**, 023842 (2015).

[36] L. Garziano, R. Stassi, V. Macrì, A. F. Kockum, S. Savasta, and F. Nori, Multiphoton quantum Rabi oscillations in ultrastrong cavity QED, Phys. Rev. A **92**, 063830 (2015).

[37] See Supplemental Material at http://link.aps.org/supplemental/10.1103/PhysRevLett.117.043601 for more details.

[38] Y. X. Liu, J. Q. You, L. F. Wei, C. P. Sun, and F. Nori, Optical Selection Rules and Phase-Dependent Adiabatic State Control in a Superconducting Quantum Circuit, Phys. Rev. Lett. **95**, 087001 (2005).

[39] F. Deppe, M. Mariantoni, E. P. Menzel, A. Marx, S. Saito, K. Kakuyanagi, H. Tanaka, T. Meno, K. Semba, H. Takayanagi, E. Solano, and R. Gross, Two-photon probe of the Jaynes Cummings model and controlled symmetry breaking in circuit QED, Nat. Phys. **4**, 686 (2008).

[40] A. Ridolfo, M. Leib, S. Savasta, and M. J. Hartmann, Photon Blockade in the Ultrastrong Coupling Regime, Phys. Rev. Lett. **109**, 193602 (2012).

[41] A. J. Hoffman, S. J. Srinivasan, S. Schmidt, L. Spietz, J. Aumentado, H. E. Türeci, and A. A. Houck, Dispersive Photon Blockade in a Superconducting Circuit, Phys. Rev. Lett. **107**, 053602 (2011).

[42] J. Majer, J. M. Chow, J. M. Gambetta, J. Koch, B. R. Johnson, J. A. Schreier, L. Frunzio, D. I. Schuster, A. A. Houck, A. Wallraff *et al.*, Coupling superconducting qubits via a cavity bus, Nature (London) **449**, 443 (2007).

[43] P. D. Nation, J. R. Johansson, M. P. Blencowe, and F. Nori, Stimulating uncertainty: Amplifying the quantum vacuum with superconducting circuits, Rev. Mod. Phys. **84**, 1 (2012).

Supplemental Material for Simultaneous Excitation of Two Atoms with a Single Photon

I. DERIVATION OF THE EFFECTIVE HAMILTONIAN

According to standard time-dependent perturbation theory, for a constant perturbation switched-on at $t = 0$, the resulting transition rate can be expressed as

$$W_{i\to f} = \frac{2\pi}{\hbar}|V_{fi}^{\text{eff}}|^2\,\delta(E_f - E_i)\,, \tag{1}$$

where i and f label the initial and final states with corresponding energies E_i and E_f, and V_{fi}^{eff} describes the effective coupling strength connecting the initial and final states. In the framework of first-order perturbation theory, this effective coupling strength coincides with the matrix element of the generic perturbing interaction $\hat{V}$: $V_{fi}^{\text{eff}} = V_{fi} = \langle f|\hat{V}|i\rangle$. If i and f are coupled only via third-order perturbation theory, the resulting effective coupling strength is

$$V_{fi}^{\text{eff}} = \sum_{m,n}\frac{V_{fn}V_{nm}V_{mi}}{(E_i - E_m)(E_i - E_n)}\,. \tag{2}$$

In the case when the states $|n\rangle$ and $|m\rangle$ are virtual intermediate states that do not conserve energy, the only effect of the perturbation is to couple, via these virtual intermediate states, the initial and final states. The same coupling can be described by the effective Hamiltonian

$$H_{\text{eff}} = V_{fi}^{\text{eff}}\,|f\rangle\langle i| + \text{H.c.}\,, \tag{3}$$

with V_{fi}^{eff} provided by Eq. (2).

We observe that, applying first-order perturbation theory by using this effective Hamiltonian, we obtain the same result of standard third-order perturbation theory with the real perturbation $\hat{V}$. Hence, Eq. (2) describes the effective coupling strength between the energy-degenerate states $|g, g, 1\rangle$ and $|e, e, 0\rangle$. We consider the case $\omega_{\text{c}} \approx 2\omega_{\text{q}}$ and a perturbation of the form:

$$\hat{V} = \lambda\hat{X}\sum_i(\cos\theta\,\hat{\sigma}_x^{(i)} + \sin\theta\,\hat{\sigma}_z^{(i)})\,. \tag{4}$$

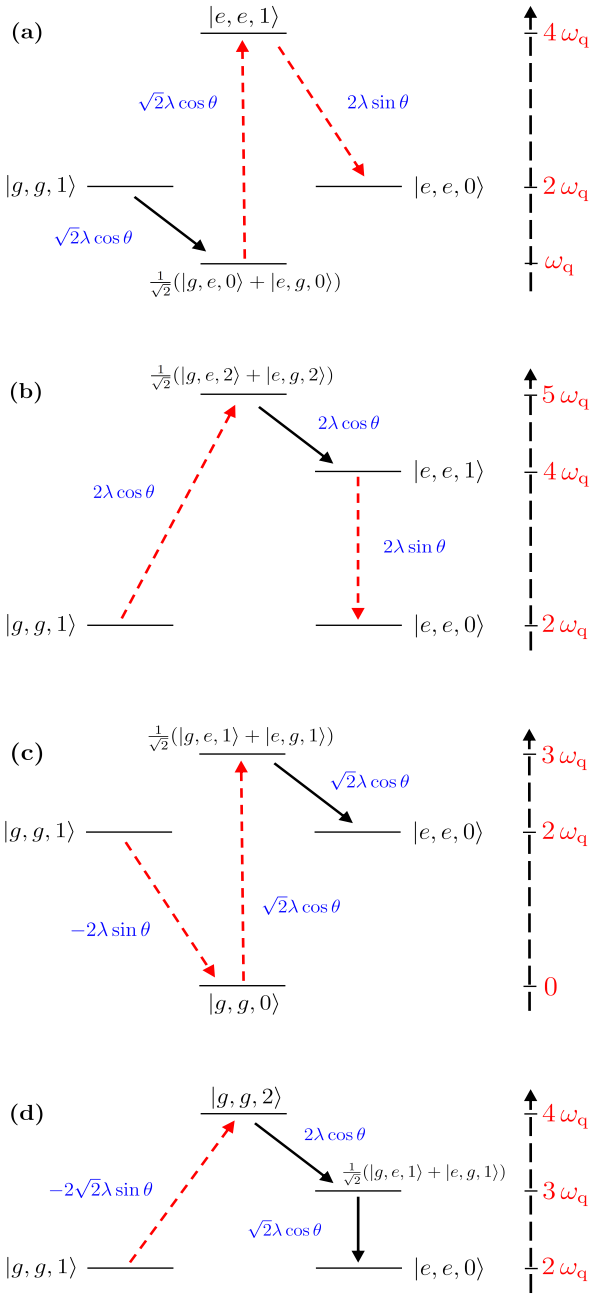

FIG. S1. (Color online) Coupling between the bare states $|g,g,1\rangle$ and $|e,e,0\rangle$ via intermediate virtual transitions. Here, the excitation-number nonconserving processes are represented by the arrowed red dashed lines. The transition matrix elements are also shown (in blue).

After carefully inspecting all the possible intermediate states, we find that only the four paths shown in Fig. S1 can connect the states $|g,g,1\rangle$ and $|e,e,0\rangle$. Applying Eq. (2), we obtain,

$$\Omega_{\rm eff} \equiv -V_{fi}^{\rm eff} = \frac{8}{3}\sin\theta\cos^2\theta\left(\frac{\lambda}{\omega_{\rm q}}\right)^3 . \tag{5}$$

Figure S2 displays the comparison of the magnitudes of the effective Rabi splitting $2\Omega_{\rm eff}/\omega_{\rm q}$ between the states $|g,g,1\rangle$ and $|e,e,0\rangle$ obtained analytically [Eq. (5)] via third-order perturbation theory and by the numerical diagonalization of the Hamiltonian in Eq. (1) (in the main text), as a function of the normalized interaction strength $\lambda/\omega_{\rm q}$. The agreement is very good, also for coupling strengths λ beyond 10% of the qubit transition frequency $\omega_{\rm q}$. This result confirms the $(\lambda/\omega_{\rm q})^3$ proportionality of the effective (one-photon)-(two-atoms) coupling predicted by the above analysis.

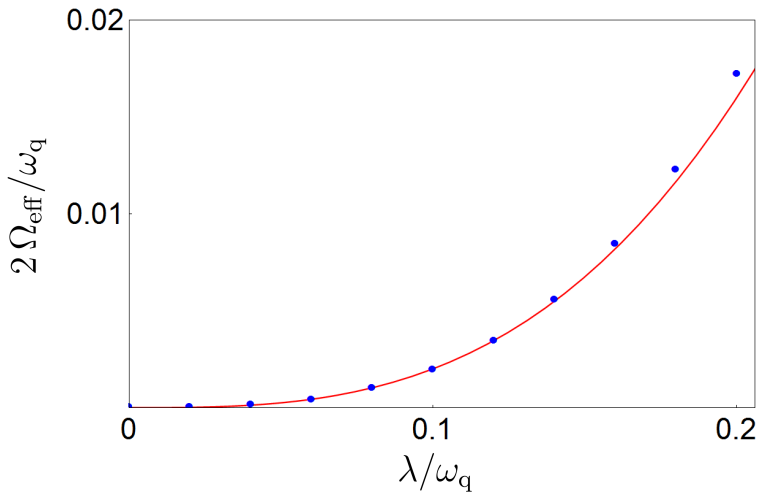

FIG. S2. (Color online) Comparison between the numerically-calculated normalized Rabi splitting (points) (corresponding to twice the effective coupling between one cavity photon and two independent atoms) and the corresponding calculation using third-order perturbation theory (continuous red curve).

II. A SINGLE PHOTON CAN SIMULTANEOUSLY EXCITE THREE QUBITS

If the resonance frequency of the optical/microwave resonator is $\omega_{\rm c} \approx 3\omega_{\rm q}$, the simultaneous excitation of three atoms: $|g,g,g,1\rangle \rightarrow |e,e,e,0\rangle$ is also possible. In contrast to

the two-atom process, the three-atom process does not need broken symmetry. This point can be understood considering one of the possible paths (involving three virtual transitions) which can determine the resonant coupling $|g,g,g,1\rangle \leftrightarrow |e,e,e,0\rangle$. In this case we consider the following perturbing potential,

$$\hat{V} = \lambda \sum_{i=1}^{3} (\hat{a}\sigma_{+}^{(i)} + \hat{a}^{\dagger}\sigma_{-}^{(i)} + \hat{a}\sigma_{-}^{(i)} + \hat{a}^{\dagger}\sigma_{+}^{(i)}) \,, \tag{6}$$

corresponding to the case $\theta = 0$, where parity symmetry is not broken. According to third order perturbation theory, one of the possible paths is: $|g,g,g,1\rangle \rightarrow |(e,g,g)_s,2\rangle \rightarrow |(e,e,g)_s,1\rangle \rightarrow |e,e,e,0\rangle$, where we indicated with $()_s$ the symmetric states of three qubits with one or two of them in the excited state. The first virtual transition $|g,g,g,1\rangle \rightarrow |(e,g,g)_s,2\rangle$ is induced by the counter rotating terms $\hat{a}^{\dagger}\sigma_{+}^{(i)}$ in Eq. (6), while the last two transitions are induced by the JC interaction terms $\hat{a}\sigma_{+}^{(i)}$.

Figure S3a displays the lowest energy states (specifically, we report the frequency differences $\omega_{i,0} = \omega_i - \omega_0$) as a function of the resonator frequency resulting from the numerical diagonalization of the total Hamiltonian including the resonator energy, the three qubits energy and the interaction energy in Eq. (6). We used $\lambda/\omega_{\rm q} = 0.3$ and $\theta = 0$. At $\omega_{\rm c} \simeq 2.86\,\omega_{\rm c}$ an apparent crossing can be observed. Actually, what appears as a crossing on this scale, it turns out to be a splitting anticrossing on an enlarged view as in Fig. S3b. The resulting states are well approximated by the states $(|e,e,e,0\rangle \pm |g,g,g,1\rangle)/\sqrt{2}$. This splitting is not present in the rotating-wave approximation (RWA), where the coherent coupling between states with a different number of excitations is not allowed. Figure S4 displays the numerically-calculated dynamics of the photon number $\langle \hat{X}^{-}\hat{X}^{+}\rangle$, of the mean excitation number $\langle \hat{C}_1^{-}\hat{C}_1^{+}\rangle$ for one of the qubits (which, of course, coincides with that of the other two), and of the three-qubit correlation $G_{\rm q}^{(3)} = \langle \hat{C}_1^{-}\hat{C}_2^{-}\hat{C}_3^{-}\hat{C}_3^{+}\hat{C}_2^{+}\hat{C}_1^{+}\rangle$. Vacuum Rabi oscillations showing the reversible excitation exchange between the three qubits and the resonator are clearly visible. We also observe a strong three-qubit correlation, since $\langle \hat{C}_1^{-}\hat{C}_1^{+}\rangle$ and $G_{\rm q}^{(3)}(t)$ are almost coincident. This is a clear signature that the three qubits are jointly excited. Moreover, we observe that $\langle \hat{X}^{-}\hat{X}^{+}\rangle$ is not zero at the photon minima. This occurs because, owing to the same processes inducing its coupling with the one-photon state, the three-qubit excited state —eee0¿ acquires a non-negligible dipole transition matrix element, so that it is able to emit photons after decaying into the lower energy states (see Fig S3a).

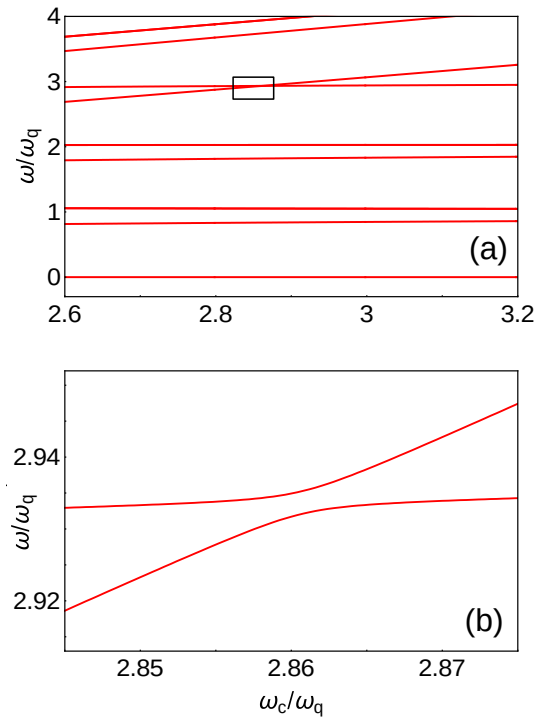

FIG. S3. (Color online) (a) Energy levels as a function of $\omega_{\rm c}/\omega_{\rm q}$ for the system of three qubits interacting with a resonator. Here we consider a normalized coupling rate $\lambda/\omega_{\rm q} = 0.1$ between the resonator and each of the qubits. We used $\theta = 0$ and $\lambda/\omega_{\rm q} = 0.3$. (b) Enlarged view of the spectral region delimited by a square in panel (a). This shows an avoided-level crossing, demonstrating the coupling between the states $|g, g, g, 1\rangle$ and $|e, e, e, 0\rangle$ due to the presence of counter-rotating terms in the system Hamiltonian.

III. ADDITIONAL ATOMIC TRANSITIONS

We discuss here the case of two identical atoms coupled to a single resonator-mode beyond the two-level system description. We consider the case where each of them has an additional higher energy state $|f\rangle$. We also assume that the transition $|g\rangle \leftrightarrow |f\rangle$, with frequency ω_{fg} is optically active. By using the results of the Supplementary Sect. I, the effective system Hamiltonian can be written as,

$$\begin{aligned}\hat{H}_{\rm eff} &= \omega_{\rm c}|g, g, 1\rangle\langle g, g, 1| + 2\omega_{eg}|e, e, 0\rangle\langle e, e, 0| + \omega_{fg}|(f, g)_s, 0\rangle\langle (f, g)_s, 0| \\ &+ \Omega_{\rm eff}(|g, g, 1\rangle\langle e, e, 0| + {\rm H.c.}) + \lambda'(|g, g, 1\rangle\langle (f, g)_s, 0| \,, \end{aligned} \tag{7}$$

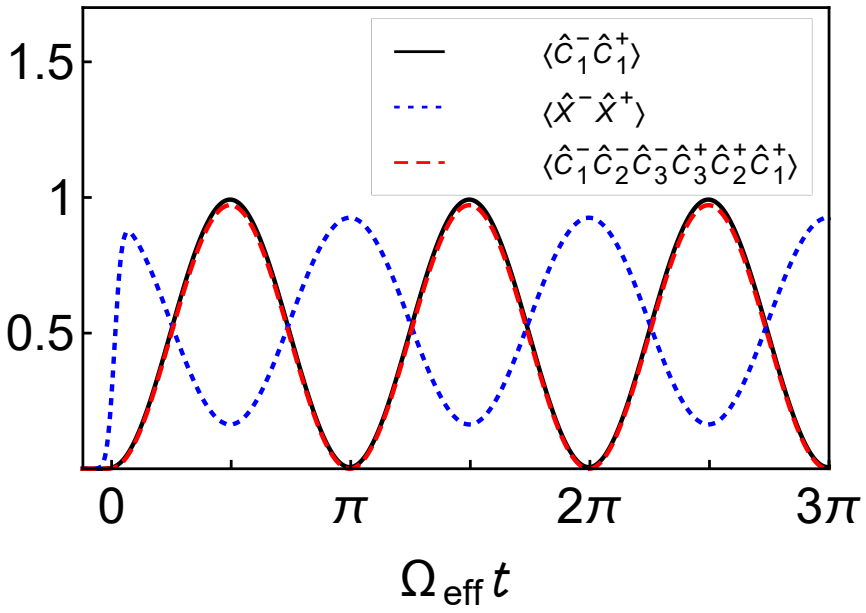

FIG. S4. (Color online) Time evolution of the cavity mean photon number $\langle \hat{X}^- \hat{X}^+ \rangle$ (dotted blue curve), qubit 1 mean excitation number $\langle \hat{C}_1^- \hat{C}_1^+ \rangle$ (continuous black curve), and the zero-delay three-qubit correlation function $G_{\rm q}^{(3)} = \langle \hat{C}_1^- \hat{C}_2^- \hat{C}_3^- \hat{C}_3^+ \hat{C}_2^+ \hat{C}_1^+ \rangle$ (dashed red curve) after the arrival of a π-like Gaussian pulse initially exciting the resonator. After the arrival of the pulse, the system undergoes vacuum Rabi oscillations showing the reversible joint absorption and re-emission of one photon by three qubits. $\langle \hat{C}_1^- \hat{C}_1^+ \rangle$ and $G_{\rm q}^{(3)}(t)$ are almost coincident.

where $|(f,g)_s,0\rangle = (|f,g,0\rangle + |g,f,0\rangle)/\sqrt{2}$, describes a symmetric superposition where only one of the two atoms is in the excited state $|f\rangle$, and λ' is the coupling rate between the cavity photon and the transition $|g\rangle \leftrightarrow |f\rangle$.

We consider the case $\omega_{\rm c} = 2\omega_{\rm eg}$. Starting from the atoms in the ground state and a single photon in the resonator: $|\psi(0)\rangle = |g,g,1\rangle$, the system will evolve towards the following superposition,

$$|\psi(t)\rangle = a(t)|g,g,1\rangle + b(t)|e,e,0\rangle + c(t)|(f,g)_s,0\rangle\,, \tag{8}$$

where the excitation of largely detuned states, as $|(f,e)_s,0\rangle$ and $|f,f\rangle$, has been neglected. We study the system dynamics for different detunings $\Delta = \omega_{fg} - \omega_{\rm c} = \omega_{fe} - \omega_{eg}$. The normalized detuning Δ/ω_{eg} also provides a measure of the atomic anharmonicity. In addition to the simultaneous excitation of two atoms (described by the ket $|e,e,0\rangle$), the excitation of

only one of them, described by the ket $|(f,g)_s,0\rangle$ in Eq. (8) is also possible. The probability that atom 1 is in an excited state can be derived from the mean value of the operator $\hat{P}_1^{\rm exc} = |e\rangle\langle e| + |f\rangle\langle f|$, where the bras and the kes here referes to states of the atom 1. The probability that both atoms are in an excited state can be expressed as the mean value of the operator $\hat{P}_{12}^{\rm exc} = |e,e\rangle\langle e,e|$.

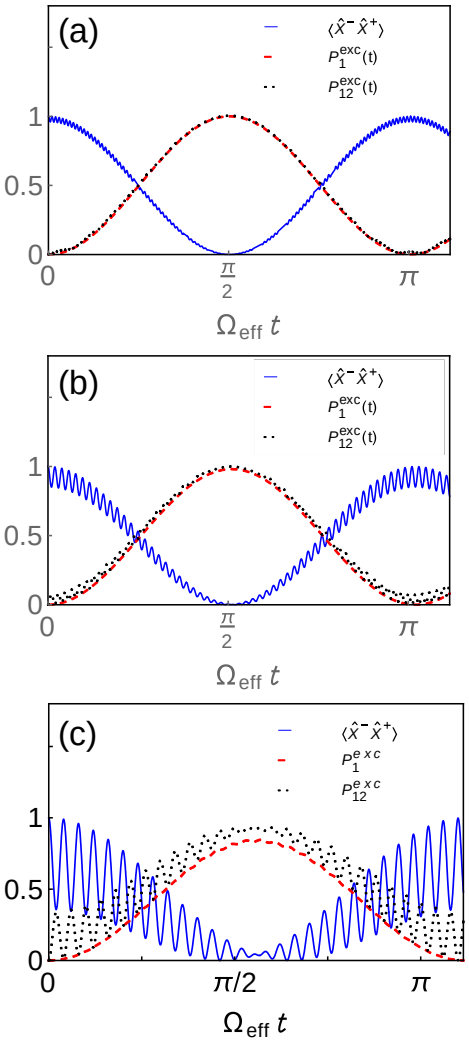

FIG. S5. (Color online) Time evolution of the mean intracavity photon number $\langle \hat{X}^- \hat{X}^+ \rangle$, of the probability that atom 1 is in one of the two excited states $P_1^{\rm exc}(t)$, and the probability that both atoms are excited $P_{12}^{\rm exc}(t)$, calculatd for different normalized detunings (from the upper to the lower panels, $\Delta/\omega_{eg} = 1,\, 0.5,\, 0.2$).

Starting from the initial state $|g,g,1\rangle$, Fig. S5 describes the time evolution of the mean

intracavity photon number $\langle \hat{X}^- \hat{X}^+ \rangle$, of the probability that atom 1 (equal to that of atom 2, being the two atoms identical) is in one of the two excited states $P_1^{\rm exc}(t)$, and the probability that both atoms are excited $P_{12}^{\rm exc}(t)$. Calculations have been carried out for different normalized detunings (from the upper to the lower panels, $\Delta/\omega_{eg} = 1,\, 0.5,\, 0.2$). We also used $\Omega_{\rm eff} = 5 \times 10^{-3} \omega_{eg}$, $\lambda' = 0.1$. Damping has not been included. Figure S5 shows that, when the detuning Δ is large as compared to the coupling strength λ', the influence of the additional transition is negligible. When Δ approaches λ', fast oscillations, due to the partial occupation of state $|f\rangle$ appears and a lowering of the two-atom correlation can be observed.

IV. NONIDENTICAL QUBITS

We have also considered the case of nonidentical qubits. The system Hamiltonian is,

$$\hat{H}_0 = \hat{H}_{\rm q} + \hat{H}_{\rm c} + \hat{X} \sum_{i=1}^{2} \lambda (\cos\theta\, \hat{\sigma}_x^{(i)} + \sin\theta\, \hat{\sigma}_z^{(i)}) \,, \tag{9}$$

where $\hat{H}_{\rm q} = \sum_{i=1}^{2} \omega_{{\rm q}i}/2 \hat{\sigma}_z^{(i)}$. It is useful to define $\omega_0 = (\omega_{\rm q1} + \omega_{\rm q2})/2$.

Figure S6a displays the lowest energy states (we report the frequency differences $\omega_{i,0} = \omega_i - \omega_0$) as a function of the resonator frequency resulting from the numerical diagonalization of the total Hamiltonian in Eq. (9). We used $\omega_{\rm q1} = 1.2\,\omega_0$, $\omega_{\rm q2} = 0.8\,\omega_0$, $\lambda_1/\omega_0 = 0.12\,\omega_0$, $\lambda_2/\omega_0 = 0.8$ and $\theta = \pi/6$. At $\omega_{\rm c} \simeq 1.974\,\omega_{\rm c}$ an apparent crossing can be observed. Actually, what appears as a crossing on this scale, it turns out to be a splitting anticrossing on an enlarged view as in Fig. S6b.

Figure S7 displays the numerically-calculated dynamics of the photon number $\langle \hat{X}^- \hat{X}^+ \rangle$, of the mean excitation number $\langle \hat{C}_i^- \hat{C}_i^+ \rangle$ for qubit1 1 and 2, and of the two-qubit correlation $G_{\rm q}^{(2)} \equiv \langle \hat{C}_1^- \hat{C}_2^- \hat{C}_2^+ \hat{C}_1^+ \rangle$. Vacuum Rabi oscillations showing the reversible excitation exchange between the qubits and the resonator are clearly visible. We find that also for nonidentical qubits, it results $\langle \hat{C}_1^- \hat{C}_1^+ \rangle \simeq \langle \hat{C}_2^- \hat{C}_2^+ \rangle \simeq G_{\rm q}^{(2)}$. This result *further confirms the simultaneous and joint nature of this multiatom process.*

V. HIGHER LIGHT-MATTER COUPLING STRENGTH

Here we present results for a qubit-cavity coupling strength higher than that consider in the main paper. Specifically, we consider a normlized coupling strength $\lambda = 0.2\,\omega_{\rm q}$. The

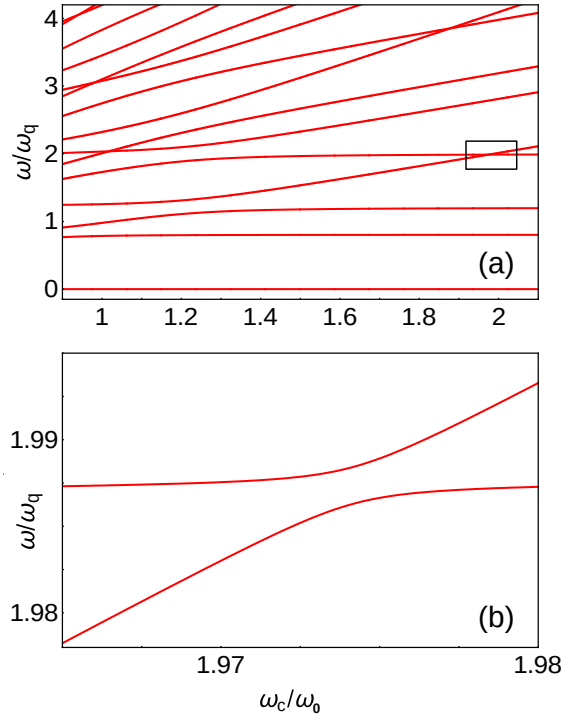

FIG. S6. (Color online) Energy levels as a function of ω_c/ω_0 for two non identical qubits qubits interacting with a resonator. (a) Frequency differences $\omega_{i,0} = \omega_i - \omega_0$ for the lowest energy eigenstates of Hamiltonian (9) as a function of ω_c/ω_0. (b) Enlarged view of the spectral region delimited by a square in panel (a). This shows an avoided-level crossing, demonstrating the coupling between the states $|g, g, 1\rangle$ and $|e, e, 0\rangle$ in the case of noidentical qubits.

other parameters are the same used for the calculation presented in Fig. 2 of the paper. Figure S8 displays the energy levels and a splittting, significantly larger than that shown Fig. 2b in the paper, can be observed in Fig. S8b.

Figure S9 displays the numerically-calculated dynamics of the photon number $\langle \hat{X}^- \hat{X}^+ \rangle$, of the mean excitation number $\langle \hat{C}_1^- \hat{C}_1^+ \rangle$ for qubit 1 (which, of course, coincides with that of qubit 2), and of the two-qubit correlation $G_q^{(2)} \equiv \langle \hat{C}_1^- \hat{C}_2^- \hat{C}_2^+ \hat{C}_1^+ \rangle$. Vacuum Rabi oscillations showing the reversible excitation exchange between the qubits and the resonator are clearly visible. The main effect of increasing the coupling strength, besides the obvious decrease of the effectiv Rabi period, is the increasing of the minimum value of $\langle \hat{X}^- \hat{X}^+ \rangle$ when $\langle \hat{C}_1^- \hat{C}_1^+ \rangle$ is maximum. This nonzero minimum occurs because the two-qubit excited state, owing to the

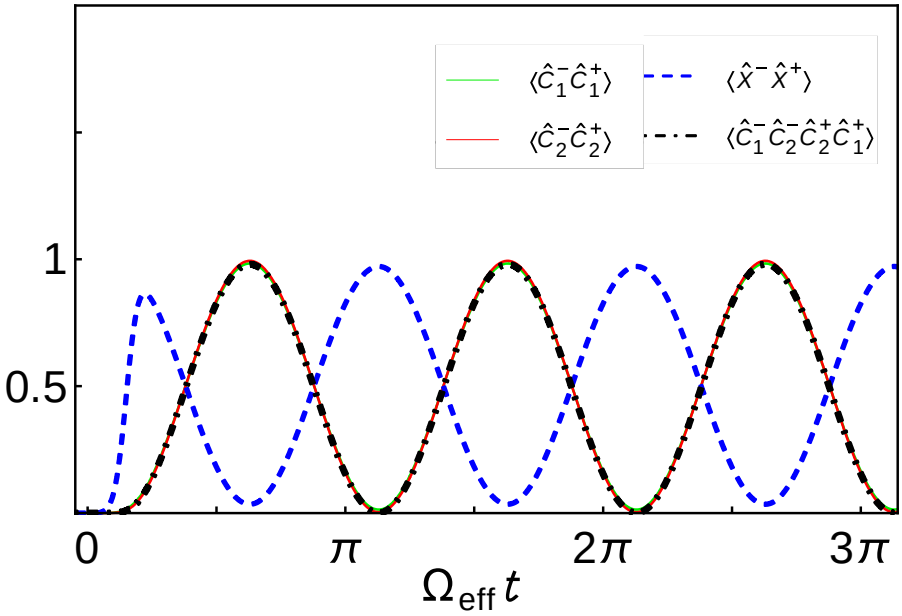

FIG. S7. (Color online) Time evolution of the cavity mean photon number $\langle \hat{X}^- \hat{X}^+ \rangle$ (dotted blue curve), qubit 1 mean excitation number $\langle \hat{C}_1^- \hat{C}_1^+ \rangle$ (continuous black curve), and the zero-delay three-qubit correlation function $G_{\rm q}^{(3)} = \langle \hat{C}_1^- \hat{C}_2^- \hat{C}_3^- \hat{C}_3^+ \hat{C}_2^+ \hat{C}_1^+ \rangle$ (dashed red curve) after the arrival of a π-like Gaussian pulse initially exciting the resonator. After the arrival of the pulse, the system undergoes vacuum Rabi oscillations showing the reversible joint absorption and re-emission of one photon by three qubits. $\langle \hat{C}_1^- \hat{C}_1^+ \rangle$ and $G_{\rm q}^{(3)}(t)$ are almost coincident.

same processes inducing its coupling with the one-photon state, acquires a dipole transition matrix element, so that this state is able to emit photons decaying to the lower energy states. The increase of its value in the present case is due to the increase of this transition matrix when the coupling strength λ increases.

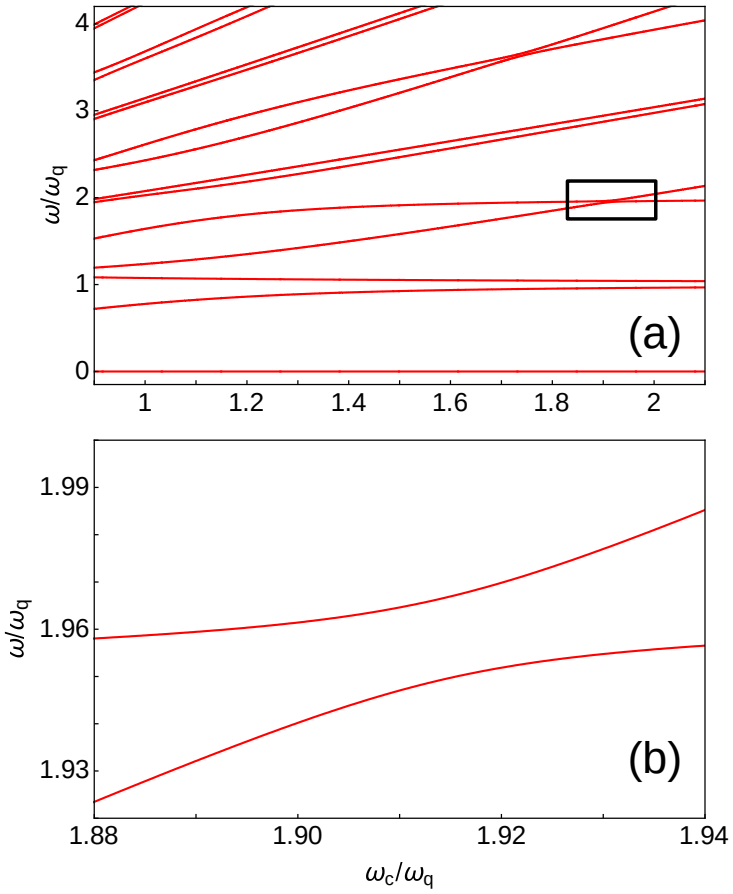

FIG. S8. (Color online) Higher light-matter coupling strength. (a) Frequency differences $\omega_{i,0} = \omega_i - \omega_0$ for the lowest energy eigenstates of Hamiltonian (9) as a function of ω_c/ω_q, obtained for an higher coupling strength $\lambda/\omega_q = 0.2$. (b) Enlarged view of the spectral region delimited by a square in panel (a). This shows an avoided-level crossing, demonstrating the coupling between the states $|g, g, 1\rangle$ and $|e, e, 0\rangle$ in the case of noidentical qubits.

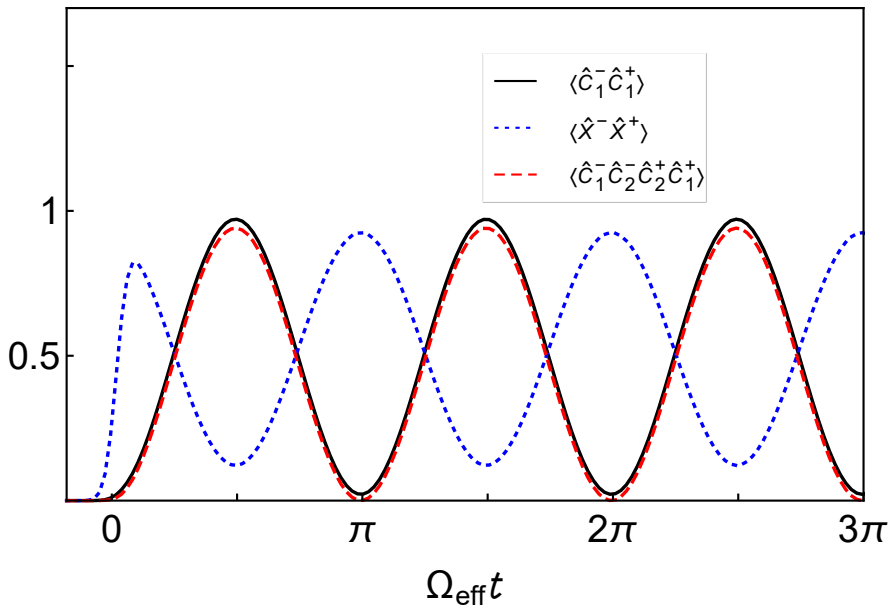

FIG. S9. (Color online) Higher light-matter coupling strength: time evolution of the cavity mean photon number $\langle \hat{X}^- \hat{X}^+ \rangle$ (dotted blue curve), qubit 1 mean excitation number $\langle \hat{C}_1^- \hat{C}_1^+ \rangle$ (continuous black curve), and the zero-delay two-qubit correlation function $G_{\text{q}}^{(2)} = \langle \hat{C}_1^- \hat{C}_2^- \hat{C}_2^+ \hat{C}_1^+ \rangle$ (dashed red curve) after the arrival of a π-like Gaussian pulse initially exciting the resonator. After the arrival of the pulse, the system undergoes vacuum Rabi oscillations showing the reversible joint absorption and re-emission of one photon by three qubits.

5.5 Paper V: Frequency conversion in ultrastrong cavity QED

SCIENTIFIC REPORTS

OPEN

Frequency conversion in ultrastrong cavity QED

Anton Frisk Kockum[1], Vincenzo Macrì[1,2], Luigi Garziano[1,2,3], Salvatore Savasta[1,2] & Franco Nori[1,4]

Received: 15 February 2017
Accepted: 10 May 2017
Published online: 13 July 2017

We propose a new method for frequency conversion of photons which is both versatile and deterministic. We show that a system with two resonators ultrastrongly coupled to a single qubit can be used to realise both single- and multiphoton frequency-conversion processes. The conversion can be exquisitely controlled by tuning the qubit frequency to bring the desired frequency-conversion transitions on or off resonance. Considering recent experimental advances in ultrastrong coupling for circuit QED and other systems, we believe that our scheme can be implemented using available technology.

Frequency conversion in quantum systems[1,2], is important for many quantum technologies. The optimal working points of devices for transmission, detection, storage, and processing of quantum states are spread across a wide spectrum of frequencies[3,4]. Interfacing the best of these devices is necessary to create quantum networks[5] and other powerful combinations of quantum hardware. Examples of frequency-conversion setups developed for such purposes include upconversion for photon detection[6] and storage[7], since both these things are easier to achieve at a higher frequency than what is optimal for telecommunications. Downconversion in this frequency range has also been demonstrated[8–10], and recently even strong coupling between a telecom and a visible optical mode[11]. Additionally, advances in quantum information processing with superconducting circuits at microwave frequencies[12,13], is driving progress on frequency conversion between optical and microwave frequencies[14–17]. We note that several types of quantum systems, suited for different tasks in quantum information processing, can operate at microwave frequencies[4]. To connect these systems, frequency conversion within this frequency range is important. Furthermore, frequency conversion can be used to create entangled states, which have applications in virtually all areas of quantum information processing, including quantum computing, quantum key distribution, and quantum teleportation[18].

Circuit quantum electrodynamics (QED)[12,19–22], offers a wealth of possibilities for frequency conversion at microwave frequencies; some of these schemes can also be generalised to optical frequencies. By modulating the magnetic flux through a superconducting quantum interference device (SQUID) in a transmission-line resonator, the frequency of the photons in the resonator can be changed rapidly[23–25], or two modes of the resonator can be coupled[26,27]. Other driven Josephson-junction-based devices can also be used for microwave frequency conversion[28,29]. Downconversion has been proposed for setups with Δ-type three-level atoms[30–32], and demonstrated with an effective three-level Λ system[33]. Upconversion of a two-photon drive has been shown for a flux qubit coupled to a resonator in a way that breaks parity symmetry[34]. Indeed, the Δ-type level structure in a flux qutrit[35] even makes possible general three-wave mixing[36]. Recently, frequency conversion was also demonstrated for two sideband-driven microwave *LC*-resonators coupled through a mechanical resonator[37].

The approach to frequency conversion that we propose in this article is based on two cavities or resonator modes coupled ultrastrongly to a two-level atom (qubit). The regime of ultrastrong coupling (USC), where the coupling strength starts to become comparable to the bare transition frequencies in the system, has only recently been reached in a number of solid-state systems[38–56]. Among these, a few circuit-QED experiments provide some of the clearest examples[39,40,49–52,54–56], including the largest coupling strength reported[51]. While the USC regime displays many striking physical phenomena[57–66], we are here only concerned with the fact that it enables higher-order processes that do not conserve the number of excitations in the system, an effect which has also been noted for a multilevel atom coupled to a resonator[67]. Examples of such processes include multiphoton Rabi oscillations[68,69], and a single photon exciting multiple atoms[70]. Indeed, almost any analogue of processes from nonlinear optics is feasible[71]; this can be regarded as an example of quantum simulation[72,73]. Just like the analytical

[1]Center for Emergent Matter Science, Riken, Saitama, 351-0198, Japan. [2]Dipartimento di Scienze Matematiche e Informatiche, Scienze Fisiche e Scienze della Terra, Università di Messina, I-98166, Messina, Italy. [3]School of Physics and Astronomy, University of Southampton, Southampton, SO17 1BJ, United Kingdom. [4]Physics Department, The University of Michigan, Ann Arbor, Michigan, 48109-1040, USA. Correspondence and requests for materials should be addressed to A.F.K. (email: anton.frisk.kockum@gmail.com)

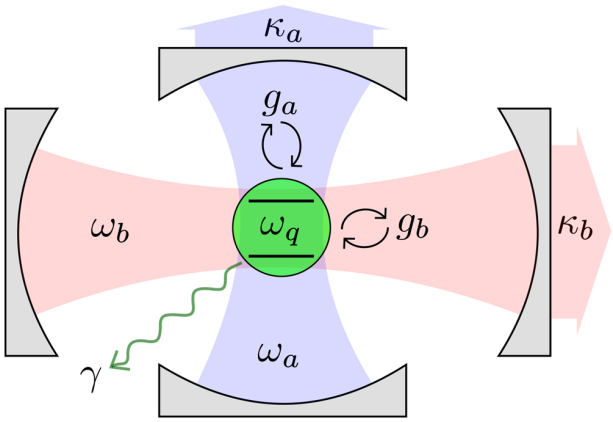

Figure 1. A sketch of the system. A qubit (green) is coupled to two resonator modes (blue, a, and red, b). Decoherence channels for the qubit (relaxation rate γ) and the resonators (relaxation rates κ_a, κ_b) are included.

solution for the quantum Rabi model[74] is now being extended to multiple qubits[75,76], and multiple resonators[77–79], we here extend the exploration of non-excitation-conserving processes to multiple resonators.

In our proposal, the qubit frequency is tuned to make various frequency-converting transitions resonant. For example, making the energy of a single photon in the first resonator equal to the sum of the qubit energy and the energy of a photon in the second resonator enables the conversion of the former (a high-energy photon) into the latter (a low-energy photon plus a qubit excitation) and vice versa. In the same way, a single photon in the first resonator can be converted into multiple photons in the second resonator (and vice versa) if the qubit energy is tuned to make such a transition resonant. The proposed frequency-conversion scheme is deterministic and allows for a variety of different frequency-conversion processes in the same setup. The setup should be possible to implement in state-of-the-art circuit QED, but the idea also applies to other cavity-QED systems.

We note that the process of parametric down-conversion in this type of circuit-QED setup has been considered previously[80], but in a regime of weaker coupling and without using the qubit to control the process. Also, it has been shown that a beamsplitter-type coupling between two resonators can be controlled by changing the qubit state[81] or induced for weaker qubit-resonator coupling by driving the qubit[82], but the proposal presented here offers greater versatility and simplicity for frequency conversion.

Model

We consider a setup where a qubit with transition frequency ω_q is coupled to two resonators with resonance frequencies ω_a and ω_b, respectively, as sketched in Fig. 1. The Hamiltonian is ($\hbar = 1$)

$$\hat{H} = \omega_a \hat{a}^\dagger \hat{a} + \omega_b \hat{b}^\dagger \hat{b} + \frac{\omega_q}{2}\hat{\sigma}_z + [g_a(\hat{a} + \hat{a}^\dagger) + g_b(\hat{b} + \hat{b}^\dagger)](\hat{\sigma}_x \cos\theta + \hat{\sigma}_z \sin\theta), \tag{1}$$

where g_a (g_b) denotes the strength of the coupling between the qubit and the first (second) resonator. The creation and annihilation operators for photons in the first (second) resonator are $\hat{a}$ and $\hat{a}^\dagger$ ($\hat{b}$ and $\hat{b}^\dagger$), respectively. The angle θ parameterises the amount of longitudinal and transverse coupling as, for example, in experiments with flux qubits[34,39,40,49,56,83]; $\hat{\sigma}_x$ and $\hat{\sigma}_z$ are Pauli matrices for the qubit.

Note that we do not include a direct coupling between the two resonators. Such a coupling is seen in experiments[49], but here we will only be concerned with situations where the resonators are far detuned from each other, meaning that this coupling term can safely be neglected. Likewise, we do not include higher modes of the resonators. While they may contribute in experiments with cavities and transmission-line resonators, they can be avoided by using lumped-element resonators[56,84].

The crucial feature of Eq. (1) for our frequency-conversion scheme is that some of the coupling terms do not conserve the number of excitations in the system. The $\hat{\sigma}_z$ coupling terms act to change the photon number in one of the resonators by one, while keeping the number of qubit excitations unchanged. Likewise, the $\hat{\sigma}_x$ coupling contains terms like $\hat{a}\hat{\sigma}_-$ and $\hat{b}^\dagger\hat{\sigma}_+$ that change the number of excitations in the system by two. For weak coupling strengths, all such terms can be neglected using the rotating-wave approximation (RWA), but in the USC regime the higher-order processes that these terms enable can become important and function as second- or third-order nonlinearities in nonlinear optics[71].

To include the effect of decoherence in our system, we use a master equation on the Lindblad form in our numerical simulations. The master equation reads

$$\dot{\hat{\rho}} = -i[\hat{H}, \hat{\rho}] + \sum_{j,k>j} \left(\Gamma_a^{jk} + \Gamma_b^{jk} + \Gamma_q^{jk}\right)\mathcal{D}[|j\rangle\langle k|]\hat{\rho}, \tag{2}$$

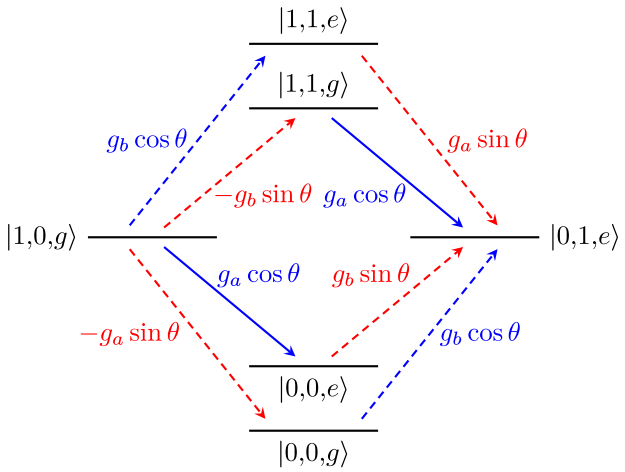

Figure 2. The four lowest-order processes contributing to a transition between $|1, 0, g\rangle$ and $|0, 1, e\rangle$. For this illustration, the parameter values $\omega_a = 3\omega_q$ and $\omega_b = 2\omega_q$ were used to set the positions of the energy levels. The transitions that do not conserve excitation number are shown as dashed lines, and the excitation-number-conserving transitions are shown as solid lines. Red lines correspond to $\hat{\sigma}_z$ (longitudinal) coupling and blue lines to $\hat{\sigma}_x$ (transverse) coupling in the Hamiltonian given in Eq. (1). Each transition is labelled by its matrix element.

where $\hat{\rho}$ is the density matrix of the system, $\mathcal{D}[\hat{c}]\rho = \hat{c}\hat{\rho}\hat{c}^\dagger - \frac{1}{2}\hat{\rho}\hat{c}^\dagger\hat{c} - \frac{1}{2}\hat{c}^\dagger\hat{c}\hat{\rho}$, and the states in the sum are eigenstates of the USC system. The relaxation rates are given by $\Gamma_a^{jk} = \kappa_a |X_a^{jk}|^2$, $\Gamma_b^{jk} = \kappa_b |X_b^{jk}|^2$, and $\Gamma_q^{jk} = \gamma |C^{jk}|^2$, where κ_a, κ_b, and γ are the relaxation rates for the bare states of the resonators and the qubit, respectively, and $c^{jk} = \langle j|\hat{c}|k\rangle$ with $\hat{X}_a = \hat{a} + \hat{a}^\dagger$, $\hat{X}_b = \hat{b} + \hat{b}^\dagger$, and $\hat{C} = \hat{\sigma}_x$[85,86], Writing the master equation in the eigenbasis of the full system avoids unphysical effects, such as emission of photons from the ground state. Similarly, to correctly count the number of photonic and qubit excitations we use $\langle \hat{X}_a^- \hat{X}_a^+ \rangle$, $\langle \hat{X}_b^- \hat{X}_b^+ \rangle$, and $\langle \hat{C}^- \hat{C}^+ \rangle$, where the plus and minus signs denote the positive and negative frequency parts, respectively, of the operators in the system eigenbasis, instead of $\langle \hat{a}^\dagger \hat{a} \rangle$, $\langle \hat{b}^\dagger \hat{b} \rangle$, and $\langle \hat{\sigma}_+ \hat{\sigma}_- \rangle$[86].

In the simulations presented in the next section, we use parameters that can be reached in circuit-QED experiments. In such experiments, the bare transition frequencies are usually in the range $\omega_{a/b/q} \sim 2\pi \times 1 - 10$ GHz. When it comes to coupling strengths, several experiments have demonstrated $g_{a/b} \gtrsim 0.1\omega_{a/b}$[39,40,49,52], and recently even $g_{a/b} \sim \omega_{a/b}$ was reached[51,56]. In all these experiments, superconducting flux qubits are coupled either to lumped-element LC oscillators[39,51,56], or transmission-line resonators[40,49,52]. For transmission-line resonators, quality factors $Q = \omega_{a/b}/\kappa_{a/b}$ exceeding 10^6 have been demonstrated[87], and flux qubit relaxation rates γ can now be as small as $\sim 2\pi \times 10$ kHz[88–90]. This brief survey of parameters indicates that $\gamma, \kappa_{a/b} \sim 10^{-6}\omega_{a/b/q}$ is possible and that $g_{a/b}$ can be a large fraction of $\omega_{a/b/q}$ if needed. In the numerical simulations for different frequency-conversion processes, we choose more conservative values for the decoherence rates (more than an order of magnitude larger than the best values discussed here), at the same time restricting the coupling strengths $g_{a/b}$ to as small values as possible (10–20% of the qubit frequency, depending on the setup) while still achieving high conversion efficiency. We note that the $g_{a/b}$ values we chose make the coupling ultrastrong with respect to ω_q, but not ultrastrong with respect to $\omega_{a/b}$.

Results

Single-photon frequency conversion. We first consider single-photon frequency conversion, where one photon in the first resonator is converted into one photon of a different frequency in the second resonator, or vice versa. The conversion is aided by the qubit. Without loss of generality, we take $\omega_a > \omega_b$. For the conversion to work, we then need $\omega_a \approx \omega_b + \omega_q$, such that the states $|1, 0, g\rangle$ and $|0, 1, e\rangle$ are close to resonant. Due to the presence of longitudinal coupling in the Hamiltonian in Eq. (1), transitions between these two states are possible even though their excitation numbers and parity differ.

The intermediate states and transitions contributing (in lowest order) to the $|1, 0, g\rangle \leftrightarrow |0, 1, e\rangle$ transition are shown in Fig. 2. Virtual transitions to and from one of the four intermediate states $|0, 0, g\rangle$, $|0, 0, e\rangle$, $|1, 1, g\rangle$, and $|1, 1, e\rangle$ connect $|1, 0, g\rangle$ and $|0, 1, e\rangle$ in two steps. This is the minimum number of steps possible, since the terms in the Hamiltonian in Eq. (1) can only create or annihilate a single photon at a time. From the figure, it is also clear that no path exists between $|1, 0, g\rangle$ and $|0, 1, e\rangle$ that does not involve longitudinal coupling (dashed red arrows in the figure).

To calculate the effective coupling between the states $|1, 0, g\rangle$ and $|0, 1, e\rangle$, we truncate the Hamiltonian from Eq. (1) to the six states shown in Fig. 2. Written on matrix form, this truncated Hamiltonian becomes

$$\hat{H} = \begin{pmatrix} -\frac{\omega_q}{2} & 0 & -g_a \sin\theta & g_b \cos\theta & 0 & 0 \\ 0 & \frac{\omega_q}{2} & g_a \cos\theta & g_b \sin\theta & 0 & 0 \\ -g_a \sin\theta & g_a \cos\theta & \omega_a - \frac{\omega_q}{2} & 0 & -g_b \sin\theta & g_b \cos\theta \\ g_b \cos\theta & g_b \sin\theta & 0 & \omega_b + \frac{\omega_q}{2} & g_a \cos\theta & g_a \sin\theta \\ 0 & 0 & -g_b \sin\theta & g_a \cos\theta & \omega_a + \omega_b - \frac{\omega_q}{2} & 0 \\ 0 & 0 & g_b \cos\theta & g_a \sin\theta & 0 & \omega_a + \omega_b + \frac{\omega_q}{2} \end{pmatrix}, \tag{3}$$

where the states are ordered from left to right as $|0, 0, g\rangle$, $|0, 0, e\rangle$, $|1, 0, g\rangle$, $|0, 1, e\rangle$, $|1, 1, g\rangle$, and $|1, 1, e\rangle$. When the condition $\omega_a \approx \omega_b + \omega_q$ is satisfied, the four intermediate states $|0, 0, g\rangle$, $|0, 0, e\rangle$, $|1, 1, g\rangle$, and $|1, 1, e\rangle$ can be adiabatically eliminated, i.e., provided that the bare coupling strengths are sufficiently small compared to the energy difference between the intermediate states and the initial and final states, we can assume that the population of the intermediate states will not change significantly, such that the effective dynamics will only involve the initial and final states. This calculation, shown in the Supplementary Information, gives an effective Hamiltonian with a coupling term

$$\hat{H}_{\mathrm{c,eff}} = g_{\mathrm{eff}}(|1, 0, g\rangle\langle 0, 1, e| + |0, 1, e\rangle\langle 1, 0, g|), \tag{4}$$

where the effective coupling between the states $|1, 0, g\rangle$ and $|0, 1, e\rangle$ has the magnitude

$$g_{\mathrm{eff}} = g_a g_b \sin 2\theta \left(\frac{1}{\omega_b} - \frac{1}{\omega_a}\right) \tag{5}$$

on resonance. Compared to the direct resonator-qubit coupling in Eq. (1), g_{eff} is weaker by a factor of order g/ω, which is why we need to at least approach the USC regime to observe the single-photon frequency conversion. We note that the effective coupling is maximised when the longitudinal and transverse coupling terms in Eq. (1) have equal magnitude. Interestingly, Eq. (5) suggests that frequency conversion can be more efficient if $\omega_b \ll \omega_a$. However, going too far in this direction violates the assumptions behind the adiabatic approximation, which relies on $g_a, g_b \ll \omega_a, \omega_b$.

The existence of this effective coupling suggests at least two ways to perform single-photon frequency conversion. The first is to use adiabatic transfer, starting in $|1, 0, g\rangle$ ($|0, 1, e\rangle$) with the qubit frequency sufficiently far detuned from the resonance $\omega_a = \omega_b + \omega_q$ and then slowly [adiabatically, i.e., slow enough that the probability of a Landau-Zener transition back to the initial state is small; note that this is a different notion of adiabaticity than that used in the adiabatic elimination used to derive Eq. (4)] changing the qubit frequency until the system ends up in the state $|0, 1, e\rangle$ ($|1, 0, g\rangle$), following one of the energy levels shown in Fig. 3(a). In this way, a single photon in the first (second) resonator is deterministically down-converted (up-converted) to a single photon of lower (higher) frequency in the second (first) resonator. We note that such adiabatic transfer has been used for robust single-photon generation in circuit QED, tuning the frequency of a transmon qubit to achieve the transition $|0, e\rangle \rightarrow |1, g\rangle$[91]. It has also been suggested as a method to generate multiple photons from a single qubit excitation in the USC regime of the standard quantum Rabi model[68].

The second approach, exemplified by a simulation including decoherence in Fig. 3(b), is to initialise the system in one of the states $|1, 0, g\rangle$ or $|0, 1, e\rangle$, far from the frequency-conversion resonance such that the effective coupling is negligible, quickly tune the qubit into resonance for the duration of half a Rabi oscillation period (set by the effective coupling to be $\pi/2g_{\mathrm{eff}}$), and then detune the qubit again (or send a pulse to deexcite it) to turn off the effective interaction. This type of scheme is, for example, commonly used for state transfer between resonators and/or qubits in circuit QED[92–96]. Letting the resonance last shorter or longer times, any superposition of $|1, 0, g\rangle$ or $|0, 1, e\rangle$ can be created. The potential for creating superpositions of photons of different frequencies (similar to ref. 27) with such a method will be explored in future work.

Since the relevant timescales for both these approaches are determined by g_{eff}, it is important to know in which parameter range the expression for g_{eff} given in Eq. (5) remains a good approximation. In Fig. 4, we show that the expression is valid up to at least $g_a = g_b = 0.2\omega_{q,0}$ for the parameters used in Fig. 3.

We note that both protocols for frequency-conversion given here can be used to transfer superposition states. For example, starting in the superposition state $a|0, 0, g\rangle + b|1, 0, g\rangle = (a|0\rangle + b|1\rangle)|0, g\rangle$, where a and b are complex numbers satisfying $|a|^2 + |b|^2 = 1$, both protocols will convert this state into $a|0, 0, g\rangle + b|0, 1, e\rangle = |0\rangle(a|0, g\rangle + b|1, e\rangle)$. If one wishes to disentangle the qubit from the second resonator mode after the transfer of the superposition, a photon-number-dependent qubit rotation, which can be implemented in the strong-dispersive regime of circuit QED[97], is one option. The remarks given here also apply to the multi-photon frequency-conversion processes studied in the next section.

Multi-photon frequency conversion. We now turn to multi-photon frequency conversion, where, aided by the qubit, one photon in the first resonator is converted into two photons in the second resonator, or vice versa. We continue to adopt the convention that $\omega_a > \omega_b$. In contrast to the single-photon frequency conversion case

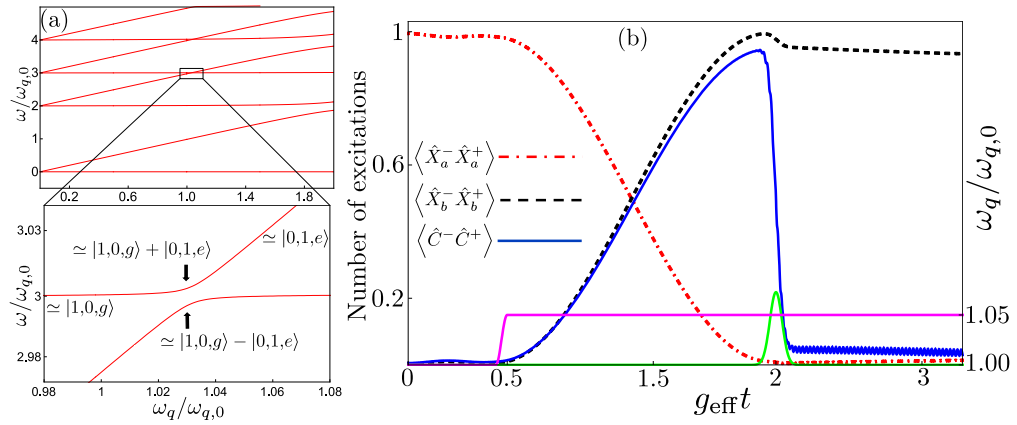

Figure 3. Two frequency conversion methods. (a) The figure shows the energy levels of our system plotted as a function of the qubit frequency ω_q, using the parameters $g_a = g_b = 0.15\omega_{q,0}$, $\theta = \pi/6$, $\omega_a = 3\omega_{q,0}$, and $\omega_b = 2\omega_{q,0}$, where $\omega_{q,0}$ is a reference point for the qubit frequency, set such that $\omega_a = \omega_b + \omega_{q,0}$. In the zoom-in, close to the resonance $\omega_a = \omega_b + \omega_q$, we see the anticrossing between $|1, 0, g\rangle$ and $|0, 1, e\rangle$ with splitting $2g_{\rm eff}$. Up- or down-conversion of single photons can be achieved by adiabatically tuning ω_q to follow one of the energy levels in the figure from $|1, 0, g\rangle$ to $|0, 1, e\rangle$, or vice versa. (b) A rapid frequency conversion can be achieved by starting in $|1, 0, g\rangle$, far from the resonance $\omega_a = \omega_b + \omega_q$, tuning the qubit frequency (pink solid curve) into resonance for half a Rabi period ($\pi/2g_{\rm eff}$) and then sending a pulse (green solid curve) to deexcite the qubit. The pink solid curve is given by $\omega_q(t) = \omega_{q,i} + \delta\omega_q\{\sin^2[A(t - t_i)]\Theta(t - t_i) + \sin^2[A(t - t_f)]\Theta(t - t_f)\}$, a smoothed step function, where $\omega_{q,i}$ is the initial qubit frequency, $\delta\omega_q$ is the change of the qubit frequency, Θ is the Heaviside step function, t_i is the time when the qubit frequency starts to change, $t_f = t_i + \pi/(2A)$, and A is a frequency setting the smoothness. The figure shows the number of excitations in the two resonators (red dashed-dotted curve for a, black dashed curve for b) and the qubit (blue solid curve) during the process, including decoherence in the form of relaxation from the resonators and the qubit. The parameters used for the decoherence are $\kappa_a = \kappa_b = \gamma = 4 \times 10^{-5}\omega_{q,0}$.

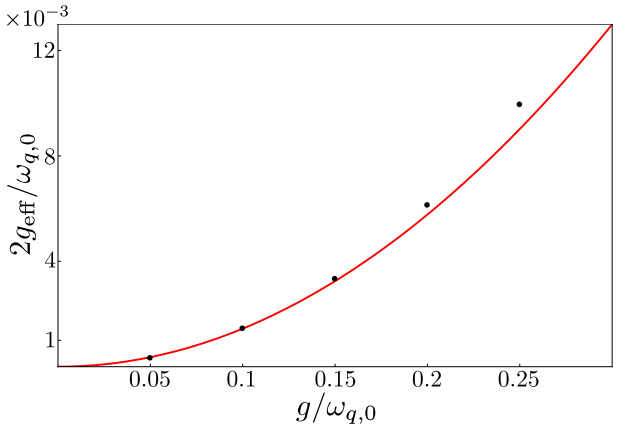

Figure 4. Comparison of analytical (red curve) and numerical (black dots) results for the effective coupling between the states $|1, 0, g\rangle$ and $|0, 1, e\rangle$. The graph shows the minimum energy splitting $2g_{\rm eff}/\omega_{q,0}$ as a function of $g/\omega_{q,0}$, where $g = g_a = g_b$, using the same parameters as in Fig. 3.

above, there are now two possibilities for how the qubit state can change during the conversion process. Below, we will study both $|1, 0, g\rangle \leftrightarrow |0, 2, e\rangle$ and $|1, 0, e\rangle \leftrightarrow |0, 2, g\rangle$. Since we wish to use the qubit to control the process, we do not consider the process $|1, 0, g\rangle \leftrightarrow |0, 2, g\rangle$, which to some extent was already included in ref. 80, although that work considered a setup with $\omega_q \approx \omega_b$ and mainly studied the squeezing produced by a strong external drive.

The $|1, 0, g\rangle \leftrightarrow |0,2,e\rangle$ process. For the process $|1, 0, g\rangle \leftrightarrow |0, 2, e\rangle$, we first of all note one more difference compared to the single-photon frequency conversion case: it changes the number of excitations from 1 to 3, which means that excitation-number parity is conserved. This makes the longitudinal coupling of Eq. (1) redundant for achieving the conversion, and to simplify our calculations we therefore hereafter work with the standard quantum Rabi Hamiltonian[98] extended to two resonators,

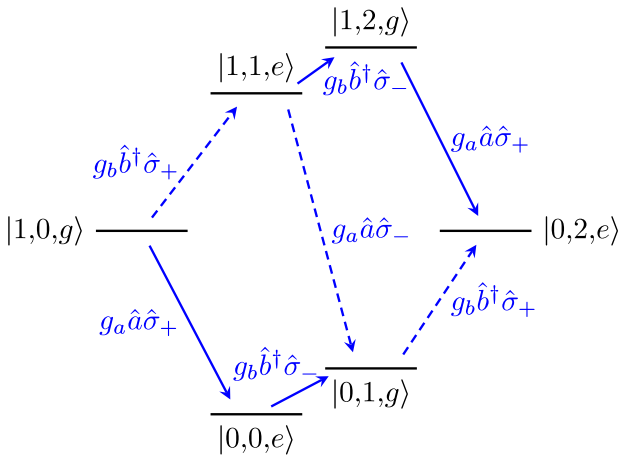

Figure 5. The lowest-order processes contributing to a transition between $|1, 0, g\rangle$ and $|0, 2, e\rangle$ in the quantum Rabi model. The transitions that do not conserve excitation number are shown as dashed blue lines and the excitation-number-conserving transitions are shown as solid blue lines. The label of each line is the term in Eq. (6) that gives rise to that transition. The parameters $\omega_a = 5\omega_q$ and $\omega_b = 2\omega_q$ were used to set the positions of the energy levels.

$$\hat{H}_{\mathrm{R}} = \omega_a\hat{a}^\dagger\hat{a} + \omega_b\hat{b}^\dagger\hat{b} + \frac{\omega_q}{2}\hat{\sigma}_z + [g_a(\hat{a} + \hat{a}^\dagger) + g_b(\hat{b} + \hat{b}^\dagger)]\hat{\sigma}_x. \tag{6}$$

Placing the system close to the resonance $\omega_a = 2\omega_b + \omega_q$, virtual transitions involving the intermediate states $|0, 0, e\rangle$, $|0, 1, g\rangle$, $|1, 1, e\rangle$, and $|1, 2, g\rangle$ (to lowest order), contribute to the process $|1, 0, g\rangle \leftrightarrow |0, 2, e\rangle$, as shown in Fig. 5. The most direct path between $|1, 0, g\rangle$ and $|0, 2, e\rangle$ involves three steps, since only one photon can be created or annihilated in each step. We note that all the paths include at least one transition that is due to terms in the Hamiltonian that do not conserve excitation number (dashed arrows in the figure).

Retaining only the states shown in Fig. 5, we can write the quantum Rabi Hamiltonian from Eq. (6) on matrix form as

$$\hat{H}_{\mathrm{R}} = \begin{pmatrix} \frac{\omega_q}{2} & g_b & g_a & 0 & 0 & 0 \\ g_b & \omega_b - \frac{\omega_q}{2} & 0 & \sqrt{2}g_b & g_a & 0 \\ g_a & 0 & \omega_a - \frac{\omega_q}{2} & 0 & g_b & 0 \\ 0 & \sqrt{2}g_b & 0 & 2\omega_b + \frac{\omega_q}{2} & 0 & g_a \\ 0 & g_a & g_b & 0 & \omega_a + \omega_b + \frac{\omega_q}{2} & \sqrt{2}g_b \\ 0 & 0 & 0 & g_a & \sqrt{2}g_b & \omega_a + 2\omega_b - \frac{\omega_q}{2} \end{pmatrix}, \tag{7}$$

where the states are ordered as $|0, 0, e\rangle$, $|0, 1, g\rangle$, $|1, 0, g\rangle$, $|0, 2, e\rangle$, $|1, 1, e\rangle$, and $|1, 2, g\rangle$. Just like before, we can adiabatically eliminate the intermediate states when the condition $\omega_a \approx 2\omega_b + \omega_q$ is satisfied. The result of this calculation, the details of which are given in the Supplementary Information, is an effective coupling between the states $|1, 0, g\rangle$ and $|0, 2, e\rangle$ with magnitude

$$g_{\mathrm{eff}} = \frac{\sqrt{2}g^3[2\omega_b(\omega_a - 2\omega_b) - g^2]}{2\omega_b^2(\omega_a - \omega_b)^2 + g^2\omega_b(5\omega_b - 3\omega_a) + g^4} \tag{8}$$

on resonance. Here, we have set $g_a = g_b \equiv g$ to simplify the expression slightly. We note that, to leading order, the coupling scales like g^3/ω^2; indeed, the leading-order term is

$$g_{\mathrm{eff}} = \frac{\sqrt{2}g^3(\omega_a - 2\omega_b)}{\omega_b(\omega_a - \omega_b)^2}. \tag{9}$$

This is a factor g/ω weaker than for the single-photon frequency conversion, and reflects the fact that an additional intermediate transition is required for the two-photon conversion. We also note that the coupling becomes

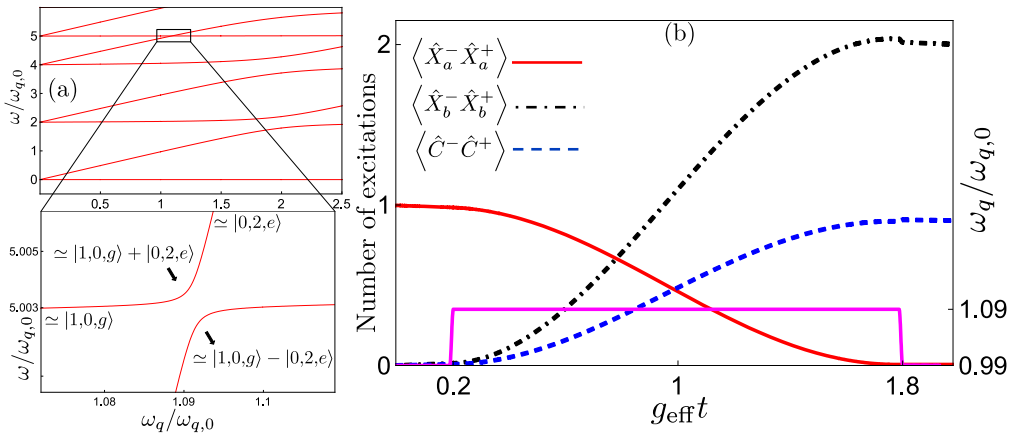

Figure 6. Two-photon frequency conversion via transitions between $|1, 0, g\rangle$ and $|0, 2, e\rangle$. (a) The energy levels of our system, given in Eq. (6), plotted as a function of the qubit frequency ω_q, using the parameters $g_a = g_b = 0.2\omega_{q,0}$, $\omega_a = 5\omega_{q,0}$, and $\omega_b = 2\omega_{q,0}$, where the reference point $\omega_{q,0}$ is set such that $\omega_a = 2\omega_b + \omega_{q,0}$. In the zoom-in, close to the resonance $\omega_a = 2\omega_b + \omega_q$, we see the anticrossing between $|1, 0, g\rangle$ and $|0, 2, e\rangle$ with the splitting $2g_{\rm eff}$ given by Eq. (8). Up-conversion of a photon pair into a single photon, or down-conversion of a single photon into a photon pair, can be achieved by adiabatically tuning ω_q to follow one of the energy levels in the figure from $|0, 2, e\rangle$ to $|1, 0, g\rangle$, or vice versa. (b) A rapid frequency conversion can be achieved by starting in $|1, 0, g\rangle$ or $|0, 2, e\rangle$, far from the resonance $\omega_a = 2\omega_b + \omega_q$, tuning the qubit frequency (pink solid curve, a smoothed step function as explained in Fig. 3) into resonance for half a Rabi period ($\pi/2g_{\rm eff}$) and then tuning it out of resonance again. The figure shows the number of excitations in the two resonators (red solid curve for a, black dashed-dotted curve for b) and the qubit (blue dashed curve) during such a process, including decoherence in the form of relaxation from the resonators and the qubit. The parameters used for the decoherence are $\kappa_a = \kappa_b = \gamma = 2 \times 10^{-5}\omega_{q,0}$.

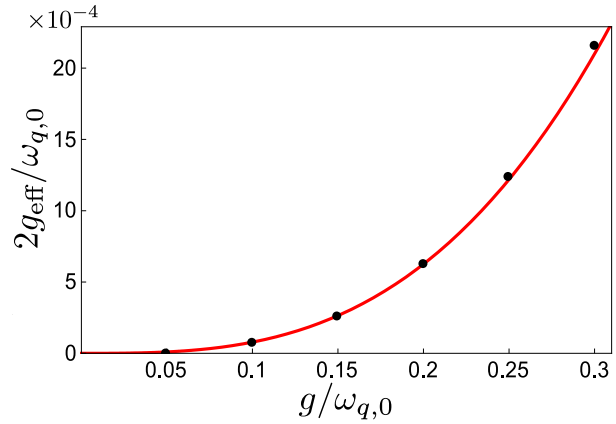

Figure 7. Comparison of analytical (red curve) and numerical (black dots) results for the effective coupling between the states $|1, 0, g\rangle$ and $|0, 2, e\rangle$. The graph shows the minimum energy splitting $2g_{\rm eff}/\omega_{q,0}$ as a function of $g/\omega_{q,0}$, using the same parameters as in Fig. 6.

small in the limit of small ω_q, i.e., when $2\omega_b \to \omega_a$. The coupling would become large if $\omega_a \to \omega_b$, but this is impossible since $\omega_a = 2\omega_b + \omega_q$ in this scheme.

The two-photon frequency conversion can be performed either by adiabatic transfer or by tuning the qubit into resonance for half a Rabi oscillation period, as explained in the section on single-photon frequency conversion. In the first approach, one adiabatically tunes the qubit energy to follow one of the energy levels shown in Fig. 6(a). A simulation of the second approach, including decoherence, is shown in Fig. 6(b). The timescale for these processes is set by the effective coupling. In Fig. 7, we show that the expression for the effective coupling given in Eq. (8) remains a good approximation up to at least $g = 0.3\omega_{q,0}$ for the parameters used in Fig. 6.

The $|1, 0, e\rangle \leftrightarrow |0, 2, g\rangle$ process. For the process $|1, 0, e\rangle \leftrightarrow |0, 2, g\rangle$, we show in Fig. 8 the virtual transitions from the quantum Rabi Hamiltonian that contribute to lowest order. We note that this process conserves the excitation number, which means that there is a path between the states that can be realised using only terms from

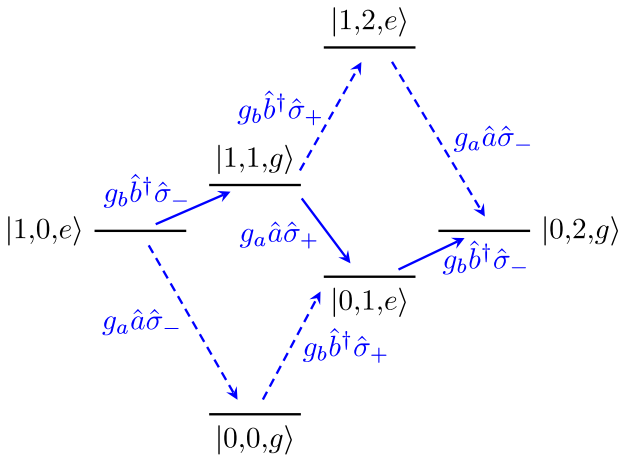

Figure 8. The lowest-order processes contributing to a transition between $|1, 0, e\rangle$ and $|0, 2, g\rangle$ in the quantum Rabi model. The transitions that do not conserve excitation number are shown as dashed blue lines and the excitation-number-conserving transitions are shown as solid blue lines. The label of each line is the term in Eq. (6) that gives rise to that transition. The parameters $\omega_a = 3\omega_q$ and $\omega_b = 2\omega_q$ were used to set the positions of the energy levels.

the Jaynes–Cummings (JC) Hamiltonian[99] (solid arrows in the figure). Below, we analyse the effective coupling both for the full quantum Rabi Hamiltonian and for the JC Hamiltonian. Usually, the JC Hamiltonian is obtained by performing the RWA on the quantum Rabi Hamiltonian when $g \ll \omega_{a/b/q}$, in which case the low coupling strength would make it very challenging to observe the frequency conversion process. However, we note that a circuit QED setup has been proposed where the pure JC Hamiltonian with ultrastrong coupling can be realised[100].

Quantum Rabi Hamiltonian. Retaining only the states shown in Fig. 8, we can write the quantum Rabi Hamiltonian from Eq. (6) on matrix form as

$$\hat{H}_{\mathrm{R}} = \begin{pmatrix} -\frac{\omega_q}{2} & g_b & g_a & 0 & 0 & 0 \\ g_b & \omega_b + \frac{\omega_q}{2} & 0 & \sqrt{2}g_b & g_a & 0 \\ g_a & 0 & \omega_a + \frac{\omega_q}{2} & 0 & g_b & 0 \\ 0 & \sqrt{2}g_b & 0 & 2\omega_b - \frac{\omega_q}{2} & 0 & g_a \\ 0 & g_a & g_b & 0 & \omega_a + \omega_b - \frac{\omega_q}{2} & \sqrt{2}g_b \\ 0 & 0 & 0 & g_a & \sqrt{2}g_b & \omega_a + 2\omega_b + \frac{\omega_q}{2} \end{pmatrix}, \tag{10}$$

where the states are ordered as $|0, 0, g\rangle$, $|0, 1, e\rangle$, $|1, 0, e\rangle$, $|0, 2, g\rangle$, $|1, 1, g\rangle$, and $|1, 2, e\rangle$. As in previous calculations, we can perform adiabatic elimination close to the resonance, which in this case is $\omega_a + \omega_q \approx 2\omega_b$. The details of the elimination are given in the Supplementary Information. The result is an effective coupling between the states $|1, 0, e\rangle$ and $|0, 2, g\rangle$ with magnitude

$$g_{\mathrm{eff}} = \frac{\sqrt{2}g^3[2\omega_b(\omega_a - 2\omega_b) - g^2]}{2\omega_b^2(\omega_a - \omega_b)^2 + g^2\omega_b(5\omega_b - 3\omega_a) + g^4} \tag{11}$$

on resonance. We have set $g_a = g_b \equiv g$ to simplify the expression slightly. Note that this expression for the coupling is actually exactly the same as the one for the process $|1, 0, g\rangle \leftrightarrow |0, 2, e\rangle$ given in Eq. (8). Even though the two processes use different intermediate states, the truncated Hamiltonians in Eqs (7) and (10) only differ in the sign of ω_q. Since ω_q is replaced on resonance by $(\omega_a - 2\omega_b)$ in the first case and by $(2\omega_b - \omega_a)$ in the second case, the formula for the effective coupling ends up being the same in both cases. The two cases still differ, however. For example, while the limit $\omega_a \to \omega_b$, which enhances the coupling, could not occur for the process $|1, 0, g\rangle \leftrightarrow |0, 2, e\rangle$, it is possible for $|1, 0, e\rangle \leftrightarrow |0, 2, g\rangle$. However, in this limit the approximations behind the adiabatic elimination break down, since the states $|1, 1, g\rangle$ and $|0, 1, e\rangle$ would also be on resonance and become populated.

The two-photon frequency conversion can again be performed either by adiabatic transfer or by tuning the qubit into resonance for half a Rabi oscillation period, as explained in the section on single-photon frequency

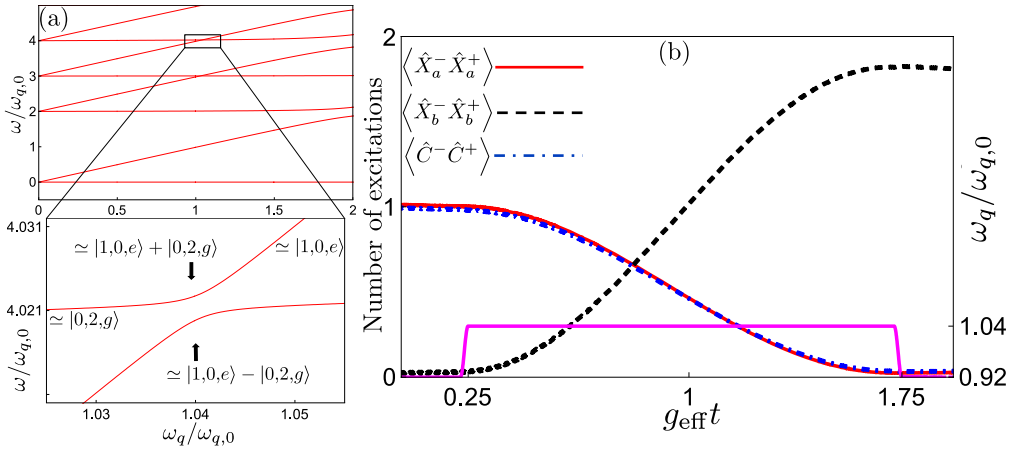

Figure 9. Two-photon frequency conversion via transitions between $|1, 0, e\rangle$ and $|0, 2, g\rangle$. (a) The energy levels of our system, given in Eq. (6), plotted as a function of the qubit frequency ω_q, using the parameters $g_a = g_b = 0.125\omega_{q,0}$, $\omega_a = 3\omega_{q,0}$, and $\omega_b = 2\omega_{q,0}$, where the reference point $\omega_{q,0}$ is set such that $\omega_a + \omega_{q,0} = 2\omega_b$. In the zoom-in, close to the resonance $\omega_a + \omega_q = 2\omega_b$, we see the anticrossing between $|1, 0, e\rangle$ and $|0, 2, g\rangle$ with the splitting $2g_{\rm eff}$ given by Eq. (11). Up-conversion of a photon pair into a single photon, or down-conversion of a single photon into a photon pair, can be achieved by adiabatically tuning ω_q to follow one of the energy levels in the figure from $|0, 2, g\rangle$ to $|1, 0, e\rangle$, or vice versa. (b) A rapid frequency conversion can be achieved by starting in $|1, 0, e\rangle$ or $|0, 2, g\rangle$, far from the resonance $\omega_a + \omega_q = 2\omega_b$, tuning the qubit frequency (pink solid curve, a smoothed step function as explained in Fig. 3) into resonance for half a Rabi period ($\pi/2g_{\rm eff}$) and then tuning it out of resonance again. The figure shows the number of excitations in the two resonators (red solid curve for a, black dashed-dotted curve for b) and the qubit (blue dashed curve) during such a process, including decoherence in the form of relaxation from the resonators and the qubit. The parameters used for the decoherence are $\kappa_a = \kappa_b = \gamma = 4 \times 10^{-5}\omega_{q,0}$.

conversion. The energy levels to follow in the first approach are plotted in Fig. 9(a) and a simulation of the second approach, including decoherence, is shown in Fig. 9(b).

Jaynes–Cummings Hamiltonian. For completeness, we calculate the effective coupling using only the JC Hamiltonian for two resonators and one qubit, i.e., we eliminate the non-excitation-conserving terms in the quantum Rabi Hamiltonian of Eq. (6), giving

$$\hat{H}_{\rm JC} = \omega_a \hat{a}^\dagger \hat{a} + \omega_b \hat{b}^\dagger \hat{b} + \frac{\omega_q}{2}\hat{\sigma}_z + g_a(\hat{a}\hat{\sigma}_+ + \hat{a}^\dagger\hat{\sigma}_-) + g_b\left(\hat{b}\hat{\sigma}_+ + \hat{b}^\dagger\hat{\sigma}_-\right). \tag{12}$$

Retaining only the states connected by solid arrows in Fig. 8, we can write the Hamiltonian from Eq. (12) on matrix form as

$$\hat{H}_{\rm JC} = \begin{pmatrix} \omega_b + \frac{\omega_q}{2} & 0 & \sqrt{2}g_b & g_a \\ 0 & \omega_a + \frac{\omega_q}{2} & 0 & g_b \\ \sqrt{2}g_b & 0 & 2\omega_b - \frac{\omega_q}{2} & 0 \\ g_a & g_b & 0 & \omega_a + \omega_b - \frac{\omega_q}{2} \end{pmatrix}, \tag{13}$$

where the states are ordered as $|0, 1, e\rangle$, $|1, 0, e\rangle$, $|0, 2, g\rangle$, and $|1, 1, g\rangle$. Again, we perform adiabatic elimination close to the resonance $\omega_a + \omega_q \approx 2\omega_b$. The details of the elimination are given in the Supplementary Information. The result is an effective coupling between the states $|1, 0, e\rangle$ and $|0, 2, g\rangle$ with magnitude

$$g_{\rm eff} = -\frac{\sqrt{2}g_a g_b^2}{g_a^2 + (\omega_a - \omega_b)^2} \tag{14}$$

on resonance. Just as for the other two-photon frequency-conversion processes, the coupling scales like g^3/ω^2 to leading order. In fact, Eq. (14) is a good approximation to Eq. (11), since the path given by the JC terms (solid lines) in Fig. 8 is far less detuned in energy from the initial and final states than all the other paths and thus gives the largest contribution to the result in Eq. (11). The remarks on the limit $\omega_a \to \omega_b$ given after Eq. (11) apply here as well. The schemes for implementing the frequency conversion are already given in Fig. 9.

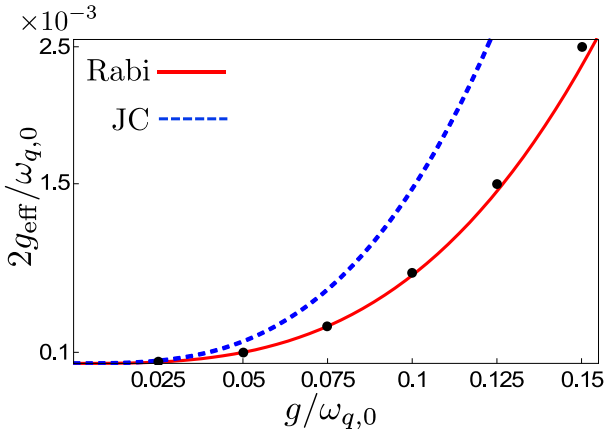

Figure 10. Comparison of analytical (JC Hamiltonian [dashed blue curve] and quantum Rabi Hamiltonian [solid red curve]) and numerical (black dots) results for the effective coupling between the states $|1, 0, e\rangle$ and $|0, 2, g\rangle$. The graph shows the minimum energy splitting $2g_{\text{eff}}/\omega_{q,0}$ as a function of $g/\omega_{q,0}$, using the same parameters as in Fig. 9.

In Fig. 10, we compare the results from Eqs (11) and (14) with a full numerical calculation using the quantum Rabi Hamiltonian. The contribution from the JC part dominates the coupling up until around $g_a = g_b = g = 0.03\omega_{q,0}$ and gives a good approximation until then. For higher values of the coupling, using the approximation from the quantum Rabi Hamiltonian instead works fine up until around $g_a = g_b = g = 0.15\omega_{q,0}$. It is interesting to note that a pure JC Hamiltonian in the USC regime would give higher effective coupling for this frequency-conversion process than the quantum Rabi Hamiltonian.

Discussion

We have shown how a system consisting of two resonators ultrastrongly coupled to a qubit can be used to realise a variety of frequency-conversion processes. In particular, we have shown how to convert a single photon into another photon of either higher or lower frequency, as well as how to convert a single photon into a photon pair and vice versa. All these processes are deterministic, can be implemented within a single setup, and do not require any external drives. The conversion is controlled by tuning the frequency of the qubit to and from values that make the desired transitions resonant.

Given the recent advances in USC circuit QED, we believe that our proposal can be implemented in such a setup. Indeed, two resonators have already been ultrastrongly coupled to a superconducting flux qubit[49]. Also, our proposal does not require very high coupling strengths. We only need that g^2/ω is appreciable (larger than the relevant decoherence rates) to realise single-photon frequency conversion; multi-photon frequency conversion can be demonstrated if g^3/ω^2 is large enough.

A straightforward extension of the current work is to extend the calculations to processes with more photons in the second resonator or to add more resonators to the setup. Some of these possibilities are discussed in ref. 71, where we explore analogies of nonlinear optics in USC systems, including the fact that the processes in the current work can be considered analogies of Raman and hyper-Raman scattering if the qubit is thought of as playing the role of a phonon. More general three-wave mixing, such as $|1, 0, 0, e\rangle \leftrightarrow |0, 1, 1, g\rangle$, or third-harmonic and -subharmonic generation such as $|1, 0, e\rangle \leftrightarrow |0, 3, g\rangle$, are examples of schemes that can be considered, but it must be kept in mind that higher-order processes with more photons involved will have lower effective coupling strengths. Another direction for future work is to investigate how the precise qubit control of the frequency-conversion processes discussed here can be used to prepare photon bundles[101] or interesting quantum superposition states with photons of different frequencies, a topic currently being explored in several frequency ranges[26,27,102].

References

1. Kumar, P. Quantum frequency conversion. *Opt. Lett.* **15**, 1476 (1990).
2. Huang, J. & Kumar, P. Observation of quantum frequency conversion. *Phys. Rev. Lett.* **68**, 2153 (1992).
3. O'Brien, J. L., Furusawa, A. & Vučković, J. Photonic quantum technologies. *Nat. Photonics* **3**, 687 (2009).
4. Buluta, I., Ashhab, S. & Nori, F. Natural and artificial atoms for quantum computation. *Reports Prog. Phys.* **74**, 104401 (2011).
5. Kimble, H. J. The quantum internet. *Nature* **453**, 1023 (2008).
6. Albota, M. A. & Wong, F. N. C. Efficient single-photon counting at 155 μm by means of frequency upconversion. *Opt. Lett.* **29**, 1449 (2004).
7. Tanzilli, S. *et al.* A photonic quantum information interface. *Nature* **437**, 116 (2005).
8. Ou, Z. Y. Efficient conversion between photons and between photon and atom by stimulated emission. *Phys. Rev. A* **78**, 023819 (2008).
9. Ding, Y. & Ou, Z. Y. Frequency downconversion for a quantum network. *Opt. Lett.* **35**, 2591 (2010).
10. Takesue, H. Single-photon frequency down-conversion experiment. *Phys. Rev. A* **82**, 013833 (2010).
11. Guo, X., Zou, C.-L., Jung, H. & Tang, H. X. On-Chip Strong Coupling and Efficient Frequency Conversion between Telecom and Visible Optical Modes. *Phys. Rev. Lett.* **117**, 123902 (2016).
12. You, J. Q. & Nori, F. Atomic physics and quantum optics using superconducting circuits. *Nature* **474**, 589 (2011).
13. Devoret, M. H. & Schoelkopf, R. J. Superconducting Circuits for Quantum Information: An Outlook. *Science* **339**, 1169 (2013).

14. Bochmann, J., Vainsencher, A., Awschalom, D. D. & Cleland, A. N. Nanomechanical coupling between microwave and optical photons. *Nat. Phys.* **9**, 712 (2013).
15. Andrews, R. W. *et al*. Bidirectional and efficient conversion between microwave and optical light. *Nat. Phys.* **10**, 321 (2014).
16. Shumeiko, V. S. Quantum acousto-optic transducer for superconducting qubits. *Phys. Rev. A* **93**, 023838 (2016).
17. Hisatomi, R. *et al*. Bidirectional conversion between microwave and light via ferromagnetic magnons. *Phys. Rev. B* **93**, 174427 (2016).
18. Bennett, C. H. & DiVincenzo, D. P. Quantum information and computation. *Nature* **404**, 247 (2000).
19. You, J. Q. & Nori, F. Quantum information processing with superconducting qubits in a microwave field. *Phys. Rev. B* **68**, 064509 (2003).
20. Wallraff, A. *et al*. Strong coupling of a single photon to a superconducting qubit using circuit quantum electrodynamics. *Nature* **431**, 162 (2004).
21. Blais, A., Huang, R.-S., Wallraff, A., Girvin, S. M. & Schoelkopf, R. J. Cavity quantum electrodynamics for superconducting electrical circuits: An architecture for quantum computation. *Phys. Rev. A* **69**, 062320 (2004).
22. Xiang, Z.-L., Ashhab, S., You, J. Q. & Nori, F. Hybrid quantum circuits: Superconducting circuits interacting with other quantum systems. *Rev. Mod. Phys.* **85**, 623 (2013).
23. Wallquist, M., Shumeiko, V. S. & Wendin, G. Selective coupling of superconducting charge qubits mediated by a tunable stripline cavity. *Phys. Rev. B* **74**, 224506 (2006).
24. Sandberg, M. *et al*. Tuning the field in a microwave resonator faster than the photon lifetime. *Appl. Phys. Lett.* **92**, 203501 (2008).
25. Johansson, J. R., Johansson, G., Wilson, C. M. & Nori, F. Dynamical Casimir effect in superconducting microwave circuits. *Phys. Rev. A* **82**, 052509 (2010).
26. Chirolli, L., Burkard, G., Kumar, S. & DiVincenzo, D. P. Superconducting Resonators as Beam Splitters for Linear-Optics Quantum Computation. *Phys. Rev. Lett.* **104**, 230502 (2010).
27. Zakka-Bajjani, E. *et al*. Quantum superposition of a single microwave photon in two different 'colour' states. *Nat. Phys.* **7**, 599 (2011).
28. Abdo, B. *et al*. Full Coherent Frequency Conversion between Two Propagating Microwave Modes. *Phys. Rev. Lett.* **110**, 173902 (2013).
29. Kamal, A., Roy, A., Clarke, J. & Devoret, M. H. Asymmetric Frequency Conversion in Nonlinear Systems Driven by a Biharmonic Pump. *Phys. Rev. Lett.* **113**, 247003 (2014).
30. Marquardt, F. Efficient on-chip source of microwave photon pairs in superconducting circuit QED. *Phys. Rev. B* **76**, 205416 (2007).
31. Koshino, K. Down-conversion of a single photon with unit efficiency. *Phys. Rev. A* **79**, 013804 (2009).
32. Sánchez-Burillo, E., Martín-Moreno, L., García-Ripoll, J. J. & Zueco, D. Full two-photon down-conversion of a single photon. *Phys. Rev. A* **94**, 053814 (2016).
33. Inomata, K. *et al*. Microwave Down-Conversion with an Impedance-Matched Λ System in Driven Circuit QED. *Phys. Rev. Lett.* **113**, 063604 (2014).
34. Deppe, F. *et al*. Two-photon probe of the Jaynes–Cummings model and controlled symmetry breaking in circuit QED. *Nat. Phys.* **4**, 686 (2008).
35. Liu, Y.-X., You, J. Q., Wei, L. F., Sun, C. P. & Nori, F. Optical Selection Rules and Phase-Dependent Adiabatic State Control in a Superconducting Quantum Circuit. *Phys. Rev. Lett.* **95**, 087001 (2005).
36. Liu, Y.-X. *et al*. Controllable microwave three-wave mixing via a single three-level superconducting quantum circuit. *Sci. Rep.* **4**, 7289 (2014).
37. Lecocq, F., Clark, J. B., Simmonds, R. W., Aumentado, J. & Teufel, J. D. Mechanically Mediated Microwave Frequency Conversion in the Quantum Regime. *Phys. Rev. Lett.* **116**, 043601 (2016).
38. Günter, G. *et al*. Sub-cycle switch-on of ultrastrong light–matter interaction. *Nature* **458**, 178 (2009).
39. Forn-Díaz, P. *et al*. Observation of the Bloch-Siegert Shift in a Qubit-Oscillator System in the Ultrastrong Coupling Regime. *Phys. Rev. Lett.* **105**, 237001 (2010).
40. Niemczyk, T. *et al*. Circuit quantum electrodynamics in the ultrastrong-coupling regime. *Nat. Phys.* **6**, 772 (2010).
41. Todorov, Y. *et al*. Ultrastrong Light-Matter Coupling Regime with Polariton Dots. *Phys. Rev. Lett.* **105**, 196402 (2010).
42. Schwartz, T., Hutchison, J. A., Genet, C. & Ebbesen, T. W. Reversible Switching of Ultrastrong Light-Molecule Coupling. *Phys. Rev. Lett.* **106**, 196405 (2011).
43. Scalari, G. *et al*. Ultrastrong Coupling of the Cyclotron Transition of a 2D Electron Gas to a THz Metamaterial. *Science* **335**, 1323 (2012).
44. Geiser, M. *et al*. Ultrastrong Coupling Regime and Plasmon Polaritons in Parabolic Semiconductor Quantum Wells. *Phys. Rev. Lett.* **108**, 106402 (2012).
45. Kéna-Cohen, S., Maier, S. A. & Bradley, D. D. C. Ultrastrongly Coupled Exciton-Polaritons in Metal-Clad Organic Semiconductor Microcavities. *Adv. Opt. Mater.* **1**, 827 (2013).
46. Gambino, S. *et al*. Exploring Light–Matter Interaction Phenomena under Ultrastrong Coupling Regime. *ACS Photonics* **1**, 1042 (2014).
47. Maissen, C. *et al*. Ultrastrong coupling in the near field of complementary split-ring resonators. *Phys. Rev. B* **90**, 205309 (2014).
48. Goryachev, M. *et al*. High-Cooperativity Cavity QED with Magnons at Microwave Frequencies. *Phys. Rev. Appl.* **2**, 054002 (2014).
49. Baust, A. *et al*. Ultrastrong coupling in two-resonator circuit QED. *Phys. Rev. B* **93**, 214501 (2016).
50. Forn-Díaz, P. *et al*. Ultrastrong coupling of a single artificial atom to an electromagnetic continuum in the nonperturbative regime. *Nat. Phys.* **13**, 39 (2017).
51. Yoshihara, F. *et al*. Superconducting qubit-oscillator circuit beyond the ultrastrong-coupling regime. *Nat. Phys.* **13**, 44 (2017).
52. Chen, Z. *et al*. Multi-photon sideband transitions in an ultrastrongly-coupled circuit quantum electrodynamics system. *arXiv:1602.01584* (2016).
53. George, J. *et al*. Multiple Rabi Splittings under Ultrastrong Vibrational Coupling. *Phys. Rev. Lett.* **117**, 153601 (2016).
54. Langford, N. K. *et al*. Experimentally simulating the dynamics of quantum light and matter at ultrastrong coupling. *arXiv:1610.10065* (2016).
55. Braumüller, J. *et al*. Analog quantum simulation of the Rabi model in the ultra-strong coupling regime. *arXiv:1611.08404* (2016).
56. Yoshihara, F. *et al*. Characteristic spectra of circuit quantum electrodynamics systems from the ultrastrong to the deep strong coupling regime. *Phys. Rev. A* **95,** 053824 (2017).
57. De Liberato, S., Ciuti, C. & Carusotto, I. Quantum Vacuum Radiation Spectra from a Semiconductor Microcavity with a Time-Modulated Vacuum Rabi Frequency. *Phys. Rev. Lett.* **98**, 103602 (2007).
58. Ashhab, S. & Nori, F. Qubit-oscillator systems in the ultrastrong-coupling regime and their potential for preparing nonclassical states. *Phys. Rev. A* **81**, 042311 (2010).
59. Cao, X., You, J. Q., Zheng, H., Kofman, A. G. & Nori, F. Dynamics and quantum Zeno effect for a qubit in either a low- or high-frequency bath beyond the rotating-wave approximation. *Phys. Rev. A* **82**, 022119 (2010).
60. Cao, X., You, J. Q., Zheng, H. & Nori, F. A qubit strongly coupled to a resonant cavity: asymmetry of the spontaneous emission spectrum beyond the rotating wave approximation. *New J. Phys.* **13**, 073002 (2011).
61. Stassi, R., Ridolfo, A., Di Stefano, O., Hartmann, M. J. & Savasta, S. Spontaneous Conversion from Virtual to Real Photons in the Ultrastrong-Coupling Regime. *Phys. Rev. Lett.* **110**, 243601 (2013).

62. Sanchez-Burillo, E., Zueco, D., Garcia-Ripoll, J. J. & Martin-Moreno, L. Scattering in the Ultrastrong Regime: Nonlinear Optics with One Photon. *Phys. Rev. Lett.* **113**, 263604 (2014).
63. De Liberato, S. Light-Matter Decoupling in the Deep Strong Coupling Regime: The Breakdown of the Purcell Effect. *Phys. Rev. Lett.* **112**, 016401 (2014).
64. Lolli, J., Baksic, A., Nagy, D., Manucharyan, V. E. & Ciuti, C. Ancillary Qubit Spectroscopy of Vacua in Cavity and Circuit Quantum Electrodynamics. *Phys. Rev. Lett.* **114**, 183601 (2015).
65. Di Stefano, O. *et al*. Feynman-diagrams approach to the quantum Rabi model for ultrastrong cavity QED: stimulated emission and reabsorption of virtual particles dressing a physical excitation. *New J. Phys***19**, 053010 (2016).
66. Cirio, M., De Liberato, S., Lambert, N. & Nori, F. Ground State Electroluminescence. *Phys. Rev. Lett.* **116**, 113601 (2016).
67. Zhu, G., Ferguson, D. G., Manucharyan, V. E. & Koch, J. Circuit QED with fluxonium qubits: Theory of the dispersive regime. *Phys. Rev. B* **87**, 024510 (2013).
68. Ma, K. K. W. & Law, C. K. Three-photon resonance and adiabatic passage in the large-detuning Rabi model. *Phys. Rev. A* **92**, 023842 (2015).
69. Garziano, L. *et al*. Multiphoton quantum Rabi oscillations in ultrastrong cavity QED. *Phys. Rev. A* **92**, 063830 (2015).
70. Garziano, L. *et al*. One Photon Can Simultaneously Excite Two or More Atoms. *Phys. Rev. Lett.* **117**, 043601 (2016).
71. Kockum, A. F., Miranowicz, A., Macrì, V., Savasta, S. & Nori, F. Deterministic quantum nonlinear optics with single atoms and virtual photons. *Phys. Rev. A arXiv:1701.05038* (2017).
72. Buluta, I. & Nori, F. Quantum Simulators. *Science* **326**, 108 (2009).
73. Georgescu, I. M., Ashhab, S. & Nori, F. Quantum simulation. *Rev. Mod. Phys.* **86**, 153 (2014).
74. Braak, D. Integrability of the Rabi Model. *Phys. Rev. Lett.* **107**, 100401 (2011).
75. Braak, D. Solution of the Dicke model for N=3. *J. Phys. B At. Mol. Opt. Phys.* **46**, 224007 (2013).
76. Peng, J., Ren, Z., Guo, G., Ju, G. & Guo, X. Exact solutions of the generalized two-photon and two-qubit Rabi models. *Eur. Phys. J. D* **67**, 162 (2013).
77. Chilingaryan, S. A. & Rodríguez-Lara, B. M. Exceptional solutions in two-mode quantum Rabi models. *J. Phys. B At. Mol. Opt. Phys.* **48**, 245501 (2015).
78. Duan, L., He, S., Braak, D. & Chen, Q.-H. Solution of the two-mode quantum Rabi model using extended squeezed states. *Europhys. Lett.* **112**, 34003 (2015).
79. Alderete, C. H. & Rodríguez-Lara, B. M. Cross-cavity quantum Rabi model. *J. Phys. A Math. Theor.* **49**, 414001 (2016).
80. Moon, K. & Girvin, S. M. Theory of Microwave Parametric Down-Conversion and Squeezing Using Circuit QED. *Phys. Rev. Lett.* **95**, 140504 (2005).
81. Mariantoni, M. *et al*. Two-resonator circuit quantum electrodynamics: A superconducting quantum switch. *Phys. Rev. B* **78**, 104508 (2008).
82. Prado, F. O., de Almeida, N. G., Moussa, M. H. Y. & Villas-Bôas, C. J. Bilinear and quadratic Hamiltonians in two-mode cavity quantum electrodynamics. *Phys. Rev. A* **73**, 043803 (2006).
83. You, J. Q., Hu, X., Ashhab, S. & Nori, F. Low-decoherence flux qubit. *Phys. Rev. B* **75**, 140515 (2007).
84. Kim, Z. *et al*. Decoupling a Cooper-Pair Box to Enhance the Lifetime to 0.2 ms. *Phys. Rev. Lett.* **106**, 120501 (2011).
85. Beaudoin, F., Gambetta, J. M. & Blais, A. Dissipation and ultrastrong coupling in circuit QED. *Phys. Rev. A* **84**, 043832 (2011).
86. Ridolfo, A., Leib, M., Savasta, S. & Hartmann, M. J. Photon Blockade in the Ultrastrong Coupling Regime. *Phys. Rev. Lett.* **109**, 193602 (2012).
87. Megrant, A. *et al*. Planar superconducting resonators with internal quality factors above one million. *Appl. Phys. Lett.* **100**, 113510 (2012).
88. Stern, M. *et al*. Flux Qubits with Long Coherence Times for Hybrid Quantum Circuits. *Phys. Rev. Lett.* **113**, 123601 (2014).
89. Orgiazzi, J.-L. *et al*. Flux qubits in a planar circuit quantum electrodynamics architecture: Quantum control and decoherence. *Phys. Rev. B* **93**, 104518 (2016).
90. Yan, F. *et al*. The flux qubit revisited to enhance coherence and reproducibility. *Nat. Commun.* **7**, 12964 (2016).
91. Johnson, B. R. *et al*. Quantum non-demolition detection of single microwave photons in a circuit. *Nat. Phys.* **6**, 663 (2010).
92. Sillanpää, M. A., Park, J. I. & Simmonds, R. W. Coherent quantum state storage and transfer between two phase qubits via a resonant cavity. *Nature* **449**, 438 (2007).
93. Hofheinz, M. *et al*. Generation of Fock states in a superconducting quantum circuit. *Nature* **454**, 310 (2008).
94. Hofheinz, M. *et al*. Synthesizing arbitrary quantum states in a superconducting resonator. *Nature* **459**, 546 (2009).
95. Wang, H. *et al*. Deterministic Entanglement of Photons in Two Superconducting Microwave Resonators. *Phys. Rev. Lett.* **106**, 060401 (2011).
96. Mariantoni, M. *et al*. Photon shell game in three-resonator circuit quantum electrodynamics. *Nat. Phys.* **7**, 287 (2011).
97. Schuster, D. I. *et al*. Resolving photon number states in a superconducting circuit. *Nature* **445**, 515 (2007).
98. Rabi, I. I. Space Quantization in a Gyrating Magnetic Field. *Phys. Rev.* **51**, 652 (1937).
99. Jaynes, E. T. & Cummings, F. W. Comparison of quantum and semiclassical radiation theories with application to the beam maser. *Proc. IEEE* **51**, 89 (1963).
100. Baksic, A. & Ciuti, C. Controlling Discrete and Continuous Symmetries in "Superradiant" Phase Transitions with Circuit QED Systems. *Phys. Rev. Lett.* **112**, 173601 (2014).
101. Sánchez Muñoz, C. *et al*. Emitters of N-photon bundles. *Nat. Photonics* **8**, 550 (2014).
102. Clemmen, S., Farsi, A., Ramelow, S. & Gaeta, A. L. Ramsey Interference with Single Photons. *Phys. Rev. Lett.* **117**, 223601 (2016).

Acknowledgements

We acknowledge useful discussions with Roberto Stassi and Adam Miranowicz. This work is partially supported by the RIKEN iTHES Project, the MURI Center for Dynamic Magneto-Optics via the AFOSR award number FA9550-14-1-0040, the Japan Society for the Promotion of Science (KAKENHI), the IMPACT program of JST, JSPS-RFBR grant No 17-52-50023, CREST grant No. JPMJCR1676, and the Sir John Templeton Foundation. A.F.K. acknowledges support from a JSPS Postdoctoral Fellowship for Overseas Researchers.

Author Contributions

A.F.K. developed the idea and performed the analytical calculations. V.M. and L.G. performed the numerical simulations. S.S. and F.N. supervised the project. A.F.K. wrote the paper with input from all authors.

Additional Information

Supplementary information accompanies this paper at doi:10.1038/s41598-017-04225-3

Competing Interests: The authors declare that they have no competing interests.

Publisher's note: Springer Nature remains neutral with regard to jurisdictional claims in published maps and institutional affiliations.

5.6 Paper VI: Deterministic quantum nonlinear optics with single atoms and virtual photons

PHYSICAL REVIEW A **95**, 063849 (2017)

Deterministic quantum nonlinear optics with single atoms and virtual photons

Anton Frisk Kockum,[1,*] Adam Miranowicz,[1,2] Vincenzo Macrì,[1,3] Salvatore Savasta,[1,3] and Franco Nori[1,4]

[1]*Center for Emergent Matter Science, RIKEN, Saitama 351-0198, Japan*

[2]*Faculty of Physics, Adam Mickiewicz University, PL-61-614 Poznan, Poland*

[3]*Dipartimento di Scienze Matematiche e Informatiche, Scienze Fisiche e Scienze della Terra, Università di Messina, I-98166 Messina, Italy*

[4]*Physics Department, University of Michigan, Ann Arbor, Michigan 48109-1040, USA*

(Received 26 January 2017; published 29 June 2017)

We show how analogs of a large number of well-known nonlinear-optics phenomena can be realized with one or more two-level atoms coupled to one or more resonator modes. Through higher-order processes, where virtual photons are created and annihilated, an effective deterministic coupling between two states of such a system can be created. In this way, analogs of three-wave mixing, four-wave mixing, higher-harmonic and -subharmonic generation (i.e., up- and down-conversion), multiphoton absorption, parametric amplification, Raman and hyper-Raman scattering, the Kerr effect, and other nonlinear processes can be realized. In contrast to most conventional implementations of nonlinear optics, these analogs can reach unit efficiency, only use a minimal number of photons (they do not require any strong external drive), and do not require more than two atomic levels. The strength of the effective coupling in our proposed setups becomes weaker the more intermediate transition steps are needed. However, given the recent experimental progress in ultrastrong light-matter coupling and improvement of coherence times for engineered quantum systems, especially in the field of circuit quantum electrodynamics, we estimate that many of these nonlinear-optics analogs can be realized with currently available technology.

DOI: 10.1103/PhysRevA.95.063849

I. INTRODUCTION

In nonlinear optics, a medium responds nonlinearly to incoming light of high intensity. This nonlinear response can give rise to a host of effects, including frequency conversion and amplification, many of which have important technological applications [1–4]. After the high-intensity light of a laser made possible the first experimental demonstration of second-harmonic generation (frequency up-conversion) in 1961 [5], many more nonlinear-optics effects were demonstrated using a variety of nonlinear media. The many applications and the fundamental nature of nonlinear optics have also inspired investigations of analogous effects in other types of waves. Prominent examples include nonlinear acoustics [6,7], nonlinear spin waves [8], nonlinear atom optics [9,10], nonlinear Josephson plasma waves [11], and nonlinear plasmonics [12]. Analogies of this kind can sometimes enable simulations or demonstrations of phenomena that are hard to realize in other systems [13–15].

In this article, we will show that analogs of many nonlinear-optics effects can also be realized by coupling one or more resonator modes to one or more two-level atoms. This stands in contrast to many other nonlinear-optics realizations, which require three or more atomic levels [4,16]. The key to the analogs we propose lies in the full interaction between a two-level atom and an electromagnetic mode, which is given by the quantum Rabi Hamiltonian [17]. This Hamiltonian includes terms that can change the number of excitations in the system, enabling higher-order processes via virtual photons. These photons are created and annihilated in a way that generates a deterministic coupling between two system states that otherwise do not have a direct coupling. In this way, we can realize analogs of various frequency-conversion processes, parametric amplification, Raman and hyper-Raman scattering, multiphoton absorption, the Kerr effect, and other nonlinear processes.

Just as nonlinear-optics effects usually require very high light intensity to manifest clearly, the higher-order processes we consider require a very strong light-matter coupling to become noticeable. Specifically, the light-matter coupling must be strong enough to ensure that the effective deterministic coupling between system states, induced by the higher-order processes, becomes larger than the relevant decoherence rates in the system. Ultrastrong coupling (USC, where the coupling strength starts to become comparable to the resonance frequencies of the bare system components) between light and matter has only recently been reached in some solid-state experiments [18–36]. Among these systems, circuit quantum electrodynamics (QED) [16,37–39] has provided some of the clearest examples [19,20,29–32,34–36], including the largest reported coupling strength [31] and the first quantum simulations of the USC regime [34,35].

The experimental progress in USC physics has motivated many theoretical studies of the interesting new effects that occur in this regime [40–51]. Some previous [52–54] and concurrent [55,56] works explore processes in the USC regime where the number of excitations is not conserved, such as multiphoton Rabi oscillations [53] and a single photon exciting multiple atoms [54]. Several of these processes can be interpreted as analogs of nonlinear-optics phenomena.

In this work, we present a unified picture of these types of processes and their relation to nonlinear optics. We also provide many more examples which together allow us to make complete tables with translations between three- and four-wave mixing in nonlinear optics and analogous processes in USC systems. It should be noted that these analogs, many of which can be realized in one universal setup, do not use

*anton.frisk.kockum@gmail.com

propagating waves, but instead mix excitations in resonators and atoms of different frequencies. We emphasize that, unlike many processes in conventional nonlinear optics, our setups do not require any external drives, but instead realize analogs of wave mixing with a minimal number of photons and unit efficiency.

Given the versatility and technological maturity of the circuit QED setups, we expect them to become the primary experimental platform for realizing these deterministic nonlinear-optics analogs with single atoms and virtual photons. We believe that these deterministic analogs can find many important applications, including frequency conversion and the creation of superposition states for use in quantum information technology. Circuit QED is already one of the most well-developed platforms for quantum information processing [57], so adding the full capabilities of nonlinear optics at the single-photon level to the toolbox of this field could result in many new exciting possibilities. Indeed, the development of nonlinear optics with single photons has been the subject of much theoretical and experimental work recently due to the wealth of potential applications [58]. We note here that although our proposal does not use propagating waves, circuit QED setups with stationary photons that mimic linear-optics experiments for itinerant photons have already been proposed [59]. Several of the nonlinear-optics analogs given in the present work could be incorporated into such an architecture.

This article is organized as follows. In Sec. II, we give a brief overview of how nonlinear processes in optics usually occur. We then describe how analogous deterministic processes become possible in the quantum Rabi model. In Secs. III and IV, we discuss three- and four-wave mixing, respectively, and give details of the analogous deterministic processes that can be realized with resonators ultrastrongly coupled to qubits. Other nonlinear processes, including higher-harmonic generation, parametric processes, and the Kerr effect, are discussed in Sec. V. In Sec. VI, we estimate achievable effective coupling strengths and decoherence rates, showing that our proposals can be realized with state-of-the-art technology in circuit QED. We conclude in Sec. VII. Some details are left for the appendices: Appendix A expands on the classical mechanisms for some nonlinear-optics phenomena, Appendix B gives a derivation of the perturbation-theory formula used to calculate the strength of the effective coupling between initial and final states in our three- and four-wave-mixing analogs, and Appendix C contains details about a few four-wave-mixing processes not treated in the main text.

II. MECHANISMS FOR NONLINEARITY

A. Nonlinear optics

In conventional classical electro-optical processes, the polarization $\mathbf{P}$ of a given medium induced by the applied electric field $\mathbf{E}$ is linearly proportional to its strength, i.e., $\mathbf{P} = \epsilon_0 \chi \mathbf{E}$, where ϵ_0 is the vacuum permittivity and $\chi \equiv \chi^{(1)}$ is the linear susceptibility of the medium, which can be considered a scalar for linear, homogeneous, and isotropic dielectric media. Usually, the real and imaginary parts of χ describe, respectively, the refraction and damping of a light beam going through such medium.

For a strong electric field $\mathbf{E}$ and nonlinear media, the above linear relation for the induced polarization is generalized to

$$\mathbf{P} = \epsilon_0(\chi^{(1)}\mathbf{E} + \chi^{(2)}\mathbf{E}^2 + \chi^{(3)}\mathbf{E}^3 + \ldots), \tag{1}$$

which is considered a core principle of nonlinear optics [1–4]. In Eq. (1), $\chi^{(2)}$ and $\chi^{(3)}$ are the second- and third-order nonlinear susceptibilities, respectively. In general, these susceptibilities are tensors $\chi^{(1)}_{kl}$, $\chi^{(2)}_{klm}$, and $\chi^{(3)}_{klmn}$. However, for simplicity, we consider them as scalars, which is usually valid for isotropic dielectric media.

Various nonlinear optical phenomena (including wave mixing) can be explained classically by recalling the nonlinear dependence of the induced polarization and electric-field strength, as given by Eq. (1). Standard examples include Pockels and Kerr effects, which are, respectively, linear and quadratic electro-optical phenomena, in which the induced polarization (and, thus, also the refractive index) of a medium is proportional to the amplitude and its square of the applied constant electric field.

For example, second-harmonic generation in a medium described by the second-order susceptibility $\chi^{(2)}$ can be described classically as follows. Assuming that a monochromatic scalar electric field $E(t) = E_0 \cos(\omega t)$ is applied to the medium, the second-order induced polarization $P^{(2)}$ of the medium is given by

$$\begin{aligned} P^{(2)} &= \epsilon_0 \chi^{(2)} E^2 = \epsilon_0 \chi^{(2)} E_0^2 \cos^2(\omega t) \\ &= \epsilon_0 \chi^{(2)} E_0^2 \left(\frac{1 + \cos(2\omega t)}{2} \right) \\ &= \frac{1}{2}\epsilon_0 \chi^{(2)} E_0^2 + \frac{1}{2}\epsilon_0 \chi^{(2)} E_0^2 \cos(2\omega t), \end{aligned} \tag{2}$$

where the first term in the last line describes frequency-independent polarization, while the second term in the last line describes the polarization oscillating at twice the frequency of the input field. This doubling of the input frequency can be interpreted as second-harmonic generation.

In Appendix A, we present a few additional pedagogical classical explanations, based on Eq. (1), of phenomena arising due to the $\chi^{(2)}$ and $\chi^{(3)}$ nonlinearities. In the following sections, we write down interaction Hamiltonians describing many of these nonlinear-optics phenomena to better compare them with our proposed analogous processes. However, it should be kept in mind that these interaction Hamiltonians only describe the higher-order interaction mediated by the $\chi^{(2)}$ and $\chi^{(3)}$ nonlinearities. The lower-order interaction due to the $\chi^{(1)}$ term remains and limits the efficiency of the higher-order processes.

B. The quantum Rabi model

The Hamiltonian for a single two-level atom (a qubit) coupled to a single resonator mode can be written as ($\hbar = 1$ here and in the rest of the article)

$$\hat{H} = \omega_a \hat{a}^\dagger \hat{a} + \omega_q \frac{\hat{\sigma}_z}{2} + \hat{H}_{\text{int}}. \tag{3}$$

In the quantum Rabi model [17], the interaction is given by

$$\hat{H}^{\text{Rabi}}_{\text{int}} = g(\hat{a} + \hat{a}^\dagger)\hat{\sigma}_x = g(\hat{a} + \hat{a}^\dagger)(\hat{\sigma}_- + \hat{\sigma}_+), \tag{4}$$

where g is the coupling strength. Here, and in the following parts of the paper that discuss deterministic realizations of nonlinear optics, we use the notation that $\hat{a}$, $\hat{b}$, $\hat{c}$, and $\hat{d}$ are the annihilation operators of resonator modes with frequencies ω_a, ω_b, ω_c, and ω_d, respectively. In setups with a single qubit, or with several identical qubits, the qubit transition frequency is denoted ω_q. In setups with qubits having different transition frequencies, the frequencies are denoted ω_{q1}, ω_{q2}, etc. The qubit operators $\hat{\sigma}_z$ and $\hat{\sigma}_x = \hat{\sigma}_- + \hat{\sigma}_+$ are Pauli matrices; $\hat{\sigma}_-$ and $\hat{\sigma}_+$ are the qubit lowering and raising operators, respectively.

In the limit $g \ll \omega_a, \omega_q$, the terms $\hat{a}^\dagger\hat{\sigma}_+$ and $\hat{a}\hat{\sigma}_-$ in $H_{\rm int}^{\rm Rabi}$ can be neglected in the rotating-wave approximation (RWA), leading to the Jaynes-Cummings (JC) model [60]

$$\hat{H}_{\rm int}^{\rm JC} = g(\hat{a}\hat{\sigma}_+ + \hat{a}^\dagger\hat{\sigma}_-). \tag{5}$$

Note that in the JC model, the number of excitations is conserved. In the quantum Rabi model, the number of excitations can change, but their parity is conserved. However, the quantum Rabi model can be generalized to

$$\hat{H}_{\rm int}^{\rm gen} = g(\hat{a} + \hat{a}^\dagger)(\hat{\sigma}_x \cos\theta + \hat{\sigma}_z \sin\theta), \tag{6}$$

where θ parametrizes the amount of longitudinal and transversal couplings. This generalized quantum Rabi model does not impose any restrictions on the number of excitations. The Hamiltonian in Eq. (6) has been realized in experiments with USC of flux qubits to resonators [19,20,29,31]. In such setups with flux qubits, the flux-qubit Hamiltonian can be written as

$$H_{\rm q} = \frac{\epsilon\hat{\tilde{\sigma}}_z + \Delta\hat{\tilde{\sigma}}_x}{2}, \tag{7}$$

where $\hat{\tilde{\sigma}}_{z,x}$ are Pauli matrices in the qubit basis given by clockwise- and anticlockwise-circulating persistent currents $\pm I_{\rm p}$ in the qubit loop, ϵ is an energy scale set by $I_{\rm p}$ and an external magnetic flux, and Δ is the tunneling energy between the two current states [61]. In this basis, the inductive coupling to the resonator is given by

$$H_{\rm int} = g_{\rm ind}(\hat{a} + \hat{a}^\dagger)\hat{\tilde{\sigma}}_z, \tag{8}$$

where the coupling strength $g_{\rm ind}$ is set by $I_{\rm p}$, the zero-point current fluctuations in the resonator, and the mutual inductance in the circuit. By rotating to the energy eigenbasis of the qubit, one arrives at the interaction in Eq. (6) [19,20,29,31,62–64]. The parameter θ can be tuned by changing ϵ or Δ.

All these models can be straightforwardly extended to include additional resonators and qubits. The presence of one or more qubits provides the necessary nonlinearity to realize various deterministic analogs of nonlinear-optics processes that we will discuss in this article. For some of these processes, such as three-wave mixing (see Sec. III), the number of excitations changes by one; this requires setups with the generalized quantum Rabi model and its extensions. For other processes, e.g., four-wave mixing (see Sec. IV), the number of excitations changes by an even number or not at all; these processes can be realized with extensions of the standard quantum Rabi model or of the JC model, respectively. The fact that we need to break the parity symmetry of the standard quantum Rabi model for the three-wave-mixing analogs, but not for the four-wave-mixing case, is reminiscent of how, in conventional nonlinear optics, inversion symmetry must be broken to realize $\chi^{(2)}$ processes, but $\chi^{(3)}$ processes can occur without breaking that symmetry [4].

In a majority of the nonlinear-optics analogs considered in this article, higher-order processes, mediated by the interaction Hamiltonians in Eqs. (4)–(6) (and their extensions to additional resonators and qubits), connect an initial state $|i\rangle$ with a final state $|f\rangle$ of the same energy through an effective interaction Hamiltonian

$$\hat{H}_{\rm int}^{\rm eff} = g_{\rm eff}|f\rangle\langle i| + {\rm H.c.}, \tag{9}$$

where $g_{\rm eff}$ is the strength of the effective coupling and H.c. denotes the Hermitian conjugate of the preceding terms. In many of the intermediate transitions that contribute to this effective coupling, virtual photons are created and destroyed. We provide a multitude of examples of this in the following sections. It is important to note here that the resonance between $|i\rangle$ and $|f\rangle$ can be set up such that all other states $|j\rangle$ which potentially could be reached through lower-order processes are far off resonance. In this way, the influence of lower-order processes can be made negligible, resulting in the higher-order process given by Eq. (9) reaching unit efficiency.

To calculate the effective coupling strength $g_{\rm eff}$ analytically, three different techniques have been employed in previous works. In Ref. [65], an effective Hamiltonian with explicit up- and down-conversion terms was derived through a series of unitary transformations combined with approximations that only retained terms of lowest order in $g_j/|\omega_n - \omega_m|$, where g_j are the relevant coupling strengths in the setup and $|\omega_n - \omega_m|$ are the energy differences of the relevant intermediate transitions. In Refs. [52,53,55], the intermediate virtual transitions were adiabatically eliminated, relying on the approximation that the population of the intermediate levels will not change significantly if $g_j \ll |\omega_n - \omega_m|$. In this article, we follow the approach of Ref. [54], which calculated $g_{\rm eff}$ using standard perturbation theory. Specifically, if the shortest path between $|i\rangle$ and $|f\rangle$ is an nth-order process, the effective coupling is given to lowest order by

$$g_{\rm eff} = \sum_{j_1, j_2, \ldots, j_{n-1}} \frac{V_{f j_{n-1}} \ldots V_{j_2 j_1} V_{j_1 i}}{(E_i - E_{j_1})(E_i - E_{j_2}) \ldots (E_i - E_{j_{n-1}})}, \tag{10}$$

where the sum goes over all virtual transitions forming n-step paths between $|i\rangle$ and $|f\rangle$, E_k denotes the energy of state $|k\rangle$, and $V_{km} = \langle k|\hat{H}_{\rm int}|m\rangle$. A derivation of this formula is given in Appendix B.

In general, the perturbation-theory method of Eq. (10) appears to be the simplest way to calculate $g_{\rm eff}$, especially for higher-order processes involving many virtual transitions. The other methods mentioned above can be more cumbersome, but provide more information such as energy-level shifts and higher-order corrections to the effective coupling.

III. THREE-WAVE MIXING

In this section, we look at three-wave mixing, starting with a general description of sum- and difference-frequency generation and then treating special cases such as up-conversion, down-conversion, and Raman scattering; see Fig. 1 for an

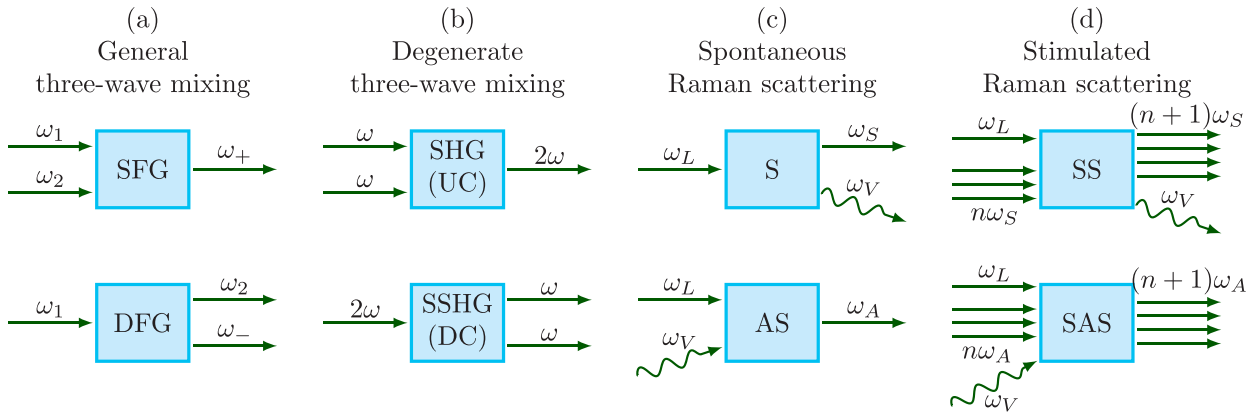

FIG. 1. Schematic representations (Feynman-like diagrams) of three-wave-mixing processes. (a) The two general types of three-wave mixing are sum-frequency generation (SFG, above) and difference-frequency generation (DFG, below). (b) When two of the involved frequencies are degenerate, we have either second-harmonic generation [SHG, or up-conversion (UC), above] or second-subharmonic generation [SSHG, or down-conversion (DC), below]. (c) Another special case is spontaneous Raman scattering, where a small part of the total energy is carried by a phonon (pictured as a wavy arrow), which is either outgoing [Stokes Raman scattering (S), above] or incoming [anti-Stokes Raman scattering (AS), also known as sideband cooling, below]. (d) In stimulated Raman scattering, the rate is increased due to the presence of n additional photons of the same frequency as the outgoing one. Stimulated Stokes Raman scattering (SS) is shown above and stimulated anti-Stokes Raman scattering (SAS) is shown below.

overview. We provide deterministic analogs based on the generalized quantum Rabi model for each case.

A. General description: Generation of sum- and difference-frequency fields

1. Nonlinear optics

The creation and annihilation of a photon with sum frequency ω_+ can be described in the Fock representation as $|n_1,n_2,n_+\rangle \to |n_1-1,n_2-1,n_++1\rangle$ and $|n_1,n_2,n_+\rangle \to |n_1+1,n_2+1,n_+-1\rangle$, respectively; see also Fig. 1(a). The interaction Hamiltonian $\hat{H}_{\rm int}^{(+)}$ for this sum-frequency generation can be given by

$$\hat{H}_{\rm int}^{(+)} = g\hat{a}_1\hat{a}_2\hat{a}_+^\dagger + g^*\hat{a}_1^\dagger\hat{a}_2^\dagger\hat{a}_+, \tag{11}$$

in terms of the annihilation ($\hat{a}_j$) and creation ($\hat{a}_j^\dagger$) operators for the input modes (for $j=1,2$) and the output sum-frequency mode (for $j=+$), and the three-mode complex coupling constant g.

Analogously, the creation and annihilation of a photon with difference frequency ω_- can be described in the Fock representation as $|n_1,n_2,n_-\rangle \to |n_1-1,n_2+1,n_-+1\rangle$ and $|n_1,n_2,n_-\rangle \to |n_1+1,n_2-1,n_--1\rangle$; see also Fig. 1(a). The interaction Hamiltonian $\hat{H}_{\rm int}^{(-)}$ describing this process can be given by

$$\hat{H}_{\rm int}^{(-)} = g\hat{a}_1\hat{a}_2^\dagger\hat{a}_-^\dagger + g^*\hat{a}_1^\dagger\hat{a}_2\hat{a}_-, \tag{12}$$

using the same notation as in Eq. (11) except that the subscript "+", corresponding to the sum-frequency mode, is replaced by "−" for the difference-frequency mode.

The energy conservation principle implies that $\omega_+ = \omega_1+\omega_2$ and $\omega_- = \omega_1-\omega_2$, and the momentum conservation principle implies that $\mathbf{k}_+ = \mathbf{k}_1+\mathbf{k}_2$ and $\mathbf{k}_- = \mathbf{k}_1-\mathbf{k}_2$ for the wave vectors $\mathbf{k}_j$.

Note that in conventional nonlinear optics, the interaction Hamiltonians given here only describe the interaction that results from the higher-order $\chi^{(2)}$ nonlinearity. The full interaction Hamiltonian for the system will also contain lower-order terms, which limit the efficiency of the sum- and difference-frequency generation described by Eqs. (11) and (12).

2. Analogous processes

There are several possible setups that can realize analogs of sum- and difference-frequency generation deterministically. One such setup would be three resonators coupled to a single qubit using the generalized Rabi interaction in Eq. (6). If the resonator frequencies satisfy $\omega_a+\omega_b \approx \omega_c$, the two states $|1,1,0,g\rangle$ and $|0,0,1,g\rangle$ become resonant. Here, and in all the following discussions of deterministic processes, kets list photon excitation numbers, starting from the resonator with frequency ω_a, followed by qubit state(s) (g for ground state, e for excited state). The transition $|1,1,0,g\rangle \to |0,0,1,g\rangle$ then corresponds to sum-frequency generation [$a=1$, $b=2$, $c=+$ makes the connection explicit with Sec. III A 1 and Fig. 1(a)] and the transition $|0,0,1,g\rangle \to |1,1,0,g\rangle$ corresponds to difference-frequency generation ($a=2$, $b=-$, $c=1$).

The transition $|1,1,0,g\rangle \to |0,0,1,g\rangle$ is enabled by paths with several intermediate virtual transitions. One example of such a path is

$$|1,1,0,g\rangle \xrightarrow{\hat{b}\hat{\sigma}_+} |1,0,0,e\rangle \xrightarrow{\hat{c}^\dagger\hat{\sigma}_-} |1,0,1,g\rangle \xrightarrow{\hat{a}\hat{\sigma}_z} |0,0,1,g\rangle,$$

where the terms from Eq. (6) that generate the transitions are shown above the arrows. Note that the last transition changes the number of excitations in the system by one, which is only possible when the interaction is given by the generalized quantum Rabi Hamiltonian of Eq. (6). The last transition is also an example of how a virtual photon is annihilated

in the process. For the transition in the opposite direction (difference-frequency generation), a virtual photon is created instead.

By adiabatic elimination, or suitable unitary transformations combined with perturbation expansion in g over some frequency, it can be shown that these virtual transitions combine to give an effective interaction Hamiltonian

$$\hat{H}_{\rm int}^{\rm eff} = g_{\rm eff}|0,0,1,g\rangle\langle 1,1,0,g| + \text{H.c.}, \tag{13}$$

where the effective coupling $g_{\rm eff}$, in general, becomes weaker the more intermediate steps are needed. Later in this section, we will provide examples with detailed diagrams of the virtual transitions and calculations of the effective coupling.

In contrast to the interaction Hamiltonians for conventional nonlinear optics given in Sec. III A 1, the effective interaction given in Eq. (13) does not need to compete with lower-order processes if the transition energies in the system are chosen appropriately. For example, given the resonance condition $\omega_a + \omega_b \approx \omega_c$, the intermediate states $|1,0,0,e\rangle$ and $|1,0,1,g\rangle$, with energies $\omega_a + \omega_q$ and $\omega_a + \omega_c$, respectively, will be far off resonance as long as ω_q is chosen sufficiently far from ω_b. Thus, even though these intermediate states can be reached via lower-order processes, they will not become populated and will not limit the efficiency of the analog of three-wave mixing.

We note that, if at least one of the excitations in the three-wave mixing can be hosted in a qubit, other setups become possible. Both a single resonator coupled to two qubits and two resonators coupled to a single qubit could be used to implement the processes in Fig. 1(a). In particular, Ref. [54] analyzed the former case with $\omega_a \approx \omega_{q1} + \omega_{q2}$, showing an effective coupling between $|1,g,g\rangle$ and $|0,e,e\rangle$. In the latter case, the effective coupling of interest would be that between the states $|1,1,g\rangle$ and $|0,0,e\rangle$ when $\omega_a + \omega_b \approx \omega_q$.

B. Degenerate three-wave mixing: Second-harmonic and second-subharmonic generation

1. Nonlinear optics

Let us assume the degenerate process of three-wave mixing for which $\hat{a}_1 = \hat{a}_2 \equiv \hat{a}$ and $\omega_1 = \omega_2 \equiv \omega$. The energy conservation principle implies $\omega_+ = 2\omega$. The processes of the creation and annihilation of photons can be written as $|n,n_+\rangle \to |n-2,n_+ + 1\rangle$ and $|n,n_+\rangle \to |n+2,n_+ - 1\rangle$; see also Fig. 1(b). The interaction Hamiltonian reads as

$$\hat{H}_{\rm int} = g\hat{a}^2\hat{a}_+^\dagger + g^*\hat{a}^{\dagger 2}\hat{a}_+. \tag{14}$$

For second-harmonic generation (also referred to as up-conversion), one can assume that the initial pure state is $|\psi(t_0)\rangle = \sum_{n=0}^{\infty} c_n|n,0\rangle$. For second-subharmonic generation (also called down-conversion), one can assume that the initial pure state is $|\psi(t_0)\rangle = \sum_{n_+=0}^{\infty} c_{n_+}|0,n_+\rangle$. Here, c_n and c_{n_+} denote arbitrary complex superposition amplitudes satisfying the normalization conditions. It is seen that our description of second-subharmonic generation can be the same as that for second-harmonic generation except with a different initial state.

2. Analogous processes

(a) Two resonators. There are, again, several possible setups to realize analogs of up- and down-conversion deterministically. In Ref. [65], it was shown that an effective Hamiltonian like that of Eq. (14) can be achieved with two resonator modes coupled to a qubit with the interaction given by Eq. (6). However, in that work some additional assumptions were made, since ultrastrong coupling had not yet been experimentally demonstrated at the time. With strong enough coupling, the virtual transitions shown in the upper left panel of Fig. 2 combine to achieve a robust effective coupling between the states $|1,0,g\rangle$ and $|0,2,g\rangle$, which results in both up- and down-conversion. Note how virtual photons and qubit excitations are created or annihilated in all transitions marked with dashed arrows.

To be precise, the full Hamiltonian of the system is here given by

$$\hat{H} = \omega_a\hat{a}^\dagger\hat{a} + \omega_b\hat{b}^\dagger\hat{b} + \omega_q\frac{\hat{\sigma}_z}{2} + \hat{H}_{\rm int}, \tag{15}$$

$$\hat{H}_{\rm int} = [g_a(\hat{a} + \hat{a}^\dagger) + g_b(\hat{b} + \hat{b}^\dagger)] \times(\hat{\sigma}_x\cos\theta + \hat{\sigma}_z\sin\theta), \tag{16}$$

and the effective interaction due to the virtual transitions shown in Fig. 2 becomes

$$\hat{H}_{\rm int}^{\rm eff} = g_{\rm eff}|1,0,g\rangle\langle 0,2,g| + \text{H.c.} \tag{17}$$

The effective coupling $g_{\rm eff}$ can be calculated with third-order perturbation theory. From Eq. (10), we have

$$g_{\rm eff} = \sum_{n,m}\frac{\langle f|\hat{H}_{\rm int}|n\rangle\langle n|\hat{H}_{\rm int}|m\rangle\langle m|\hat{H}_{\rm int}|i\rangle}{(E_i - E_n)(E_i - E_m)}. \tag{18}$$

Looking at the upper left panel of Fig. 2, we see that there are 12 paths contributing to the effective coupling between $|i\rangle = |0,2,g\rangle$ and $|f\rangle = |1,0,g\rangle$. Three of these paths consist solely of $\hat{\sigma}_z$-mediated transitions (dashed red arrows in the figure). Their contribution is

$$\sqrt{2}g_a g_b^2\sin^3\theta\left(\frac{1}{\omega_a\Delta_{ba}} - \frac{1}{\omega_b\Delta_{ba}} - \frac{1}{2\omega_b^2}\right), \tag{19}$$

where we introduced the notation $\Delta_{nm} = \omega_n - \omega_m$. This contribution sums to zero on resonance ($\omega_a = 2\omega_b$). The contribution from the remaining 9 paths is (introducing the notation $\Omega_{nm} = \omega_n + \omega_m$)

$$\sqrt{2}g_a g_b^2\sin\theta\cos^2\theta\left[\frac{1}{(\Delta_{ab}+\omega_q)\Omega_{aq}} - \frac{1}{\omega_a(\Delta_{ab}+\omega_q)} - \frac{1}{(\Delta_{ab}+\omega_q)\Delta_{bq}} + \frac{1}{\omega_b(\Delta_{ab}+\omega_q)} - \frac{1}{\Delta_{ab}\Omega_{aq}} + \frac{1}{\Delta_{ab}\Delta_{bq}} + \frac{1}{(2\omega_b-\omega_q)\Omega_{aq}} - \frac{1}{\omega_b(2\omega_b-\omega_q)} - \frac{1}{2\omega_b\Delta_{bq}}\right], \tag{20}$$

which on resonance reduces to

$$g_{\rm eff} = \frac{3\sqrt{2}g_a g_b^2\omega_q^2\sin(2\theta)\cos\theta}{4\omega_b^4 - 5\omega_b^2\omega_q^2 + \omega_q^4}. \tag{21}$$

Since the transition paths in the upper left panel of Fig. 2 go via two intermediate levels, $g_{\rm eff}$ becomes on the order

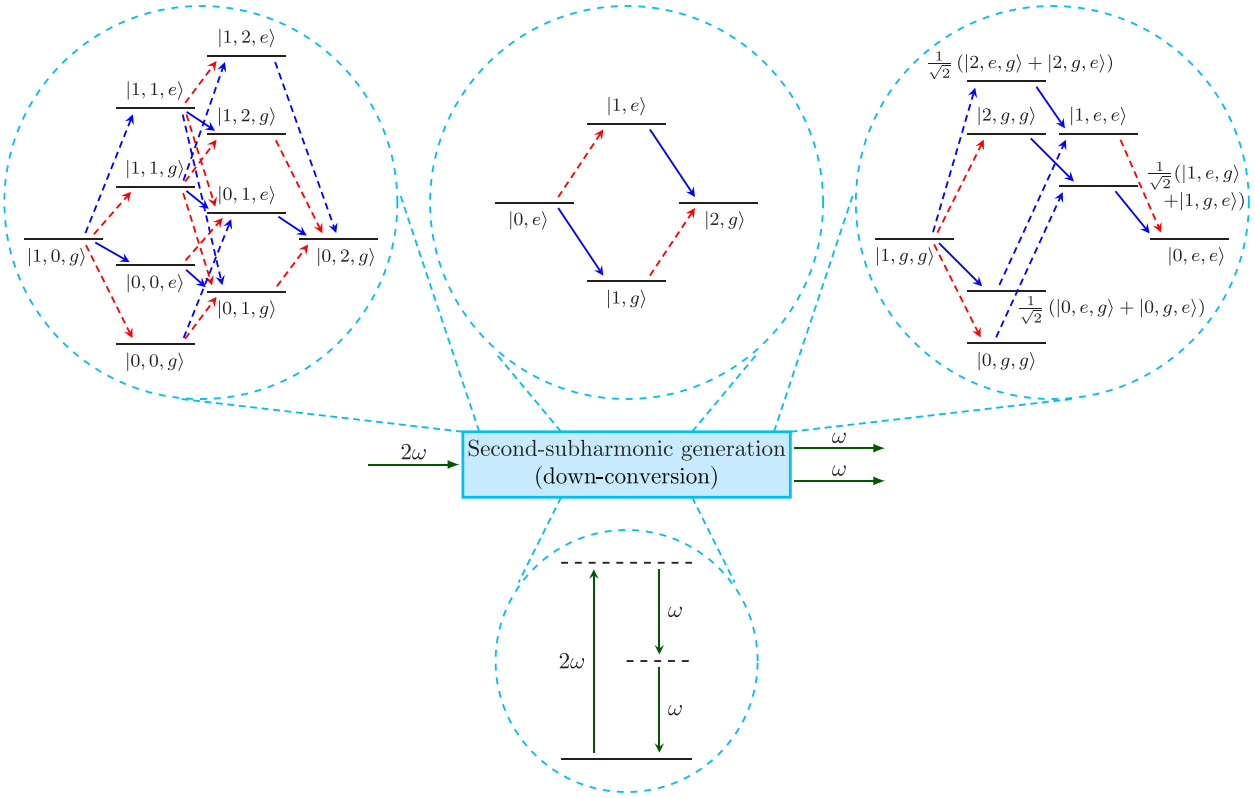

FIG. 2. Realizations of down- and up-conversion. The upper left panel shows all virtual transitions that contribute to the down-conversion process (second-subharmonic generation) $|1,0,g\rangle \rightarrow |0,2,g\rangle$ to lowest order. Blue solid arrows mark transitions that do *not* change the number of excitations [these transitions are mediated by the terms in the JC model, Eq. (5)], blue dashed arrows correspond to transitions that change the number of excitations by *two* [these transitions are mediated by the non-JC terms in the quantum Rabi model, Eq. (4)], and red dashed arrows show transitions that change the number of excitations by *one* [these transitions are mediated by the additional terms in the generalized Rabi model, Eq. (6)]. We have set $\omega_a = 2\omega_b$ and $\omega_q = 1.5\omega_b$. Similarly, the upper middle panel shows all virtual transitions that contribute to the down-conversion process $|0,e\rangle \rightarrow |2,g\rangle$ to lowest order. Here, we have set $\omega_q = 2\omega_a$. The upper right panel shows all virtual transitions that contribute to the down-conversion process $|1,g,g\rangle \rightarrow |0,e,e\rangle$ to lowest order. In this case, we have set $\omega_a = 2\omega_q$. Note that all intermediate energy levels in the upper panels are detuned far off resonance from the initial and final states, which means that lower-order processes will not be part of the effective interaction Hamiltonians given in the text of Sec. III B 2. The lower panel shows the generic level diagram for the process in nonlinear optics. Dashed horizontal lines denote virtual levels. If the directions of all arrows in the entire figure are reversed, up-conversion (second-harmonic generation) is shown instead.

of $(g_j/\omega)^2$ weaker than g_j $(j = a,b)$. This expression is slightly more complicated than that derived in Ref. [65], where unitary transformations were combined with perturbation expansions using the additional simplifying assumptions that $g_b \ll |\omega_q - \omega_b| \ll \omega_a$.

A further demonstration of the effective coupling in Eq. (17) is given in Fig. 3, where we plot some of the energy levels in the system as a function of ω_a for the JC (dashed-dotted lines), Rabi (dashed lines), and generalized Rabi (solid lines) interactions. The inset shows a clear avoided crossing between $|1,0,g\rangle$ and $|0,2,g\rangle$; the splitting is set by $g_{\rm eff}$. The JC and Rabi interactions do not give rise to such an avoided crossing since they cannot change the excitation number by one. However, all three interactions give rise to an avoided crossing between $|1,0,g\rangle$ and $|0,0,e\rangle$ to the left in the figure, since those two states have the same number of excitations.

(b) Multiphoton Rabi oscillations. An alternative implementation of up- and down-conversion is multiphoton Rabi oscillations, illustrated in the upper middle panel of Fig. 2 and discussed in Ref. [53]. In this case, virtual transitions induce an effective coupling (and, thus, Rabi oscillations) between the states $|0,e\rangle$ and $|2,g\rangle$ for a single resonator coupled to a single qubit with $\omega_q \approx 2\omega_a$. The transitions are mediated by the generalized Rabi Hamiltonian Eq. (6) and give rise to an effective interaction

$$\hat{H}_{\rm int}^{\rm eff} = g_{\rm eff}|0,e\rangle\langle 2,g| + \text{H.c.} \tag{22}$$

The effective coupling is easily calculated with second-order perturbation theory. With $|i\rangle = |2,g\rangle$ and $|f\rangle = |0,e\rangle$, Eq. (10) gives

$$g_{\rm eff} = \sqrt{2}g^2 \sin\theta\cos\theta\left(\frac{1}{\Delta_{aq}} - \frac{1}{\omega_a}\right). \tag{23}$$

Using that on resonance $\omega_a = \omega_q/2$, this reduces to

$$g_{\rm eff} = -2\sqrt{2}\sin(2\theta)\frac{g^2}{\omega_q}, \tag{24}$$

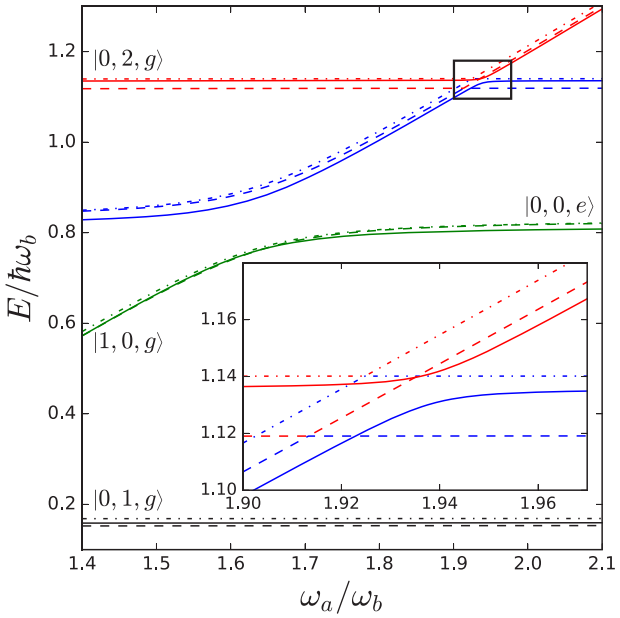

FIG. 3. Energy levels for two resonator modes coupled to a qubit via the JC [Eq. (5), dashed-dotted lines], quantum Rabi [Eq. (4), dashed lines], and generalized quantum Rabi [Eq. (6), solid lines] interactions, as a function of the resonance frequency ω_a of the first resonator mode. The inset shows a zoom-in of the area marked by the black rectangle in the upper right corner. Parameters: $\omega_q = 1.6\omega_b$, $g_a = 0.07\omega_b$, $g_b = 2g_a$, and $\theta = \pi/6$. The numerical simulations were performed in QuTiP [66,67].

which was also derived in Ref. [53] using adiabatic elimination. We note that the effective coupling acquires a factor g/ω_q due to the fact that each path between $|i\rangle$ and $|f\rangle$ contains one intermediate level.

(c) Two identical qubits. Yet another option, illustrated in the upper right panel of Fig. 2 and discussed in Ref. [54], is to couple a single resonator to two identical qubits such that the process $|1,g,g\rangle \leftrightarrow |0,e,e\rangle$ is realized. The Hamiltonian for this setup is

$$\hat{H} = \omega_a \hat{a}^\dagger \hat{a} + \sum_{j=1}^{2} \omega_q \frac{\hat{\sigma}_z^{(j)}}{2} + \hat{H}_{\rm int}, \tag{25}$$

$$\hat{H}_{\rm int} = g(\hat{a} + \hat{a}^\dagger) \sum_{j=1}^{2} (\hat{\sigma}_x^{(j)} \cos\theta + \hat{\sigma}_z^{(j)} \sin\theta), \tag{26}$$

and the effective interaction becomes

$$\hat{H}_{\rm int}^{\rm eff} = g_{\rm eff} |1,g,g\rangle\langle 0,e,e| + {\rm H.c.} \tag{27}$$

The third-order-perturbation-theory calculations for this process following Eq. (10) were already performed in the appendix of Ref. [54]. Here, we merely restate their result

$$g_{\rm eff} = -\frac{8}{3}\frac{g^3}{\omega_q^2} \sin\theta \cos^2\theta, \tag{28}$$

which is valid on resonance, when $\omega_a = 2\omega_q$. Again, we see that the effective coupling has a factor $(g/\omega)^2$, since each path contributing to the coupling contains two intermediate states.

In conclusion, we note that the multiphoton Rabi oscillation only requires two intermediate transitions, while the other two proposals require three. This means that the multiphoton Rabi oscillation has a larger effective coupling than the other two setups and is easier to implement.

C. Raman scattering

1. Nonlinear optics

In nonlinear optics, Raman scattering is a special case of nondegenerate three-wave mixing, mixing photons and optical phonons of the scattering nonlinear medium. Usually Raman scattering refers to the scattering of a light beam on optical phonons, which results in changing the frequency of the light beam [68]. We note that analogous scattering of photons on acoustic phonons is referred to as Brillouin scattering.

We consider the following fields: a driving laser (L) mode of frequency ω_L, a Stokes (S) mode of frequency ω_S, an anti-Stokes (A) mode of frequency ω_A, and optical vibrational phonon (V) modes of frequencies ω_{Vj} ($j = 1,2,\ldots$) as described by the corresponding creation ($\hat{a}_k^\dagger$) and annihilation ($\hat{a}_k$) operators for $k = L,A,S,Vj$.

(a) Stokes Raman scattering. Raman scattering with Stokes frequency $\omega_S < \omega_L$ is shortly referred to as Stokes (Raman) scattering. The process is illustrated in Fig. 1(c) and the interaction Hamiltonian can be written as

$$\hat{H}_{\rm int}^{(S)} = \sum_j g_{Sj} \hat{a}_L \hat{a}_S^\dagger \hat{a}_{Vj}^\dagger + {\rm H.c.}, \tag{29}$$

or its simpler single-phonon version

$$\hat{H}_{\rm int}^{(S)} = g_S \hat{a}_L \hat{a}_S^\dagger \hat{a}_V^\dagger + {\rm H.c.} \tag{30}$$

(b) Anti-Stokes Raman scattering (sideband cooling). One can also analyze the Raman scattering with anti-Stokes frequency $\omega_A > \omega_L$, referred to as anti-Stokes (Raman) scattering and illustrated in Fig. 1(c). The interaction Hamiltonian for the anti-Stokes Raman scattering can be written as

$$\hat{H}_{\rm int}^{(A)} = \sum_j g_{Aj}^* \hat{a}_L \hat{a}_A^\dagger \hat{a}_{Vj} + {\rm H.c.}, \tag{31}$$

or its simpler single-phonon version

$$\hat{H}_{\rm int}^{(A)} = g_A^* \hat{a}_L \hat{a}_A^\dagger \hat{a}_V + {\rm H.c.} \tag{32}$$

Since a phonon is absorbed in this process, it can also be referred to as sideband cooling of the phononic mode.

(c) Stimulated Raman scattering. The presence of additional photons in the S or A modes, as shown in Fig. 1(d), can increase the rate of Raman scattering. This is called stimulated Raman scattering. To further distinguish the processes in Fig. 1(c) from those in Fig. 1(d), the former can be referred to as spontaneous Raman scattering.

2. Analogous processes

We can achieve close analogs of Raman scattering in our deterministic setups by letting a qubit play the role of a phonon. The qubit is coupled to two resonators, one representing the

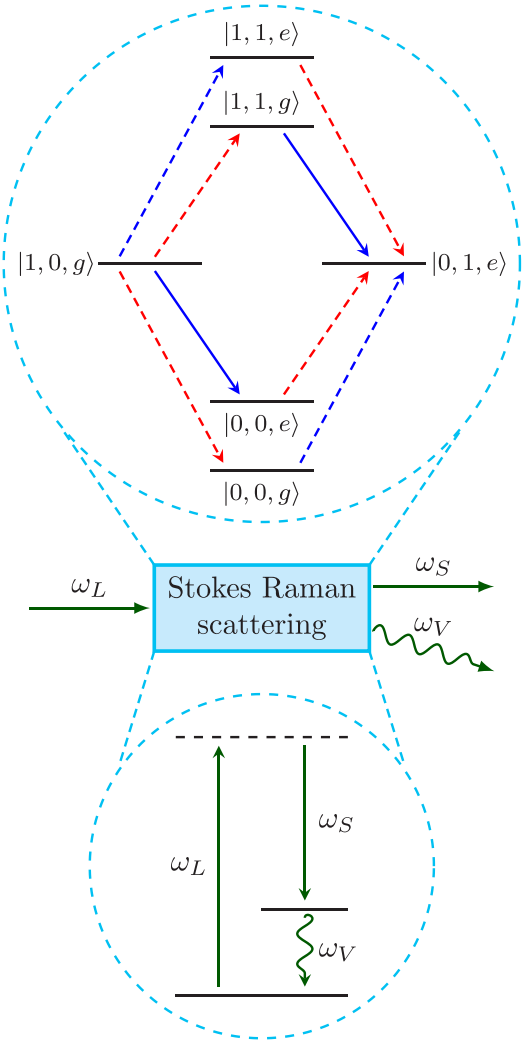

FIG. 4. Raman scattering and its deterministic analog. The upper panel shows all virtual transitions that contribute, to lowest order, to the process $|1,0,g\rangle \to |0,1,e\rangle$, which corresponds to Stokes Raman scattering. The lower panel shows the generic level diagram for the process in nonlinear optics. The same arrow and level styles as in Fig. 2 are used; we have set $\omega_a = 3\omega_q$ and $\omega_b = 2\omega_q$. If the directions of all arrows in the entire figure are reversed, and the labels are changed such that $S \to L$ and $L \to A$, anti-Stokes scattering is shown instead. Stimulated Stokes (anti-Stokes) Raman scattering is given by adding n to the photon number in the second (first) resonator mode in the upper panel and adding n incoming and outgoing photons to the S (A) mode in the rest of the figure.

laser mode and the other representing the Stokes or anti-Stokes mode. The Hamiltonian of the system is given by Eqs. (15) and (16).

(a) Stokes Raman scattering. Setting $\omega_a = \omega_b + \omega_q$, and making the connections $a = L$, $b = S$, and $q = V$, the transition $|1,0,g\rangle \to |0,1,e\rangle$ emulates Stokes Raman scattering. The virtual transitions involved are shown in Fig. 4. This process is further discussed in the concurrent work of Ref. [55] as a means to achieve single-photon frequency conversion controlled by the qubit. The effective interaction due to the virtual transitions when $\omega_q \approx \omega_a - \omega_b$ becomes

$$\hat{H}_{\rm int}^{\rm eff} = g_{\rm eff}|1,0,g\rangle\langle 0,1,e| + \text{H.c.} \tag{33}$$

Second-order perturbation theory using Eq. (10) and Fig. 4 gives

$$g_{\rm eff} = g_a g_b \sin\theta\cos\theta\left(\frac{1}{-\omega_a} - \frac{1}{\Delta_{qa}} + \frac{1}{\omega_b} - \frac{1}{\Omega_{bq}}\right), \tag{34}$$

which reduces to

$$g_{\rm eff} = g_a g_b\left(\frac{1}{\omega_b} - \frac{1}{\omega_a}\right)\sin(2\theta) \tag{35}$$

on resonance ($\omega_q = \omega_a - \omega_b$). This agrees with the result obtained using adiabatic elimination in Ref. [55].

We also note that it has been shown that a photon scattering off a qubit ultrastrongly coupled to an open transmission line can be down-converted in frequency, leaving some of its energy with the qubit [48]. However, this down-conversion process is not deterministic.

(b) Anti-Stokes Raman scattering. The same setup as for Stokes Raman scattering, but considering the reverse transition $|0,1,e\rangle \to |1,0,g\rangle$, implements anti-Stokes Raman scattering. In this case, we need to make the identifications $a = A$, $b = L$, and $q = V$.

(c) Stimulated Raman scattering. We can again consider the same setup, but instead look at the transitions $|1,n,g\rangle \to |0,n+1,e\rangle$ and $|n,1,e\rangle \to |n+1,0,g\rangle$ to obtain stimulated Stokes Raman scattering and stimulated anti-Stokes Raman scattering, respectively. In calculating the effective coupling $g_{\rm eff}$ between the initial and final states, as done above and in Ref. [55] for the case $n = 0$, we will, for each possible path between them, multiply the corresponding transition matrix elements. As can be seen from Fig. 4, each path contains exactly one transition that changes the number of excitations in one of the modes from n to $n+1$. This contributes a factor $\sqrt{n+1}$ to the effective coupling, showing that the presence of the additional photons stimulates the transition.

IV. FOUR-WAVE MIXING

In this section, we treat four-wave mixing, starting as in Sec. III with a general description and then treating special cases, such as degenerate four-wave mixing and hyper-Raman scattering. An overview of these processes is given in Fig. 5. We again provide deterministic analogs for each case. Since there are many similarities to the material presented in Sec. III, the treatment here will be a little more concise. However, compared to Sec. III there are more processes to cover and longer paths of virtual transitions to consider in calculating the effective coupling for those processes.

A. General description

1. Nonlinear optics

Four-wave mixing comes in three types, as illustrated in Fig. 5(a). Type I, with the interaction Hamiltonian

$$\hat{H}_{\rm int} = g\hat{a}_1\hat{a}_2\hat{a}_3^\dagger\hat{a}_4^\dagger + g^*\hat{a}_1^\dagger\hat{a}_2^\dagger\hat{a}_3\hat{a}_4, \tag{36}$$

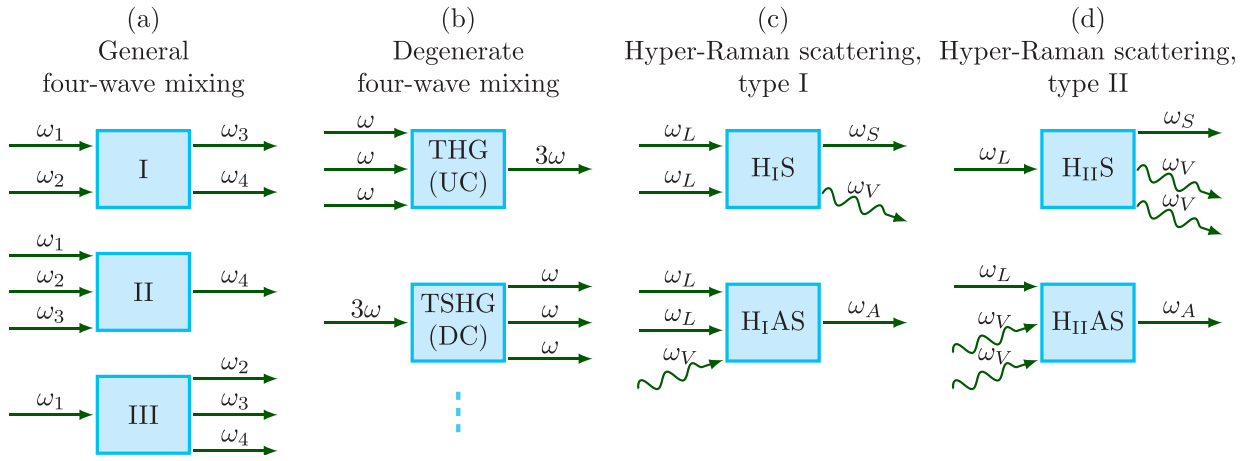

FIG. 5. Schematic representations (Feynman-like diagrams) of four-wave-mixing processes. (a) Four-wave mixing can be divided into three general categories: type I, with two incoming and two outgoing signals (above), type II, with three incoming signals and one outgoing (middle), and type III, with one incoming signal and three outgoing ones (below). (b) When three of the frequencies are degenerate, we have either third-harmonic generation (THG, or up-conversion, above) or third-subharmonic generation (TSHG, or down-conversion, below). When two of the frequencies are degenerate, four processes are possible (not pictured here, but shown in Appendix C). (c) When a phonon is involved, the process is called hyper-Raman scattering of type I. The only change to Stokes (H_IS, above) and anti-Stokes (H_IAS, below) Raman scattering from the three-wave-mixing case [see Fig. 1(c)] is that there are two (degenerate) incoming photons instead of one. (d) With two degenerate phonons, the process is called hyper-Raman scattering of type II. The two phonons replace the single one in the Stokes ($H_{II}S$, above) and anti-Stokes ($H_{II}AS$, below) versions of ordinary Raman scattering from Fig. 1(c).

has two incoming and two outgoing signals. Processes with three incoming signals and one outgoing are here called type II, and processes with one incoming signal and three outgoing ones are here referred to as type III. The interaction Hamiltonian for both types II and III can be written as

$$\hat{H}_{\rm int} = g\hat{a}_1\hat{a}_2\hat{a}_3\hat{a}_4^\dagger + g^*\hat{a}_1^\dagger\hat{a}_2^\dagger\hat{a}_3^\dagger\hat{a}_4. \tag{37}$$

2. *Analogous processes*

There are, just as for three-wave mixing, several possible setups that allow deterministic analogs of the four-wave mixing processes. The clearest analogy is probably four resonators all coupled to a single qubit. Adjusting the resonator frequencies to satisfy the condition $\omega_a + \omega_b \approx \omega_c + \omega_d$, the states $|1,1,0,0,g\rangle$ and $|0,0,1,1,g\rangle$ become resonant and the transitions between these states will constitute type-I four-wave mixing. Similarly, if $\omega_a + \omega_b + \omega_c \approx \omega_d$, the transition $|1,1,1,0,g\rangle \rightarrow |0,1,1,1,g\rangle$ corresponds to type-II mixing and the reverse process $|0,1,1,1,g\rangle \rightarrow |1,0,0,0,g\rangle$ will be type-III mixing.

If at least one of the excitations in the four-wave mixing can be hosted in a qubit, additional setups are possible. With three resonators coupled to a single qubit, $|1,1,0,g\rangle \leftrightarrow |0,0,1,e\rangle$ corresponds to type-I mixing and the processes $|1,1,1,g\rangle \leftrightarrow |0,0,0,e\rangle$ corresponds to type-II ($\rightarrow$) and type-III ($\leftarrow$) mixing, respectively. In the same way, with two resonators coupled to two qubits, $|1,1,g,g\rangle \leftrightarrow |0,0,e,e\rangle$ are analogs of type-I mixing and the processes $|0,1,e,e\rangle \leftrightarrow |1,0,g,g\rangle$ are some possible analogs for type-II ($\rightarrow$) and type-III ($\leftarrow$) mixing, respectively. Finally, with a single resonator coupled to three qubits, $|1,e,g,g\rangle \leftrightarrow |0,g,e,e\rangle$ corresponds to type-I mixing and the processes $|0,e,e,e\rangle \leftrightarrow |1,g,g,g\rangle$ corresponds to type-II ($\rightarrow$) and type-III ($\leftarrow$) mixing, respectively. Hosting at least one excitation in a qubit may be preferable, since such setups, in general, will require one less intermediate virtual transition than the setup with four resonators and a qubit. Barring destructive interference between the various virtual transition paths, this implies that the effective coupling will be weaker in the latter setup.

All these processes can occur due to intermediate virtual transitions as before. However, in contrast to three-wave mixing, the four-wave mixing analogs do not require the generalized Rabi interaction Hamiltonian from Eq. (6). The standard quantum Rabi model in Eq. (4) is sufficient, since the parity of the number of excitation is conserved in four-wave mixing. In fact, for type-I processes, which do not change the number of excitations, the interaction terms from the JC model in Eq. (5) are sufficient to mediate the required virtual transitions. However, terms from the full quantum Rabi model can still give a significant contribution to the effective coupling between the initial and final states of such processes.

B. Degenerate four-wave mixing: Third-harmonic and third-subharmonic generation

In this subsection, we limit our analysis to the cases where three of the signals involved are degenerate. The cases with two degenerate signals are reviewed briefly in Appendix C.

1. *Nonlinear optics*

Let us analyze a degenerate case of four-wave mixing assuming $\hat{a}_1 = \hat{a}_2 = \hat{a}_3 \equiv \hat{a}$, $\hat{a}_4 \equiv \hat{a}_+$, and $\omega_+ = 3\omega$. The creation and annihilation of a photon in the Fock basis can be given as $|n,n_+\rangle \rightarrow |n-3,n_+ + 1\rangle$ for third-harmonic generation (up-conversion) and $|n,n_+\rangle \rightarrow |n+3,n_+ - 1\rangle$ for third-subharmonic generation (down-conversion); see also

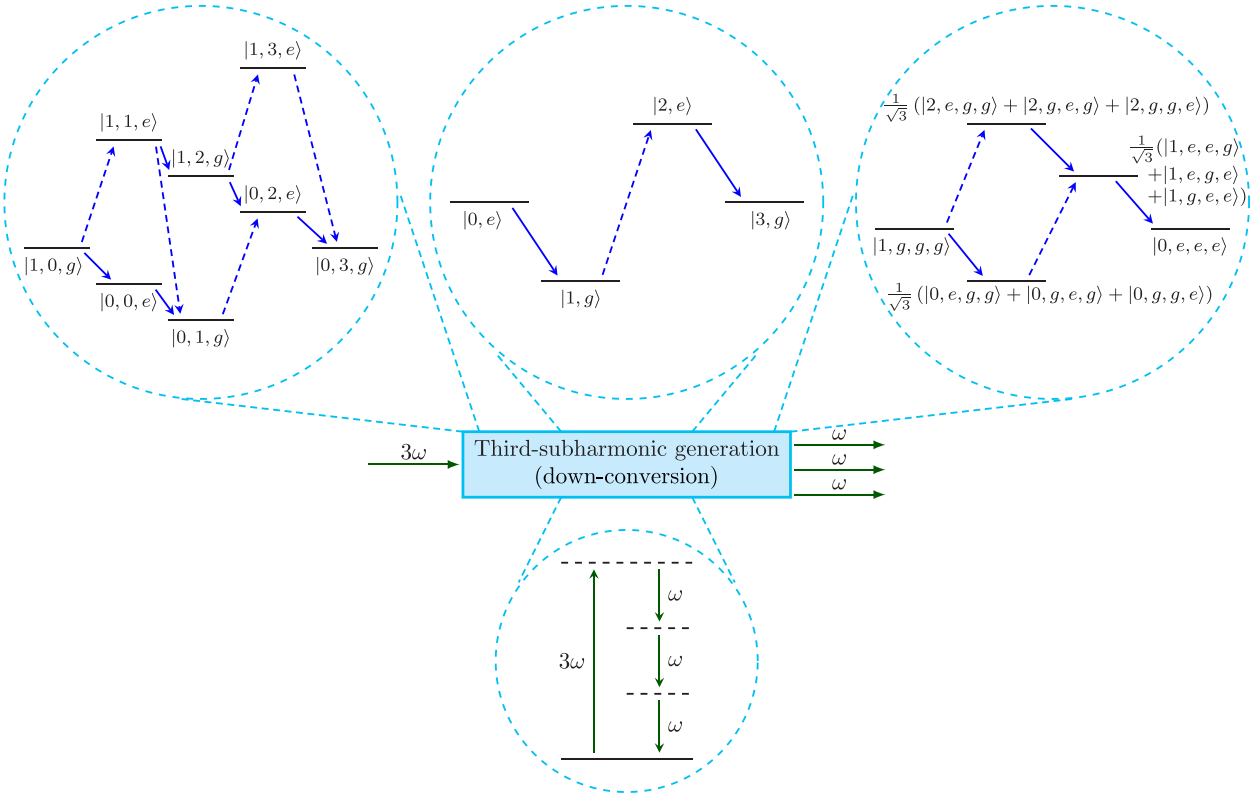

FIG. 6. Realizations of down- and up-conversion with four-wave mixing. The upper left panel shows all virtual transitions that contribute to the down-conversion process (third-subharmonic generation) $|1,0,g\rangle \to |0,3,g\rangle$ to lowest order. Similarly, the upper middle panel shows all virtual transitions that contribute to the down-conversion process $|0,e\rangle \to |3,g\rangle$ to lowest order, and the upper right panel shows all virtual transitions that contribute to the down-conversion process $|1,g,g,g\rangle \to |0,e,e,e\rangle$ to lowest order. The lower panel show the generic level diagram for the process in nonlinear optics. The same arrow and level styles as in Fig. 2 are used. In the upper left panel, $\omega_a = 3\omega_b$ and $\omega_q = 2\omega_b$; in the upper middle panel, we have set $\omega_q = 3\omega_a$; in the upper right panel, $\omega_a = 3\omega_q$. If the directions of all arrows in the entire figure are reversed, up-conversion (third-harmonic generation) is shown instead.

Fig. 5(b). The interaction Hamiltonian for both processes reads as

$$\hat{H}_{\rm int} = g\hat{a}^3\hat{a}_+^\dagger + g^*\hat{a}^{\dagger 3}\hat{a}_+. \tag{38}$$

The initial pure state for third-subharmonic generation is usually chosen as $|\psi(t_0)\rangle = \sum_{n=0}^{\infty} c_n|n,0\rangle$, while that for third-harmonic generation can read as $|\psi(t_0)\rangle = \sum_{n_+=0}^{\infty} c_{n_+}|0,n_+\rangle$, where c_n and c_{n_+} are arbitrary complex amplitudes like in Sec. III B 1.

2. *Analogous processes*

Also in this case, there are various possible deterministic setups, extensions of those discussed in Sec. III B 2. The three most straightforward setups are illustrated in Fig. 6. We note from the figure that although these setups in general require one more intermediate step than in the three-wave-mixing case, the calculations of the effective coupling are simplified by the fact that we only need to use transitions mediated by the quantum Rabi Hamiltonian (blue arrows in the figure), and not the $\hat{\sigma}_z$ terms of the generalized Rabi Hamiltonian (red arrows in Fig. 2), since the excitation-number parity is conserved.

(a) Two resonators. The first analog, shown in the upper left panel of Fig. 6, utilizes two resonators, with frequencies $\omega_a \approx 3\omega_b$, coupled to a single qubit such that virtual intermediate transitions enable the process $|1,0,g\rangle \leftrightarrow |0,3,g\rangle$, which realizes both up- and down-conversion. The full Hamiltonian for this system is given by Eq. (15) and

$$\hat{H}_{\rm int} = [g_a(\hat{a} + \hat{a}^\dagger) + g_b(\hat{b} + \hat{b}^\dagger)]\hat{\sigma}_x. \tag{39}$$

We can derive, in the same way as before, an effective Hamiltonian

$$\hat{H}_{\rm int}^{\rm eff} = g_{\rm eff}|1,0,g\rangle\langle 0,3,g| + \text{H.c.} \tag{40}$$

The effective coupling requires fourth-order perturbation theory to calculate. Summing the four contributing paths using Eq. (10) with $|i\rangle = |0,3,g\rangle$ and $|f\rangle = |1,0,g\rangle$ gives

$$g_{\rm eff} = \sqrt{6}g_a g_b^3\Bigg[-\frac{1}{(\Omega_{aq} - 2\omega_b)\Delta_{ab}\Omega_{aq}} + \frac{1}{(\Omega_{aq} - 2\omega_b)\Delta_{ab}\Delta_{bq}} - \frac{1}{2\omega_b(\Omega_{aq} - 2\omega_b)\Delta_{bq}} + \frac{1}{2\omega_b(3\omega_b + \omega_q)\Delta_{bq}}\Bigg]. \tag{41}$$

Applying the resonance condition $\omega_a = 3\omega_b$ simplifies this result to

$$g_{\rm eff} = \frac{\sqrt{6}g_a g_b^3}{2\omega_b}\left[\frac{1}{\Delta_{bq}(3\omega_b-\omega_q)} - \frac{1}{\Omega_{bq}(3\omega_b+\omega_q)}\right] = \frac{4\sqrt{6}g_a g_b^3\omega_q}{9\omega_b^4 - 10\omega_b^2\omega_q^2+\omega_q^4}, \quad (42)$$

which scales as $(g_j/\omega)^3$, $j = a,b$, as expected for a fourth-order process.

(b) Multiphoton Rabi oscillations. The second option, shown in the upper middle panel of Fig. 6, is multiphoton Rabi oscillations between the states $|0,e\rangle$ and $|3,g\rangle$ with a single resonator coupled to a single qubit ($\omega_q \approx 3\omega_a$), a process studied in Refs. [52,53]. The Hamiltonian for the system is given by Eqs. (3) and (4).

The effective interaction Hamiltonian for this process is

$$\hat{H}_{\rm int}^{\rm eff} = g_{\rm eff}|0,e\rangle\langle 3,g| + {\rm H.c.} \quad (43)$$

The effective coupling for three-photon Rabi oscillations follows immediately from third-order perturbation theory as there is only a single path contributing. With $|i\rangle = |3,g\rangle$ and $|f\rangle = |0,e\rangle$, Eq. (10) gives

$$g_{\rm eff} = \frac{\sqrt{6}g^3}{2\omega_a\Delta_{aq}} = -\frac{9\sqrt{6}g^3}{4\omega_q^2}, \quad (44)$$

where we used the resonance condition $\omega_q = \omega_a/3$ in the last step. This result was also derived in Ref. [52] using adiabatic elimination.

(c) Three identical qubits. A third possibility, shown in the upper right panel of Fig. 6, is coupling a single resonator to three identical qubits ($\omega_a = 3\omega_q$), such that the process $|1,g,g,g\rangle \leftrightarrow |0,e,e,e\rangle$ is implemented, as discussed in Ref. [54]. In this case, the Hamiltonian for the system is

$$\hat{H} = \omega_a\hat{a}^\dagger\hat{a} + \sum_{j=1}^{3}\omega_q\frac{\hat{\sigma}_z^{(j)}}{2} + \hat{H}_{\rm int}, \quad (45)$$

$$\hat{H}_{\rm int} = g(\hat{a}+\hat{a}^\dagger)\sum_{j=1}^{3}\hat{\sigma}_x^{(j)}, \quad (46)$$

and the effective interaction Hamiltonian of interest is

$$\hat{H}_{\rm int}^{\rm eff} = g_{\rm eff}|1,g,g,g\rangle\langle 0,e,e,e| + {\rm H.c.} \quad (47)$$

The effective coupling can be calculated with third-order perturbation theory. Following Eq. (10), adding up the contributions from the two paths with $|i\rangle = |0,e,e,e\rangle$ and $|f\rangle = |1,g,g,g\rangle$, leads to

$$g_{\rm eff} = g^3\left(\frac{3}{\Delta_{qa}^2} + \frac{6}{2\omega_q\Delta_{qa}}\right) = -\frac{3g^3(\omega_a-3\omega_q)}{\omega_q\Delta_{qa}^2}, \quad (48)$$

which goes to zero on resonance ($\omega_a = 3\omega_q$); the two paths interfere destructively then. However, as shown numerically in the appendix of Ref. [54], a coupling between the states $|1,g,g,g\rangle$ and $|0,e,e,e\rangle$ nevertheless exists close to that resonance. This is partly due to the fact that the energy levels are shifted from their bare-state values to the dressed states induced by the ultrastrong interaction and partly due to the influence of higher-order processes.

Comparing the three analogs given here, we note that the multiphoton Rabi oscillations and the single photon exciting three qubits both require one less intermediate step than the setup with two resonators and one qubit. However, in the three-qubit case this does not necessarily translate into a stronger effective coupling due to destructive interference between the virtual transitions. The possibility of such destructive interference diminishing the effective coupling needs to be kept in mind when designing analogs of nonlinear optics in these setups. We will see one more example of this phenomenon below.

C. Hyper-Raman scattering, type I: Two-photon processes

1. Nonlinear optics

Hyper-Raman scattering is a generalization of Raman scattering (see Sec. III C) to include either multiple incoming photons or multiple phonons. Here, we first analyze hyper-Raman scattering based on two-photon processes (we refer to this as type-I hyper-Raman scattering), as described by the following Hamiltonians for Stokes frequency,

$$\hat{H}_{\rm int}^{(S)} = g_S\hat{a}_L^2\hat{a}_S^\dagger\hat{a}_V^\dagger + {\rm H.c.}, \quad (49)$$

and anti-Stokes frequency (which could also be called sideband hypercooling of type I),

$$\hat{H}_{\rm int}^{(A)} = g_A^*\hat{a}_L^2\hat{a}_A^\dagger\hat{a}_V + {\rm H.c.} \quad (50)$$

These processes are sketched in Fig. 5(c). We note that here $\omega_S > \omega_L$, contrary to the standard Raman scattering case. For simplicity, we have omitted multiphonon versions analogous to Eq. (29).

2. Analogous processes

Just as in Sec. III C 2, we consider setups where qubit excitations play the role of phonons in the deterministic analogs of hyper-Raman scattering. For the type-I process, two resonators (one corresponding to the L mode, one corresponding to the S or A mode) are coupled to a single qubit. This setup is studied further in our concurrent work Ref. [55] as a means to implement deterministic up- and down-conversions controlled by a qubit.

(a) Stokes Hyper-Raman scattering, type I. Setting $\omega_a + \omega_q \approx 2\omega_b$ and making the connections $a = S$, $b = L$, and $q = V$, we see that the process $|0,2,g\rangle \to |1,0,e\rangle$ corresponds to Stokes hyper-Raman scattering of type I. In the upper panel of Fig. 7, we show the virtual transitions contributing to this process. From the full system Hamiltonian, given by Eqs. (15) and (39) just as for the three-photon frequency conversion in Sec. IV B 2 a, we can derive the effective Hamiltonian

$$\hat{H}_{\rm int,H_IS}^{\rm eff} = g_{\rm eff}|0,2,g\rangle\langle 1,0,e| + {\rm H.c.} \quad (51)$$

Third-order perturbation theory following Eq. (10) gives

$$g_{\rm eff} = \sqrt{2}g_a g_b^2\left(\frac{1}{-2\omega_b\Delta_{qb}} + \frac{1}{\Delta_{ab}\Delta_{qb}} + \frac{1}{\Delta_{ab}\Omega_{aq}}\right) = \frac{\sqrt{2}g_a g_b^2(\omega_a-2\omega_b)}{\omega_b\Delta_{ab}^2}, \quad (52)$$

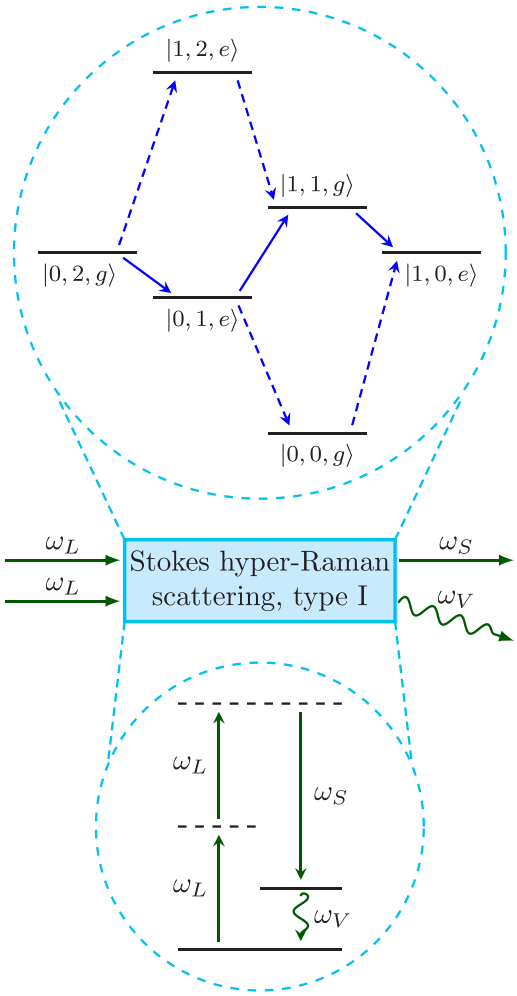

FIG. 7. Stokes hyper-Raman scattering of type I and its deterministic analog. The upper panel shows all virtual transitions that contribute to lowest order to the transition $|0,2,g\rangle \rightarrow |1,0,e\rangle$. The lower panel shows the generic level diagram for the process in nonlinear optics. The connection becomes clear with the identifications $a = S$, $b = L$, and $q = V$. The same arrow and level styles as in Fig. 2 are used; we have set $\omega_a = 3\omega_q$ and $\omega_b = 2\omega_q$.

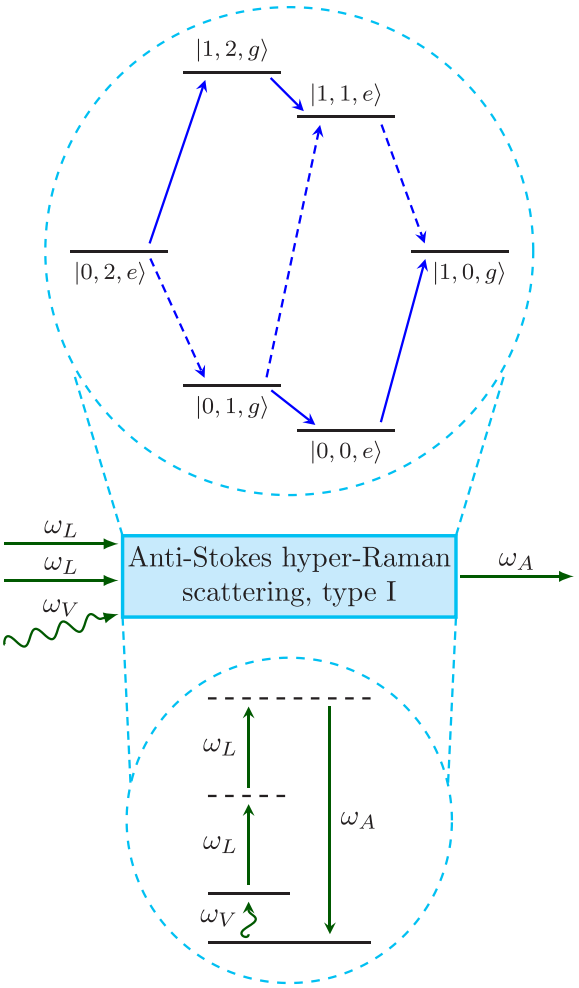

FIG. 8. Anti-Stokes hyper-Raman scattering of type I (sideband hypercooling) and its deterministic analog. The upper panel shows all virtual transitions that contribute to lowest order to the transition $|0,2,e\rangle \rightarrow |1,0,g\rangle$. The lower panel shows the generic level diagram for the process in nonlinear optics. The connection becomes clear with the identifications $a = A$, $b = L$, and $q = V$. The same arrow and level styles as in Fig. 2 are used; we have set $\omega_a = 5\omega_q$ and $\omega_b = 2\omega_q$.

where we used the resonance condition $\omega_q = 2\omega_b - \omega_a$ in the last step.

We note that one of the paths contributing to the coupling [the second term in Eq. (52)] only requires interactions given by the JC version of the interaction Hamiltonian,

$$\hat{H}_{\rm int} = g_a(\hat{a}\hat{\sigma}_+ + \hat{a}^\dagger\hat{\sigma}_-) + g_b(\hat{b}\hat{\sigma}_+ + \hat{b}^\dagger\hat{\sigma}_-). \tag{53}$$

Omitting the other terms from Eq. (52) and setting $\omega_q = 2\omega_b - \omega_a$, the result is

$$g_{\rm eff} = -\frac{\sqrt{2}g_a g_b^2}{\Delta_{ab}^2}. \tag{54}$$

These effective couplings are also calculated in Ref. [55] using adiabatic elimination. In that case, the results are a little more complicated since some higher-order contributions are included, but to lowest order the results coincide with those given here.

(b) Anti-Stokes Hyper-Raman scattering, type I. If we instead set $\omega_a \approx 2\omega_b + \omega_q$ in the same setup as for Stokes hyper-Raman scattering of type I (and make the connections $a = A$, $b = L$, and $q = V$), the transition $|0,2,e\rangle \rightarrow |1,0,g\rangle$ corresponds to anti-Stokes hyper-Raman scattering of type I. The effective interaction Hamiltonian becomes

$$\hat{H}^{\rm eff}_{\rm int,H_IAS} = g_{\rm eff}|0,2,e\rangle\langle 1,0,g| + {\rm H.c.} \tag{55}$$

The virtual transitions contributing to the process $|0,2,e\rangle \rightarrow |1,0,g\rangle$ are shown in Fig. 8. Third-order perturbation theory

following Eq. (10) gives

$$g_{\rm eff} = \sqrt{2} g_a g_b^2 \left(\frac{1}{2\omega_b \Omega_{qb}} - \frac{1}{\Delta_{ab}\Omega_{qb}} + \frac{1}{\Delta_{ab}\Delta_{aq}} \right) = \frac{\sqrt{2} g_a g_b^2 (\omega_a - 2\omega_b)}{\omega_b \Delta_{ab}^2}, \quad (56)$$

where we used the resonance condition $\omega_q = \omega_a - 2\omega_b$ in the last step. We note that the expression is the same as the one obtained for type-I Stokes hyper-Raman scattering in Eq. (52), despite the resonance condition being different.

This effective coupling is also calculated in Ref. [55] using adiabatic elimination. Again, in that case, the result is a little more complicated since some higher-order contributions are included, but to lowest order it coincides with Eq. (56).

D. Hyper-Raman scattering, type II: Two-phonon processes

1. Nonlinear optics

Hyper-Raman scattering can also be based on two-phonon processes (we refer to this as type-II hyper-Raman scattering), as described by the following interaction Hamiltonians with Stokes frequency,

$$\hat{H}_{\rm int}^{(S)} = g_S \hat{a}_L \hat{a}_S^\dagger \hat{a}_{V1}^\dagger \hat{a}_{V2}^\dagger + \text{H.c.}, \quad (57)$$

and with anti-Stokes frequency (which could also be called sideband hypercooling of type II),

$$\hat{H}_{\rm int}^{(A)} = g_A^* \hat{a}_L \hat{a}_A^\dagger \hat{a}_{V1} \hat{a}_{V2} + \text{H.c.} \quad (58)$$

These processes are sketched in Fig. 5(d).

2. Analogous processes

The closest analog here is a setup with two resonators both coupled to two identical qubits. The full system Hamiltonian is given by

$$\hat{H} = \omega_a \hat{a}^\dagger \hat{a} + \omega_b \hat{b}^\dagger \hat{b} + \sum_{j=1}^{2} \omega_q \frac{\hat{\sigma}_z^{(j)}}{2} + \hat{H}_{\rm int}, \quad (59)$$

$$\hat{H}_{\rm int} = [g_a(\hat{a} + \hat{a}^\dagger) + g_b(\hat{b} + \hat{b}^\dagger)] \sum_{j=1}^{2} \hat{\sigma}_x^{(j)}. \quad (60)$$

If the frequencies satisfy the resonance condition $\omega_a \approx \omega_b + 2\omega_q$, the process $|1,0,g,g\rangle \to |0,1,e,e\rangle$, whose virtual transitions are shown in Fig. 9, corresponds to Stokes hyper-Raman scattering of type II, given that we make the connections $a = L$, $b = S$, and $q = V$. The reverse process corresponds to anti-Stokes hyper-Raman scattering of type II, if we instead identify $a = A$ and $b = L$.

The virtual transitions give rise to the effective Hamiltonian

$$\hat{H}_{\rm int}^{\rm eff} = g_{\rm eff} |1,0,g,g\rangle\langle 0,1,e,e| + \text{H.c.}, \quad (61)$$

which describes both processes. Adding up the two paths in Fig. 9 using second-order perturbation theory following Eq. (10), we obtain

$$g_{\rm eff} = 2 g_a g_b \left(\frac{1}{\Delta_{qa}} + \frac{1}{\Omega_{bq}} \right) = -\frac{2 g_a g_b (\Delta_{ba} + 2\omega_q)}{\Delta_{aq}\Omega_{bq}}, \quad (62)$$

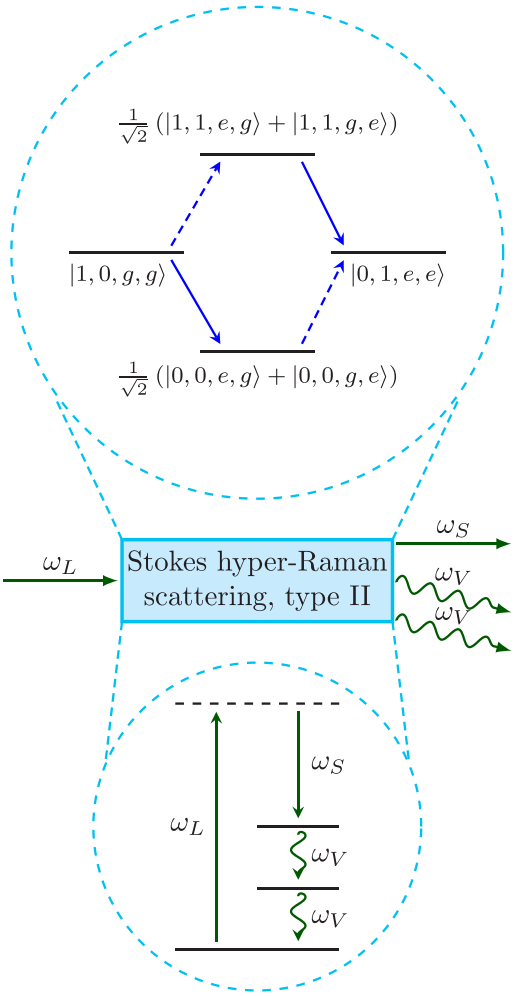

FIG. 9. Stokes hyper-Raman scattering of type II and its deterministic analog. The upper panel shows all virtual transitions that contribute to lowest order to the transition $|1,0,g,g\rangle \to |0,1,e,e\rangle$. The lower panel shows the generic level diagram for the process in nonlinear optics. The connection becomes clear with the identifications $a = L$, $b = S$, and $q = V$. The same arrow and level styles as in Fig. 2 are used; we have set $\omega_a = 2\omega_b = 4\omega_q$. If the directions of all arrows in the entire figure are reversed, and the labels are changed such that $S \to L$ and $L \to A$, anti-Stokes hyper-Raman scattering of type II is shown instead.

which goes to zero on resonance ($\omega_a = \omega_b + 2\omega_q$). However, a finite coupling should result from the fact that bare energy levels are shifted to dressed ones and higher-order processes can contribute, analogous to the situation for the single photon exciting three qubits discussed in Sec. IV B 2 c.

V. OTHER NONLINEAR PROCESSES

While three- and four-wave mixing have been the main focus of this article, there are several other nonlinear-optics processes for which analogs can be found. In this section, we treat a few of these.

A. Higher-harmonic and -subharmonic generation

A plethora of processes are possible when considering wave-mixing involving five or more frequencies. To shed light on the relevant considerations for the deterministic analogs of these processes, it is sufficient to consider higher-harmonic and -subharmonic generation as a simple representative example.

1. Nonlinear optics

We consider the degenerate case of m-wave mixing assuming $\hat{a}_1 = \hat{a}_2 = \ldots = \hat{a}_{m-1} \equiv \hat{a}, \hat{a}_m \equiv \hat{a}_+$, and $\omega_+ = (m-1)\omega$. The creation and annihilation of a photon in the Fock basis can then be given as $|n,n_+\rangle \to |n-m+1,n_+ +1\rangle$ for $(m-1)$th-harmonic generation (up-conversion) and $|n,n_+\rangle \to |n+m-1,n_+ -1\rangle$ for $(m-1)$th-subharmonic generation (down-conversion). The interaction Hamiltonian for both processes can be written as

$$\hat{H}_{\rm int} = g\hat{a}^{m-1}\hat{a}_+^\dagger + g^*\hat{a}^{\dagger(m-1)}\hat{a}_+, \tag{63}$$

generalizing Eq. (14) for three-wave mixing and Eq. (38) for four-wave mixing.

2. Analogous processes

It is straightforward to extend the three approaches discussed in Sec. III B 2 for three-wave mixing and in Sec. IV B 2 for four-wave mixing. One can use two resonators, with frequencies $\omega_a = (m-1)\omega_b$, coupled to a single qubit such that the process $|1,0,g\rangle \leftrightarrow |0,m-1,g\rangle$ is enabled by virtual intermediate transitions, realizing both up- and down-conversion. The other approaches are to use multiphoton Rabi oscillations between $|0,e\rangle$ and $|m-1,g\rangle$ using a single resonator coupled to a single qubit with $\omega_q = (m-1)\omega_a$ [53]; or to couple a single resonator to $m-1$ identical qubits [$\omega_a = (m-1)\omega_q$] such that the process $|1,g,\ldots,g\rangle \leftrightarrow |0,e,\ldots,e\rangle$ is realized [54].

What these three approaches, and all other analogs of m-wave mixing, have in common are that they require an increasing number of intermediate virtual transitions as m increases. In general, the effective coupling $g_{\rm eff}$, determining the transition rate, will be proportional to $(g/\omega)^{n-1}$ if n steps of intermediate virtual transitions are required to go between the initial and final states. Here, g and ω are the coupling and the relevant system frequencies, respectively, in the quantum Rabi model discussed in Sec. II B. Considering this, the fact that the multiphoton Rabi oscillations require one less intermediate step than the other two approaches described above (see Secs. III B 2 and IV B 2) makes them the most suited to implement an analog of higher-harmonic and -subharmonic generation.

We also note that the standard quantum Rabi model, Eq. (4), is sufficient to mediate the virtual transitions needed for m-wave mixing when m is even. If m is odd, the interaction terms from the generalized quantum Rabi model, Eq. (6), are necessary to realize the analogs discussed here.

B. Multiphoton absorption

1. Nonlinear optics

Simultaneous absorption of multiple photons in a system is a nonlinear process, first predicted by Göppert-Mayer [69]. Unlike most of the wave-mixing processes discussed above (except Raman scattering), this process changes the net energy of the system.

2. Analogous processes

A clear analogy of multiphoton absorption is provided by the multiphoton Rabi oscillations [53] already discussed in the context of harmonic and subharmonic generation in Secs. III B 2, IV B 2, and V A 2. During a multiphoton Rabi oscillation, a single qubit absorbs n photons from the resonator it is coupled to; this is the process $|n,g\rangle \to |0,e\rangle$. We also note that circuit-QED experiments with flux qubits have demonstrated multiphoton absorption in a driven qubit-resonator system [32,63].

C. Parametric processes

1. Nonlinear optics

Many of the processes discussed above can be analyzed for the case where one of the fields is a strong drive that can be approximated as classical. As an example, consider the general three-wave-mixing processes described by Eqs. (11) and (12) in Sec. III A 1. We denote the frequencies by $\omega_p \equiv \omega_1$ for the pump (drive) mode, $\omega_s \equiv \omega_2$ for the signal mode, and $\omega_i \equiv \omega_\pm$ for the idler mode. We then apply the parametric approximation $\hat{a}_p(t) \approx \langle \hat{a}_p(t)\rangle \approx \alpha_p(t) \equiv |\alpha_p|\exp[-i(\omega t+\phi_p)]$, which is usually valid if $\langle \hat{n}_p(t)\rangle \approx \langle \hat{n}_p(t_0)\rangle \gg \max\{1,\langle \hat{n}_s(t)\rangle,\langle \hat{n}_i(t)\rangle\}$, where $\hat{n}_x$ is the number of photons in mode x. For the case $\omega_p = \omega_s + \omega_i$, Eq. (12) then becomes

$$\begin{aligned}\hat{H}^{\rm (amp)} &= g^*\alpha_p^*\hat{a}_i\hat{a}_s + g\alpha_p\hat{a}_i^\dagger\hat{a}_s^\dagger \\ &= \kappa[\hat{a}_i\hat{a}_s e^{i(\omega t+\phi)} + \hat{a}_i^\dagger\hat{a}_s^\dagger e^{-i(\omega t+\phi)}],\end{aligned} \tag{64}$$

where $\omega \equiv \omega_p$, the coupling constant g is rescaled as $\kappa = |g\alpha_p|$, and $\phi = \phi_p - \arg(g)$. This equation describes parametric amplification (down-conversion). For the special case $\omega_s = \omega_i$, it corresponds to degenerate parametric down-conversion. Similarly, under the parametric approximation, with $\hat{a}_1 \equiv \hat{a}_p \approx \alpha_p$, Eq. (11) describes parametric frequency conversion.

2. Analogous processes

As discussed in Sec. III B 2 a, Ref. [65] showed that a setup with two resonator modes coupled to a qubit with the interaction of Eq. (6) can give an effective interaction of the form

$$\hat{H}_{\rm int}^{\rm eff} = \zeta(\hat{a}^{\dagger 2}\hat{b} + \hat{a}^2\hat{b}^\dagger)\hat{\sigma}_z, \tag{65}$$

where

$$\zeta = \frac{g_a^2 g_b^2 \sin\theta\sin(2\theta)}{\omega_a(\omega_q - \omega_b)}. \tag{66}$$

This interaction results in degenerate parametric down-conversion and squeezing. Note that the qubit state will affect the process since the interaction is proportional to $\hat{\sigma}_z$, which is absent in Eq. (64). However, if we assume that the qubit remains in its ground (or excited) state during the system evolution, we can recover Eq. (64) from Eq. (65). Such qubit "freezing" can be achieved, e.g., by Zeno-type effects.

In general, similar effective interaction Hamiltonians should be possible to derive for all setups considered in this article where the initial and final states for the system have the same qubit state. Thus, most parametric processes from nonlinear optics have deterministic analogs involving virtual photons.

D. Kerr, cross-Kerr, and Pockels effects

1. Nonlinear optics

The Kerr, cross-Kerr, and Pockels effects differ from the other nonlinear-optics phenomena discussed so far in that they do not involve any change in the number of excitations in some mode. Instead, the frequency of a mode a is modified, either through self-interaction (Kerr effect) or through interaction with a second mode b (Pockels effect when the change is proportional to the amplitude of the field; cross-Kerr effect when the change is proportional to the square of said amplitude). These effects can be described by the following Hamiltonians:

$$\hat{H}_{\rm K} = \chi_{\rm K}(\hat{a}^\dagger\hat{a})^2, \tag{67}$$

$$\hat{H}_{\rm cK} = \chi_{\rm cK}\hat{a}^\dagger\hat{a}\hat{b}^\dagger\hat{b}, \tag{68}$$

$$\hat{H}_{\rm P} = \chi_{\rm P}\hat{a}^\dagger\hat{a}(\hat{b}+\hat{b}^\dagger), \tag{69}$$

where χ_x gives the strength of the nonlinear interaction.

2. Analogous processes

The Kerr effect can be realized with a single qubit coupled to a resonator with only the JC interaction of Eq. (5). In the dispersive regime, where $g \ll |\omega_a - \omega_q|$, a perturbation expansion in the small parameter $g/(\omega_a - \omega_q)$ yields a term [70]

$$\hat{H}_{\rm K}^{\rm disp} = \chi_{\rm K}(\hat{a}^\dagger\hat{a})^2\hat{\sigma}_z, \tag{70}$$

where

$$\chi_{\rm K} = -\frac{g^4}{(\omega_a-\omega_q)^3}. \tag{71}$$

This Hamiltonian reduces to the standard Kerr Hamiltonian, given in Eq. (67), if we can assume that the qubit remains in one and the same state during the system evolution, as discussed above in Sec. V C 2. More general derivations for multiple resonator modes and a multilevel atom in the dispersive regime have shown how both Kerr and cross-Kerr effects can be realized [71,72]. In particular, Ref. [72] demonstrates clearly how an atom coupled to two resonators in the dispersive regime via a general coupling like Eq. (6) gives rise to the Kerr and cross-Kerr effects due to fourth-order processes involving virtual photons in the same way as all other analogs of nonlinear optics discussed previously in this article. We note that these Kerr and cross-Kerr terms, just like in Eqs. (65) and (70), involve sums over the diagonal qubit operators $|g\rangle\langle g|$ and $|e\rangle\langle e|$.

Based on the above theory, experiments in circuit QED have recently demonstrated both the single-photon Kerr [73] and cross-Kerr effects [74]. A large cross-Kerr effect for propagating photons interacting with a three-level artificial atom in circuit QED has also been studied theoretically [75] and experimentally [76]. However, to the best of our knowledge, no such experimental demonstrations exists for the Pockels effect and we have been unable to find a mechanism for engineering it in the setups we consider.

VI. EXPERIMENTAL FEASIBILITY

In this section, we evaluate the experimental feasibility of our proposed analogs of nonlinear-optics processes. In most of these analogs, the process consists of transferring population from an initial state $|i\rangle$ to a final state $|f\rangle$. The time scale for this process is given by the inverse of the effective coupling strength $g_{\rm eff}$ for the interaction that connects the two states [see Eq. (9)]. For the transfer to be successful, $g_{\rm eff}$ must exceed the relevant decoherence rates in the system: qubit decoherence (relaxation and dephasing) at a rate γ and resonator losses at a rate κ. To observe energy-level anticrossings in spectroscopy, revealing the effective coupling between $|i\rangle$ and $|f\rangle$, it is sufficient that $g_{\rm eff} > \kappa,\gamma$; for the transfer to be essentially deterministic, i.e., have close to unit efficiency, $g_{\rm eff} \gg \kappa,\gamma$ is required. Note that when either $|i\rangle$ or $|f\rangle$ contain multiple excitations, the relevant loss rates that $g_{\rm eff}$ should be compared to are the total loss rates for those states. For example, in the case of nth-subharmonic generation through multiphoton Rabi oscillations with $|i\rangle = |0,e\rangle$ and $|f\rangle = |n,g\rangle$, discussed in Sec. V A 2, the effective coupling must be compared to γ and $n\kappa$.

Although USC has been realized in several solid-state systems, as noted in Sec. I, we limit the discussion here to circuit QED, where we believe the proposed experiments are easiest to implement. The experimental demonstrations of USC with qubits coupled to resonators in circuit QED have all used flux qubits, coupled either to lumped-element LC oscillators [19,31,36] or transmission-line resonators [20,29,32]. In such circuit QED experiments, qubit and resonator frequencies are usually in the range $\omega_q,\omega_a \sim 2\pi \times 1$–$10\,$GHz. Recent experimental work on flux qubits has demonstrated γ on the order of $2\pi \times 10\,$kHz [77,78], and an improvement of the flux qubit design [79], which comes at the price of reduced anharmonicity, has been shown to reduce γ even further [80]. Superconducting transmon qubits, which have lower anharmonicity than flux qubits, can have γ approaching $2\pi \times 1\,$kHz [81,82]. For transmission-line resonators, quality factors $Q = \omega_a/\kappa$ on the order of 10^6 have been demonstrated [83]. Recently, superconducting qubits are often coupled to 3D cavities, where the quality factor can be another two orders of magnitude larger [84].

Taken together, the numbers above indicate that $\gamma,\kappa \sim 10^{-6}\omega_a$ can be reached in state-of-the-art circuit-QED experiments. Regarding the coupling strength, Refs. [19,20,29,32] have reached $g \gtrsim 0.1\omega_a$ and Refs. [31,36] demonstrated $g \sim \omega_a$. Using the lower of these values as a very conservative estimate, we calculate most of the effective coupling strengths derived in Secs. III and IV. The results are given in Table I. We see that even with this conservative estimate for the bare coupling, and even though processes up to fourth order are considered, the effective coupling strengths are orders of magnitude larger than the decoherence rates that have been demonstrated in experiments. If such low decoherence rates would be hard to reach, the effective coupling can instead be much strengthened by a modest increase of the bare coupling.

We note that already one of the first circuit QED experiments to reach the USC regime, Ref. [20], achieved

TABLE I. Conservative estimates of the effective coupling strengths g_{eff} for most of the analogs of three- and four-wave mixing processes given in this article. In each case, we have assumed the bare coupling g to be 10% of the lowest transition frequency in the setup. The effective coupling is given in units of that transition frequency. We note that the parameter θ can be chosen quite freely in experiments with flux qubits.

Process	Parameters	Equation	Effective coupling $\lvert g_{\text{eff}}\rvert$
$\lvert 1,0,g\rangle \leftrightarrow \lvert 0,2,g\rangle$	$\omega_a = 2\omega_b$, $\omega_q = 1.5\omega_b$, $g_{a/b} = 0.1\omega_b$, $\theta = \pi/6$	Eq. (21)	$3 \times 10^{-3}\omega_b$
$\lvert 0,e\rangle \leftrightarrow \lvert 2,g\rangle$	$\omega_q = 2\omega_a$, $g = 0.1\omega_a$, $\theta = \pi/4$	Eq. (24)	$1 \times 10^{-2}\omega_a$
$\lvert 1,g,g\rangle \leftrightarrow \lvert 0,e,e\rangle$	$\omega_a = 2\omega_q$, $g = 0.1\omega_q$, $\theta = \pi/6$	Eq. (28)	$1 \times 10^{-3}\omega_q$
$\lvert 1,0,g\rangle \leftrightarrow \lvert 0,1,e\rangle$	$\omega_a = 3\omega_q$, $\omega_b = 2\omega_q$, $g_{a/b} = 0.1\omega_q$, $\theta = \pi/4$	Eq. (35)	$2 \times 10^{-3}\omega_q$
$\lvert 1,0,g\rangle \leftrightarrow \lvert 0,3,g\rangle$	$\omega_a = 3\omega_b$, $\omega_q = 2\omega_b$, $g_{a/b} = 0.1\omega_b$	Eq. (42)	$1 \times 10^{-4}\omega_b$
$\lvert 0,e\rangle \leftrightarrow \lvert 3,g\rangle$	$\omega_q = 3\omega_a$, $g = 0.1\omega_a$	Eq. (44)	$6 \times 10^{-4}\omega_a$
$\lvert 0,2,g\rangle \leftrightarrow \lvert 1,0,e\rangle$	$\omega_a = 3\omega_q$, $\omega_b = 2\omega_q$, $g_{a/b} = 0.1\omega_q$	Eq. (52)	$7 \times 10^{-4}\omega_q$
$\lvert 0,2,e\rangle \leftrightarrow \lvert 1,0,g\rangle$	$\omega_a = 5\omega_q$, $\omega_b = 2\omega_q$, $g_{a/b} = 0.1\omega_q$	Eq. (56)	$2 \times 10^{-4}\omega_q$

sufficiently small decoherence to clearly observe an energy-level anticrossing due to effective coupling between states $|1,0,g\rangle$ and $|0,1,e\rangle$. Furthermore, as noted in Sec. V D 2, the single-photon Kerr and cross-Kerr effects, even though these are fourth-order processes, have also been experimentally demonstrated in circuit QED using transmon qubits and 3D cavities [73,74]. In the case of the Kerr effect, the Kerr coefficient was $\chi_{\text{K}} = 2\pi \times 325\,\text{kHz}$, much larger than $\gamma,\kappa \sim 2\pi \times 10$–$20\,\text{kHz}$ [73].

From the estimates in this section, we conclude that most, if not all, of the nonlinear-optics analogs proposed in this article can be implemented with existing experimental technology in circuit QED. It appears that the effective coupling strengths can be orders of magnitude larger than the system decoherence rates, ensuring that the relevant processes can reach close to unit efficiency.

VII. SUMMARY AND OUTLOOK

We have shown how analogs of nonlinear optics can be realized in systems where one or more qubits are coupled to one or more resonator modes. These analogous processes are all based on the light-matter interaction between a qubit and a photonic mode described by the quantum Rabi Hamiltonian or some generalized version thereof. This interaction allows the number of excitations in the system to change, which makes possible the creation and annihilation of virtual photons and qubit excitations. In this way, initial and final states of the nonlinear-optics processes can be connected via a number of virtual transitions, creating an effective deterministic coupling between the states. The effective coupling decreases when the number of intermediate transition steps increases. However, with the recent experimental demonstrations of USC in a variety of systems, circuit QED in particular, it should now be possible to observe many of these nonlinear-optics phenomena in new settings. When the light-matter coupling becomes ultrastrong, even the weaker effective coupling can be larger than the relevant decoherence rates in the system.

For the case of three-wave mixing, we have shown how analogs can be constructed for sum- and difference-frequency generation, including the special cases of second-harmonic generation (up-conversion) and second-subharmonic generation (down-conversion) as well as Stokes and anti-Stokes spontaneous and stimulated Raman scattering. A summary of all the three-wave-mixing processes and their analogs is given in Table II.

Similarly, for the case of four-wave mixing, we have shown how analogs can be realized for all types of nondegenerate and degenerate mixing, including third-harmonic and third-subharmonic generation as well as all forms of hyper-Raman scattering. We provide a summary of all the four-wave-mixing processes and their analogs in Table III. Finally, we have also shown that analogs working according to the same principle are available for higher-harmonic and -subharmonic generation, multiphoton absorption, parametric processes, and the Kerr and cross-Kerr effects.

It is noteworthy that some of the setups we consider, especially the relatively simple setups of a single qubit coupled to one or two resonators, can be used to realize many analogs of nonlinear-optics phenomena in one universal system. It is also remarkable that these analogs work at unit efficiency with a minimal number of photons without any need for external drives, which is not the case for conventional nonlinear optics. While some processes that we discuss here have been investigated in previous and concurrent publications, we have now provided a unified and clear picture of how and why nonlinear-optics analogs can be constructed in these setups. One important difference to conventional nonlinear optics is that we are able to suppress lower-order processes by making the final state of such processes far off-resonant with the initial state.

There are many directions for future work following this article. They include deriving effective Hamiltonians for more parametric processes based on the setups discussed here and finding an analog of the Pockels effect. An interesting way to take the ideas of the current work one step further is to consider analogs of nonlinear-optics processes where the excitations are exchanged only between atoms and any resonators in the setups are only excited virtually, which is treated in a concurrent publication [56]. We also see a great potential for using the

TABLE II. A summary of three-wave-mixing processes in nonlinear optics and their deterministic analogs with single atoms and virtual photons. In the case of nondegenerate three-wave mixing, with the exception of Raman scattering, the given frequencies and transitions are just some of the possibilities.

Nonlinear-optics process			**Analogous setup**	**Frequencies**	**Transition**	**Hamiltonian**	**Reference**
Degenerate three-wave mixing	Second-harmonic generation (upconversion)		1 resonator, 1 qubit	$\omega_q = 2\omega_a$	$\|2,g\rangle \to \|0,e\rangle$	Gen. Rabi	Sec. III B, [53]
			2 resonators, 1 qubit	$\omega_a = 2\omega_b$	$\|0,2,g\rangle \to \|1,0,g\rangle$	Gen. Rabi	Sec. III B, [65]
			1 resonator, 2 qubits	$\omega_a = 2\omega_q$	$\|0,e,e\rangle \to \|1,g,g\rangle$	Gen. Rabi	Sec. III B, [54]
	Second-subharmonic generation (downconversion)		1 resonator, 1 qubit	$\omega_q = 2\omega_a$	$\|0,e\rangle \to \|2,g\rangle$	Gen. Rabi	Sec. III B, [53]
			2 resonators, 1 qubit	$\omega_a = 2\omega_b$	$\|1,0,g\rangle \to \|0,2,g\rangle$	Gen. Rabi	Sec. III B, [65]
			1 resonator, 2 qubits	$\omega_a = 2\omega_q$	$\|1,g,g\rangle \to \|0,e,e\rangle$	Gen. Rabi	Sec. III B, [54]
Non-degenerate three-wave mixing	Spontaneous Raman scattering	Stokes	2 resonators, 1 qubit	$\omega_a = \omega_b + \omega_q$	$\|1,0,g\rangle \to \|0,1,e\rangle$	Gen. Rabi	Sec. III C, [55]
		anti-Stokes			$\|0,1,e\rangle \to \|1,0,g\rangle$	Gen. Rabi	Sec. III C, [55]
	Stimulated Raman scattering	Stokes			$\|1,n,g\rangle \to \|0,n+1,e\rangle$	Gen. Rabi	Sec. III C
		anti-Stokes			$\|n,1,e\rangle \to \|n+1,0,g\rangle$	Gen. Rabi	Sec. III C
	Sum-frequency generation		1 resonator, 2 qubits	$\omega_a = \omega_{q1} + \omega_{q2}$	$\|0,e,e\rangle \to \|1,g,g\rangle$	Gen. Rabi	Sec. III A, [54]
			2 resonators, 1 qubit	$\omega_a + \omega_b = \omega_q$	$\|1,1,g\rangle \to \|0,0,e\rangle$	Gen. Rabi	Sec. III A
			3 resonators, 1 qubit	$\omega_a + \omega_b = \omega_c$	$\|1,1,0,g\rangle \to \|0,0,1,g\rangle$	Gen. Rabi	Sec. III A
	Difference-frequency generation		1 resonator, 2 qubits	$\omega_a = \omega_{q1} + \omega_{q2}$	$\|1,g,g\rangle \to \|0,e,e\rangle$	Gen. Rabi	Sec. III A, [54]
			2 resonators, 1 qubit	$\omega_a + \omega_b = \omega_q$	$\|0,0,e\rangle \to \|1,1,g\rangle$	Gen. Rabi	Sec. III A
			3 resonators, 1 qubit	$\omega_a + \omega_b = \omega_c$	$\|0,0,1,g\rangle \to \|1,1,0,g\rangle$	Gen. Rabi	Sec. III A

TABLE III. A summary of four-wave-mixing processes in nonlinear optics and their deterministic analogs with single atoms and virtual photons. In the case of nondegenerate four-wave mixing, the given frequencies and transitions are just some of the possibilities. For degenerate four-wave mixing with two degenerate signals, see Appendix C.

Nonlinear-optics process			**Analogous setup**	**Frequencies**	**Transition**	**Hamiltonian**	**Reference**
Degenerate four-wave mixing	Third-harmonic generation (upconversion)		1 resonator, 1 qubit	$\omega_q = 3\omega_a$	$\|3,g\rangle \to \|0,e\rangle$	Rabi	Sec. IV B, [52, 53]
			2 resonators, 1 qubit	$\omega_a = 3\omega_b$	$\|0,3,g\rangle \to \|1,0,g\rangle$	Rabi	Sec. IV B
			1 resonator, 3 qubits	$\omega_a = 3\omega_q$	$\|0,e,e,e\rangle \to \|1,g,g,g\rangle$	Rabi	Sec. IV B, [54]
	Third-subharmonic generation (downconversion)		1 resonator, 1 qubit	$\omega_q = 3\omega_a$	$\|0,e\rangle \to \|3,g\rangle$	Rabi	Sec. IV B, [52, 53]
			2 resonators, 1 qubit	$\omega_a = 3\omega_b$	$\|1,0,g\rangle \to \|0,3,g\rangle$	Rabi	Sec. IV B
			1 resonator, 3 qubits	$\omega_a = 3\omega_q$	$\|1,g,g,g\rangle \to \|0,e,e,e\rangle$	Rabi	Sec. IV B, [54]
	Hyper-Raman scattering, type I	Stokes	2 resonators, 1 qubit	$\omega_a + \omega_q = 2\omega_b$	$\|0,2,g\rangle \to \|1,0,e\rangle$	JC	Sec. IV C, [55]
		anti-Stokes		$\omega_a = 2\omega_b + \omega_q$	$\|0,2,e\rangle \to \|1,0,g\rangle$	Rabi	Sec. IV C, [55]
	Hyper-Raman scattering, type II	Stokes	2 resonators, 2 qubits	$\omega_a = \omega_b + 2\omega_q$	$\|1,0,g,g\rangle \to \|0,1,e,e\rangle$	Rabi	Sec. IV D
		anti-Stokes			$\|0,1,e,e\rangle \to \|1,0,g,g\rangle$	Rabi	Sec. IV D
Non-degenerate four-wave mixing	Type I (2 inputs, 2 outputs)		3 resonators, 1 qubit	$\omega_a + \omega_b = \omega_c + \omega_q$	$\|1,1,0,g\rangle \to \|0,0,1,e\rangle$	JC	Sec. IV A
			4 resonators, 1 qubit	$\omega_a + \omega_b = \omega_c + \omega_d$	$\|1,1,0,0,g\rangle \to \|0,0,1,1,g\rangle$	JC	Sec. IV A
			2 resonators, 2 qubits	$\omega_a + \omega_b = \omega_{q1} + \omega_{q2}$	$\|1,1,g,g\rangle \to \|0,0,e,e\rangle$	JC	Sec. IV A
			1 resonator, 3 qubits	$\omega_a + \omega_{q1} = \omega_{q2} + \omega_{q3}$	$\|1,e,g,g\rangle \to \|0,g,e,e\rangle$	JC	Sec. IV A
	Type II (3 inputs, 1 output)		3 resonators, 1 qubit	$\omega_a + \omega_b + \omega_c = \omega_q$	$\|1,1,1,g\rangle \to \|0,0,0,e\rangle$	Rabi	Sec. IV A
			4 resonators, 1 qubit	$\omega_a + \omega_b + \omega_c = \omega_d$	$\|1,1,1,0,g\rangle \to \|0,0,0,1,g\rangle$	Rabi	Sec. IV A
			2 resonators, 2 qubits	$\omega_a = \omega_b + \omega_{q1} + \omega_{q2}$	$\|0,1,e,e\rangle \to \|1,0,g,g\rangle$	Rabi	Sec. IV A
			1 resonator, 3 qubits	$\omega_a = \omega_{q1} + \omega_{q2} + \omega_{q3}$	$\|0,e,e,e\rangle \to \|1,g,g,g\rangle$	Rabi	Sec. IV A
	Type III (1 input, 3 outputs)		3 resonators, 1 qubit	$\omega_a + \omega_b + \omega_c = \omega_q$	$\|0,0,0,e\rangle \to \|1,1,1,g\rangle$	Rabi	Sec. IV A
			4 resonators, 1 qubit	$\omega_a = \omega_b + \omega_c + \omega_d$	$\|1,0,0,0,g\rangle \to \|0,1,1,1,g\rangle$	Rabi	Sec. IV A
			2 resonators, 2 qubits	$\omega_a = \omega_b + \omega_{q1} + \omega_{q2}$	$\|1,0,g,g\rangle \to \|0,1,e,e\rangle$	Rabi	Sec. IV A
			1 resonator, 3 qubits	$\omega_a = \omega_{q1} + \omega_{q2} + \omega_{q3}$	$\|1,g,g,g\rangle \to \|0,e,e,e\rangle$	Rabi	Sec. IV A

processes described here to create various superposition states with applications in quantum information processing, and we expect that adding the capabilities of nonlinear optics at the single-photon level to current quantum technology will spawn many more important applications. Considering an experimental implementation, we have shown that most, if not all, of the processes discussed here can be realized with currently available technology in circuit QED. Given that ultrastrong light-matter coupling has been demonstrated in several other solid-state systems as well, the processes proposed here could potentially also be implemented in other setups in the future.

ACKNOWLEDGMENTS

A.F.K. acknowledges support from a JSPS Postdoctoral Fellowship for Overseas Researchers. A.M. and F.N. acknowledge the support of a grant from the John Templeton Foundation. F.N. was also partially supported by the RIKEN iTHES Project, the MURI Center for Dynamic Magneto-Optics via AFOSR Award No. FA9550-14-1-0040, the Japan Society for the Promotion of Science (KAKENHI), the IMPACT program of JST, JSPS-RFBR Grant No. 17-52-50023, and CREST Grant No. JPMJCR1676.

APPENDIX A: CLASSICAL DESCRIPTION OF NONLINEAR OPTICAL PHENOMENA

Here we give a few examples showing how mixing of classical waves can be explained classically by applying the principal relation of nonlinear optics,

$$\begin{aligned}\mathbf{P} &= \epsilon_0(\chi^{(1)}\mathbf{E} + \chi^{(2)}\mathbf{E}^2 + \chi^{(3)}\mathbf{E}^3 + \ldots)\\ &= \mathbf{P}^{(1)} + \mathbf{P}^{(2)} + \mathbf{P}^{(3)} + \ldots.\end{aligned} \tag{A1}$$

In this pedagogical introduction to nonlinear optics, based on Ref. [1], we give the classical explanations of a few standard wave-mixing processes by applying the lowest-order required nonlinear polarization $\mathbf{P}^{(n)}$ and the corresponding nonlinear susceptibility $\chi^{(n)}$. Our examples include the linear (Pockels) and quadratic (Kerr) electro-optical phenomena. Second-harmonic generation in a $\chi^{(2)}$ medium was already treated in Sec. II A.

1. Wave mixing in a $\chi^{(2)}$ medium and the Pockels effect

Assume that two monochromatic scalar electric waves, $E_1(t) = E_{10}\cos(\omega_1 t)$ and $E_2(t) = E_{20}\cos(\omega_2 t)$, are applied to a medium described by the second-order frequency-independent susceptibility $\chi^{(2)}$. Then, the induced second-order polarization $P^{(2)}$ is given by

$$\begin{aligned}P^{(2)} &= \epsilon_0\chi^{(2)}E^2 = \epsilon_0\chi^{(2)}\{E_{10}\cos(\omega_1 t) + E_{20}\cos(\omega_2 t)\}^2\\ &= \epsilon_0\chi^{(2)}\big\{E_{10}^2\cos^2(\omega_1 t) + E_{20}^2\cos^2(\omega_2 t)\\ &\quad + 2E_{10}E_{20}\cos(\omega_1 t)\cos(\omega_2 t)\big\}\\ &= \frac{1}{2}\epsilon_0\chi^{(2)}\big\{E_{10}^2[1+\cos(2\omega_1 t)] + E_{20}^2[1+\cos(2\omega_2 t)]\\ &\quad + 2E_{10}E_{20}(\cos[(\omega_1-\omega_2)t] + \cos[(\omega_1+\omega_2)t])\big\}\\ &= \frac{1}{2}\epsilon_0\chi^{(2)}\big\{\big(E_{10}^2 + E_{20}^2\big) + E_{10}^2\cos(2\omega_1 t)\\ &\quad + E_{20}^2\cos(2\omega_2 t) + 2E_{10}E_{20}\cos[(\omega_1-\omega_2)t]\\ &\quad + 2E_{10}E_{20}\cos[(\omega_1+\omega_2)t]\big\}\\ &\equiv P_0^{(2)} + P_{2\omega_1}^{(2)} + P_{2\omega_2}^{(2)} + P_{\omega_1-\omega_2}^{(2)} + P_{\omega_1+\omega_2}^{(2)},\end{aligned} \tag{A2}$$

where the induced second-order nonlinear polarization $P_{\omega_x}^{(2)}$, oscillating with frequency $\omega_x = 0, 2\omega_1, \ldots$, is defined by the corresponding ω_x-dependent term in the second-last equation in Eq. (A2).

We see that this process can be interpreted as mixing of two waves with frequencies ω_1 and ω_2. Alternatively, in a general case, this effect can be interpreted as six-wave mixing if we include also the four output (mixed) frequencies $2\omega_1$, $2\omega_2$, $|\omega_1-\omega_2|$, and $\omega_1+\omega_2$. In a quantum description, the latter interpretation is conventionally applied.

In a special case, let us assume that $\omega_2 = 0$; then $E_2 = E_{20} =$ constant, and

$$P_{\omega_1-\omega_2}^{(2)} + P_{\omega_1+\omega_2}^{(2)} = 2P_{\omega_1}^{(2)} = \epsilon_0(2\chi^{(2)}E_{20})E_1(t). \tag{A3}$$

We see that the effective first-order-like susceptibility $\chi_{\text{eff}}^{(1)} \equiv 2\chi^{(2)}E_{20}$ is proportional to the amplitude of the constant electric field. This phenomenon is usually referred to as the (linear) Pockels effect or linear electro-optical effect.

A few comments can be made on the momentum (and energy) conservation when fields of frequencies ω_1 and ω_2 are mixed to generate fields with sum ($\omega_+ = \omega_1+\omega_2$) and difference ($\omega_- = |\omega_1-\omega_2|$) frequencies. These new fields can be amplified depending on which momentum condition $\mathbf{k}_+ = \mathbf{k}_1+\mathbf{k}_2$ or $\mathbf{k}_- = \mathbf{k}_1-\mathbf{k}_2$ is satisfied for the corresponding wave vectors $\mathbf{k}_j$. Usually only one of these conditions is satisfied. If both conditions are fulfilled, then the wave mixing has a local character. For example, if $\omega_1 = \omega_2 \equiv \omega$ and $\mathbf{k}_1 = \mathbf{k}_2 \equiv \mathbf{k}$, then $\omega_+ = 2\omega$, $\omega_- = 0$, $k_+ = 2k$, and $k_- = 0$.

2. Third-harmonic generation in a $\chi^{(3)}$ medium

Assume that a monochromatic electric wave $E(t) = E_0\cos(\omega t)$ is applied to a medium described solely by a third-order susceptibility $\chi^{(3)}$. Then we observe

$$\begin{aligned}P^{(3)} &= \epsilon_0\chi^{(3)}E^3 = \epsilon_0\chi^{(3)}E_0^3\cos^3(\omega t)\\ &= \epsilon_0\chi^{(3)}E_0^3\left[\frac{3\cos(\omega t)+\cos(3\omega t)}{4}\right]\\ &= \frac{3}{4}\epsilon_0\chi^{(3)}E_0^3\cos(\omega t) + \frac{1}{4}\epsilon_0\chi^{(3)}E_0^3\cos(3\omega t)\\ &= P_\omega^{(3)} + P_{3\omega}^{(3)},\end{aligned} \tag{A4}$$

where the term $P_{3\omega}^{(3)}$ describes the induced polarization, oscillating with triple the frequency of the input field, which can be interpreted as third-harmonic generation.

3. Wave mixing in a $\chi^{(3)}$ medium and the Kerr effect

Assume that two monochromatic electric beams, $E_1(t) = E_{10}\cos(\omega_1 t)$ and $E_2(t) = E_{20}\cos(\omega_2 t)$, are applied to a medium described by a third-order susceptibility $\chi^{(3)}$, and that $\chi^{(3)}$ is frequency independent. Then the third-order induced

polarization $P^{(3)}$ of the medium is given by

$$\begin{aligned} P^{(3)} &= \epsilon_0 \chi^{(3)} E^3 = \epsilon_0 \chi^{(3)} [E_{10}\cos(\omega_1 t) + E_{20}\cos(\omega_2 t)]^3 \\ &= P^{(3)}_{\omega_1} + P^{(3)}_{\omega_2} + P^{(3)}_{3\omega_1} + P^{(3)}_{3\omega_2} + P^{(3)}_{2\omega_1-\omega_2} \\ &\quad + P^{(3)}_{2\omega_1+\omega_2} + P^{(3)}_{2\omega_2-\omega_1} + P^{(3)}_{2\omega_2+\omega_1}, \end{aligned} \tag{A5}$$

where we do not give (except two terms) an explicit form of these induced third-order nonlinear polarizations $P^{(3)}_{\omega_x}$, but only indicate their frequencies ω_x.

Analogously to wave mixing in a $\chi^{(2)}$ medium, one can interpret this process as mixing of two waves with frequencies ω_1 and ω_2. Alternatively, this effect, in a general case, can be interpreted as mixing of eight waves (including the output waves) with frequencies ω_1, ω_2, $3\omega_1$, $3\omega_2$, $|2\omega_1 \pm \omega_2|$, and $|2\omega_2 \pm \omega_1|$. In a quantum description, the latter convention is usually applied.

In a special case, we have

$$P^{(3)}_{2\omega_2\pm\omega_1} = \tfrac{3}{4}\epsilon_0 \chi^{(3)} E_{20}^2 E_{10}\cos[(2\omega_2 \pm \omega_1)t]. \tag{A6}$$

If we assume that $\omega_2 = 0$, we obtain

$$P^{(3)}_{2\omega_2\pm\omega_1} = \tfrac{3}{4}\epsilon_0 \chi^{(3)} E_{20}^2 E_{10}\cos(\omega_1 t) \equiv \epsilon_0 \chi^{(1)}_{\text{eff}} E_1(t). \tag{A7}$$

Thus, the effective first-order-like susceptibility $\chi^{(1)}_{\text{eff}} \equiv \frac{3}{4}\chi^{(3)} E_{20}^2$ is proportional to the square of the constant electric field $E_2(t) = E_{20}$. This is a standard classical explanation of the Kerr effect, which is also referred to as the quadratic electro-optical effect.

APPENDIX B: PERTURBATION THEORY

In this Appendix, we show how to derive the expression for the effective coupling given in Eq. (10). In all processes we considered in Secs. III and IV, there is an initial state $|i\rangle$ and a final state $|f\rangle$ connected by the effective coupling in an effective interaction Hamiltonian

$$\hat{H}^{\text{eff}}_{\text{int}} = g_{\text{eff}} |f\rangle\langle i| + \text{H.c.} \tag{B1}$$

As stated in Sec. II B, if the shortest path between $|i\rangle$ and $|f\rangle$ is an nth-order process, the effective coupling g_{eff} is given to lowest order by

$$g_{\text{eff}} = \sum_{j_1, j_2, \ldots, j_{n-1}} \frac{V_{f j_{n-1}} \ldots V_{j_2 j_1} V_{j_1 i}}{(E_i - E_{j_1})(E_i - E_{j_2}) \ldots (E_i - E_{j_{n-1}})}, \tag{B2}$$

where the sum goes over all virtual transitions forming n-step paths between $|i\rangle$ and $|f\rangle$. The formula in Eq. (B2) can be derived by considering the Dyson series of the time evolution operator in the interaction picture,

$$\begin{aligned} \hat{U}_I(t,t_0) &= 1 - i\int_{t_0}^{t} dt' \hat{H}_{\text{int}}(t') \\ &\quad + (-i)^2 \int_{t_0}^{t} dt' \int_{t_0}^{t'} dt'' \hat{H}_{\text{int}}(t')\hat{H}_{\text{int}}(t'') + \ldots, \end{aligned} \tag{B3}$$

when the interaction Hamiltonian $\hat{H}_{\text{int}}$ is time-independent. Assuming the system starts in the eigenstate $|i\rangle$ of the noninteracting Hamiltonian at time t_0, the probability of the transition $|i\rangle \to |f\rangle$ is given to lowest (nth) order by the nth-order term in Eq. (B3), $U^{(n)}_I(t,t_0)$, through

$$\begin{aligned} &P(|i\rangle \to |f\rangle) \\ &= |\langle f|\hat{U}^{(n)}_I(t,t_0)|i\rangle|^2 = \frac{(1 - e^{i(E_f - E_i)})^2}{(E_f - E_i)^2} \\ &\quad \times \left| \sum_{j_1, j_2, \ldots, j_{n-1}} \frac{V_{f j_{n-1}} \ldots V_{j_2 j_1} V_{j_1 i}}{(E_i - E_{j_1})(E_i - E_{j_2}) \ldots (E_i - E_{j_{n-1}})} \right|^2, \end{aligned} \tag{B4}$$

which in the limit $t \to \infty$ gives the transition rate

$$\begin{aligned} &W_{(|i\rangle \to |f\rangle)} = 2\pi\delta(E_f - E_i) \\ &\quad \times \left| \sum_{j_1, j_2, \ldots, j_{n-1}} \frac{V_{f j_{n-1}} \ldots V_{j_2 j_1} V_{j_1 i}}{(E_i - E_{j_1})(E_i - E_{j_2}) \ldots (E_i - E_{j_{n-1}})} \right|^2. \end{aligned} \tag{B5}$$

This is just Fermi's golden rule, showing that the effective Hamiltonian in Eq. (B1) with the coupling strength g_{eff} given by Eq. (10) gives the correct coupling matrix element between $|i\rangle$ and $|f\rangle$.

APPENDIX C: FOUR-WAVE MIXING WITH TWO DEGENERATE FREQUENCIES

For completeness, we here show, in Fig. 10, schematic representations of the four degenerate four-wave-mixing processes where two frequencies are degenerate (omitted from Fig. 5). Analogs for these processes can be constructed in the same way as for the other four-wave mixing processes treated in Sec. IV and listed in Table III. The most obvious setup is three resonators all coupled to a single qubit. In that case, the process $|2,0,0,g\rangle \leftrightarrow |0,1,1,g\rangle$ corresponds to the type-I mixing shown in the figure. Similarly, $|2,1,0,g\rangle \leftrightarrow |0,0,1,e\rangle$ realizes analogs of the pictured type-II ($\to$) and type-III ($\leftarrow$) processes, respectively.

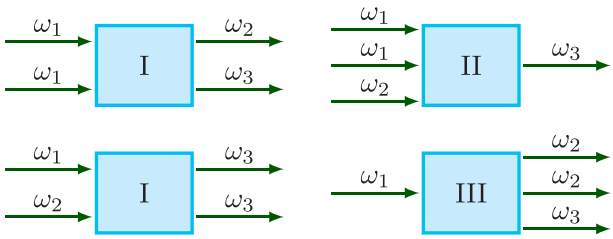

FIG. 10. Schematic representations (Feynman-like diagrams) of the four-wave-mixing processes with two degenerate frequencies. Going clockwise from the upper left corner, they are as follows: type-I four-wave mixing with the frequencies of the two incoming signals degenerate ($2\omega_1 = \omega_2 + \omega_3$), type-II four-wave mixing with the frequencies of two of the incoming signals degenerate ($2\omega_1 + \omega_2 = \omega_3$), type-III four-wave mixing with the frequencies of two of the outgoing signals degenerate ($\omega_1 = 2\omega_2 + \omega_3$), and type-I four-wave mixing with the frequencies of the two outgoing signals degenerate ($\omega_1 + \omega_2 = 2\omega_3$).

Just as for the nondegenerate mixing processes discussed in Secs. III A 2 and IV A 2, additional setups become possible if we allow at least one of the excitations to be hosted in a qubit. With two resonators coupled to a single qubit, the two type-I mixing processes shown in Fig. 10 could be emulated by $|2,0,g\rangle \leftrightarrow |0,1,e\rangle$, which we recognize as the analog of type-I hyper-Raman scattering already treated in Sec. IV C 2. The pictured type-II and type-III mixing could similarly be emulated by, e.g., the process $|2,1,g\rangle \leftrightarrow |0,0,e\rangle$. In the same way, a setup with a single resonator coupled to two qubits could realize analogs of the pictured type-I processes through the transition $|2,g,g\rangle \leftrightarrow |0,e,e\rangle$, and of the pictured type-II and type-III processes through the transition $|2,e,g\rangle \leftrightarrow |0,g,e\rangle$.

[1] P. A. Lindsay, *Introduction to Quantum Electronics* (Pitman, London, 1975).

[2] S. Kielich, *Molecular Nonlinear Optics* (Nauka, Moscow, 1981).

[3] Y. R. Shen, *The Principles of Nonlinear Optics* (Wiley, New York, 1984).

[4] R. W. Boyd, *Nonlinear Optics*, 3rd ed. (Elsevier, Amsterdam, 2008).

[5] P. A. Franken, A. E. Hill, C. W. Peters, and G. Weinreich, Generation of Optical Harmonics, Phys. Rev. Lett. **7**, 118 (1961).

[6] F. V. Bunkin, Y. A. Kravtsov, and G. A. Lyakhov, Acoustic analogues of nonlinear-optics phenomena, Sov. Phys. Usp. **29**, 607 (1986).

[7] M. F. Hamilton and D. T. Blackstock (eds.), *Nonlinear Acoustics: Theory and Applications* (Academic Press, New York, 1998).

[8] M. G. Cottam (ed.), *Linear and Nonlinear Spin Waves in Magnetic Films and Superlattices* (World Scientific, Singapore, 1994).

[9] G. Lenz, P. Meystre, and E. M. Wright, Nonlinear Atom Optics, Phys. Rev. Lett. **71**, 3271 (1993).

[10] S. L. Rolston and W. D. Phillips, Nonlinear and quantum atom optics, Nature (London) **416**, 219 (2002).

[11] S. Savel'ev, A. L. Rakhmanov, V. A. Yampol'skii, and F. Nori, Analogues of nonlinear optics using terahertz Josephson plasma waves in layered superconductors, Nat. Phys. **2**, 521 (2006).

[12] M. Kauranen and A. V. Zayats, Nonlinear plasmonics, Nat. Photonics **6**, 737 (2012).

[13] I. Buluta and F. Nori, Quantum simulators, Science **326**, 108 (2009).

[14] P. D. Nation, J. R. Johansson, M. P. Blencowe, and F. Nori, Colloquium: Stimulating uncertainty: Amplifying the quantum vacuum with superconducting circuits, Rev. Mod. Phys. **84**, 1 (2012).

[15] I. M. Georgescu, S. Ashhab, and F. Nori, Quantum simulation, Rev. Mod. Phys. **86**, 153 (2014).

[16] J. Q. You and F. Nori, Atomic physics and quantum optics using superconducting circuits, Nature (London) **474**, 589 (2011).

[17] I. I. Rabi, Space quantization in a gyrating magnetic field, Phys. Rev. **51**, 652 (1937).

[18] G. Günter, A. A. Anappara, J. Hees, A. Sell, G. Biasiol, L. Sorba, S. De Liberato, C. Ciuti, A. Tredicucci, A. Leitenstorfer, and R. Huber, Sub-cycle switch-on of ultrastrong light-matter interaction, Nature (London) **458**, 178 (2009).

[19] P. Forn-Díaz, J. Lisenfeld, D. Marcos, J. J. García-Ripoll, E. Solano, C. J. P. M. Harmans, and J. E. Mooij, Observation of the Bloch-Siegert Shift in a Qubit-Oscillator System in the Ultrastrong Coupling Regime, Phys. Rev. Lett. **105**, 237001 (2010).

[20] T. Niemczyk, F. Deppe, H. Huebl, E. P. Menzel, F. Hocke, M. J. Schwarz, J. J. Garcia-Ripoll, D. Zueco, T. Hümmer, E. Solano, A. Marx, and R. Gross, Circuit quantum electrodynamics in the ultrastrong-coupling regime, Nat. Phys. **6**, 772 (2010).

[21] Y. Todorov, A. M. Andrews, R. Colombelli, S. De Liberato, C. Ciuti, P. Klang, G. Strasser, and C. Sirtori, Ultrastrong Light-Matter Coupling Regime with Polariton Dots, Phys. Rev. Lett. **105**, 196402 (2010).

[22] T. Schwartz, J. A. Hutchison, C. Genet, and T. W. Ebbesen, Reversible Switching of Ultrastrong Light-Molecule Coupling, Phys. Rev. Lett. **106**, 196405 (2011).

[23] G. Scalari, C. Maissen, D. Turcinkova, D. Hagenmuller, S. De Liberato, C. Ciuti, C. Reichl, D. Schuh, W. Wegscheider, M. Beck, and J. Faist, Ultrastrong coupling of the cyclotron transition of a 2D electron gas to a THz metamaterial, Science **335**, 1323 (2012).

[24] M. Geiser, F. Castellano, G. Scalari, M. Beck, L. Nevou, and J. Faist, Ultrastrong Coupling Regime and Plasmon Polaritons in Parabolic Semiconductor Quantum Wells, Phys. Rev. Lett. **108**, 106402 (2012).

[25] S. Kéna-Cohen, S. A. Maier, and D. D. C. Bradley, Ultrastrongly coupled exciton-polaritons in metal-clad organic semiconductor microcavities, Adv. Opt. Mater. **1**, 827 (2013).

[26] S. Gambino, M. Mazzeo, A. Genco, O. Di Stefano, S. Savasta, S. Patanè, D. Ballarini, F. Mangione, G. Lerario, D. Sanvitto, and G. Gigli, Exploring light-matter interaction phenomena under ultrastrong coupling regime, ACS Photonics **1**, 1042 (2014).

[27] C. Maissen, G. Scalari, F. Valmorra, M. Beck, J. Faist, S. Cibella, R. Leoni, C. Reichl, C. Charpentier, and W. Wegscheider, Ultrastrong coupling in the near field of complementary split-ring resonators, Phys. Rev. B **90**, 205309 (2014).

[28] M. Goryachev, W. G. Farr, D. L. Creedon, Y. Fan, M. Kostylev, and M. E. Tobar, High-Cooperativity Cavity QED with Magnons at Microwave Frequencies, Phys. Rev. Appl. **2**, 054002 (2014).

[29] A. Baust, E. Hoffmann, M. Haeberlein, M. J. Schwarz, P. Eder, J. Goetz, F. Wulschner, E. Xie, L. Zhong, F. Quijandría, D. Zueco, J.-J. García Ripoll, L. García-Álvarez, G. Romero, E. Solano, K. G. Fedorov, E. P. Menzel, F. Deppe, A. Marx, and R. Gross, Ultrastrong coupling in two-resonator circuit QED, Phys. Rev. B **93**, 214501 (2016).

[30] P. Forn-Díaz, J. J. García-Ripoll, B. Peropadre, J.-L. Orgiazzi, M. A. Yurtalan, R. Belyansky, C. M. Wilson, and A. Lupascu, Ultrastrong coupling of a single artificial atom to an electromagnetic continuum in the nonperturbative regime, Nat. Phys. **13**, 39 (2017).

[31] F. Yoshihara, T. Fuse, S. Ashhab, K. Kakuyanagi, S. Saito, and K. Semba, Superconducting qubit-oscillator circuit beyond the ultrastrong-coupling regime, Nat. Phys. **13**, 44 (2017).

[32] Z. Chen, Y. Wang, T. Li, L. Tian, Y. Qiu, K. Inomata, F. Yoshihara, S. Han, F. Nori, J. S. Tsai, and J. Q. You, Multiphoton sideband transitions in an ultrastrongly coupled circuit quantum electrodynamics system, arXiv:1602.01584.

[33] J. George, T. Chervy, A. Shalabney, E. Devaux, H. Hiura, C. Genet, and T. W. Ebbesen, Multiple Rabi Splittings under Ultrastrong Vibrational Coupling, Phys. Rev. Lett. **117**, 153601 (2016).

[34] N. K. Langford, R. Sagastizabal, M. Kounalakis, C. Dickel, A. Bruno, F. Luthi, D. J. Thoen, A. Endo, and L. DiCarlo, Experimentally simulating the dynamics of quantum light and matter at ultrastrong coupling, arXiv:1610.10065.

[35] J. Braumüller, M. Marthaler, A. Schneider, A. Stehli, H. Rotzinger, M. Weides, and A. V. Ustinov, Analog quantum simulation of the Rabi model in the ultrastrong-coupling regime, arXiv:1611.08404.

[36] F. Yoshihara, T. Fuse, S. Ashhab, K. Kakuyanagi, S. Saito, and K. Semba, Characteristic spectra of circuit quantum electrodynamics systems from the ultrastrong to the deep strong coupling regime, Phys. Rev. A **95**, 053824 (2017).

[37] A. Wallraff, D. I. Schuster, A. Blais, L. Frunzio, R.-S. Huang, J. Majer, S. Kumar, S. M. Girvin, and R. J. Schoelkopf, Strong coupling of a single photon to a superconducting qubit using circuit quantum electrodynamics, Nature (London) **431**, 162 (2004).

[38] A. Blais, R.-S. Huang, A. Wallraff, S. M. Girvin, and R. J. Schoelkopf, Cavity quantum electrodynamics for superconducting electrical circuits: An architecture for quantum computation, Phys. Rev. A **69**, 062320 (2004).

[39] Z.-L. Xiang, S. Ashhab, J. Q. You, and F. Nori, Hybrid quantum circuits: Superconducting circuits interacting with other quantum systems, Rev. Mod. Phys. **85**, 623 (2013).

[40] S. De Liberato, C. Ciuti, and I. Carusotto, Quantum Vacuum Radiation Spectra from a Semiconductor Microcavity with a Time-Modulated Vacuum Rabi Frequency, Phys. Rev. Lett. **98**, 103602 (2007).

[41] S. Ashhab and F. Nori, Qubit-oscillator systems in the ultrastrong-coupling regime and their potential for preparing nonclassical states, Phys. Rev. A **81**, 042311 (2010).

[42] X. Cao, J. Q. You, H. Zheng, A. G. Kofman, and F. Nori, Dynamics and quantum Zeno effect for a qubit in either a low- or high-frequency bath beyond the rotating-wave approximation, Phys. Rev. A **82**, 022119 (2010).

[43] J. Casanova, G. Romero, I. Lizuain, J. J. García-Ripoll, and E. Solano, Deep Strong Coupling Regime of the Jaynes-Cummings Model, Phys. Rev. Lett. **105**, 263603 (2010).

[44] F. Beaudoin, J. M. Gambetta, and A. Blais, Dissipation and ultrastrong coupling in circuit QED, Phys. Rev. A **84**, 043832 (2011).

[45] A. Ridolfo, M. Leib, S. Savasta, and M. J. Hartmann, Photon Blockade in the Ultrastrong Coupling Regime, Phys. Rev. Lett. **109**, 193602 (2012).

[46] R. Stassi, A. Ridolfo, O. Di Stefano, M. J. Hartmann, and S. Savasta, Spontaneous Conversion from Virtual to Real Photons in the Ultrastrong-Coupling Regime, Phys. Rev. Lett. **110**, 243601 (2013).

[47] S. De Liberato, Light-Matter Decoupling in the Deep Strong Coupling Regime: The Breakdown of the Purcell Effect, Phys. Rev. Lett. **112**, 016401 (2014).

[48] E. Sanchez-Burillo, D. Zueco, J. J. Garcia-Ripoll, and L. Martin-Moreno, Scattering in the Ultrastrong Regime: Nonlinear Optics with One Photon, Phys. Rev. Lett. **113**, 263604 (2014).

[49] J. Lolli, A. Baksic, D. Nagy, V. E. Manucharyan, and C. Ciuti, Ancillary Qubit Spectroscopy of Vacua in Cavity and Circuit Quantum Electrodynamics, Phys. Rev. Lett. **114**, 183601 (2015).

[50] M. Cirio, S. De Liberato, N. Lambert, and F. Nori, Ground State Electroluminescence, Phys. Rev. Lett. **116**, 113601 (2016).

[51] O. Di Stefano, R. Stassi, L. Garziano, A. F. Kockum, S. Savasta, and F. Nori, Feynman-diagrams approach to the quantum Rabi model for ultrastrong cavity QED: Stimulated emission and reabsorption of virtual particles dressing a physical excitation, New J. Phys. **19**, 053010 (2017).

[52] K. K. W. Ma and C. K. Law, Three-photon resonance and adiabatic passage in the large-detuning Rabi model, Phys. Rev. A **92**, 023842 (2015).

[53] L. Garziano, R. Stassi, V. Macrì, A. F. Kockum, S. Savasta, and F. Nori, Multiphoton quantum Rabi oscillations in ultrastrong cavity QED, Phys. Rev. A **92**, 063830 (2015).

[54] L. Garziano, V. Macrì, R. Stassi, O. Di Stefano, F. Nori, and S. Savasta, One Photon Can Simultaneously Excite Two or More Atoms, Phys. Rev. Lett. **117**, 043601 (2016).

[55] A. F. Kockum, V. Macrì, L. Garziano, S. Savasta, and F. Nori, Frequency conversion in ultrastrong cavity QED, arXiv:1701.07973 [Sci. Rep. (to be published)].

[56] R. Stassi, V. Macrì, A. F. Kockum, O. Di Stefano, A. Miranowicz, S. Savasta, and F. Nori, Quantum nonlinear optics without photons, arXiv:1702.00660.

[57] M. H. Devoret and R. J. Schoelkopf, Superconducting circuits for quantum information: An outlook, Science **339**, 1169 (2013).

[58] D. E. Chang, V. Vuletić, and M. D. Lukin, Quantum nonlinear optics—photon by photon, Nat. Photonics **8**, 685 (2014).

[59] B. Peropadre, G. G. Guerreschi, J. Huh, and A. Aspuru-Guzik, Proposal for Microwave Boson Sampling, Phys. Rev. Lett. **117**, 140505 (2016).

[60] E. T. Jaynes and F. W. Cummings, Comparison of quantum and semiclassical radiation theories with application to the beam maser, Proc. IEEE **51**, 89 (1963).

[61] T. P. Orlando, J. E. Mooij, L. Tian, C. H. van der Wal, L. S. Levitov, S. Lloyd, and J. J. Mazo, Superconducting persistent-current qubit, Phys. Rev. B **60**, 15398 (1999).

[62] T. Lindström, C. H. Webster, J. E. Healey, M. S. Colclough, C. M. Muirhead, and A. Y. Tzalenchuk, Circuit QED with a flux qubit strongly coupled to a coplanar transmission line resonator, Supercond. Sci. Technol. **20**, 814 (2007).

[63] F. Deppe, M. Mariantoni, E. P. Menzel, A. Marx, S. Saito, K. Kakuyanagi, H. Tanaka, T. Meno, K. Semba, H. Takayanagi, E. Solano, and R. Gross, Two-photon probe of the Jaynes-Cummings model and controlled symmetry breaking in circuit QED, Nat. Phys. **4**, 686 (2008).

[64] J. Bourassa, J. M. Gambetta, A. A. Abdumalikov, O. Astafiev, Y. Nakamura, and A. Blais, Ultrastrong coupling regime of cavity QED with phase-biased flux qubits, Phys. Rev. A **80**, 032109 (2009).

[65] K. Moon and S. M. Girvin, Theory of Microwave Parametric Down-Conversion and Squeezing Using Circuit QED, Phys. Rev. Lett. **95**, 140504 (2005).

[66] J. R. Johansson, P. D. Nation, and F. Nori, QuTiP: An open-source Python framework for the dynamics of open quantum systems, Comput. Phys. Commun. **183**, 1760 (2012).

[67] J. R. Johansson, P. D. Nation, and F. Nori, QuTiP 2: A Python framework for the dynamics of open quantum systems, Comput. Phys. Commun. **184**, 1234 (2013).

[68] A. Miranowicz and S. Kielich, Quantum-statistical theory of Raman scattering processes, Adv. Chem. Phys. **85**(III), 531 (1994).

[69] M. Göppert-Mayer, Über elementarakte mit zwei quantensprüngen, Ann. Phys. **401**, 273 (1931).

[70] M. Boissonneault, J. M. Gambetta, and A. Blais, Dispersive regime of circuit QED: Photon-dependent qubit dephasing and relaxation rates, Phys. Rev. A **79**, 013819 (2009).

[71] S. E. Nigg, H. Paik, B. Vlastakis, G. Kirchmair, S. Shankar, L. Frunzio, M. H. Devoret, R. J. Schoelkopf, and S. M. Girvin, Black-Box Superconducting Circuit Quantization, Phys. Rev. Lett. **108**, 240502 (2012).

[72] G. Zhu, D. G. Ferguson, V. E. Manucharyan, and J. Koch, Circuit QED with fluxonium qubits: Theory of the dispersive regime, Phys. Rev. B **87**, 024510 (2013).

[73] G. Kirchmair, B. Vlastakis, Z. Leghtas, S. E. Nigg, H. Paik, E. Ginossar, M. Mirrahimi, L. Frunzio, S. M. Girvin, and R. J. Schoelkopf, Observation of quantum state collapse and revival due to the single-photon Kerr effect, Nature (London) **495**, 205 (2013).

[74] E. T. Holland, B. Vlastakis, R. W. Heeres, M. J. Reagor, U. Vool, Z. Leghtas, L. Frunzio, G. Kirchmair, M. H. Devoret, M. Mirrahimi, and R. J. Schoelkopf, Single-Photon-Resolved Cross-Kerr Interaction for Autonomous Stabilization of Photon-Number States, Phys. Rev. Lett. **115**, 180501 (2015).

[75] B. Fan, A. F. Kockum, J. Combes, G. Johansson, I.-C. Hoi, C. M. Wilson, P. Delsing, G. J. Milburn, and T. M. Stace, Breakdown of the Cross-Kerr Scheme for Photon Counting, Phys. Rev. Lett. **110**, 053601 (2013).

[76] I.-C. Hoi, A. F. Kockum, T. Palomaki, T. M. Stace, B. Fan, L. Tornberg, S. R. Sathyamoorthy, G. Johansson, P. Delsing, and C. M. Wilson, Giant Cross-Kerr Effect for Propagating Microwaves Induced by an Artificial Atom, Phys. Rev. Lett. **111**, 053601 (2013).

[77] M. Stern, G. Catelani, Y. Kubo, C. Grezes, A. Bienfait, D. Vion, D. Esteve, and P. Bertet, Flux Qubits with Long Coherence Times for Hybrid Quantum Circuits, Phys. Rev. Lett. **113**, 123601 (2014).

[78] J.-L. Orgiazzi, C. Deng, D. Layden, R. Marchildon, F. Kitapli, F. Shen, M. Bal, F. R. Ong, and A. Lupascu, Flux qubits in a planar circuit quantum electrodynamics architecture: Quantum control and decoherence, Phys. Rev. B **93**, 104518 (2016).

[79] J. Q. You, X. Hu, S. Ashhab, and F. Nori, Low-decoherence flux qubit, Phys. Rev. B **75**, 140515 (2007).

[80] F. Yan, S. Gustavsson, A. Kamal, J. Birenbaum, A. P. Sears, D. Hover, T. J. Gudmundsen, D. Rosenberg, G. Samach, S. Weber, J. L. Yoder, T. P. Orlando, J. Clarke, A. J. Kerman, and W. D. Oliver, The flux qubit revisited to enhance coherence and reproducibility, Nat. Commun. **7**, 12964 (2016).

[81] C. Rigetti, J. M. Gambetta, S. Poletto, B. L. T. Plourde, J. M. Chow, A. D. Córcoles, J. A. Smolin, S. T. Merkel, J. R. Rozen, G. A. Keefe, M. B. Rothwell, M. B. Ketchen, and M. Steffen, Superconducting qubit in a waveguide cavity with a coherence time approaching 0.1 ms, Phys. Rev. B **86**, 100506 (2012).

[82] X. Y. Jin, A. Kamal, A. P. Sears, T. Gudmundsen, D. Hover, J. Miloshi, R. Slattery, F. Yan, J. Yoder, T. P. Orlando, S. Gustavsson, and W. D. Oliver, Thermal and Residual Excited-State Population in a 3D Transmon Qubit, Phys. Rev. Lett. **114**, 240501 (2015).

[83] A. Megrant, C. Neill, R. Barends, B. Chiaro, Y. Chen, L. Feigl, J. Kelly, E. Lucero, M. Mariantoni, P. J. J. O'Malley, D. Sank, A. Vainsencher, J. Wenner, T. C. White, Y. Yin, J. Zhao, C. J. Palmstrøm, J. M. Martinis, and A. N. Cleland, Planar superconducting resonators with internal quality factors above one million, Appl. Phys. Lett. **100**, 113510 (2012).

[84] M. Reagor, H. Paik, G. Catelani, L. Sun, C. Axline, E. Holland, I. M. Pop, N. A. Masluk, T. Brecht, L. Frunzio, M. H. Devoret, L. Glazman, and R. J. Schoelkopf, Reaching 10 ms single photon lifetimes for superconducting aluminum cavities, Appl. Phys. Lett. **102**, 192604 (2013).

5.7 Paper VII: Quantum Nonlinear Optics without Photons

PHYSICAL REVIEW A **96**, 023818 (2017)

Quantum nonlinear optics without photons

Roberto Stassi,[1] Vincenzo Macrì,[1,2] Anton Frisk Kockum,[1] Omar Di Stefano,[1] Adam Miranowicz,[1,3] Salvatore Savasta,[1,2] and Franco Nori[1,4]

[1]*Center for Emergent Matter Science, RIKEN, Saitama 351-0198, Japan*

[2]*Dipartimento di Scienze Matematiche e Informatiche, Scienze Fisiche e Scienze della Terra, Università di Messina, I-98166 Messina, Italy*

[3]*Faculty of Physics, Adam Mickiewicz University, PL-61-614 Poznan, Poland*

[4]*Physics Department, University of Michigan, Ann Arbor, Michigan 48109-1040, USA*

(Received 28 February 2017; published 9 August 2017)

Spontaneous parametric down-conversion is a well-known process in quantum nonlinear optics in which a photon incident on a nonlinear crystal spontaneously splits into two photons. Here we propose an analogous physical process where one excited atom directly transfers its excitation to a pair of spatially separated atoms with probability approaching 1. The interaction is mediated by the exchange of *virtual* rather than *real* photons. This nonlinear atomic process is coherent and reversible, so the pair of excited atoms can transfer the excitation back to the first one: the atomic analog of sum-frequency generation of light. The parameters used to investigate this process correspond to experimentally demonstrated values in ultrastrong circuit quantum electrodynamics. This approach can be extended to realize other nonlinear interatomic processes, such as four-atom mixing, and is an attractive architecture for the realization of quantum devices on a chip. We show that four-qubit mixing can efficiently implement quantum repetition codes and, thus, can be used for error-correction codes.

DOI: 10.1103/PhysRevA.96.023818

I. INTRODUCTION

It is highly desirable to couple distant qubits for quantum-information applications [1,2]. One implementation of such a quantum bus has been demonstrated using microwave photons confined in a transmission-line cavity to couple two superconducting qubits on opposite sides of a chip [3]. Interestingly, the interaction between the two qubits is mediated by the exchange of *virtual* rather than *real* photons, avoiding cavity-induced losses [3]. The effective qubit-qubit interaction is the result of the exchange of virtual photons with the cavity and gives rise to a qubit-qubit avoided level crossing. At the minimum splitting, the eigenstates of the system are symmetric and antisymmetric superpositions of the two qubit states $|e,g\rangle$ and $|g,e\rangle$, where $|g\rangle$ ($|e\rangle$) labels the ground (excited) state of the qubits. When the two qubits have the *same* transition energy, an excitation in one qubit can be coherently transferred to the other qubit by virtually becoming a photon in the cavity [3]. When the qubits have different transition energies, the interaction is effectively turned off. The absence of cavity-induced losses, due to the virtual nature of the quantum bus, is useful especially in the presence of intrinsically lossy interaction channels. For example, it has been shown theoretically [4] that virtual plasmon polaritons in realistic one-dimensional subwavelength waveguides are excellent candidates to act as mediators for achieving a high degree of entanglement between two distant qubits.

Here we propose a generalization of the qubit-qubit coupling via virtual bosons, which enables the interaction of multiple ($N > 2$) spatially separated qubits with *different* transition frequencies. For example, we show that, in analogy to the frequency-mixing processes of nonlinear optics, one qubit of given transition frequency ω_3 can coherently transfer its excitation to a pair of qubits (1 and 2) if $\omega_1 + \omega_2 = \omega_3$. The results presented here open the way to *nonlinear optical processes without real photons*. Instead, virtual photons, which are *not* subject to cavity-induced losses and decoherence, drive the interaction between spatially separated and non-degenerate qubits. While the qubit-qubit resonant excitation transfer can be well described by the Tavis-Cummings (TC) model [5], the process proposed here cannot be described without including the counter-rotating terms in the atom-field interaction Hamiltonian, neglected in the TC model. Although the Hamiltonian of a realistic atom-cavity system contains counter-rotating terms (allowing the simultaneous creation or annihilation of an excitation in both atom and cavity mode), these terms can be safely neglected for coupling rates that are small with respect to the atomic transition frequency and the cavity-mode resonance frequency. However, when the coupling rate increases, the counter-rotating terms start to play an important role, giving rise to a new regime of cavity quantum electrodynamics (QED). This ultrastrong-coupling (USC) regime was recently realized in a variety of solid-state systems [6–22]. This opens the door to the study of the physics of virtual processes that do not conserve the number of excitations [23–31]. Recently, it has been shown that, through higher-order processes where virtual photons are created and annihilated, an effective deterministic coupling between two states of such a system can be created giving rise to new effects such as multiphoton Rabi oscillations [32–34] and a single photon exciting multiple atoms [35]. Moreover, it has been shown that almost any analog of nonlinear optical processes is feasible [36] without the need for high-intensity driving fields. The results presented here go one remarkable step forward, beyond Ref. [36], showing that nonlinear optical processes involving only atoms, without the need for *real* photons, are also feasible.

In quantum nonlinear optics, the effective interaction Hamiltonian for a three-mode parametric process can be written as [37]

$$\hat{V}_{\rm c}^{(3)} = K^{(3)}\,\hat{a}_1^\dagger \hat{a}_2^\dagger \hat{a}_3 + \text{H.c.}, \tag{1}$$

where $\hat{a}_i$ and $\hat{a}_i^\dagger$ are photon destruction and creation operators for the ith mode, and $K^{(3)}$ is a constant describing the strength of the nonlinear interaction. This Hamiltonian describes well-known nonlinear optical processes, such as sum-frequency generation and spontaneous parametric down-conversion. The latter process is used especially as a source of entangled photon pairs and of single photons. Analogously, the process proposed here can be described by the following effective three-qubit Hamiltonian,

$$\hat{V}^{(3)} = J^{(3)}\,\hat{\sigma}_+^{(1)}\hat{\sigma}_+^{(2)}\hat{\sigma}_-^{(3)} + \text{H.c.}, \tag{2}$$

where $\hat{\sigma}_\pm^{(i)}$ are the raising (+) and lowering (−) Pauli operators for qubit i, and the effective coupling $J^{(3)}$, as we show, can be calculated by perturbation theory. This three-body effective interatomic interaction describes three-qubit-mixing (3QM) processes as the coherent and reversible transfer of an excitation from one qubit to two spatially separated qubits or vice versa. We show that four-qubit mixing (4QM), described by the effective Hamiltonian

$$\hat{V}_I^{(4)} = J^{(4)}\,\hat{\sigma}_-^{(1)}\hat{\sigma}_-^{(2)}\hat{\sigma}_+^{(3)}\hat{\sigma}_+^{(4)} + \text{H.c.}, \tag{3}$$

is also possible, where $J^{(4)}$ is the effective coupling strength. The four-wave mixing of light [38] arises from third-order optical nonlinearities. In typical cases, a photon of frequency ω_4 results from the annihilation of photons at ω_1 and ω_2 and the stimulated emission of one at ω_3 with $\omega_4 + \omega_3 = \omega_1 + \omega_2$. The process can also be spontaneous, occurring even in the absence of stimulation at ω_3. The effective potential in Eq. (3) enables the simultaneous excitation transfer from qubits 1 and 2 to qubits 3 and 4 when the qubit transition frequencies satisfy the relation $\omega_1 + \omega_2 = \omega_3 + \omega_4$, which is an interatomic scattering process without the presence of real photons. This process is the qubit analog of the spontaneous four-wave mixing of light (see, e.g., Ref. [39]). In the following we refer to it as type-I 4QM in order to distinguish it from a different type of 4QM (type II), achievable in our system in the USC regime when $\omega_4 = \omega_1 + \omega_2 + \omega_3$. This latter process can efficiently perform quantum repetition codes after a proper evolution time. We show that such spontaneous evolution of the system can be used for error-correction codes [40,41] for encoding, decoding, and error-syndrome detection.

Note that the framework proposed here is different from nonlinear atom optics [42], where the atomic center-of-mass degree of freedom is involved. Coherent matter waves in the form of Bose-Einstein condensates have led to the development of nonlinear and quantum atom optics, where atomic waves are manipulated in a manner analogous to the manipulation of light [43,44]. For example, coherent four-wave mixing (in which three sodium matter waves of differing momenta mix to produce a fourth wave with another momentum) has been demonstrated experimentally [45].

It has also been shown that a system of trapped ions can be used to implement spin models with three-body interactions [46]. However, in contrast to the framework proposed here, where the effective interaction is enforced by the field quantum vacuum only, in trapped ions the effective three-spin interactions are induced by external lasers.

As we show below, the effective Hamiltonians in Eqs. (2) and (3) can be derived from a generalized Dicke Hamiltonian [47], describing three or more qubits interacting with the same oscillator (cavity mode). The interaction Hamiltonian also includes a longitudinal coupling term [48], which arises when the inversion symmetry of the potential energy of the artificial atoms (qubits) is broken [49,50].

II. RESULTS

A. Description of the system

Here we examine a quantum system of N two-level atoms (with possible symmetry-broken potentials) coupled to a single-mode resonator. The Hamiltonian describing this system is (e.g., Refs. [10,28])

$$\hat{H}_0 = \hat{H}_\text{q} + \hat{H}_\text{c} + \hat{V}, \tag{4}$$

where (using $\hbar = 1$) $\hat{H}_\text{q} = \sum_i (\omega_i/2)\,\hat{\sigma}_z^{(i)}$ and $\hat{H}_\text{c} = \omega_\text{c}\,\hat{a}^\dagger\hat{a}$ describe the qubit and cavity Hamiltonians, respectively, in the absence of interaction. The qubits-cavity interaction is

$$\hat{V} = \hat{X}\sum_i \lambda_i\left(\cos\theta_i\,\hat{\sigma}_x^{(i)} + \sin\theta_i\,\hat{\sigma}_z^{(i)}\right), \tag{5}$$

where $\hat{X} = \hat{a} + \hat{a}^\dagger$, $\hat{\sigma}_x^{(i)}$ and $\hat{\sigma}_z^{(i)}$ are Pauli operators for the ith qubit, λ_i are the coupling rates of each qubit to the cavity mode, and θ_i are parameters determining the relative contribution of the transverse and longitudinal couplings. For $\theta_i = 0$, the parity of qubit i is conserved. For flux qubits, the angles θ_i, as well as the transition frequencies ω_i, can be continuously and individually tuned by changing the external flux biases [10,48]. In contrast to the TC model, the Hamiltonian in Eq. (4) explicitly contains counter-rotating terms of the form $\hat{\sigma}_+^{(i)}\hat{a}^\dagger$, $\hat{\sigma}_-^{(i)}\hat{a}$, $\hat{\sigma}_z^{(i)}\hat{a}^\dagger$, and $\hat{\sigma}_z^{(i)}\hat{a}$. The first (second) term creates (destroys) two excitations, while the third (fourth) term creates (destroys) one excitation. Equation (4) represents the simplest Hamiltonian describing the interaction of N atoms (with possible symmetry-broken potentials) with the electromagnetic field of a cavity beyond the rotating-wave approximation (RWA). This model is well suited for describing atoms with very large anharmonicity, such as flux qubits. However, we expect that the results presented below also apply, at least qualitatively, to more general atom-cavity systems when additional atomic levels are involved.

In the case of two qubits ($i = 1,2$), dropping the counter-rotating terms, considering the dispersive regime ($|\Delta_i| = |\omega_i - \omega_\text{c}| \gg \lambda_i$), and applying second-order perturbation theory, it is possible to derive from the atom-cavity interaction Hamiltonian [see Eq. (4)] the following effective interaction Hamiltonian [3,51]:

$$\hat{V}^{(2)} = J^{(2)}\,\hat{\sigma}_+^{(2)}\hat{\sigma}_-^{(1)} + \text{H.c.}, \tag{6}$$

where $J^{(2)} = \lambda_1\,\lambda_2(1/\Delta_1 + 1/\Delta_2)/2$. In this regime, no energy is exchanged between the qubits and the cavity. This qubit-qubit interaction is the result of virtual exchange of photons with the cavity. It gives rise to a qubit-qubit avoided level crossing when the transition energy of one of the two qubits is continuously tuned across the fixed transition energy of the other. When the qubits are degenerate, an excitation in one qubit can be transferred to the other qubit by virtually becoming a photon in the cavity. However, when the qubits are nondegenerate, $|\omega_1 - \omega_2| \gg J^{(2)}$, this process does not

conserve energy and, therefore, the interaction is effectively turned off.

The dispersive-regime condition $|\Delta_i| = |\omega_i - \omega_c| \gg \lambda_i$ is necessary to enable the virtual exchange of photons. Moreover, in order to ensure that only a negligible population of real photons is present, the atom-cavity detuning has to be much larger than the atomic and photonic decoherence rates.

Throughout this paper, we consider a single-mode optical resonator. Many circuit-QED experiments use an LC resonator, which only has a single mode. When additional modes are considered, the dispersive-regime conditions have to hold for all the modes. Defining $|\Delta_{i,n}| = |\omega_i - \omega_{c,n}|$, where $\omega_{c,n}$ is the nth mode frequency, the conditions are $|\Delta_{i,n}| \gg \lambda_i$ and $|\Delta_{i,n}| \gg \kappa_n$, where κ_n is the decay rate of the nth mode. If these conditions are satisfied, following the procedure of Ref. [51], it is straightforward to find $J^{(2)} = \sum_n [\lambda_{1,n}\,\lambda_{2,n}(1/\Delta_{1,n} + 1/\Delta_{2,n})/2]$. This series is expected to converge, owing to the suppression of light-matter coupling $\lambda_{i,n}$ at high frequencies (see, e.g., Ref. [52]). If the lowest-frequency mode is not too far detuned from the atomic transition frequencies, and the modes are well separated spectrally, only the lowest-frequency mode will provide a significant contribution. The experimental results shown in Ref. [3], obtained using a $\lambda/4$ coplanar waveguide resonator, are very well described considering a single mode, since higher-energy modes are too far off resonance to give a significant contribution. Analogous considerations apply to the processes described here. On the contrary, in a large cavity ($l \gg \lambda_i$) or in a transmission line, the modes constitute either a quasicontinuum or a continuum, and the single-mode description adopted here does not work. In this case, one possibility to realize a qubit-qubit interaction mediated by virtual photons is to consider atoms with transition frequencies outside the frequency bandwidth of the photonic system.

In the following, we show how the Hamiltonian in Eq. (4) can also give rise to effective qubit-qubit interactions involving more than two qubits. Specifically, we consider nonlinear interatomic processes involving nondegenerate qubits, such as 3QM and 4QM.

B. Three-qubit mixing

Here we consider three nondegenerate qubits of transition frequencies $\omega_1 \neq \omega_2 \neq \omega_3$ coupled to a cavity mode [see Fig. 1(a)]. Figure 1(b) shows the energy levels for the excited lowest-energy states as a function of the frequency of qubit 3, obtained by numerically diagonalizing Eq. (4). For each value of ω_3, the energy scale is chosen such that the ground-state energy is equal to zero. All the parameters are provided in terms of a fixed reference frequency ω_0. We assume that qubits 1 and 2 are ultrastrongly coupled to the cavity mode, while the coupling strength of qubit 3 with the cavity mode is lower. We used $\lambda_3/\omega_0 = 5 \times 10^{-3}$, $\lambda_1/\omega_0 = \lambda_2/\omega_0 = 0.13$, $\theta_i = \pi/6$ for all the qubits, $\omega_1/\omega_0 = 0.4$, $\omega_2/\omega_0 = 0.6$, and $\omega_c = \omega_0 + 2.5\lambda_1$. The lowest-energy horizontal line (with $\omega/\omega_0 \approx 0.4$) corresponds to the excitation of qubit 1. We indicate this state as $|\psi_1\rangle = |e,g,g,0\rangle$, where the first three entries in the ket describe the states of the three qubits and the last entry describes the cavity-mode state. We observe that this eigenstate, corresponding to the excitation of the *physical* qubit 1, can differ from the bare state $|e,g,g,0\rangle_b$, describing the excitation of qubit 1 in the absence of its interaction with the cavity mode (see, e.g., Ref. [53]). Owing to the dressing effects induced by the counter-rotating terms in the interaction Hamiltonian, differences between bare and physical states occur for all the energy eigenstates. The second horizontal line (with $\omega/\omega_0 \approx 0.6$) corresponds to $|\psi_2\rangle = |g,e,g,0\rangle$. A signature of the discussed dressing is the slight frequency shift occurring between the bare qubit frequencies ω_2 and ω_3 and the two lowest-energy (horizontal) levels displayed in Fig. 1(b) (with $\omega/\omega_0 \approx 0.4$ and 0.6) corresponding to the *physical* transition frequencies of qubits 1 and 2 (in the presence of the interaction with the cavity mode), respectively. In the region much below the first (apparent) crossing ($\omega_3/\omega_0 < 0.95$), the third level corresponds to $|\psi_3\rangle = |g,g,e,0\rangle$, as can also be inferred from its linear dependence on ω_3. In the same frequency region, the fourth level (with $\omega/\omega_0 \approx 0.97$)

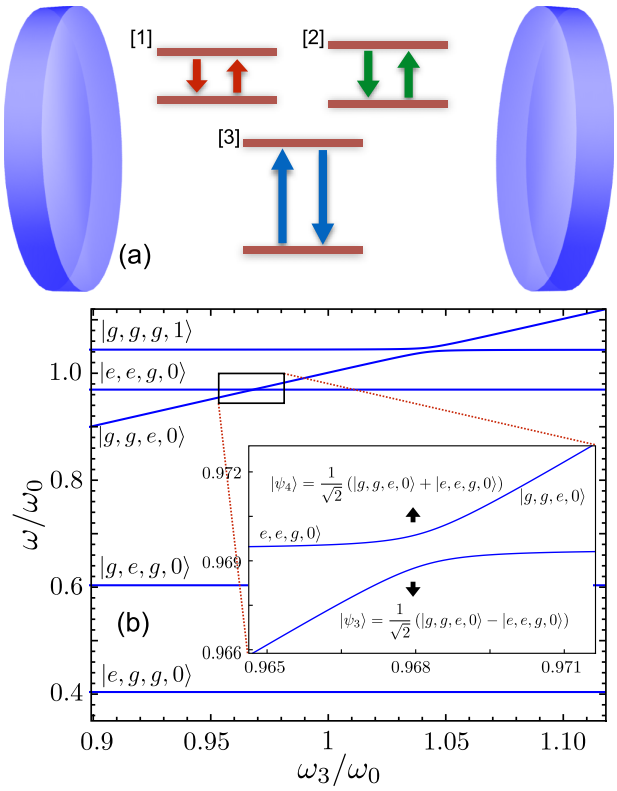

FIG. 1. (a) Schematic representation of three nondegenerate qubits interacting with the electromagnetic field of a cavity. (b) Lowest-energy levels, indicated with ω ($\hbar = 1$), of the system constituted by three qubits interacting with a cavity mode as a function of the normalized frequency of qubit 3, obtained by numerically diagonalizing the Hamiltonian in Eq. (4). The transition frequencies of the other two qubits, as well as the resonance frequency of the cavity mode, are kept fixed. All the parameters used here are specified in the text. The enlarged view of the boxed *apparent* crossing in the inset displays a clear anticrossing level splitting. When the splitting is at its minimum, the eigenstates of the system are approximately symmetric and antisymmetric superpositions of the states $|g,g,e,0\rangle$ and $|e,e,g,0\rangle$.

corresponds to the simultaneous excitation of qubits 1 and 2, $|\psi_4\rangle = |e,e,g,0\rangle$, while the fifth level (with $\omega/\omega_0 \approx 1.04$) corresponds to the one-photon state $|\psi_5\rangle = |g,g,g,1\rangle$. When increasing ω_3/ω_0, the energy level associated with $|g,g,e,0\rangle$ rises, and it reaches the energy levels corresponding to $|e,e,g,0\rangle$ and $|g,g,g,1\rangle$. When the (dressed) energy of qubit 3 approaches that of the cavity mode, a clear anticrossing can be observed. This is the ordinary vacuum Rabi splitting, which can also be reproduced within the RWA. When this splitting is at its minimum, the eigenstates of the system are the symmetric and antisymmetric superpositions of the states $|g,g,g,1\rangle$ and $|g,g,e,0\rangle$, as confirmed by numerical calculations. More interestingly, Fig. 1(b) also displays an apparent crossing at lower energy when $\omega_3 \simeq \omega_1 + \omega_2$ ($\approx 0.4 + 0.6$). The enlarged view in the inset shows that this is actually an anticrossing level splitting. When this splitting is at its minimum [see inset in Fig. 1(b)], the two system eigenstates $|\psi_{3,4}\rangle$ are, respectively, the antisymmetric and symmetric superpositions of the states $|g,g,e,0\rangle$ and $|e,e,g,0\rangle$. This avoided level crossing indicates a coherent coupling, which does not conserve the number of excitations, of the three spatially separated qubits.

The origin of this coupling can be understood using time-dependent fourth-order perturbation theory, identifying the resulting transition amplitude between the initial state $|i\rangle \equiv |e,g,g,0\rangle_b$ and the final state $|f\rangle \equiv |g,e,e,0\rangle_b$ (or vice versa) with the effective coupling strength determining this level splitting. According to fourth-order perturbation theory, this coupling can be expressed as [36]

$$\lambda_{\rm eff} = \sum_{n,m,k} \frac{V_{fn} V_{nm} V_{mk} V_{ki}}{(E_i - E_n)(E_i - E_m)(E_i - E_k)}, \tag{7}$$

where $V_{n,m} = \langle n|\hat{V}|m\rangle$. Although the initial and final states do not contain photons, the coupling is determined by the interaction of the qubits with the cavity field. States with nonzero photon number play a role only as intermediate levels ($|n\rangle$, $|m\rangle$, and $|k\rangle$) reached by virtual transitions (see diagrams in Appendix B). The two states $|i\rangle$ and $|f\rangle$ are connected via a fourth-order process and there are no lower-order contributions. There are 48 paths connecting the states to this order, as shown in Fig. 8. These paths clearly show that the three qubits are connected by a nonlinear optical process involving *only* virtual photons. This analysis has been performed for two-level atoms, which is a good approximation for flux qubits where the next higher level can be energetically very far (see, e.g., Ref. [54]). Of course, additional paths must be taken into account for multilevel systems. The resulting effective coupling between the states $|g,g,e,0\rangle$ and $|e,e,g,0\rangle$ can be described by the effective Hamiltonian in Eq. (2), where $J^{(3)} = \lambda_{\rm eff}$ [corresponding to half the minimum level splitting shown in the inset in Fig. 1(b)].

The analytical expression obtained from Eq. (7), which considers the 48 contributions, is very cumbersome. However, it can be simplified considerably if we assume $\lambda_1 = \lambda_2 = \lambda_3 = \lambda$ and $\omega_1 = \omega_2 = \omega_3/2$. In this case, the final result is

$$J^{(3)} = \frac{64\lambda^4\omega_c^2\left(4\omega_c^2 - 7\omega_3^2\right)\sin\theta\cos^3\theta}{\omega_3\left(\omega_3^2 - \omega_c^2\right)\left(\omega_3^2 - 4\omega_c^2\right)^2}. \tag{8}$$

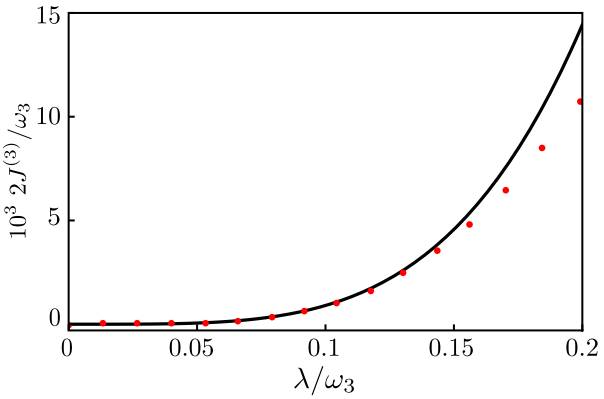

FIG. 2. Comparison between the numerically calculated normalized effective Rabi splitting (points) corresponding to $J^{(3)}$ in Appendix B and the corresponding calculations using fourth-order perturbation theory (continuous black curve), as a function of the normalized interaction strength λ/ω_3.

We note that the effective coupling becomes zero when $\omega_c = \frac{\sqrt{7}}{2}\omega_3$. It is not easy to see how the interference between the 48 paths becomes destructive for this particular value of ω_c. Looking at the denominator of Eq. (8), we see that $J^{(3)} \to \infty$ when $\omega_c \to \omega_3$ or $\omega_c \to \frac{1}{2}\omega_3$, i.e., when the cavity becomes resonant with one of the qubits. Perturbation theory is not valid around those points. We also note that the coupling, also in the unsimplified general case, is proportional to $\sin\theta\cos^3\theta$, which implies that the maximum coupling is achieved when $\theta = \pi/6$. Figure 2 displays a comparison of the magnitudes of the effective Rabi splitting $2J^{(3)}/\omega_3$ obtained analytically [Eq. (8)] via fourth-order perturbation theory (black continuous curve) and by numerical diagonalization of the Hamiltonian in Eq. (4), as a function of the normalized interaction strength λ/ω_3 ($\lambda = \lambda_{1,2,3}$). The other parameters are the same as those used to obtain the results in Fig. 1. The agreement is very good for normalized interaction strengths $\lambda/\omega_3 \lesssim 0.15$. Figure 2 shows that an effective coupling rate well beyond typical decoherence rates of circuit-QED systems (see, e.g., Ref. [55]) can be obtained already at a coupling strength $\lambda/\omega_3 \sim 0.1$.

In order to demonstrate the simultaneous excitation transfer from qubit 3 to qubits 1 and 2, we fix $\omega_3 \simeq \omega_1 + \omega_2$, so that the system is at its minimum-level splitting [see inset in Fig. 1(b)]. The minimum occurs when the transition energy of the dressed qubit 3 is equal to the energy level corresponding to the simultaneous excitation of the dressed qubits 1 and 2. We study the dynamics after initial preparation of the system in the symmetric superposition of the eigenstates associated with the two split energy levels: $(|\psi_3\rangle + |\psi_4\rangle)/\sqrt{2} = |g,g,e,0\rangle$, corresponding to the excitation of the dressed qubit 3. The system can be prepared in this state by directly exciting the detuned qubit 3 by sending a π electromagnetic pulse, followed by a flux shift that brings the qubit into resonance (minimum splitting). Another possibility is to start with qubit 3 already on resonance and excite it by a π pulse much faster than $\pi/J^{(3)}$.

The influence of the cavity-field damping and atomic decay on the process can be studied by the master-equation

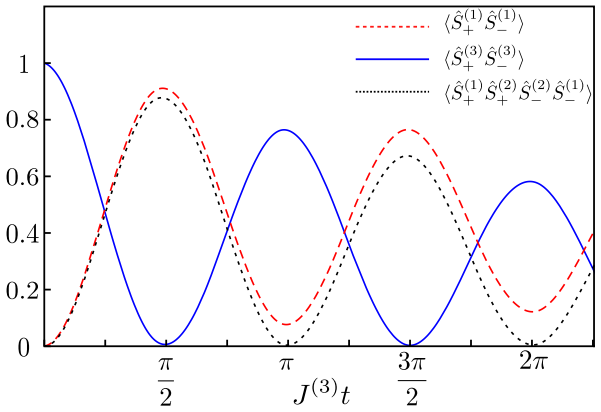

FIG. 3. Time evolution of the mean excitation probabilities of qubits 1 and 3, $\langle\hat{S}_+^{(1)}\hat{S}_-^{(1)}\rangle$ and $\langle\hat{S}_+^{(3)}\hat{S}_-^{(3)}\rangle$, and of the two-qubit correlation function $\langle\hat{S}_+^{(1)}\hat{S}_+^{(2)}\hat{S}_-^{(2)}\hat{S}_-^{(1)}\rangle$. The initial state is $|g,g,e,0\rangle$.

approach in the dressed picture [56,57]. We consider the system interacting with zero-temperature baths. The master equation is obtained by using the Born-Markov approximation without the post-trace RWA [33]. We study the dynamics of the relevant system population and correlation functions by introducing the dressed-qubit lowering and raising operators $\hat{S}_-^{(i)}$ and $\hat{S}_+^{(i)} = (\hat{S}_-^{(i)})^\dagger$. They are a direct generalization of $\hat{\sigma}_-^{(i)}$ and $\hat{\sigma}_+^{(i)}$. For qubit 1,

$$\hat{S}_-^{(1)} = \sum_{n=0}^{\infty}\sum_{\alpha,\beta=g}^{e} |g,\alpha,\beta,n\rangle\langle e,\alpha,\beta,n|. \tag{9}$$

In the absence of interaction, when $|p,q,r,n\rangle$ are bare states, the operators $\hat{S}_-^{(i)}$ coincide with the usual lowering Pauli operators $\hat{\sigma}_-^{(i)}$. Figure 3 displays the time evolution of the mean excitation probability $\langle\hat{S}_+^{(i)}\hat{S}_-^{(i)}\rangle$ of qubits 1 and 3 (the dynamics of qubit 1 coincides with that of qubit 2), as well as that of the two-qubit correlation function $\langle\hat{S}_+^{(1)}\hat{S}_+^{(2)}\hat{S}_-^{(2)}\hat{S}_-^{(1)}\rangle$. The initial state is $|g,g,e,0\rangle = (|\psi_3\rangle + \psi_4\rangle)/\sqrt{2}$. The parameters are those used to obtain the energy levels in Fig. 1(b). For the decay rates of the qubit (γ) and the cavity (κ), we used $\gamma = \kappa = 3\times10^{-5}\omega_0$. Quantum Rabi oscillations, showing the reversible excitation exchange between qubit 3 and qubits 1 and 2, can be clearly observed. Note that, during the time evolution displayed in Fig. 3, the photon population (not shown) reaches a maximum value $\sim1.5\times10^{-2}$. This small population decreases rapidly when increasing the detuning Δ_3 between the cavity mode and qubit 3. We also checked that increasing the photon damping, provided that $\kappa \lesssim 2\Delta_3$, does not affect the displayed dynamics. After half a Rabi period ($t = \pi/2J^{(3)}$), the excitation is fully transferred from qubit 3 to qubits 1 and 2, which reach their maximum excitation probability. The presence of damping prevents $\langle\hat{S}_+^{(1)}\hat{S}_-^{(1)}\rangle$ from reaching 1. We observe that the single-qubit excitations and the two-qubit correlation function $\langle\hat{S}_+^{(1)}\hat{S}_+^{(2)}\hat{S}_-^{(2)}\hat{S}_-^{(1)}\rangle$ almost coincide at early times. This almost-perfect two-qubit correlation is a clear signature of the joint excitation of qubits 1 and 2: if one qubit becomes excited, the probability that the other one is excited is also very close to 1. However, as expected, the two-qubit correlation is more fragile to losses. We also observe that, at time $t = \pi/4J^{(3)}$, this process spontaneously gives rise to the maximally entangled three-qubit state $(|g,g,e\rangle - i|e,e,g\rangle)/\sqrt{2}$ when damping can be neglected (the factorized photonic vacuum state has been disregarded). This state is the Greenberger-Horne-Zeilinger (GHZ) state, up to a local transformation.

We observe that, during the time evolution displayed in Fig. 3, the photon population (not shown) reaches a maximum value of $\sim1.5\times10^{-2}$. This small population decreases rapidly when increasing the detuning Δ_3 between the cavity mode and qubit 3. We also checked that increasing the photon damping, provided that $\kappa \lesssim 2\Delta_3$, does not affect the displayed dynamics. This result shows that the 3QM process is not influenced by the cavity-loss rate κ, owing to the negligible probability to have real photons in the cavity. This result, however, does not imply a total immunity to losses of the quantum bus. For example, if an impurity atom, almost resonant with the transition energy of qubit 3, is present inside the bus, the excitation would be partly transferred to the impurity atom.

This 3QM offers also the possibility to encode an arbitrary qubit state $a|g\rangle + b|e\rangle$ into a two-qubit entangled state so that $(a|g\rangle + b|e\rangle)|g\rangle|g\rangle \rightarrow |g\rangle(a|g\rangle|g\rangle - ib|e\rangle|e\rangle)$. This operation can be realized by just letting the system evolve spontaneously for a time $t = \pi/2J^{(3)}$.

C. Four-qubit mixing

Here we consider four nondegenerate qubits coupled to a cavity mode in the dispersive regime and investigate the 4QM process. Figure 4 shows the energy levels for the lowest-energy excited states as a function of the frequency of qubit 1, obtained by numerically diagonalizing the Hamiltonian in Eq. (4). Also in this case, for each value of ω_1, the energy scale is chosen such that the ground-state energy is equal to zero. All the values are provided in terms of a fixed reference frequency ω_0. We used $\lambda_i/\omega_0 = 0.15$ and $\theta_i = \pi/6$ for all the qubits. We also set the transition frequencies of qubits 2, 3, and 4 as $\omega_2/\omega_0 = 0.4$, $\omega_3/\omega_0 = 0.55$, and $\omega_4/\omega_0 = 0.7$, and the resonance frequency of the cavity mode as $\omega_c/\omega_0 = 1.4$.

The figure displays several *apparent* level crossings and anticrossings, corresponding to different kinds of normal-mode couplings. The avoided level crossings indicated by the red circles originate from two-qubit resonant interactions described by the effective Hamiltonian in Eq. (6). In the time domain, this type of interaction leads to two-qubit mixing (2QM). The *apparent* level crossings labeled by the orange triangles give rise to 3QM. For example, the lowest-energy orange triangle (at $\omega/\omega_0 \simeq 0.6$) marks the coupling between the states $|g,g,e,g,0\rangle$ and $|e,e,g,g,0\rangle$. The stars in the higher-energy region describe the coupling of a single photon to two (open star) or three (solid star) qubits, studied in Ref. [35]. Type-I 4QM processes are denoted by open squares. An enlarged view of the *apparent* crossing (⊠) in Fig. 4 is plotted in Fig. 5(a). There, an anticrossing level splitting of $\sim10^{-3}\omega_0$ can be observed. When the splitting is at its minimum, the two system eigenstates are the symmetric and antisymmetric superpositions of the states $|e,g,g,e,0\rangle$ and $|g,e,e,g,0\rangle$. This avoided level crossing is the signature of a four-qubit coherent coupling.

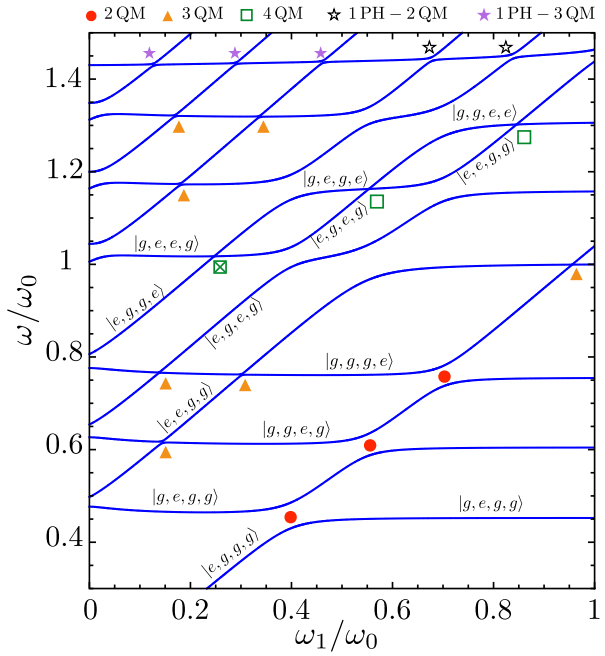

FIG. 4. Four nondegenerate qubits dispersively coupled to a cavity mode at higher energy. Lowest-energy levels of the system as a function of the frequency of qubit 1, obtained by numerical diagonalization of the Hamiltonian in Eq. (4) with four qubits. The transition frequencies of the other three qubits as well as the resonance frequency of the cavity mode are kept fixed. All the parameters used are provided in the text.

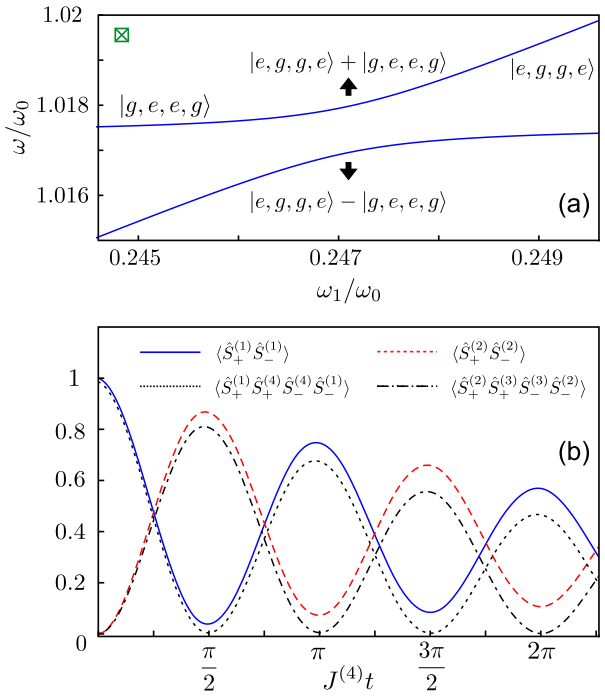

FIG. 5. (a) Enlarged view of the *apparent* crossing (⊠) in Fig. 4 determining a type-I 4QM. (b) Type-I 4QM: Time evolution of the mean excitation probability of qubits 1 and 2, $\langle\hat{S}_+^{(1)}\hat{S}_-^{(1)}\rangle$ and $\langle\hat{S}_+^{(2)}\hat{S}_-^{(2)}\rangle$, and of the two-qubit correlation functions $\langle\hat{S}_+^{(1)}\hat{S}_+^{(4)}\hat{S}_-^{(4)}\hat{S}_-^{(1)}\rangle$ and $\langle\hat{S}_+^{(2)}\hat{S}_+^{(3)}\hat{S}_-^{(3)}\hat{S}_-^{(2)}\rangle$. The initial state is $|e,g,g,e,0\rangle$.

Also in this case, the origin of this coupling can be understood using time-dependent fourth-order perturbation theory, using Eq. (7) and considering the states $|e,g,g,e,0\rangle_{\rm b}$ and $|g,e,e,g,0\rangle_{\rm b}$ as the initial and final states (see Appendix C). We notice that type-I 4QM, in contrast to the 3QM process, conserves the number of excitations. Hence we can expect that it can be described within the RWA (for the TC model). However, by numerically diagonalizing the TC model we find no avoided level splitting. As shown in Appendix C, the fourth-order perturbation theory shows that the coupling goes to zero, owing to perfect cancellation between the different contributions to the matrix element. This 4QM process can be described by the effective interaction Hamiltonian in Eq. (3), which determines the coupling between the states $|g,g,e,e,0\rangle$ and $|e,e,g,g,0\rangle$.

Figure 5(b) displays the time evolution of the mean excitation probability of qubits 1 and 2 (the dynamics of qubits 3 and 4 coincide with that of qubits 1 and 2, respectively), as well as that of the two-qubit correlation functions $\langle\hat{S}_+^{(1)}\hat{S}_+^{(4)}\hat{S}_-^{(4)}\hat{S}_-^{(1)}\rangle$ and $\langle\hat{S}_+^{(2)}\hat{S}_+^{(3)}\hat{S}_-^{(3)}\hat{S}_-^{(2)}\rangle$. The parameters are those used to obtain the energy levels in Fig. 4. We also set $\gamma = \kappa = 3\times10^{-5}\omega_0$. The initial state is $|e,g,g,e,0\rangle$. The system can be prepared in this state by setting the qubit frequencies such that $\omega_1+\omega_4 \neq \omega_2+\omega_3$ and directly exciting qubits 1 and 4 by sending a π pulse to each of them, followed by a flux shift to one of the four qubits that brings the four-qubit system into resonance [corresponding to the minimum splitting in Fig. 5(a)]. At $t=0$, qubits 1 and 4 are excited and the minimum-splitting condition is satisfied. Figure 5(b) clearly demonstrates the excitation transfer $|e,g,g,e,0\rangle \to |g,e,e,g,0\rangle$, which is also reversible as the time evolution for $\pi/2 \leqslant J^{(4)}t \leqslant \pi$ shows. If damping is absent or negligible, the transfer can be deterministic at $J^{(4)}t=\pi/2$, and a maximally entangled four-qubit state (GHZ-type state) is obtained at $J^{(4)}t=\pi/4$.

This 4QM process can be used to transfer the entanglement from a pair of qubits to another spatially separated pair, initially in a factorized state. Specifically, if the system is initially prepared in the two-qubit entangled state $(a|g,g\rangle + b|e,e\rangle)|g,g\rangle$, after a time $t=\pi/2J^{(4)}$, the entanglement will be transferred from qubits 1 and 2 to qubits 3 and 4: $(a|g,g\rangle+b|e,e\rangle)|g,g\rangle \to |g,g\rangle(a|g,g\rangle - ib|e,e\rangle)$.

Adjusting the transition frequencies of the qubits, a four-qubit down-conversion (type-II 4QM) analogous to that studied above for three qubits can also occur. This process is enabled by the resonant coupling between the states $|e,g,g,g,0\rangle \leftrightarrow |g,e,e,e,0\rangle$ and can be described by the effective Hamiltonian

$$\hat{V}_{\rm II}^{(4)} = J^{(4)}(\hat{\sigma}_-^{(1)}\hat{\sigma}_+^{(2)}\hat{\sigma}_+^{(3)}\hat{\sigma}_+^{(4)} + \text{H.c.}). \tag{10}$$

As shown in Appendix A, the resulting splitting is of the same order as that shown in Fig. 5(a). The spontaneous evolution of the Dicke USC system, effectively described by the Hamiltonian (10), corresponding to a type-II 4QM,

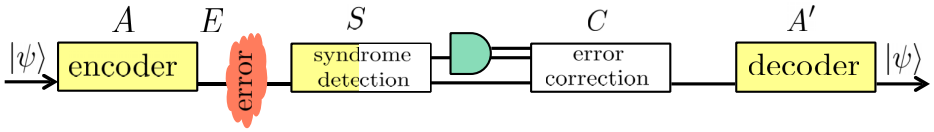

FIG. 6. Basic modules of a standard ECC. These include encoding (A) and decoding (A') modules (usually based on quantum repetition codes using multiple CNOT gates), a dissipative channel or evolution when the error (E) happens, error-syndrome detection (S), and error-correction (C) modules. Sometimes, the modules S and C are combined. Here, single (double) lines denote quantum (classical) channels, and a half-circle denotes detectors. In Appendix D, we consider in detail an ECC (see, e.g., Ref. [41]) for correcting either a single bit-flip or single phase-flip error. Then, modules A and A' can be entirely implemented (as marked in yellow) by a type-II 4QM, described by $\hat{V}_{\rm II}^{(4)}$ for the evolution time (length) $t' = \pi/(2J^{(4)})$. Typically, modules A and A' are realized with four CNOT gates in total. Moreover, the error-syndrome module S can be implemented by 4QM and two additional CNOT gates, instead of typically four CNOT gates. The detected error can be corrected by a single-qubit rotation (NOT gate) applied to a proper qubit, based on the results of the detectors, as discussed in Appendix D.

performs the transformation

$$(a|g\rangle + b|e\rangle)|ggg\rangle \rightarrow |g\rangle(a|ggg\rangle - ib|eee\rangle) \qquad (11)$$

after the evolution time $t' = \pi/(2J^{(4)})$. This operation corresponds, up to a single-qubit phase gate, to a three-qubit repetition code, which is usually implemented with two controlled-NOT (CNOT) gates. Repetition codes are basic elements of error-correction codes (ECCs) [40,58], in particular, for encoding A and decoding A', as shown and explained in Fig. 6. Note that the error E can be corrected in the module C by a single qubit flip conditioned on the classical information obtained from the detectors in the module S. In Appendix D, we analyze in detail an ECC [41] for correcting either a single bit-flip or phase-flip error. In this ECC, a type-II 4QM can be used for three purposes: to implement encoding A and decoding A', but also to replace two CNOT gates in the error-syndrome-detection module S (see the modules depicted in yellow in Fig. 6). We note that CNOT-based ECCs (including the double-controlled-NOT gate, i.e., the Toffoli gate) were first implemented experimentally in a liquid NMR system [59] and, later, with trapped ions [60,61], linear optics [62], homogenous [63] and heterogeneous [64] solid-state spin systems, and a circuit-QED system [65–68]. Usually, the CNOT and Toffoli gates are realized by long sequences of pulses or using qudits instead of qubits [65,69]. In our proposal, the total number of eight CNOT gates in the five-qubit ECC is reduced from eight to only two, and we are not using the Toffoli gate.

Finally, we note that any entangling operation (like the type-II 4QM) is universal for quantum computing [58]. Specifically, by using many copies of such a gate together with single-qubit operations, an arbitrary quantum algorithm (i.e., not only the ECC) can be performed. However, here we focus on a direct and simple application of the spontaneous evolution of the Dicke system. Thus, we do not express the two remaining CNOT gates for the syndrome detection S via a sequence of 4QM and single-qubit operations.

III. CONCLUSIONS

In this article, we described nonlinear optical processes with qubits, where only virtual photons are involved. The results presented here show that N spatially separated and nondegenerate qubits can coherently exchange energy in analogy with light modes in nonlinear optics. The energy exchange is also reversible. This few-body interaction is mediated by the exchange of virtual rather than real photons and is protected against photon losses in the bus. The coherent coupling between the N superconducting qubits can be switched on or off by tuning the transition energy of one of them. These results can be regarded as the generalization to $N > 2$ qubits of the two-qubit coherent state transfer mediated by virtual photons experimentally demonstrated with superconducting artificial atoms [3].

These processes can produce multiparticle entanglement simply starting from one or more qubits in their excited state and letting the system evolve spontaneously. The spontaneous time evolution is also able to transfer the entanglement from one pair of qubits to a different one. The processes proposed here extend further the broad field of nonlinear optics. This architecture can be extended to consider qubits in different coupled cavities and opens up new possibilities for quantum-information processing on a chip. As an example, we have demonstrated that four-qubit mixing can be used as a replacement for the standard quantum repetition codes based on CNOT gates. Then, we have discussed a practical application of type-II four-qubit mixing for quantum-information processing, i.e., an error-correction code for encoding, decoding, and error-syndrome detection, as shown in Fig. 12 and discussed in detail in Appendix D. Finally, we observe that these effective three- and four-body interactions can give rise to exotic phases not seen in usual condensed-matter experiments [70].

ACKNOWLEDGMENTS

We thank S. Devitt for useful comments. A.F.K. acknowledges support from a JSPS Postdoctoral Fellowship for Overseas Researchers. A.M. and F.N. acknowledge the support of a grant from the John Templeton Foundation. F.N. was also partially supported by the RIKEN iTHES Project, the MURI Center for Dynamic Magneto-Optics via the AFOSR Grant No. FA9550-14-1-0040, the IMPACT program of JST, CREST Grant No. JPMJCR1676, the Japan Society for the Promotion of Science (KAKENHI), JSPS-RFBR Grant No. 17-52-50023, and the RIKEN-AIST Joint Research Fund. S.S. acknowledges the partial support of MPNS COST Action MP1403 Nanoscale Quantum Optics.

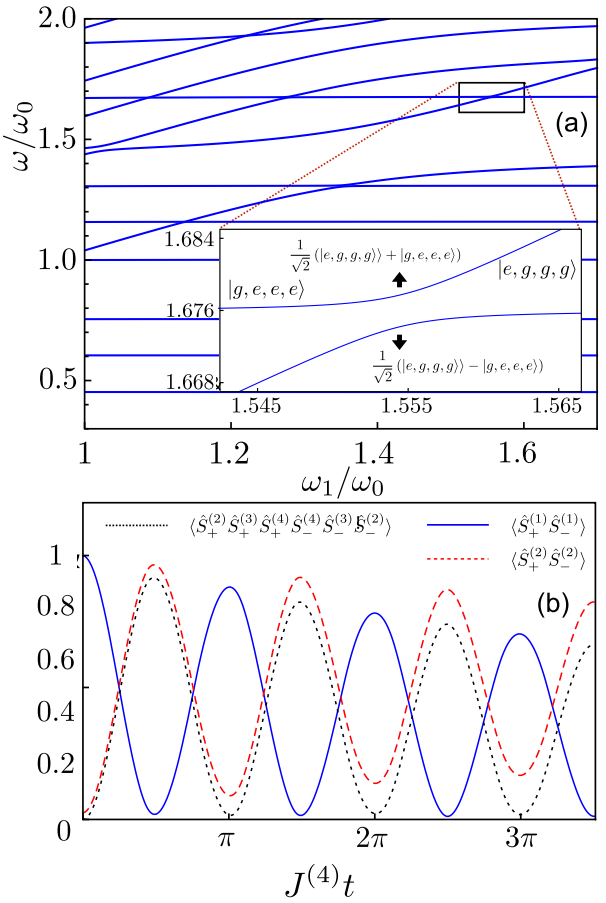

FIG. 7. Type-II 4QM. (a) Lowest-energy levels of the system constituted by four qubits interacting with a cavity mode as a function of the normalized frequency of qubit 1, obtained by numerically diagonalizing the Hamiltonian in Eq. (4). We used the following parameters in units of ω_0: $\omega_2 = 0.4, \omega_3 = 0.55, \omega_4 = 0.7, \omega_c = 1.75$, $\lambda_1 = 0.05, \lambda_i = 0.15$ (for $i = 2$–4), and $\theta_i = \pi/6$ for all four qubits. The enlarged view of the boxed *apparent* crossing in the inset displays a clear anticrossing level splitting. When the splitting is at its minimum, the eigenstates of the system are approximately symmetric and antisymmetric superpositions of the states $|e,g,g,g,0\rangle$ and $|g,e,e,e,0\rangle$. (b) Time evolution of the mean excitation probabilities of qubits 1 and 2, and of the three-qubit correlation function $\langle \hat{S}_+^{(2)}\hat{S}_+^{(3)}\hat{S}_+^{(4)}\hat{S}_-^{(4)}\hat{S}_-^{(3)}\hat{S}_-^{(2)}\rangle$, obtained fixing $\omega_1 = 1.6448$, so that the splitting in the inset is minimum. The initial state is $|e,g,g,g,0\rangle$ and we used $\gamma = \kappa = 3 \times 10^{-5}\omega_0$.

APPENDIX A: ENERGY LEVELS AND DYNAMICS FOR TYPE-II FOUR-QUBIT MIXING

Figure 7 presents the numerical calculations for type-II 4QM. Figure 7(a) displays the lowest-energy levels as a function of the normalized frequency of qubit 1, obtained by numerically diagonalizing the Hamiltonian in Eq. (4). Parameters are provided in the figure caption. Figure 7(a) also shows the enlarged view of the boxed *apparent* crossing. Figure 7(b) shows the time evolution of the mean excitation probabilities of qubits 1 and 2, and of the three-qubit correlation function $\langle \hat{S}_+^{(2)}\hat{S}_+^{(3)}\hat{S}_+^{(4)}\hat{S}_-^{(4)}\hat{S}_-^{(3)}\hat{S}_-^{(2)}\rangle$, obtained fixing $\omega_1 = 1.6448$, so that the splitting in the inset in Fig. 7(a) is minimum. The initial state is $|e,g,g,g,0\rangle$.

APPENDIX B: ANALYTICAL DERIVATION OF THE THREE-QUBIT COUPLING STRENGTH $J^{(3)}$

Our system consists of three qubits, all ultrastrongly coupled to a cavity mode. The Hamiltonian for the system is given in Eq. (4). In this appendix, we calculate the effective 3QM coupling strength $J^{(3)}$ between the two states $|i\rangle = |e,g,g,0\rangle$ and $|f\rangle = |g,e,e,0\rangle$ (equivalent to the 3QM $|g,g,e,0\rangle \leftrightarrow |e,e,g,0\rangle$, discussed in the main text, with a permutation of the qubit indices). These states are connected via 48 fourth-order paths, as shown in Fig. 8.

We can treat the interaction part of the Hamiltonian, given in Eq. (5), as a perturbation. As discussed in the main text, the effective coupling is then given by Eq. (7), where the sum goes over all paths shown in Fig. 8. There are no contributions from terms of order lower than four. Note that $E_i = E_f = 0$ when $\omega_1 = \omega_2 + \omega_3$, which is the case considered here.

In the rest of this appendix, for brevity, we use the notation $\Delta_{nm} = \omega_n - \omega_m$, $\Delta_{Cn} = 2\omega_c - \omega_n$, $\Omega_{nm} = \omega_n + \omega_m$, $\Omega_{Cn} = 2\omega_c + \omega_n$, $\lambda_{\pm\pm\pm} = \pm\lambda_1 \pm \lambda_2 \pm \lambda_3$, $\Lambda_3 = \lambda_1\lambda_2\lambda_3$, and $\Lambda_4 = \lambda_1\lambda_2\lambda_3\lambda_4$. With this notation, the contribution from the terms in diagram 1 of Fig. 8 becomes

$$\begin{aligned}\lambda_{\text{eff}}^{(1)} = -\frac{\Lambda_3 \sin\theta\cos^3\theta}{\Delta_{c1}}\Bigg[&2\frac{\lambda_{-++}}{\omega_c\Delta_{C3}} + 2\frac{\lambda_{-+-}}{\Delta_{C2}\Delta_{c3}} \\ &+ 2\frac{\lambda_{-++}}{\omega_c\Delta_{C2}} + 2\frac{\lambda_{--+}}{\Delta_{C2}\Delta_{c2}} + 2\frac{\lambda_{---}}{\Delta_{C1}\Delta_{c3}} + 2\frac{\lambda_{---}}{\Delta_{C1}\Delta_{c1}} \\ &+ \frac{\lambda_{-++}}{\omega_c(-\omega_3)} + \frac{\lambda_{-+-}}{(-\omega_1)\Delta_{c1}} + \frac{\lambda_{-++}}{\omega_c(-\omega_2)} + \frac{\lambda_{--+}}{(-\omega_2)\Delta_{c2}} \\ &+ \frac{\lambda_{---}}{(-\omega_1)\Delta_{c3}} + \frac{\lambda_{---}}{(-\omega_1)\Delta_{c2}}\Bigg].\end{aligned} \tag{B1}$$

To check our calculations, we can compare with the calculation in Ref. [35], which treated the process $|g,g,1\rangle \to |e,e,0\rangle$. This is exactly the process in diagram 1 after the first transition, ignoring the first qubit. If we insert the values $\omega_c = 2\omega_q$, $\omega_2 = \omega_3 = \omega_0$, $\omega_1 = 2\omega_0$ [recall that we have used the fact that $\omega_1 = \omega_2 + \omega_3$ to derive Eq. (B1)], $\lambda_2 = \lambda_3 = \lambda$, and $\lambda_1 = 0$ in Eq. (B1), and remove the factor $-\lambda_1\cos\theta/\Delta_{c1}$ (which comes from the first transition in the diagram), we obtain

$$\lambda_{\text{eff}}^{(1\text{ph},2\text{qb})} = -\frac{8}{3}\sin\theta\cos^2\theta\frac{\lambda^3}{\omega_0^2}, \tag{B2}$$

which is exactly the result from Ref. [35].

If we make the simplifying assumptions $\lambda_1 = \lambda_2 = \lambda_3 \equiv \lambda$, $\omega_1 \equiv \omega_0$, and $\omega_2 = \omega_3 = \omega_0/2$, the contribution from diagram 1 to the coupling becomes

$$\begin{aligned}\lambda_{\text{eff}}^{(1)} = -\frac{2\lambda^4\sin\theta\cos^3\theta}{\omega_c - \omega_0}\Bigg[&\frac{2}{\omega_c\left(2\omega_c - \frac{1}{2}\omega_0\right)} \\ &- \frac{2}{\left(\omega_c - \frac{1}{2}\omega_0\right)\left(2\omega_c - \frac{1}{2}\omega_0\right)} - \frac{12}{(2\omega_c - \omega_0)^2} \\ &- \frac{2}{\omega_c\omega_0} + \frac{5}{\omega_0\left(\omega_c - \frac{1}{2}\omega_0\right)}\Bigg].\end{aligned} \tag{B3}$$

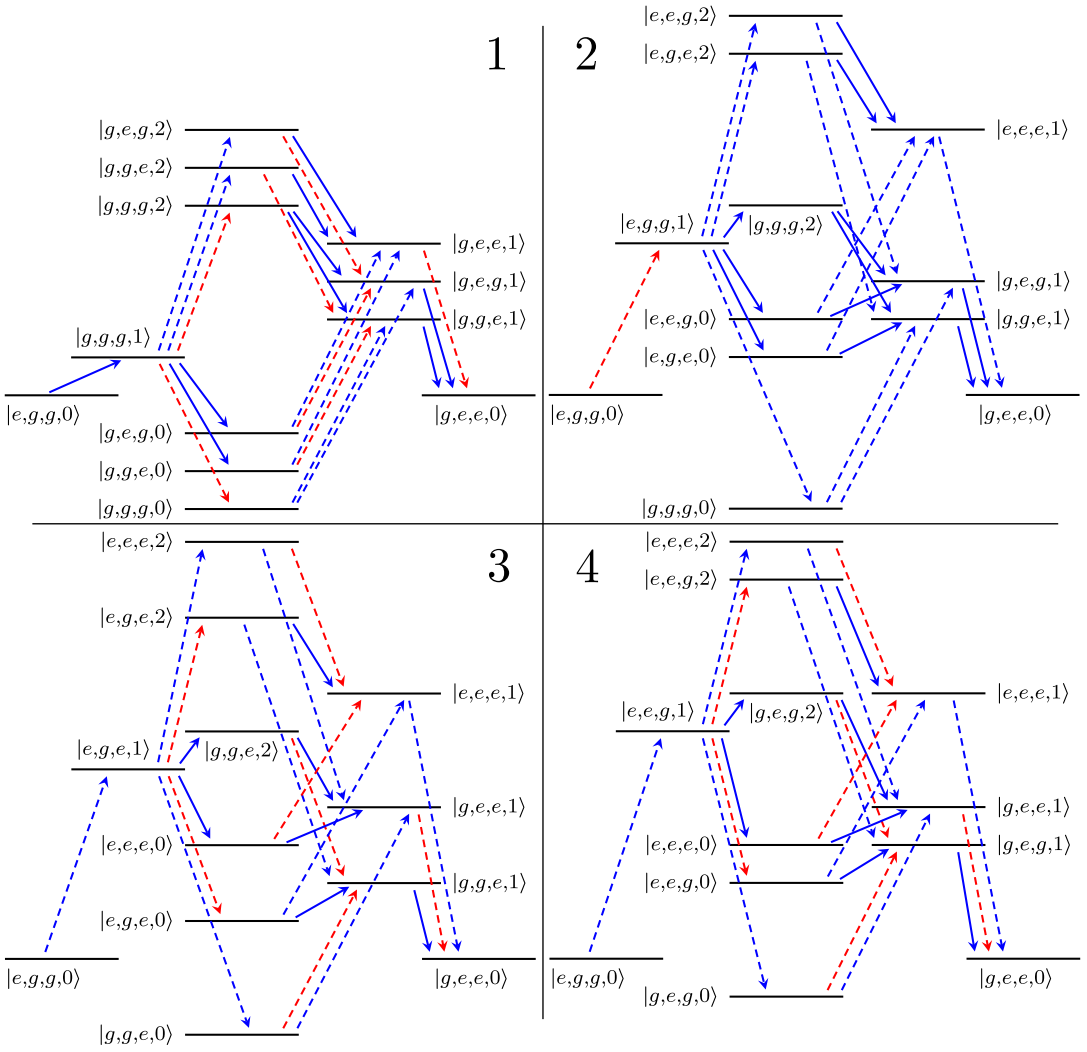

FIG. 8. The 48 fourth-order paths connecting the states $|e,g,g,0\rangle$ and $|g,e,e,0\rangle$. The four diagrams show 12 paths each. Diagram 1 shows the paths starting with $|e,g,g,0\rangle \to |g,g,g,1\rangle$, diagram 2 shows the paths starting with $|e,g,g,0\rangle \to |e,g,g,1\rangle$, diagram 3 shows the paths starting with $|e,g,g,0\rangle \to |e,g,e,1\rangle$, and diagram 4 shows the paths starting with $|e,g,g,0\rangle \to |e,e,g,1\rangle$. Transitions that do not conserve the number of excitations in the system are marked by dashed lines, while transitions that conserve the number of excitations are marked by solid lines. The red lines mark the transitions mediated by the $\hat{\sigma}_z$ part of the coupling and the blue lines mark the transitions mediated by the $\hat{\sigma}_x$ part of the coupling. To set the energy levels, we have used the parameter values $\omega_c = 4\omega_3$, $\omega_1 = 3\omega_3$, and $\omega_2 = 2\omega_3$.

The terms from diagram 2 add up to

$$\lambda_{\text{eff}}^{(2)} = -\frac{\Lambda_3\lambda_{+--}\sin\theta\cos^3\theta}{\omega_c}\left[\frac{2}{\Omega_{C2}\Omega_{c1}} + \frac{2}{\Omega_{C2}\Delta_{c3}} + \frac{2}{\Omega_{C3}\Omega_{c1}} + \frac{2}{\Omega_{C3}\Delta_{c2}} + \frac{2}{\Delta_{C1}\Delta_{c3}} + \frac{2}{\Delta_{C1}\Delta_{c2}} + \frac{1}{\omega_2\Omega_{c1}} + \frac{1}{\omega_2\Delta_{c3}} + \frac{1}{\omega_3\Omega_{c1}} + \frac{1}{\omega_3\Delta_{c2}} + \frac{1}{(-\omega_1)\Delta_{c3}} + \frac{1}{(-\omega_1)\Delta_{c2}}\right], \tag{B4}$$

and with the same assumptions as above ($\lambda_1 = \lambda_2 = \lambda_3 \equiv \lambda$, $\omega_1 \equiv \omega_0$, and $\omega_2 = \omega_3 = \omega_0/2$) this simplifies to

$$\lambda_{\text{eff}}^{(2)} = \frac{2\lambda^4\sin\theta\cos^3\theta}{\omega_c}\left[\frac{2}{\left(2\omega_c + \frac{1}{2}\omega_0\right)\left(\omega_c + \omega_0\right)} + \frac{2}{\left(2\omega_c + \frac{1}{2}\omega_0\right)\left(\omega_c - \frac{1}{2}\omega_0\right)} + \frac{4}{\left(2\omega_c - \omega_0\right)^2} + \frac{2}{\omega_0(\omega_c + \omega_0)} + \frac{1}{\omega_0\left(\omega_c - \frac{1}{2}\omega_0\right)}\right]. \tag{B5}$$

The terms from diagram 3 add up to

$$\lambda_{\text{eff}}^{(3)} = -\frac{\Lambda_3 \sin\theta\cos^3\theta}{\Omega_{c3}}\Bigg[2\frac{\lambda_{+++}}{\Omega_{C1}\Omega_{c1}} + 2\frac{\lambda_{-++}}{\Omega_{C1}\omega_c} + 2\frac{\lambda_{+-+}}{\Omega_{C3}\Omega_{c1}} + 2\frac{\lambda_{+-+}}{\Omega_{C3}\Delta_{c2}} + 2\frac{\lambda_{-++}}{\Delta_{C2}\omega_c} + 2\frac{\lambda_{--+}}{\Delta_{C2}\Delta_{c2}} + \frac{\lambda_{+++}}{\omega_1\Omega_{c1}} + \frac{\lambda_{-++}}{\omega_1\omega_c} + \frac{\lambda_{+-+}}{\omega_3\Omega_{c1}} + \frac{\lambda_{+-+}}{\omega_3\Delta_{c2}} + \frac{\lambda_{-++}}{(-\omega_2)\omega_c} + \frac{\lambda_{--+}}{(-\omega_2)\Delta_{c2}}\Bigg], \tag{B6}$$

and with the same assumptions as above this simplifies to

$$\lambda_{\text{eff}}^{(3)} = -\frac{\lambda^4\sin\theta\cos^3\theta}{\omega_c+\frac{1}{2}\omega_0}\Bigg[\frac{6}{(2\omega_c+\omega_0)(\omega_c+\omega_0)} + \frac{2}{(2\omega_c+\omega_0)\omega_c} + \frac{2}{\left(2\omega_c+\frac{1}{2}\omega_0\right)(\omega_c+\omega_0)} + \frac{2}{\left(2\omega_c+\frac{1}{2}\omega_0\right)\left(\omega_c-\frac{1}{2}\omega_0\right)} + \frac{2}{\left(2\omega_c-\frac{1}{2}\omega_0\right)\omega_c} - \frac{2}{\left(2\omega_c-\frac{1}{2}\omega_0\right)\left(\omega_c-\frac{1}{2}\omega_0\right)} + \frac{5}{\omega_0(\omega_c+\omega_0)} - \frac{1}{\omega_0\omega_c} + \frac{4}{\omega_0\left(\omega_c-\frac{1}{2}\omega_0\right)}\Bigg]. \tag{B7}$$

The terms from diagram 4 add up to $\lambda_{\text{eff}}^{(4)}$, which is given by Eq. (B6) but with the indices 2 and 3 interchanged everywhere. With the same assumptions as above $\lambda_{\text{eff}}^{(4)}$ simplifies to exactly the same expression as for diagram 3, given in Eq. (B7). Adding up all the terms from the four diagrams in the simplified case gives

$$\begin{aligned}\lambda_{\text{eff}} = -2\lambda^4\sin\theta\cos^3\theta\Bigg\{&\frac{1}{\omega_c-\omega_0}\Bigg[\frac{2}{\omega_c\left(2\omega_c-\frac{1}{2}\omega_0\right)} - \frac{2}{\left(2\omega_c-\frac{1}{2}\omega_0\right)\left(\omega_c-\frac{1}{2}\omega_0\right)} - \frac{12}{(2\omega_c-\omega_0)^2} \\ &- \frac{2}{\omega_c\omega_0} + \frac{5}{\left(\omega_c-\frac{1}{2}\omega_0\right)\omega_0}\Bigg] - \frac{1}{\omega_c}\Bigg[\frac{2}{\left(2\omega_c+\frac{1}{2}\omega_0\right)\left(\omega_c+\omega_q\right)} + \frac{2}{\left(2\omega_c+\frac{1}{2}\omega_0\right)\left(\omega_c-\frac{1}{2}\omega_0\right)} \\ &+ \frac{4}{(2\omega_c-\omega_0)^2} + \frac{2}{\omega_0(\omega_c+\omega_0)} + \frac{1}{\omega_0\left(\omega_c-\frac{1}{2}\omega_0\right)}\Bigg] + \frac{1}{\omega_c+\frac{1}{2}\omega_0}\Bigg[\frac{6}{(2\omega_c+\omega_0)(\omega_c+\omega_0)} \\ &+ \frac{2}{(2\omega_c+\omega_0)\omega_c} + \frac{2}{\left(2\omega_c+\frac{1}{2}\omega_0\right)(\omega_c+\omega_0)} + \frac{2}{\left(2\omega_c+\frac{1}{2}\omega_0\right)\left(\omega_c-\frac{1}{2}\omega_0\right)} + \frac{2}{\left(2\omega_c-\frac{1}{2}\omega_0\right)\omega_c} \\ &- \frac{2}{\left(2\omega_c-\frac{1}{2}\omega_0\right)\left(\omega_c-\frac{1}{2}\omega_0\right)} + \frac{5}{\omega_q(\omega_c+\omega_0)} - \frac{1}{\omega_0\omega_c} + \frac{4}{\omega_0\left(\omega_c-\frac{1}{2}\omega_0\right)}\Bigg]\Bigg\}.\end{aligned} \tag{B8}$$

We note that the part from diagram 1 gives the largest contribution, since the first transition in that diagram has a smaller energy difference than the first transitions in the other diagrams, resulting in a smaller denominator.

The expression in Eq. (B8) turns out to simplify much further when everything is put on a common denominator.

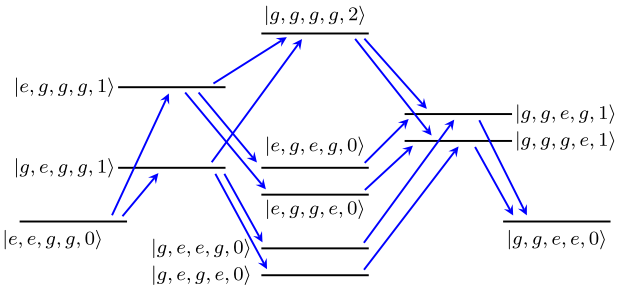

FIG. 9. The eight fourth-order paths connecting the states $|e,e,g,g,0\rangle$ and $|g,g,e,e,0\rangle$ using only the TC terms. To set the energy levels, we have used the parameter values $\omega_c = 6\omega_2$, $\omega_1 = 4\omega_2$, $\omega_3 = 3\omega_2$, and $\omega_4 = 2\omega_2$.

The final result is

$$\lambda_{\text{eff}} = J^{(3)} = \frac{64\lambda^4\omega_c^2\left(4\omega_c^2-7\omega_0^2\right)\sin\theta\cos^3\theta}{\omega_0\left(\omega_0^2-\omega_c^2\right)\left(\omega_0^2-4\omega_c^2\right)^2}, \tag{B9}$$

which is discussed further in the main text.

We note that the coupling, also in the unsimplified case, is proportional to $\sin\theta\cos^3\theta$. Differentiating this with respect to θ and setting the derivative to zero, we obtain

$$0 = \cos^2\theta(\cos^2\theta - 3\sin^2\theta). \tag{B10}$$

Since $\cos\theta = 0$ implies $\lambda_{\text{eff}} = 0$, Eq. (B10) gives that the maximum coupling is achieved when

$$\theta = \pm\arctan\frac{1}{\sqrt{3}} = \pm\frac{\pi}{6}. \tag{B11}$$

APPENDIX C: ANALYTICAL CALCULATIONS WITH FOUR QUBITS

Our system now consists of four qubits, all ultrastrongly coupled to a cavity mode. We calculate the effective

coupling strength between the two states $|i\rangle = |e,e,g,g,0\rangle$ and $|f\rangle = |g,g,e,e,0\rangle$ (equivalent to the 4QM $|e,g,g,e,0\rangle \leftrightarrow |g,e,e,g,0\rangle$, discussed in the main text, with a permutation of the qubit indices). Since this transition conserves the total number of excitations in the system, we limit our study to the case where $\theta_i = 0$ for all four qubits in the interaction Hamiltonian Eq. (5). The Hamiltonian we work with is thus

$$\hat{H} = \omega_c \hat{a}^\dagger \hat{a} + \sum_{i=1}^{4} \frac{\omega_i}{2} \hat{\sigma}_z^{(i)} + (\hat{a} + \hat{a}^\dagger) \sum_{i=1}^{4} \lambda_i \hat{\sigma}_x^{(i)}. \tag{C1}$$

In fact, since the number of excitations is conserved, we can also consider only the TC terms in Eq. (C1), i.e., the TC Hamiltonian

$$\hat{H} = \omega_c \hat{a}^\dagger \hat{a} + \sum_{i=1}^{4} \frac{\omega_i}{2} \hat{\sigma}_z^{(i)} + \sum_{i=1}^{4} \lambda_j \left(\hat{a} \hat{\sigma}_+^{(i)} + \hat{a}^\dagger \hat{\sigma}_-^{(i)} \right). \tag{C2}$$

The two states $|e,e,g,g,0\rangle$ and $|g,g,e,e,0\rangle$ are connected via fourth-order processes. If we use Eq. (C2), there are eight paths connecting the states to this order, as shown in Fig. 9. If we use Eq. (C1) instead, there are 48 paths connecting the states to this order, as shown in Fig. 10.

1. Calculations with the Tavis-Cummings Hamiltonian

We use the same calculation method, as well as the notation, as in Appendix B. From Eqs. (7) and (C2) and Fig. 9, we then obtain the effective coupling

$$\begin{aligned}
\lambda_{\text{eff}} = -\Lambda_4 \Bigg[& \frac{2}{\Delta_{c2}(\Delta_{c1}+\Delta_{c2})(\Delta_{c1}+\Delta_{32})} + \frac{2}{\Delta_{c2}(\Delta_{c1}+\Delta_{c2})(\Delta_{c1}+\Delta_{42})} \\
& + \frac{1}{\Delta_{c2}\Delta_{32}(\Delta_{c1}+\Delta_{32})} + \frac{1}{\Delta_{c2}\Delta_{42}(\Delta_{c1}+\Delta_{42})} + \frac{2}{\Delta_{c1}(\Delta_{c1}+\Delta_{c2})(\Delta_{c1}+\Delta_{32})} \\
& + \frac{2}{\Delta_{c1}(\Delta_{c1}+\Delta_{c2})(\Delta_{c1}+\Delta_{42})} + \frac{1}{\Delta_{c1}\Delta_{31}(\Delta_{c1}+\Delta_{32})} + \frac{1}{\Delta_{c1}\Delta_{41}(\Delta_{c1}+\Delta_{42})} \Bigg] \\
= & \frac{\Lambda_4(\Delta_{13}+\Delta_{24})(\Delta_{13}\Delta_{24}+\Delta_{14}\Delta_{23})}{\Delta_{13}\Delta_{23}\Delta_{14}\Delta_{24}\Delta_{1c}\Delta_{2c}}.
\end{aligned} \tag{C3}$$

Because of the factor $\omega_1 + \omega_2 - \omega_3 - \omega_4$ in the numerator, this expression goes to zero on resonance ($\omega_1 + \omega_2 = \omega_3 + \omega_4$).

2. Calculations with the quantum Rabi Hamiltonian

The first diagram in Fig. 10 gives the following contribution to the effective coupling:

$$\begin{aligned}
\lambda_{\text{eff}}^{(1)} = -\frac{\Lambda_4}{\Omega_{c3}} \Bigg[& \frac{2}{(\Omega_{c3}+\Omega_{c4})(\Omega_{c3}+\Delta_{42})} + \frac{2}{(\Omega_{c3}+\Omega_{c4})(\Omega_{c3}+\Delta_{41})} \\
& + \frac{2}{(\Omega_{c3}+\Delta_{c2})(\Omega_{c3}+\Delta_{42})} + \frac{2}{(\Omega_{c3}+\Delta_{c2})(\Omega_{c3}-\Omega_{12})} + \frac{2}{(\Omega_{c3}+\Delta_{c1})(\Omega_{c3}+\Delta_{41})} \\
& + \frac{2}{(\Omega_{c3}+\Delta_{c1})(\Omega_{c3}-\Omega_{12})} + \frac{1}{\Omega_{34}(\Omega_{c3}+\Delta_{42})} + \frac{1}{\Omega_{34}(\Omega_{c3}+\Delta_{41})} \\
& + \frac{1}{\Delta_{32}(\Omega_{c3}+\Delta_{41})} + \frac{1}{\Delta_{32}(\Omega_{c3}-\Omega_{12})} + \frac{1}{\Delta_{31}(\Omega_{c3}+\Delta_{41})} + \frac{1}{\Delta_{31}(\Omega_{c3}-\Omega_{12})} \Bigg].
\end{aligned} \tag{C4}$$

Note that the six last terms are just the six first terms with 2 replaced by 1 in the numerator and $2\omega_c$ replaced by zero in the denominator. This holds for all four diagrams. The terms in the second diagram contribute with

$$\begin{aligned}
\lambda_{\text{eff}}^{(2)} = -\frac{\Lambda_4}{\Omega_{c4}} \Bigg[& \frac{2}{(\Omega_{c3}+\Omega_{c4})(\Omega_{c3}+\Delta_{42})} + \frac{2}{(\Omega_{c3}+\Omega_{c4})(\Omega_{c3}+\Delta_{41})} \\
& + \frac{2}{(\Omega_{c4}+\Delta_{c2})(\Omega_{c3}+\Delta_{42})} + \frac{2}{(\Omega_{c4}+\Delta_{c2})(\Omega_{c4}-\Omega_{12})} + \frac{2}{(\Omega_{c4}+\Delta_{c1})(\Omega_{c3}+\Delta_{41})} \\
& + \frac{2}{(\Omega_{c4}+\Delta_{c1})(\Omega_{c4}-\Omega_{12})} + \frac{1}{\Omega_{34}(\Omega_{c3}+\omega_4-\omega_2)} + \frac{1}{\Omega_{34}(\Omega_{c3}+\omega_4-\omega_1)} \\
& + \frac{1}{\Delta_{42}(\Omega_{c3}+\Delta_{42})} + \frac{1}{\Delta_{42}(\Omega_{c4}-\Omega_{12})} + \frac{1}{\Delta_{41}(\Omega_{c3}+\Delta_{41})} + \frac{1}{\Delta_{41}(\Omega_{c4}-\Omega_{12})} \Bigg],
\end{aligned} \tag{C5}$$

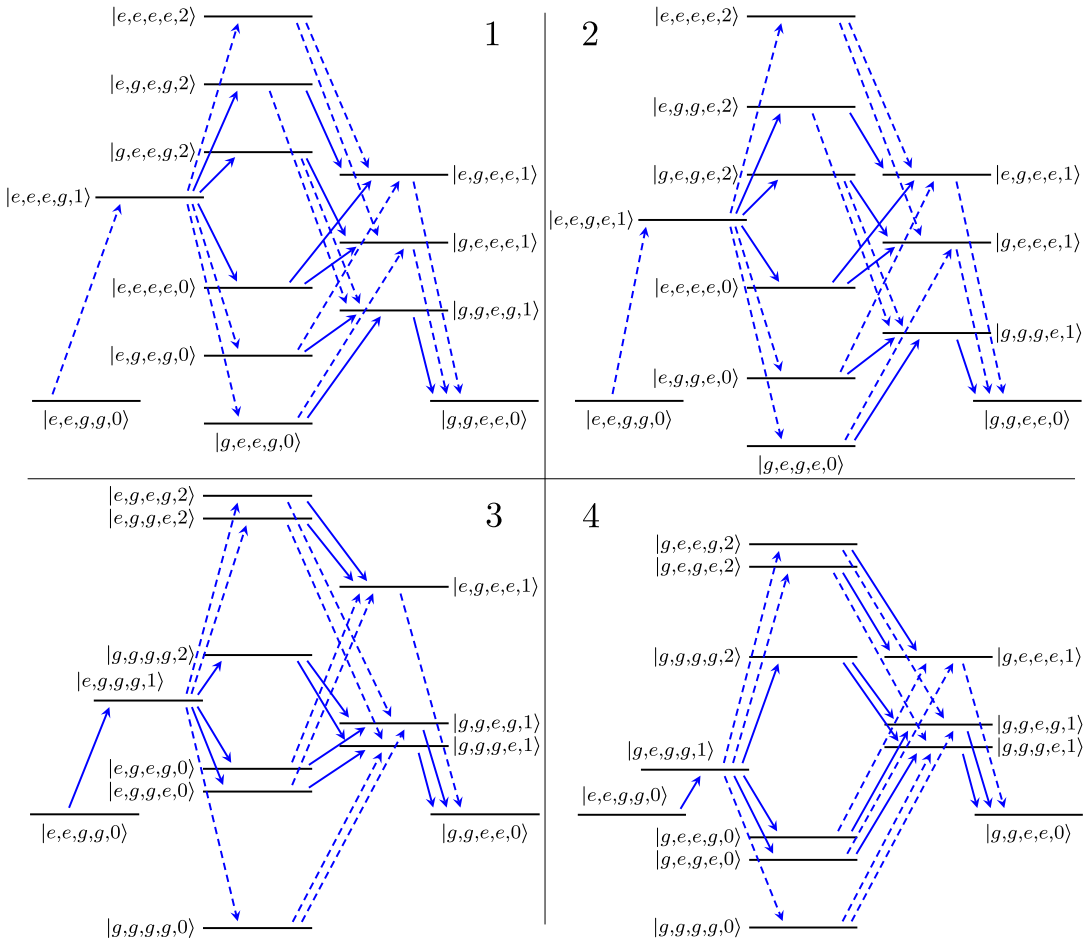

FIG. 10. The 48 fourth-order paths connecting the states $|e,e,g,g,0\rangle$ and $|g,g,e,e,0\rangle$. The four diagrams show 12 paths each. Diagram 1 shows the paths starting with $|e,e,g,g,0\rangle \to |e,e,e,g,1\rangle$, diagram 2 shows the paths starting with $|e,e,g,g,0\rangle \to |e,e,g,e,1\rangle$, diagram 3 shows the paths starting with $|e,e,g,g,0\rangle \to |e,g,g,g,1\rangle$, and diagram 4 shows the paths starting with $|e,e,g,g,0\rangle \to |g,e,g,g,1\rangle$. Transitions that do not conserve the number of excitations in the system are marked by dashed lines, while the transitions that conserve the number of excitations are marked by solid lines. To set the energy levels, we have used the same parameter values as in Fig. 9.

the terms in the third diagram give

$$\begin{aligned}\lambda_{\text{eff}}^{(3)} = -\frac{\Lambda_4}{\Delta_{c2}}\Bigg[&\frac{2}{(\Omega_{c3}+\Delta_{c2})(\Omega_{c3}+\Delta_{42})} + \frac{2}{(\Omega_{c3}+\Delta_{c2})(\Omega_{c3}-\Omega_{12})} \\ &+ \frac{2}{(\Omega_{c4}+\Delta_{c2})(\Omega_{c3}+\Delta_{42})} + \frac{2}{(\Omega_{c4}+\Delta_{c2})(\Omega_{c4}-\Omega_{12})} + \frac{2}{(\Delta_{c1}+\Delta_{c2})(\Omega_{c3}-\Omega_{12})} \\ &+ \frac{2}{(\Delta_{c1}+\Delta_{c2})(\Omega_{c4}-\Omega_{12})} + \frac{1}{\Delta_{32}(\Omega_{c3}+\Delta_{42})} + \frac{1}{\Delta_{32}(\Omega_{c3}-\Omega_{12})} + \frac{1}{\Delta_{42}(\Omega_{c3}+\Delta_{42})} \\ &+ \frac{1}{\Delta_{42}(\Omega_{c4}-\Omega_{12})} + \frac{1}{-\Omega_{12}(\Omega_{c3}-\Omega_{12})} + \frac{1}{-\Omega_{12}(\Omega_{c4}-\Omega_{12})}\Bigg],\end{aligned} \tag{C6}$$

and the terms in the fourth diagram give

$$\begin{aligned}\lambda_{\text{eff}}^{(4)} = -\frac{\Lambda_4}{\Delta_{c1}}\Bigg[&\frac{2}{(\Omega_{c3}+\Delta_{c1})(\Omega_{c3}+\Delta_{41})} + \frac{2}{(\Omega_{c3}+\Delta_{c1})(\Omega_{c3}-\Omega_{12})} \\ &+ \frac{2}{(\Omega_{c4}+\Delta_{c1})(\Omega_{c3}+\Delta_{41})} + \frac{2}{(\Omega_{c4}+\Delta_{c1})(\Omega_{c4}-\Omega_{12})} + \frac{2}{(\Delta_{c1}+\Delta_{c2})(\Omega_{c3}-\Omega_{12})}\end{aligned}$$

$$+\frac{2}{(\Delta_{c1}+\Delta_{c2})(\Omega_{c4}-\Omega_{12})}+\frac{1}{\Delta_{31}(\Omega_{c3}+\Delta_{41})}+\frac{1}{\Delta_{31}(\Omega_{c3}-\Omega_{12})}+\frac{1}{\Delta_{41}(\Omega_{c3}+\Delta_{41})}$$
$$+\frac{1}{\Delta_{41}(\Omega_{c4}-\Omega_{12})}+\frac{1}{-\Omega_{12}(\Omega_{c3}-\Omega_{12})}+\frac{1}{-\Omega_{12}(\Omega_{c4}-\Omega_{12})}\Big]. \tag{C7}$$

Adding up all these terms gives the complicated expression

$$\begin{aligned}\lambda_{\rm eff} = {}& \Lambda_4\big(\Omega_{12}-\Omega_{34}\big)\big(3\omega_2\omega_3\omega_4\Delta_{23}\Delta_{24}\Omega_{34}+\big\{2\omega_c\big[\Delta_{23}-\omega_4\big]-4\omega_c^2\big\}\big\{\omega_3^2\omega_4^2-3\omega_2\omega_3\omega_4\Omega_{34}+\omega_2^2\big[\omega_3^2+3\omega_3\omega_4+\omega_4^2\big]\big\}\\
&+\omega_1^2\big\{\Omega_{12}-\Omega_{34}-2\omega_c\big\}\big\{3\Delta_{23}\Delta_{24}\Omega_{34}+2\omega_c\big[\omega_2^2+\omega_3^2+\omega_4^2+3\omega_3\omega_4-3\omega_2\Omega_{34}\big]\big\}\\
&+\omega_1\big\{12\omega_c^2\Delta_{23}\Delta_{24}\Omega_{34}-3\Delta_{23}\Delta_{24}\Omega_{34}\big[\omega_2\Omega_{34}-\omega_3\omega_4\big]\\
&+2\omega_c\big[\omega_2^2\big(7\omega_3^2+15\omega_3\omega_4+7\omega_4^2\big)+\omega_3\omega_4\big(3\omega_3^2+7\omega_3\omega_4+3\omega_4^2\big)\\
&-3\omega_2\Omega_{34}\big(\omega_2^2+\omega_3^2+4\omega_3\omega_4\big)\big]\big\}\big)/\Omega_{12}\Omega_{34}\Omega_{c3}\Omega_{c4}\Delta_{13}\Delta_{14}\Delta_{23}\Delta_{24}\Delta_{c1}\Delta_{c2}.\end{aligned} \tag{C8}$$

Because of the factor $\omega_1+\omega_2-\omega_3-\omega_4$ in the numerator, this expression goes to zero when $\omega_1+\omega_2=\omega_3+\omega_4$. However, ω_i describe bare qubit transition frequencies. Owing to the presence of the counter-rotating terms in the atom-cavity interaction Hamiltonian, the physical transition frequencies are somewhat different from the bare ones. Hence at the physical resonance $\omega_1+\omega_2\neq\omega_3+\omega_4$.

APPENDIX D: HOW TO APPLY QUBIT MIXING IN AN ERROR-CORRECTION CODE

Here we present a possible application of the spontaneous time evolution of the Dicke model, which leads to 4QM, for the qubit encoding, decoding, and error-syndrome detection modules in an ECC.

1. Quantum repetition codes via qubit mixing

As shown in Sec. II B, 4QM can occur in a system described by the Dicke model in the ultrastrong-coupling regime, which can be described by the effective Hamiltonian ($\hbar=1$)

$$\hat{V}_{\rm II}^{(4)}=J^{(4)}\,(\hat{\sigma}_-^{(1)}\hat{\sigma}_+^{(2)}\hat{\sigma}_+^{(3)}\hat{\sigma}_+^{(4)}+{\rm H.c.}) \tag{D1}$$

and is referred to as type-II 4QM. The spontaneous evolution operator $\hat{U}_t$ after the time $t'=\pi/(2J^{(4)})$ is simply given by

$$\begin{aligned}\hat{U}_{t'}^{(4)}=\exp\left(-i\,\hat{V}_{\rm II}^{(4)}t'\right)=\hat{I}^{(4)}&-|0111\rangle\langle 0111|\\&-|1000\rangle\langle 1000|-i(|0111\rangle\langle 1000|+{\rm H.c.}),\end{aligned} \tag{D2}$$

where $\hat{I}^{(4)}={\rm eye}(16)$ is the four-qubit identity operator and, for simplicity, hereafter we denote $|0\rangle\equiv|g\rangle$ and $|1\rangle\equiv|e\rangle$. Thus, an initial arbitrary state $|\psi_1\rangle=a|0\rangle+b|1\rangle$ of a single qubit and the other three qubits in the ground state $|0\rangle$ is transformed as

$$\hat{S}_4\hat{U}_{t'}^{(4)}(a|0\rangle+b|1\rangle)|000\rangle=|0\rangle(a|000\rangle+b|111\rangle), \tag{D3}$$

as shown in Fig. 11(c). Note that the $(\pi/4)$-phase gate $\hat{S}_n={\rm diag}(1,i)$ can be applied to any qubit n except $n=1$. It is seen that the first qubit is decoupled (disentangled) from the others at $t=0$ and $t=t'$, so it can be discarded. Thus, Eq. (D2) effectively describes the standard $(N=3)$-qubit repetition code

$$\begin{aligned}\hat{U}_{\rm rep}^{(N)}|\psi_1\rangle|0\rangle^{\otimes(N-1)}&=\hat{U}_{\rm CNOT}^{12}\hat{U}_{\rm CNOT}^{13}\cdots\hat{U}_{\rm CNOT}^{1N}|\psi_1\rangle|0\rangle^{\otimes(N-1)}\\&=a|0\rangle^{\otimes N}+b|1\rangle^{\otimes N}\equiv|\psi_N\rangle,\end{aligned} \tag{D4}$$

where $\hat{U}_{\rm CNOT}^{1n}$ denotes the CNOT gate with the control (target) qubit 1 (n) for $n=2,\ldots,N$. More precisely, $\hat{S}_4\hat{U}_{t'}^{(4)}|\psi_1\rangle|000\rangle=(\hat{I}^{(1)}\otimes\hat{U}_{\rm rep}^{(3)})|0\rangle|\psi_1\rangle|00\rangle$, where $\hat{I}^{(1)}$ is the single-qubit identity operator and we have an auxiliary qubit in the state $|0\rangle$ in addition to those in Eq. (D4). Analogously, it can be shown that the 3QM in the model described by the effective interaction Hamiltonian

$$\hat{V}^{(3)}=J^{(3)}\,(\hat{\sigma}_+^{(1)}\hat{\sigma}_+^{(2)}\hat{\sigma}_-^{(3)}+{\rm H.c.}) \tag{D5}$$

after the time $t'=\pi/(2J^{(3)})$ is given by

$$\begin{aligned}\hat{U}_{t'}^{(3)}=\exp\left(-i\,\hat{V}^{(3)}t'\right)=\hat{I}^{(3)}&-|011\rangle\langle 011|-|100\rangle\langle 100|\\&-i(|011\rangle\langle 100|+{\rm H.c.}),\end{aligned} \tag{D6}$$

which realizes the two-qubit repetition code, as shown in Fig. 11(b), since

$$\hat{S}_3\hat{U}_{t'}^{(3)}(a|0\rangle+b|1\rangle)|00\rangle=|0\rangle(a|00\rangle+b|11\rangle), \tag{D7}$$

In Eq. (D6), $\hat{I}^{(3)}={\rm eye}(8)$ is the three-qubit identity operator.

2. Error-correction code

Now we present the implementation of a toy version of an ECC (for a pedagogical description, see Ref. [41]) for correcting a single phase-flip error or a bit-flip error. We apply the ECC circuit shown in Fig. 12, and show that the quantum repetition codes, based on the CNOT gates in the modules depicted in yellow, can be replaced by the type-II 4QM described above.

Figure 11(a) shows a standard N-qubit repetition code implemented with N CNOT gates. Although CNOT gates have been implemented in circuit-QED systems, these implementations are based on a sequence of a few pulses using, usually, higher-excited levels [71,72]. Thus, it is desirable to reduce the number of CNOT gates or other entangling gates, which

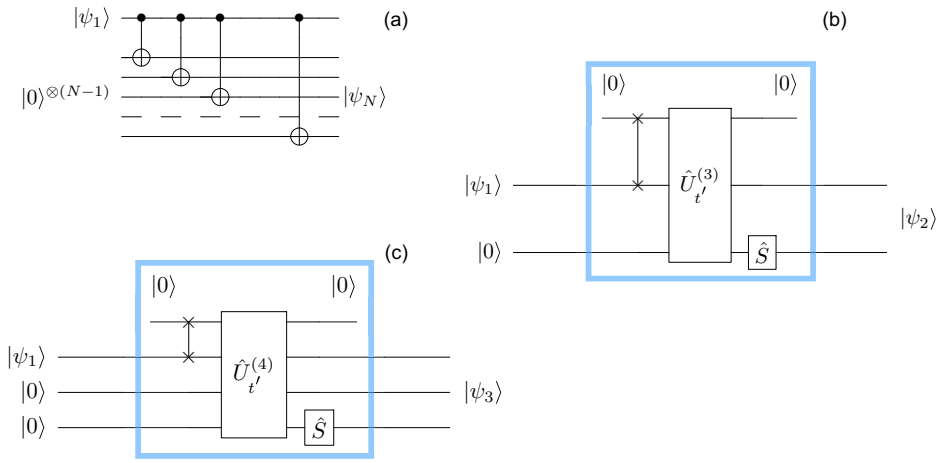

FIG. 11. (a) Standard N-qubit repetition code based on N CNOT gates for generating $|\psi_N\rangle = a|0\rangle^{\otimes N} + b|1\rangle^{\otimes N}$ (for $N = 2,3,\ldots$). Repetition codes for (b) three and (c) four qubits based on qubit mixing corresponding to the spontaneous evolution operations $\hat{U}^{(3)}_{t'}$ and $\hat{U}^{(4)}_{t'}$, given by Eqs. (D6) and (D2), respectively, followed by the $(\pi/4)$-phase gate $\hat{S}$ acting on the Nth qubit. The operation marked by $\times-\times$ corresponds to the classical SWAP gate, which is not necessary but is added to show the correspondence of all the panels. In (b) and (c), the first qubit is finally disentangled from the others, so it can be discarded after the operation. In a special case, the four-qubit repetition code can implement the encoder A and decoder A', and can be used for the error-syndrome detection in the ECC shown in Fig. 12.

cannot be implemented easily like those corresponding to the spontaneous evolution of a given system.

Figure 12 shows a standard circuit implementing the ECC, which enables the correction of a single phase-flip error, or of a single bit-flip error if the blocks B and B' are omitted. These blocks B and B' are composed of three single-qubit rotations $\hat{Y}(\pi/2)$ and $\hat{Y}(-\pi/2)$ about angles of $\pm\pi/2$ around the y axis, respectively. The $\hat{Y}$ rotation about an arbitrary angle θ is defined by $\hat{Y}(\theta) = [\cos\frac{\theta}{2}, -\sin\frac{\theta}{2}; \sin\frac{\theta}{2}, \cos\frac{\theta}{2}]$. Thus, the rotations $\hat{Y}(\pm\pi/2)$ effectively realize Hadamard-like gates corresponding to rotations of the basis states $\{|0\rangle,|1\rangle\}$ into (from) $\{|\pm\rangle = (|+\rangle + |-\rangle)/\sqrt{2}\}$ in B (B'). The modules A and B (B' and A') enable encoding (decoding) a single qubit against a single phase-flip error, while the gates A (A'), without B and B', enable encoding (decoding) a single qubit against a single bit-flip error. The module E in Fig. 12 describes a dissipative evolution or a channel, which introduces a single error (either a bit flip or a phase flip) in one of the qubits. The error-syndrome detection is performed by the four CNOT gates in the modules S_1 and S_2 using two additional qubits, which are then measured by two detectors yielding the values $m,n \in \{0,1\}$. The error correction is done in the module C

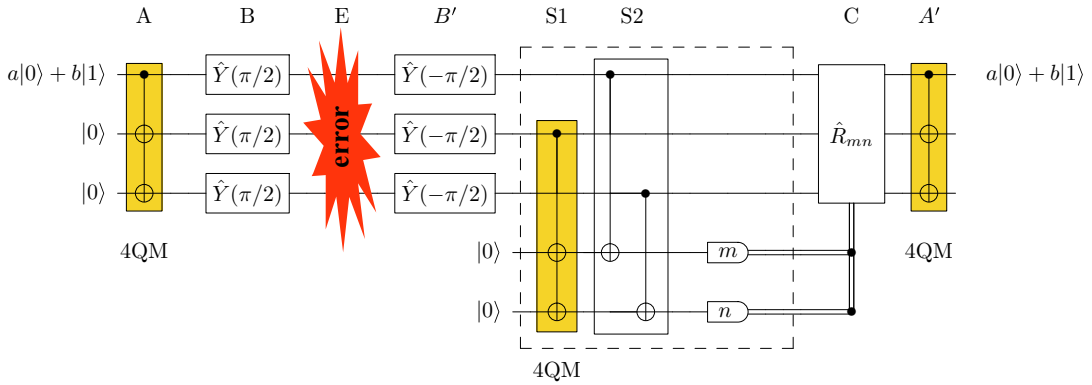

FIG. 12. Circuit implementing an ECC correcting a single phase-flip error. If the modules B and B' are omitted, then the circuit corrects a single bit-flip error. The circuit modules include encoder A, basis rotator B (from the basis $\{|0\rangle,|1\rangle\}$ into $\{|+\rangle,|-\rangle\}$) corresponding to the Hadamard gates or rotations $\hat{Y}(\pi/2)$, dissipative channel or evolution (E, when the error happens), basis rotator B' (from $\{|+\rangle,|-\rangle\}$ into $\{|0\rangle,|1\rangle\}$ being inverse to B), error-syndrome detector S (composed of blocks S_1, S_2, and detectors with two possible outcomes $m,n = 0,1$), error corrector [C, where the single-qubit operation R_{nm}, given by Eq. (D8), is conditioned on the classical information from the detectors], and decoder A'. In our implementation, the blocks A, A', and S_1, which are composed of two CNOT gates with two qubits in $|0\rangle$, can be replaced by type-II 4QM, i.e., by spontaneous evolution for the time $t = \pi/(2J^{(4)})$ of the system governed by the effective interaction Hamiltonian $\hat{V}^{(4)}$, given in Eq. (D1).

by rotating (flipping) a proper qubit as conditioned on the measured values m,n:

$$\hat{R}_{mn} = \hat{\sigma}_x^{(n-m+2)} \approx \hat{Y}_{n-m+2}(\pi), \tag{D8}$$

where we define $\hat{\sigma}_x^{(4)} \approx \hat{Y}_4(\pi)$ to be the identity operator.

As marked in yellow in Fig. 12, the encoder A, decoder A', but also the error-syndrome module S_1 can be implemented via the type-II 4QM, i.e., the spontaneous evolution of the system described by Eq. (D2). In fact, the error-syndrome module S_2 can also be expressed via the sequence of the type-II 4QM operations $\hat{U}^{(4)}$ applied to different qubits, together with single-qubit rotations. This possibility comes from the fundamental theorem about the universality of an arbitrary entangling gate (thus, including $\hat{U}^{(4)}$). However, we focus here on simple and direct applications of $\hat{U}^{(4)}$. Thus, a lengthy circuit implementing the module S_2 via $\hat{U}^{(4)}$ is not presented here.

Finally, we make three remarks:

(1) In our proposal we need to apply the 4QM between different qubits. Thus, the question arises whether one can efficiently tune the ultrastrong coupling between a chosen fraction of a collection of six qubits and a cavity field. For switching on and off the coupling it is possible to change the transition energy of the qubits involved. This can be easily done by applying, e.g., a flux offset to the qubits.

(2) By using three times the 4QM operations instead of the six CNOT gates, we need an extra qubit in addition to the five qubits shown in Fig. 11(c).

(3) In a specific physical system, it might be easier to perform 3QM rather than 4QM. Then, the six CNOT gates in the modules A, A', and S_1, shown in Fig. 11(c), can be replaced by the 3QM corresponding to the spontaneous evolution $\hat{U}_{t'}^{(3)}$, given by Eq. (D6).

[1] L. M. Duan, M. D. Lukin, J. I. Cirac, and P. Zoller, Long-distance quantum communication with atomic ensembles and linear optics, Nature (London) **414**, 413 (2001).

[2] C. W. Chou, J. Laurat, H. Deng, K. S. Choi, H. De Riedmatten, D. Felinto, and H. J. Kimble, Functional quantum nodes for entanglement distribution over scalable quantum networks, Science **316**, 1316 (2007).

[3] J. Majer, J. M. Chow, J. M. Gambetta, J. Koch, B. R. Johnson, J. A. Schreier, L. Frunzio, D. I. Schuster, A. A. Houck, A. Wallraff, A. Blais, M. H. Devoret, S. M. Girvin, and R. J. Schoelkopf, Coupling superconducting qubits via a cavity bus, Nature (London) **449**, 443 (2007).

[4] A. Gonzalez-Tudela, D. Martin-Cano, E. Moreno, L. Martin-Moreno, C. Tejedor, and F. J. Garcia-Vidal, Entanglement of Two Qubits Mediated by One-Dimensional Plasmonic Waveguides, Phys. Rev. Lett. **106**, 020501 (2011).

[5] M. Tavis and F. W. Cummings, Exact solution for an N-molecule–radiation-field Hamiltonian, Phys. Rev. **170**, 379 (1968).

[6] G. Günter, A. A. Anappara, J. Hees, A. Sell, G. Biasiol, L. Sorba, S. De Liberato, C. Ciuti, A. Tredicucci, A. Leitenstorfer, and R. Huber, Sub-cycle switch-on of ultrastrong light-matter interaction, Nature (London) **458**, 178 (2009).

[7] P. Forn-Díaz, J. Lisenfeld, D. Marcos, J. J. García-Ripoll, E. Solano, C. J. P. M. Harmans, and J. E. Mooij, Observation of the Bloch-Siegert Shift in a Qubit-Oscillator System in the Ultrastrong Coupling Regime, Phys. Rev. Lett. **105**, 237001 (2010).

[8] Y. Todorov, A. M. Andrews, R. Colombelli, S. De Liberato, C. Ciuti, P. Klang, G. Strasser, and C. Sirtori, Ultrastrong Light-Matter Coupling Regime with Polariton Dots, Phys. Rev. Lett. **105**, 196402 (2010).

[9] P. Forn-Díaz, J. J. García-Ripoll, B. Peropadre, J.-L. Orgiazzi, M. A. Yurtalan, R. Belyansky, C. M. Wilson, and A. Lupascu, Ultrastrong coupling of a single artificial atom to an electromagnetic continuum in the nonperturbative regime, Nat. Phys. **13**, 39 (2016).

[10] T. Niemczyk, F. Deppe, H. Huebl, E. P. Menzel, F. Hocke, M. J. Schwarz, J. J. García-Ripoll, D. Zueco, T. Hümmer, E. Solano, A. Marx, and R. Gross, Circuit quantum electrodynamics in the ultrastrong-coupling regime, Nat. Phys. **6**, 772 (2010).

[11] T. Schwartz, J. A. Hutchison, C. Genet, and T. W. Ebbesen, Reversible Switching of Ultrastrong Light-Molecule Coupling, Phys. Rev. Lett. **106**, 196405 (2011).

[12] G. Scalari, C. Maissen, D. Turčinková, D. Hagenmüller, S. De Liberato, C. Ciuti, C. Reichl, D. Schuh, W. Wegscheider, M. Beck, and J. Faist, Ultrastrong coupling of the cyclotron transition of a 2D electron gas to a THz metamaterial, Science **335**, 1323 (2012).

[13] M. Geiser, F. Castellano, G. Scalari, M. Beck, L. Nevou, and J. Faist, Ultrastrong Coupling Regime and Plasmon Polaritons in Parabolic Semiconductor Quantum Wells, Phys. Rev. Lett. **108**, 106402 (2012).

[14] S. Kéna-Cohen, S. A Maier, and D. D. C. Bradley, Ultrastrongly coupled exciton-polaritons in metal-clad organic semiconductor microcavities, Adv. Opt. Mater. **1**, 827 (2013).

[15] S. Gambino, M. Mazzeo, A. Genco, O. Di Stefano, S. Savasta, S. Patane, D. Ballarini, F. Mangione, G. Lerario, D. Sanvitto, and G. Gigli, Exploring light-matter interaction phenomena under ultrastrong coupling regime, ACS Photonics **1**, 1042 (2014).

[16] C. Maissen, G. Scalari, F. Valmorra, M. Beck, J. Faist, S. Cibella, R. Leoni, C. Reichl, C. Charpentier, and W. Wegscheider, Ultrastrong coupling in the near field of complementary split-ring resonators, Phys. Rev. B **90**, 205309 (2014).

[17] M. Goryachev, W. G. Farr, D. L. Creedon, Y. Fan, M. Kostylev, and M. E. Tobar, High-Cooperativity Cavity QED with Magnons at Microwave Frequencies, Phys. Rev. Appl. **2**, 054002 (2014).

[18] A. Baust, E. Hoffmann, M. Haeberlein, M. J. Schwarz, P. Eder, J. Goetz, F. Wulschner, E. Xie, L. Zhong, F. Quijandría, D. Zueco, J.-J. García-Ripoll, L. García-Álvarez, G. Romero, E. Solano, K. G. Fedorov, E. P. Menzel, F. Deppe, A. Marx, and R. Gross, Ultrastrong coupling in two-resonator circuit QED, Phys. Rev. B **93**, 214501 (2016).

[19] F. Yoshihara, T. Fuse, S. Ashhab, K. Kakuyanagi, S. Saito, and K. Semba, Superconducting qubit-oscillator circuit beyond the ultrastrong-coupling regime, Nat. Phys. **13**, 44 (2016).

[20] N. K. Langford, R. Sagastizabal, M. Kounalakis, C. Dickel, A. Bruno, F. Luthi, D. J. Thoen, A. Endo, and L. DiCarlo,

Experimentally simulating the dynamics of quantum light and matter at ultrastrong coupling, arXiv:1610.10065.

[21] Z. Chen, Y. Wang, T. Li, L. Tian, Y. Qiu, K. Inomata, F. Yoshihara, S. Han, F. Nori, J. S. Tsai, and J. Q. You, Single-photon-driven high-order sideband transitions in an ultrastrongly coupled circuit-quantum-electrodynamics system, Phys. Rev. A **96**, 012325 (2017).

[22] J. Braumüller, M. Marthaler, A. Schneider, A. Stehli, H. Rotzinger, M. Weides, and A. V. Ustinov, Analog quantum simulation of the Rabi model in the ultra-strong coupling regime, arXiv:1611.08404.

[23] S. De Liberato, D. Gerace, I. Carusotto, and C. Ciuti, Extracavity quantum vacuum radiation from a single qubit, Phys. Rev. A **80**, 053810 (2009).

[24] Q. Ai, Y. Li, H. Zheng, and C. P. Sun, Quantum anti-Zeno effect without rotating wave approximation, Phys. Rev. A **81**, 042116 (2010).

[25] R. Stassi, A. Ridolfo, O. Di Stefano, M. J. Hartmann, and S. Savasta, Spontaneous Conversion from Virtual to Real Photons in the Ultrastrong-Coupling Regime, Phys. Rev. Lett. **110**, 243601 (2013).

[26] A. Ridolfo, S. Savasta, and M. J. Hartmann, Nonclassical Radiation from Thermal Cavities in the Ultrastrong Coupling Regime, Phys. Rev. Lett. **110**, 163601 (2013).

[27] L. Garziano, A. Ridolfo, R. Stassi, O. Di Stefano, and S. Savasta, Switching on and off of ultrastrong light-matter interaction: Photon statistics of quantum vacuum radiation, Phys. Rev. A **88**, 063829 (2013).

[28] L. Garziano, R. Stassi, A. Ridolfo, O. Di Stefano, and S. Savasta, Vacuum-induced symmetry breaking in a superconducting quantum circuit, Phys. Rev. A **90**, 043817 (2014).

[29] J.-F. Huang and C. K. Law, Photon emission via vacuum-dressed intermediate states under ultrastrong coupling, Phys. Rev. A **89**, 033827 (2014).

[30] Y.-J. Zhao, Y.-L. Liu, Y.-X. Liu, and F. Nori, Generating nonclassical photon states via longitudinal couplings between superconducting qubits and microwave fields, Phys. Rev. A **91**, 053820 (2015).

[31] A. F. Kockum, V. Macrì, L. Garziano, S. Savasta, and F. Nori, Frequency conversion in ultrastrong cavity QED, Scientific Reports **7**, 5313 (2017).

[32] G. Zhu, D. G. Ferguson, V. E. Manucharyan, and J. Koch, Circuit QED with fluxonium qubits: Theory of the dispersive regime, Phys. Rev. B **87**, 024510 (2013).

[33] K. K. W. Ma and C. K. Law, Three-photon resonance and adiabatic passage in the large-detuning Rabi model, Phys. Rev. A **92**, 023842 (2015).

[34] L. Garziano, R. Stassi, V. Macrì, A. F. Kockum, S. Savasta, and F. Nori, Multiphoton quantum Rabi oscillations in ultrastrong cavity QED, Phys. Rev. A **92**, 063830 (2015).

[35] L. Garziano, V. Macrì, R. Stassi, O. Di Stefano, F. Nori, and S. Savasta, One Photon Can Simultaneously Excite Two or More Atoms, Phys. Rev. Lett. **117**, 043601 (2016).

[36] A. F. Kockum, A. Miranowicz, V. Macrì, S. Savasta, and F. Nori, Deterministic quantum nonlinear optics with single atoms and virtual photons, Phys. Rev. A **95**, 063849 (2017).

[37] L. Mandel and E. Wolf, *Optical Coherence and Quantum Optics* (Cambridge University Press, Cambridge, U.K., 1995).

[38] Y. R. Shen, *Principles of Nonlinear Optics* (Wiley-Interscience, New York, 1984).

[39] H. I. Takesue and K. Inoue, Generation of polarization-entangled photon pairs and violation of Bell's inequality using spontaneous four-wave mixing in a fiber loop, Phys. Rev. A **70**, 031802 (2004).

[40] P. W. Shor, Scheme for reducing decoherence in quantum computer memory, Phys. Rev. A **52**, R2493(R) (1995).

[41] R. T. Perry, *Quantum Computing from the Ground Up* (World Scientific, Singapore, 2012).

[42] S. L. Rolston and W. D. Phillips, Nonlinear and quantum atom optics, Nature (London) **416**, 219 (2002).

[43] G. Lenz, P. Meystre, and E. M. Wright, Nonlinear Atom Optics, Phys. Rev. Lett. **71**, 3271 (1993).

[44] M. Trippenbach, Y. Band, and P. Julienne, Four wave mixing in the scattering of Bose-Einstein condensates, Opt. Express **3**, 530 (1998).

[45] L. Deng, E. W. Hagley, J. Wen, M. Trippenbach, Y. Band, P. S. Julienne, J. E. Simsarian, K. Helmerson, S. L. Rolston, and W. D. Phillips, Four-wave mixing with matter waves, Nature (London) **398**, 218 (1999).

[46] A. Bermudez, D. Porras, and M. A. Martin-Delgado, Competing many-body interactions in systems of trapped ions, Phys. Rev. A **79**, 060303 (2009).

[47] R. H. Dicke, Coherence in spontaneous radiation processes, Phys. Rev. **93**, 99 (1954).

[48] Y. X. Liu, J. Q. You, L. F. Wei, C. P. Sun, and F. Nori, Optical Selection Rules and Phase-Dependent Adiabatic State Control in a Superconducting Quantum Circuit, Phys. Rev. Lett. **95**, 087001 (2005).

[49] J. Q. You and F. Nori, Atomic physics and quantum optics using superconducting circuits, Nature (London) **474**, 589 (2011).

[50] X. Gu, A. F. Kockum, A. Miranowicz, Y. X. Liu, and F. Nori, Microwave photonics with superconducting quantum circuits, arXiv:1707.02046.

[51] A. Blais, J. Gambetta, A. Wallraff, D. I. Schuster, S. M. Girvin, M. H. Devoret, and R. J. Schoelkopf, Quantum-information processing with circuit quantum electrodynamics, Phys. Rev. A **75**, 032329 (2007).

[52] M. Malekakhlagh, A. Petrescu, and H. E. Türeci, Cutoff-free circuit quantum electrodynamics, arXiv:1701.07935.

[53] O. Di Stefano, R. Stassi, L. Garziano, A. F. Kockum, S. Savasta, and F. Nori, Feynman-diagrams approach to the quantum Rabi model for ultrastrong cavity QED: Stimulated emission and reabsorption of virtual particles dressing a physical excitation, New J. Phys. **19**, 053010 (2017).

[54] I. Chiorescu, P. Bertet, K. Semba, Y. Nakamura, C. J. P. M. Harmans, and J. E. Mooij, Coherent dynamics of a flux qubit coupled to a harmonic oscillator, Nature (London) **431**, 159 (2004).

[55] F. Yan, S. Gustavsson, A. Kamal, J. Birenbaum, A. P. Sears, D. Hover, T. J. Gudmundsen, D. Rosenberg, G. Samach, S. Weber, J. L. Yoder, T. P. Orlando, J. Clarke, A. J. Kerman, and W. D. Oliver, The flux qubit revisited to enhance coherence and reproducibility, Nat. Commun. **7**, 12964 (2016).

[56] F. Beaudoin, J. M. Gambetta, and A. Blais, Dissipation and ultrastrong coupling in circuit QED, Phys. Rev. A **84**, 043832 (2011).

[57] A. Ridolfo, M. Leib, S. Savasta, and M. J. Hartmann, Photon Blockade in the Ultrastrong Coupling Regime, Phys. Rev. Lett. **109**, 193602 (2012).

[58] M. A. Nielsen and I. L. Chuang, *Quantum Computation and Quantum Information* (Cambridge University Press, Cambridge, U.K., 2000).

[59] D. G. Cory, M. D. Price, W. Maas, E. Knill, R. Laflamme, W. H. Zurek, T. F. Havel, and S. S. Somaroo, Experimental Quantum Error Correction, Phys. Rev. Lett. **81**, 2152 (1998).

[60] J. Chiaverini, D. Leibfried, T. Schaetz, M. D. Barrett, R. B. Blakestad, J. Britton, W. M. Itano, J. D. Jost, E. Knill, C. Langer, R. Ozeri, and D. J. Wineland, Realization of quantum error correction, Nature (London) **432**, 602 (2004).

[61] P. Schindler, J. T. Barreiro, T. Monz, V. Nebendahl, D. Nigg, M. Chwalla, M. Hennrich, and R. Blatt, Experimental repetitive quantum error correction, Science **332**, 1059 (2011).

[62] T. B. Pittman, B. C. Jacobs, and J. D. Franson, Demonstration of quantum error correction using linear optics, Phys. Rev. A **71**, 052332 (2005).

[63] O. Moussa, J. Baugh, C. A. Ryan, and R. Laflamme, Demonstration of Sufficient Control for Two Rounds of Quantum Error Correction in a Solid State Ensemble Quantum Information Processor, Phys. Rev. Lett. **107**, 160501 (2011).

[64] G. Waldherr, Y. Wang, S. Zaiser, M. Jamali, T. Schulte-Herbrüggen, H. Abe, T. Ohshima, J. Isoya, J. F. Du, P. Neumann, and J. Wrachtrup, Quantum error correction in a solid-state hybrid spin register, Nature (London) **506**, 204 (2014).

[65] M. D. Reed, L. DiCarlo, S. E. Nigg, L. Sun, L. Frunzio, S. M. Girvin, and R. J. Schoelkopf, Realization of three-qubit quantum error correction with superconducting circuits, Nature (London) **482**, 382 (2012).

[66] D. Ristè, S. Poletto, M.-Z. Huang, A. Bruno, V. Vesterinen, O.-P. Saira, and L. DiCarlo, Detecting bit-flip errors in a logical qubit using stabilizer measurements, Nat. Commun. **6**, 6983 (2015).

[67] J. Kelly, R. Barends, A. G. Fowler, A. Megrant, E. Jeffrey, T. C. White, D. Sank, J. Y. Mutus, B. Campbell, Yu Chen, Z. Chen, B. Chiaro, A. Dunsworth, I.-C. Hoi, C. Neill, P. J. J. O'Malley, C. Quintana, P. Roushan, A. Vainsencher, J. Wenner, A. N. Cleland, and J. M. Martinis, State preservation by repetitive error detection in a superconducting quantum circuit, Nature (London) **519**, 66 (2015).

[68] M. Takita, A. D. Córcoles, E. Magesan, B. Abdo, M. Brink, A. Cross, J. M. Chow, and J. M. Gambetta, Demonstration of Weight-Four Parity Measurements in the Surface Code Architecture, Phys. Rev. Lett. **117**, 210505 (2016).

[69] B. P. Lanyon, M. Barbieri, M. P. Almeida, T. Jennewein, T. C. Ralph, K. J. Resch, G. J. Pryde, J. L. O'Brien, A. Gilchrist, and A. G. White, Simplifying quantum logic using higher-dimensional Hilbert spaces, Nat. Phys. **5**, 134 (2008).

[70] X.-G. Wen, *Quantum Field Theory of Many-Body Systems: From the Origin of Sound to an Origin of Light and Electrons* (Oxford University Press, Oxford, U.K., 2004).

[71] L. DiCarlo, J. M. Chow, J. M. Gambetta, L. S. Bishop, B. R. Johnson, D. I. Schuster, J. Majer, A. Blais, L. Frunzio, S. M. Girvin, and R. J. Schoelkopf, Demonstration of two-qubit algorithms with a superconducting quantum processor, Nature (London) **460**, 240 (2009).

[72] L. DiCarlo, M. D. Reed, L. Sun, B. R. Johnson, J. M. Chow, J. M. Gambetta, L. Frunzio, S. M. Girvin, M. H. Devoret, and R. J. Schoelkopf, Preparation and measurement of three-qubit entanglement in a superconducting circuit, Nature (London) **467**, 574 (2010).

5.8 Paper VIII: Nonperturbative Dynamical Casimir Effect in Optomechanical Systems: Vacuum Casimir-Rabi Splittings

Non-Perturbative Dynamical Casimir Effect in Optomechanical Systems: Vacuum Casimir-Rabi Splittings

Vincenzo Macrì,[1,2] Alessandro Ridolfo,[2] Omar Di Stefano,[2]
Anton Frisk Kockum,[2] Franco Nori,[2,3] and Salvatore Savasta[1,2]

[1] *Dipartimento di Scienze Matematiche e Informatiche, Scienze Fisiche e Scienze della Terra, Università di Messina, I-98166 Messina, Italy*
[2] *Center for Emergent Matter Science, RIKEN, Saitama 351-0198, Japan*
[3] *Physics Department, The University of Michigan, Ann Arbor, Michigan 48109-1040, USA*

We study the dynamical Casimir effect using a fully quantum-mechanical description of both the cavity field and the oscillating mirror. We do not linearize the dynamics, nor do we adopt any parametric or perturbative approximation. By numerically diagonalizing the full optomechanical Hamiltonian, we show that the resonant generation of photons from the vacuum is determined by a ladder of mirror-field *vacuum Rabi splittings*. We find that vacuum emission can originate from the free evolution of an initial pure mechanical excited state, in analogy with the spontaneous emission from excited atoms. By considering a coherent drive of the mirror, using a master-equation approach to take losses into account, we are able to study the dynamical Casimir effect for optomechanical coupling strengths ranging from weak to ultrastrong. We find that a resonant production of photons out of the vacuum can be observed even for mechanical frequencies lower than the cavity-mode frequency. Since high mechanical frequencies, which are hard to achieve experimentally, were thought to be imperative for realizing the dynamical Casimir effect, this result removes one of the major obstacles for the observation of this long-sought effect. We also find that the dynamical Casimir effect can create entanglement between the oscillating mirror and the radiation produced by its motion in the vacuum field, and that vacuum Casimir-Rabi oscillations can occur. Finally, we also show that all these findings apply not only to optomechanical systems, but also to parametric amplifiers operating in the fully quantum regime.

PACS numbers: 42.50.Pq, 42.50.Ct

I. INTRODUCTION

Quantum-field theory predicts that vacuum fluctuations can be converted into real particles by the energy provided through certain external perturbations [1–8]. Examples include the Schwinger effect [1], predicting the production of electron-positron pairs from the vacuum under the application of intense electrical fields; Hawking radiation [3, 9], which is caused by the bending of spacetime in intense gravitational fields and determines the evaporation of black holes; the Unruh effect [10], predicting that an accelerating observer will observe blackbody radiation where an inertial observer would observe none; and the dynamical Casimir effect (DCE) [2, 6, 7] describing the generation of photons from the quantum vacuum due to rapid changes of the geometry (in particular, the positions of some boundaries) or material properties of electrically neutral macroscopic or mesoscopic objects.

The creation of photons by moving mirrors was first predicted by Moore [2] in 1970, for a one-dimensional cavity. In 1976, Fulling and Davis [11] demonstrated that photons can be generated even by a single mirror, when it is subjected to a nonuniform acceleration. Since the first prediction of the DCE, many different experimental setups, able to produce sudden nonadiabatic changes inducing light emission from the quantum vacuum, have been proposed [12]. These proposals can be divided into two main groups: setups where the photons are created due to the movement of mirrors [11, 13–17] [mechanical (M) DCE], and systems where the boundary conditions are modulated by some effective motion producing a parametric amplification of vacuum fluctuations [6–8, 18–25] [parametric (P) DCE].

The experimental detection of the DCE is challenging owing to the difficulty in changing the boundary conditions, e.g., by moving physical objects, such as massive mirrors, sufficiently fast for generation of a significant number of photons. In 1996, Lambrecht, Jaekel, and Reynaud [14] provided a quantitative estimate of the photon flux radiated from an optomechanical system consisting of a cavity with oscillating mirrors. Taking advantage of resonance-enhancement effects, they showed that a significant number of microwave photons, sufficient to allow detection, can be produced in realistic high-Q cavities with a moderate peak velocity of the mirrors. However, the resonance condition, requiring that the mechanical oscillation frequency $\omega_{\rm m}$ be at least twice that of the lowest-frequency cavity mode $\omega_{\rm c}$, remains a major barrier to the experimental demonstration of the MDCE. Recently, high-frequency mechanical oscillators, [$\omega_{\rm m}/(2\pi) \sim 6$ GHz] [26] have been realized. However, to produce vacuum radiation at a frequency $\omega_{\rm c}/(2\pi) \sim 5$ GHz, a still higher mechanical frequency $\omega_{\rm m}/(2\pi) \sim 10$ GHz is required.

In order to circumvent these difficulties, a number of theoretical proposals has suggested to use experimental

setups where the boundary conditions are modulated by some effective motion instead (PDCE). Examples of such proposals include: (i) using lasers to rapidly modulate the reflectivity of thin semiconductor films [18, 20, 21], (ii) modulating the resonance frequency of a superconducting stripline resonator [22], non-adiabatic time-modulation of (iii) the light-matter coupling strength in cavity QED systems [23, 27–33], or (iv) of the background in which the field propagates [5, 7, 19], and (v) to use a superconducting quantum interference device (SQUID) to modulate the boundary condition of a superconducting waveguide or resonator [6, 24, 25].

Recently, using superconducting circuits [34–37], the DCE (specifically, the PDCE) has been demonstrated experimentally, implementing proposals (iv) and (v). In particular, it was observed [6] in a coplanar transmission line terminated by a SQUID whose inductance was modulated at high frequency (> 10 GHz). This was also demonstrated by modulating the index of refraction of a Josephson metamaterial embedded in a microwave cavity [7]. Of course, these all-optical experiments do not demonstrate the conversion of *mechanical* energy into photons, as predicted by the DCE. Such a direct observation is still lacking.

Moreover, it is worth noting that the interpretation of these *all-optical* experiments is not unique. Although these experiments demonstrate key features of the DCE physics, the question may arise if these can be regarded as direct observations of the DCE or quantum simulations of the DCE. Specifically, these experiments can also be considered as examples of spontaneous parametric down-conversion [38, 39] in a waveguide or in a cavity (see, e.g., [37] for implementations with superconducting quantum circuits). In this optical quantum process, incident photons at frequency ω are converted into pairs of photons at lower frequencies ω_1 and ω_2, such that $\omega_1+\omega_2=\omega$. This process is determined by the nonlinearities of the material system and the vacuum fluctuations of the electromagnetic field. The validity of this description is confirmed by looking at the interaction Hamiltonians describing the investigated systems [7, 24, 25]. In both cases, they can be written as $\lambda(\delta\Phi_{\rm ext}/\Phi_0)\Phi^2$, where $\Phi_{\rm ext}$ is the external driving flux, Φ_0 is the flux quantum, Φ is the flux field in the waveguide or in the cavity, and λ is a coupling coefficient depending on the specific system. In this Hamiltonian, the amplitude of the driving field is multiplied with the square of the amplitude of the excited field, just like in the Hamiltonians that describe second-order nonlinear optical processes. Furthermore, conceptually there are subtle differences between moving boundaries and moving sources (see, e.g., [40]). We also observe that other proposed all-optical PDCE setups [such as (i) and (iii)], might have undesired background signals, due to the undesired excitations arising from the driving fields which can overwhelm the expected signal (see, e.g. [41]). Hence, direct observations of the conversion of mechanical energy into photon pairs (MDCE) would be highly desirable.

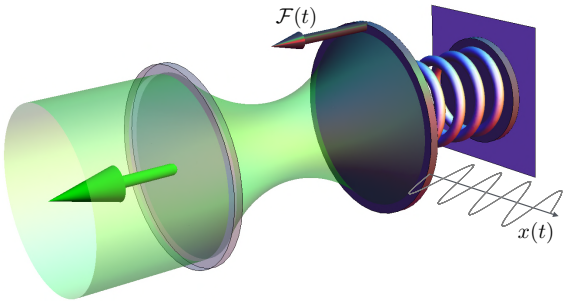

Figure 1. Schematic of a generic optomechanical system where one of the mirrors in an optical cavity can vibrate at frequency $\omega_{\rm m}$. If the vibrating mirror is excited by an external drive $\mathcal{F}(t)$, able to create a k-phonon state with a non-negligible probability, the vibrating mirror can emit photon pairs if $k\omega_{\rm m}\simeq 2\omega_{\rm c}$, where $\omega_{\rm c}$ is the resonance frequency of the cavity.

Most theoretical studies of the MDCE consider the mirror that scatters the vacuum field to follow a prescribed motion [2, 11–13, 15, 42–44]. Therefore the photon creation from the initial vacuum state is usually described as a parametric amplification process, just as in the case of the PDCE. Exceptions consider fluctuations of the position of the mirror driven by vacuum radiation pressure using linear dispersion theory [45, 46] or focus on the mirror motion as the main dynamical degree of freedom. In the latter case, studies have shown how the DCE induces friction forces on the mirror [47, 48] or leads to decoherence of mechanical quantum superposition states [49].

In this article, we investigate the MDCE in cavity optomechanical systems [50], treating both the cavity field and the moving mirror as quantum-mechanical systems. Calculations are made *without* performing any linearization of the dynamical equations. Multiple scattering between the two subsystems is taken into account nonperturbatively. The interactions of the two subsystems with the environment is described by using a master equation [51, 52]. A surprising feature of this approach is that the DCE can be described *without* the need for a time-dependent light-matter interaction. The only time-dependent Hamiltonian term considered here is the one describing the external drive of the vibrating mirror. Actually, within this approach, the DCE effect can be described, at least in principle, even *without* considering any time-dependent Hamiltonian. Specifically, we find that vacuum radiation can originate from the free evolution of an initial pure mechanical excited state, in analogy with the spontaneous emission from excited atoms. We believe that this theoretical framework provides a more fundamental explanation of the DCE. Note that fundamental processes in quantum field theory are described by interaction Hamiltonians which do *not* depend parametrically on time. We find that the resonant generation of photons from the vacuum is determined by a ladder of mirror-field vacuum Rabi-like energy splittings. When the loss rates are lower than the corresponding frequency

splittings, a reversible exchange of energy between the vibrating mirror and the cavity field, which we call *vacuum Casimir-Rabi oscillations*, can be observed.

Cavity-optomechanics experiments are rapidly approaching the regime where the radiation pressure of a single photon displaces the mechanical oscillator by more than its zero-point uncertainty [53–59]. Specifically, in circuit optomechanics, it has been shown that the radiation pressure effect can be strongly enhanced by introducing a qubit-mediated [56, 57] or modulated [60] interaction between the mechanical and the electromagnetic resonator. This ultrastrong coupling (USC) regime, where the optomechanical coupling rate is comparable to the mechanical frequency, can give rise to strong nonlinearities even in systems described by the standard optomechanics interaction Hamiltonian, which depends linearly on the mirror displacement [61, 62]. This regime favours the observation of macroscopic mechanical oscillators in a nonclassical state of motion [61–64]. This requires a full quantum treatment of both the mechanical and optical degrees of freedom, and multiple-scattering effects between the field and the mechanical oscillator cannot be ignored.

The approach considered here allows us to extend the investigation of the DCE to the USC limit of cavity optomechanics. We find that this regime is able to remove one of the major obstacles for the experimental observation of this long-sought effect. Indeed, we show that, approaching USC, a resonant production of photons out from the vacuum can be observed for mechanical frequencies lower than the lowest cavity-mode frequency. Approximately, the resonance condition for the production of photon pairs out from the vacuum is $k\,\omega_{\rm m} \simeq 2\omega_{\rm c}$, with k integer. This corresponds to processes where k phonons in the mechanical oscillator are converted into two cavity photons. The matrix element for this transition decreases rapidly for increasing k, but increases when the optomechanical coupling g increases. Already the resonance condition with $k = 2$, corresponding to $\omega_{\rm m} \simeq \omega_{\rm c}$, where DCE matrix elements display reasonable amplitude even at moderate coupling, is promising for the observation of the MDCE. Indeed, this resonance condition can be achieved in the GHz spectral range using ultra-high-frequency mechanical micro- or nano-resonators [26, 59].

Very recently, new resonance conditions in the DCE that potentially allow the production of photons for $\omega_{\rm m} < \omega_{\rm c}$ have been found assuming a classical prescribed anharmonic motion of the mirror [65]. This model, however, describes photon emission from vacuum fluctuations only in the instability region and the resulting time evolution of the mean photon number grows exponentially even in the presence of cavity losses. On the contrary, in our approach, the vibrating mirror is treated as a harmonic (anharmonicity only originates from the interaction) quantum degree of freedom on the same footing as the cavity field and we do not find unstable regions.

II. RESULTS

A. Model

We consider the case of a cavity with a movable end mirror (see Fig. 1) and focus on the simplest possible model system in cavity optomechanics, which has been used to successfully describe most of such experiments to date. A detailed derivation of the optomechanical Hamiltonian can be found in Ref. [66]. Both the cavity field and the position of the mirror are treated as dynamical variables and a canonical quantization procedure is adopted. By considering only one mechanical mode with resonance frequency $\omega_{\rm m}$ and bosonic operators $\hat{b}$ and $\hat{b}^\dagger$, and only the lowest-frequency optical mode $\omega_{\rm c}$ of the cavity, with bosonic operators $\hat{a}$ and $\hat{a}^\dagger$, the system Hamiltonian can be written as $\hat{H}_{\rm s} = \hat{H}_0 + \hat{H}_{\rm I}$, where

$$\hat{H}_0 = \hbar\omega_{\rm c}\hat{a}^\dagger\hat{a} + \hbar\omega_{\rm m}\hat{b}^\dagger\hat{b} \tag{1}$$

is the unperturbed Hamiltonian. The Hamiltonian describing the mirror-field interaction is

$$\hat{H}_{\rm I} = \frac{\hbar G}{2}(\hat{a} + \hat{a}^\dagger)^2\hat{x}\,, \tag{2}$$

where $\hat{x} = x_{\rm ZPF}(\hat{b} + \hat{b}^\dagger)$ is the mechanical displacement ($x_{\rm ZPF}$ is the zero-point fluctuation amplitude of the vibrating mirror) and G is a coupling parameter. By developing the photonic factor in normal order, and by defining new bosonic phonon and photon operators and a renormalized photon frequency, $\hat{H}_{\rm s}$ can be written as

$$\hat{H}_{\rm s} = \hat{H}_0 + \hat{V}_{\rm om} + \hat{V}_{\rm DCE}\,, \tag{3}$$

where $\hat{H}_0$ formally coincides with Eq. (1),

$$\hat{V}_{\rm om} = \hbar g\hat{a}^\dagger\hat{a}(\hat{b} + \hat{b}^\dagger) \tag{4}$$

is the standard optomechanical interaction conserving the number of photons, and

$$\hat{V}_{\rm DCE} = \frac{\hbar g}{2}(\hat{a}^2 + \hat{a}^{\dagger 2})(\hat{b} + \hat{b}^\dagger)\,, \tag{5}$$

describes the creation and annihilation of photon pairs [67], where $g = G\,x_{\rm ZPF}$ is the optomechanical coupling rate. As we will see in detail below, $\hat{V}_{\rm DCE}$ determines the DCE. The Hamiltonian (3) describes the interaction between a moving mirror and the radiation pressure of a cavity field. However, the same radiation-pressure-type coupling is obtained for microwave optomechanical circuits (see, e.g., Ref. [56]).

When describing most of the optomechanics experiments to date [50], $\hat{V}_{\rm DCE}$ is neglected. This is a very good approximation when the mechanical frequency is much smaller than the cavity frequency (which is the most common experimental situation), since $\hat{V}_{\rm DCE}$ connects bare states with an energy difference $2\hbar\omega_{\rm c} \pm \hbar\omega_{\rm m}$ much larger

than the coupling strength $\hbar g$. With this approximation, the resulting Hamiltonian, $\hat{H}_0 + \hat{V}_{\rm om}$, conserves the number of photons and can be analytically diagonalized. The full Hamiltonian in Eq. (3) provides the simplest unified description of cavity-optomechanics experiments and the DCE in a cavity with a vibrating mirror.

In order to properly describe the system dynamics, including external driving, dissipation and decoherence, the coupling to external degrees of freedom needs to be considered. A coherent external drive of the vibrating mirror can be described by including the following time-dependent Hamiltonian,

$$\hat{V}_{\rm m}(t) = \mathcal{F}(t)\,(\hat{b} + \hat{b}^\dagger)\,, \tag{6}$$

where $\mathcal{F}(t)$ is proportional to the external force applied to the mirror. Analogously, the coherent optical excitation of the cavity mode can be described by

$$\hat{V}_{\rm c}(t) = \mathcal{E}(t)\,(\hat{a} + \hat{a}^\dagger)\,, \tag{7}$$

where $\mathcal{E}(t)$ is proportional to the coherent optical field exciting the cavity. In the following, we will only consider the external excitation of the mirror [$\mathcal{E}(t) = 0$] by a continuous-wave drive or by a pulse, in contrast to most cavity optomechanical experiments, where the system is optically excited.

B. Vacuum Casimir-Rabi splittings

We begin by numerically diagonalizing the system Hamiltonian $\hat{H}_{\rm s}$ in Eq. (3). Figure 2(a) displays the lowest energy levels as a function of the ratio between the cavity and the mechanical frequency, using an optomechanical coupling $g/\omega_{\rm m} = 0.04$. For comparison, we also show in Fig. 2(a) (dashed grey lines) the lowest energy levels

$$E_{n,k} = \hbar\omega_{\rm c} n - \hbar g^2 n^2/\omega_{\rm m} + \hbar\omega_m k$$

for the standard optomechanics Hamiltonian $\hat{H}_0 + \hat{V}_{\rm om}$. In this case, the system eigenstates can be written as

$$|n, k_n\rangle = |n\rangle_{\rm c} \otimes \hat{D}(n\beta)|k\rangle_{\rm m}\,, \tag{8}$$

where n is the cavity photon number and the mechanical state $|k_n\rangle$ is a displaced Fock state, determined by the displacement operator $\hat{D}(n\beta) = \exp[n\beta(\hat{b}^\dagger - \hat{b})]$, with $\beta = g/\omega_{\rm m}$. The dashed grey horizontal lines in Fig. 2(a) correspond to states $|0, k_0\rangle \equiv |0, k\rangle$ belonging to the $n = 0$ manifold. The dashed grey lines with lower non-zero slope (slope 1) describes the $n = 1$ manifold ($|1, k_1\rangle$), while those with slope 2 describe the energy levels of the manifold with $n = 2$.

The continuous blue lines correspond to the energy levels obtained by numerically diagonalizing the system Hamiltonian $\hat{H}_{\rm s}$ in Eq. (3). The main difference compared to the grey lines is the appearance of level anticrossings of increasing size at increasing eigenenergy values when $E_{0,k} = E_{2,k-1}$ (corresponding to a cavity frequency $\omega_{\rm c} = \omega_{\rm m}/2 + 2g^2/\omega_{\rm m} \simeq \omega_{\rm m}/2$). We observe that the condition $\omega_{\rm c} \simeq \omega_{\rm m}/2$ is the standard resonance condition ($\omega_{\rm m} = 2N\omega_{\rm c}$) for the DCE in a cavity with a vibrating mirror [14], with $N = 1$. These avoided crossings arise from the coherent coupling induced by $\hat{V}_{\rm DCE}$ between the states $|0, k\rangle \leftrightarrow |2, (k-1)_2\rangle$ with $k \geq 1$. If the optomechanical coupling is not too strong, the size of the anticrossings can be analytically calculated by using first-order perturbation theory. By approximating $|k_2\rangle \simeq |k\rangle$, for the energy splittings, we obtain the simple expression

$$2\hbar\Omega_{0,k}^{2,k-1} = 2\langle 2, (k-1)_2|\hat{V}_{\rm DCE}|0, k\rangle \simeq \hbar g\sqrt{2k},$$

in very good agreement with the numerical results in Fig. 2(a). When the splitting is at its minimum ($\omega_{\rm c} = \omega_{\rm m}/2 + 2g^2/\omega_{\rm m}$), the two system eigenstates are approximately (not exactly, owing to dressing effects induced by $\hat{V}_{\rm DCE}$) the symmetric and antisymmetric superposition states

$$|\psi_{2(3)}\rangle \simeq \frac{1}{\sqrt{2}}(|0, 1\rangle \pm |2, 0_2\rangle)\,. \tag{9}$$

These *vacuum Casimir-Rabi splittings*, demonstrating optomechanical-induced hybridization of zero- and two-photon states, establish a close analogy between the DCE and cavity QED, where the atom-photon vacuum Rabi splitting and quantum Rabi oscillations in the time domain have been observed in many systems and widely exploited for many applications [68]. We observe, however, that, while quantum Rabi splittings in cavity QED describe coherent coupling between states with the same number of excitations, Casimir-Rabi splittings involve pairs of states with different number of excitations. In this case, for example, a state with k excitations (phonons) hybridizes with a state with $k + 1$ excitations ($k - 1$ phonons and 2 photons). This non-conservation of excitation numbers is reminiscent of cavity QED in the USC regime, where the counter-rotating terms in the atom-field interaction Hamiltonian enable the coupling of states with different excitation numbers [69–74]. More generally, the DCE Hamiltonian in Eq. (5) gives rise to several additional avoided-level crossings, describing resonant optomechanical scattering processes $|n, k_n\rangle \leftrightarrow |n+2, (k-q)_{n+2}\rangle$, which occur when the energies of the final and initial states coincide ($2\omega_{\rm c} \sim q\,\omega_{\rm m}$).

These coherent couplings induced by $\hat{V}_{\rm DCE}$ constitute the fundamental quantum mechanism through which mechanical energy is transferred to the vacuum electromagnetic field, giving rise to the DCE. For example, in the absence of losses, an initial 1-phonon-0-photon state $|0, 1\rangle$ (not being a system eigenstate) will evolve as

$$|\psi(t)\rangle = \cos\left(\Omega_{0,1}^{2,0}\,t\right)|0, 1\rangle - i\sin\left(\Omega_{0,1}^{2,0}\,t\right)|2, 0_2\rangle\,, \tag{10}$$

and thus, after a time $t = \pi/(2\Omega_{0,1}^{2,0})$, will spontaneously

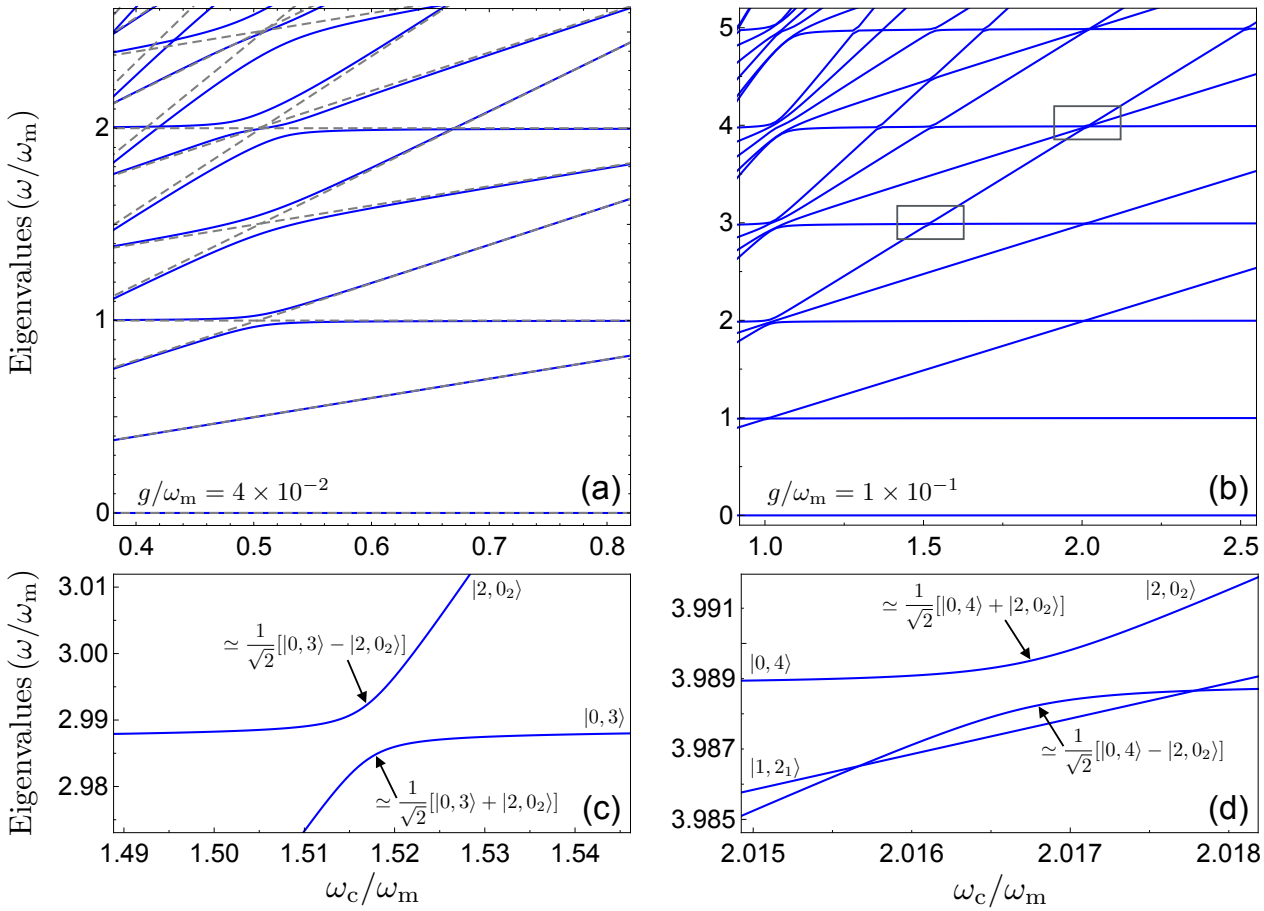

Figure 2. Lowest energy levels of the system Hamiltonian as a function of the ratio between the cavity frequency and the mechanical frequency. In (a) an optomechanical coupling $g/\omega_m = 0.04$ has been used. The dashed grey lines describe the eigenenergies of the standard optomechanics Hamiltonian $\hat{H}_0 + \hat{V}_{om}$. The blue continuous curves are the eigenvalues of $\hat{H}_s = H_0 + \hat{V}_{om} + \hat{V}_{DCE}$, which have also been calculated for a coupling $g/\omega_m = 0.1$ as shown in (b). Panels (c) and (d) display enlarged views of the two boxed regions in (b) showing avoided level crossings due to optomechanical hybridizations of zero- and two-photon states (vacuum Casimir-Rabi splittings).

evolve into a photon pair. This elementary analysis shows that, if the mechanical and photonic loss rates are much lower than the coupling rate $\Omega_{0,1}^{2,0}$, mechanical energy can be converted, at least in principle, into light with 100% efficiency. Moreover, according to Eq. (10), at $t = \pi/(4\Omega_{0,1}^{2,0})$, the moving mirror and the cavity field become maximally entangled. Figure 2(b) shows the lowest energy eigenvalues of $\hat{H}_s$ for larger cavity-mode frequencies, using a stronger optomechanical coupling $g/\omega_m = 0.1$. The figure [see also the boxed details enlarged in panels 2(c) and (d)] shows that optomechanical resonant couplings occur also for $\omega_m < 2\omega_c$. In particular, vacuum Casimir-Rabi splittings occur when $E_{0,k} = E_{2,k-q}$, corresponding to a cavity frequency $\omega_c - 2g^2/\omega_m \simeq q\,\omega_m/2$, also when $q > 1$. Avoided level crossings for $q = 2$ are clearly visible in Fig. 2(b). Smaller splittings for $q = 3$ and $q = 4$ are indicated by black boxes and their enlarged views are shown in Figs. 2(c) and (d). By using first-order perturbation theory, the size of these avoided level crossings can be calculated analytically:

$$\begin{aligned} 2\hbar\Omega_{0,k}^{2,k-q} &= 2\langle 0,k|\hat{V}_{DCE}|2,(k-q)_2\rangle \\ &= \sqrt{2}\,\hbar g\left[\sqrt{k+1}D_{k+1,k-q}(2\beta)\right. \\ &\quad \left. + \sqrt{k}D_{k-1,k-q}(2\beta)\right], \end{aligned} \tag{11}$$

where the matrix elements of the displacement operators can be expressed in terms of associated Laguerre polynomials: $D_{k',k}(\alpha) = \sqrt{k!/k'!}\alpha^{k'-k}e^{-|\alpha|^2/2}L_k^{k'-k}(|\alpha|^2)$. We note that the resonance conditions with $\omega_m \leq \omega_c$ have nonzero DCE matrix elements (11) thanks to the non-orthogonality of mechanical Fock states with different phonon numbers, belonging to different photonic manifolds:

$$\langle k|k'_2\rangle = D_{k,k'}(2\beta) \neq 0$$

(see, e.g., Ref. [64]). Note also that, for $\beta \to 0$,

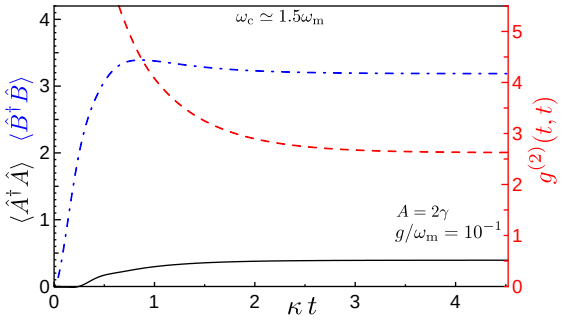

Figure 3. System dynamics for $\omega_c \simeq 1.5\omega_m$ under continuous-wave drive of the vibrating mirror. The blue dash-dotted curve describes the mean phonon number $\langle \hat{B}^\dagger \hat{B} \rangle$, while the black solid curve describes the mean intracavity photon number $\langle \hat{A}^\dagger \hat{A} \rangle$ rising thanks to the DCE. The zero-delay normalized photon-photon correlation function $g^{(2)}(t,t)$ is also plotted as a red dashed curve with values given on the y-axis on the right. All parameters are given in the text.

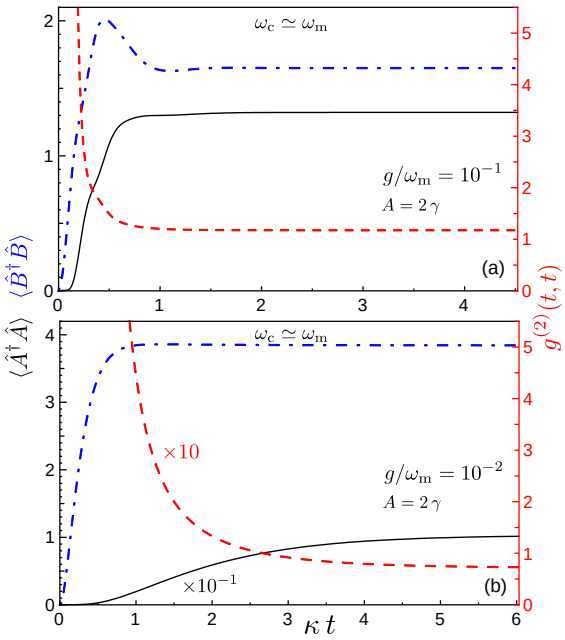

Figure 4. System dynamics for $\omega_c \simeq \omega_m$ under continuous-wave drive of the vibrating mirror. The blue dash-dotted curves describe the mean phonon number $\langle \hat{B}^\dagger \hat{B} \rangle$, while the black solid curves describe the mean intracavity photon number $\langle \hat{A}^\dagger \hat{A} \rangle$ rising thanks to the DCE. The zero-delay normalized photon-photon correlation function $g^{(2)}(t,t)$ is also plotted (red dashed curve with values given on the y-axis on the right). Panel (a) has been obtained using $g/\omega_m = 0.1$; panel (b) with $g/\omega_m = 10^{-2}$. All the other parameters are given in the text.

$\langle k|k_2' \rangle \to \delta_{k,k'}$. Examples of analytically-calculated splittings $2\Omega_{0,k}^{2,k-q}$ are displayed in Appendix A, where we also present a comparison between the numerically-calculated vacuum Rabi splitting and the corresponding analytical calculations, obtained with first-order perturbation theory for $2\Omega_{0,3}^{2,0}$ and $2\Omega_{0,4}^{2,0}$. Also for resonance conditions with $q > 1$, when the splitting is at its minimum (corresponding to values of ω_c such that $E_{0,k} \simeq E_{2,k-q}$), the two system eigenstates are essentially symmetric and antisymmetric linear superpositions. For example, for the boxed splitting at lower ω_c,

$$|\psi_{5(6)}\rangle \simeq \frac{1}{2}(|0,3\rangle \pm |2,0_2\rangle)\,. \tag{12}$$

Neglecting losses, an initial 3-phonon state $|0,3\rangle$ (not being a system eigenstate) will thus evolve spontaneously as

$$|\psi(t)\rangle = \cos(\Omega_{0,3}^{2,0}\, t)\,|0,3\rangle - i \sin(\Omega_{0,3}^{2,0}\, t)\,|2,0\rangle\,, \tag{13}$$

giving rise to a 100% mechanical-to-optical energy transfer and to vacuum-induced entanglement.

C. DCE in the weak-coupling regime

Here we investigate the dynamics giving rise to the DCE, numerically solving the system master equation (described in Appendix B). We focus on some experimentally promising cases, with $\omega_c \geq \omega_m$. In this subsection, we limit our investigations to the *weak-coupling regime*, which, however, does not refer to the optomechanical coupling strength (we use g/ω_m up to 0.1). Instead, following the terminology of cavity QED, by the term *weak*, we mean Casimir-Rabi splittings $2\Omega_{0,k}^{2,k-q}$ smaller than the total decoherence rate $\gamma + \kappa$, where γ and κ are the mechanical and photonic loss rates respectively (see Appendix B). We consider the optomechanical system initially in its ground state and numerically solve the master equation (B1) including the excitation of the moving mirror by a single-tone continuous-wave mechanical drive $\mathcal{F}(t) = A\cos(\omega_d t)$. Figure 3 shows the time evolution of the mean phonon number $\langle \hat{B}^\dagger \hat{B} \rangle$ (blue dash-dotted curve), the intracavity mean photon number $\langle \hat{A}^\dagger \hat{A} \rangle$ (black solid curve), and the equal-time photonic normalized second-order correlation function (red dashed curve)

$$g^{(2)}(t,t) = \frac{\langle \hat{A}^\dagger(t)\hat{A}^\dagger(t)\hat{A}(t)\hat{A}(t)\rangle}{\langle \hat{A}^\dagger(t)\hat{A}(t)\rangle^2}\,, \tag{14}$$

where $\hat{A}, \hat{B}$ are dressed photonic and phononic operators, as explained in Appendix B. We assume a zero-temperature reservoir and use $\kappa/\omega_m = 3 \times 10^{-3}$ and $\gamma = 10\kappa$ for the photonic and mechanical loss rates. We consider a weak ($A/\gamma = 2$) resonant excitation of the vibrating mirror ($\omega_d = \omega_m$). Figure 3 shows the system dynamics for the case $\omega_c \simeq 3\omega_m/2$ [corresponding to the minimum level-splitting shown in Fig. 2(c)]. We used a normalized coupling $g/\omega_m = 0.1$. The results demon-

strate that a measurable rate of photons is produced. In particular, a steady-state mean intra-cavity photon number $\langle \hat{A}^\dagger \hat{A} \rangle_{\rm ss} \simeq 0.3$ is obtained, corresponding (for a resonance frequency of the cavity mode $\omega_{\rm c}/(2\pi) = 6$ GHz) to a steady-state output photon flux $\Phi = \kappa \langle \hat{A}^\dagger \hat{A} \rangle_{\rm ss} \sim 3 \times 10^6$ photons per second. The output photon flux is remarkable, taking into account the weak mechanical drive, corresponding to a steady-state mean phonon number $\langle \hat{b}^\dagger \hat{b} \rangle_{\rm ss} = 4$ for $g/\omega_{\rm m} = 0$, and the quite low cavity quality factor $Q_{\rm c} = \omega_{\rm c}/\kappa = 500$ used in the numerical calculations. Note that $Q_{\rm c}$-values beyond 10^6 are obtained in microwave resonators (see, e.g., [75]). Also, the mechanical loss rate γ used here corresponds to a quality factor $Q_{\rm m}$ one order of magnitude lower than the experimentally measured values in ultra-high-frequency mechanical resonators [26, 59]. Such a low driving amplitude and quality factors were used in order to reduce both memory and numerical effort. We observe that the steady-state phonon number does not reach the value $\langle \hat{B}^\dagger \hat{B} \rangle_{\rm ss} = 4$ obtained in the absence of $\hat{V}_{\rm DCE}$. This is an expected result, since the calculations fully take into account the correlated field-mirror dynamics induced by the DCE. The calculated second-order correlation function $g^{(2)}(t,t)$, also displayed in Fig. 3, starts with very high values, confirming that photons are emitted in pairs. As time goes on, it decreases significantly, due to losses which affect the photon-photon correlation and to the increase in the mean photon number (note that $g^{(2)}(t,t)$, owing to the squared denominator, is intensity dependent).

Figure 4 displays results for the case $\omega_{\rm c} \simeq \omega_{\rm m}$. In this case, a higher-frequency mechanical oscillator is required. However, as we pointed out in the introduction, mechanical oscillators with resonance frequencies $\omega_{\rm m}/(2\pi) \sim 6$ GHz have been realized [26]. In the present case, the DCE can be observed by coupling such a mechanical oscillator to a microwave resonator with the same resonance frequency. The advantage of this configuration is that the corresponding matrix elements (vacuum Casimir-Rabi splittings) $\Omega_{0,k}^{2,k-2}$ are non-negligible even for quite low optomechanical couplings. Figure 4(a), obtained using a coupling $g/\omega_{\rm m} = 0.1$, shows a remarkable energy transfer from the moving mirror to the cavity field which in its steady state contains more than 1 photon, corresponding to a steady-state output photon flux Φ beyond 10^7 photons per second. Figure 4(b) has been obtained using an optomechanical coupling one order of magnitude lower. The resulting steady-state mean intracavity photon number decreases by one order of magnitude to $\langle \hat{A}^\dagger \hat{A} \rangle_{\rm ss} \simeq 0.1$, but it is still measureable. This result is particularly interesting because it shows that the MDCE can be observed with state-of-the-art ultra-high-frequency mechanical resonators [26, 59] and with normalized coupling rates β below those already achieved in circuit optomechanics [53]. We can conclude that the MDCE can be observed at $\omega_{\rm c} \simeq \omega_{\rm m}$ even when the optomechanical USC regime is not reached, although reaching it can significantly enhance the emission rate.

Quantum correlations in microwave radiation produced by the DCE in a superconducting waveguide terminated and modulated by a SQUID have been investigated [76]. The results indicate that the produced radiation can be strictly nonclassical and can display a measurable amount of intermode entanglement. In the approaches where the real or effective mirror is assumed to follow a prescribed classical motion, the entanglement between the moving mirror and the emitted electromagnetic field cannot be investigated. On the contrary, the present theoretical framework, fully taking into account the quantum correlations between the moving mirror and the cavity field, induced by $\hat{V}_{\rm DCE}$, allows us to investigate if the DCE creates optomechanical entanglement. In the present case, the dynamics involve many system states and, owing to the presence of losses, the system is far from being in a pure state during its time evolution. We quantify the entanglement using the negativity $\mathcal{N}$ (see Appendix C). By considering the same, numerically calculated, density matrix used to derive the results shown in Fig. 3, we find a steady-state negativity oscillating around $\mathcal{N} \simeq 5 \times 10^{-2}$, attesting that the DCE is able to produce mirror-field steady-state entanglement. For comparison, a maximally entangled Bell-like state, like that described by Eq. (13) at time $t = \pi/(4\Omega_{0,3}^{2,0})$, has a negativity $\mathcal{N} = 0.5$. Using the parameters of Fig. 4(a), we find a larger steady-state negativity, oscillating around $\mathcal{N} \simeq 0.1$. However, we find no entanglement ($\mathcal{N} \simeq 0$) for the parameters of Fig. 4(b), when the influence of the DCE on the dynamics of the moving mirror is small.

D. Vacuum Casimir-Rabi oscillations

Here we investigate the DCE in the *strong-coupling regime*, when the Casimir-Rabi splittings $2\Omega_{0,k}^{2,k-q}$ are larger than the total decoherence rate $\gamma + \kappa$. This regime is particularly interesting, since it provides direct evidence of the level structure determining the DCE and the multiple-scattering effects between the two sub-systems. Moreover, as we are going to show, it gives rise to non-perturbative entangled dynamics of the cavity field and the moving mirror.

We numerically solve the master equation (B1), assuming the optomechanical system prepared in its ground state and including the vibrating mirror excitation by an ultrafast resonant pulse $\mathcal{F}(t) = \mathcal{A}\,\mathcal{G}(t - t_0)\cos(\omega_{\rm d}\, t)$, where $\mathcal{G}(t)$ is a normalized Gaussian function. We consider an optomechanical coupling $g/\omega_{\rm m} = 0.1$ and set the cavity frequency at the value providing the minimum level-splitting $2\Omega_{0,3}^{2,0}/\omega_{\rm m} \simeq 8 \times 10^{-3}$ shown in Fig. 2(c) ($\omega_{\rm c} \simeq 3\omega_{\rm m}/2$). We consider pulses with central frequency resonant with the mechanical oscillator ($\omega_{\rm d} = \omega_{\rm m}$), and with standard deviation $\sigma = (20\Omega_{0,3}^{2,0})^{-1} \simeq 12/\omega_{\rm m}$. For the loss rates, we use $\gamma = 0.15\ \Omega_{0,3}^{2,0} \simeq 6 \times 10^{-4}\,\omega_{\rm m}$ and $\kappa = \gamma/2$.

Figure 5 displays the system dynamics after the pulse

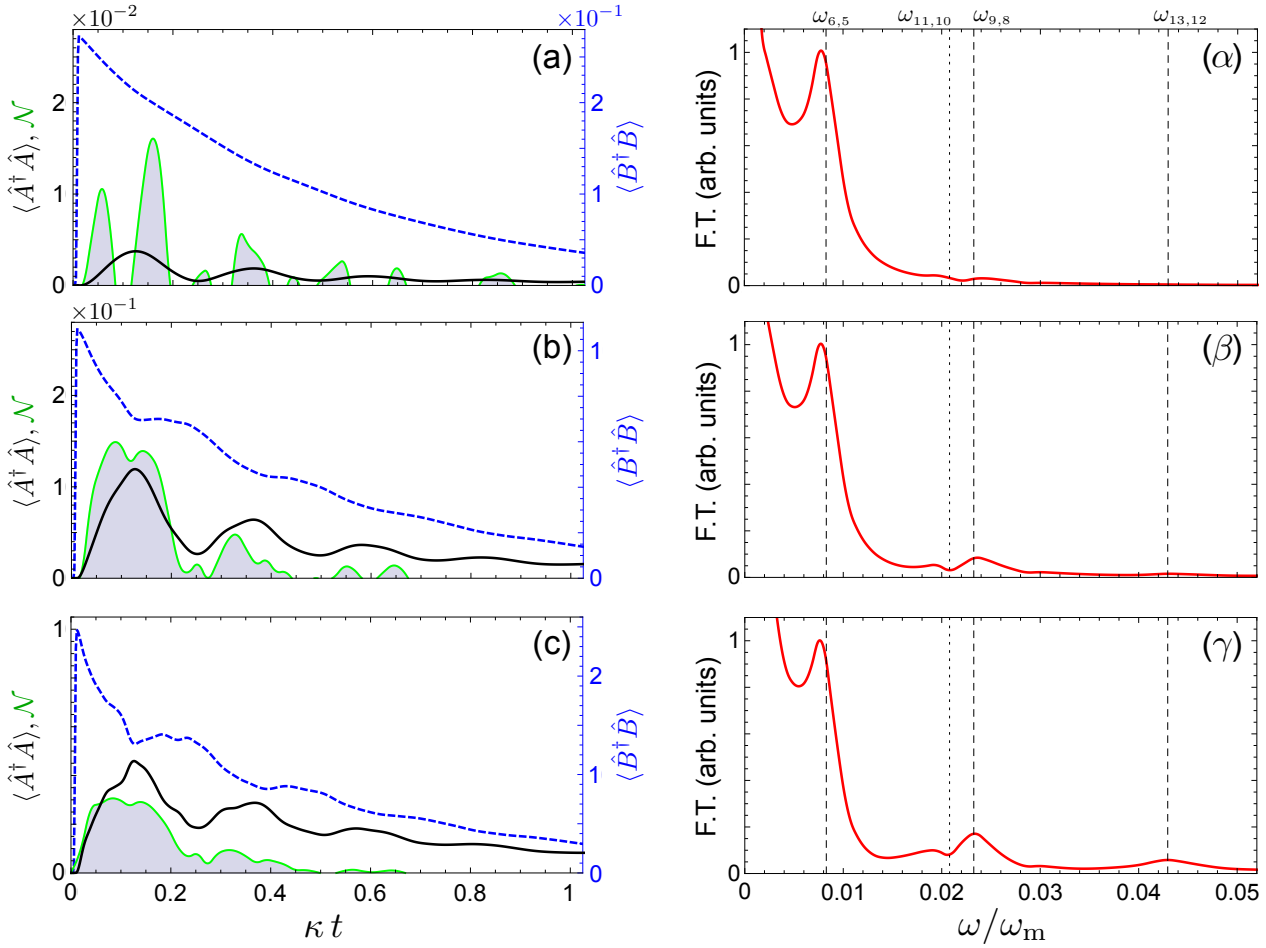

Figure 5. System dynamics after the pulse arrival, obtained for pulses with amplitudes increasing from top to bottom: $\mathcal{A} = \pi/3$ (a), $2\pi/3$ (b), and π (c). Specifically, panels (a-c) display the mean intracavity photon number $\langle \hat{A}^\dagger \hat{A} \rangle$ (black solid curves), the mean phonon number $\langle \hat{B}^\dagger \hat{B} \rangle$ (blue dashed curves), and the negativity $\mathcal{N}$ (green filled curve). Panels (α-γ) display the Fourier transform of the mean photon number shown in the corresponding panel on the left.

arrival and the Fourier transform of the mean photon number, obtained for pulses with amplitudes increasing from top to bottom: $\mathcal{A} = \pi/3, 2\pi/3, \pi$. Figures 5(a)-(c) show (Casimir-Rabi) nutations (superimposed on the exponential decay due to the presence of losses) of the signals $\langle \hat{A}^\dagger \hat{A} \rangle$ (black solid curves) and $\langle \hat{B}^\dagger \hat{B} \rangle$ (blue dashed curves). The mean phonon number displays much less pronounced oscillations which are anticorrelated with the photonic oscillations. When the pulse amplitude is small ($A = \pi/3$), the time evolution of the mean photon number is sinusoidal-like with peak amplitudes decaying exponentially. Initially, the ultrafast kick produces a coherent mechanical state. The lowest Fock state in this mechanical coherent superposition, which is able to resonantly produce photon pairs, is $|0,3\rangle$ (see Fig. 2). This state is coherently coupled to the state $|2,0_2\rangle$ by $\hat{V}_{\rm DCE}$, giving rise to the avoided-crossing states $|\psi_5\rangle$ and $|\psi_6\rangle$ given in Eq. (12). These two levels display a frequency vacuum Casimir-Rabi splitting $2\Omega_{0,3}^{2,0}$, which, as also shown in Fig. 5(α), corresponds to the frequency of the observed Rabi-like oscillations. The small difference between the peak in Fig. 5(α) and $\omega_{6,5} \equiv (E_6 - E_5)/\hbar = 2\Omega_{0,3}^{2,0}$ is due to the presence of the nearby higher peak at $\omega = 0$. For the amplitude $A = \pi/3$, the peak phonon number, reached just after the kick, is significantly below one, and thus the occupation probability for the state $|3\rangle_{\rm m}$ is very low. This explains the weakness of the photonic signal in Fig. 5(a) and the smallness of the oscillations superimposed on the exponential decay in the mechanical signal $\langle \hat{B}^\dagger \hat{B} \rangle$. Indeed, the mechanical states $|1\rangle_{\rm m}$ and $|2\rangle_{\rm m}$ in the initial coherent superposition have a much larger probability than $|3\rangle_{\rm m}$ and evolve unaffected by the vacuum field. Higher energy mechanical states $|k\rangle_{\rm m}$ with $k > 3$ can also produce photon pairs at a rate $\Omega_{0,k}^{2,k-3}$, but their occupation probability is negligible at such a low pulse amplitude. The non-monotonous dy-

namics of the signals indicates that the DCE effect is, at least partially, a reversible process: the emitted photon pairs can be reabsorbed by the moving mirror and then re-emitted, if the effective DCE rates are larger than the losses. However, if one of the photons in the pair is lost, the surviving one-photon state is no longer resonant with the vibrating mirror and undergoes a standard exponential decay. This effect gives rise to a decay of the oscillation amplitude faster than the signal decay.

When increasing the pulse amplitude [Figs. 5(b) and 5(c)], the mean photon number grows significantly and no longer oscillates sinusoidally. In addition, the mechanical signal deviates significantly from the exponential decay, owing to increased population of the mechanical states with phonon number $k \geq 3$ that are able to produce photon pairs.

Figures 5(α) to 5(γ) show the Fourier transforms of the photonic nutation signals. For $A = \pi/3$, besides the intense peak at $\omega = 0$ (describing the exponential decay induced by losses, always superimposed on the nutations), only an additional peak at $\omega \simeq \Omega_{0,3}^{2,0}$ is visible, in full agreement with the sinusoidal signal in Fig. 5(a). Increasing the pulse amplitude, a second peak at higher frequency [Fig. 5(β)], followed by a third at still higher frequency [Fig. 5(γ)] appears. These two additional peaks in the Fourier transform clarify the origin of the non-sinusoidal behaviour of signals in Figs. 5(b) and 5(c). They correspond to the higher-energy processes associated with the effective coupling strengths $\Omega_{0,4}^{2,1}$ and $\Omega_{0,5}^{2,2}$, both larger than $\Omega_{0,3}^{2,0}$. However, these two peak frequencies are slightly larger than the corresponding minimum half-splittings $\Omega_{0,4}^{2,1}$ and $\Omega_{0,5}^{2,2}$. This difference occurs because the ladder of vacuum Casimir-Rabi splittings, occurring at a given cavity frequency when $2\omega_c \simeq 3\omega_m$, is not perfectly vertical (see Fig. 2), owing to energy shifts induced by $\hat{V}_{\rm DCE}$. Hence, if ω_c, as in this case, is tuned to ensure that the minimum level splitting $E_6 - E_5 = 2\hbar\Omega_{0,3}^{2,0}$, the higher-energy split levels will not be at their minimum. The peaks clearly visible in Fig. 5(γ) occur at frequencies $\omega = 0$, $\omega \simeq \omega_{6,5} = 2\Omega_{0,3}^{2,0}$, $\omega \simeq \omega_{9,8} > 2\Omega_{0,4}^{2,1}$, and $\omega \simeq \omega_{13,12} > 2\Omega_{0,5}^{2,2}$. A further structure with a dip is also visible in Figs 5(β) and 5(γ) around $\omega = \omega_{11,10}$. This corresponds to the coherent coupling of the states $|1, 3_1\rangle$ and $|3, 0\rangle$, producing the eigenstates $|\psi_{10}\rangle$ and $|\psi_{11}\rangle$. These states are neither directly excited by the external mechanical pulse which generates zero-photon states, nor by $\hat{V}_{\rm DCE}$, which creates or destroy photon pairs. However, the cavity losses can give rise to the decay $|2, 3_1\rangle \rightarrow |1, 3_1\rangle$. Hence, also the states $|\psi_{10}\rangle$ and $|\psi_{11}\rangle$ can be indirectly involved in the signal dynamics.

Analogous quantum Rabi oscillations, giving rise to discrete Fourier components, have been experimentally observed for circular Rydberg atoms in a high-Q cavity [77]. In this system, however, the different level anticrossings are not affected by different energy shifts.

In cavity QED, the strong-coupling dynamics produces atom-field entanglement [78]. We investigate if this non-

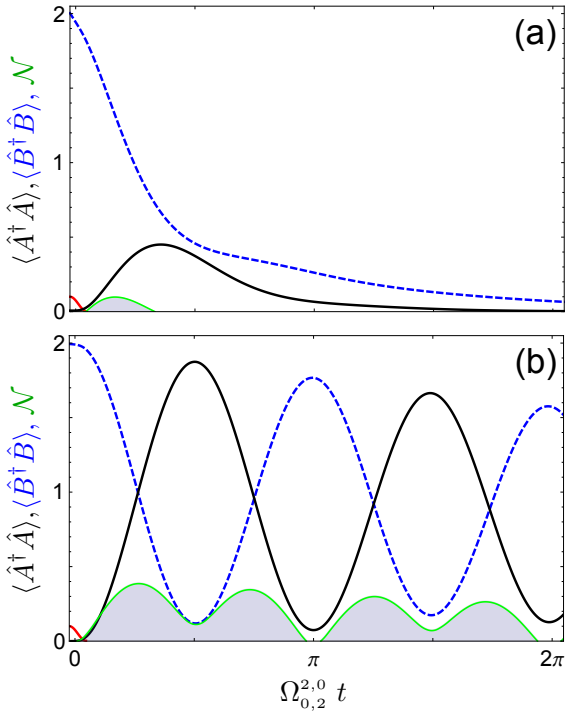

Figure 6. Dynamics starting from a mechanical Fock state. The blue dashed curves decribe the mechanical signal $\langle \hat{B}^\dagger \hat{B} \rangle$, while the black solid curves describe the optical signal $\langle \hat{A}^\dagger \hat{A} \rangle$. The green curves correspond to the negativity $\mathcal{N}$. The cavity frequency is initially detuned from the DCE resonance ($\delta\omega_c = 0.1$), and the system is initially prepared in the state $|0, 2\rangle$. Then the cavity is quickly tuned to the DCE resonance ($\delta\omega_c \rightarrow 0$). The initial detuning $\delta\omega_c$ is displayed as a small red solid curve in the lower left corner of both panels, near $t = 0$. In panel (a), the dynamics is evaluated in the weak-coupling regime. Panel (b) displays the vacuum Casimir-Rabi oscillations that arise when the system loss rates are low. The parameters used are provided in the text.

perturbative regime of the DCE is able to produce entanglement between the mobile-mirror and the cavity field, when the mirror is excited by a coherent pulse and in the presence of mechanical and optical dissipations. The time evolution of the negativity is displayed in Figs. 5(a)-(c). As expected, $\mathcal{N}$ increases noticeably when the pulse amplitude increases, so that the mirror dynamics is significantly affected by the DCE. We observe that, while decaying as a consequence of losses, the negativity displays a non-monotonous behaviour analogous to that observed in cavity-QED [79].

E. Radiative decay of a mechanical excited state

Spontaneous emission is the process in which a quantum emitter, such as a natural or an artificial atom, or a molecule, decays from an excited state to a lower energy state and emits a photon. This cannot be described within the classical electromagnetic theory and is fun-

damentally a quantum process. Here we present numerical calculations showing that a vibrating mirror prepared in an excited state (mechanical Fock state) can spontaneously emit photons like a quantum emitter. In this case, however, instead of a single photon, a photon pair is emitted. Here, instead of considering the coherent excitation of the vibrating mirror as in usual descriptions of the DCE, we assume that it is initially prepared in a Fock state. We consider the case $\omega_{\rm c} \simeq \omega_{\rm m}$ and the system is initialised in the state $|0,2\rangle$, with $\omega_{\rm c}$ sufficiently detuned from the DCE resonance (minimum avoided-level crossing) at $\omega_{\rm c}^0 \simeq \omega_{\rm m}$, with $\delta\omega_{\rm c} \equiv \omega_{\rm c} - \omega_{\rm c}^0 = 0.1\omega_{\rm c}^0$, such that the effective resonant DCE coupling is negligible. This $k = 2$ mechanical Fock state can be prepared, for example, if the vibrating mirror is strongly coupled to an addtional qubit [26], using the same protocols realized in circuit QED [80]. After preparation, the cavity can be quickly tuned into resonance: $\omega_{\rm c} \to \omega_{\rm c}^0$. If the cavity resonator is an LC superconducting circuit, its resonance frequency can be tuned by using a SQUID. In order to not affect the mechanical Fock state during this non-adiabatic process, the tuning time must be shorter than $2\pi/\Omega_{0,2}^{2,0}$.

Figure 6 displays the mean phonon number $\langle \hat{B}^\dagger \hat{B}\rangle$ (dashed blue curve), the mean intracvity photon number $\langle \hat{A}^\dagger \hat{A}\rangle$ (black solid curve), and the negativity (green filled curve) calculated for $g/\omega_{\rm m} = 0.1$. Figure 6 also displays the initial detuning $\delta\omega_{\rm c}$ (red solid curve). Figure 6(a), obtained using $\gamma = \Omega_{0,2}^{2,0}/5$ and $\kappa = 2.5\gamma$, describes the irreversible mechanical decay due to both non-radiative (induced by the mechanical loss rate γ) and radiative decay (induced by $\hat{V}_{\rm DCE}$). The radiative decay gives rise to non-negligible light emission (black solid curve), and to transient mirror-field entanglement. Figure 6(b), obtained using the lower loss rates $\gamma = \kappa = \Omega_{0,2}^{2,0}/80$, shows vacuum Casimir-Rabi oscillations. In this case, a photon pair can be produced at $t = \pi/(2\Omega_{0,2}^{2,0})$ with probability close to one.

F. Analog non-perturbative DCE in all-optical systems

The non-perturbative description of the DCE in optomechanical systems, presented here, can also be applied to other all-optical quantum systems such as parametric amplifiers [8, 81]. Specifically, we consider systems operating as spontaneous parametric down-converters. A degenerate parametric amplifier can be described by the interaction Hamiltonian (see, e.g, [82])

$$\hat{V}_{\rm DPA} = \lambda \hat{\Phi}_{\rm p} \hat{\Phi}_{\rm s}^2 \,, \tag{15}$$

where the pump (p) and signal (s) field coordinates can be expressed in terms of bosonic annihilation and creation operators: $\hat{\Phi}_{\rm p} = \Phi_{\rm p}^{\rm ZPF}(\hat{b} + \hat{b}^\dagger)$, $\Phi_{\rm s} = \Phi_{\rm s}^{\rm ZPF}(\hat{a} + \hat{a}^\dagger)$, and where $\Phi_j^{\rm ZPF}$ $(j = s, p)$ is the zero-point-fluctuation amplitude of the field $\hat{\Phi}_j$. In most cases, when the system is used as a parametric amplifier or as a spontaneous down-converter, the pump mode is quite strongly driven at frequency $\omega_{\rm p}$, and thus it can be considered as a classical pump field of amplitude p, leading to the quadratic Hamiltonian

$$\hat{V}_{\rm DPA} = \hbar\lambda\Phi_{\rm p}^{\rm ZPF}(p e^{-i\omega_{\rm p}t} + p^* e^{i\omega_{\rm p}t})\hat{\Phi}_{\rm s}^2 \,. \tag{16}$$

This Hamiltonian (usually further simplified discarding rapidly oscillating terms) describes many parametric processes (see, e.g., [81]), including the resonant spontaneous parametric down-conversion when $\omega_{\rm p} = 2\omega_{\rm s}$. However, if the pump field is weak or if the pump mode is prepared in a nonclassical state, and/or the coupling strength is sufficiently strong, this approximation fails, and the full quantum Hamiltonian (15) has to be considered. Using the bosonic operators, the resulting interaction Hamiltonian reads

$$\hat{V}_{\rm NDPA} = \frac{\hbar g}{2}(\hat{b} + \hat{b}^\dagger)(\hat{a} + \hat{a}^\dagger)^2 \,, \tag{17}$$

which is formally identical to the optomechanical interaction in Eq. (2) $[g = 2\lambda\Phi_{\rm p}^{\rm ZPF}(\Phi_{\rm s}^{\rm ZPF})^2]$.

This result shows that the nonperturbative analysis presented in this paper is not confined to optomechanical systems, but can also be applied to parametric amplifiers in the full quantum regime, when the pump field is not replaced by a classical amplitude and the rotating-wave approximation is not applied. According to this analysis, emission processes such as $|n,0\rangle \to |n-q,2\rangle$ are possible even for $q \geq 2$, if $q\omega_{\rm p} \simeq 2\omega_{\rm s}$. Hence, spontaneous vacuum emission is possible even for pump frequencies *lower* than the signal frequency. This is a result which cannot be obtained within the usual approximate quadratic Hamiltonian in Eq. (16).

Since experiments on these all-optical systems can be simpler than experiments in optomechanical systems, they could be used as analog quantum simulators of the non-perturbative MDCE. Just as for the MDCE, significant deviations from the ordinary DCE analysis occur when the coupling strength is not too small compared to the resonance frequencies of the system. This can be difficult to achieve with parametric amplifiers at optical frequencies. However, this regime can be achieved at microwave frequencies, using superconducting quantum circuits. For example, a fully quantum device, described by the Hamiltonian in Eq. (17), could be obtained modifying flux-driven amplifiers [6, 83], so that the SQUID is coupled to an additional resonator (determining the pump mode) instead of being directly driven by an external flux.

Analogous nonperturbative parametric scattering processes, requiring further theoretical analysis, can be obtained by considering non-degenerate parametric amplifiers described by the interaction Hamiltonian

$$\hat{V}_{\rm DP} = \lambda \hat{\Phi}_{\rm p} \hat{\Phi}_{\rm s} \hat{\Phi}_{\rm i} \,, \tag{18}$$

where $\hat{\Phi}_{\rm i}$ is the quantum field describing the additional mode (idler). Such a non-degenerate amplifier at microwave frequencies was first proposed and realized in 2010 [82, 84].

III. CONCLUSIONS

We have analyzed the DCE in cavity optomechanical systems, describing quantum-mechanically both the cavity field and the vibrating mirror, fully including multiple scattering between the two subsystems. The full quantum approach developed here describes the DCE *without* introducing a time-dependent light-matter interaction. The only time-dependent Hamiltonian term considered in this work was the one describing the external drive of the moving mirror. Actually, we can conclude that the DCE can be described even without considering any time-dependent Hamiltonian. Vacuum emission can originate from the free evolution of an initial pure mechanical excited state, in analogy with the spontaneous emission from excited atoms.

Using numerical diagonalization of the optomechanical Hamiltonian [66], including those terms usually neglected for describing current optomechanics experiments [50], we have shown that the resonant generation of photons from the vacuum is determined by a ladder of mirror-field vacuum Rabi-like splittings. These avoided-level crossings describe the energy-conserving conversion of phonons (quanta of mechanical vibration) into photon pairs. More generally, the DCE Hamiltonian in Eq. (5) describes many resonant optomechanical scattering processes $|n, k_n\rangle \leftrightarrow |n+2, (k-q)_{n+2}\rangle$ which occur when the energies of the final and initial states coincide ($2\omega_{\rm c} \sim q\,\omega_{\rm m}$).

The standard resonance condition for the DCE requires a mechanical resonance frequency at least double that of the lowest mode frequency of the cavity. We have shown instead that, when the coupling between the moving mirror and the cavity field is non-negligible compared to the mechanical and optical resonance frequencies, a resonant production of photons out from the vacuum can be observed for mechanical frequencies equal to or lower than the cavity-mode frequencies. Hence, the present analysis demonstrates that optomechanical systems with coupling strengths which experiments already started to approach, and with vibrating mirrors working in the GHz spectral range, can be used to observe light emission from mechanical motion.

We have also analyzed the non-perturbative regime of the DCE, which, we showed, provides direct access to the level structure determining the DCE and can display Rabi-like nutations of the cavity-field and oscillating mirror signals. Finally, we have shown that the oscillating mirror can evolve into a state which is entangled with the radiation emitted by the mirror itself.

Appendix A: DCE Matrix Elements

The matrix elements $\hbar\Omega_{0,k}^{2,k-q} = \langle 0,k|\hat{V}_{\rm DCE}|2,(k-q)_2\rangle$ play a key role in the MDCE, since they determine the rate at which a mechanical Fock state $|k\rangle_{\rm m}$ can generate a photon pair. Figure 7 displays $2\hbar\Omega_{0,k}^{2,k-q} = 2\langle 0,k|\hat{V}_{\rm DCE}|2,(k-q)_2\rangle$ evaluated for $q = 2, 3, 4$, as a function of the initial Fock state k, obtained for $g/\omega_{\rm m} = 0.1$ (upper panels) and 0.01 (lower panels). The two panels on the left, obtained for $q = 2$, correspond to the approximate resonance condition $\omega_{\rm c} \simeq \omega_{\rm m}$. The central panels correspond to $\omega_{\rm c} \simeq 1.5\omega_{\rm m}$, and the panels on the left correspond to $\omega_{\rm c} \simeq 2\omega_{\rm m}$. Going from left to right, the matrix elements decrease. However, as long as they are comparable to the mechanical and photonic decay rates, a mechanical-optical energy exchange (at least partial) can occur, giving rise to the DCE.

The analytically calculated matrix elements (11) displayed in Fig. 7 describe the phonon-photon DCE coherent couplings obtained using first-order perturbation theory. In order to test their accuracy, we compared them to the corresponding vacuum Casimir-Rabi splittings obtained by numerical diagonalization of $\hat{H}_{\rm s}$ in Eq. (3). Specifically, Fig. 8 shows a comparison for $2\Omega_{0,3}^{2,0}$ [panel (a)] and $2\Omega_{0,4}^{2,0}$ [panel (b)], as a function of the normalized optomechanical coupling $g/\omega_{\rm m}$. The agreement is very good for $g/\omega_{\rm m}$ below 0.1.

Appendix B: Master equation

We take into account dissipation and decoherence effects by adopting a master-equation approach. For strongly-coupled hybrid quantum systems, the description offered by the standard quantum-optical master equation breaks down [52, 85]. Following Refs. [51, 52, 70], we express the system-bath interaction Hamiltonian in the basis formed by the energy eigenstates of $\hat{H}_{\rm s}$. By applying the standard Markov approximation and tracing out the reservoir degrees of freedom, we arrive at the master equation for the density-matrix operator $\hat{\rho}(t)$,

$$\begin{aligned}\dot{\hat{\rho}}(t) =& \frac{i}{\hbar}[\hat{\rho}(t), \hat{H}_{\rm s} + \hat{V}_{\rm m}(t)] \\ &+ \kappa\,\mathcal{D}[\hat{A}]\hat{\rho}(t) + \gamma\,\mathcal{D}[\hat{B}]\hat{\rho}(t)\,.\end{aligned} \tag{B1}$$

Here the constants κ and γ correspond to the cavity-field and mirror damping rates. The dressed photon and phonon lowering operators $\hat{O} = \hat{A}, \hat{B}$ are defined in terms of their bare counterparts $\hat{o} = \hat{a}, \hat{b}$ as [86]

$$\hat{O} = \sum_{E_n > E_m} \langle\psi_m|(\hat{o} + \hat{o}^\dagger)|\psi_n\rangle\,|\psi_m\rangle\langle\psi_n|\,, \tag{B2}$$

where $|\psi_n\rangle$ ($n = 0\,,1\,,2\,\ldots$) are the eigenvectors of $\hat{H}_{\rm s}$ and E_n the corresponding eigenvalues. The superopera-

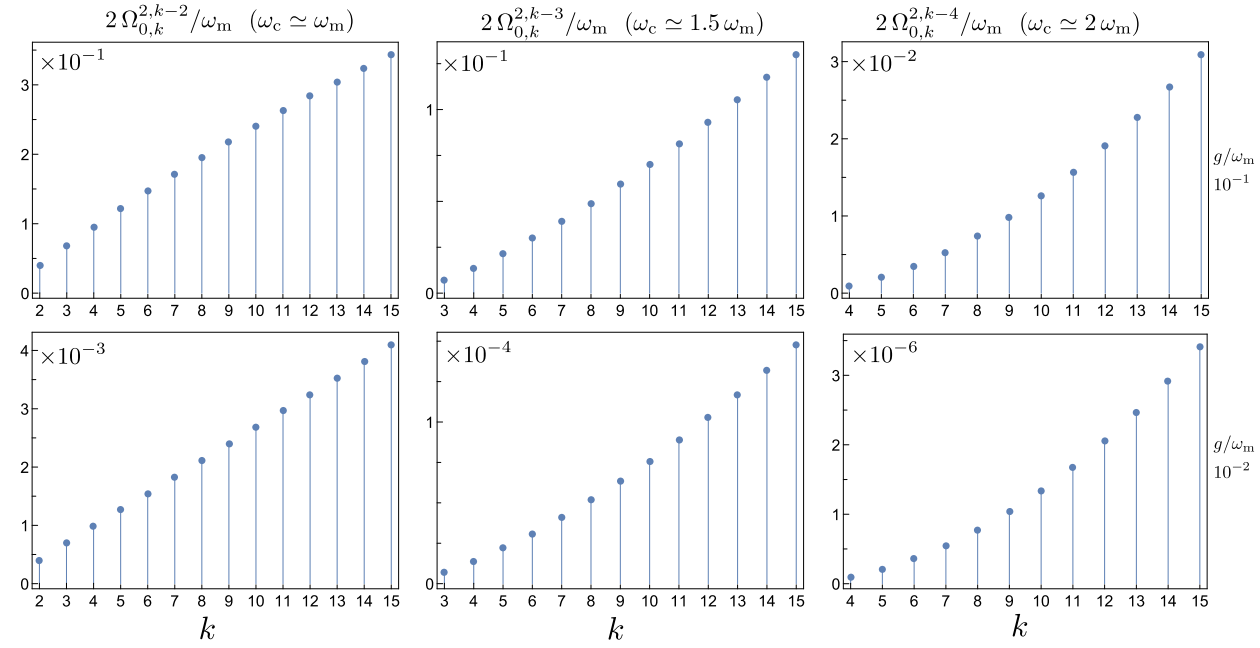

Figure 7. Normalized effective vacuum Rabi splittings $2\Omega_{0,k}^{2,k-q}/\omega_{\rm m}$ of $\hat{V}_{DCE}$ between the eigenstates of $\hat{H}_0+\hat{V}_{\rm om}$, evaluated for $q=2$, 3, 4, as a function of k.

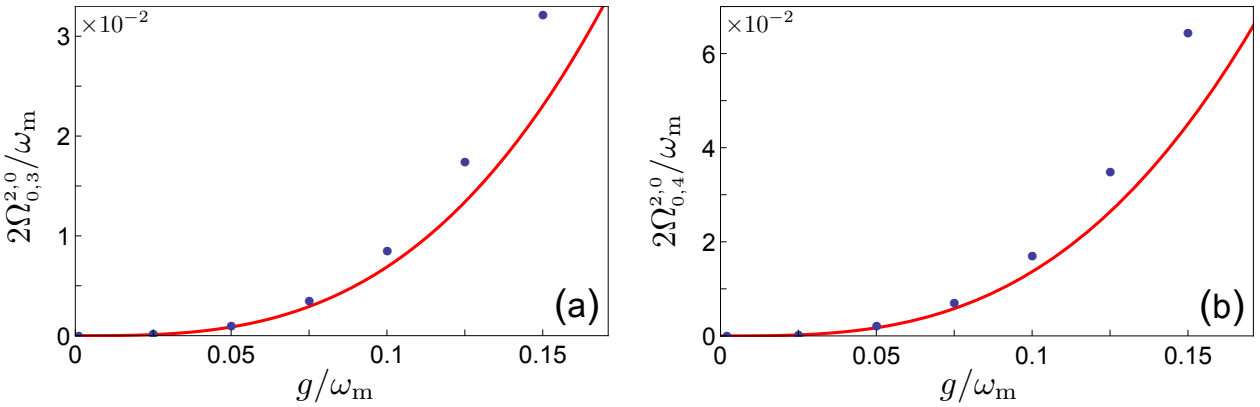

Figure 8. Comparison between the numerically-calculated normalized vacuum Rabi splitting (points) and the corresponding analytical calculations (red solid curve), obtained using first-order perturbation theory for (a) $2\Omega_{0,3}^{2,0}$, and (b) $2\Omega_{0,4}^{2,0}$.

tor $\mathcal{D}$ is defined as

$$\mathcal{D}[\hat{O}]\,\hat{\rho}=\frac{1}{2}(2\hat{O}\,\hat{\rho}\,\hat{O}^{\dagger}-\hat{O}^{\dagger}\hat{O}\,\hat{\rho}-\hat{\rho}\,\hat{O}^{\dagger}\hat{O})\,. \tag{B3}$$

The spectrum and the eigenstates of $\hat{H}_{\rm s}$ are obtained by standard numerical diagonalization in a truncated finite-dimensional Hilbert space. The truncation is realized by only including the lowest-energy $N_{\rm c}$ photonic and $N_{\rm m}$ mechanical Fock states. These truncation numbers are chosen in order to ensure that the lowest $M<N_{\rm c}\times N_{\rm m}$ energy eigenvalues and the corresponding eigenvectors, which are involved in the dynamical processes investigated here, are not significantly affected when increasing $N_{\rm c}$ and $N_{\rm m}$. Then the density matrix in the basis of the system eigenstates is truncated in order to exclude all the higher-energy eigenstates which are not populated during the dynamical evolution. This truncation, of course, depends on the excitation strength $\mathcal{F}(t)$ in Eq. (6). The system of differential equations resulting from the master equation is then solved by using a standard Runge-Kutta method with step control. In this way, the mechanical-optical quantum correlations are taken into account to all significant orders.

In writing the master equation, we have assumed that

the baths are at zero temperature. The generalization to $T \neq 0$ reservoirs can be derived following Ref. [52]. Note that the photonic and mechanical lowering operators only involve transitions from higher to lower energy states. If $\hat{V}_{\rm DCE}$ is neglected, $\hat{A} = \hat{a}$ and $\hat{B} = \hat{b} - (g/\omega_{\rm m})\hat{a}^\dagger\hat{a}$. Following Ref. [70], the master equation (B1) has been derived without making the post-trace rotating-wave approximation used in Ref. [85], which is not applicable in the presence of equally spaced (even approximately) energy levels, as in the present case.

Appendix C: Negativity

Negativity is an entanglement monotone and does not increase under local operations and classical communication [87]. Hence, it represents a proper measure of entanglement, although it can be zero even if the state is entangled, for a specific class of entangled states [87]. The negativity of a subsystem A can be defined as the absolute sum of the negative eigenvalues of the partial transpose ρ^{T_A} of the density matrix ρ with respect to a subsystem A: $\mathcal{N}(\rho) = \sum_i (|\lambda_i| - \lambda_i)/2$, where λ_i are the eigenvalues of ρ^{T_A}. In this case, the subsystems A and B are the cavity field and the vibrating mirror, respectively.

[1] J. Schwinger, "On gauge invariance and vacuum polarization," Phys. Rev. **82**, 664–679 (1951).
[2] G. T. Moore, "Quantum theory of the electromagnetic field in a variable-length one-dimensional cavity," J. Math. Phys. **11**, 2679 (1970).
[3] S. W. Hawking, "Black hole explosions," Nature **248**, 30–31 (1974).
[4] J. Schwinger, "Casimir light: the source." PNAS **90**, 2105–2106 (1993).
[5] E. Yablonovitch, "Accelerating reference frame for electromagnetic waves in a rapidly growing plasma: Unruh-Davies-Fulling-DeWitt radiation and the nonadiabatic Casimir effect," Phys. Rev. Lett. **62**, 1742 (1989).
[6] C. M. Wilson, G. Johansson, A. Pourkabirian, M. Simoen, J. R. Johansson, T. Duty, F. Nori, and P. Delsing, "Observation of the dynamical Casimir effect in a superconducting circuit," Nature **479**, 376 (2011).
[7] P. Lähteenmäki, G. S. Paraoanu, J. Hassel, and P. J. Hakonen, "Dynamical Casimir effect in a Josephson metamaterial," Proc. Natl. Acad. Sci. USA **110**, 4234–4238 (2013).
[8] P. D. Nation, J. R. Johansson, M. P. Blencowe, and Franco Nori, "Colloquium: Stimulating uncertainty: Amplifying the quantum vacuum with superconducting circuits," Rev. Mod. Phys. **84**, 1–24 (2012).
[9] S. W. Hawking, "Particle creation by black holes," Commun. Math. Phys. **43**, 199–220 (1975).
[10] W. G. Unruh, "Notes on black-hole evaporation," Phys. Rev. D **14**, 870–892 (1976).
[11] S. A. Fulling and P. C. W. Davies, "Radiation from a moving mirror in two dimensional space-time: conformal anomaly," in *Proc. R. Soc. Lond. A Math. Phys. Sci.*, Vol. 348 (The Royal Society, 1976) pp. 393–414.
[12] V. V. Dodonov, "Current status of the dynamical Casimir effect," Phys. Scr. **82**, 038105 (2010).
[13] E. Sassaroli, Y. N. Srivastava, and A. Widom, "Photon production by the dynamical Casimir effect," Phys. Rev. A **50**, 1027–1034 (1994).
[14] A. Lambrecht, M.-T. Jaekel, and S. Reynaud, "Motion induced radiation from a vibrating cavity," Phys. Rev. Lett. **77**, 615–618 (1996).
[15] V. V. Dodonov and A. B. Klimov, "Generation and detection of photons in a cavity with a resonantly oscillating boundary," Phys. Rev. A **53**, 2664–2682 (1996).
[16] G. Schaller, R. Schützhold, G. Plunien, and G. Soff, "Dynamical Casimir effect in a leaky cavity at finite temperature," Phys. Rev. A **66**, 023812 (2002).
[17] W.-J. Kim, J. H. Brownell, and R. Onofrio, "Detectability of dissipative motion in quantum vacuum via superradiance," Phys. Rev. Lett. **96**, 200402 (2006).
[18] Yu. E. Lozovik, V. G. Tsvetus, and E. A. Vinogradov, "Femtosecond parametric excitation of electromagnetic field in a cavity," JETP Lett. **61**, 723 (1995).
[19] M. Uhlmann, G. Plunien, R. Schützhold, and G. Soff, "Resonant cavity photon creation via the dynamical Casimir effect," Phys. Rev. Lett. **93**, 193601 (2004).
[20] M. Crocce, D. A. R. Dalvit, F. C. Lombardo, and F. D. Mazzitelli, "Model for resonant photon creation in a cavity with time-dependent conductivity," Phys. Rev. A **70**, 033811 (2004).
[21] C. Braggio, G. Bressi, G. Carugno, C. Del Noce, G. Galeazzi, A. Lombardi, A. Palmieri, G. Ruoso, and D. Zanello, "A novel experimental approach for the detection of the dynamical Casimir effect," EPL **70**, 754 (2005).
[22] E. Segev, B. Abdo, O. Shtempluck, E. Buks, and B. Yurke, "Prospects of employing superconducting stripline resonators for studying the dynamical Casimir effect experimentally," Phys. Lett. A **370**, 202 – 206 (2007).
[23] S. De Liberato, C. Ciuti, and I. Carusotto, "Quantum Vacuum Radiation Spectra from a Semiconductor Microcavity with a Time-Modulated Vacuum Rabi Frequency," Phys. Rev. Lett. **98**, 103602 (2007).
[24] J. R. Johansson, G. Johansson, C. M. Wilson, and F. Nori, "Dynamical Casimir effect in a superconducting coplanar waveguide," Phys. Rev. Lett. **103**, 147003 (2009).
[25] J. R. Johansson, G. Johansson, C. M. Wilson, and F. Nori, "Dynamical Casimir effect in superconducting microwave circuits," Phys. Rev. A **82**, 52509 (2010).
[26] A. D. O'Connell, M. Hofheinz, M. Ansmann, R. C. Bialczak, M. Lenander, E. Lucero, M. Neeley, D. Sank,

H. Wang, M. Weides, *et al.*, "Quantum ground state and single-phonon control of a mechanical resonator," Nature **464**, 697–703 (2010).
[27] S. De Liberato, D. Gerace, I. Carusotto, and C. Ciuti, "Extracavity quantum vacuum radiation from a single qubit," Phys. Rev. A **80**, 053810 (2009).
[28] L. Garziano, A. Ridolfo, R. Stassi, O. Di Stefano, and S. Savasta, "Switching on and off of ultrastrong light-matter interaction: Photon statistics of quantum vacuum radiation," Phys. Rev. A **88**, 063829 (2013).
[29] L. Garziano, R. Stassi, A. Ridolfo, O. Di Stefano, and S. Savasta, "Vacuum-induced symmetry breaking in a superconducting quantum circuit," Phys. Rev. A **90**, 043817 (2014).
[30] D. Hagenmüller, "All-optical dynamical Casimir effect in a three-dimensional terahertz photonic band gap," Phys. Rev. B **93**, 235309 (2016).
[31] O. Di Stefano, R. Stassi, L. Garziano, A. F. Kockum, S. Savasta, and F. Nori, "Feynman-diagrams approach to the quantum rabi model for ultrastrong cavity qed: stimulated emission and reabsorption of virtual particles dressing a physical excitation," New J. Phys. **19**, 053010 (2017).
[32] M. Cirio, K. Debnath, N. Lambert, and F. Nori, "Amplified optomechanical transduction of virtual radiation pressure," Phys. Rev. Lett. **119**, 053601 (2017).
[33] S. De Liberato, "Impact of losses and detuning on quantum vacuum emission," arXiv preprint arXiv:1609.04249 (2016).
[34] J.Q. You and F. Nori, "Superconducting circuits and quantum information," Physics today **58**, 42–47 (2005).
[35] J. Q. You and F. Nori, "Atomic physics and quantum optics using superconducting circuits," Nature **474**, 589–597 (2011).
[36] Z.-L. Xiang, S. Ashhab, J. Q. You, and F. Nori, "Hybrid quantum circuits: Superconducting circuits interacting with other quantum systems," Rev. Mod. Phys. **85**, 623 (2013).
[37] X. Gu, A. F. Kockum, A. Miranowicz, Y-x. Liu, and F. Nori, "Microwave photonics with superconducting quantum circuits," arXiv preprint arXiv:1707.02046 (2017).
[38] W. H. Louisell, A. Yariv, and A. E. Siegman, "Quantum fluctuations and noise in parametric processes. I." Phys. Rev. **124**, 1646–1654 (1961).
[39] S. E. Harris, M. K. Oshman, and R. L. Byer, "Observation of tunable optical parametric fluorescence," Phys. Rev. Lett. **18**, 732–734 (1967).
[40] P. D. Noerdlinger, "Boundary conditions for moving magnetic fields and lorentz transformation of surface currents," Am. J. Phys **39**, 191–192 (1971).
[41] M. Kira, W. Hoyer, and S. W. Koch, "Terahertz signatures of the exciton formation dynamics in non-resonantly excited semiconductors," Solid State Commun. **129**, 733–736 (2004).
[42] G. Plunien, R. Schützhold, and G. Soff, "Dynamical Casimir effect at finite temperature," Phys. Rev. Lett. **84**, 1882–1885 (2000).
[43] J. Haro and E. Elizalde, "Hamiltonian approach to the dynamical Casimir effect," Phys. Rev. Lett. **97**, 130401 (2006).
[44] V. V. Dodonov, "Dynamical Casimir effect in a nondegenerate cavity with losses and detuning," Phys. Rev. A **58**, 4147–4152 (1998).
[45] M.-T. Jaekel and S. Reynaud, "Quantum fluctuations of position of a mirror in vacuum," J. Phys. I **3**, 1–20 (1993).
[46] P. A. Maia Neto and S. Reynaud, "Dissipative force on a sphere moving in vacuum," Phys. Rev. A **47**, 1639–1646 (1993).
[47] M. Kardar and R. Golestanian, "The "friction" of vacuum, and other fluctuation-induced forces," Rev. Mod. Phys. **71**, 1233–1245 (1999).
[48] M. F. Maghrebi, R. Golestanian, and M. Kardar, "Scattering approach to the dynamical Casimir effect," Phys. Rev. D **87**, 025016 (2013).
[49] D. A. R. Dalvit and P. A. Maia Neto, "Decoherence via the dynamical Casimir effect," Phys. Rev. Lett. **84**, 798–801 (2000).
[50] M. Aspelmeyer, T. J. Kippenberg, and F. Marquardt, "Cavity optomechanics," Rev. Mod. Phys. **86**, 1391–1452 (2014).
[51] H.-P. Breuer and F. Petruccione, *The Theory of Open Quantum Systems* (Oxford University Press, 2002).
[52] D. Hu, S.-Y. Huang, J.-Q. Liao, L. Tian, and H.-S. Goan, "Quantum coherence in ultrastrong optomechanics," Phys. Rev. A **91**, 013812 (2015).
[53] J. D. Teufel, D. Li, M. S. Allman, K. Cicak, A. J. Sirois, J. D. Whittaker, and R. W. Simmonds, "Circuit cavity electromechanics in the strong-coupling regime," Nature **471**, 204–208 (2011).
[54] J. Chan, T. P. M. Alegre, A. H. Safavi-Naeini, J. T. Hill, A. Krause, S. Gröblacher, M. Aspelmeyer, and O. Painter, "Laser cooling of a nanomechanical oscillator into its quantum ground state," Nature **478**, 89–92 (2011).
[55] A. J. Rimberg, M. P. Blencowe, A. D. Armour, and P. D. Nation, "A cavity-Cooper pair transistor scheme for investigating quantum optomechanics in the ultra-strong coupling regime," New J. Phys. **16**, 055008 (2014).
[56] T. T. Heikkilä, F. Massel, J. Tuorila, R. Khan, and M. A. Sillanpää, "Enhancing optomechanical coupling via the Josephson effect," Phys. Rev. Lett. **112**, 203603 (2014).
[57] J.-M. Pirkkalainen, S. U. Cho, F. Massel, J. Tuorila, T. T. Heikkilä, P. J. Hakonen, and M. A. Sillanpää, "Cavity optomechanics mediated by a quantum two-level system," Nat. Commun. **6** (2015).
[58] P. D. Nation, J. Suh, and M. P. Blencowe, "Ultrastrong optomechanics incorporating the dynamical Casimir effect," Phys. Rev. A **93**, 022510 (2016).
[59] F. Rouxinol, Y. Hao, F. Brito, A. O. Caldeira, E. K. Irish, and M. D. LaHaye, "Measurements of nanoresonator-qubit interactions in a hybrid quantum electromechanical system," Nanotechnology **27**, 364003 (2016).
[60] J.-Q. Liao, K. Jacobs, F. Nori, and R. W. Simmonds, "Modulated electromechanics: large enhancements of nonlinearities," New J. Phys. **16**, 072001 (2014).
[61] A. Nunnenkamp, K. Børkje, and S. M. Girvin, "Single-photon optomechanics," Phys. Rev. Lett. **107**, 063602 (2011).
[62] L. Garziano, R. Stassi, V. Macrí, S. Savasta, and O. Di Stefano, "Single-step arbitrary control of mechanical quantum states in ultrastrong optomechanics," Phys. Rev. A **91**, 023809 (2015).
[63] K. Stannigel, P. Komar, S. J. M. Habraken, S. D. Bennett, M. D. Lukin, P. Zoller, and P. Rabl, "Optomechanical quantum information processing with photons and phonons," Phys. Rev. Lett. **109**, 013603 (2012).

[64] V. Macrí, L. Garziano, A. Ridolfo, O. Di Stefano, and S. Savasta, "Deterministic synthesis of mechanical NOON states in ultrastrong optomechanics," Phys. Rev. A **94**, 013817 (2016).

[65] B. E. Ordaz-Mendoza and S. F. Yelin, "A novel regime for the dynamical Casimir effect," arXiv preprint arXiv:1612.02525 (2016).

[66] C. K. Law, "Interaction between a moving mirror and radiation pressure: A hamiltonian formulation," Phys. Rev. A **51**, 2537–2541 (1995).

[67] S. Butera and R. Passante, "Field fluctuations in a one-dimensional cavity with a mobile wall," Phys Rev Lett **111**, 060403 (2013).

[68] S. Haroche, "Nobel Lecture: Controlling photons in a box and exploring the quantum to classical boundary," Rev. Mod. Phys. **85**, 1083 (2013).

[69] T. Niemczyk, F. Deppe, H. Huebl, E. P. Menzel, F. Hocke, M. J. Schwarz, J. J. Garcia-Ripoll, D. Zueco, T. Hümmer, E. Solano, A. Marx, and R. Gross, "Circuit quantum electrodynamics in the ultrastrong-coupling regime," Nat. Phys. **6**, 772 (2010).

[70] K. W. Ma and C. K. Law, "Three-photon resonance and adiabatic passage in the large-detuning Rabi model," Phys. Rev. A **92**, 023842 (2015).

[71] L. Garziano, R. Stassi, V. Macrì, A. F. Kockum, S. Savasta, and F. Nori, "Multiphoton quantum Rabi oscillations in ultrastrong cavity QED," Phys. Rev. A **92**, 063830 (2015).

[72] L. Garziano, R. Stassi, V. Macrì, O. Di Stefano, F. Nori, and S. Savasta, "One photon can simultaneously excite two or more atoms," Phys. Rev. Lett. **117**, 043601 (2016).

[73] A. F. Kockum, A. Miranowicz, V. Macrì, S. Savasta, and F. Nori, "Deterministic quantum nonlinear optics with single atoms and virtual photons," Phys. Rev. A **95**, 063849 (2017).

[74] R. Stassi, V. Macrì, A. F. Kockum, O. Di Stefano, A. Miranowicz, S. Savasta, and F. Nori, "Quantum nonlinear optics without photons," Phys. Rev. A **96**, 023818 (2017).

[75] A. Megrant, C. Neill, R. B., B. Chiaro, Y. Chen, L. Feigl, J. Kelly, E. Lucero, M. Mariantoni, P. J. J. O'Malley, *et al.*, "Planar superconducting resonators with internal quality factors above one million," Appl. Phys. Lett. **100**, 113510 (2012).

[76] J. R. Johansson, G. Johansson, C. M. Wilson, P. Delsing, and F. Nori, "Nonclassical microwave radiation from the dynamical Casimir effect," Phys. Rev. A **87**, 043804 (2013).

[77] M. Brune, F. Schmidt-Kaler, A. Maali, J. Dreyer, E. Hagley, J. M. Raimond, and S. Haroche, "Quantum Rabi oscillation: A direct test of field quantization in a cavity," Phys. Rev. Lett. **76**, 1800–1803 (1996).

[78] J. M. Raimond, M. Brune, and S. Haroche, "Manipulating quantum entanglement with atoms and photons in a cavity," Rev. Mod. Phys. **73**, 565–582 (2001).

[79] B. Bellomo, R. Lo Franco, and G. Compagno, "Non-Markovian effects on the dynamics of entanglement," Phys. Rev. Lett. **99**, 160502 (2007).

[80] M. Hofheinz, H. Wang, M. Ansmann, R. C. Bialczak, E. Lucero, M. Neeley, A. D. O'Connell, D. Sank, J. Wenner, J. M. Martinis, and A. N. Cleland, "Synthesizing arbitrary quantum states in a superconducting resonator," Nature **459**, 546–549 (2009).

[81] L. Mandel and E. Wolf, *Optical coherence and quantum optics* (Cambridge university press, 1995).

[82] N. Bergeal, R. Vijay, V. E. Manucharyan, I. Siddiqi, R. J. Schoelkopf, S. M. Girvin, and M. H. Devoret, "Analog information processing at the quantum limit with a Josephson ring modulator," Nat. Phys. **6**, 296 (2010).

[83] T. Yamamoto, K. Inomata, M. Watanabe, K. Matsuba, T. Miyazaki, W. D. Oliver, Y. Nakamura, and J. S. Tsai, "Flux-driven Josephson parametric amplifier," Appl. Phys. Lett. **93**, 042510 (2008).

[84] N. Bergeal, F. Schackert, M. Metcalfe, R. Vijay, V. E. Manucharyan, L. Frunzio, D. E. Prober, R. J. Schoelkopf, S. M. Girvin, and M. H. Devoret, "Phase preserving amplification near the quantum limit with a Josephson ring modulator," Nature **465**, 64 (2010).

[85] F. Beaudoin, J. M. Gambetta, and A. Blais, "Dissipation and ultrastrong coupling in circuit QED," Phys. Rev. A **84**, 043832 (2011).

[86] A. Ridolfo, M. Leib, S. Savasta, and M. J. Hartmann, "Photon Blockade in the Ultrastrong Coupling Regime," Phys. Rev. Lett. **109**, 193602 (2012).

[87] G. Vidal and R. F. Werner, "Computable measure of entanglement," Phys. Rev. A **65**, 032314 (2002).

Chapter 6

Summary and Outlook

In this thesis, I presented the research activity developed during my Ph.D. program. I have studied several physical processes in cavity QED and cavity optomechanics in the ultrastrong coupling (USC) regime. This light-matter regime signicantly changes the standard scenarios in cavity QED and cavity optomechanics and, can give rise to a great variety of new exciting phenomena, which cannot be observed in the conventional weak and strong coupling regimes. Most of the physical processes studied in this thesis work can be explained and understood in terms of *avoided level crossings* arising from some type of light-matter interaction. Indeed, in quantum systems whose Hamiltonian depends on a variable parameter, two energy levels can cross for some value of this parameter. When the Hamiltonian is perturbed by an interaction which couples the levels, the degeneracy at the crossing is broken and the levels repel. In these cases, the light-matter interaction gives rise to *coherent resonant coupling* between states nearly degenerate, including those which not conserve the number of excitations (if the counter-rotating terms in the interaction Hamiltonian are taken into account).

For instance, anomalous *vacuum Rabi oscillations*, where two or more photons are jointly emitted by the qubit into the resonator and reabsorbed by the qubit in a reversible and coherent process are show in Paper 5.2 in terms of avoided level crossings resulting from the coupling between states with different excitation numbers (due to the presence of counterrotating terms in the system Hamiltonian). Also, in Paper 5.4 we show that an avoided level crossing underlies the process where a *single photon is able to excite two or more atoms at the same time*. Moreover, analogues of a large

number of well-known nonlinear optics phenomena can be realized with one or more two-level atoms coupled to one or more resonator modes. Through higher-order processes, where virtual photons are created and annihilated, an effective deterministic coupling between two states of such a system can be created. In this way, *frequency conversion* and, analogues *higher-harmonic*, *subharmonic-generation* (up and down-conversion), *multiphoton absorption*, *parametric amplification*, *Raman* and *hyper -Raman* scattering, the *Kerr effect*, and other nonlinear processes can be realized (see Paper 5.5,5.6). More generally, it has been shown that the USC regime opens the door to higher-order processes, where virtual photons are created and annihilated, and an effective deterministic coupling between two levels (whose degeneracy at the crossing is broken) of such a system can be created. Indeed, in Paper 5.7 it has been shown a physical process where one excited atom directly transfers its excitation to a pair of spatially separated atoms with probability approaching one, the interaction being mediated by the exchange of *virtual* rather than *real* photons.

The most important work developed during my Ph.D., is the study of the dynamical Casimir effect (DCE), describing quantum mechanically both the cavity field and the oscillating mirror (cavity optomechanics). Actually, within this approach, the DCE effect can be described, at least in principle, without considering any time-dependent Hamiltonian, parametric or perturbative approximations nor dynamics linearization (see Paper 5.8). I have shown that the resonant generation of photons from the vacuum is determined by a ladder of mirror-field vacuum Rabi splittings. We find that, vacuum emission and *Casimir-Rabi* oscillations can even originate from the free evolution of an initial pure mechanical excited state, in analogy with the spontaneous emission from excited atoms. By considering a coherent drive of the mirror and a master equation approach to take into account the losses, we were able to study the DCE from the weak to the ultrastrong limit. Also, we found that a resonant production of *Casimir* photons can be observed for mechanical frequencies lower than the cavity mode frequency, when the coupling strength is not a negligible amount of the mechanical and optical resonance frequencies. Hence, this coupling regime, which experiments are

rapidly approaching, removes one of the major obstacles to the observation of this effect. I hope that the investigations performed in this thesis will stimulate experimental research aiming at verifying these effects.

In conclusion, looking at the recent scientific literature, there is a very fast increase in the interest in studying light-matter interactions in the ultrastrong coupling (USC) regime. I believe that quite soon this interest will spread towards many different hybrid quantum systems. This is a very hot and important area of research, and our results so far have been very well received by the referees of various journals, and are receiving several citations. I am quite confident that future works in this research field, will have a significant impact in the field of interacting quantum systems, and may contribute to the development of novel quantum technologies.

Appendix A

Derivazione of the effective coupling by perturbation theory

Here we analyze, by means of the time-dependent perturbation theory, the *resonant coupling* between two degenerate quantum states (which also could have different numbers of excitation), induced by a constant perturbation. According to first-order time-dependent perturbation theory, for a constant perturbation $V(t) = V$ switched-on at $t = 0$, the resulting transition rate can be expressed as

$$W_{i\to n} = \frac{2\pi}{\hbar}|V_{ni}|^2\,\delta(E_n - E_i)\,, \tag{A.1}$$

where $V_{ni} = \langle n|V|i\rangle$, is the coupling matrix element between the initial and the final state. If this matrix element is zero, by using higher order perturbation theory, it is possible to show that, the resulting transition rate can be expressed as

$$W_{i\to n} = \frac{2\pi}{\hbar}|V^{\text{eff}}_{ni}|^2\,\delta(E_n - E_i)\,, \tag{A.2}$$

where V^{eff}_{ni}, as we will show below, contains a summation over intermediate states and products of matrix elements $V_{jk} = \langle j|V|k\rangle$ associated to virtual transitions. Comparing Eqs. (A.1) and (A.2), V^{eff}_{ni} can be interpreted as the effective coupling matrix element between the states $|i\rangle$ and $|n\rangle$, also known as *avoided level crossing* resonant coupling (see Fig. A.1). In general the Hamiltonian operator can be separated in two parts $H = H_0 + V(t)$: one time-independent H_0 whose we know eigenvalues and eigenstates , one

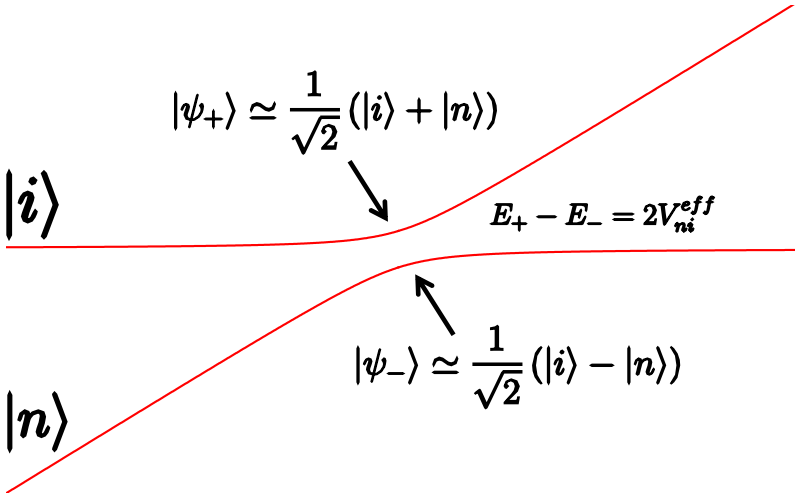

Figure A.1: Schematic picture of an *Avoided level crossing*. $|i\rangle, |n\rangle$ are the eigenstates (*bare* states) of the time-independent part of the total Hamiltonian $H = H_0 + V(t)$. $|\psi_\pm\rangle$ are the eigenstates (*dressed* states) of the of the total Hamiltonian. They are symmetric and anti-symmetric superposition of the *bare* states. Finally, the difference of the eigenvalues of the *bare* states is equals to two times the resonant effective coupling V_{ni}^{eff} between the *bare* states

time-dependent $V(t)$ which is considered small as compared to the stationary part. Let us consider time evolution in the interaction picture:

$$|\Psi(t,t_0)\rangle_I = U_I(t,t_0)\,|\Psi(t)\rangle_S = \sum_n C_n(t)\,|n\rangle\ , \tag{A.3}$$

where $|\Psi(t)\rangle_S$ is a general time-dependent state in the Schrödinger picture and $U_I(t,t_0)$ is the time evolution operator which can be expanded by the Dyson series, ($\hbar = 1$)

$$\begin{aligned} U_I(t,t_0) = 1 - i\int_{t_0}^{t} dt^{'} V_I(t^{'}) + (-i)^2 \int_{t_0}^{t} dt^{'} \int_{t_0}^{t^{'}} dt^{''} V_I(t^{'}) V_I(t^{''}) + ... \\ .. + (-i)^j \int_{t_0}^{t} dt^{'} \int_{t_0}^{t^{'}} dt^{''} ..... \int_{t_0}^{t^{(j-1)}} dt^{(j)} V_I(t^{'}) V_I(t^{''}) ... V_I(t^{(j)}) + ..., \end{aligned} \tag{A.4}$$

If the initial state is an eigenstate $|\Psi(t,0)\rangle_I = |i\rangle$, of H_0, the coefficients of the superposition Eq. (A.3) can be expressed as

$$C_n(t) = \langle n|\, U_I(t,t_0)\,|i\rangle\ . \tag{A.5}$$

Using the Dyson series, it is possible to express the time dependent coefficients as a perturbative expansion:

$$C_n(t) = C_n^{(0)}(t) + C_n^{(1)}(t) + C_n^{(2)}(t) + ...C_n^{(j)}(t) + ... \tag{A.6}$$

comparing Eq. (A.4) with Eq. (A.6) and using the closure relation $j-1$ times, the jth term of the perturbation expansion can be expressed as:

$$\begin{aligned} C_n^{(j)}(t) =& (-i)^j \sum_{\underbrace{m,l,..,k}_{j-1}} \int_{t_0}^{t} dt^{'} \int_{t_0}^{t^{'}} dt^{''} ..... \int_{t_0}^{t^{(j-1)}} dt^{(j)} \times \\ & \times e^{i\omega_{nm}t} V_{nm}(t^{'}) e^{i\omega_{ml}t} V_{ml}(t^{''}) ..... e^{i\omega_{ki}t} V_{ki}(t^{(j)}) ... \,. \end{aligned} \tag{A.7}$$

The transition probability for $|i\rangle \to |n\rangle$ with $n \neq i$ is obtained by $P_{(i\to n)} = \left| C_n^{(1)}(t) + C_n^{(2)}(t) + ... \right|^2$.

A.1 explicit calculation of the coefficients

Let us consider a constant perturbation which is on at $t = 0$: $V(t) = 0$ for $t < 0$, $V(t) = V$ for $t \geq 0$. If the ket $|n\rangle$ is the final state, we can calculate explicitly the terms of the perturbation expansion up to the desired order, as follows ($E_n - E_i = \omega_{ni}$):

- **Zero order**

$$C_n^{(0)}(t) = \delta_{ni} = 0 \tag{A.8}$$

- **First order**

$$C_n^{(1)}(t) = -iV_{ni} \int_0^t dt' e^{i\omega_{ni}t'} = \frac{1 - e^{i\omega_{ni}t}}{E_n - E_i} V_{ni} \,. \tag{A.9}$$

  For times sufficiently long with respect to the transition frequency ($\omega_{ni}t \gg 1$), the resulting coefficient determines non-zero transition probabilities ($|C_n^{(1)}(t)|^2$) only when $E_n \simeq E_i$.

- **Second order**

$$\begin{aligned} C_n^{(2)}(t) &= (-i)^2 \sum_m V_{nm}V_{mi} \int_0^t dt' e^{i\omega_{nm}t'} \int_0^{t'} dt'' e^{i\omega_{mi}t''} \\ &= i \sum_m \frac{V_{nm}V_{mi}}{\omega_{mi}} \int_0^t dt' e^{i\omega_{nm}t'} \, [e^{i\omega_{mi}t'} - 1] \\ &= i \sum_m \frac{V_{nm}V_{mi}}{\omega_{mi}} \int_0^t dt' [e^{i\omega_{ni}t'} - e^{i\omega_{nm}t'}] \,. \end{aligned} \tag{A.10}$$

  In this case, for times sufficiently long with respect to the transition frequencies, the resulting coefficient determines non-zero transition probabilities ($|C_n^{(2)}(t)|^2$) only when $E_n \simeq E_i$ or $E_n \simeq E_m$. Assuming that level n has an energy which is different from all the intermediate levels m, the second term inside the integral in Eq. (A.10) can be neglected. Thus, the only important contribution arises when $E_n \simeq E_i$ as in first-

order perturbation theory. Equation (A.10) becomes

$$C_n^{(2)}(t) = \frac{1 - e^{i\omega_{ni}t}}{E_n - E_i} \sum_m \frac{V_{nm}V_{mi}}{E_i - E_m}\,. \tag{A.11}$$

- **Third order** In a similar way, we can calculate the third order coefficient as follows:

$$\begin{aligned} C_n^{(3)}(t) &= (-i)^3 \sum_{m,l} V_{nl}V_{lm}V_{mi} \int_{t_0}^{t} dt' e^{i\omega_{nl}t'} \int_{t_0}^{t'} dt'' e^{i\omega_{lm}t''} \int_{t_0}^{t''} dt''' e^{i\omega_{mi}t'''} \\ &= \sum_{m,l} \frac{V_{nl}V_{lm}V_{mi}}{(E_i - E_m)(E_i - E_l)} \int_0^t dt' [e^{i\omega_{ni}t'} + \dots] \\ &\simeq \frac{1 - e^{i\omega_{ni}t}}{E_n - E_i} \sum_{m,l} \frac{V_{nl}V_{lm}V_{mi}}{(E_i - E_m)(E_i - E_l)} \end{aligned} \tag{A.12}$$

  The dots in the second line of Eq. (A.12), describes additional rapidly time-oscillating terms of the kind $e^{i\omega_{nk}t}$, where k indicates a possible intermediate level. Like in the derivation of Eq. (A.11), we can neglect these terms.

This last observation allows us to generalize the calculation of the j-*th* term of the perturbation expansion:

$$C_n^{(j)}(t) = \frac{1 - e^{i\omega_{ni}t}}{E_n - E_i} \sum_{\underbrace{m,l,..,k}_{j-1}} \frac{V_{nl}V_{lm}....V_{ki}}{(E_i - E_k)....(E_i - E_m)(E_i - E_l)} \tag{A.13}$$

The transition probability for $|i\rangle \to |n\rangle$ with $n \neq i$ is:

$$P_{(i\to n)} = \frac{(1 - e^{i\omega_{ni}t})^2}{(E_n - E_i)^2} \left| \sum_j \sum_{\underbrace{m,l,..,k}_{j-1}} \frac{V_{nl}V_{lm}....V_{ki}}{(E_i - E_k)....(E_i - E_m)(E_i - E_l)} \right|^2 \tag{A.14}$$

As $t \to \infty$, in order to evaluate the time dependent term, we can use

$$\lim_{t\to\infty} \frac{(1-e^{i\omega_{ni}t})^2}{(E_n-E_i)^2} = \lim_{t\to\infty} \frac{4}{(E_n-E_i)^2} \sin^2\left[\frac{(E_n-E_i)t}{2}\right] = 2\pi t\, \delta(\Delta E_{n,i})\,. \tag{A.15}$$

Considering the transition probability per unit time and using Eq. (A.15), we obtain the generalized Fermi's golden rule:

$$W_{(i\to n)} = \left| \sum_j \sum_{\underbrace{m,l,..,k}_{j-1}} \frac{2\pi V_{nl}V_{lm}....V_{ki}}{(E_i-E_k)....(E_i-E_m)(E_i-E_l)} \right|^2 \delta(\Delta E_{n,i}) \tag{A.16}$$

As an example we consider the case where the states $|i\rangle$ and $|n\rangle$ are connected at loew order by forth-order perturbation theory. Specifically, we assume that the lowest order coeffficents do not provide contribution. We obtain

$$W_{(i\to n)} = 2\pi \left|V_{ni}^{\text{eff}}\right|^2 \delta(\Delta E_{n,i})\,, \tag{A.17}$$

where

$$V_{ni}^{\text{eff}} = \sum_{m,l,k} \frac{V_{nl}V_{lm}V_{mk}V_{ki}}{(E_i-E_k)(E_i-E_m)(E_i-E_l)}\,. \tag{A.18}$$

Eq. (A.17) has the following physical interpretation. We visualize that the transition due to the fourth-order term takes place in four steps. First, $|i\rangle$ makes an energy nonconserving transition to $|k\rangle$; subsequently, $|k\rangle$ makes an energy nonconserving transition to $|m\rangle$, $|m\rangle$ makes an energy nonconserving transition to $|l\rangle$. Finally, $|l\rangle$ makes an energy nonconserving transition to $|n\rangle$, while between $|n\rangle$ and $|i\rangle$ there is overall energy conservation. Such energy nonconserving transitions are often called virtual transitions. Energy need not be conserved for those virtual transitions into (or from) virtual intermediate states. In contrast, the first-order term V_{ni} is often said to represent a direct energy-conserving "real" transition.

Bibliography

[1] C. Cohen-Tannoudji, B. L. Diu, C. C.-T. Franck, F. L. Bernard Diu, *et al.*, *Quantum mechanics*. 2005.

[2] J. Sakurai, "Modern quantum mechanics," 1995.

[3] P. Goy, J. M. Raimond, M. Gross, and S. Haroche, "Observation of cavity-enhanced single-atom spontaneous emission," *Phys. Rev. Lett.*, vol. 50, pp. 1903–1906, Jun 1983.

[4] W. Jhe, A. Anderson, E. A. Hinds, D. Meschede, L. Moi, and S. Haroche, "Suppression of spontaneous decay at optical frequencies: Test of vacuum-field anisotropy in confined space," *Phys. Rev. Lett.*, vol. 58, pp. 666–669, Feb 1987.

[5] M. Brune, J. M. Raimond, P. Goy, L. Davidovich, and S. Haroche, "Realization of a two-photon maser oscillator," *Phys. Rev. Lett.*, vol. 59, pp. 1899–1902, Oct 1987.

[6] S. Haroche, "Nobel lecture: Controlling photons in a box and exploring the quantum to classical boundary," *Rev. Mod. Phys.*, vol. 85, pp. 1083–1102, Jul 2013.

[7] D. J. Wineland, "Nobel lecture: Superposition, entanglement, and raising schrödinger's cat," *Rev. Mod. Phys.*, vol. 85, pp. 1103–1114, Jul 2013.

[8] D. J. Wineland, R. E. Drullinger, and F. L. Walls, "Radiation-pressure cooling of bound resonant absorbers," *Phys. Rev. Lett.*, vol. 40, pp. 1639–1642, Jun 1978.

[9] J. C. Bergquist, R. G. Hulet, W. M. Itano, and D. J. Wineland, "Observation of quantum jumps in a single atom," *Phys. Rev. Lett.*, vol. 57, pp. 1699–1702, Oct 1986.

[10] C. Monroe, D. M. Meekhof, B. E. King, S. R. Jefferts, W. M. Itano, D. J. Wineland, and P. Gould, "Resolved-sideband raman cooling of a bound atom to the 3d zero-point energy," *Phys. Rev. Lett.*, vol. 75, pp. 4011–4014, Nov 1995.

[11] C. Monroe, D. M. Meekhof, B. E. King, W. M. Itano, and D. J. Wineland, "Demonstration of a fundamental quantum logic gate," *Phys. Rev. Lett.*, vol. 75, pp. 4714–4717, Dec 1995.

[12] A. Blais, R.-S. Huang, A. Wallraff, S. M. Girvin, and R. J. Schoelkopf, "Cavity quantum electrodynamics for superconducting electrical circuits: An architecture for quantum computation," *Phys. Rev. A*, vol. 69, p. 062320, Jun 2004.

[13] A. Wallraff, D. Schuster, A. Blais, L. Frunzio, R.-S. Huang, J. Majer, S. Kumar, S. M. Girvin, and R. J. Schoelkopf, "Strong coupling of a single photon to a superconducting qubit using circuit quantum electrodynamics," *Nature*, vol. 431, p. 162, Jun 2004.

[14] J. You and F. Nori, "Superconducting circuits and quantum information," *Phys. Today*, vol. 58, no. 11, p. 42, 2005.

[15] R. J. Schoelkopf and S. M. Girvin, "Wiring up quantum systems," *Nature*, vol. 451, no. 7179, pp. 664–669, 2008.

[16] J. Clarke and F. Wilhelm, "Superconducting quantum bits," *Nature*, vol. 453, no. 7198, pp. 1031–1042, 2008.

[17] B. Josephson, "Possible new effects in superconductive tunnelling," *Physics Letters*, vol. 1, no. 7, pp. 251 – 253, 1962.

[18] T. Niemczyk, F. Deppe, H. Huebl, E. Menzel, F. Hocke, M. Schwarz, J. García-Ripoll, D. Zueco, T. Hümmer, E. Solano, A. Marx, and

R. Gross, "Circuit quantum electrodynamics in the ultrastrong-coupling regime," *Nature Phys.*, vol. 6, no. 10, pp. 772–776, 2010.

[19] T. Kippenberg and K. Vahala, "Cavity optomechanics: back-action at the mesoscale," *Science*, vol. 321, no. 5893, pp. 1172–1176, 2008.

[20] I. Favero and K. Karrai, "Optomechanics of deformable optical cavities," *Nat. Photonics*, vol. 3, no. 4, pp. 201–205, 2009.

[21] F. Marquardt and S. Girvin, "Optomechanics," *Physics*, vol. 2, p. 40, May 2009.

[22] M. Poot and H. van der Zant, "Mechanical systems in the quantum regime," *Phys. Rep.*, vol. 511, no. 5, pp. 273 – 335, 2012. Mechanical systems in the quantum regime.

[23] M. Aspelmeyer, T. J. Kippenberg, and F. Marquardt, "Cavity optomechanics," *Rev. Mod. Phys.*, vol. 86, pp. 1391–1452, Dec 2014.

[24] O. Arcizet, P. Cohadon, T. Briant, M. Pinard, and A. Heidmann, "Radiation-pressure cooling and optomechanical instability of a micromirror," *Nature*, vol. 444, no. 7115, pp. 71–74, 2006.

[25] A. Schliesser, P. Del'Haye, N. Nooshi, K. J. Vahala, and T. J. Kippenberg, "Radiation pressure cooling of a micromechanical oscillator using dynamical backaction," *Phys. Rev. Lett.*, vol. 97, p. 243905, Dec 2006.

[26] J. Thompson, B. Zwickl, A. Jayich, F. Marquardt, S. Girvin, and J. Harris, "Strong dispersive coupling of a high-finesse cavity to a micromechanical membrane," *Nature*, vol. 452, no. 7183, pp. 72–75, 2008.

[27] G. Anetsberger, O. Arcizet, Q. P. Unterreithmeier, R. Rivière, A. Schliesser, E. M. Weig, J. P. Kotthaus, and T. J. Kippenberg, "Near-field cavity optomechanics with nanomechanical oscillators," *Nature Physics*, vol. 5, no. 12, pp. 909–914, 2009.

[28] M. Eichenfield, R. Camacho, J. Chan, K. Vahala, and O. Painter, "A picogram-and nanometre-scale photonic-crystal optomechanical cavity," *Nature*, vol. 459, no. 7246, pp. 550–555, 2009.

[29] J. R. Johansson, G. Johansson, and F. Nori, "Optomechanical-like coupling between superconducting resonators," *Phys. Rev. A*, vol. 90, p. 053833, Nov 2014.

[30] R. C. Jaklevic, J. Lambe, A. H. Silver, and J. E. Mercereau, "Quantum interference effects in josephson tunneling," *Phys. Rev. Lett.*, vol. 12, pp. 159–160, Feb 1964.

[31] G. T. Moore, "Quantum theory of the electromagnetic field in a variable length one dimensional cavity," *J. Math. Phys.*, no. 2679, p. 11, 1970.

[32] C. Wilson, G. Johansson, A. Pourkabirian, M. Simoen, J. Johansson, T. Duty, F. Nori, and P. Delsing, "Observation of the dynamical casimir effect in a superconducting circuit," *Nature*, vol. 479, no. 7373, pp. 376–379, 2011.

[33] J. R. Johansson, G. Johansson, C. M. Wilson, and F. Nori, "Dynamical casimir effect in a superconducting coplanar waveguide," *Phys. Rev. Lett.*, vol. 103, p. 147003, Sep 2009.

[34] J. R. Johansson, G. Johansson, C. M. Wilson, and F. Nori, "Dynamical casimir effect in superconducting microwave circuits," *Phys. Rev. A*, vol. 82, p. 052509, Nov 2010.

[35] P. D. Nation, J. R. Johansson, M. P. Blencowe, and F. Nori, "Colloquium," *Rev. Mod. Phys.*, vol. 84, pp. 1–24, Jan 2012.

[36] M. Uhlmann, G. Plunien, R. Schützhold, and G. Soff, "Resonant cavity photon creation via the dynamical casimir effect," *Phys. Rev. Lett.*, vol. 93, p. 193601, Nov 2004.

[37] M. Crocce, D. A. R. Dalvit, F. C. Lombardo, and F. D. Mazzitelli, "Model for resonant photon creation in a cavity with time-dependent conductivity," *Phys. Rev. A*, vol. 70, p. 033811, Sep 2004.

[38] S. De Liberato, C. Ciuti, and I. Carusotto, "Quantum vacuum radiation spectra from a semiconductor microcavity with a time-modulated vacuum rabi frequency," *Phys. Rev. Lett.*, vol. 98, p. 103602, Mar 2007.

[39] Z.-L. Xiang, S. Ashhab, J. Q. You, and F. Nori, "Hybrid quantum circuits: Superconducting circuits interacting with other quantum systems," *Rev. Mod. Phys.*, vol. 85, pp. 623–653, Apr 2013.

[40] H. Kimble, "The quantum internet," *Nature*, vol. 453, no. 7198, pp. 1023–1030, 2008.

[41] L. Zhou, H. Dong, Y.-x. Liu, C. P. Sun, and F. Nori, "Quantum supercavity with atomic mirrors," *Phys. Rev. A*, vol. 78, p. 063827, Dec 2008.

[42] E. M. Purcell, "Spontaneous emission probabilities at radio frequencies," in *Confined Electrons and Photons*, pp. 839–839, Springer, 1995.

[43] M. O. Scully and M. S. Zubairy, "Quantum optics," 1999.

[44] S. De Liberato, D. Gerace, I. Carusotto, and C. Ciuti, "Extracavity quantum vacuum radiation from a single qubit," *Phys. Rev. A*, vol. 80, no. 5, p. 053810, 2009.

[45] P. Forn-Díaz, J. Lisenfeld, D. Marcos, J. J. García-Ripoll, E. Solano, C. J. P. M. Harmans, and J. E. Mooij, "Observation of the bloch-siegert shift in a qubit-oscillator system in the ultrastrong coupling regime," *Phys. Rev. Lett.*, vol. 105, p. 237001, Nov 2010.

[46] R. Stassi, A. Ridolfo, O. Di Stefano, M. Hartmann, and S. Savasta, "Spontaneous conversion from virtual to real photons in the ultrastrong-coupling regime," *Phys. Rev. Lett.*, vol. 110, no. 24, p. 243601, 2013.

[47] A. Ridolfo, S. Savasta, and M. Hartmann, "Nonclassical radiation from thermal cavities in the ultrastrong coupling regime," *Phys. Rev. Lett.*, vol. 110, no. 16, p. 163601, 2013.

[48] R. H. Dicke, "Coherence in spontaneous radiation processes," *Phys. Rev.*, vol. 93, pp. 99–110, Jan 1954.

[49] P. A. Lindsay, *Introduction to Quantum Electronics*. London: Pitman, 1975.

[50] S. Kielich, *Molecular Nonlinear Optics*. Moscow: Nauka, 1981.

[51] Y. R. Shen, *The Principles of Nonlinear Optics*. New York: Wiley, 1984.

[52] R. W. Boyd, *Nonlinear Optics*. Amsterdam: Elsevier, 3 ed., 2008.

[53] P. A. Franken, A. E. Hill, C. W. Peters, and G. Weinreich, "Generation of Optical Harmonics," *Physical Review Letters*, vol. 7, p. 118, 1961.

[54] F. V. Bunkin, Y. A. Kravtsov, and G. A. Lyakhov, "Acoustic analogues of nonlinear-optics phenomena," *Soviet Physics Uspekhi*, vol. 29, p. 607, 1986.

[55] M. F. Hamilton and D. T. Blackstock, eds., *Nonlinear Acoustics: Theory and Applications*. New York: Academic Press, 1998.

[56] M. G. Cottam, ed., *Linear and Nonlinear Spin Waves in Magnetic Films and Superlattices*. Singapore: World Scientific, 1994.

[57] G. Lenz, P. Meystre, and E. M. Wright, "Nonlinear atom optics," *Physical Review Letters*, vol. 71, p. 3271, nov 1993.

[58] S. L. Rolston and W. D. Phillips, "Nonlinear and quantum atom optics," *Nature*, vol. 416, p. 219, 2002.

[59] S. Savel'ev, A. L. Rakhmanov, V. A. Yampol'skii, and F. Nori, "Analogues of nonlinear optics using terahertz Josephson plasma waves in layered superconductors," *Nature Physics*, vol. 2, p. 521, 2006.

[60] M. Kauranen and A. V. Zayats, "Nonlinear plasmonics," *Nature Photonics*, vol. 6, p. 737, 2012.

[61] C. K. Law, "Interaction between a moving mirror and radiation pressure: A hamiltonian formulation," *Phys. Rev. A*, vol. 51, pp. 2537–2541, Mar 1995.

[62] A. Baust, E. Hoffmann, M. Haeberlein, M. J. Schwarz, P. Eder, J. Goetz, F. Wulschner, E. Xie, L. Zhong, F. Quijandría, D. Zueco, J.-J. G. Ripoll, L. García-Álvarez, G. Romero, E. Solano, K. G. Fedorov, E. P. Menzel, F. Deppe, A. Marx, and R. Gross, "Ultrastrong coupling in two-resonator circuit qed," *Phys. Rev. B*, vol. 93, p. 214501, Jun 2016.

[63] A. Ridolfo, M. Leib, S. Savasta, and M. J. Hartmann, "Photon blockade in the ultrastrong coupling regime," *Phys. Rev. Lett.*, vol. 109, p. 193602, Nov 2012.

[64] F. Beaudoin, M. Gambetta, J, and A. Blais, "Dissipation and ultrastrong coupling in circuit qed," *Phys. Rev. A*, vol. 84, p. 043832, Oct 2011.

[65] E. Jaynes and F. Cummings, "Comparison of quantum and semiclassical radiation theories with application to the beam maser," *Proceedings of the IEEE*, vol. 51, no. 1, pp. 89–109, 1963.

[66] M. Devoret, S. Girvin, and R. Schoelkopf, "Circuit-qed: How strong can the coupling between a josephson junction atom and a transmission line resonator be?," *Ann. Phys.*, vol. 16, no. 10-11, pp. 767–779, 2007.

[67] J. Bourassa, J. M. Gambetta, A. A. Abdumalikov Jr, O. Astafiev, Y. Nakamura, and A. Blais, "Ultrastrong coupling regime of cavity qed with phase-biased flux qubits," *Phys. Rev. A*, vol. 80, no. 3, p. 032109, 2009.

[68] T. Schwartz, J. Hutchison, C. Genet, and T. Ebbesen, "Reversible switching of ultrastrong light-molecule coupling," *Phys. Rev. Lett.*, vol. 106, no. 19, p. 196405, 2011.

[69] A. A. Anappara, S. De Liberato, A. Tredicucci, C. Ciuti, G. Biasiol, L. Sorba, and F. Beltram, "Light-matter excitations in the ultra-strong coupling regime," *Phys. Rev. B*, vol. 79, p. 201303, 2009.

[70] G. Günter, A. A. Anappara, J. Hees, A. Sell, G. Biasiol, L. Sorba, S. De Liberato, C. Ciuti, A. Tredicucci, A. Leitenstorfer, *et al.*, "Sub-cycle switch-on of ultrastrong light–matter interaction," *Nature*, vol. 458, no. 7235, pp. 178–181, 2009.

[71] G. Scalari, C. Maissen, D. Turčinková, D. Hagenmüller, S. De Liberato, C. Ciuti, C. Reichl, D. Schuh, W. Wegscheider, M. Beck, and J. Faist, "Ultrastrong coupling of the cyclotron transition of a 2D electron gas to a THz metamaterial," *Science*, vol. 335, no. 6074, pp. 1323–1326, 2012.

[72] J. Casanova, G. Romero, I. Lizuain, J. J. García-Ripoll, and E. Solano, "Deep strong coupling regime of the jaynes-cummings model," *Phys. Rev. Lett.*, vol. 105, p. 263603, Dec 2010.

[73] D. Braak, "Integrability of the rabi model," *Phys. Rev. Lett.*, vol. 107, p. 100401, Aug 2011.

[74] J. Huang and C. K. Law, "Photon emission via vacuum-dressed intermediate states under ultrastrong coupling," *Phys. Rev. A*, vol. 89, p. 033827, Mar 2014.

[75] L. Garziano, A. Ridolfo, R. Stassi, O. Di Stefano, and S. Savasta, "Switching on and off of ultrastrong light-matter interaction: Photon statistics of quantum vacuum radiation," *Phys. Rev. A*, vol. 88, p. 063829, Dec 2013.

[76] L. Garziano, R. Stassi, A. Ridolfo, O. Di Stefano, and S. Savasta, "Vacuum-induced symmetry breaking in a superconducting quantum circuit," *Phys. Rev. A*, vol. 90, p. 043817, Oct 2014.

[77] Y. Nakamura, Y. A. Pashkin, and J. Tsai, "Coherent control of macroscopic quantum states in a single-cooper-pair box," *Nature*, vol. 398, no. 6730, p. 786, 1999.

[78] M. H. devoret and J. M. Martinis, "Implementing qubits with superconducting integrated circuits," *Quantum Information Processing*, vol. 3, pp. 163–203, Oct 2004.

[79] O. Astafiev, A. M. Zagoskin, A. A. Abdumalikov, Y. A. Pashkin, T. Yamamoto, K. Inomata, Y. Nakamura, and J. S. Tsai, "Resonance fluorescence of a single artificial atom," *Science*, vol. 327, no. 5967, pp. 840–843, 2010.

[80] L. Frunzio, A. Wallraff, D. Schuster, J. Majer, and R. Schoelkopf, "Fabrication and characterization of superconducting circuit qed devices for quantum computation," *IEEE Transactions on Applied Superconductivity*, vol. 15, pp. 860–863, June 2005.

[81] M. Göppl, A. Fragner, M. Baur, R. Bianchetti, S. Filipp, J. Fink, P. Leek, G. Puebla, L. Steffen, and A. Wallraff, "Coplanar waveguide resonators for circuit quantum electrodynamics," *J. Appl. Phys.*, vol. 104, no. 11, p. 113904, 2008.

[82] J. Q. You and F. Nori, "Quantum information processing with superconducting qubits in a microwave field," *Phys. Rev. B*, vol. 68, p. 064509, Aug 2003.

[83] S. J. Srinivasan, A. J. Hoffman, J. M. Gambetta, and A. A. Houck, "Tunable coupling in circuit quantum electrodynamics using a superconducting charge qubit with a v-shaped energy level diagram," *Phys. Rev. Lett.*, vol. 106, p. 083601, Feb 2011.

[84] J. M. Gambetta, A. A. Houck, and A. Blais, "Superconducting qubit with purcell protection and tunable coupling," *Phys. Rev. Lett.*, vol. 106, p. 030502, Jan 2011.

[85] A. J. Hoffman, S. J. Srinivasan, J. M. Gambetta, and A. A. Houck, "Coherent control of a superconducting qubit with dynamically tunable qubit-cavity coupling," *Phys. Rev. B*, vol. 84, p. 184515, Nov 2011.

[86] J. D. Whittaker, F. C. S. da Silva, M. S. Allman, F. Lecocq, K. Cicak, A. J. Sirois, J. D. Teufel, J. Aumentado, and R. W. Simmonds, "Tunable-cavity qed with phase qubits," *Phys. Rev. B*, vol. 90, p. 024513, Jul 2014.

[87] Y. x. Liu, C.-X.Yang, H.-C. Sun, and X.-B. Wang, "Coexistence of single- and multi-photon processes due to longitudinal couplings between superconducting flux qubits and external fields," *New J. Phys.*, vol. 16, no. 1, p. 015031, 2014.

[88] Y.-J. Zhao and Y.-x. N. F. Liu, Y.-L.and Liu, "Generating nonclassical photon states via longitudinal couplings between superconducting qubits and microwave fields," *Phys. Rev. A*, vol. 91, p. 053820, May 2015.

[89] D. Rugar, R. Budakian, H. Mamin, and B. Chui, "Single spin detection by magnetic resonance force microscopy," *Nature*, vol. 430, no. 6997, pp. 329–332, 2004.

[90] A. Krause, M. Winger, T. Blasius, Q. Lin, and O. Painter, "A high-resolution microchip optomechanical accelerometer," *Nat. Photon.*, vol. 6, no. 11, pp. 768–772, 2012.

[91] S. Bose, K. Jacobs, and P. L. Knight, "Scheme to probe the decoherence of a macroscopic object," *Phys. Rev. A*, vol. 59, pp. 3204–3210, May 1999.

[92] W. Marshall, C. Simon, R. Penrose, and D. Bouwmeester, "Towards quantum superpositions of a mirror," *Phys. Rev. Lett.*, vol. 91, p. 130401, Sep 2003.

[93] B. Pepper, R. Ghobadi, E. Jeffrey, C. Simon, and D. Bouwmeester, "Optomechanical superpositions via nested interferometry," *Phys. Rev. Lett.*, vol. 109, p. 023601, Jul 2012.

[94] M. Hofheinz, H. Wang, M. Ansmann, R. Bialczak, E. Lucero, M. Neeley, A. O'Connell, D. Sank, J. Wenner, J. Martinis, and A. Cleland, "Synthesizing arbitrary quantum states in a superconducting resonator," *Nature*, vol. 459, no. 7246, pp. 546–549, 2009.

[95] M. LaHaye, J. Suh, P. Echternach, K. C. Schwab, and M. L. Roukes, "Nanomechanical measurements of a superconducting qubit," *Nature*, vol. 459, no. 7249, p. 960, 2009.

[96] S. Etaki, M. Poot, I. Mahboob, K. Onomitsu, H. Yamaguchi, and H. Van der Zant, "Motion detection of a micromechanical resonator embedded in a dc squid," *Nat. Phys.*, vol. 4, no. 10, p. 785, 2008.

[97] L. F. Wei, Y.-x. Liu, C. P. Sun, and F. Nori, "Probing tiny motions of nanomechanical resonators: Classical or quantum mechanical?," *Phys. Rev. Lett.*, vol. 97, p. 237201, Dec 2006.

[98] M. Grajcar, S. Ashhab, J. R. Johansson, and F. Nori, "Lower limit on the achievable temperature in resonator-based sideband cooling," *Phys. Rev. B*, vol. 78, p. 035406, Jul 2008.

[99]

[100] A. D. Armour, M. P. Blencowe, and K. C. Schwab, "Entanglement and decoherence of a micromechanical resonator via coupling to a cooper-pair box," *Phys. Rev. Lett.*, vol. 88, p. 148301, Mar 2002.

[101] Y.-x. Liu, L. F. Wei, and F. Nori, "Generation of nonclassical photon states using a superconducting qubit in a microcavity," *EPL (Europhysics Letters)*, vol. 67, no. 6, p. 941, 2004.

[102] X.-W. Xu, H. Wang, J. Zhang, and Y.-x. Liu, "Engineering of nonclassical motional states in optomechanical systems," *Phys. Rev. A*, vol. 88, p. 063819, Dec 2013.

[103] J. Pirkkalainen, S. Cho, J. Li, G. Paraoanu, P. Hakonen, and M. Sillanpää, "Hybrid circuit cavity quantum electrodynamics with a micromechanical resonator," *Nature*, vol. 494, no. 7436, pp. 211–215, 2013.

[104] A. Rimberg, M. Blencowe, A. Armour, and P. Nation, "A cavity-cooper pair transistor scheme for investigating quantum optomechanics in the ultra-strong coupling regime," *New J. Phys.*, vol. 16, no. 5, p. 055008, 2014.

[105] A. Nunnenkamp, K. Børkje, and S. M. Girvin, "Publisher's note: Single-photon optomechanics [phys. rev. lett. 107, 063602 (2011)]," *Phys. Rev. Lett.*, vol. 107, p. 099901, Aug 2011.

[106] M. Castagnino and R. Ferraro, "The radiation from moving mirrors: The creation and absorption of particles," *Ann. Phys.*, vol. 154, no. 1, pp. 1 – 23, 1984.

[107] S. Sarkar, "Photon statistics and moving mirrors," *Journal of the European Optical Society*, vol. 4, no. 6, p. 345, 1992.

[108] G. Barton and C. Eberlein, "On quantum radiation from a moving body with finite refractive index," *Ann. Phys.*, vol. 227, no. 2, pp. 222 – 274, 1993.

[109] G. Plunien, B. Mller, and W. Greiner, "The casimir effect," *Phys. Rep.*, vol. 134, no. 2, pp. 87 – 193, 1986.

[110] P. W. Milonni, R. J. Cook, and M. E. Goggin, "Radiation pressure from the vacuum: Physical interpretation of the casimir force," *Phys. Rev. A*, vol. 38, pp. 1621–1623, Aug 1988.

[111] R. J. Glauber, "The quantum theory of optical coherence," *Phys. Rev.*, vol. 130, pp. 2529–2539, Jun 1963.

[112] P. W. Milonni, D. F. V. James, and H. Fearn, "Photodetection and causality in quantum optics," *Phys. Rev. A*, vol. 52, pp. 1525–1537, Aug 1995.

[113] C. Gardiner and P. Zoller, *Quantum noise*, vol. 56. Springer Science & Business Media, 2004.

[114] D. Walls and G. Milburn, *Quantum optics*. Springer, 2008.

[115] H. Carmichael, *An open systems approach to Quantum Optics*, vol. 18. Springer, 1993.

[116] H.-P. Breuer and F. Petruccione, *The theory of open quantum systems*. Oxford University Press, 2002.

[117] F. Haake, "Statistical treatment of open systems by generalized master equations," in *Springer tracts in modern physics*, pp. 98–168, Springer, 1973.

[118] S.-Y. Hu, D.and Huang, J.-Q. Liao, L. Tian, and H.-S. Goan, "Quantum coherence in ultrastrong optomechanics," *Phys. Rev. A*, vol. 91, p. 013812, Jan 2015.

[119] C. Genes, D. Vitali, P. Tombesi, S. Gigan, and M. Aspelmeyer, "Ground-state cooling of a micromechanical oscillator: Comparing cold damping and cavity-assisted cooling schemes," *Phys. Rev. A*, vol. 77, p. 033804, Mar 2008.

[120] K. W. Ken and C. K. Law, "Three-photon resonance and adiabatic passage in the large-detuning rabi model," *Phys. Rev. A*, vol. 92, p. 023842, Aug 2015.